THÈSE DE DOCTORAT DE L'UNIVERSITÉ PIERRE ET MARIE CURIE

Spécialité: Paléocéanographie

Ecole doctorale des Sciences de l'Environnement d'Ile de France (ED129)

Présentée par Renato SALVATTECI

Variabilité multi-décennale et millénaire de l'intensité de la Zone de Minimum d'Oxygène, de la production exportée et des populations de poissons pélagiques à partir de sédiments marins laminés à Pisco, Pérou, au cours des derniers 25 000 ans.

Multi-decadal to millennial scale variability in Oxygen Minimum Zone intensity, export production and pelagic fish abundances from marine laminated sediments off Pisco, Peru during the last 25 000 years.

Pour obtenir le grade de :
Docteur de l'UNIVERSITÉ PIERRE ET MARIE CURIE

Soutenue le 25 Janvier 2013

Devant le jury composé de :

Damien Cardinal (LOCEAN, UPMC)	Président
Luc Ortlieb (LOCEAN, IRD)	Directeur de thèse
Dimitri Gutierrez (IMARPE, Pérou)	Co-directeur de thèse
Arnaud Bertrand (IRD)	Rapporteur
Franck Bassinot (LSCE)	Rapporteur
Ellen Druffel (UC Irvine, États-Unis)	Examinateur
Philippe Béarez (CNRS, MNHN)	Examinateur

ACKNOWLEDGMENTS

INDEX

RESUME EN FRANÇAIS

1. Introduction

Les Systèmes d'Upwelling de Bord Est (EBUS) des Canaries, de Benguela, de Californie et de Humboldt sont caractérisés par des vents alizés qui provoquent la remontée d'eaux froides riches en nutriments fournissant des conditions adéquates pour le développement d'une production primaire élevée et d'abondantes ressources halieutiques (Carr, 2002; Carr and Kearns, 2003; Chavez et al., 2008; Messié et al., 2009). Le Système du Courant de Humboldt (HCS) situé au large du Pérou et du Chili, est le troisième EBUS en termes de productivité primaire par unité de surface, mais le premier en termes de tonnage des pêches, notamment d'anchois (*Engraulis ringens)* (Chavez et al., 2008; Messié et al., 2009). La variabilité interannuelle de la biomasse d'anchois, aux échelles interannuelle à décennale, provoque des variations importantes des prises (Schwartzlose et al., 1999; Chavez et al., 2003). La variabilité interannuelle est en partie due aux impacts du phénomène El Niño/Oscillation Australe (ENSO) et à l'intensité de la pression de pêche, mais la variabilité décennale reste mal comprise et n'a pas encore été bien expliquée par des mécanismes physiques et biologiques. Comme cela a été observé dans d'autres écosystèmes d'upwelling du monde, la diminution des débarquements d'anchois dans le HCS a été suivie par une augmentation des prises de sardine (*Sardinops sagax sagax*) qui coïncide avec une période d'anomalies océanographiques en face du Pérou (Alheit and Bakun, 2010; Bertrand et al., 2011; Moron et al., en prep.). La compréhension de la variabilité naturelle des abondances relatives de ces deux espèces de poissons pélagiques, à différentes échelles temporelles (décennale à séculaire), est devenue indispensable pour la gestion efficace de ces ressources.

Le système du Courant de Humboldt se caractérise par la présence d'une Zone de Minimum d'Oxygène (ZMO) très proche de la surface et particulièrement étendue qui est le résultat d'une ventilation limitée et d'un fort taux de respiration (Helly and Levin, 2004; Karstensen et al., 2008; Paulmier and Ruiz-Pino, 2009). Cette ZMO intense au large des côtes du Pérou central et notamment face à Pisco (~14 °S) permet la formation et la bonne préservation de sédiments finement laminés sur la marge continentale. Ces conditions qui limitent efficacement la bioturbation induite par les organismes benthiques rendent possible des études paléocéanographiques à très haute résolution temporelle. L'intensité de la ZMO en face du Pérou et du Chili montre une forte variabilité aux échelles interannuelle à millénaire (Sanchez et al,. 2000; Agnihotri et al., 2006 ; 2008; Gutierrez et al., 2009). La présente étude est consacrée aux analyses sédimentologiques permettant de reconstruire l'intensité de la ZMO, la productivité exportée et la variabilité des populations de poissons pélagiques au cours des derniers 25 kyr BP (Before Present = 1950 AD) et aux interprétations proposées pour expliquer ces conditions et leurs variations dans le temps.

2. Méthodologie

Les carottes sédimentaires étudiées dans ce mémoire ont été prélevées sur la marge continentale face à Pisco, dans la zone affectée par la ZMO, à des profondeurs variant entre 200 et 400 m de profondeur, et ont été datées par plusieurs techniques complémentaires. L'établissement d'un cadre chronologie précis de ces enregistrements sédimentaires est compliquée par trois particularités de la région: l'activité sismique récurrente (Dorbath et al., 1990; Tavera et Buforn, 2001; Okal et al., 2006; Okal, 2011) qui provoque des glissement et discordances dans la colonne de sédiments, la fiabilité relative des datations au radiocarbone du fait de variations de l'effet réservoir et de l'impact des fluctuations d'intensité des remontées d'eaux froides et «plus âgées» (Ortlieb et al., 2011), et enfin l'existence de courants de fond susceptibles de balayer localement l'interface eau-sédiment et de causer ainsi la formation de hiatus sédimentaires (Reinhardt et al., 2002). Afin d'obtenir une chronologie la plus fiable possible pour les derniers ~500 ans, nous avons sélectionné parmi la trentaine de carottes disponibles pour cette région 4 carottes extraites par carottier de gravité (diamètre ~8 cm) et 4 autres obtenues par carottier-boîte (20 x 20 cm). Les 4 carottes «boîte» fournissant suffisamment de matériel ont été datées avec des techniques utilisant les radioéléments ^{210}Pb, ^{241}Am et ^{14}C. Les données géochronologiques ont ensuite été intégrées dans une corrélation latérale entre les 8 carottes fondées sur une analyse fine des caractéristiques sédimentologiques de chacune d'elles. Cette étude a conduit à la construction des modèles d'âge et à la détection d'un grand nombre d'anomalies stratigraphiques (hiatus, slumps, etc.). L'important résultat obtenu démontre qu'aucune des carottes prise isolément n'était susceptible de constituer une archive complète et continue des conditions paléocéanographiques du dernier demi-millenaire. Par ailleurs, deux carottes de ~5.3 mètres obtenues par carottier à gravité à une profondeur de 300 et 400 mètres (campagne Galathea III) ont été étudiées pour reconstruire la variabilité d'une série de proxies depuis 25 kyr BP. Dans ces deux carottes une trentaine d'intervalles ont été datés par ^{14}C mesuré dans la matière organique décarbonatée.

La variabilité de l'intensité de la ZMO, la productivité exportée, et les variations des abondances de poissons pélagiques ont été reconstruites à partir de plusieurs proxies géochimiques et de techniques paléontologiques. Les apports terrigènes continentaux, qui dépendent principalement du ruissellement de surface et du transport éolien, ont été reconstruites à partir des teneurs en Aluminium (Al), Titane (Ti) et Fer (Fe), éléments étroitement liés au signal détritique. Les variations de la productivité exportée ont été étudiées à travers les fluctuations de teneur en Carbone Organique Total (COT), carbonates (Ca), silice (Si), ainsi que par l'examen du facteur d'enrichissement de métaux traces tels que le Nickel (Ni) et le Cuivre (Cu). Le degré de préservation de la matière organique a été déduit de l'indice d'hydrogène (HI). Les variations passées des conditions d'oxygénation à l'interface eau/sédiment ont été déduites des fluctuations des facteurs

d'enrichissement de Molybdène (Mo), Rhénium (Re) et Vanadium (Va), métaux fortement associés aux conditions redox. L'intensité de la ZMO a été déduite des variations de teneurs en $\delta^{15}N$ dans la matière organique sédimentaire, laquelle reflète le processus de dénitrification dans la colonne d'eau. Finalement, la variabilité naturelle de la biomasse d'anchois et de sardines (avant le développement de la pêche industrielle) a été reconstruite à partir de l'étude des variations d'abondance des écailles et os de poissons accumulés dans les sédiments marins non perturbés déposés en environnement anoxique (Soutar et Isaacs, 1974; Baumgartner et al., 1992; Field et al., 2009). La dégradation diagénétique des écailles, qui fournit également des informations pertinentes sur l'évolution des conditions du milieu de sédimentation, a été évaluée à partir de plusieurs indices de préservation (Salvatteci et al., 2012). Les variations de composition en métaux traces (Al, Ti, Fe, Ni, Cu, Ca, Mo, Re et V) des sédiments ont été déterminées à partir des analyses ICP-MS (Inductively coupled plasma mass spectrometry), tandis que la variabilité à haute résolution temporelle des teneurs en Al, Ti, Fe, Ca et Si a été reconstruite à partir d'analyses XRF (analyse automatisée de spectrométrie de fluorescence X). Finalement l'identification et la quantification des diverses catégories de restes de poissons ont été faites par observation à la loupe binoculaire.

3. Principaux résultats

La corrélation stratigraphique des structures sédimentaires et des profils de ^{210}Pb et ^{241}Am entre plusieurs carottes confirment que les sédiments de la marge péruvienne présentent des discontinuités fréquentes, causées par des processus d'érosion et des événements de transport latéral (slumps) qui peuvent soit éliminer, soit rajouter des sédiments dans la colonne sédimentaire. Entre ~1550 et 1800 AD, trois slumps ont été observés dans toutes les carottes examinées. Les datations effectuées montrent que les slumps coïncident avec les trois plus forts tremblements de terre et tsunamis historiques survenus dans la région de Pisco, en 1604, 1687 et 1746 AD (Dorbath et al., 1990; Okal et al., 2006). Par ailleurs, la présence de traces de cendres volcaniques, très probablement associées à l'explosion du volcan Huaynaputina en 1600 AD, dans les quatre carotte 4 carottes « boîte » analysées, constitue un marqueur chronologique précieux qui confirme les interprétations chronologiques proposées. La continuité latérale observée entre lamines des diverses carottes indique sans ambigüité que c'est un processus régional qui détermine la formation de ces lamines. Cette analyse détaillée démontre la complexité des reconstructions paléocéanographiques à partir de carottes sédimentaire de la marge continentale du Pérou et met clairement en évidence les précautions qui doivent être prises en matière d'interprétations paléo-climatiques à haute résolution.

La concentration de matériel détritique provenant du continent, l'intensité de la ZMO, la productivité exportée et les conditions redox à l'interface eau – sédiment présentent une grande variabilité au cours des derniers 25 kyr. Une augmentation de la productivité exportée et des

conditions anoxiques dans les sédiments est mise en évidence depuis ~8 kyr BP. Le début de la Dernière Période Glaciaire (25.5 – 23 kyr BP) et le Dernier Maximum Glaciaire (23 – 19 kyr BP) se caractérisent par une grande quantité de matériel détritique, une ZMO faible, une productivité exportée limitée, des conditions suboxiques au sein du sédiment et une mauvaise préservation de la matière organique. Le période entre 18 et 14.7 kyr BP qui contient l'épisode Heinrich 1, est caractérisé par une forte variabilité multiséculaire des teneurs en matériel détritique, une rapide et importante augmentation de la dénitrification de la colonne d'eau (induite par des processus lointains), une légère augmentation de la productivité exportée, une bonne préservation de carbonates, une haute concentration de silice biogénique, et des conditions anoxiques dans les sédiments. L'Holocène Inférieur (10.7 – 8 kyr BP) est caractérisé par une forte diminution de matériel détritique, une forte ZMO, une productivité exportée plus élevée que pendant le début du Dernier Glaciaire, le Dernier Maximum Glaciaire et l'épisode Heinrich 1, et des conditions anoxiques dans les sédiments. L'Holocène Moyen (8 – 4 kyr BP) est caractérisé par une ZMO moins forte que pendant le début du Dernier Glaciaire, de conditions généralement suboxiques dans les sédiments et une productivité exportée comparable à celle du début de l'Holocène. L'Holocène Supérieur (4 – 0 kyr BP) est caractérisé par une très forte variabilité multiséculaire de tous les proxies. La productivité exportée, les conditions redox dans les sédiments et la dénitrification dans la colonne d'eau montrent une étroite relation. La ZMO faible, les conditions suboxiques dans les sédiments et la faible productivité exportée pendant le Petit Age de la Glace (1500 - 1850 AD) est comparable aux conditions reconstituées pendant le début du Dernier Glaciaire et le Dernier Maximum Glaciaire. En revanche, l'Anomalie Chaude Médiévale (900 - 1350 AD) montre dans sa phase terminale (1130 – 1350 AD) une ZMO forte, une forte productivité et des conditions anoxiques dans les sédiments. Enfin, les derniers 100 ans sont caractérisés par une forte diminution des apports continentaux, une forte ZMO, une productivité exportée élevée, des conditions fortement anoxiques dans les sédiments et une excellente préservation de la matière organique.

Les vertèbres d'anchois, plus résistantes à la dégradation que les écailles, montrent une augmentation depuis l'Holocène Inférieur, ce qui est concordant avec l'augmentation de la productivité exportée et les conditions redox dans les sédiments. Les écailles et vertèbres de toutes les espèces de poissons pélagiques sont peu abondantes pendant le Dernière Période Glaciaire et le Dernier Maximum Glaciaire, et les écailles montrent une forte dégradation associée à une ZMO faible. Le période entre 18 et 14.7 kyr BP qui contient l'épisode Heinrich 1est caractérisé par une forte abondance d'écailles d'anchois, très peu de vertèbres, la présence de quelques écailles d'espèces océaniques, une très bonne préservation des écailles et une ZMO forte, ce qui indique une faible abondance d'anchois mais légèrement supérieure à celle du début de dernier Glaciaire et du Dernier Maximum Glaciaire. L'Holocène montre une préservation très variable des écailles et une tendance à l'augmentation de l'abondance des anchois. La première phase de l'Holocène Inférieur (épisode

chaud dans l'hémisphère nord) est caractérisée par une forte abondance des écailles et vertèbres d'anchois et des espèces océaniques dont les sardines. L'Holocène Moyen montre une variable préservation des écailles, et des conditions favorables pour les anchois et les espèces océaniques. L'Holocène Supérieur montre une abondance très variable des vertèbres d'anchois et autres espèces, associée à la variabilité de la productivité exportée. Les derniers 1 800 ans sont caractérisés par une alternance de périodes chaudes et froides. Les périodes froides (Dark Ages Cold Period et Petit Age Glaciaire) sont caractérisées par une faible abondance d'anchois et d'espèces océaniques qui contrastent avec les fortes abondances observées durant les périodes chaudes (l'Anomalie Chaude Médiévale et les derniers 150 ans).

Finalement, la reconstruction de la variabilité des populations de poissons pélagiques à haute résolution effectuée dans une série de carottes pendant les dernières 150 ans met en évidence deux épisodes favorables pour les espèces océaniques et une augmentation de l'abondance des anchois depuis ~1900 AD. Le premier épisode favorable pour les espèces océaniques (1855 – 1905 AD) est associé à une forte diminution des anchois, des températures superficielles élevées, et des conditions océanographiques plus variables que pendant les 50 ans suivants. La seconde période (1975-2000) est favorable aux espèces océaniques, comme cela est confirmé par les statistiques de pêche, et caractérisée par une forte variabilité des conditions océanographiques. La tendance positive d'augmentation des populations d'anchois depuis ~1900AD jusqu'à l'heure actuelle coïncide avec une intensification des vents locaux, une diminution de la température superficielle, une augmentation de la productivité exportée, ce qui se traduit par une augmentation de l'upwelling côtier.

4. Conclusions générales

Toutes les analyses paléoenvironnementales et paléocéanographiques et les variations d'abondance de poissons pélagiques à partir des divers proxies géochimiques et de techniques paléontologiques, et la comparaison des résultats obtenus au cours des derniers 25 kyr BP, nous permet de conclure qu'il y a une forte relation entre forçages climatiques et populations de poissons. Les variations détectées de productivité exportée et de dénitrification de la colonne d'eau indiquent que la ZMO est contrôlée à la fois par des forçages locaux et par des causes plus lointaines. La ZMO a été contrôlée par des forçages lointains depuis le début du Dernier Glaciaire jusqu'à ~14.7 kyr BP, comme suggéré par la faible relation entre productivité exportée et dénitrification de la colonne d'eau. Par contre, à partir de ~14.7 kyr BP jusqu'à présent, la relation étroite entre productivité locale et dénitrification de la colonne d'eau, indique que ce sont essentiellement des processus locaux qui régularisent l'oxygénation de l'eau. La biomasse d'anchois est fortement liée à l'augmentation de la productivité exportée. Cette situation est possiblement liée à une augmentation graduelle d'insolation dans l'hémisphère sud depuis le début de l'Holocène qui favorise la stratification de la colonne d'eau. Les périodes froides (début du Dernier Glaciaire, Dernier Maximum Glaciaire, Dark Ages Cold

Period et Petit Age Glaciare) ont été défavorables pour les anchois et les autres espèces de poissons. En revanche, le début de l'Holocène, l'Anomalie Chaude Médiévale et les derniers 150 ans ont été favorables pour les anchois et les espèces océaniques. L'intensification de l'upwelling côtier en face de Pisco a conduit à une augmentation de la productivité primaire (Gutierrez et al., 2011). Ceci a des conséquences importantes pour toute la chaine trophique, comme indiqué par l'augmentation de la biomasse des anchois et également de la population des oiseaux marins prédateurs de ces anchois.

5. Bibliographie

Agnihotri, R., M. A. Altabet, and T. D. Herbert. 2006. Influence of marine denitrification on atmospheric N_2O variability during the Holocene. Geophysical Research Letters 33(L13704).

Agnihotri, R., M. A. Altabet, T. Herbert, and J. E. Tierney. 2008. Subdecadally resolved paleoceanography of the Peru margin during the last two millennia. Geochemistry Geophysics Geosystems 9(5):1-15.

Alheit, J., and A. Bakun. 2010. Population synchronies within and between ocean basins: Apparent teleconnections and implications as to physical–biological linkage mechanisms. Journal of Marine Systems 79(3-4):267-285.

Baumgartner, T., A. Soutar, and V. Ferreira-Bartrina. 1992. Reconstruction of the history of pacific sardine and northern anchovy populations over the past two millennia from sediments of the Santa Barbara basin, California. CalCOFI Rep. 33:24-40.

Bertrand, A., A. Chaigneau, S. Peraltilla, J. Ledesma, M. Graco, F. Monetti, and F. Chavez. 2011. Oxygen: A Fundamental Property Regulating Pelagic Ecosystem Structure in the Coastal Southeastern Tropical Pacific. PLoS ONE 6(12):e29558.

Carr, M.-E., and E. J. Kearns. 2003. Production regimes in four Eastern Boundary Current systems. Deep-Sea Research Part II 50:3199-3221.

Carr, M.-E. 2002. Estimation of potential productivity in Eastern Boundary Currents using remote sensing. Deep-Sea Research Part II 49:59-80.

Chavez, F., J. Ryan, S. Lluch-Cota, and M. Niquen. 2003. From Anchovies to Sardines and Back: Multidecadal Change in the Pacific Ocean. Science 299:217-221.

Chavez, F., A. Bertrand, R. Guevara-Carrasco, P. Soler, and J. Csirke. 2008. The northern Humboldt Current System: Brief history, present status and a view towards the future. Progress in Oceanography 79:95-105.

Dorbath, L., A. Cisternas, and C. Dorbath. 1990. Assessment of the size of large and great historical earthquakes in Peru. Bulletin of the Seismological Society of America 80(3):551-576.

Field, D. B., T. R. Baumgartner, V. Ferreira, D. Gutierrez, H. Lozano-Montes, R. Salvatteci, and A. Soutar. 2009. Variability from scales in marine sediments and other historical records. Pp. 45-63. In D. Checkley, C. Roy, J. Alheit, and Y. Oozeki, eds. Climate Change and Small Pelagic Fish. Cambridge University Press.

Gutierrez, D., A. Sifeddine, D. B. Field, L. Ortlieb, G. Vargas, F. Chavez, F. Velazco, V. Ferreira, P. Tapia, R. Salvatteci, H. Boucher, M. C. Morales, J. Valdes, J. L. Reyss, A. Campusano, M. Boussafir, M. Mandeng-Yogo, M. Garcia, and T. Baumgartner. 2009. Rapid reorganization in ocean biogeochemistry off Peru towards the end of the Little Ice Age. Biogeosciences 6:835-848.

Gutierrez, D., I. Bouloubassi, A. Sifeddine, S. Purca, K. Goubanova, M. Graco, D. Field, L. Méjanelle, F. Velazco, A. Lorre, R. Salvatteci, D. Quispe, G. Vargas, B. Dewitte, and L. Ortlieb. 2011. Coastal cooling and increased productivity in the main upwelling zone off Peru since the mid-twentieth century. Geophysical Research Letters 38:L07603.

Helly, J., and L. Levin. 2004. Global distribution of naturally occurring marine hypoxia on continental margin. Deep-Sea Research I 51:1159-1168.

Karstensen, J., L. Stramma, and M. Visbeck. 2008. Oxygen minimum zones in the eastern tropical Atlantic and Pacific oceans. Progress in Oceanography 77:331-350.

Messié, M., J. Ledesma, D. D. Kolber, R. P. Michisaki, D. G. Foley, and F. P. Chavez. 2009. Potential new production estimates in four eastern boundary upwelling ecosystems. Progress in Oceanography 83:151-158.

Moron, O., W. Garcia, and M. Sarmiento. Promedios y variabilidad interanual de la salinidad frente a la costa peruana. In prep.

Okal, E. A., J. C. Borrero, and C. E. Synolakis. 2006. Evaluation of tsunami risk from regional earthquakes at Pisco, Peru. Bulletin of the Seismological Society of America 96(5):1634-1648.

Okal, E. A. 2011. Tsunamigenic Earthquakes: Past and Present Milestones. Pure Appl. Geophys. 168:969-995.

Ortlieb, L., G. Vargas, and J.-F. Saliège. 2011. Marine radiocarbon reservoir effect along the northern Chile-southern Peru coast (14-24°S) throughout the Holocene. Quaternary Research 75:91-103.

Paulmier, A., and D. Ruiz-Pino. 2009. Oxygen minimum zones (OMZs) in the modern ocean. Progress in Oceanography 80:113-128.

Reinhardt, L., H.-R. Kudrasss, A. Lückge, M. Wiedicke, J. Wunderlich, and G. Wendt. 2002. High-resolution sediment echosounding off Peru: Late Quaternary depositional sequences and sedimentary structures of a current-dominated shelf Marine Geophysical Researches 23(4):335-351.

Salvatteci, R., D. B. Field, T. Baumgartner, V. Ferreira, and D. Gutierrez. 2012. Evaluating fish scale preservation in sediment records from the oxygen minimum zone off Peru. Paleobiology 38(1):766-792.

Sanchez, G., R. Calienes, and S. Zuta. 2000. The 1997-98 el Nino and its effects on the coastal marine ecosystem off Peru. CalCOFI Rep. 41:62-86.

Schwartzlose, R. A., J. Alheit, A. Bakun, T. R. Baumgartner, R. Cloete, R. J. M. Crawford, W. J. Fletcher, Y. Green-Ruiz, E. Hagen, T. Kawasaki, D. Lluch-Belda, S. E. Lluch-Cota, A. D. MacCall, Y. Matsuura, M. O. Nevarez-Martinez, R. H. Parrish, C. Roy, R. Serra, K. V. Shust, M. N. Ward, and J. Z. Zuzunaga. 1999. Worldwide large-scale fluctuations of sardine and anchovy populations. South African Journal of Marine Science 21:289-347.

Soutar, A., and J. Isaacs. 1974. Abundance of pelagic fish during the 19th and 20th century as recorded in anaerobic sediment off the Californias. Fisheries Bulletin 72:257-273

Tavera, H., and E. Buforn. 2001. Source mechanism of earthquakes in Peru. Journal of Seismology 5:519-539.

PREFACE

The Peruvian Upwelling Ecosystem (PUE) is notable for several reasons. First, as a result of enhanced productivity the marine ecosystem off central and northern Peru produces more than 10 times the tonnage of fishery landings compared to other regions that are characterized by similar or even greater basic primary production (Carr et al., 2002; Bakun and Weeks, 2008; Chavez et al., 2008). Second, the upper continental margin of Peru (~50 to 600 meters depth) is intersected by a strong and shallow Oxygen Minimum Zone (OMZ; $[O_2] < 0.5$ ml.L^{-1}) that results from the lack of ventilation, long residence times, and the decay of biological production that consumes O_2 (Helly and Levin, 2004; Pennington et al., 2006). Third, the PUE is subject to large interannual to centennial fluctuations in climate, ecosystems and in the fish resources (Bertrand et al., 2004; Agnihotri et al., 2008; Gutierrez et al., 2009). Fourth, the PUE is experiencing an increase in coastal upwelling and productivity during the last decades (Jahncke et al., 2004; Demarcq, 2009; Gutierrez et al., 2011) presumable linked to anthropogenic global warming through local land-ocean interactions (Bakun 1990; Bakun et al., 2010). Therefore, given the uncertainty of the PUE to the effects of global warming there is concern that the upwelling and productivity in the PUE may experience strong changes in the future as climate change proceeds.

As a result of the intense OMZ, laminated sediments are preserved in suitable topographic conditions permitting the reconstruction of past ecosystem changes at high temporal resolution (Krissek and Scheidegger, 1983; Reinhardt et al., 2002). In the present work, a multi-proxy approach using paleontological techniques, organic and inorganic proxies was carried out on several laminated cores retrieved off Pisco, Peru, in the core of the Oxygen Minimum Zone (OMZ) to elucidate: 1) **Which were the driving mechanisms originating the changes in OMZ intensity and export production off Peru during the last 25 kyr,** and 2) **which were the the factors influencing anchovy and sardine fluctuations during the last 25 kyr**.

The thesis is divided in 7 chapters. **Chapter I** contains the introduction and the background of the two scientific questions that build the backbone of the thesis. **Chapter II** focuses on determining the continuity/discontinuity of multiple sediment cores retrieved off Pisco covering the last ~600 years. In this chapter, 8 sediments cores were selected in order to perform a cross-correlation of sedimentary structures based on X-ray images, proxy records, and ^{210}Pb, ^{241}Am and ^{14}C profiles. All the cores evaluated showed evidence of multiple discontinuities, due to loss of sequences and instantaneous deposit arising from slumps, possibly triggered by tsunamogenic earthquakes, which indicate frequent violation of the assumption of record continuity. Consequently, the reconstruction of past climate variability at high resolution level using one single core is subject to temporal gaps that could lead to erroneous interpretations. Therefore, prior to the subsampling a

stratigraphic approach should be done using X-ray images, to determine the samples that will be used to date the core and to develop the proxies. This chapter was submitted to *Marine Geology* on July 30 2012, and is now under revision.

Chapter III focuses on the question whether the OMZ off Peru was more dominated by remote ventilation or by the oxygen demand imposed by local productivity during the last 25 kyr. Therefore a multi-proxy approach was conducted to infer subsurface oxygenation, sediment redox conditions and export production on three cores that cover the last 25.5 kyr BP. The results show that the intensity of the OMZ off Peru during the last ~25.5 kyr BP was controlled by local and remote forcings. The weak export production from 25 to 14.7 kyr BP did not leave a strong imprint in the water column denitrification indicating that the OMZ signal was mainly originated by remote forcings (changes in ventilation of the source water mass and/or increase in export production and then in sub-surface oxygen demand in the eastern equatorial Pacific), as proposed in earlier works (Higginson and Altabet, 2004; De Pol-Holz et al., 2006; Martinez and Robinson, 2010). In contrast from ~14.7 kyr to the present, the increase in export production exerts a strong control on the water column oxygenation. In this chapter all proxies developed in the cores are shown. This chapter was not written as a manuscript, because at least 2 publications will be drawn from this chapter in the near future.

Chapter IV focuses on the centennial to millennial-scale variability in pelagic fish populations during the last 25 kyr BP. The cores evaluated in this chapter are the same as in chapter III. The results of this chapter indicate that climatic forcing plays a major role in regulating fish stocks in the PUE. Anchovy biomass appears to be strongly linked with the positive trend towards enhanced upwelling, an increase in export production and more reducing conditions in the sediments since ~ 8 kyr BP. The Holocene was favorable for anchovies and oceanic species, and the warmer Northern Hemisphere Early Holocene was more favorable for oceanic species. In contrast, the climatic-oceanographic conditions during the Northern Hemisphere cold periods were unfavorable for anchovy and oceanic species. This manuscript will be submitted shortly.

Chapter V focuses on the response of the PUE to centennial-scale global change during the last 2 millennia. Throughout the last 2 millennia an alternation of warm and cold events were registered in the Northern Hemisphere. The reconstructed changes in terrestrial runoff, export production, water column oxygenation and sediment REDOX conditions off Peru consistently suggest that the centennial-scale variations have been linked to global climate variability. In general, the response of the PUE to the Northern Hemisphere cold periods consisted in a weak OMZ, sub-oxic conditions in the sediments, low export production and low fish abundance. In contrast the response of the PUE to the warm periods consisted in a stronger OMZ, anoxic sediment conditions, higher

export production and higher fish biomass. The observed changes in the PUE are concordant with the ocean thermostat mechanism proposed by Clement et al. (1996). This manuscript will be submitted shortly to *Biogeosciences*.

Chapter VI focuses on the sub-decadal to multidecadal-scale changes in fish abundances during the last 150 years using 5 sediment cores retrieved in the Humboldt Current System. This chapter combines new as well as previously published records (Valdes et al., 2008; Gutierrez et al., 2009). All the fish scale records show a positive trend towards increased anchovy abundance since the beginning of the 20th century, which is supported by an increase in upwelling favorable winds, a tendency towards lower SST and higher productivity (Gutierrez et al., 2011). The productivity trend propagates from the base (i.e. anchovy) to higher trophic levels such as hake and sea birds. Additionally, a strong multidecadal period favorable to oceanic species was recorded from 1855 to 1905AD, which seems to be stronger in comparison to the last multidecadal period favorable to sardines that occurred from ~1975 to ~2000 AD. During this former period, anchovies were extremely reduced (in terms of biomass) and displaced to refuge areas in the south and close to the coast as registered in a core retrieved in the Mejillones bay off Chile. This manuscript will be submitted shortly. Finally, in **Chapter VII** a general discussion and conclusions of the thesis are proposed.

Bibliography

Agnihotri, R., M. A. Altabet, T. Herbert, and J. E. Tierney. 2008. Subdecadally resolved paleoceanography of the Peru margin during the last two millennia. Geochemistry Geophysics Geosystems 9(5):1-15.

Bakun, A. 1990. Global climate change and intensification of coastal upwelling. Science 247(4939):198-201.

Bakun, A., and S. J. Weeks. 2008. The marine ecosystem off Peru: What are the secrets of its fishery productivity and what might its future hold? Progress in Oceanography 79:290-299.

Bakun, A., D. Field, A. Redondo-Rodriguez, and S. J. Weeks. 2010. Greenhouse gas, upwelling-favorable winds, and the future of coastal ocean upwelling ecosystems. Global Change Biology 16:1213-1228.

Bertrand, A., M. Segura, M. Gutiérrez, and L. Vásquez. 2004. From small-scale habitat loopholes to decadal cycles: a habitat-based hypothesis explaining fluctuation in pelagic fish populations off Peru. Fish and Fisheries 5:296-316.

Carr, M.-E. 2002. Estimation of potential productivity in Eastern Boundary Currents using remote sensing. Deep-Sea Research Part II 49:59-80.

Chavez, F., A. Bertrand, R. Guevara-Carrasco, P. Soler, and J. Csirke. 2008. The northern Humboldt Current System: Brief history, present status and a view towards the future. Progress in Oceanography 79:95-105.

Clement, A. C., R. Seager, M. A. Cane, and S. E. Zebiak. 1996. An ocean dynamical thermostat. Journal of Climate 9(9):2190-2196.

De Pol-Holz, R., O. Ulloa, L. Dezileau, J. Kaiser, F. Lamy, and D. Hebbeln. 2006. Melting of the Patagonian Ice Sheet and deglacial perturbations of the nitrogen cycle in the eastern South Pacific. Geophysical Research Letters 33:L04704.

Demarcq, H. 2009. Trends in primary production, sea surface temperature and wind in upwelling systems (1998–2007). Progress in Oceanography 83:376-385.

Gutierrez, D., A. Sifeddine, D. B. Field, L. Ortlieb, G. Vargas, F. Chavez, F. Velazco, V. Ferreira, P. Tapia, R. Salvatteci, H. Boucher, M. C. Morales, J. Valdes, J. L. Reyss, A. Campusano, M. Boussafir, M. Mandeng-Yogo, M. Garcia, and T. Baumgartner. 2009. Rapid reorganization in ocean biogeochemistry off Peru towards the end of the Little Ice Age. Biogeosciences 6:835-848.

Gutierrez, D., I. Bouloubassi, A. Sifeddine, S. Purca, K. Goubanova, M. Graco, D. Field, L. Méjanelle, F. Velazco, A. Lorre, R. Salvatteci, D. Quispe, G. Vargas, B. Dewitte, and L. Ortlieb. 2011. Coastal cooling and increased productivity in the main upwelling zone off Peru since the mid-twentieth century. Geophysical Research Letters 38:L07603.

Helly, J., and L. Levin. 2004. Global distribution of naturally occurring marine hypoxia on continental margin. Deep-Sea Research I 51:1159-1168.

Higginson, M. J., and M. A. Altabet. 2004. Initial test of the silicic acid leakage hypothesis using sedimentary biomarkers. Geophysical Research Letters 31:L18303.

Jahncke, J., D. M. Checkley, and G. L. Hunt. 2004. Trends in carbon flux to seabirds in the Peruvian upwelling system: effects of wind and fisheries on population regulation. Fisheries Oceanography 13(3):208-223.

Krissek, L. A., and K. F. Scheidegger. 1983. Environmental controls on sediment texture and composition in low oxygen zones off Peru and Oregon. Pp. 163-180. *In* E. Suess, and J. Thiede, eds. Coastal upwelling, its sediment record, Part B: Sedimentary records of ancient coastal upwelling. Plenum Press, New York.

Martinez, P., and R. S. Robinson. 2010. Increase in water column denitrification during the last deglaciation: the influence of oxygen demand in the eastern equatorial Pacific. Biogeosciences 7:1-9.

Pennington, J. T., K. L. Mahoney, V. S. Kuwahara, D. D. Kolber, R. Calienes, and F. P. Chavez. 2006. Primary production in the eastern tropical Pacific: A review. Progress in Oceanography 69:285-317.

Reinhardt, L., H.-R. Kudrasss, A. Lückge, M. Wiedicke, J. Wunderlich, and G. Wendt. 2002. High-resolution sediment echosounding off Peru: Late Quaternary depositional sequences and sedimentary structures of a current-dominated shelf Marine Geophysical Researches 23(4):335-351.

Valdés, J., L. Ortlieb, D. Gutierrez, L. Marinovic, G. Vargas, and A. Sifeddine. 2008. 250 years of sardine and anchovy scale deposition record in Mejillones Bay, northern Chile. Progress in Oceanography 79:198-207.

CHAPTER I:

INTRODUCTION

I. 1. Background

I. 1.1. The Peruvian Upwelling Ecosystem

The regions associated with the Atlantic and Pacific equatorward-flowing Eastern Boundary Upwelling Ecosystems (EBUE), i.e. California, Canary, Peru-Chile and Benguela (Fig. I-1), are worldwide recognized for their high productivity (Carr et al., 2002). The integrated area of these EBUS is less than 1% of the world's oceans but accounts for 11% of global new production and 17% of global fish catch (Pauly and Christensen, 1995; Carr et al., 2002; Messié et al., 2009). In all these EBUS, upwelling of cool waters brings phytoplankton nutrients to the surface, dramatically increasing biological productivity (Chavez et al., 2008). Among all the EBUEs the Peruvian Upwelling Ecosystem (PUE), that forms part of the larger Humboldt Current System (HCS), produces more than 10 times the tonnage of fish landings produced by other comparable regions exhibiting similar or even greater basic primary production (Bakun and Weeks, 2008). For example the primary productivity in the Benguela Current or off Northwest Africa is higher compared to off Peru but the fish catch is lower (Fig. I-2). Through ocean-atmosphere coupling, the northern HCS is intimately linked to equatorial Pacific dynamics and is subject to large interannual to multidecadal fluctuations in climate, with consequences for the whole ecosystem and fisheries (Chavez et al., 2008).
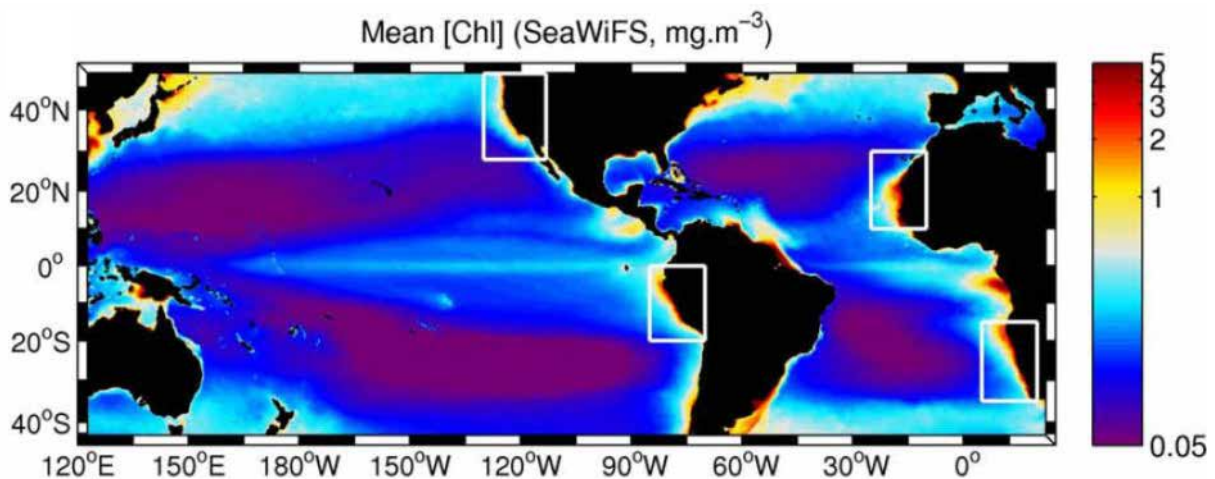
Figure I-1. Basin-scale map of Chlorophyll obtained from SeaWiFS monthly climatology averaged over the year, showing the location of the Eastern Boundary Upwelling Ecosystems (EBUE) discussed in the present work (Chavez and Messié, 2009).
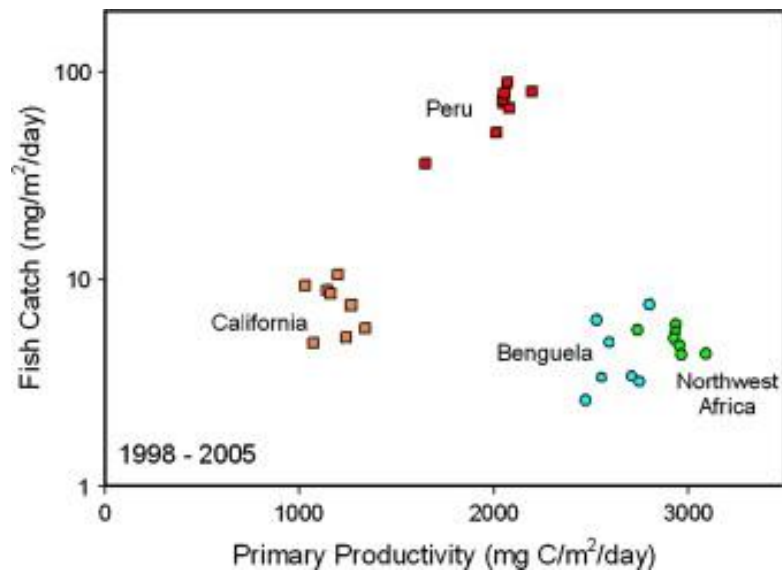
Figure I-2. Fish catch versus primary productivity for the four main eastern boundary coastal upwelling ecosystems for the years 1998–2005. It was assumed that the reported fish catches (Fish and Agriculture Organization, FAO) were made within 100 km from the coast. The catches were then normalized by area. Primary productivity was estimated from satellite remote sensing of chlorophyll and the Behrenfeld and Falkowski (1997) model. Even during the El Niño year of 1998 Peru fish catch still exceeded that from the other areas by several fold. Taken from Chavez et al. (2008).

The upper continental margin of Peru (~50 to 600 meters depth) is intersected by a strong and shallow Oxygen Minimum Zone (OMZ; $[O_2] < 0.5$ ml.L^{-1}; Fig. I-3). The OMZ off Peru and off Chile is one of the three main open-ocean oxygen deficient regions of the global ocean (Ulloa and Pantoja, 2009). The OMZ results from the lack of ventilation, long residence times, and the decay of biological production that consumes O_2 (Helly and Levin, 2004; Pennington et al., 2006). The intensity of the OMZ off Peru has been observed to vary on interannual time scales driven by El Niño events, for example during the extreme El Niño 1997–98, the upper boundary of the OMZ deepened to 250 m (Sánchez et al., 2000). The presence of the OMZ inhibits bioturbation and facilitates the preservation of high-resolution records of past ecosystem changes in suitable topographic conditions (Krissek and Scheidegger, 1983). Past studies of marine sediments within the OMZ show that the intensity of the OMZ has varied on decadal- to centennial-scale time scales as inferred by δ^{15}N of organic matter and other proxies in sediment records (Agnihotri et al., 2008; Gutierrez et al., 2009). Although the OMZs occupy only ~1% of the volume of the global ocean, they disproportionately affect global biogeochemical cycles, particularly the nitrogen cycle (Ulloa and Pantoja, 2009). Moreover, the OMZs are the main areas of nitrogen loss (as N_2, N_2O) to the atmosphere through denitrification and anammox (anaerobic oxidation of NH_4^+ using NO_2^-), and could even indirectly mitigate the oceanic biological sequestration of CO_2 (Paulmier and Ruiz-Pino, 2009). Finally, the expansion of oceanic low-oxygen waters is suggested by observations in the tropical oceans (Stramma et al., 2008).
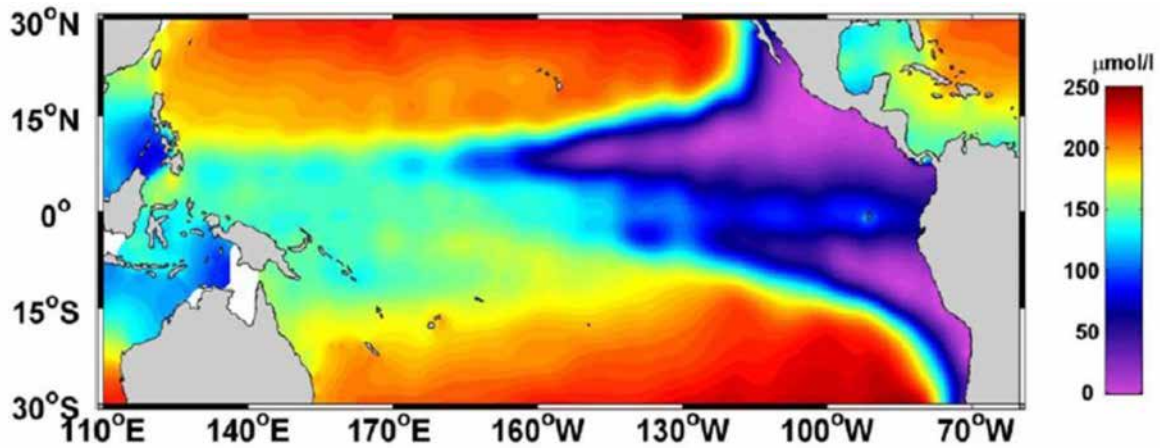
Figure I-3. Present day climatological map of dissolved oxygen at 150 m depth (μmol.L^{-1}), from the World Ocean Data Center, showing the persistently low oxygen in the Eastern Tropical Pacific. Figure taken from Gutierrez et al. (2009).

I-1.2. Present-day atmospheric and oceanographic conditions

The atmospheric forcing in the PUE is driven by the southeastern Pacific Subtropical Anticyclone or also named the South Pacific High (Fig. I-4) that drives equatorward winds along the coasts of Chile and Peru (Strub et al., 1998). The limits of the south Pacific High are the Inter-Tropical Convergence Zone (ITCZ) in the north and the polar front in the south (Strub et al., 1998). The ITCZ displays annual latitudinal displacements, moving from ~10 °N during the austral winter (June to September) to 2-5 °N in austral summer (December-March). Local semi-permanent low-pressure areas are found along the coast of Peru associated with the arid regions inshore of upwelling centers, especially to the south of Bahia Paracas at 14 °S which coincides with the Ica Desert. Higher aridity and frequency of clear-sky conditions on land causes stronger alongshore winds in general because of the enhanced land-sea temperature gradient, these winds are enhanced during the afternoon due to enhanced insolation (Rutland et al., 1990). The strong winds resulting from the land-sea temperature gradient produce upwelling reinforcing the difference in temperature and pressure across the coastline.

The coastal currents in the HCS are similar as those observed in other EBUE, consisting by one equatorward current (Peruvian Current [PC]) and a poleward sub-surface current (Poleward undercurrent [PUC]; Figs. I-4 and I-5). The West Wind Drift bifurcates at ~ 43 °S into two currents: the equatorward PC and the poleward Cape Horn current (Fig. I-4), ultimately after flowing parallel to the Peruvian coast, the PC flows westward near the Equator into the South Equatorial Current (SEC). The equatorward Peruvian Coastal Current (PCC) is strongest in austral winter when equatorward winds are maximum carrying upwelled colder and saltier water to the Equatorial Cold Tongue. The surface currents are dominated by equatorward flows, but the sub-surface currents are dominated by

poleward currents. The origin of the PUC is associated with the equatorial sub-surface currents (Figs. I-4 and I-5). The Equatorial Undercurrent (EUC) splits at the Galápagos Island and one branch continues as an undercurrent that reaches South America near the equator and turns south to become the PUC. The other branch of the EUC flows to the Southeast of the Galápagos and approaches the coast at ~6 °S forming the Peru-Chile countercurrent (PCCC). The undercurrents that feed the PUC are the primary and secondary Southern Subsurface Countercurrent (SSSC) and contribute in higher proportion to the PUC in comparison with the EUC (Montes et al., 2010). The 30% of the PUC is fed by the EUC and SSSC while the remaining part comes from an alongshore recirculation associated with flows below it, and from undercurrents south of ~9 °S (Montes et al., 2010). The PUC is clearly identified by its water mass characteristics because it is saltier, richer in nutrients and lower in oxygen than the surrounding waters (Strub et al., 1998).
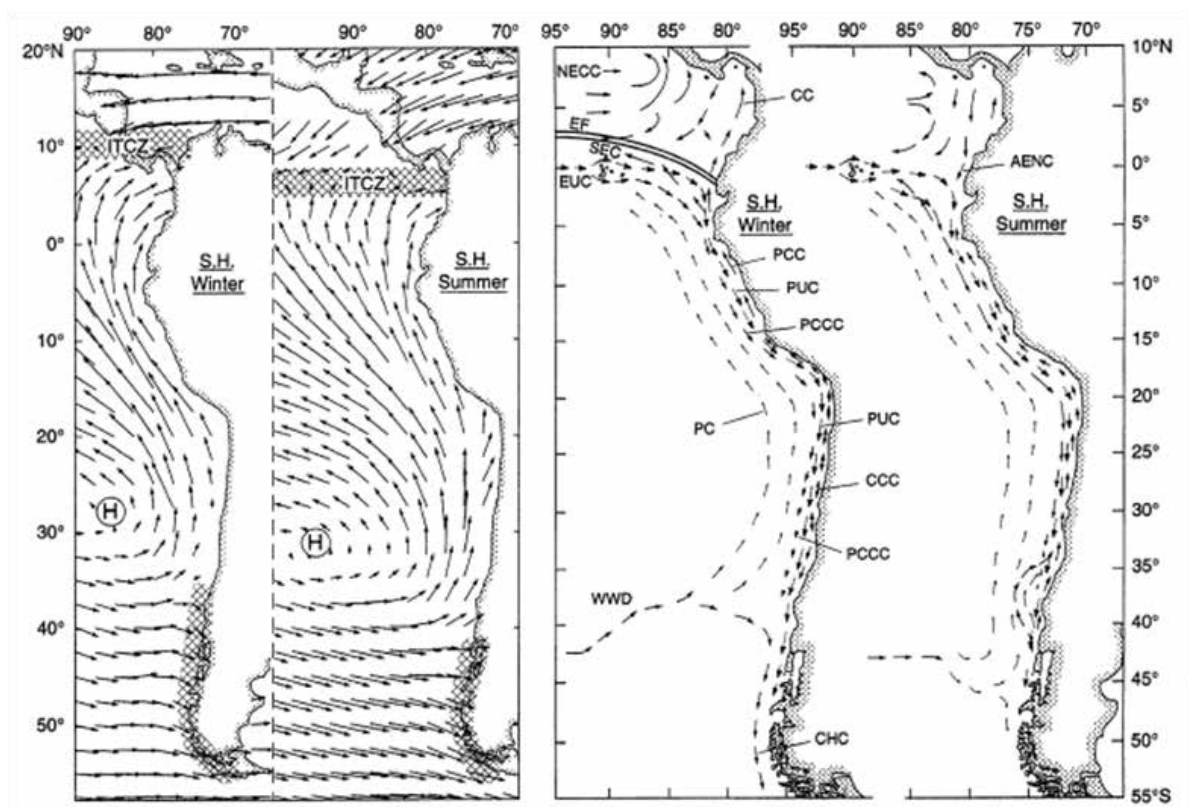
Figure I-4. Climatologically winds and currents during austral winter and summer. Taken from Strub et al. (1998).
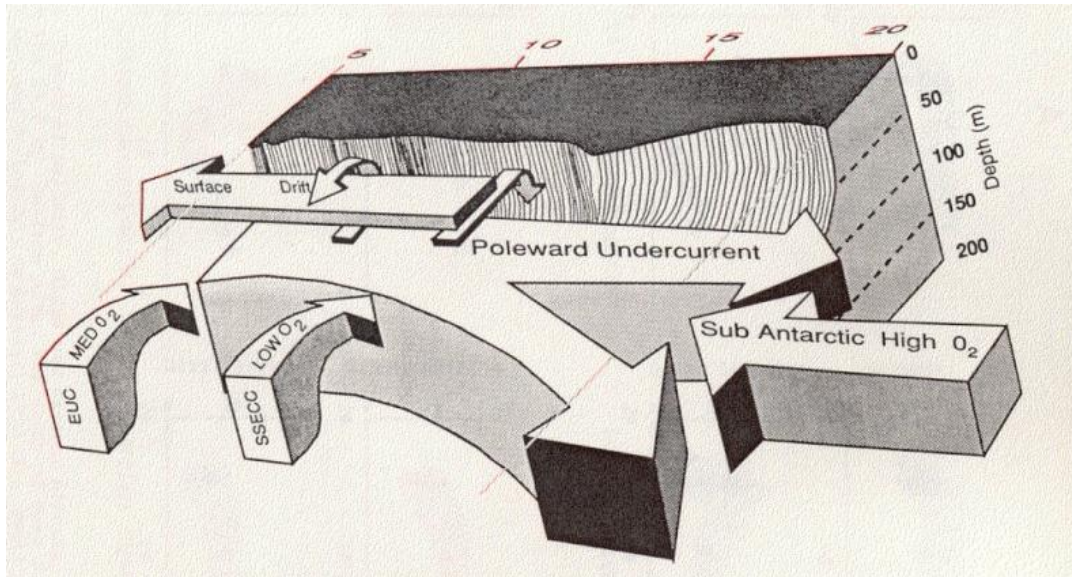
Figure I-5. Schema showing the Poleward Undercurrent, the surface "wind-drift" and the three advective sources of oxygen for the Undercurrent which are the Equatorial Undercurrent, the Subsurface South Equatorial Countercurrent, and the equatorward flow of the subantarctic waters in the Peru Oceanic Current. Figure taken from Codispoti (1989).

In the PUE the seasonal cycles in production are out of phase with seasonal upwelling winds, in clear contrast to the other EBUS (Fig. I-6; Pennington et al., 2006; Chavez and Messié, 2009; Gutierrez et al., 2011). The seasonal changes in winds and productivity in the Peruvian upwelling ecosystem are associated with the movement of the ITCZ from 10°N in austral winter (June-September) to 2-5°N in austral summer (December-March) (Strub et al., 1998). Upwelling favorable winds occur during the entire year but are stronger during austral winter and spring (Strub et al., 1998; Gutierrez et al., 2011). In contrast primary productivity is higher during austral spring and summer when surface waters are more stratified (Pennington et al., 2006; Chavez and Messié, 2009; Gutierrez et al., 2011). In particular, the Pisco area (~14° S) is subjected to the most intense alongshore winds in the Peruvian coast (Goubanova et al., 2010). In this area during August, the alongshore winds reach a maximum value, the Sea Surface Temperatures (SST) reach a minimum value, while the primary productivity (estimated by Chlorophyll-a) is lower (Fig. I-6). In contrast, from December to March the primary productivity is higher, when the surface waters are more stratified (Gutierrez et al., 2011).
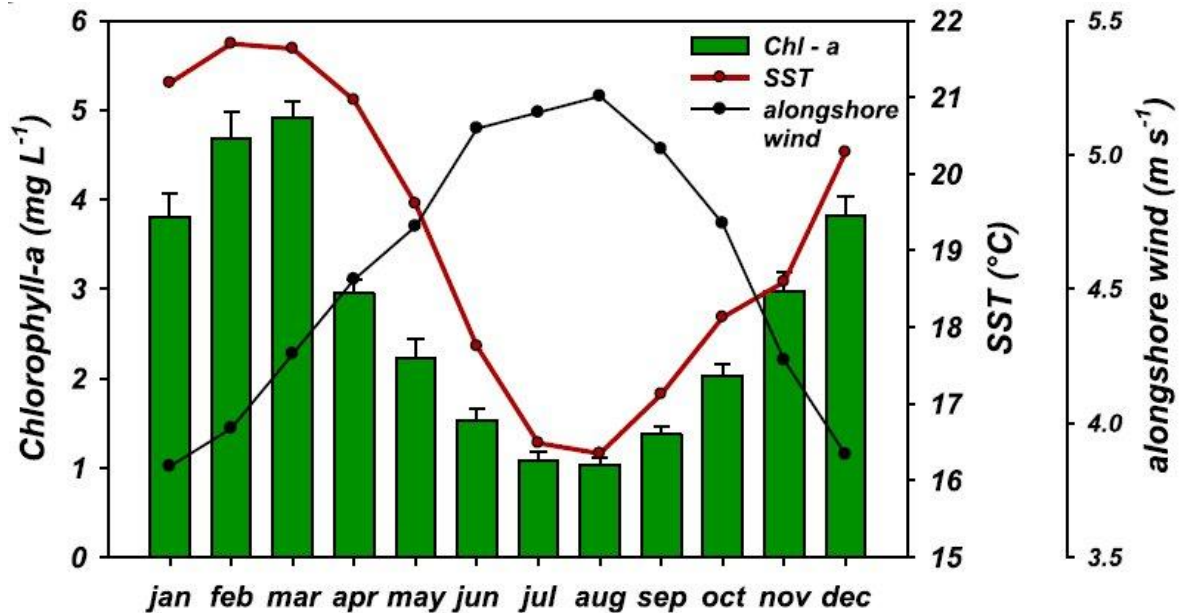
Figure I-6. Climatology of Chl-a based on Sea-WiFS color data (1997–2006) and of the alongshore wind velocities (ECMWF–ERA40) inside a coastal area off Pisco. The red line joins the monthly SST means, based on a least squares fit between Pisco pier SST and GHRSST. Taken from Gutiérrez et al. (2011)

I-1.3. ENSO events and the interannual variability

The main cause of interannual variability in the HCS are El Niño events that produce anomalously warm SST in the equatorial and eastern Pacific every three to eight years (Chavez et al., 2011). During El Niño events the equatorial Walker circulation is weakened, and the coast of Peru is characterized by an increase in SST, sub-surface oxygenation and reduced productivity due to a deepening of the thermocline; however the Pisco area retains a small upwelling plume even during El Niño events (Barber and Chavez, 1983). During El Niño events the upwelling favorable winds off Peru increase in response to an increase in water vapor within the low-pressure cell that forms over the Peruvian landmass (Bakun and Weeks, 2008; Bakun et al., 2010). However, because the thermocline/nutricline is located deeper than during normal conditions, there is no fertilization of the upper section of the water column. In contrast, the La Niña events are characterized by lower than normal SST in the eastern central equatorial Pacific and enhanced Walker Circulation. Figure I-7 depicts the climatic and oceanographic changes that occur during El Niño and La Niña events, and are compared with the "normal" conditions.
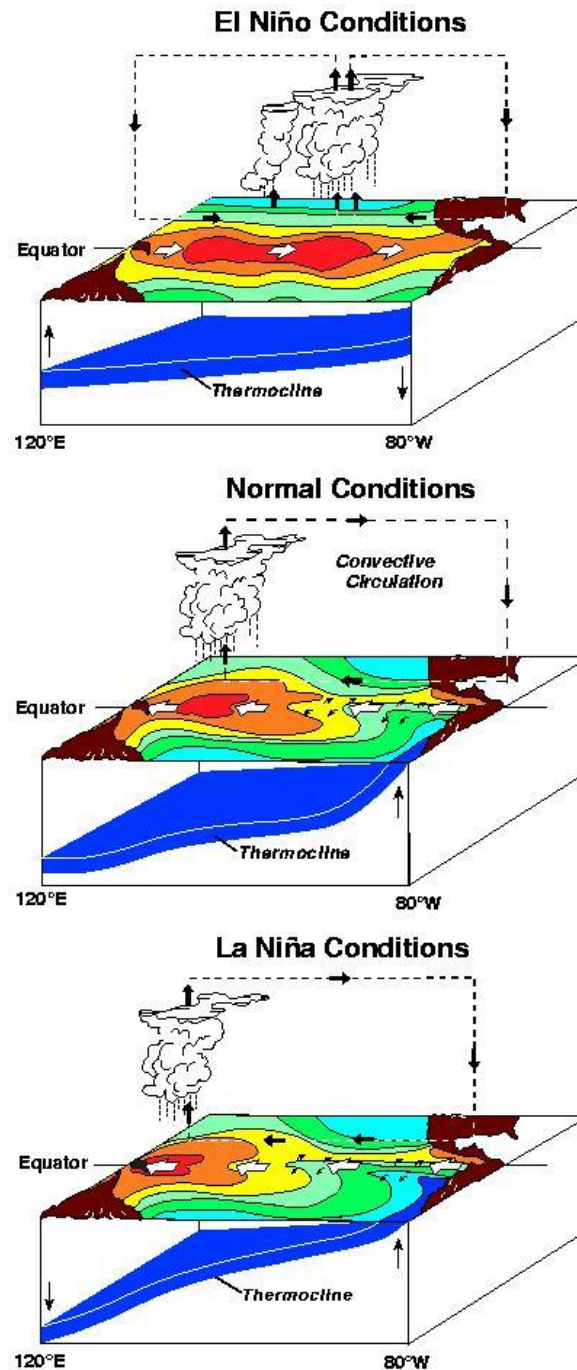
Figure I-7. Atmospheric and oceanographic changes during El Niño (top), Normal (middle) and La Niña conditions (bottom). Figure taken from the NOAA web page (http://www.noaa.gov/).

It is well known that each El Niño event is associated with different regional climate, and that the response of the ecosystem (and particularly fishes) is not similar during each El Niño event (Kao and Yu, 2009; Dewitte et al., 2011). The ENSO has been categorized into two types of El Niño: the traditional Cold tongue El Niño or Eastern Pacific El Niño that consists of the SST anomaly developing and peaking in the eastern equatorial Pacific (Fig. I-7), and the Modoki El Niño (Ashok et al., 2007) or Central Pacific El Niño (Kao and Yu, 2009) that consists of the SST anomaly developing and persisting in the central Pacific. The teleconnections patterns of each type of El Niño are

different (Dewitte et al., 2011). The effect of El Niño conditions on anchovy and other species differ from one event to another (Bakun and Broad, 2003; Alheit and Ñiquen, 2004; Bertrand et al., 2004). For example the recovery of anchovy was slow after El Niño events in 1972-73, 1977-78, and 1982-83, rapid after El Niño 1987 and 1997-98, and finally the El Niño of 1992-93 and 2002-03 seemed to have no perceptible impact on anchovy biomass (Alheit and Ñiquen, 2004; Bertrand et al., 2004). Consequenlty no generalization can be made on the response of fishes to El Niño events.

I-1.4. Anchovy and Sardine biomass fluctuations during the last 50 years

The highly productive upwelling environment off the coast of Peru sustains one of the world's largest fisheries, the Peruvian anchoveta (*Engraulis ringens*), but biomass variability on inter-annual to decadal timescales results in dramatic variations in catch (Schwartzlose et al., 1999, Chavez et al., 2003). The Peruvian fishery for anchovy developed rapidly during the late 1950s and early 1960s and quickly became the largest in the world, reaching more than 12 million tons in 1970 (Fig. I-8). By 1972 the anchoveta fishery collapsed in part due to the intense fishing on a resource made vulnerable by the El Niño conditions. However the anchovy biomass didn't recover the following years and in the middle of the 1970s, sardines (*Sardinops sagax sagax*) appeared in abundances to support an alternative fishery. The presence of sardine off Peru lasted until the late 1990s; in contrast the anchovy biomass increased in the late 1980s to the date. The large-scale fluctuations of anchovy and sardine populations observed off Peru were also observed in other major ocean ecosystems like off California, Japan, Namibia, among other sites (Schwartzlose et al., 1999).

The fluctuations between anchovy and sardine cannot be principally explained by interspecies predation because these species do not seem to compete. First, anchovy prey on larger zooplankton while sardine is a more efficient filter feeder on phytoplankton and small zooplankton (Espinoza and Bertrand, 2008; Espinoza et al., 2009; Alheit and Bakun, 2010). Second, there is a strong relationship linking anchovy distribution to the highly productive upwelled coastal waters while sardine had a slight (though not statistically significant) preference for surface subtropical waters (Gutierrez et al., 2007; Swartzman et al., 2008). Third, sardines migrate more in comparison with anchovies (Alheit and Bakun, 2010). Finally, anchovy and sardine cannibalize their own eggs and larvae as readily as predating upon other's (Alheit, 1987). Consequently the interspecies predation cannot be seen as mechanism to explain that one species could depress the other (Alheit and Bakun, 2010). Thus, changes in the favorable habitat for each species linked to changes in climate-ocean interactions seem to better explain the fluctuations in anchovy and sardine populations (Bertrand et al., 2004).
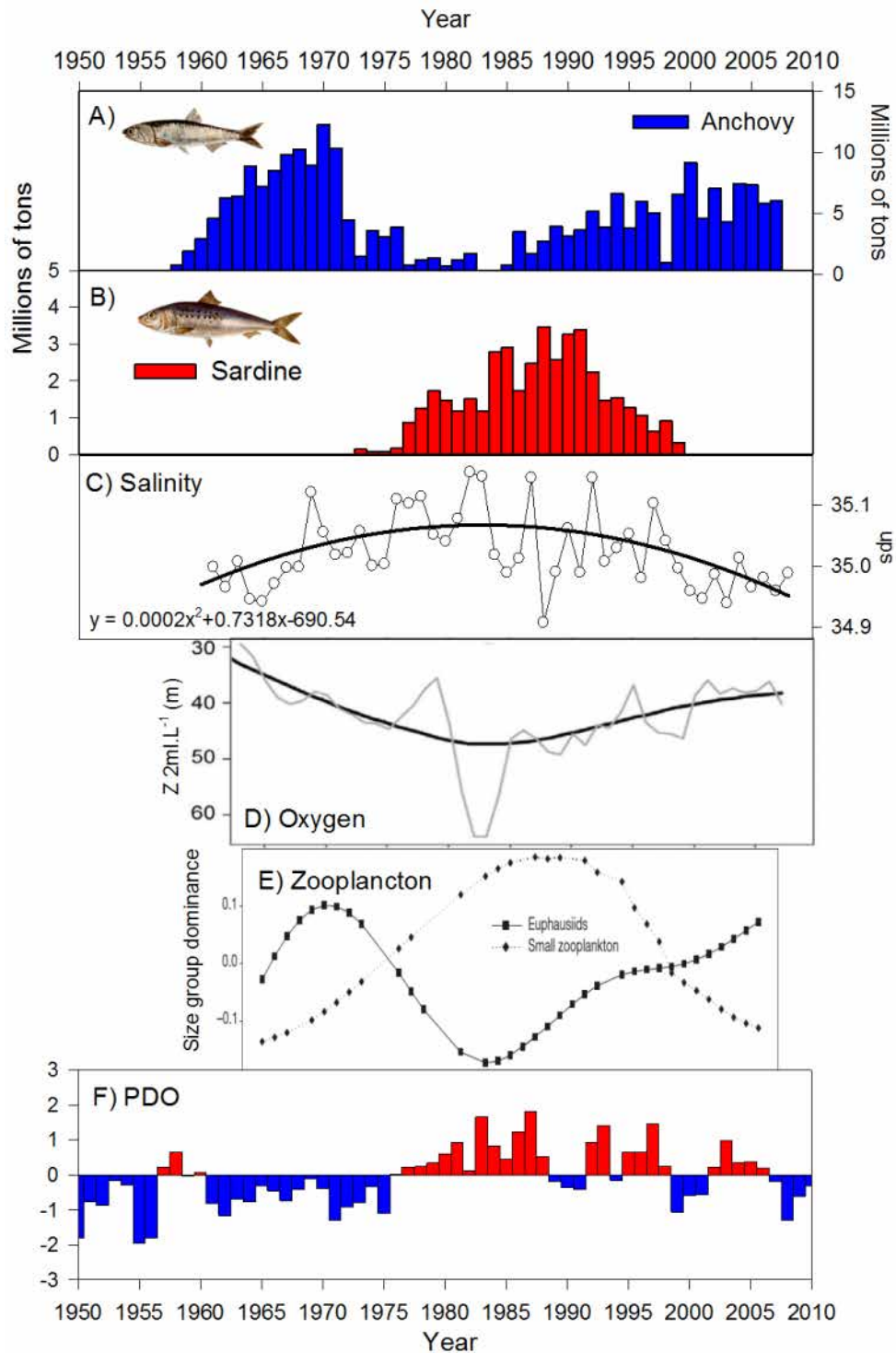
Figure. I-8. Time series of anchovy (*Engraulis ringens*) and sardine (*Sardinops sagax sagax*) landings and other biological and oceanographic parameters. A) Anchovy landings off Peru. B) Sardine landings off Peru. C) Salinity measurements between 11 and 12 °S, the black line represent the polynomial function obtained from the data set, data taken from Moron et al, in prep. D) Depth at which the 2 ml.L^{-1} were found, black solid line shows the smoothed time series, taken from Bertrand et al. (2011). E) Dominance of euphasiids and small zooplankton from generalized additive model results, taken from Ayon et al. (2011). F) Pacific Decadal Oscillation (PDO) index, which is defined as the leading principal component of North Pacific monthly sea surface temperature variability (poleward of 20 °N for the 1900-93 period).

The fluctuations between anchovy and sardine populations are associated with the advance or retreat of the coastal cold and oxygen-poor upwelled waters and the warm and more oxygenated subtropical oceanic waters to the coast of Peru and Chile (Alheti and Bakun, 2010; Bertrand et al. 2011; Moron et al. in prep.). The advance of the subtropical waters towards the coast seems to be adverse for anchovy, but favorable for sardine (Fig. I-8). Analysis of long-term salinity data from waters off Peru, up to 60 nm offshore shows that the shifts in anchovy and sardines abundances are related to the advance and retreat of oceanic subtropical high salinity water masses (Moron et al., in prep). From 1960 to the late 1960s, coastal waters off Peru were dominated by cold coastal water (CCW; 14–18 °C; 34.9–35.0 PSU). Thereafter, from the late 1960s to the mid-1980s, subtropical surface water (SSW; 18–27 °C; 35.1–35.7 PSU) approached the coast. Since the 1990s the SSW retreated again offshore, being replaced by CCW. Moreover, nowadays the spatial distribution of anchovy and sardine schools indicate a greater tolerance of anchovy to water hypoxia, compared to sardine (Bertrand et al., 2011). Additionally available time-series indicate that anchovy were more abundant during periods with shallow oxycline conditions while sardine peaked during the period with deeper oxycline (Fig. I-8D). The cool conditions favorable to anchovies were accompanied by more nutrients in the euphotic layer and the development of large phytoplankton (chain forming centric diatoms) and zooplankton (large copepods and euphasiids) which favors anchovy that feed primarily by direct biting on large zooplankton (Espinoza and Bertrand, 2008; Bertrand et al., 2011). In contrast, the period favorable for sardine was associated with lower nutrients in the euphotic layer that favored the development of smaller phytoplankton and zooplankton that sardines can more efficiently filter feed (Espinoza et al., 2009; Bertrand et al., 2011). The changes in the range of anchovy and sardine habitat induced by climatic changes at different temporal scales (annual to multi-decadal), and the resulting shift of dominance between anchovy and sardine lead to the habitat-based hypothesis (Bertrand et al., 2004) to explain the changes in anchovy and sardine populations given the ecological differences between these two species.

Given these relationships between the environmental conditions and the fluctuations of anchovy and sardine biomasses, several authors have tried to link these observations to large-scale atmospheric or oceanic forcings as the Pacific Oscillation Index (PDO, Chavez et al., 2003). The period of higher sardine abundance occurred during the warm phase of the PDO (from 1975 to the mid-1990s), while the periods with increased anchovy population sizes have occurred during the cool phase of the PDO (from 1950 to 1975, and from the early 1990s to the present). However, Gutierrez et al. (2009) and Valdes et al. (2008) show evidence, based on anchovy and sardine biomass reconstruction using fish scale deposited in laminated sediments, that the warm phases of the PDO are not always associated with sardine given that no sardine were found during a former warm phase of the PDO (from 1925 to 1950).

I-1.5. Cooling and enhanced productivity in the Peruvian upwelling during the last decades

The PUE is experiencing an increase in coastal upwelling and productivity during the last decades (Jahncke et al., 2004; Demarcq, 2009; Gutierrez et al., 2011) presumable linked to anthropogenic global warming through local land-ocean interactions. There is a long-term increase in wind stress observed in the International Comprehensive Ocean-Atmosphere Data Set (ICOADS) that could support the enhanced upwelling as a consequence of enhanced upwelling favorable wind stress (Jahncke et al., 2004; Bakun et al., 2010). However the data are highly controversial because the long-term increasing trend in the data base may be artificially created by temporal trends in ship sizes and associated anemometer heights, trends in relative frequencies of measured and estimated winds, and no homogeneities in recording and archiving practices (Bakun et al., 2010). The increase in upwelling is also observed in paleoceanographic data off Chile (Vargas et al., 2007) and other EBUS (McGregor et al., 2007; Leduc et al., 2010) suggesting a somewhat similar forcing in each one of the EBUS. The physical driving forcing is not yet fully understood, however Bakun (1990), suggests a mechanism related to the 'thermal' low-pressure cell that builds up over the coastal landmass due to heating of the continental surface relative to the more slowly heating ocean (Fig. I-9). This continent-ocean system exerts an equatorward geostrophic wind stress on the sea surface that, in turn, drives offshore-directed Ekman transport of ocean surface water and corresponding upwelling of deeper waters required to replace the surface waters transported offshore (Bakun, 1990; Bakun et al., 2010). In Peru this mechanism should be more evident in two local semi permanent low-pressure areas, south of Punta Aguja (Bahia Sechura) at 6 °S, where the coastal desert widens, and to the south of Bahia Paracas at 14 °S, coinciding with the Ica desert, where the sediment cores used in the present thesis were taken. Another possibly mechanism that could explain the intensification in coastal upwelling is related to the intensification of the South Pacific High Pressure Cell which is also possible triggered by anthropogenic global warming (Falvey and Garreaud, 2009).
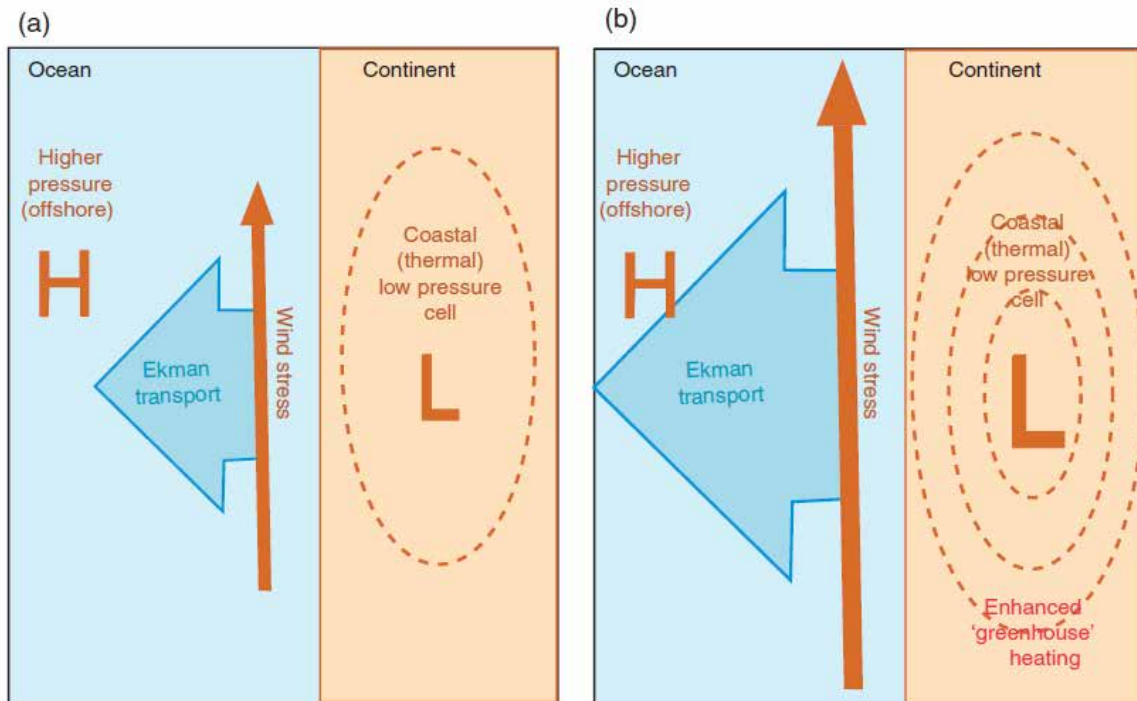
Figure I-9. Diagram of the upwelling intensification mechanism upon Bakun et al. (2010): (a) a 'thermal' low-pressure cell builds up over the coastal landmass due to heating of the continental surface relative to the more slowly heating ocean, exerting equatorward geostrophic wind stress on the sea surface that, in turn, drives offshore-directed Ekman transport of ocean surface water and corresponding upwelling of deeper waters required to replace the surface waters transported offshore; (b) buildup of greenhouse gases in the atmosphere inhibits nighttime cooling of the heated coastlands, increasing average intensity of the coastal low-pressure cell and associated upwelling-favorable wind, which in terms drives increases in offshore surface transport and in resulting upwelling.

I-1.6. Fish scales deposited in undisturbed marine sediments as a proxy for pelagic fish abundance variability

Testing hypotheses of mechanisms driving decadal or longer variability in fish abundances and determining the role of fisheries in affecting population sizes require long records of fish population variability prior to the development of industrial fishing. This is best achieved through the development of fish scale records from marine undisturbed anoxic marine sediments (Soutar and Isaacs, 1974; Baumgartner et al., 1992). Over time fish scales and bones as well as debris of many organisms fall to the ocean floor, bury and accumulated, and if the conditions are favorable a record may be preserved providing a history of pelagic communities which inhabited the area. Variation in scale deposition with fish population size is attributable to natural scale shedding while the majority of bones and vertebrae arrive to sediments by passing through the guts of predators (Field et al., 2009, Salvatteci et al., 2012). However in order to preserve the record, a strong OMZ is required to avoid the presence of benthic fauna that can bioturbated or bio-irrigate the sediments. Fortunately high resolution laminated sediments within the OMZ are present off Central Peru, especially in front of

13

Pisco (Gutierrez et al., 2006 and IMARPE surveys). Also anoxic conditions in the sediment are more favorable for the preservation of fish remains, since the organic matrix and the mineral composition are very sensitive to the oxygenation of the microenvironment (Salvatteci et al., 2012).

One of the best examples of past population variability of pelagic fishes inferred by fish scale deposition rates is the one developed in the Santa Barbara Basin off Southern California (Baumgartner et al., 1992). This basin contains annually layered sediments that can be counted to establish a precise chronology (e.g. Soutar and Crill, 1977; Baumgartner et al., 1992; Biondi et al, 1997; Field and Baumgartner, 2000; Schimmelmann et al., 2006). Scale deposition rates in 2 cores retrieved in this basin show a similar pattern indicating the good reproducibility of the data set (Baumgartner et al., 1992). The anchovy and sardine scale deposition rates obtained from a Kasten core retrieved in this basin (Fig. I-10), show periods with low abundance of sardine and high abundance of anchovy (e.g. ~500 and ~900AD), high abundance of sardine and low abundance of anchovy (e.g. ~1070 AD), and relatively high abundance of both species (e.g. ~430 and ~1300 AD). These results imply that multiple scenarios may exist instead of just an alternation between anchovy and sardine populations. Consequently the term of "fluctuation" rather than "alternation" is used in the present thesis when referring to the changes in anchovy and sardine biomass through time.
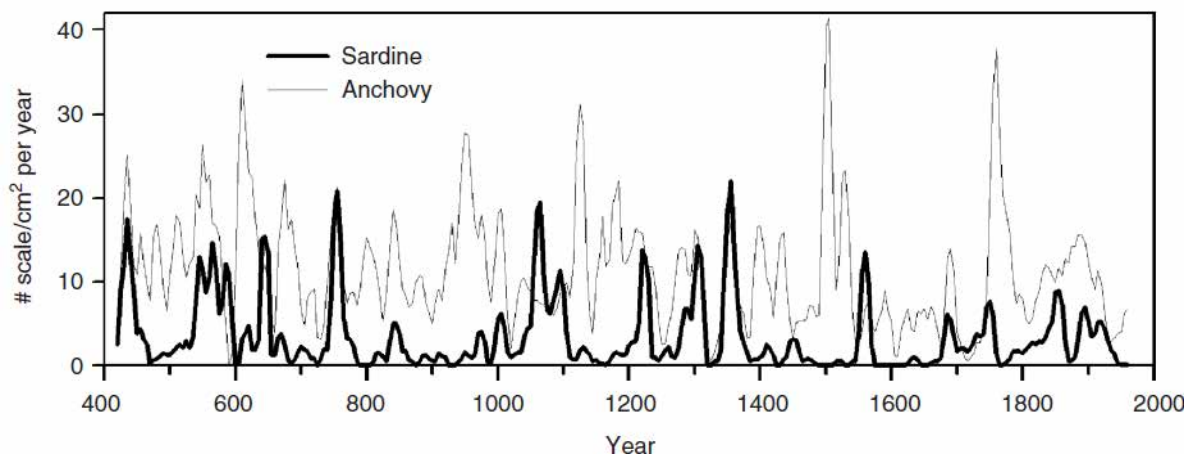
Figure I-10.Sardine and anchovy scale deposition rates in the Santa Barbara Basin from Kasten core SBKC 9110–1301. The lines are three-term smoothing of continuous 5-year sampling intervals. Figure taken from Field et al. (2009), which was updated from Baumgartner et al. (1992).

Previous work using laminated sediments retrieved off Callao (~12 °S) and off Pisco (~14 °S) show strong changes in the HCS throughout the last 500 years (Diaz-Ochoa et al., 2008; Sifeddine et al., 2008; Gutiérrez et al., 2009). During the globally cold Little Ice Age period (LIA, from ~1500 to ~1850 AD), the PUE was characterized by lower productivity, weaker OMZ and low abundances of all type of fish scales (Fig. I-11). In contrast the last ~150 years were characterized by an increase in export production, a strong OMZ and high fluxes of anchovy scales. These results show that the PUE

was sensitive to global climate changes and that these changes affected the biomass of anchovy and other pelagic fishes.

The low abundance of anchovy scales during the LIA was in part due to strong degradation of fish scales, suggesting a possible direct or indirect effect of oxygen concentration in the degradation process of fish scales (Salvatteci et al., 2012). In contrast fish scales after the LIA were better preserved and the fish scale deposition rates can be directly linked to changes in past fish biomass (Salvatteci et al., 2012). Thus, fish scale preservation in the sediment record is variable in time, depends on the environmental conditions, and can bias the record if the preservation issues are not taken into account. Salvatteci et al. (2012) showed several means to evaluate fish scale degradation on the sedimentary record that must be evaluated prior to any interpretation.
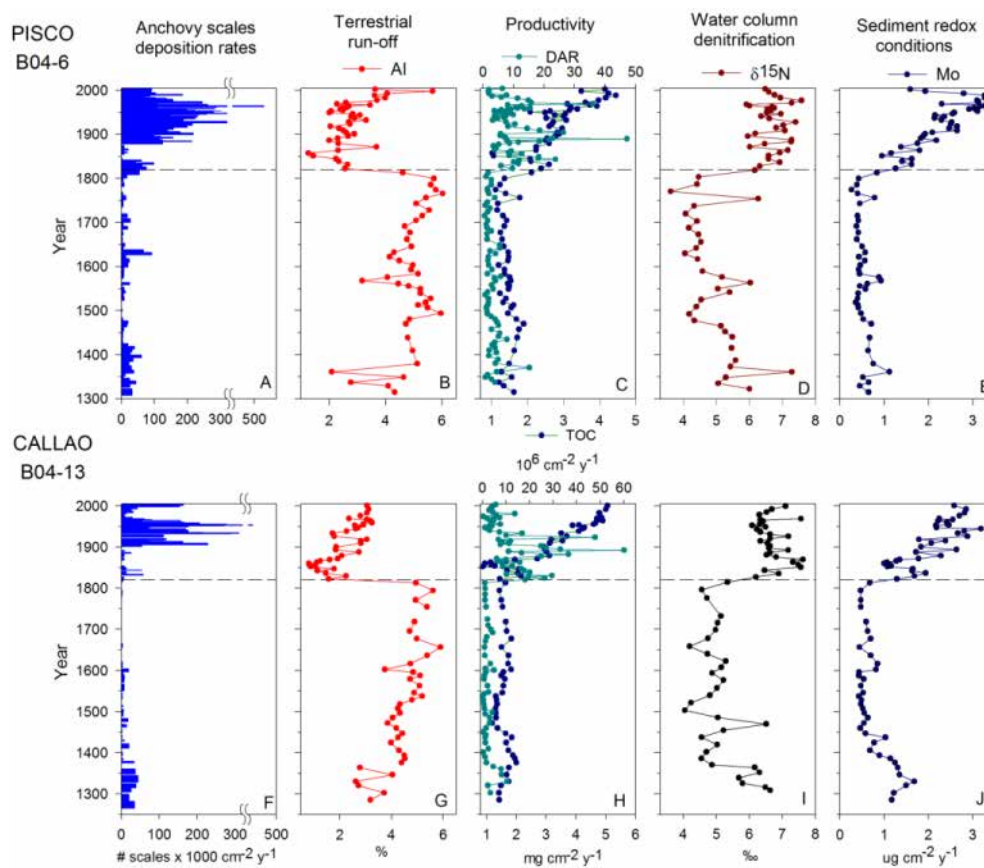
Figure I-11. Fish scale deposition rates and proxies of environmental conditions developed in cores B04-6 (299 m depth) and B04-13 (189 m depth) retrieved off Pisco and Callao, respectively. Records are anchovy scale fluxes as indicators of anchovy biomass (A, F); Aluminum (Al) contents as proxy for terrestrial run-off (B and G); fluxes of total organic carbon (TOC) and diatom accumulation rates (DAR) as proxies of primary productivity (C, H); δ¹⁵N values of organic matter as an indicator of water column oxygenation, where higher values indicate lower oxygenation (D, I); and molybdenum (Mo) fluxes as an indicator of redox conditions where higher values indicate more anoxic conditions) (E, J). The dashed lines indicate a shift from a period characterized by lower productivity and weaker OMZ to a period characterized by higher productivity and intense OMZ, (following Sifeddine et al., (2008) and Gutierrez et al., (2009). Figure redrawn using data from Gutierrez et al. (2009).

One of the uncertainties that often arise while using fish scales records is about how well do local fish abundances over a given area reflect fish abundance over a boundary current (Field et al., 2009). On multi-decadal timescales, paleoceanographic studies by Valdes et al. (2008) and Gutierrez et al. (2009) on sediment cores off Peru (~12 and 14 °S) and Northern Chile (~23 °S) retrieved within the OMZ, have shown the potential to replicate similar changes in fish scale fluxes. However it is known that the pelagic fishes like anchovy changes its distribution during interannual and interdecadal time-scales. At interannual timescale, El Niño events cause the expansion or contraction of pelagic species distribution and abundance, and the latitudinal effect of each El Niño seems to be different and not directly related to its strength (Bertrand et al., 2004; Ñiquen and Bouchon, 2004; Gutierrez et al., 2012). In general during an El Niño event anchovy is distributed very close to the coast (Bertrand et al., 2004; Ñiquen and Bouchon, 2004). At interdecadal timescales the gravity centre of anchovy seems to present a north trend since the 1960s (Gutierrez et al., 2012). Following this line of reasoning, during multi-decadal periods with unfavorable conditions for anchovy (e.g. a reduction of the habitat favorable for anchovy), the spatial distribution of anchovy should be distributed very close to the coast. Thus, well dated sediment records collected in a latitudinal and a longitudinal gradient may record the multidecadal changes in anchovy distribution.

Another problem of using fish scales buried in laminated sediments in order to construct high resolution records is the complicated sedimentological pattern of the sediment cores retrieved on the continental margin that could lead to misleading interpretations in the fish scale downcore variability. While considerable effort is usually made to construct chronological models, it is usually assumed stratigraphic continuity of the sedimentary column; however this assumption may not be correct. For example, careful examination of annually laminated sediments off Guaymas (Gulf of California) clearly revealed that stratigraphic disruptions and missing laminae within a sequence occurs in every core taken (Baumgartner et al., 1991). Sediments of the Peru slope present large discontinuities (in longer timescales) caused by erosive processes and events of lateral transportation possibly originated by tectonically processes that can frequently eliminate laminae or bands sequences previously deposited and add material from upslope (Reinhardt et al., 2002). Therefore, the development of stratigraphic sequences from multiple cores in one particular region is a crucial first step in order to infer the sub decadal and decadal-scale variability of any proxy, avoiding the misleading interpretation arising from only one record (Baumgartner et al., 1991, Field et al., 2009). Despite all the sedimentological problems that may complicate the interpretation of the fish scale records, important insights of the impacts of past climate variability in the pelagic community can be learned from an accurate study of the sedimentary column.

The response of anchovy and sardine populations to global climate change on longer time scales is poorly known. De Vries and Pearcy (1982) quantified the fish debris in multiple cores off

Peru covering only small time windows since ~16 000 years cal BP (Fig. I-12), given that the cores presented multiple unconformities and slumped sections. The results of De Vries and Pearcy (1982) show that scales and vertebrae of anchovy and hake were the dominant constituents of fish debris, the anchoveta was the dominant pelagic fish off central Peru for much of the past recorded 16 kyr, and that there was an increase in oceanic species (i.e. sardine) between ~11.8 and ~11.4 kyr cal BP. Thus, the results of this work indicate that the anchovy and sardine biomass has varied considerably in the past; however the limited time windows did not permit to establish which climatic and environmental conditions were the ones that favored anchovy and sardine.
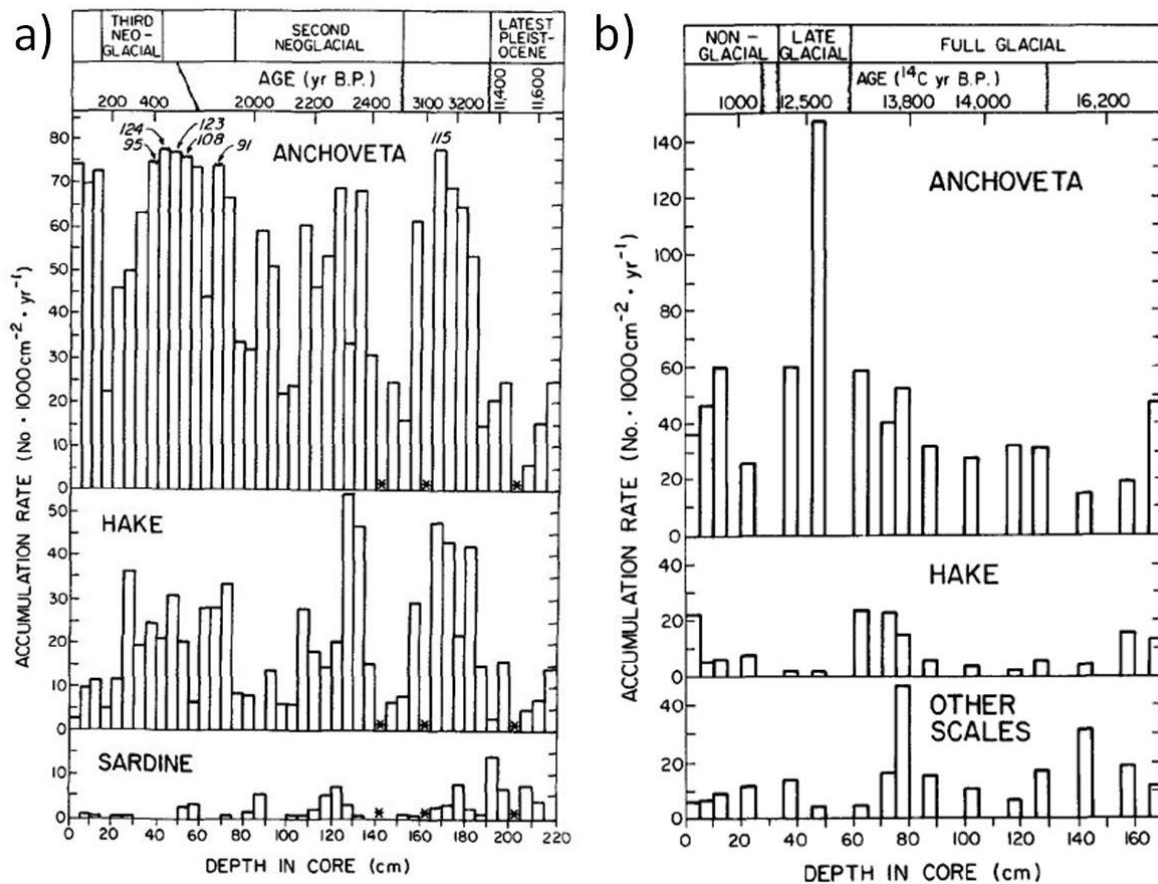
Figure I-12. Anchovy, hake sardine and other scales accumulation rates in two cores retrieved off central Peru. A) Core 7706-40 retrieved at ~11 °S and B) Core 7706-37 retrieved at ~13 °S. Figures were taken from DeVries and Pearcy (1982).

I-1.7. Summary of the global climatic changes since the Last Glacial Maximum

The Last Glacial Maximum (from 23 to 19 kyr cal BP) is the most recent interval when global ice sheets reached their maximum integrated volume during the last glaciations and caused profound climate changes around the world (Mix et al., 2001). During the Last Glacial Maximum the eustatic sea level was 125 ±5 m lower than the present day (Fleming et al., 1998) and consequently the

coastlines were different than today. The Eastern Tropical Pacific (ETP) experienced large changes in circulation and in oceanographic conditions: the ETP was 3-5 °C cooler than at present (Fig. I-13E), the Hadley and the Walker circulation were reduced, and the ITCZ was displaced to the south; all of these characteristics are consistent with an El Niño-like pattern in the Tropical Pacific (Feldberg and Mix, 2002; Koutavas et al., 2002). These observations in the Eastern Pacific are consistent with paleoceanographic studies in the Indo-Pacific Warm Pool (IPWP), where the SSTs during the Last Glacial Maximum were ~3 °C cooler than at present (Gagan et al., 2004; de Garidel-Thoron et al., 2007), indicating a cooler background level. Off Peru (~12 °S) SSTs reconstruction during the Last Glacial Maximum shows the lowest temperatures in the record (Fig. I-13F; Rein et al., 2005) which is also concordant with the low temperatures observed in the IPWP and the Eastern Tropical Pacific.

The last deglacial period (Termination 1, between the Last Glacial Maximum and the Holocene), was marked by large, hemispheric, millennial-scale climate variations: the Heinrich Event 1, the Bølling-Allerød and the Younger Dryas in the Northern Hemisphere, and the Antarctic Cold Reversal (ACR) in the Southern Hemisphere (Morgan et al., 2002; Fig. I-13). The Termination 1 is the last major climate transition of the Earth's recent geological history and is thus crucial for our understanding of modern climate processes and the validation of climate models (Lamy and Kaiser, 2009). During the period between ~18 – 14.5 kyr cal BP, a cold interval was observed in records from Greenland and other North Hemisphere records (Fig. I-13A). This period is called the Heinrich Stadial 1or the "Mystery Interval" (Denton et al., 2006), and contains the Heinrich event 1 characterized by a massive ice rafting episode (Bond et al., 1992; Barker et al., 2009). The Bølling-Allerød was warm event between the cold Heinrich 1 Stadial and the Younger Dryas (Fig. I-13A; Weaver et al., 2003). The Younger Dryas (12.9 – 11.7 kyr cal BP) was a millennial-duration cold snap that punctuated the termination of the last glacial period (Broecker et al., 2010). The Atlantic Meridional Overturning Circulation (AMOC) is widely believed to affect global climate and its strength was inferred using the ratio $^{231}Pa/^{230}Th$ in a sediment core from the subtropical North Atlantic Ocean (McManus et al., 2004). The reconstructed AMOC strength (Fig. I-13B) shows that this circulation was nearly eliminated during the coldest deglacial interval in the North Atlantic region (Heinrich 1 Stadial), show an abrupt resumption (~14.7 kyr cal BP) associated with the warm Bølling-Allerød, and showed low values again during the Younger Dryas (~12.7 kyr cal BP; McManus et al., 2004). In the Southern Hemisphere the ACR (Figs. I-13F and G; from 14 to 12.5 kyr cal BP) marks a period where the Antarctic deglacial warming trend pauses, beginning with a temperature maximum around 15 to 14 kyr cal BP and ending with resumption of warming ~1.5 kyr later (Jouzel et al., 1995; Blunier and Brooks, 2001; Morgan et al., 2002).

The warm climate of the Holocene (last 11.7 kyr BP) is generally viewed as climatically stable because there is little evidence of the abrupt millennial-scale climatic shift that characterized

glacial periods (Daansgard et al., 1993; deMenocal et al., 2000); however paleoclimatic and modeling studies indicate considerable global changes throughout the Holocene. Northern summer (July) insolation shows a maximum centered at about 10 kyr BP and has been declining ever since (Berger et al., 1998). The insolation maximum is associated with the Early Holocene Climatic Optimum (from ~10 to 6 kyr cal BP) observed in several high-latitudes records as for example the NGRIP ice core in Greenland (Fig. I-13A). This period was also marked by a northward displacement of the ITCZ as inferred by the Ti contents in sediments retrieved in the Cariaco Basin (Fig. I-13C; Haug et al., 2001). In Peru and Bolivia, the Lake Titicaca reached its lowest levels between 8 to 5.5 kyr BP which is consistent with an inferred dry condition in Peru during the Holocene Climatic Optimum (Baker et al., 2000). Additionally during the Early Holocene, alkenone SST records show high values off Peru (Rein et al., 2005; Chazen et al., 2009). The SST gradient in the Tropical Pacific also showed considerable changes throughout the Holocene implying large changes in ocean and atmospheric circulation. SST reconstructions in the Western Pacific Warm Pool (Kienast et al., 2001; Gagan et al., 2004; Linsley et al., 2010) and in the Cold tongue (Koutavas et al., 2002) show that during the Early and Mid Holocene, the SST gradient was higher in comparison to the deglaciation, implying a "La Niña-like" conditions (Figs. I-13D and E). Finally throughout the last 2000 years, warmer (the Roman Warm Period [RWP], the Medieval Climate Anomaly [MCA] and the Current Warm Period [CWP]), and colder (the Dark Ages Cold Period [DACP] and Little Ice Age [LIA]) intervals occurred with considerable changes around the globe (Mann et al., 2009; Graham et al., 2011; Yan et al., 2011).
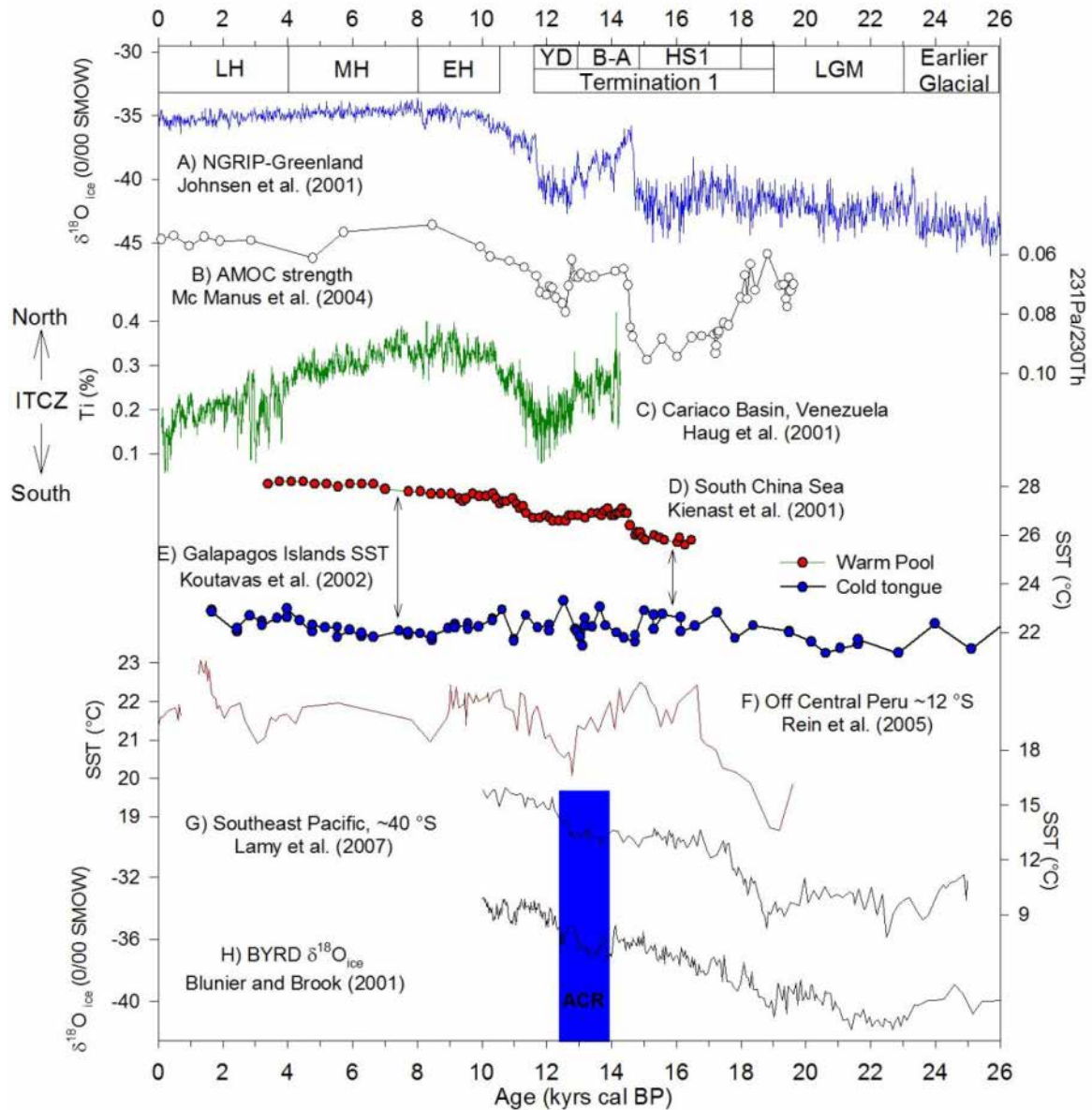
Figure I-13. A) Greenland temperature estimated by $\delta^{18}O$ in the GISP2 ice core (Johnsen et al., 2001). **B)** AMOC strength derived from sedimentary $^{231}Pa/^{230}Th$ ratio (Mc Manus et al., 2004). **C)** Titanium contents of Cariaco Basin sediments (~10 °N, Haug et al., 2001). **D)** SST reconstruction in South China Sea (Kienast et al., 2001). **E)** SST reconstruction off Galapagos Islands (Koutavas et al., 2002). **F)** Alkenone SST record off Central Peru (Rein et al., 2005). **G)** Alkenone SST record at ~ 40 °S (Lamy et al., 2007). **H)** West Antarctic temperatures estimated by $\delta^{18}O$, showing the cooling episode between ~14 to 12.5 kyr kyr named the Antarctic Cold Reversal (ACR, Blunier and Brook, 2001). The acronyms used are: Last Glacial Maximum (LGM), Heinrich 1 Stadial (H1S), Bølling-Allerød (B-A), Younger Dryas (YD), Early Holocene (EH), Mid-Holocene (MH) and Late Holocene (LH)

I-2. Scientific questions of the thesis

During the last decades the EBUEs are experiencing large changes in upwelling intensity and ocean productivity likely linked to current global change as evidenced by paleoceanographic reconstructions, observational data and analysis of satellite images (Bakun 1990; Jahncke et al. 2004;

McGregor et al., 2007; Vargas et al., 2007; Demarcq, 2009; Narayan et al., 2010; Leduc et al., 2010; Gutierrez et al., 2011). However, productivity cannot increase continuously, and feedbacks via denitrification or other processes will eventually rectify the system (Chavez et al., 2011). The PUE response to future climate scenarios indicate that surface along-shore winds off central Peru will weaken during austral summer (Goubanova et al., 2010; Echevin et al., 2011), which contradict the the mechanism proposed by Bakun (1990) explained in sub-chapter I-1.5. In a broader geographical area, climate model simulations indicate that the trade winds in the equatorial Pacific have weakened during the twentieth century in response to the progressive build up of atmospheric greenhouse gases (Vecchi et al., 2006), but recent studies indicate that there is no trend in the tropical Pacific Walker Circulation (Compo et al., 2011), or even that the tropical Pacific trade winds strengthened in the past two decades probably due to a warming of the Indian Ocean relative to the Pacific (Luo et al., 2012). Therefore, given the uncertainty of the the PUE and the tropical Pacific to the effects of global warming there is concern that the upwelling, primary productivity and fish biomass in the PUE may experience strong changes in the future as climate change proceeds.

Anchovy and sardine population response to future climatic change is also very uncertain. If local upwelling continues to intensify, then the rates of offshore transport and wind-driven turbulent mixing would also increase (Bakun and Weeks, 2008). One expected scenario under these conditions is that anchoveta dominance may give way to the sardine dominance that seems to characterize the other EBUS that are currently subject to relatively stronger winds and more intense turbulence generation (Bakun and Weeks, 2008). Alternatively, the increase in winds will push offshore the front between the subtropical oceanic waters and the coastal cold waters displacing the sardines offshore given the preference of sardine to subtropical oceanic waters. Thus, it is important to understand the response of anchovy and sardine populations to past climatic changes to know the natural range of biomass variability of these species. For example, the response of the PUE to the Little Ice Age period, included a weak OMZ, low export production, and very low anchovy and sardine abundances inferred by fish scale deposition rates (Gutierrez et al., 2009). Consequently, records that extend beyond the available historical period are needed to define variability that occurs over multi-decadal time scales in order to help understand the processes underlying fluctuations in fish stocks (Finney et al., 2010).

Studying the response of the PUE and particularly the response of the pelagic fishes to past climate changes during the last glacial and interglacial should give insights about the mechanism that controlled the changes in the PUE and the factors that affected the biomass fluctuations of these two species. In this thesis I propose a multi-proxy approach using paleontological techniques, organic and inorganic proxies to respond the following questions: **1) Which were the driving mechanisms originating the changes in OMZ intensity and export production off Peru during the last 25**

kyr?, and **2) which were the factors influencing anchovy and sardine fluctuations during the last 25 kyr?.** Productivity and OMZ intensity are taken as the factors that may principally influence anchovy and sardine fluctuations (Bertrand et al., 2011). SST is not taken into account as an important factor because anchovy and sardine can tolerate a wide range of temperature and several works raise the question about the role of temperature on anchovy and sardine fluctuations (Bertrand et al., 2004; 2011). By answering the questions proposed in this thesis we will be able to determine 1) if the changes in export production, the OMZ, and the pelagic abundance changes off Peru are better explained by northern hemisphere climate changes or by more regional processes, and 2) the role of productivity and OMZ in regulating the fluctuations of anchovy and sardine populations at different timescales.

The results of the thesis will serve to better understand the ecosystem variability and the physical regulating processes in the HCS. The good management of pelagic fisheries is strongly associated with understanding the natural response of pelagic stocks to the climate changes and the underlying mechanisms. While the year-to- year management does not require full understanding of the cause of the fluctuations in anchovy and sardine biomass in long time scales, long-term management and investment planning would certainly benefit from a model capable of predicting the long-term dynamics of anchovy and sardine with and without fishing, or as a combined outcome of the interacting drivers of fishing and the environment (Checkley et al., 2009). Moreover given the uncertainty of the response of the anchovy and sardine populations to future climate change, the study of past biomass fluctuations of these two species to northern hemisphere warm periods like the deglaciation, the early Holocene or the MCA, may give important insight, although the causes of the warming are different in each of the different periods. Additionally, the response of the upwelling ecosystem, the export production, and the OMZ intensity off Peru to the increase in Southern Hemisphere summer insolation from the Early Holocene to the present, will illustrate the fundamental mechanisms behind the natural responses of anchovy and sardine under climate mean state changes.

I-3. Bibliography

Agnihotri, R., M. A. Altabet, T. Herbert, and J. E. Tierney. 2008. Subdecadally resolved paleoceanography of the Peru margin during the last two millennia. Geochemistry Geophysics Geosystems 9(5):1-15.

Alheit, J. 1987. Egg cannibalism versus egg predation: their significance in anchovies. South African Journal of Marine Science 5:467-470.

Alheit, J., and M. Ñiquen. 2004. Regime shifts in the Humboldt Current ecosystem. Progress in Oceanography 60:201-222.

Alheit, J., and A. Bakun. 2010. Population synchronies within and between ocean basins: Apparent teleconnections and implications as to physical–biological linkage mechanisms. Journal of Marine Systems 79(3-4):267-285.-285.

Ashok, K., S. K. Behera, S. A. Rao, H. Weng, and T. Yamagata. 2007. El Niño Modoki and its possible teleconnection. Journal of Geophysical Research 112:C11007.

Ayón, P., G. Swartzman, P. Espinoza, and A. Bertrand. 2011. Long-term changes in zooplankton size distribution in the Peruvian Humboldt Current System: conditions favouring sardine or anchovy. Marine Ecology Progress Series 422:211-222.

Baker, P. A., G. O. Seltzer, S. C. Fritz, R. B. Dunbar, M. J. Grove, P. M. Tapia, S. L. Cross, H. D. Rowe, and J. P. Broda. 2001. The history of South American tropical precipitation for the past 25,000 years. Science 291(5504):640-643.

Bakun, A. 1990. Global climate change and intensification of coastal upwelling. Science 247(4939):198-201.

Bakun, A., and K. Broad. 2003. Environmental 'loopholes' and fish population dynamics: comparative pattern recognition with focus on El Niño effects in the Pacific. Fisheries Oceanography 12(4/5):458-473.

Bakun, A., and S. J. Weeks. 2008. The marine ecosystem off Peru: What are the secrets of its fishery productivity and what might its future hold? Progress in Oceanography 79:290-299.

Bakun, A., D. Field, A. Redondo-Rodriguez, and S. J. Weeks. 2010. Greenhouse gas, upwelling-favorable winds, and the future of coastal ocean upwelling ecosystems. Global Change Biology 16:1213-1228.

Barber, R. T., and F. Chavez. 1983. Biological consequences of El Niño. Science 222:1203-1210.

Barker, S., P. Diz, M. J. Vautravers, J. Pike, G. Knorr, I. R. Hall, and W. S. Broecker. 2009. Interhemispheric Atlantic seesaw response during the last deglaciation. Nature 457:1097-1102.

Baumgartner, T. R., V. Ferreira-Bartrina, J. Cowen, and A. Soutar. 1991. Reconstruction of a 20th century varve chronology from the central Gulf of California. The Gulf and Peninsular Province of the Californias.

Baumgartner, T., A. Soutar, and V. Ferreira-Bartrina. 1992. Reconstruction of the history of pacific sardine and northern anchovy populations over the past two millennia from sediments of the Santa Barbara basin, California. CalCOFI Rep. 33:24-40.

Behrenfeld, R. T., and P. G. Falkowski. 1997. Photosynthetic rates derived from satellite-based chlorophyll concentration. Limnology and Oceanography 42:1-20.

Berger, A. 1988. Milankovitch Theory and climate. Reviews of Geophysics 26(4):624-657.

Bertrand, A., M. Segura, M. Gutiérrez, and L. Vásquez. 2004. From small-scale habitat loopholes to decadal cycles: a habitat-based hypothesis explaining fluctuation in pelagic fish populations off Peru. Fish and Fisheries 5:296-316.

Bertrand, A., A. Chaigneau, S. Peraltilla, J. Ledesma, M. Graco, F. Monetti, and F. Chavez. 2011. Oxygen: A Fundamental Property Regulating Pelagic Ecosystem Structure in the Coastal Southeastern Tropical Pacific. PLoS ONE 6(12):e29558.

Biondi, F., C. B. Lange, M. K. Hughes, and W. H. Berger. 1997. Inter-decadal signals during the last millennium (AD 1117-1992) in the varve record of Santa Barbara basin, California. Geophysical Research Letters 24(2):193-196.

Blunier, T. and E. J. Brook 2001. Timing of Millennial-Scale Climate Change in Antarctica and Greenland During the Last Glacial Period. Science 291(5501): 109-112.

Bond, G., H. Heinrich, W. S. Broecker, L. Labeyrie, J. McManus, J. Andrews, S. Huon, R. Jantschik, S. Clasen, C. Simet, K. Tedesco, M. Klas, G. Bonani, and S. Ivy. 1992. Evidence for massive discharge of icebergs into the glacial Northern Atlantic. Nature 360:245-249.

Broecker, W. S., G. H. Denton, R. Lawrence Edwards, H. Cheng, R. B. Alley, and A. E. Putnam. 2010. Putting the Younger Dryas cold event into context. Quaternary Science Reviews 29:1078-1081.

Carr, M.-E. 2002. Estimation of potential productivity in Eastern Boundary Currents using remote sensing. Deep-Sea Research Part II 49:59-80.

Chavez, F., J. Ryan, S. Lluch-Cota, and M. Niquen. 2003. From Anchovies to Sardines and Back: Multidecadal Change in the Pacific Ocean. Science 299:217-221.

Chavez, F., A. Bertrand, R. Guevara-Carrasco, P. Soler, and J. Csirke. 2008. The northern Humboldt Current System: Brief history, present status and a view towards the future. Progress in Oceanography 79:95-105.

Chavez, F. P., and M. Messié. 2009. A comparison of Eastern Boundary Upwelling Ecosystems. Progress in Oceanography 83(1-4):80-96.

Chavez, F. P., M. Messie, and J. T. Pennington. 2011. Marine Primary Production in Relation to Climate Variability and Change. Annu. Rev. Mar. Sci. 3:227-260.

Chazen, C. R., M. A. Altabet, and T. D. Herbert. 2009. Abrupt mid-Holocene onset of centennial-scale climate variability on the Peru-Chile Margin. Geophysical Research Letters 36:L18704.

Checkley, D. M., A. Bakun, M. Barange, L. R. Castro, P. Freon, R. Guevara-Carrasco, S. F. Herrick, A. D. MacCall, R. Ommer, Y. Oozeki, C. Roy, L. Shannon, and C. D. van der Lingen. 2009. Synthesis and perspectives. *In* D. Checkley, C. Roy, J. Alheit, and Y. Oozeki, eds. Climate change and small pelagic fish. Cambridge University Press.

Codispoti, L. A., R. T. Barber, and G. E. Friederich. 1989. Do nitrogen transformations in the Poleward Undercurrent off Peru and Chile have a globally significant influence? Pp. 281-314. In S. J. Neshyba, ed. Poleward Flows Along Eastern Ocean Boundaries, Coastal Estuarine Studies.

Compo, G. P., J. S. Whitaker, P. D. Sardeshmukh, N. Matsui, R. J. Allan, X. Yin, B. E. Gleason, R. S. Vose, G. Rutledge, P. Bessemoulin, S. Brönnimann, M. Brunet, R. I. Crouthamel, A. N. Grant, P. Y. Groisman, P. D. Jones, M. C. Kruk, A. C. Kruger, G. J. Marshall, M. Maugeri, H. Y. Mok, Ø. Nordli, T. F. Ross, R. M. Trigo, X. L. Wang, S. D. Woodruff, and S. J. Worley. 2011. The Twentieth Century Reanalysis Project. Quarterly Journal of the Royal Meteorological Society Part A 137(654):1-28.

Dansgaard, W., S. J. Johnsen, H. B. Clausen, D. Dahl-Jensen, N. S. Gundestrup, C. U. Hammer, C. S. Hvidberg, J. P. Steffensen, A. E. Sveinbjörnsdottir, J. Jouzel, and G. Bond. 1993. Evidence for general instability of past climate from a 250-kyr ice-core record. Nature 364:218-220.

de Garidel-Thoron, T., Y. Rosenthal, L. Beaufort, E. Bard, C. Sonzogni, and A. C. Mix. 2007. A multiproxy assessment of the western equatorial Pacific hydrography during the last 30 kyr. Paleoceanography 22:PA3204.

De Vries, T., and W. Pearcy. 1982. Fish debris in sediments of the upwelling zone off central Peru: a late Quaternary record. Deep-Sea Research 28:87-109.

Demarcq, H. 2009. Trends in primary production, sea surface temperature and wind in upwelling systems (1998–2007). Progress in Oceanography 83:376-385.

deMenocal, P., J. Ortiz, T. Guilderson, and M. Sarnthein. 2000. Coherent High- and Low-Latitude Climate Variability During the Holocene Warm Period. Science 288:2198-2202.

Denton, G. H., W. S. Broecker, and R. B. Alley. 2006. The Mystery Interval 17.5 to 14.5 kyrs ago. PAGES News 14:14-16.

Dewitte, B., J. Vazquez-Cuervo, K. Goubanova, S. Illig, K. Takahashi, G. Cambon, S. Purca, D. Correa, D. Gutierrez, A. Sifeddine, and L. Ortlieb. 2012. Changes in el Niño flavours over 1958-2008: Implications for the long-term trend of the upwelling off Peru. Deep-Sea Research II 77-80:143-156.

Diaz-Ochoa, J. A., C. B. Lange, S. Pantoja, G. J. De Lange, D. Gutierrez, P. Muñoz, and M. Salamanca. 2008. Fish scales in sediments from off Callao, central Peru. Deep-Sea Research Part II 56:1124–1135.

Echevin, V., K. Goubanova, A. Belmadani, and B. Dewitte. 2011. Sensitivity of the Humboldt Current system to global warming: a downscaling experiment of the IPSL-CM4 model. Climate Dynamics.

Espinoza, P., A. Bertrand, C. D. van der Lingen, S. Garrido, and B. Rojas de Mendiola. 2009. Diet of sardine (Sardinops sagax) in the northern Humboldt Current system and comparison with the diets of clupeoids in this and other eastern boundary upwelling systems. Progress in Oceanography 83:242-250.

Espinoza, P., and A. Bertrand. 2008. Revisiting Peruvian anchovy (*Engraulis ringens*) trophodynamics provides a new vision of the Humboldt Current system. Progress in Oceanography 79:215-227.

Falvey, M., and R. D. Garreaud. 2008. Regional cooling in a warming world: Recent temperature trends in the southeast Pacific and along the west coast of subtropical South America (1979–2006). Journal of Geophysical Research 114:D04102.

Feldberg, M. J., and A. C. Mix. 2002. Sea-surface temperature estimates in the Southeast Pacific based on planktonic foraminiferal species; modern calibration and Last Glacial Maximum. Marine Micropaleontology 44:1-29.

Field, D., and T. Baumgartner. 2000. A 900 year stable isotope record of interdecadal and centennial change from the California Current Paleoceanography 15(6):695-708.

Field, D. B., T. R. Baumgartner, V. Ferreira, D. Gutierrez, H. Lozano-Montes, R. Salvatteci, and A. Soutar. 2009. Variability from scales in marine sediments and other historical records. Pp. 45-63. In D. Checkley, C. Roy, J. Alheit, and Y. Oozeki, eds. Climate Change and Small Pelagic Fish. Cambridge University Press.

Finney, B. P., J. Alheit, K. C. Emeis, D. B. Field, D. Gutierrez, and U. Struck. 2010. Paleoecological studies on variability in marine fish populations: A long-term perspective on the impacts of climatic change on marine ecosystems. Journal of Marine Systems 79(3-4):316-326.

Fleming, K., P. Johnston, D. Zwartz, Y. Yokoyama, K. Lambeck, and J. Chappell. 1998. Refining the eustatic sea-level curve since the Last Glacial Maximum using far- and intermediate-field sites. Earth and Planetary Science Letters 163(1-4):327-342.

Gagan, M. K., E. J. Hendy, S. G. Haberle, and W. S. Hantoro. 2004. Post-glacial evolution of the Indo-Pacific Warm Pool and El Niño-Southern oscillation. Quaternary International 118-119:127-143.

Goubanova, K., V. Echevin, B. Dewitte, F. Codron, K. Takahashi, P. Terray, and M. Vrac. 2010. Statistical downscaling of sea-surface wind over the Peru–Chile upwelling region: diagnosing the impact of climate change from the IPSL-CM4 model. Climate Dynamics. doi: 10.1007/s00382-010-0824-0

Graham, N. E., C. M. Ammann, D. Fleitmann, K. M. Cobb, and J. Luterbacher. 2011. Support for global climate reorganization during the ''Medieval Climate Anomaly''. Climate Dynamics 37:1217-1245.

Gutierrez, D., A. Sifeddine, J. L. Reyss, G. Vargas, F. Velazco, R. Salvatteci, V. Ferreira-Bartrina, L. Ortlieb, D. Field, T. Baumgartner, M. Boussafir, H. Boucher, J. Valdes, L. Marinovic, P. Soler, and P. Tapia. 2006. Anoxic sediments off Central Peru record interannual to multidecadal changes of climate and upwelling ecosystems during the last two centuries. Advances in Geosciences 6:119-125.

Gutierrez, M., G. Swartzman, A. Bertrand, and S. Bertrand. 2007. Anchovy (*Engraulis ringens*) and sardine (*Sardinops sagax*) spatial dynamics and aggregation patterns in the Humboldt Current ecosystem, Peru, from 1983–2003. Fisheries Oceanography 16(2):155-168.

Gutierrez, D., A. Sifeddine, D. B. Field, L. Ortlieb, G. Vargas, F. Chavez, F. Velazco, V. Ferreira, P. Tapia, R. Salvatteci, H. Boucher, M. C. Morales, J. Valdes, J. L. Reyss, A. Campusano, M. Boussafir, M. Mandeng-Yogo, M. Garcia, and T. Baumgartner. 2009. Rapid reorganization in ocean biogeochemistry off Peru towards the end of the Little Ice Age. Biogeosciences 6:835-848.

Gutierrez, D., I. Bouloubassi, A. Sifeddine, S. Purca, K. Goubanova, M. Graco, D. Field, L. Méjanelle, F. Velazco, A. Lorre, R. Salvatteci, D. Quispe, G. Vargas, B. Dewitte, and L. Ortlieb. 2011. Coastal cooling and increased productivity in the main upwelling zone off Peru since the mid-twentieth century. Geophysical Research Letters 38:L07603.

Haug, G. H., K. A. Hughen, D. M. Sigman, L. C. Peterson, and U. Rohl. 2001. Southward Migration of the Intertropical Convergence Zone Through the Holocene. Science 293:1304-1308.

Helly, J., and L. Levin. 2004. Global distribution of naturally occurring marine hypoxia on continental margin. Deep-Sea Research I 51:1159-1168.

Jahncke, J., D. M. Checkley, and G. L. Hunt. 2004. Trends in carbon flux to seabirds in the Peruvian upwelling system: effects of wind and fisheries on population regulation. Fisheries Oceanography 13(3):208-223.

Jouzel, J., R. Vaikmae, J. R. Petit, M. Martin, Y. Duclos, M. Stievenard, C. Lorius, M. Toots, M. A. Melieres, H. Burckle, N. I. Barkov, and V. M. Kotlyakov. 1995. The two-step shape and timing of the last deglaciation in Antarctica. Climate Dynamics 11(3):151-161.

Kao, H.-Y., and J.-Y. Yu. 2009. Contrasting Eastern-Pacific and Central-Pacific types of ENSO. Journal of Climate 22:615-632.

Kienast, M., S. Steinke, K. Stattegger, and S. E. Calvert. 2001. Synchronous tropical South China Sea SST change and Greenland warming during deglaciation. Science 291:2132-2134.

Koutavas, A., J. Lynch-Stieglitz, T. M. Marchitto, and J. P. Sachs. 2002. El Niño-like pattern in ice age tropical Pacific sea surface temperature. Science 297(5579):226-230.

Krissek, L. A., and K. F. Scheidegger. 1983. Environmental controls on sediment texture and composition in low oxygen zones off Peru and Oregon. Pp. 163-180. *In* E. Suess, and J. Thiede, eds. Coastal upwelling, its sediment record, Part B: Sedimentary records of ancient coastal upwelling. Plenum Press, New York.

Lamy, F., and J. Kaiser. 2009. Glacial to Holocene Paleoceanographic and Continental Paleoclimate Reconstructions Based on ODP Site 1233/GeoB 3313 Off Southern Chile Developments in Paleoenvironmental Research 14(Part 1):129-156.

Lamy, F., J. Kaiser, H. W. Arz, D. Hebbeln, U. Ninnnemann, O. Timm, A. Timmermann, and J. R. Toggweiler. 2007. Modulation of the bipolar seesaw in the Southeast Pacific during Termination 1. Earth and Planetary Science Letters 259:400-413.

Leduc, G., T. Herbert, T. Blanz, P. Martinez, and R. Schneider. 2010. Contrasting evolution of sea surface temperature in the Benguela upwelling system under natural and anthropogenic climate forcings. Geophysical Research Letters 37:L20705.

Linsley, B., Y. Rosenthal, and D. W. Oppo. 2010. Holocene evolution of the Indonesian throughflow and the western Pacific warm pool. Nature Geoscience 3:578-583.

Luo, J.-J., W. Sasaki, and Y. Masumoto. 2012. Indian Ocean warming modulates Pacific climate change. PNAS Early Edition.

Mann, M. E., Z. Zhang, S. Rutherford, R. S. Bradley, M. K. Hughes, D. Shindell, C. Ammann, G. Faluvegi, and F. Ni. 2009. Global Signatures and Dynamical Origins of the Little Ice Age and Medieval Climate Anomaly. Science 326:1256-1260.

McGregor, H. V., M. Dima, H. W. Fischer, and S. Mulitza. 2007. Rapid 20th-Century Increase in Coastal Upwelling off Northwest Africa. Science 315:637-639.

McManus, J. F., R. Francois, J.-M. Gherardi, L. D. Keigwin, and S. Brown-Leger. 2004. Collapse and rapid resumption of Atlantic meridional circulation linked to deglacial climate changes. Nature 428:834-837.

Messié, M., J. Ledesma, D. D. Kolber, R. P. Michisaki, D. G. Foley, and F. P. Chavez. 2009. Potential new production estimates in four eastern boundary upwelling ecosystems. Progress in Oceanography 83:151-158.

Mix, A. C., E. Bard, and R. Schneider. 2001. Environmental processes of the ice age: land, oceans, glaciers (EPILOG). Quaternary Science Reviews 20:627-657.

Montes, I., F. Colas, X. Capet, and W. Schneider. 2010. On the pathways of the equatorial subsurface currents in the eastern equatorial Pacific and their contributions to the Peru-Chile Undercurrent. Journal of Geophysical Research 115:C09003.

Morgan, V., M. Delmotte, T. van Ommen, J. Jouzel, J. Chappellaz, S. Woon, V. Masson-Delmotte, and D. Raynaud. 2002. Relative Timing of Deglacial Climate Events in Antarctica and Greenland. Science 297:1862-1864.

Moron, O., W. Garcia, and M. Sarmiento. in prep. Promedios y variabilidad interanual de la salinidad frente a la costa peruana.

Narayan, N., A. Paul, S. Mulitza, and M. Schulz. 2010. Trends in coastal upwelling intensity during the late 20th century. Ocean Science 6:815-823.

Ñiquen, M., and M. Bouchon. 2004. Impact of El Niño events on pelagic fisheries in Peruvian waters. Deep-Sea Research II 51:563-574.

Paulmier, A., and D. Ruiz-Pino. 2009. Oxygen minimum zones (OMZs) in the modern ocean. Progress in Oceanography 80:113-128.

Pauly, D., and V. Christensen. 1995. Primary production required to sustain global fisheries. Nature 374:255-257.

Pennington, J. T., K. L. Mahoney, V. S. Kuwahara, D. D. Kolber, R. Calienes, and F. P. Chavez. 2006. Primary production in the eastern tropical Pacific: A review. Progress in Oceanography 69:285-317.

Rein, B., A. Lückge, L. Reinhardt, F. Sirocko, A. Wolfe, and W.-C. Dullo. 2005. El Niño variability off Peru during the last 20,000 years. Paleoceanography 20:PA4003.

Reinhardt, L., H.-R. Kudrasss, A. Lückge, M. Wiedicke, J. Wunderlich, and G. Wendt. 2002. High-resolution sediment echosounding off Peru: Late Quaternary depositional sequences and sedimentary structures of a current-dominated shelf Marine Geophysical Researches 23(4):335-351.

Rutlant, J. A. 1990. Natural desertification mechanisms along the arid west coast of South America. Pp. 235-253. Proc. International Workshop on Sand Transport and Desertification in Arid Lands. Khartoum (Sudan).

Salvatteci, R., D. B. Field, T. Baumgartner, V. Ferreira, and D. Gutierrez. 2012. Evaluating fish scale preservation in sediment records from the oxygen minimum zone off Peru. Paleobiology 38(1):766-792.

Sanchez, G., R. Calienes, and S. Zuta. 2000. The 1997-98 El Niño and its effects on the coastal marine ecosystem off Peru. CalCOFI Rep. 41:62-86.

Schimmelmann, A., C. B. Lange, E. B. Roark, and B. L. Ingram. 2006. Resources for paleoceanographic and paleoclimatic analysis: a 6,700-year stratigraphy and regional radiocarbon reservoir-age (DR) record based on varve counting and 14C-AMS dating for the Santa Barbara basin, offshore California, U.S.A. Journal of Sedimentary Research 76:74-80.

Schwartzlose, R. A., J. Alheit, A. Bakun, T. R. Baumgartner, R. Cloete, R. J. M. Crawford, W. J. Fletcher, Y. Green-Ruiz, E. Hagen, T. Kawasaki, D. Lluch-Belda, S. E. Lluch-Cota, A. D. MacCall, Y. Matsuura, M. O. Nevarez-Martinez, R. H. Parrish, C. Roy, R. Serra, K. V. Shust, M. N. Ward, and J. Z. Zuzunaga. 1999. Worldwide large-scale fluctuations of sardine and anchovy populations. South African Journal of Marine Science 21:289-347.

Sifeddine, A., D. Gutierrez, L. Ortlieb, H. Boucher, F. Velazco, D. Field, G. Vargas, M. Boussafir, R. Salvatteci, V. Ferreira, M. García, J. Valdes, S. Caquineau, M. Mandeng-Yogo, F. Cetin, J. Solis, P. Soler, and T. Baumgartner. 2008. Laminated sediments from the central Peruvian continental slope: A 500 year record of upwelling system productivity, terrestrial runoff and redox conditions. Progress in Oceanography 79:190–197.

Soutar, A., and J. Isaacs. 1974. Abundance of pelagic fish during the 19th and 20th century as recorded in anaerobic sediment off the Californias. Fisheries Bulletin 72:257-273.

Soutar, A., and P. A. Crill. 1977. Sedimentation and climatic patterns in the Santa Barbara Basin during the 19th and 20th centuries. Geol.Soc. Am. Bull. 88:1161-1172.

Stramma, L., G. C. Johnson, J. Sprintall, and V. Mohrholz. 2008. Expanding Oxygen-Minimum Zones in the Tropical Oceans. Science 320(5876):655-658.

Strub, P. T., J. M. Mesias, V. Montecino, J. Rutllant, and S. Salinas. 1998. Coastal ocean circulation off Western South America. Coastal segment (6,E). Pp. 273-313. In A. Robinson, and K. Brink, eds. The Sea. John Wiley & Sons, Inc., New York.

Swartzman, G., A. Bertrand, M. Gutiérrez, S. Bertrand, and L. Vasquez. 2008. The relationship of anchovy and sardine to water masses in the Peruvian Humboldt Current System from 1983 to 2005. Progress in Oceanography 79:228-237

Ulloa, O., and S. Pantoja. 2009. The oxygen minimum zone of the eastern South Pacific. Deep-Sea Research II 56:987-991.

Valdés, J., L. Ortlieb, D. Gutierrez, L. Marinovic, G. Vargas, and A. Sifeddine. 2008. 250 years of sardine and anchovy scale deposition record in Mejillones Bay, northern Chile. Progress in Oceanography 79:198-207.

Vargas, G., S. Pantoja, J. A. Rutlant, C. Lange, and L. Ortlieb. 2007. Enhancement of coastal upwelling and interdecadal ENSO-like variability in the Peru-Chile Current since late 19th century. Geophysical Research Letters 34.

Vecchi, G. A., B. Soden, A. T. Wittenberg, I. M. Held, A. Leetmaa, and M. J. Harrison. 2006. Weakening of tropical Pacific atmospheric circulation due to anthropogenic forcing. Nature 44:73-76.

Weaver, A. J., O. A. Saenko, P. U. Clark, and J. X. Mitrovica. 2003. Meltwater Pulse 1A from Antarctica as a Trigger of the Bølling-Allerød Warm Interval. Science 299(5613):1709-1713.

Yan, H., L. Sun, Y. Wang, W. Huang, S. Qiu, and C. Yang. 2011. A record of the Southern Oscillation Index for the past 2,000 years from precipitation proxies. Nature geoscience 4:611-614.

CHAPTER II:

CROSS-STRATIGRAPHIES FROM A SEISMICALLY ACTIVE MUD LENS OFF PERU INDICATE HORIZONTAL EXTENSIONS OF LAMINAE, MISSING SEQUENCES, AND A NEED FOR MULTIPLE CORES FOR HIGH RESOLUTION RECORDS

Renato Salvatteci[1,2], David Field[3], Abdel Sifeddine[1,4], Luc Ortlieb[1], Vicente Ferreira[5], Tim Baumgartner[5], Sandrine Caquineau[1], Federico Velazco[2], Jean-Louis Reyss[6], Joan Albert Sanchez-Cabeza[7,8], Dimitri Gutierrez[1,9]

Affiliations:

1 LOCEAN, UMR 7159 (IRD, CNRS, UPMC, MNHN), Institut Pierre Simon Laplace, Laboratoire d'Océanographie et du Climat: Expérimentations et Analyses Numériques. Centre IRD France Nord, 32 avenue Henri Varagnat, 93143 Bondy cedex, France

2 Instituto del Mar del Perú, Esquina Gamarra y General Valle s/n, Callao, 22000 Perú

3 Hawaii Pacific University, College of Natural Sciences, 45-045 Kamehameha Highway, Kaneohe, Hawaii, 96744-5297

4 Departamento de Geoquimica, Universidade Federal Fluminense, Niteroi, Brasil.

5 Centro de Investigación Científica y de Educación Superior de Ensenada, Apartado Postal 2732, Ensenada, Baja California C.P., 22860, México

6 Laboratoire des Sciences de Climat et de l'Environnement, UMR CEA – CNRS-Univ. Versailles-Saint Quentin en Yveline, 91 198 Gif-sur-Yvette, France

7 Instituto de Ciencias de Mar y Limnología, Universidad Nacional Autónoma de México, Ciudad Universitaria, 04510 Ciudad de México, Distrito Federal, México.

8 Institut de Ciència i Tecnologia Ambientals, and Departament de Fisica, Universitat Autonoma de Barcelona, 08193 Bellaterra, Spain.

9 Programa Maestría en Ciencias del Mar, Universidad Peruana Cayetano Heredia, Lima, Perú.

II-1. Abstract

Marine laminated sediments that accumulate over time in disoxic areas of the ocean floor are an excellent archive for high-resolution climate reconstructions. While the existence of discontinuities produced by natural events such as strong bottom currents, bioturbation or lateral depositions are usually acknowledged, particularly for long records, the extent of their influence on high-resolution sequences is not carefully considered. In the present work we show widespread evidence for stratigraphic discontinuities from multiple gravity and box-cores retrieved off Pisco (Peru). Chronostratigraphies are largely based on correlation of distinct sedimentary structures (determined by X-ray image analysis) and validated using ^{210}Pb, ^{241}Am, and ^{14}C profiles, as well as proxy records. The lateral correlation of distinct stratigraphic layers clearly shows that some sedimentary sequences are continuous across scales of tens of kilometers, indicating that regional processes often determine laminae formation. However, some laminated sequences visible in some cores are notably lacking in other cores. These discontinuities may frequently be due to erosion caused by slumps, possibly triggered by tsunamogenic earthquakes. However erosion caused by bottom currents, spatial variability distribution in deposition events (e.g. diatom blooms) and other factors may account for the differences among cores. In spite of the missing sequences in some cores, a continuous composite record of the last several centuries was reconstructed from spliced sequences of the different cores, which provides a well constrained temporal framework to develop further high resolution proxies in this region. Proxy records developed from single cores, particularly in areas with steep slopes and seismic instabilities, are subject to both temporal gaps and instantaneous depositions from upslope, which could commonly be inferred to represent abrupt changes or anomalous climate events. Thus, the results of the present work indicate the need for multiple cores for determining whether high-resolution records are continuous and establishing chronologies for such records, while much greater caution is needed for interpreting paleo records from a single core.

Keywords: High-resolution records; Laminated sediments; Hiatus; Slumps; lateral correlation; Composite record

II-2. Introduction

Marine laminated sediments that accumulate over time on the ocean floor are an excellent archive of past climate variability with high temporal resolution. Continuous sequences necessary for high resolution reconstructions require an accurate chronological model which is usually based on natural (^{210}Pb and ^{14}C) and artificial (^{241}Am and ^{137}Cs) radionuclides from nuclear weapons testing fallout, as well as varve counts and extrapolation of sedimentation rates (Appleby, 2001; 2008; Kirchner, 2011; Sanchez-Cabeza and Ruiz-Fernández, 2012). While considerable effort is usually

made to construct chronological models; stratigraphic continuity of the sediments is often assumed, despite evidence for discontinuities in some settings. For example, careful examination of annually laminated sediments off Guaymas (Gulf of California) clearly showed that stratigraphic disruptions and missing laminae within a sequence occurs in every core taken (Baumgartner et al., 1991). Widespread evidence for discontinuities on longer timescales (late Pleistocene and Holocene) off Peru has also been noticed (De Vries and Pearcy, 1982; Reinhardt et al., 2002; Skilbeck and Flink, 2006). Therefore, the development of stratigraphic sequences from multiple cores in one particular region is desirable to infer the sub decadal and decadal-scale variability of any proxy, avoiding the misleading interpretations arising from only one record (Baumgartner et al., 1991; Field et al. 2009). In the present work we used 8 sediment cores taken off Pisco, Peru to i) document the stratigraphic continuity between sites, ii) determine the continuity or discontinuities of the records, and iii) develop a high resolution composite sequence derived from cross stratigraphy among cores, using prominent laminae and radionuclides (^{241}Am, ^{210}Pb and ^{14}C) as markers, covering the last ~600 years. We show clear evidence of widespread and frequent discontinuities that are only apparent after detailed comparisons among cores.

Correlations of prominent laminae and discontinuities between cores in Guaymas and the Santa Barbara Basin indicate considerable variability in laminae sequences with many slumps that are not resolvable with single cores (Baumgartner et al., 1991; Schimmelmann et al., 2006; Field et al. 2009). The correlation of laminae sequences off Guaymas among five box-cores taken along the Guaymas slope reveal multiple small-scale, secondary mass movements that disrupted the varve record throughout the 20th century at each of the core sites (Baumgartner et al., 1991). However, only one discontinuity (associated with a large-magnitude earthquake occurred in 1907) was present in all cores, which helped constrain the development of a continuous varve chronostratigraphy from spliced segments (Baumgartner et al., 1991). The correlation of laminae sequences off Santa Barbara also show slumps of varying thickness, which indicates that they are instantaneous deposits from upslope rather than bioturbation events (Field et al., 2009). At both sites, some laminae are present or better preserved in some cores, while they are absent in others (Baumgartner et al., 1991; Field et al., 2009). Therefore, it is clear that variations between cores exist, although the extent of such variations in different environments is not established.

Paleoceanographic studies by Gutierrez et al. (2009) on sediment cores off Peru and Northern Chile retrieved within the Oxygen Minimum Zone (OMZ) show the potential to replicate decadal to multidecadal scale changes as the sediments are laminated, but not annually varved (though this might occur occasionally). However, numerous sediment cores retrieved off Peru covering the Late Pleistocene and the Holocene periods reveal widespread occurrences of large discontinuities. For example cores retrieved off Callao show hiatuses of up to 9 kyr between 13 to ~4 kyr BP (De Vries

and Pearcy, 1982; Skilbeck and Flink, 2006; Makou et al., 2010) or perhaps very low sedimentation rates between ~9 to 4 kyr BP (Rein et al., 2005). The only known sediment core off Peru with presumed continuous sedimentation from ~10 kyr BP to 1.5 kyr BP was reported by Chazen et al. (2009), but unfortunately only one ^{14}C date was determined during the period where the hiatuses in other cores were identified (~5 – ~8 kyr BP), and no X-ray images were shown in this work. The discontinuities are not limited to the late- to mid-Holocene period, since older sediments also show hiatuses (Reinhardt et al., 2002; Contreras et al., 2011).

The principal factors affecting the records continuity off Peru are lateral depositions of sediments from upslope and/or down slope sediment slumps (Duperret et al., 1995; Greene et al., 2006; Field et al., 2009; Shanmugam, 2010), changes in the intensity of the poleward undercurrent (Suess et al., 1987; Reinhardt et al., 2002) and periodic bioturbation events (Kim and Burnett, 1988; Levin et al., 2003). The extent of the influence of these events on high-resolution sequences has not been well documented in order to develop chronological models for high resolution studies.

Strong seismic events induce gravity instability in the sedimentary sequences (Duperret et al., 1995; Blais-Stevens and Clague, 2001; Schnellmann et al., 2002; Vargas et al., 2005; Greene et al., 2006; Goldfinger, 2010), triggering slumps especially in steep platforms. The plate boundary between the South American plate and the subducting Nazca plate along the coast of Peru is one of the most active subduction zones and subject to large destructive earthquakes (Audin et al., 2008). Recorded historical earthquakes (M_w> 7.5) that had their ruptures zones near the Pisco area occurred in 1586, 1604, 1664, 1687, 1746, 1784, 1868, 1942, 1974, 1996 and 2001 AD (Dorbath et al., 1990; Giovanni et al., 2002; Okal et al., 2006) and at least four of them (1604, 1687, 1746 and 1868), which were the most intense ones (Mw = 8.7, 8.4, 8.6 and 8.8 respectively), were tsunamogenic and caused major destruction of Pisco city.

The poleward undercurrent off Peru, coinciding with the sea floor between ~150 m to ~ 400 m, is exceptionally strong during El Niño events (Hill et al., 1998) and has been inferred to generate erosional unconformities, winnowing of the sediments and to have created mudwaves between 250 m to 400 m (Reinhardt et al., 2002). The discontinuities during the late Pleistocene and early to mid-Holocene have been attributed to variations in the activity of the poleward undercurrent causing sediment erosion and sediment redistribution (Suess et al., 1987; Reinhardt et al., 2002; Skilbeck and Flink, 2006). Thus, temporal changes in strength and size of the poleward undercurrent may cause discontinuities in the sediment records. In contrast, bioturbation disturbs the continuity of the laminated sequences but generally does not result in a loss of material.

The OMZ intensity may vary on seasonal to inter annual-scale (Gutierrez et al., 2008) inducing sediment mixing by benthic fauna in shallower cores (Kim and Burnett, 1988, Levin et al., 2003). For example during the strong El Niño event of 1997-98 the upper boundary of the OMZ deepened to 250 m allowing the presence of benthic fauna (Sanchez et al., 2000). The intensity of the OMZ has also changed in longer time scales as inferred by $\delta^{15}N$ of organic matter and other proxies in sediment records (Agnihotri et al., 2008; Sifeddine et al., 2008; Chazen et al., 2009; Gutierrez et al., 2009). These different processes of tectonic or oceanographic origins may have distinct impacts upon the continuity or stratigraphic preservation of the sedimentary column along and across the continental platform.

Therefore, it is important to detect the discontinuities in every core and to try to assign them to one or the other cause. It is only if a number of cores are available, and if the missing sections are not the same in all the archives, that a selection of the most complete sedimentary sequences will eventually be possible and lead to a compiled continuous record. Missing sequences and unidentified instantaneous deposits can introduce fundamental errors into paleo-climate interpretations. For example, i) slump material may provide ages older than the neighboring sequences, resulting in age inversions in the chronological model, ii) cores containing many slump material depositions can be misinterpreted as sites with high sedimentation rates or iii) records with hiatus would wrongly show low sedimentation rates. Additionally, discontinuities could clearly result in erroneous climatic interpretations. Thus, the present study aims to determine differences and similarities in stratigraphic structure from multiple cores to develop a well constrained temporal framework for proxy records off Pisco, Peru. Sequences of laminated sediments that could be identified across cores were used to construct a composite sequence to obtain the most complete sequence of laminae and bands (thicker layers) to interpret paleo records (Baumgartner et al., 1991).

II-3. Regional Setting

The Peruvian upwelling ecosystem is an Eastern Boundary Upwelling System characterized by a shallow surface mixed layer, a shallow thermocline, and high productivity driven by coastal upwelling of nutrient-rich cold waters that are poorly ventilated (Barber and Chavez, 1983; Pennington et al., 2006). The upper continental margin of Peru (~50 to 600 m depth) is intersected by a strong and shallow OMZ that results from decay of biological production, lack of ventilation and long residence times (Helly and Levin, 2004; Pennington et al., 2006). The presence of the OMZ inhibits bioturbation and preserves high-resolution records of past ecosystem changes in certain areas on the shelf and upper slope of the Peruvian margin (Krissek and Scheidegger, 1983; Suess and von Huene, 1988; Reinhardt et al., 2002; Gutierrez et al., 2006). The principal biogenic components of Pliocene to Quaternary sediments off Peru are diatom frustules and benthic foraminifers, although

foraminifers are more variable in abundance and are intermittently dissolved in the sediment. Planktonic foraminifers, radiolarians and coccoliths are only rarely observed (Kemp, 1990). The terrigenous fraction is principally composed by quartz, feldspar and clay (Kemp, 1990). Although most of the laminae or bands consist on diatom ooze, laminae spacing (which ranges from submilimeter to decimeter size), and thickness (ranging from less than 1 mm to decimeters), and their internal structure (from pure ooze to mixed-ooze/terrigenous sediment) varies considerably (Kemp, 1990).

II-4. Methodology

II-4.1 Sampling sites

After an exploratory coring cruise in 2003, two coring cruises (2004 and 2005) were carried out off Pisco in order to obtain short gravity and box cores for paleoceanographic studies (Fig. II-1). All the box-cores retrieved superficial sediments as evidenced by protruding filaments of the giant sulphur bacteria *Thioploca sp*. (Gutierrez et al., 2009), which live in the sediment water interface. In contrast, the gravity cores did not recover the sediment surface most probably caused by loss of surface sediments at the impact of the corer on the ocean floor. The two uppermost centimeters (2 cm) of cores GC-17 and GC-18 were extruded and sub-sampled on board for other purposes.
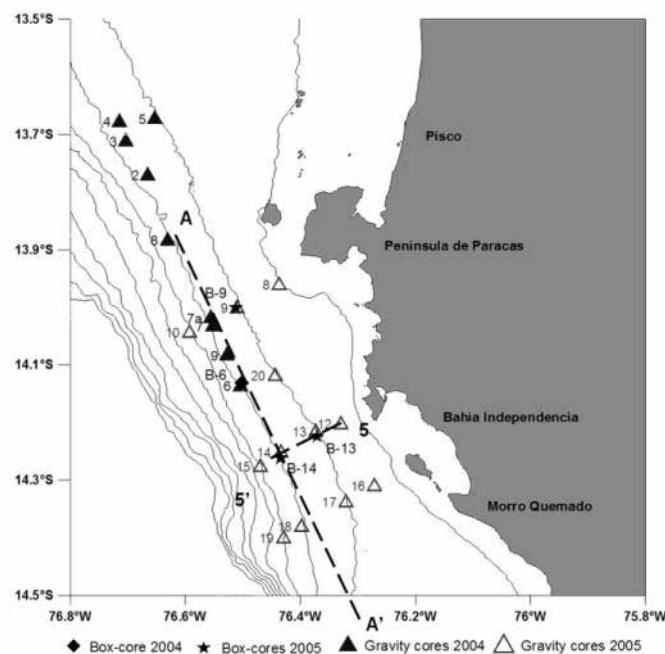
Figure II-1. Location of box-cores (stars and diamond) and gravity cores (triangles) collected off the south-central Peruvian coast during 2004 and 2005. The primary cores examined in the present study comprise GC-18, B-14, B-6, GC-9, GC- 7 retrieved at ~300 meters depth and cores GC-17, B-13, and B-9 retrieved at ~200 meters depth. Bathymetric contour lines are in 100 meters intervals. Dashed lines show the position of high-resolution sediment echo sounder profiles.

II-4.2 High-resolution sediment echo sounder profiles

High-resolution seismic profiles were obtained with an echo sounder Bathy 2000P during the cruise "Paleomap 2006" on board of RV Olaya to examine the nature of the mud lens. High-resolution acoustic profiles were obtained along multiple transects that were parallel and perpendicular to the coast over 515 km, taking also into account the coring sites performed during the 2004 and 2005 cruises (Fig. II-1). In the present work we focus on two transects (A-A' and 5-5'). Transect A-A' crosses the position of G-18, B-14, B-6, G-9, and G-7, while transect 5-5' crosses the position of G-13, G-14, and G-15 (Fig. II-1).

II-4.3 X-ray images

In order to examine the sediment structures, conventional X-ray images and/or Scopix (digital X-ray imaging system, Migeon et al., 1999) were obtained for each core. Box-cores were cut into four horizontal sections and six vertical slabs. In each box-core, two vertical slabs separated by 5 cm were used to obtain conventional X-ray and Scopix images. In order to reveal structures that cannot be seen using only one focus, two X-ray images were obtained in each slab, one focusing at ~5cm from the top of the slab and the other at ~5 cm from the base. The best parts of the X-ray images were compiled to form a composite image of each box-core. When both X-ray and Scopix images were available, we used the image that best resolved the structure of the sedimentary sequence (usually the conventional X-ray images). Gravity cores were cut lengthwise into two sections and Scopix images were obtained from each section. Conventional X-ray images were obtained in a medical facility in Lima, Peru and the Scopix images were obtained at EPOC (*Environnements et Paléoenvironnements Océaniques et Continentaux*) Laboratories at the University of Bordeaux 1.

II-4.4 Major sedimentary shift as a stratigraphic marker

A distinct sedimentary shift dating ~1820 AD in 2 box-cores collected off Pisco (B-6) and Callao (~12 °S) separated by ~300 km (Fig. II-1) has been described by Sifeddine et al. (2008) and Gutierrez et al. (2009). The cores were independently dated using ^{241}Am, ^{210}Pb and ^{14}C as described by Gutierrez et al. (2009). Both cores show similar changes in numerous environmental properties such as sediment density, productivity and oxygen proxies. Below the shift, sediments are denser, more finely laminated and present low total organic carbon (TOC) values. Above the shift the sediments are less dense and have fewer distinct laminae even though there is an increase in TOC and a decrease in oxygen (Gutierrez et al. 2009). Since the Pisco and Callao core sites are 300 km apart, we expect closer cores to show the same sedimentary shift and use it as an anchor layer in order to correlate the cores.

In order to identify the sedimentary shift, we determined density and proxies for export productivity in each core. To determine the sediment density we calculated the dry bulk density (DBD) of 0.5 cm^3 samples in the box-cores and used Gray Level (GL) values from the SCOPIX images in the gravity cores by using the software ImageJ. In order to infer productivity, the percentage of Nitrogen (N) was determined in cores B-9, B-13 and B-14 at 0.5 cm resolution in the same samples used for DBD assays. For core B-6 we used the TOC data reported by Sifeddine et al. (2008). %N and %TOC in core B-6 are well correlated (r^2=0.80) and thus %N can be used in the other box-cores to indicate major productivity changes, as established by Sifeddine et al. (2008) and Gutierrez et al. (2009) from multiple proxies.

II-4.5 ^{210}Pb and ^{241}Am profiles as stratigraphic markers

^{210}Pb and ^{241}Am activities were measured in all box-cores and the profiles were used to correlate the cores using several characteristics of the profiles. The presence of ^{241}Am is due to global fallout following nuclear bomb testing. Three specific dates associated with the radiometric patterns caused by bomb testing can be used to interpret and develop a chrono-stratigraphy in the marine sediment records and to correlate the cores: 1) the onset of nuclear testing at ~1953 AD, 2) a period of maximum bomb fallout from 1961 to 1966 AD, and 3) another period of intense bomb testing in the South Pacific at the early 1970s (UNSCEAR, 2000). Additionally, ^{210}Pb (half life 22.3 years) can be used to date sediments up to ~150 years old, and the activities of ^{210}Pb are commonly measured by alpha and gamma spectrometry (Appleby, 2001; Zaborska et al., 2007; Sanchez-Cabeza and Ruiz-Fernández, 2012). Gamma spectrometry allows for the analysis of other gamma emitting radionuclides (Zaborska et al., 2007). The total activity of ^{210}Pb measured on a sample (^{210}Pb$_{tot}$) consists of two components: the supported ^{210}Pb (^{210}Pb$_{supp}$), which is originated by in situ decay of ^{226}Ra, and the excess or unsupported ^{210}Pb (^{210}Pb$_{ex}$). The activity of the ^{210}Pb$_{ex}$ decreases over time while ^{210}Pb$_{supp}$ activity remains in equilibrium with its parent radionuclide ^{226}Ra. Changes in the ^{210}Pb$_{ex}$ profiles can also be used to correlate stratigraphies among box-cores.

Sub sampling for gamma measurements of ^{210}Pb and ^{241}Am in all box-cores was done in samples from finely sampled stratigraphic units (Gutierrez et al., 2009; Salvatteci et al., 2012). Briefly, the X-ray images of the box-cores were used in order to construct a high-resolution sub-sampling template following the stratigraphy. Each sampling interval consisted of a couplet of dark and light laminae or a thicker band in the X-ray image. Any couplet or band thicker than 0.6 cm was sub-sampled into thinner samples of similar thickness (no less than 0.3 cm). The activities of ^{210}Pb and ^{241}Am were measured at LSCE on 1-2 g of dried sediment by gamma spectrometry using high-efficiency, very-low-background well-type Germanium detectors in the Underground Laboratory of Modane (Reyss et al., 1995). ^{226}Ra activities were inferred from gamma spectra following Reyss et al.

(2005). $^{210}Pb_{ex}$ activities were calculated by subtracting the ^{226}Ra from the total ^{210}Pb activity (Appleby, 2001; Zaborska et al., 2007).

Core B-13 was sub-sampled at 1 cm resolution for analysis by alpha spectrometry at the laboratories of the Marine Environment Laboratories of the International Atomic Energy Agency in Monaco. Analyses were performed following the method by Sanchez-Cabeza et al. (1998), assuming that ^{210}Pb is in equilibrium with ^{210}Po. Base ^{210}Pb was determined from deep samples in the core where no $^{210}Pb_{ex}$ was present (Sanchez-Cabeza and Ruiz-Fernandez, 2012). ^{210}Pb activities measured by gamma and alpha spectrometry were corrected for decay between sampling and measurement.

II-4.6 Radiometric analysis ^{14}C

Radiocarbon was analyzed to identify the origin of homogeneous deposits and to establish a preliminary chronology. ^{14}C dates from bulk organic matter (instead of foraminifera) are commonly used in Peruvian marine sediments (Rein et al., 2005; Chazen et al., 2009; Makou et al., 2010) due to extensive periods of dissolution of benthic and planktonic foraminifera (Kemp, 1990; Morales et al., 2006). In order to verify the upslope origin of the homogeneous deposits, ^{14}C measurements from laminated sediments in B-14 were compared with measurements from several homogeneous deposits. Remobilized upslope sediments should show older ages than adjacent laminated sections. Radiocarbon measurements were performed by Accelerator Mass Spectrometry (AMS) at the "*Laboratoire de mesures du Carbone-14*" (LMC14, Gif-sur Yvette, France). In the present work, conventional radiocarbon ages are indicated (i.e. without calibration by reservoir effect) to avoid additional bias in the data set (e. g. temporal changes in upwelling intensity and changes in the source of organic matter).

II-4.7 Lateral correlation of sediment structures and construction of the composite sequence

After the identification of the sedimentary shift in each core, laminae correlation among the cores was done by visual inspection of the X-ray images. The pattern of variation in tonal contrast on the X-radiographs, produced by the internal structure of the laminae, provides unique signatures which can be used to define the stratigraphic position of the laminae sequence (Baumgartner et al., 1991). Sequences of laminae detected in all cores were correlated and defined as stratigraphic markers. After the identification of the stratigraphic markers, the X-ray images of the contemporaneous laminated sequences were overlapped to assess the completeness of the surrounding laminated sequences in each core. Homogeneous deposits were identified as upslope lateral depositions when at least one slump characteristics was found: 1) internal deformation of the laminae sequences (e.g. presence of laminae diagonal or perpendicular to the sedimentation plane), 2) different

thicknesses of contemporaneous deposits in different cores with the same identified laminae above the deposit, or 3) laminae erosion below the deposit. When the homogeneous deposit was identified as a slump, it was removed from the record.

To reconstruct the high resolution composite record, the sedimentary sequences of the box-cores that presented more and better defined laminae were selected. If two or more sections were equally preserved in several box-cores we chose the cores retrieved at 300 m because there is evidence of better preservation in sediments retrieved in the core of the OMZ off Pisco (Salvatteci et al., 2012). The box-cores were used to reconstruct the composite sequence while the gravity cores were mainly used for the determination of the extent of lateral correlation.

II-5. Results

II-5.1 Coring site and cores selection

The bathymetry of the zone indicates important changes in the slope off Pisco (Fig. II-1), being steeper at 14.1 °S where core B-6 and B-9 were retrieved, and less steep at ~14.3 °S where cores B-13, B-14, G-17 and G-18 were taken. The seismic acoustic profiles off Pisco (Figs. II-2A and II-2B) reveal a sediment layer varying between around 10 -15 meters at ~300 m depth, containing laminated sediments as evidenced by the X-ray images of the cores (Fig. II-2C). Parallel to the coast there is little evidence for large scale changes in the upper sedimentary sequence in the seismic acoustic profile (Fig. II-2A). However the perpendicular profile (Fig. II-2B) shows the thinning of the mud lens with depth, which can be explained by lower sedimentation rates and/or by sediment erosion. Between 400 to 500 m depth the sediment layer is very thin leaving only dense consolidated sediment (Fig. II-2B), which likely explains the difficulties experienced in recovering gravity cores at depths > 400 meters (e.g., G-15, Fig. II-2D).
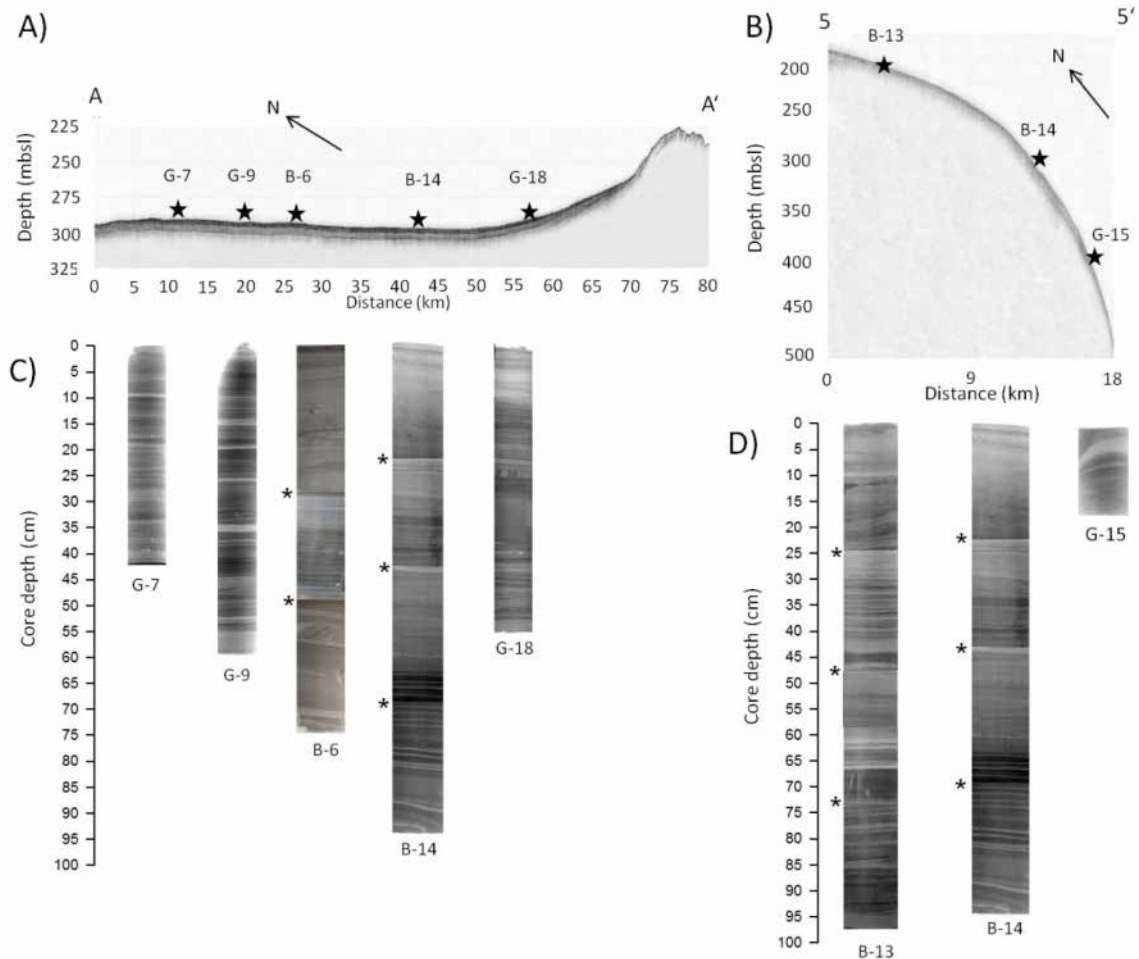
Figure II-2. Seismic profiles, position and positive X-ray images of the cores associated with the acoustic seismic profiles. A) Seismic profile A-A′ at ~300 meters below sea level (mbsl) showing a thick layer (~10- ~15 meters) and the approximate position of the cores. B) Seismic profile 5-5′ showing the thinning of the mud lens with depth beneath ~350 m and the approximately position of the cores. C) X-ray images of the gravity cores and box-cores associated with the A-A′ profile showing finely laminated sediments. D) X-ray images of the gravity core and box-cores associated with the 5-5′ profile. The asterisks indicate the transitions between slabs of the same box-core where the apparent differences in color between slabs do not represent a real change in density. In all the X-ray and SCOPIX images the colors were inverted, thus the darker (lighter) laminae represent dense (less dense) sediments.

From the 25 gravity and box-cores retrieved off Pisco (Fig. II-1), 4 box-cores and 4 gravity cores were selected in order to determine the record continuity and the spatial extent of laminae between sites (Fig. II-3). The cores selected were located between ~200 to ~300 meters depth, within the core of the OMZ, where the cores with better laminations are found, with the intention of covering the largest possible area. The cores retrieved north-west of the Paracas peninsula do not show good laminations in comparison to the southern cores and are not included. The X-ray images of the selected cores are shown in Figure II-3 as well as the DBD or gray level.
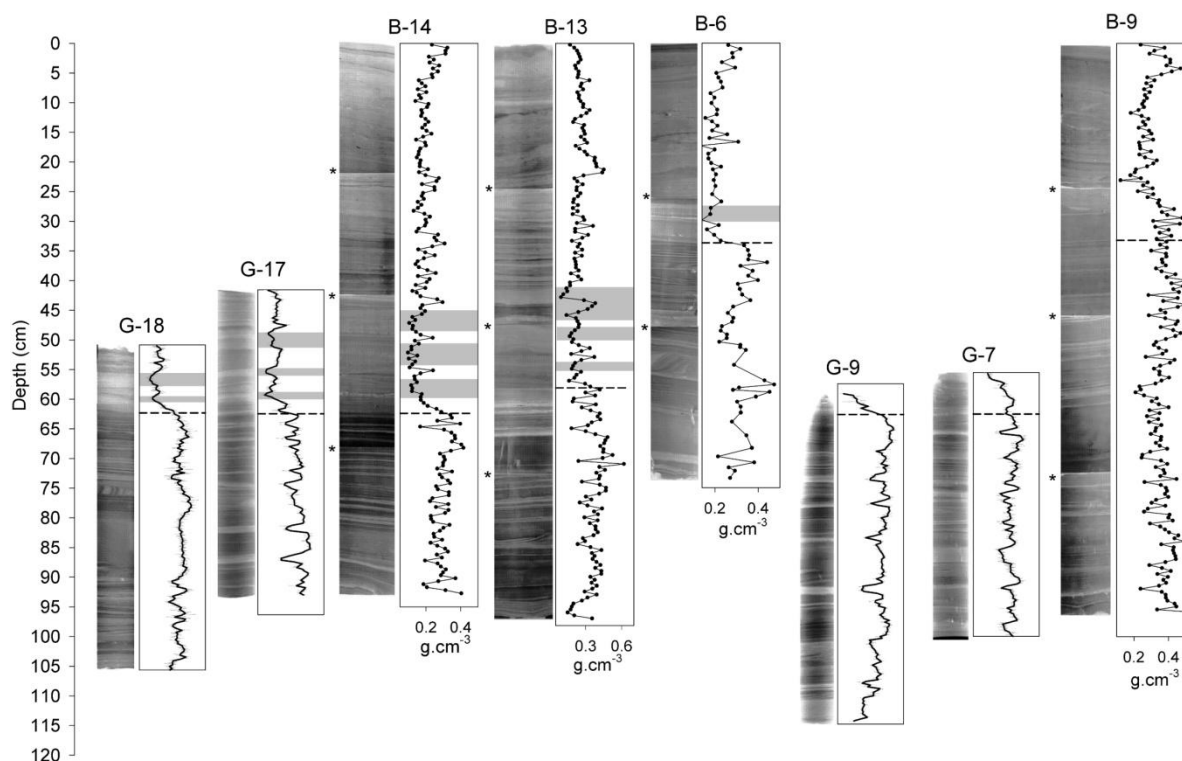
Figure II-3. Positive X-ray (box-cores) and SCOPIX (gravity cores) images and density of the cores selected for the present study. The density values in the box-cores were calculated from dry bulk density (DBD) while in the gravity cores the sediment density was inferred by the gray level values obtained from the SCOPIX images. The bold lines superimposed in the gray level plots of the gravity cores indicate a 10 point moving average. The asterisks indicate the transition between slabs of the same core, artificially indicating differences in density. The vertical dashed lines indicate the sedimentological shift reported by Gutierrez et al. (2009) and Sifeddine et al. (2008), which is established by the change in sediment density. The highlighted areas correspond to the position of the diatom layers (see Fig. II-4). The gravity cores were positioned accordingly to the depth of the sedimentological shift in B-14. In all the X-ray and SCOPIX images the colors were inverted, thus the darker (lighter) laminae represent dense (less dense) sediments.

II-5.2 Correlation of the sedimentary shift and diatom bands

All cores showed a change in density as inferred by the DBD and GL, indicated by vertical dashed lines in Figure II-3. While the DBD changes do not appear identical with one another, they are supported by different lines of evidence including i) the similar laminated sequence among cores below the sedimentary shift, ii) the changes in export productivity proxies and iii) the position of the diatom layers. We describe the sedimentological characteristics first, followed by the support from proxies of export productivity and the position of the diatom bands that help to establish the sedimentary shift. The density shift is located closer to the top in cores B-6 (~34 cm) and B-9 (~34 cm), and further down in cores B-13 (~58 cm) and B-14 (~62.5 cm). The density change is abrupt in cores B-6, B-9 and B-14 while it is more gradual in core B-13. This density change can be correlated with cores B6, B-13 and B-14, where the sedimentary shift has already been identified (Gutierrez et

al., 2009; Salvatteci et al., 2012; Sifeddine et al., 2008). Below the sedimentary shift, where the sediments are denser, all cores are characterized by finely laminated sequences interspersed with homogeneous or slumped sections (Fig. II-3), and few bands or laminae with lower density (e.g. at 82 and 87 cm depth in core G-17, Fig. II-3). In contrast, above the shift the sediments are less dense and have fewer distinct laminae. Because there is a possibility of a shift in density resulting from a turbidite, slump or erosional features, it is important to confirm that the shift in each core is contemporaneous and corresponds to the oceanographic shift documented by Gutierrez et al. (2009).

All box-cores show a change of export productivity associated with the sedimentological shift, which helps confirm its oceanographic origin, although, like the DBD profiles, the transition between the pre and post-shift periods is different among cores (Fig. II-4). Cores B-9 and B-6 show lower productivity during the pre-shift period, an increase after the shift, followed by a decrease and finally an increase towards the top. In contrast, cores B-13 and B-14 show strong variability in export productivity associated with changes in DBD values (Fig. II-3) after the sedimentary shift, and from ~40 cm to ~23 cm there is an increase in export productivity in both cores. From ~23 cm to the top, B-14 shows a decrease followed by an increase towards the top whereas B-13 shows a decrease towards the top (Fig. II-4). The downcore patterns observed above the sedimentary shift in B-13 and B-14 are consistent with higher sedimentation rates that resolve greater downcore variations in comparison to B-6 and B-9.

One of the most prominent characteristics in many cores retrieved off Pisco was the presence of yellowish layers mainly composed of large diatoms, such as *Coscinodiscus asteromphalus* (Fig. II-4). The diatom layers are interspersed throughout the cores but they are thicker and most evident in the first centimeters above the sedimentary shift. The "spongy" appearance of these layers, along with low values of DBD (Fig. II-3) and a decrease of export productivity (Fig. II-4) were used to correlate the cores and helped to determine the position of the sedimentary shift. Right above the shift, successive diatom packages interspersed with laminated sections can be observed in all cores except GC-7, GC-9 and B-9 (Fig. II-4). Cores GC-17, B-13 and B-14 show 3 diatoms packages, GC-18 show 2 and B-6 shows only one package above the sedimentary shift (Fig. II-4). Within the upper diatom package in core B-13 (~45 cm depth) a dense band can be observed (Figs. II-3 and II-4). Diatom layers served as anchor layers, but were used along with other stratigraphic markers as not all cores showed the same number of apparent bloom deposits.
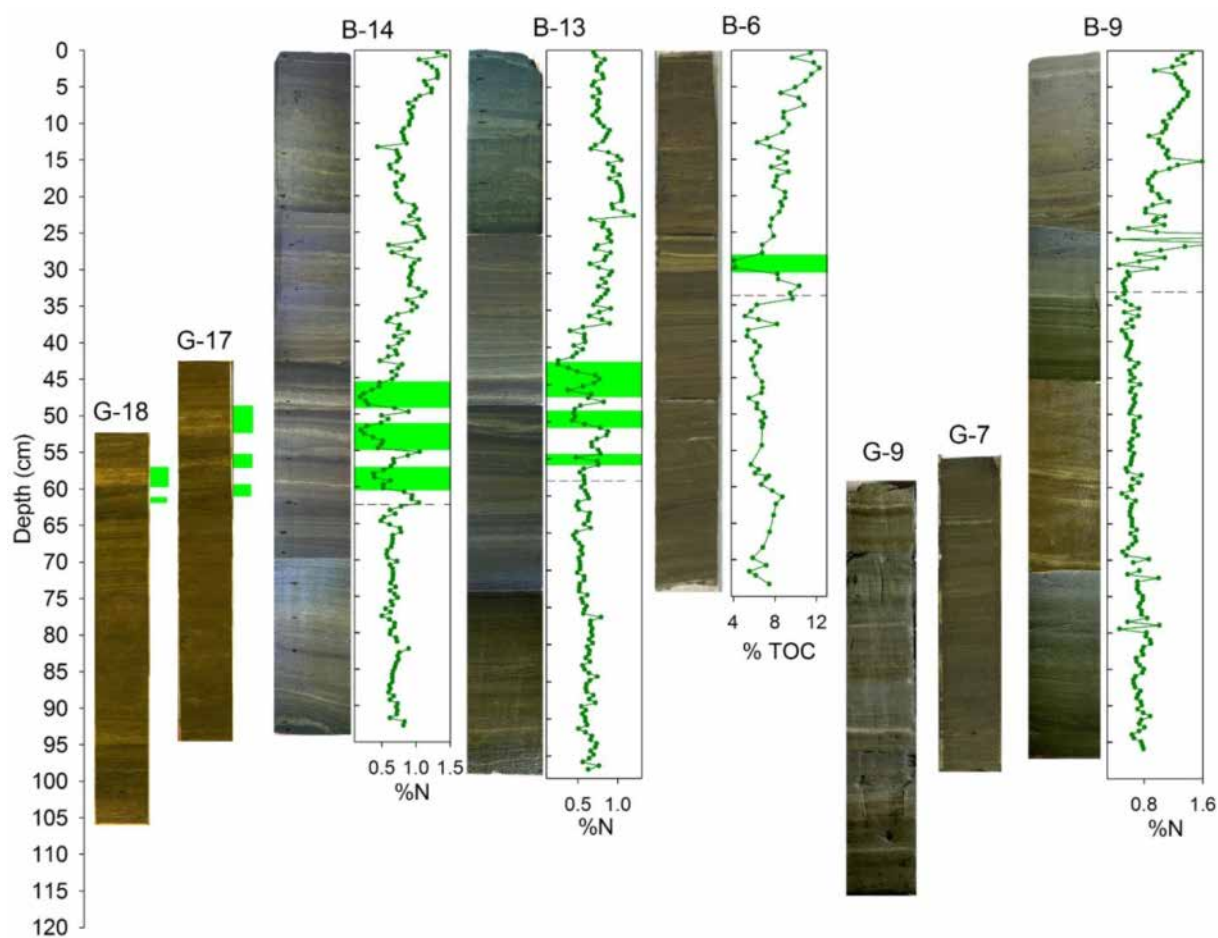
Figure II-4. Photograph images and proxies for productivity (%TOC or %N) in cores GC-18, GC-17, B-14, B-13, B-6, GC-9, GC-7 and B-9. The black dashed horizontal lines indicate the position of the sedimentological shift in each core as inferred by DBD or GL (Fig. II-3). Highlighted areas correspond to the position of the diatoms layers. The gravity cores were positioned accordingly to the depth of the sedimentological shift in B-14 (see Fig. II-3).

II-5.3 [241]Am and ^{210}Pb profiles

The depth at which [241]Am becomes clearly detectable (~0.15 dpm.g[-1]) was used as a tie point among the box-cores in order to further develop the correlation (Fig. II-5). This point is closer to the top in B-6 (12 cm) and in B-9 (11 cm) while it is located deeper in cores B-14 (15 cm) and B-13 (17 cm). The expected peaks of [241]Am are not well defined in all cores and therefore lead to uncertainties for the correlation: B-6 shows the characteristic double peak at ~7.4 (0.94 dpm.g[-1]) and 5 cm (0.78 dpm.g[-1]), whereas cores B-13 and B-14 show only one clear peak located at ~ 12.4 cm (0.66 dpm.g[-1]) and 4.5 cm (0.74 dpm.g[-1]) respectively. B-9 shows only one weak peak at ~8.6 cm with an activity (0.46 dpm.g[-1]) lower than the maximum concentration in the other cores. The double peak in core B-6 is located within a laminated section, the peak in B-13 is located above a section with evidence of sediment mixing and the peaks in cores B-14 and B-9 are located within sections with more homogeneous material (Fig. II-5). Thus, it is very likely that the original [241]Am signal in cores B-9,

B-13 and B-14 was not preserved. Due to the uncertainty in correlating the ^{241}Am peaks, the possible correlation of the ^{241}Am maxima is indicated with dashed bold lines in Fig. II-5. Despite the uncertainties in correlating the peaks, the ^{241}Am profiles indicate higher sedimentation rates in B-13 and B-14 in comparison to B-6 and B-9.

^{210}Pb$_{ex}$ activities in all box-cores show a clear decline with depth with some scatter and a variable penetration (^{210}Pb$_{ex}$ >1 dpm.g^{-1}). The activities and the profiles of ^{210}Pb$_{ex}$ for the top ~23 cm of B-13 by alpha and gamma spectrometry were similar (Fig. II-5); confirming the comparability of both techniques. In B-13 and B-14 the ^{210}Pb$_{ex}$ penetration is ~49.5 and 46 cm respectively, while in cores B-6 and B-9 is ~24 and ~26 cm respectively. The ^{210}Pb$_{ex}$ penetration in core B-6 is above the only discernible diatom layer, in B-13 is in the second diatom layer while in B-14 is in the first diatom package from the top (Fig. II-5). The difference in the ^{210}Pb$_{ex}$ penetration between cores B-13 and B-14 in comparison with B-6 and B-9 confirms a consistent difference between the cores taken in a more gentle slope (B-13 and B-14) in comparison with the cores taken in a steeper slope (B-6 and B-9). Even though the ^{210}Pb$_{ex}$ profiles are quite complex, the difference in the depth at which ^{210}Pb$_{ex}$ ends further indicate that the sedimentation rates are higher in B-13 and B-14 in comparison to B-6 and B-9.
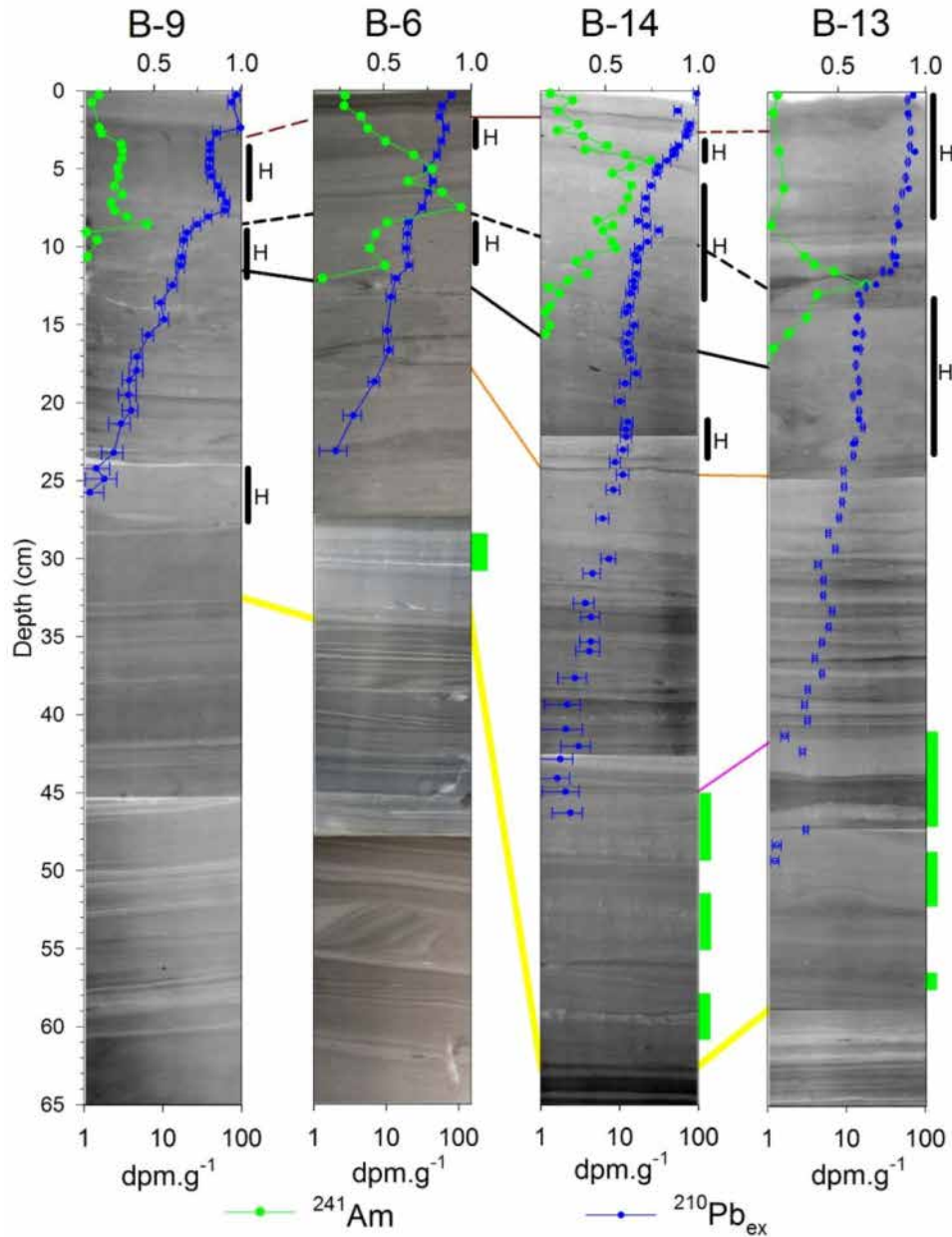
Figure II-5. Positive X-ray images of box-cores B-9, B-6, B-14 and B-13, with profiles of ^{210}Pb$_{ex}$ (blue) and ^{241}Am (green) activities (± analytical error) superimposed. The full (open) circles indicate ^{210}Pb$_{ex}$ gamma (alpha) counting. The yellow lines between cores indicate the position of the sedimentological shift as shown in Figures II-3 and 4. The black bold lines between cores indicate the correlation of events of the ^{241}Am profiles (see text). The other color lines correlate laminae sequences as in Figure II-6. Black bars at the right side of the cores indicate the extent of homogeneous sections (H) as determined by the relatively constant profile and homogenous sediment types in the X-ray images or sections with evidence of physical or biological sediment mixing. Green bars indicate the extent of the diatom layers. In all the X-ray images the colors were inverted, thus the darker (lighter) laminae represent dense (less dense) sediments.

II-5.4 Horizontal continuity of laminae

The combined results obtained from the anchor layers indicate higher sedimentation rates in B-13 and B-14 in comparison to B-6 and B-9. As anchor layers we used: 1) the sedimentary shift identified by the change in sediment density and productivity (yellow lines in Figs. II-3 and II-4); 2) the presence of diatom layers associated with a dilution of the productivity proxies and low values of sediment density (highlighted areas in Figs. II-3 and II-4); and 3) the end of ^{241}Am profiles (black bold lines in Fig. II-5). Additionally the end of the ^{210}Pb$_{ex}$ further confirms the differences in sedimentation rates between B-13 and B-14 with B-6 and B-9 but it cannot be used as a strong anchor layer because of the error associated with the measurement of low values of ^{210}Pb.

In order to further develop the correlation among cores, we used clearly defined laminae sequences as stratigraphic markers. Stratigraphic markers are well-defined laminae sequences identified in nearly all cores that were used to correlate the cores in a more detailed approach (thin color lines in Fig. II-6). The sedimentary shift represents a boundary with more clearly defined laminae prior to the shift, which usually allowed the correlation of the first group of laminae above a homogeneous or slumped deposit (Fig. II-6). In contrast, from the sedimentary shift to ~25 cm depth, only B-13 and B-14 can be correlated because they show laminated sequences that cannot be observed in the others cores (Fig. II-6). From ~ 25 cm to the top in B-13 and B-14 there are few laminae or bands that can be correlated (Fig. II-6), due to sediment mixing or rapid sedimentation events as evidenced by the ^{210}Pb$_{ex}$ profiles (Fig. II-5).

The identification of the anchor layers and the stratigraphic markers allowed the division of the cores into contemporaneous sections (capital letters in Fig. II-6). The base of section A and D is defined by the limit of detection of ^{241}Am and the sedimentary shift respectively, while the base of the other sections is defined by the stratigraphic markers (thin color lines in Fig. II-6). Each stratigraphic marker presents a unique characteristic that can be observed in most cores.

- Section A comprises the part from the top of the box-cores to the limit of detection of ^{241}Am (Fig. II-5).

- The base of section B presents two dense laminae in cores B-14, B-13 and B-6, also associated with an increase in DBD at ~25 cm, 24 cm and 17 cm, respectively (Fig. II-3) which confirms that they are the same layer.

- The base of section C is characterized by a finely laminated sequence above the uppermost diatom package shown in Figs. II-4 and II-5 (well defined in G-17, B-13 and B-14).

- The base of section D is the sedimentary shift identified in all the cores.

- The base of section E is a light lamina above a homogeneous deposit.

- The base of section F starts with two well-defined clear laminae present in all cores.

- The base of section G is a finely laminated sequence right above an evident slump, better observed in cores B-6 and G-18.

- The base of section H is characterized by a diatom band observed in cores B-6 and B-14 (Figs. II-4 and II-6).

- The base of section I is another diatom layer associated with low values of DBD and that can be better observed near the base in B-6, at 80 cm in B-9 and at 92 cm in G-9 (Figs. II-3, II-4 and II-6).

- The base of section J is an alternation of clear and dark laminae within a dense sequence (better observed in core G-9, Figs. II-3 and II-6).

- Finally, the base of section K is a thin diatom lamina observed at 97, 112 cm, 92 depth in cores G-18, G-9 and B-9 respectively (Figs. II-4 and II-6). As evidenced by the correlations of stratigraphic markers in Fig. II-6, cores G-18, G-9 and B-9 present older sedimentary sequences.
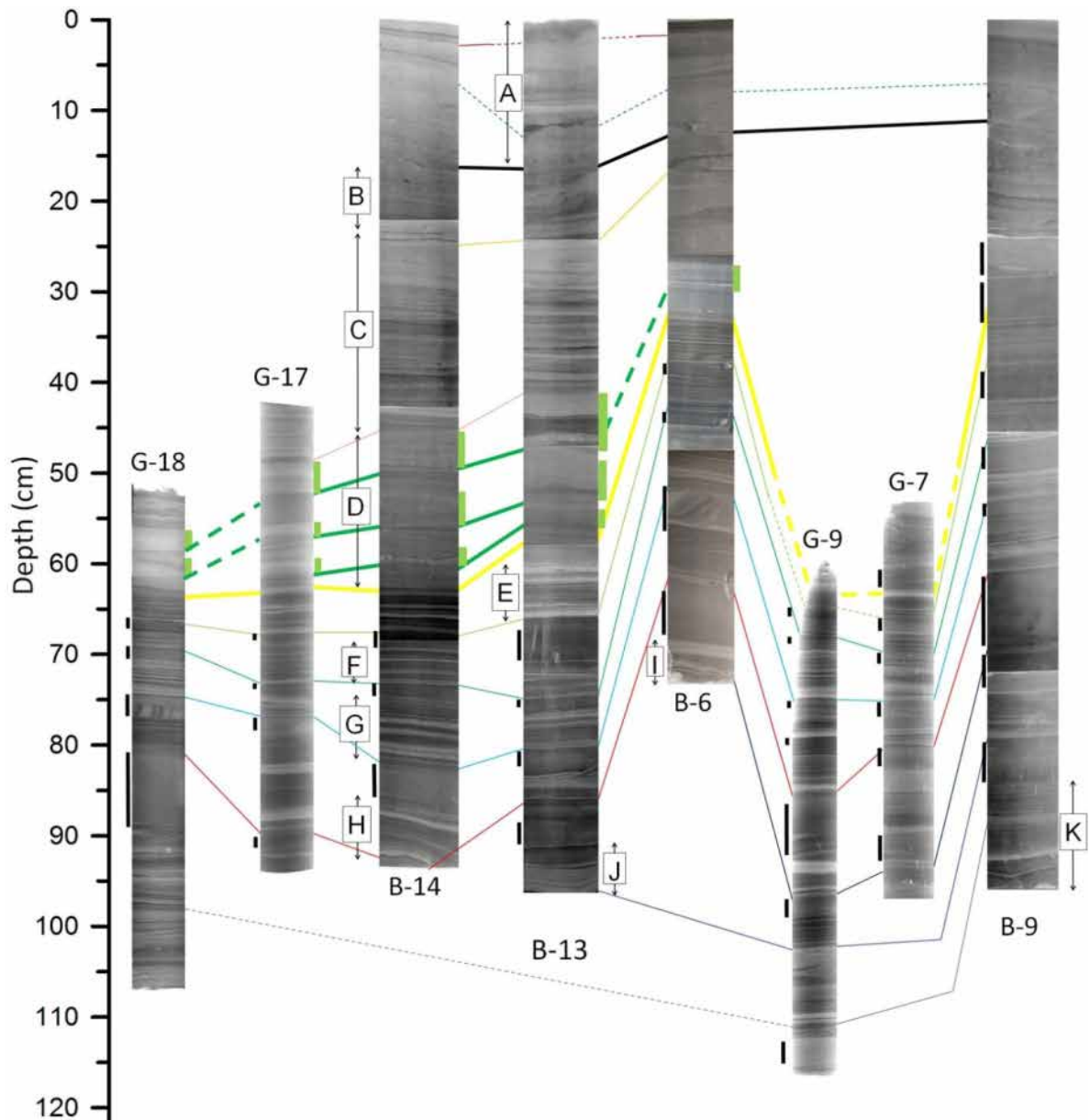
Figure II-6. Lateral correlation of sediment sequences among the gravity cores (G) and box cores (B) retrieved off Pisco. The yellow lines indicate the position of the sedimentological shift as shown in Figures II-3, II-4 and II-5, the upper black bold lines indicate the start of [241]Am activities as in Fig. II-5 and the green thick lines indicate the correlations of the diatom layers. The stratigraphic markers are represented by the continuous (dashed) colored thin lines that indicate possible (less obvious) correlations and represent the base of the sediment sequences (from A to K) shown in Fig. II-7 except for the sections A and D where the base is defined by the limit of detection of [241]Am and the sedimentary shift respectively (see text). The capital letters from A to K at the right or left side of some cores indicate the sediment sequences that were used to reconstruct the composite record (Fig. II-9A) and the arrows indicate the extent of the sediment sequences. Black bars at the left side of the cores indicate homogeneous deposits, while green bars at the right side indicate the extent of the diatom layers as in Figures II-4 and II-5. Given that the box-cores recovered surface sediments they are aligned at 0 cm, in contrast the gravity cores are aligned to the position of the shift in core B-14. In all the X-ray and SCOPIX images the colors were inverted, thus the darker (lighter) laminae represent dense (less dense) sediments.

46

II-5.5 Continuity and discontinuity of the records

The comparison of contemporaneous sequences using stratigraphic markers as tie points provides evidence of erosion, discontinuities, and/or non-continuous laminae structure (Fig. II-7). In order to compare the contemporaneous sediment sequences between cores, we first discarded all the homogeneous or slumped deposits shown by bars in Figure II-6. Then, the contemporaneous sections (capital letters in Fig. II-6) from different cores were overlapped with the aid of the stratigraphic markers and other prominent laminae. Slight differences in the visual appearance of the laminae (e.g. differences in lamina thickness and density) can be explained by oceanographic and/or sedimentological processes (e. g. patchiness of diatom bloom sedimentation and differences in sedimentation rates between core sites). In these cases, some slight adjustments (enlargements or reduction) of the X-ray images helped to find the correspondence among laminae. In the sediment sequence A, the sections corresponding to core B-9, B-6 and B-14 were separated in two parts in order to fit the laminae present in the sequence A of B-13. The division point in cores B-6 and B-9 was the base of the homogeneous section located at ~ 4 and ~8 cm depth respectively (Fig. II-5) and in B-14 the division point was an angular discordance located at ~4 cm depth (Fig. II-5). Only the sediment sequences corresponding to section B in cores B-6, B-9, B-13 and B-14 could not be correlated due to the lack of laminated or banded sequences (Fig. II-7). The rest of the sediment sequences were overlapped with confidence.

After overlapping the contemporaneous sediment sequences of different cores, we carefully evaluated evidence of erosion, differences in laminae appearance among cores discontinuities, and/or non-continuous laminae structure. Some sediment sequences in some cores present more laminae than in others (Fig. II-7A to K). For example, cores G-18 and B-14 present more laminae in comparison with G-17, G-7, B-13 and B-9 (Fig. II-7G). The presence of laminae in some cores but not in others may indicate a sediment loss. Many sequences are similar among some cores without an apparent loss of laminae at any core site or alternatively (but less likely) with exactly the same loss of laminae in all cores. For example the sediment sequence F shows the same pattern in all the cores studied with exception of cores G-18 and G-9 (Fig. II-7F). There is also evidence of large changes in the thickness of individual laminae. For example in Fig. II-7 panel E, the first light laminae from the top of the sequence (mainly composed by diatoms) is very thin in core B-9 and is thicker in cores B-14 and B-13.
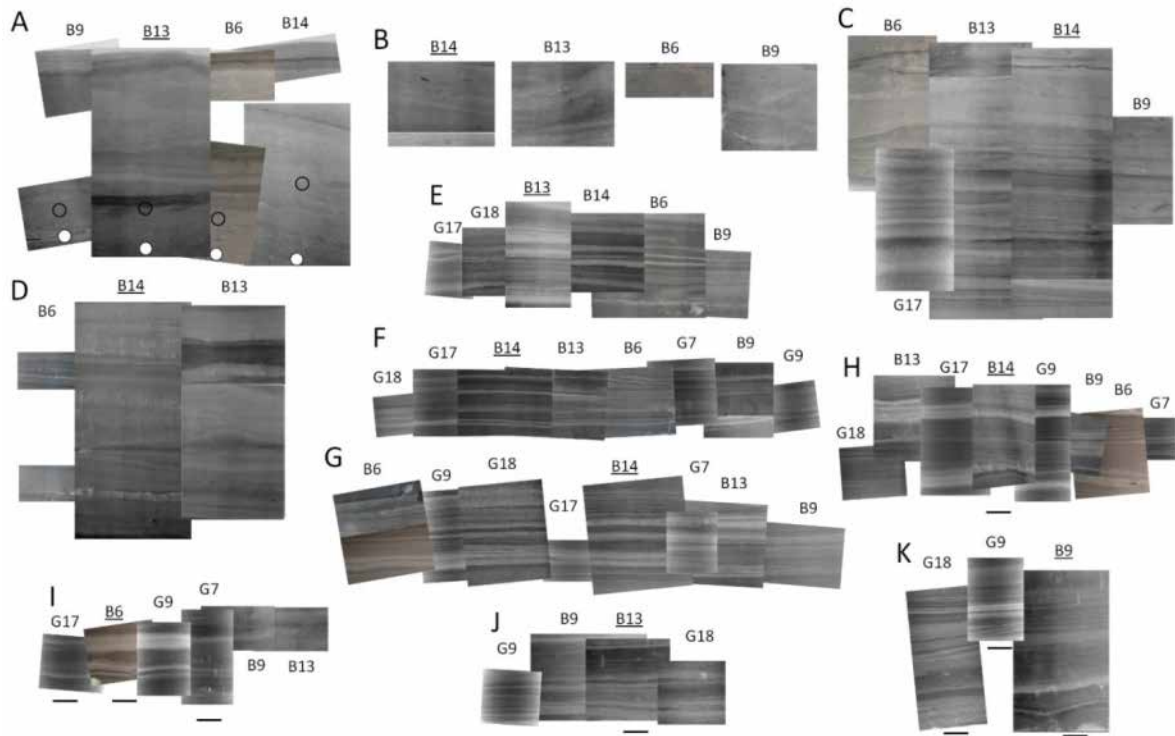
Figure II-7. Overlap of positive X-ray images of laminae sequences shown by capital letters in Figure II-6. The homogeneous deposits shown in Figure II-6 were removed. The underlined labels indicate the sections that were used to construct the composite record (Fig. II-9B). The open (full) circles indicate the peak (end) in ^{241}Am profiles. The horizontal bars at the base of some X-ray images indicate the base of the core. The X-ray images are not to scale; the sections were enlarged or reduced in order to show the best fit, yet some small offsets and/or variations in laminae thickness still exist between cores. In all the X-ray and SCOPIX images the colors were inverted, thus the darker (lighter) laminae represent dense (less dense) sediments.

Similar thickness of equivalent laminated sedimentary sequences indicates similar sediment deposition rates during the pre-shift period. The similar thickness of the temporally equivalent laminated sequences (up to some mm's difference) is in clear contrast with the large differences (up to several cm's difference) of the homogeneous layers (Table II-1). Given that some cores have more laminae in comparison with others, caution was taken to measure the sedimentary sequence from the base of the sedimentary sequence (i.e. the stratigraphic marker) to a well identifiable laminae observed in all cores (Fig. II-7). For example, sequence F measures 4.0, 4.1, 3.9 and 3.8 cm in cores B-14, B-13, B-6 and B-9 respectively. Another example is sequence G which measures 5.2, 5.0 and 5.1 cm in cores B-14, B-13 and B-6 respectively (core B-9 did not show enough laminae in sequence G to be included in the analysis). After the sedimentary shift, only B-13 and B-14 show laminated sequences that can be correlated with reliability (Fig. II-6) and the thickness of the equivalent sedimentary sequences are also similar (Fig. II-7C and D). However, as mentioned above, the sedimentation rates of cores B-6 and B-9 during the post-shift period is lower in comparison to B-13 and B-14 as supported by the ^{210}Pb and ^{241}Am profiles (Fig. II-5).

Table II-1. Thickness (cm) of the homogeneous/slumped deposits in box-cores B-14, B-13, B-6 and B-9 during the pre-shift period. The roman numerals indicate the position of the deposits according to Figure II-8.

Homogeneous/ slumped deposit	B-14	B-13	B-6	B-9
I	not observed	not observed	not observed	4.1
II	2.3	4.5	1.2	3.2
III	1.5	1	0.9	3
IV	3.9	1.4	4.5	1.6
V	-	1.2	5.3	7.9
VI	-	-	-	4.2
VII	-	-	-	5.3

In order to evaluate the record continuity, it was crucial to determine if the homogeneous deposits (Figs. II-6 and II-8) were caused by upslope sediment deposition or by bioturbation. This evaluation was done in the pre-shift part of the record because the presence of slumped material is more evident and the multiple cores are well-correlated. The millimeter to centimeter-scale homogenous layers or slumps, between laminated sequences for the pre-shift period, are shown by bars in Figure II-8. The roman numerals (from I to VII) at the left side of each bar in Figure II-8 indicate contemporaneous deposits as established by the stratigraphic markers in Figure II-6. The following observations at each deposit were made:

- The homogeneous deposit I, which can be clearly observed only in B-9 and is overlying the sedimentary shift, is characterized by massive homogeneous sediments without internal deformation and without strong evidence of laminae erosion.

- Deposit II can be observed in all the cores. Although there is no clear evidence of internal deformation of the sediment structure, below this deposit in B-6 there is clear evidence of laminae erosion (see inset panel in Fig. II-8). Furthermore, the thickness varies from 1.2 to 4.5 cm in B-6 and B-13 respectively (Table II-1).

- Deposit III does not show internal deformation. The laminae below this structure in core B-13 appear to be affected by erosion (Fig. II-8, top of section G) and sequences of laminated sediments were erased in many cores, implying that this deposit was caused by a slump rather than a bioturbation event. For example in B-13 and in G-17 (Fig. II-7G) there is no evidence of the faintly and finely laminated sequence observed in B-14 below deposit III, but the subsequent downcore laminae are very well defined in B-13 and G-17. If this lack of laminae below the deposit III in B-13 and G-17 was caused by bioturbation, then the thickness of the homogeneous deposit plus the faintly laminated sequence in B-14 (3.5 cm)

should be relatively similar to the thickness of the homogeneous deposit in B-13 (1.4 cm), which is not the case (Table II-1).

- Deposit IV is a clear and characteristic slump as demonstrated by the perpendicular/diagonal laminae to the sedimentation plane in G-18 and B-6 (see inset panels in Fig. II-8). This slump is also associated with laminae deformation in the top of sequence H in core B-13 (see inset panels in Fig. II-8). Additionally, the thickness of this deposit varies from 1.4 to 4.5 cm in B-13 and B-6 respectively (Table II-1) confirming a slump origin for this deposit. The slump IV in B-6 also serves as an example of how this slump in a core site near from B-6 site may not show internal deformation. The slump IV in B-6 is composed of laminae diagonal to the sedimentation plane (from the center of the slump to the left side) and homogeneous sediments (at the right side of the slump); this structure implies that the same slump in neighboring cores may look like homogeneous deposits without internal deformation. Additionally, slump IV in G-18 is composed by laminae perpendicular to the sedimentation plane and an overlying homogeneous deposit.

- Deposit V is a thick homogeneous deposit in G-18, B-6, G-9, G-7 and B-9, although the thickness of this deposit varies from 1.2 to 7.9 cm in B-13 and B-9 respectively. There is also evidence of laminae erosion below this slump in G-18, G-9 and B-9 (~27 cm depth in G-18 and G-9, and ~69 cm depth in B-9). Additionally, there is support of sediment reworking within this deposit in core B-9, which is better observed in the photographs images as evidenced by traces of a diatom layer diagonal to the sedimentation plane, confirming the origin of this deposit (Fig. II-4; B-9 ~65 cm depth).

- The homogeneous deposit VI can only be observed in G-9, G-7 and B-9, all of which contain older material. This deposit in B-9 has similar evidence of reworked material as the slump V, as indicated by the traces of laminae that can be observed within the deposit from ~38 to ~40 cm depth (Fig. II-8).

- Finally deposit VII, which is also present only in G-9 and B-9 containing older sequences, shows reworked material in core G-9 while in B-9 it is homogeneous with a faint couplet of laminae in the middle of the deposit. Given that the deposits VI and VII are only present in one box-core, is not clear if these deposits were originated by a slump or by bioturbation.
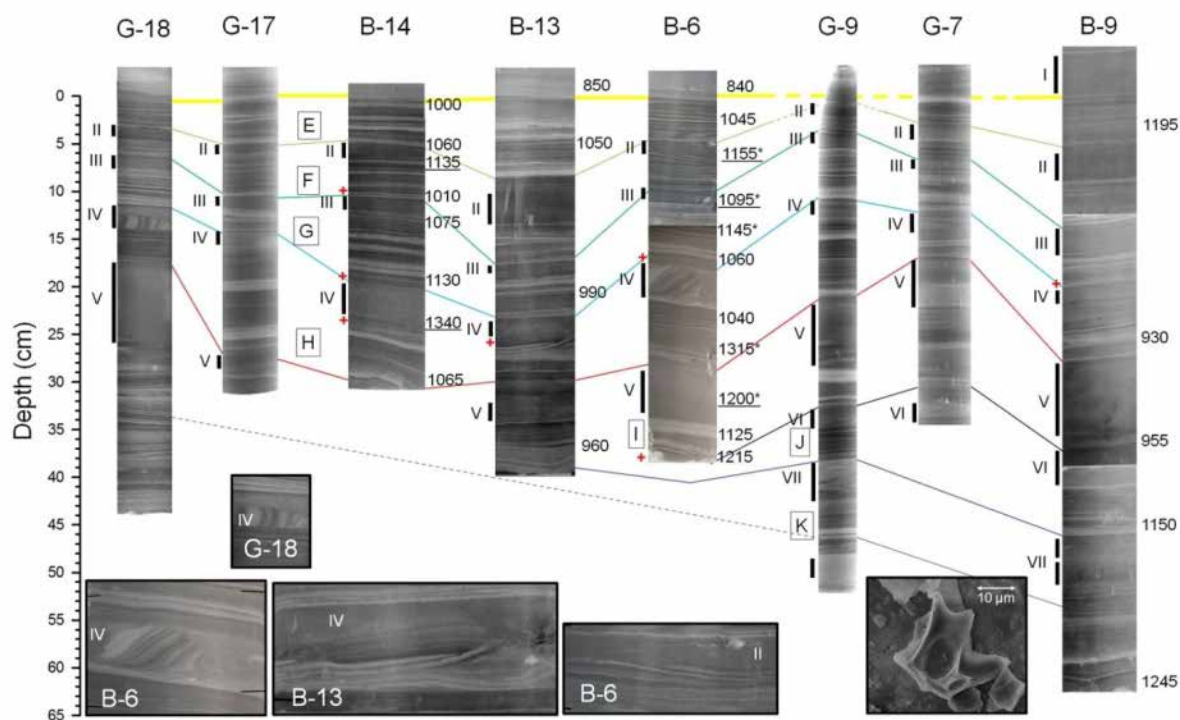
Figure II-8. Lateral correlation during the pre-shift period (as in Fig. II-6), emphasizing the different thicknesses of contemporaneous homogeneous or slumped deposits (roman numerals) below the sediment shift (which is assigned a depth of 0). The yellow lines indicate the position of the sedimentological shift as shown in Figures II-3, II-4, II-5 and II-6. The stratigraphic markers are represented by the colored thin lines as in Fig. II-6 and the capital letters indicate contemporaneous sediment sequences as in Figs. II-6 and II-7. Bars indicate the extent of the homogeneous/slumped deposits. The red crosses at the left side of some sedimentary sequences indicate the presence of the volcanic ashes. Numbers at the right of the box-cores indicate conventional radiocarbon ages (years BP) where underlined values indicate samples associated with slumps, and asterisks in core B-6 indicate samples that were not used in the chronological model by Gutierrez et al. (2009). All the ^{14}C data have an analytical error of ± 30 years BP with exception of 3 ^{14}C dates in core B-6 (1060, 1040 and 1215) which have an analytical error of ± 45 years BP. The inset panels show the X-ray images (augmented 50%) of the evident slump IV in G-18 and in B-6, laminae deformation below slumps IV in B-13, laminae erosion below slump II in B-6, and a volcanic glass found in core B-6 above slump IV. Note that, in the inset panel the slump in B-6 is composed of laminae diagonal to the sedimentation plane (from the center of the slump to the left side) and homogeneous sediments (at the right side of the slump) and in GC-18 a homogeneous layer is overlying the evident slump (see text). In all the X-ray and SCOPIX images the colors were inverted, thus the darker (lighter) laminae represent dense (less dense) sediments.

II-5.6 Radiometric ages of bulk organic matter

The conventional ^{14}C ages prior to the shift are scattered and there are many age inversions (e.g. core B-9, Fig. II-8) or ages do not notably change downcore (e.g. core B-13, Fig. II-8). However, radiocarbon data in the contemporaneous sediment sequences in different cores are generally consistent with the lateral correlations. For example the age of the samples close to the sedimentary shift in the sediment sequence E (Fig. II-8) are 1060 ± 30, 1050 ± 30 and 1045 ± 30 yr

BP in cores B-14, B-13 and B-6 respectively. The exception is B-9, which shows an anomalously high ^{14}C date (1195 ± 30 yr BP) in this part of the record. However, some other factors (e.g. reworking, sources of organic carbon [labile vs. refractory, terrestrial vs. marine, etc.], differences in reservoir age between sites, etc.) may contribute considerably to dating differences as well. Therefore, it is not surprising that in many correlated sequences the age of the samples varied considerably and in some cases showed younger dates than the more recent sedimentary shift. For example in section J (Fig. II-8) the ^{14}C date in core B-13 is 960 ± 30 yr BP while in core B-9 is 1150 ± 30 yrs BP. Surprisingly, young ^{14}C dates (with regard to the depth at which the samples were taken) were found in section H in cores B-14, B-6 and B-9 (1065 ± 30, 1040 ± 45 and 930 ± 30 yrs BP respectively) possibly indicating that the organic matter source and the reservoir age were similar in all the cores sites at that particular time.

The older conventional ^{14}C dates in some homogeneous deposits during the pre-shift period are consistent with an origin of these deposits from older sediments upslope rather than bioturbated sequences (underlined values in cores B-14 and B-6, Fig. II-8). Indeed, in core B-14 the ages of two samples associated with slumps II and IV consistently showed older ages (1135 ± 30 and 1340 ± 30 yr BP, Fig. II-8) than the closest sample (1010 ± 30 and 1130 ± 30 yr BP, respectively). In core B-6, Gutierrez et al. (2009) discarded 5 radiocarbon ages (indicated by an asterisk at the right side of the ^{14}C age in Fig. II-8) because samples were associated with allochtonous, reworked or even terrestrial organic matter. Three of the discarded ages in core B-6 belonged to slumps II, III and V, and two of them (^{14}C dates associated with slumps II and V) presented slightly older ages (1155 ± 30 and 1200 ± 30 yr BP respectively) than the next down-core samples (1060 ± 45 and 1125 ± 30 yr BP) that were used in the chronological model by Gutierrez et al. (2009, supplementary material).

II-5.7 Construction of the composite sequence

The lateral correlation of stratigraphic markers and the identification of slumps permitted estimates of sedimentary sequences lost in each core (Fig. II-9A). B-14, collected in the core of the OMZ where best preservation was expected, contained the best sequences in terms of completeness, laminae definition and contrast. Taking B-14 as a reference, contemporaneous sediment sequences of other box-cores (Fig. II-7) were positioned according to the depth of the equivalent sediment sequence in B-14 (Fig. II-9A). The ^{241}Am and ^{210}Pb$_{ex}$ profiles indicate lower sedimentation rates in B-6 and B-9 in comparison to B-13 and B-14 above the sedimentary shift (Fig. II-5). Consequently, contemporaneous sediment sequences in B-6 and B-9 do not have the same sizes as in B-13 and B-14 (Fig. II-7), thus the blank areas between sediment sequences in B-6 and B-9 (first ~30 cm in Fig. II-9A) are mainly explained by the differences in sedimentation rates and do not represent sedimentary losses as no direct evidence of discontinuities was found. All the cores showed evidence of sediment

losses (hatched areas in Fig. II-9A). B-13 and B-14 are the most complete records while B-6 and B-9 (both located in a steeper slope, Fig. II-1) likely lost most of the laminated sequences between ~35 to ~60 cm in B-13 and B-14 (Fig. II-9A) which comprise the sediment sequences containing the diatom layers and the laminated sequences between them. The lack of sedimentary sequences in cores B-6 and B-9 cannot be explained only by different sedimentation rates between core sites since no evidence of the sediment structures were found in B-9, and B-6 only contains some laminae and one diatom band of the sediment sequences present in B-13 and B-14. Additionally, small-scale losses of sediment sequences can also be observed below ~60 cm in all the cores (Fig. II-9A) as shown by the overlap of lamina sequences (Fig. II-7).

The composite sequence (Fig. II-9B) was mainly assembled from B-14 sections and completed with the other cores. The boundaries between sections were defined by the anchor layers and the stratigraphic markers shown in Fig. II-6. The composite sequence is composed from the top of the core down to the limit of detection of ^{241}Am (sedimentary sequence A; Figs. II-6 and II-7) by sediment sequences from B-13. Although B-13 shows a segment likely characterized by bioturbation and/or the flux of a more homogenous sediment type, its more regular ^{210}Pb$_{ex}$ profile (Fig. II-6) indicates less discontinuities compared with the other cores. From the limit of detection of ^{241}Am to the sedimentary shift, core B-14 shows the most complete sediment sequences which comprise sediment sequences B, C and D (Fig. II-6) and covers the entire ^{210}Pb$_{ex}$ domain. From the sedimentary shift to the base of the composite sequence, sediment sequences of cores B-13, B-14, B-6 and B-9 were selected. Section E, which is the first sediment sequence below the sedimentary shift, was taken from B-13. Sections F, G and H were taken from B-14. Sections I, J and K were taken from B-6, B-13 and B-9 respectively.
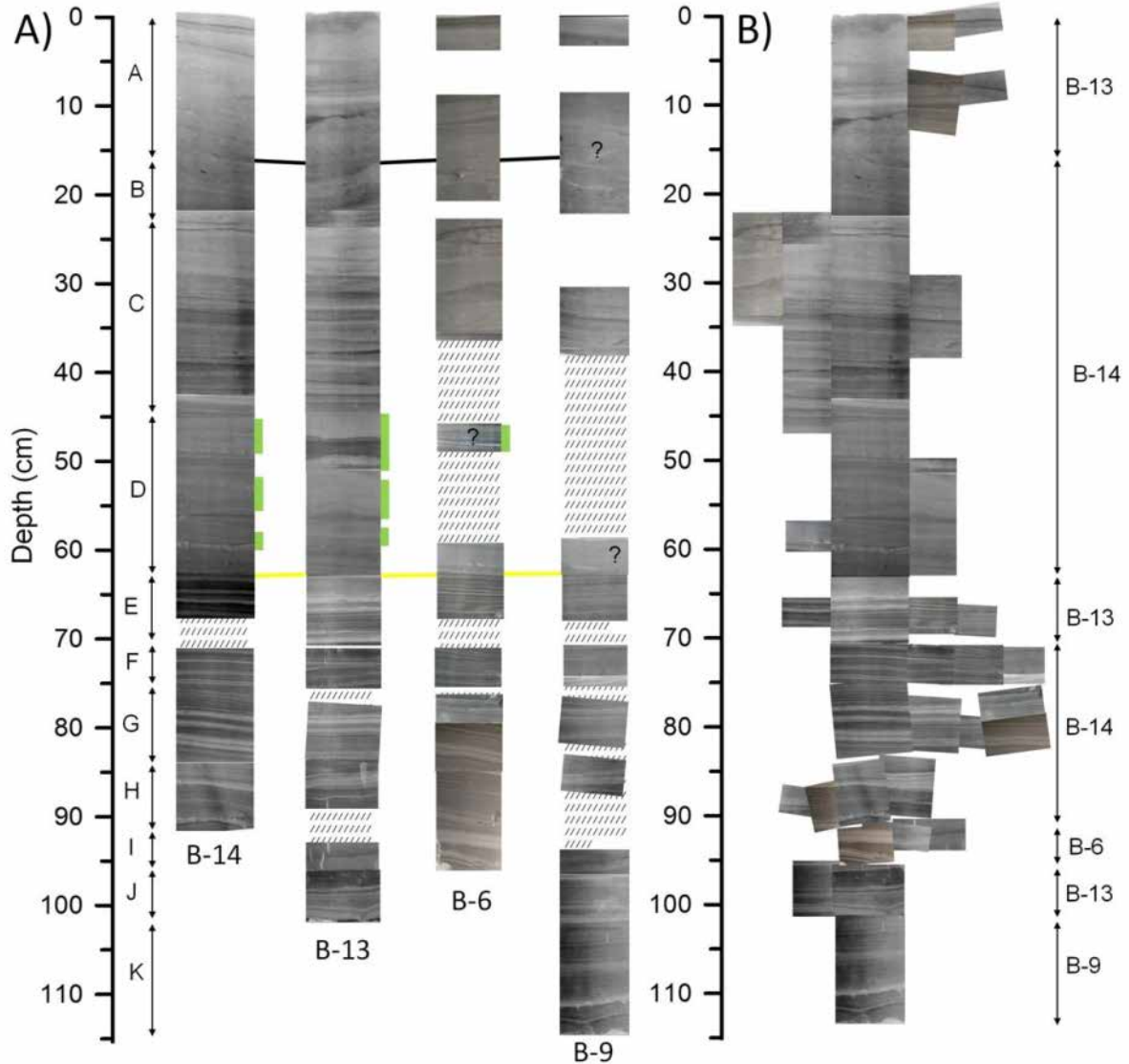
Figure II-9. A) The full sequences of the box-cores showing discontinuities (hatched areas) inferred from the removal of slumps and lateral correlation of laminae. Taking B-14 as a reference, contemporaneous sediment sequences of cores B-13, B-6 and B-9 shown in Figure II-7 were positioned according to the depth of the equivalent sediment sequence in B-14. Given that the sedimentation rate of cores B-6 and B-9 is lower than B-13 and B-14, the contemporaneous sediment sequences in B-6 and B-9 are smaller in comparison to B-13 and B-14, thus some of the blank areas may be possible explained by changes in sedimentation rates. The black and yellow lines indicate the depth at which the ^{241}Am becomes detectable (0.15 dpm.g^{-1}) and the sedimentary shift respectively. The green bars at the right side of some sedimentary sequences indicate the extent of the diatom layers as in Figures II-4, II-5 and II-6. The "?" inside some sediment sequences indicate uncertainty in the position of these segments. The capital letters from A to K indicate the contemporaneous sediment sequences as in Figures II-6, II-7 and II-8. The homogeneous deposits (bars in Fig. II-8) were removed in all cores. B) The composite sequence reconstructed from the selected spliced sedimentary sequences of all the box-cores shown in Figure II-7. The labels at the right side of the composite sequence indicate the cores that present the more continuous sedimentary sequence in each contemporaneous sediment sequences (capital letters from A to K, see Fig. II-7), and these selected sediment sequences were placed in the middle of the composite sequence. The sedimentary sequences were slighted reduced or augmented as in Figure II-7.

II-6. Discussion

A lateral correlation of sedimentary sequences among four gravity cores and four box-cores was done in order to document the spatial extent of laminae between sites, to determine the record continuity and to develop a high resolution composite sequence derived from the cross-stratigraphy. The stratigraphic markers correlation among the cores (Fig. II-6) clearly shows that some laminae can be traced across at least 40 km, implying regional processes of laminae formation. However some laminae couldn't be clearly identified across the region. The differences among core sites may be due to patchiness of diatom bloom deposits, differences in sedimentation rates among core sites, better contrast in sediment fluxes in some sites, slight changes of bioturbation intensity (driven by oxygenation events) and differences in the extent of sediment erosion. Additionally, all core sites presented events of lateral deposition that have disrupted the stratigraphic continuity of the laminae sequence (Fig. II-8), indicating frequent violation of the assumption of continuous records in this region and implying frequent major displacements of sediments. In some sites the slump deposits eroded previously deposited laminae sequences, which was only apparent after detailed comparisons among cores (Fig. II-7).

II-6.1 Spatial continuity of sediment sequences

The lateral correlation of stratigraphic markers among the 8 cores shows that there are many identifiable laminae but there are also unidentifiable sequences (Fig. II-6), which was not the case in other regions such as the Santa Barbara or Guaymas basins (Baumgartner et al., 1991; Field et al., 2009). The fact that some stratigraphic markers could be correlated among cores retrieved up to 40 km apart indicates that laminae formation is driven by regional processes. Below the sedimentary shift, where the stratigraphic markers are well observed in all cores, the laminated sequences in one core match the laminated sequences of the other cores after a slight reduction or expansion of the images (Fig. II-7). The lateral correlation of stratigraphic markers below the shift is due to well defined laminae sequences, although some laminae could not be correlated. In contrast, above the sedimentary shift the correlations are less obvious, because laminae are less defined. Furthermore, post-shift sequences were only retrieved in four cores, and two of them presented large discontinuities (Fig. II-9).

The prominent diatom layers above the sedimentary shift (~1820 AD) present in many of the cores retrieved off Pisco (Fig. II-4) were likely originated by regional oceanographic events. These events had a large geographical extension since also a box-core retrieved off Callao (~12° S; Gutierrez et al., 2009; Sifeddine et al., 2008) and 2 sediment cores retrieved off Mejillones (~23° S; ~70° 25'W; Diaz-Ochoa et al., 2011) show evidence of thick diatom layers after the sedimentary shift.

The mechanism could be a strong variability in the position of the oceanic front between the cold coastal waters and the warm subtropical oceanic waters off Peru and Chile that favored the bloom and subsequent sedimentation of some diatom species. The different number of diatom layers after the sedimentary shift in B-13 and B-14 in comparison to B-6 and the absence of diatom layers (and the intermediate sediment sequences) in B-9 was due to the discontinuity observed in this part of the record in B-6 and B-9 and also in part by lower sedimentation rates (Fig. II-9A).

Several independent lines of evidence indicate that some homogeneous sections (Figs. II-6 and II-8) were caused by instantaneous deposits from upslope rather than by bioturbation events or rapid sedimentation events. First and most important, within the slump IV in cores B-6 and GC-18, some laminae are perpendicular or diagonal to the sedimentation plane (Fig. II-8 inset panels) which is strong evidence of typical deformation of soft laminae sequences associated to a slump (Shanmugam, 2010). Second, complete dissolution of foraminifera was observed in the laminated sequences above the slumps in B-6 (Fig. II-8) while in the first centimeters below the slumps II, III and IV the foraminifera were well preserved, which indicates that the rapid deposition of the slump favored the preservation of foraminifera (Morales et al., 2006). Third, the lateral correlation of the equivalent homogeneous sections among cores (Figs. II-6 and II-8) indicates dramatically different thickness in each core (Table II-1), which stands in clear contrast to the relatively similar thickness of equivalent laminae sequences. Fourth, laminae erosion can be observed in many cores below the homogeneous deposits (Fig. II-8, inset panels). Fifth, below some homogeneous deposit there are more laminae in some of the cores suggesting that the slump eroded previously deposited sediments (Fig. II-7). Finally, the ^{14}C ages in these homogeneous layers indicate older ages (Fig. II-8) and very negative δ^{13}C values (Gutierrez et al., 2009). In some cores the slumps or homogeneous deposits were observed only as millimeter scale bands that could have passed unobserved if a detailed lateral correlation had not been done. Given that these homogeneous sections were instantaneously deposited from upslope, they were removed from the records.

II-6.2 Implications for geochronology studies

Chronologies based on ^{210}Pb$_{ex}$ and validated by independent markers (e.g. ^{241}Am, ^{137}Cs) are widely used for dating marine sediments and considered sufficiently robust to develop high resolution records (Appleby, 2001, 2008; Kirchner, 2011; Sanchez-Cabeza and Ruiz-Fernández, 2012). However, off Pisco the radioisotope profiles do not necessarily reveal record discontinuities. Cores that present interspersed losses of sedimentary sequences may be interpreted as records with low sedimentation rates. For example, the ^{210}Pb$_{ex}$ profiles are deeper in cores B-13 and B-14 in comparison with B-6 and B-9 (Fig. II-5), which could be erroneously explained just by changes in sedimentation rates. After a detailed analysis of the X-ray images among cores, there were clearly

several centimeters of sedimentary sequences present in cores B-13 and B-14, but absent in cores B-6 and B-9 (Fig. II-9A), indicating large discontinuities, particularly in B-9. Additionally, cores retrieved from 200 m and 300 m depth show similar sediment accumulation rates (e.g. B-13 and B-14) despite the differences in depth, while cores retrieved at the same depth (e.g. B-6 and B-14) show differences in sediment accumulation rates (Fig. II-5). Lower rates are associated to a steeper slope (Figure II-1), suggesting that the bottom topography rather than the water column depth is the major factor that determines sediment accumulation rates off Pisco. Radiocarbon dating of slumps may lead to age inversions and should therefore be avoided. These structures could be erroneously interpreted as mixed- or rapid pelagic deposition layers. The results of the present work highlight the necessity of combining the radioisotopes profiles with a detailed sedimentological approach in order to develop a chronological model for high resolution studies.

Despite the findings above, some sequences likely result from episodes of sediment mixing, as inferred from the constant values of the $^{210}Pb_{ex}$ in some parts of the profiles and the detailed study of the X-ray images (Fig. II-5). Some sequences show mixing events covering up to ~10 cm (Fig. II-5), likely triggered by bottom water oxygenation during strong El Niño events. If the mixing events were originated by slumps (containing older sediments from upslope), then the sediments should present low $^{210}Pb_{ex}$ activities, which is not the case in any of the cores (Fig. II-5). Additionally, the laminated sequences between diatom layers in B-14 and B-13 are better preserved in the deepest core (B-14). X-radiographs of cores retrieved off Callao in the OMZ during the strong El Niño 1997-1998 reveal the presence of bioturbated zones in the first centimeters of the cores associated with the presence of oligochaetes (Levin et al., 2003). This result implies that short-term changes in oxygenation can have profound effects on the preservation of the sedimentary sequences of the cores. As a consequence, cores at 300 meters depth should be less subject to the influence of bioturbation.

The scattering of the conventional ^{14}C age profiles (Figs. II-8 and II-9) implies that the ^{14}C ages from bulk organic matter cannot be used to resolve absences or discontinuities in the sedimentary record for high resolution studies in the region. The observed scattering is mainly due to changes in the organic matter source (i.e. terrestrial vs. marine) and changes in the local reservoir age. The comparison of ^{14}C measurements from bulk organic matter and alkenone to date cores covering the last 13 000 yr BP suggests a bias between these two sources (Makou et al., 2010 supplementary information). For example, a sample located at 165 cm depth in a core retrieved at ~11 °S (ODP site 1228D, Leg 201) has a bulk organic carbon conventional date of 2660 ±40 yr while the alkenone date is 2910 ±110 yr (Makou et al., 2010 supplementary information). Although this difference is relatively small, it is too large to resolve a high resolution record for the past centuries. Given the potential errors of ^{14}C dating of sedimentary organic matter, radiocarbon measurements should be

done in samples that share the same fraction of organic matter, e.g. biomarker-specific (e.g. alkenone) compounds which contains organic matter exclusively of marine origin (Makou et al., 2010), or at least in previously isolated material following a petrographic study. Local reservoir (delta-R) changes through time due to changes of coastal upwelling intensity and water mass properties are another likely source of geochronological errors. Delta-R values vary by a factor of 2 ($226 \pm 98 - 511 \pm 278$ y) at centennial to millennial time-scales off Southern Peru/Northern Chile during the Holocene (Ortlieb et al., 2011). Similarly, a large difference of delta-R values since ~500 BP to the present off Central Peru has been inferred by comparisons of radiocarbon and ^{210}Pb ages (Gutiérrez et al., 2009). Therefore, even if the carbon source is accounted in radiocarbon dating, it is of primary importance to use an independent chronological marker in order to develop robust age models.

II-6.3 Preliminary chronology prior to the sedimentary shift and slump origin

The ^{14}C dates help to constrain the chronologies but show considerable uncertainty for developing a reliable high-resolution chronological model of high resolution using the ^{14}C dates alone. Therefore, we gave them low consideration but present them here to test if the slumps originated by strong tsunamogenic earthquakes. A sedimentation rate for the period below the sedimentary shift was calculated using the ^{14}C data of core B-6 (Gutierrez et al., 2009) after identifying and removing the slumps in the core. Core B-6 was used because it has more ^{14}C dates in comparison with other cores (Fig. II-8) and an organic petrography (palynofacies) study had already been conducted to discard samples associated with allochtonous, reworked or terrestrial organic matter. First, using a preliminary dating of the sedimentary shift at ~1820 AD (Gutierrez et al., 2009), we calculated the accumulated mass in core B-6 during the pre-shift period by eliminating all the samples associated with the inferred slumps (Fig. II-8). The local reservoir age (ΔR), needed to estimate the calibrated ^{14}C ages, was calculated with a linear regression between conventional ^{14}C age and the accumulated mass before the sedimentary shift as explained by Gutierrez et al. (2009, supplementary material) and was found to be 367 ± 40 yr. Then, the ^{14}C ages in core B-6 were calibrated with the software CALIB v. 6.1 (Stuiver and Reimer, 1993). Finally, a chronological model was constructed using the calibrated ^{14}C ages and the accumulated mass. This model gave a preliminary sedimentation rate of 0.69 ± 0.05 mm yr^{-1}, which indicates that the B-6 core base is ~1407 ± 32 AD. The sedimentation rate estimated in core B-6 for the pre-shift period should be valid as well for the other cores given that the thickness of the laminae sequences are similar among the cores (Fig. II-7).

The strong tsunamogenic earthquakes that hit the city of Pisco may be the principal cause that triggered the slumps observed in the records (Fig. II-6). Applying the estimated sedimentation rate to core B-6, the age of the samples above slumps II, III and IV (Fig. II-8) are 1755 ± 13, 1686 ± 16 and

1592 ±21 AD, which are very close to the strongest tsunamogenic earthquakes that hit Pisco in 1746, 1687 and 1604 AD (Dorbath et al., 1990, Okal et al., 2006). The other strong tsunamogenic earthquake that hit the city of Pisco (1868 AD) could be responsible for the large hiatus in core B-6 and B-9 (Fig. II-9A). The sediment sequences lacking in B-6 and B-9, which correspond to the diatom layers in B-13 and B-14 (~45 to 60 cm), are located between the limit of $^{210}Pb_{ex}$ (Fig. II-5) and the sedimentary shift (Fig. II-6), thus they were deposited between ~1870 and ~1820 AD. Consequently, is very likely that the 1868 earthquake, the largest to affect Peru in historical times and responsible for the total destruction of the city of Pisco, caused large hiatus in cores B-6 and B-9, located in a steeper slope and more vulnerable affected than the other cores.

To corroborate the dates calculated, we searched for independent evidence such as volcanic ashes which have been used to date, correlate cores, and infer paleo-volcanism in many regions of the world (Pouclet et al., 1990; Hart and Miller, 2006; Lowe, 2011). Detailed examination of cores retrieved off Peru show thick ash layers in Miocene, Pliocene, Pleistocene, and Holocene sediments (Pouclet et al., 1990; Hart and Miller, 2006), suggesting that the volcanic layers in sediments off Peru may be used to infer paleo-volcanism. The 1600 AD eruption of Huaynaputina, in southern Peru, has been speculated to be one of the largest eruptions of the past 500 years, with a similar or larger magnitude than the Krakatau (de Silva and Zielinski, 1998; Adams et al., 2001). The fall deposit covered an area of at least 300 000 km^2 in southern and west central Peru, western Bolivia and north Chile, and the ash fall was reported in Lima, La Paz (Bolivia), Arica (Chile) and on a ship 1 000 km to the west of the coast (de Silva and Zielinski, 1998). Therefore, we would expect that the volcanic ashes from the Huaynaputina volcanic eruption reached the sea floor off Pisco and serve as an independent time-marker.

We found sparse volcanic glasses during the pre-shift period in some laminae (red crosses and inset panel in Fig. II-8), especially below slump IV in cores B-13 and B-14, in the first laminae right after the slump IV in cores B-6, B-9 and B-14, at the bottom of section I in B-6, and in the first pair of laminae of section F in B-14 (on top of slump III; Fig. II-8). If the repeated presence of dispersed volcanic ashes in a given core can be explained by events of terrestrial runoff after the volcanic eruption, then it is most likely that the first stratigraphic layer in several cores with volcanic glasses would be the closest stratigraphic marker of the volcanic eruption. As most of the ash presence occurs above and below slump IV, the first laminae in contact with the base of slump IV could correspond to the 1600 AD Huaynaputina eruption. The relative position of slump IV is consistent with the occurrence of the very strong earthquake that hit Pisco in 1604 AD, considered as the second one in intensity and rupture area since the sixteenth century (Dorbath et al., 1990). The estimated age from of slump IV using the volcanic ashes is consistent with the age of this slump calculated using the ^{14}C ages (1592 ±21 AD), providing an independent validation of the chronology up to the sedimentary

shift, within estimation errors. Although we found some dispersed volcanic ashes, we were not able to detect a defined ash layer. Its absence could be attributed to a mechanism of transport towards the seafloor from the eruption. It is possible that, depending on the volume of the atmospheric plume over the sea, that the ashes could be diluted and redistributed by currents away from the original zone of deposition. It is also possible that post-deposition processes may erode or rework the ash signal, for example the slump IV could be responsible for the erosion of the volcanic ash layer.

Slope instabilities occur when the loads acting on sediment mass exceed the resistance offered by the sediment strength (Duperret et al., 1995). The two major factors that are responsible for slope instabilities are a) a downslope stress increase by external load (resulting from slope angle steepening which may occur by tectonic effect or by high sedimentation rates) or by basal unload, and b) an excess of pore water pressure that can result from allochtonous fluid accumulation, from high sedimentation rates or from earthquakes (Duperret et al., 1995; Greene et al., 2006). The steepness of the slope can also be a factor that affects the stability of the sedimentary record; cores B-6 and B-9 that were retrieved in a steeper part of the shelf show larger discontinuities (Fig. II-9A) in comparison to cores B-13 and B14 that were retrieved in a gentler sloping platform (Fig. II-1). Thus, slumps can be triggered by earthquakes and other non-seismic mechanisms. Although we did not conduct a full study to determine the causes of the slumps we speculate that the presence of numerous slumps before the sedimentary shift can be better explained by strong tsunamogenic earthquakes as explained above. A more detailed chronology (e.g. sedimentation rates inferred by ^{32}Si) is required to explore the possible seismic origin of the other slumps.

II-6.4 Composite sequence

The selection of the most complete sediment sequences shown in Fig. II-7 permitted assembling a composite sequence which contains the most complete record off Pisco (Fig. II-9B) and can be used as the chronological basis for downcore paleoceanographic studies. This composite sequence contains sediment sequences that would not be available if only one core was analyzed. The composite sequence was assembled from cores retrieved at 200 and 300 m depth and this difference in depth may have an influence in some proxies, as the redox sensitive metals, in which needs to be accounted in the interpretation of the data. Consequently, when deriving proxy records it would be better to average the proxy values to account for the lateral variability.

The reconstruction of a composite sequence off Guaymas by Baumgartner et al. (1991) was possible by the fact that each core site presented small-scale mass movements but the same mass movements did not affect all the core sites. Moreover Baumgartner et al. (1991) only found one large discontinuity that cut across the core sites. In contrast, the mass movements observed in all the cores

off Pisco affected all the core sites and the composite sequence may still present missing sediment sequences that were possibly eroded in all the core sites. However, in spite of these uncertainties, it should be clear that a composite sequence has overwhelming advantages with respect to sedimentary sequences that contain unknown numbers of hiatus interspersed within laminated sequences.

II-6.5 Implications for other high resolution studies

The results of the present work have many implications for paleo reconstructions off Peru and in other areas that may present similar characteristics. Prior to the present study, several sediment cores retrieved off Peru revealed widespread occurrences of large discontinuities (DeVries and Pearcy, 1982; Skilbeck and Fink, 2006; Makou et al., 2010). The present work casts uncertainties to the interpretations of high resolution records obtained from marine cores retrieved off Peru in order to infer changes in the frequency of former El Niño events (Rein et al., 2004; Rein et al., 2005; Rein et al. 2007) or to infer changes in productivity at sub-decadal resolution (Agnihotri et al., 2008). All the cores evaluated in the present work show discontinuities and the addition of upslope material (Figs. II-8 and II-9). These processes are not trivial; core B-9 (total length 97 cm) shows a hiatus of up to 25 cm in comparison to B-14, and also contains a total of 32 cm of slumped and homogeneous sediment sequences along the core (Fig. II-6). The presence of slumped material and the existence of hiatuses are not proper to Pisco cores; box-cores retrieved off Callao also show evidence of slumped material (Gutierrez et al., 2009). Even if sediments from other sites are unlikely to have the same degree of discontinuity, they are probably occasionally subjected to discontinuities. The homogeneous sections found in the cores need to be identified as slumps, bioturbation events or rapid sedimentation events. If the homogeneous deposits were originated from slumps they must be removed from the records. The bioturbated sections must remain in the record but need to be identified as such, since they must be taken into consideration during paleoceanographic interpretation. The temporal variability of the proxies developed within homogeneous, slumped or bio-turbated sections may be small in comparison to laminated sequences and could be interpreted erroneously as periods of inferred low climate variability. Additionally, temporal gaps within the cores could lead to reductions of the sedimentation rates that dilute the fluxes of the proxies. Thus, high resolution studies should indicate the laminated sections in the cores (Cartapanis et al., 2011), identify the slumps and the homogeneous sections, and base their interpretations of high resolution climate variability on the results obtained on the laminated parts of the record.

II-7. Conclusions

This study showed widespread and frequent discontinuities that are only apparent after detailed comparisons of X-ray images, radionuclide profiles and other stratigraphic indicators among cores. All the cores evaluated in the present work show evidence of multiple discontinuities, due to loss of sequences and instantaneous deposit arising from slumps, possibly triggered by tsunamogenic earthquakes, which indicate frequent violation of the assumption of record continuity. The discontinuities observed in all the cores indicate that the reconstruction of past climate variability at high resolution level using one single core in this region is subject to temporal gaps that could lead to erroneous interpretations in regions of active slumping, due either to tectonic activity, steep slopes or other reasons. Therefore, multiple cores must be studied in order to reconstruct a master chronology for accurate high resolution studies.

A regional process is involved in the laminae formation since the lateral continuity of laminae can be traced along at least 40 kilometers. Moreover the presence of diatom layers right after the sedimentary shift in cores retrieved off Pisco (~14 °S), off Callao (~12 °S) and even off Chile (~23 °S) indicates a period of particular regional oceanographic conditions favoring the occurrence of large-scale diatom bloom events.

Chronological models of sediment cores from areas with characteristics similar to the Peruvian shelf should be developed by combining a detailed sedimentological approach with radioisotopes profiles for high resolution studies. Moreover, the scattering and inversions of ^{14}C ages from bulk organic matter clearly indicate that this approach must be avoided for high resolution models. Additionally, an independent time marker, like the volcanic ashes or another decaying isotope like ^{32}Si must be further developed in order to construct a robust chronological model for high resolution studies.

II-8. Acknowledgments

II-9. Bibliography

Adams, N.K., de Silva, S.L., Self, S., Salas, G., Schubring, S., Permenter, J.L., Arbesman, K., 2001. The physical volcanology of the 1600 eruption of Huaynaputina, southern Peru. Bulletin of Volcanology 62, 493-518.

Agnihotri, R., Altabet, M.A., Herbert, T., Tierney, J.E., 2008. Subdecadally resolved paleoceanography of the Peru margin during the last two millennia. Geochemistry Geophysics Geosystems 9(5), 1-15.

Appleby, P.G., 2001. Chronostratigraphic techniques in recent sediments, in: Last, W.M., Smol, .J.P. (Eds.), Tracking Environmental Change Using Lake Sediments. Volume 1: Basin Analysis, Coring, and Chronological Techniques. Kluwer Academic Publishers, Dordrecht, The Netherlands, pp. 171-203

Appleby, P.G., 2008. Three decades of dating recent sediments by fallout radionuclides: a review. The Holocene 18(1), 83-93.

Audin, L., Lacan, P., Tavera, H., Bondoux, F., 2008. Upper plate deformation and seismic barrier in front of Nazca subduction zone: The Chololo Fault System and active tectonics along the Coastal Cordillera, southern Peru. Tectonophysics 459, 174-185.

Barber, R.T., Chavez, F., 1983. Biological consequences of El Niño. Science 222, 1203-1210.

Baumgartner, T.R., Ferreira-Bartrina, V., Cowen, J., Soutar, A., 1991. Reconstruction of a 20th century varve chronology from the central Gulf of California, in: Dauphin, J.P., Simoneit, B.R.T. (Eds.), The Gulf and Peninsular Province of the Californias. American Association of Petroleum Geologists, Tulsa, Oklahoma, U.S.A.

Blais-Stevens, A., Clague, J.J., 2001. Paleoseismic signature in late Holocene sediment cores from Saanich Inlet, British Columbia. Marine Geology 175, 131-148.

Cartapanis, O., Tachikawa, K., Bard, E., 2011. Northeastern Pacific oxygen minimum zone variability over the past 70 kyr: Impact of biological production and oceanic ventilation. Paleoceanography 26, PA4208.

Chazen, C.R., Altabet, M.A., Herbert, T.D., 2009. Abrupt mid-Holocene onset of centennial-scale climate variability on the Peru-Chile Margin. Geophysical Research Letters 36, L18704.

Contreras, S., Lange, C.B., Pantoja, S., Lavik, G., Rincón-Martínez, D., Kuypers, M.M., 2011. A rainy northern Atacama Desert during the last interglacial. Geophysical Research Letters 37, L23612.

de Silva, S.L., Zielinski, G.A., 1998. Global influence of the AD1600 eruption of Huaynaputina, Peru. Nature 393, 455-458.

De Vries, T., Pearcy, W., 1982. Fish debris in sediments of the upwelling zone off central Peru: a late Quaternary record. Deep-Sea Research 28, 87-109.

Diaz-Ochoa, J.A., Pantoja, S., De Lange, G.J., Lange, C.B., Sanchez, G.E., Acuña, V.R., Muñoz, P. Vargas, G., 2011. Oxygenation variability in Mejillones Bay, off northern Chile, during the last two centuries. Biogeosciences 8, 137-146.

Dorbath, L., Cisternas, A., Dorbath, C., 1990. Assessment of the size of large and great historical earthquakes in Peru. Bulletin of the Seismological Society of America 80(3), 551-576.

Duperret, A., Bourgois, J., Lagabrielle, Y., Suess, E., 1995. Slope instabilities at an active continental margin: large-scale polyphase submarine slides along the northern Peruvian margin, between 5°S and 6° S. Marine Geology 122, 303-328.

Field, D.B., Baumgartner, T.R., Ferreira, V., Gutierrez, D., Lozano-Montes, H., Salvatteci, R., Soutar, A., 2009. Variability from scales in marine sediments and other historical records, in: Checkley, D., Roy, C., Alheit, J., Oozeki, Y. (Eds.), Climate Change and Small Pelagic Fish. Cambridge University Press, pp. 45-63.

Giovanni, M.K., Beck, S.L., Wagner, L., 2002. The June 23, 2001 Peru earthquake and the southern Peru subduction zone. Geophysical Research Letters 29(21), 21018.

Goldfinger, C., 2010. Submarine paleoseismology based on turbidite records. Annual Review of Marine Science 3, 35-66.

Greene, H.G., Murai, L.Y., Watts, P., Maher, N.A., Fisher, M.A., Paull, E., Eichhubl, P., 2006. Submarine landslides in the Santa Barbara Channel as potential tsunami sources. Natural Hazards and Earth System Sciences 6, 63-88.

Gutierrez, D., Sifeddine, A., Reyss, J.L., Vargas, G., Velazco, F., Salvatteci, R., Ferreira-Bartrina, V., Ortlieb, L., Field, D., Baumgartner, T., Boussafir, M., Boucher, H., Valdes, J., Marinovic, L., Soler, P., Tapia, P., 2006. Anoxic sediments off Central Peru record interannual to multidecadal changes of climate and upwelling ecosystems during the last two centuries. Advances in Geosciences 6, 119-125.

Gutierrez, D., Enriquez, E., Purca, S., Quipuzcoa, L., Marquina, R., Flores, G., Graco, M., 2008. Oxygenation episodes on the continental shelf of central Peru: Remote forcing and benthic ecosystem response. Progress in Oceanography 79, 177-189.

Gutierrez, D., Sifeddine, A., Field, D.B., Ortlieb, L., Vargas, G., Chavez, F., Velazco, F., Ferreira, V., Tapia, P., Salvatteci, R., Boucher, H., Morales, M.C., Valdes, J., Reyss, J.L., Campusano, A., Boussafir, M., Mandeng-Yogo, M., Garcia, M., Baumgartner, T., 2009. Rapid reorganization in ocean biogeochemistry off Peru towards the end of the Little Ice Age. Biogeosciences 6, 835-848.

Hart, D., Miller, D.J., 2006. Analysis and correlation of volcanic ash in marine sediments from the Peru margin, Ocean Drilling Program Leg 201: explosive volcanic cycles of the north-central Andes, in: Jørgensen, B.B., D'Hondt, S.L., Miller, D.J. (Eds.) Proceedings of the Ocean Drilling Program, Scientific Results Volume 201, pp. 1-43.

Helly, J., Levin, L., 2004. Global distribution of naturally occurring marine hypoxia on continental margin. Deep-Sea Research I 51, 1159-1168.

Hill, E.A., Hickey, B.M., Shillington, F.A., Strub, P.T., Brink, K.H., Barton, E.D., Thomas, A.C., 1998. Eastern Ocean Boundaries Coastal Segment (E), in: Robinson, A.R., Brink, K.H., (Eds.), The Sea. The Global Coastal Ocean. John Wiley & Sons Inc., New York, pp. 29-67.

Kemp, A.E., 1990. Sedimentary fabrics and variation in lamination style in Peru continental margin upwelling sediments, in: Suess, E., von Huene, R., et al. (Eds.), Proceedings of the Ocean Drilling Program, Scientific Results, Vol. 112, pp. 43-58.

Kim, K.H., Burnett, W.C., 1988. Accumulation and biological mixing of Peru margin sediments. Marine Geology 80, 181-194.

Kirchner, G., 2011. ^{210}Pb as a tool for establishing sediment chronologies: examples of potentials and limitations of conventional dating models. Journal of Environmental Radioactivity 102, 490-494.

Krissek, L.A., Scheidegger, K.F., 1983. Environmental controls on sediment texture and composition in low oxygen zones off Peru and Oregon, in: Suess, E., Thiede, J. (Eds.), Coastal upwelling; its sediment record, Part B: Sedimentary records of ancient coastal upwelling. Plenum Press, New York, pp. 163-180.

Levin, L.A., Rathburn, A.E., Gutiérrez, D., Muñoz, P., Shankle, A., 2003. Bioturbation by symbiont-bearing annelids in near-anoxic sediments: Implications for biofacies models and paleo-oxygen assessments. Palaeogeography, Palaeoclimatology, Palaeoecology 199, 129-140.

Lowe, D.J., 2011. Tephrochronology and its application: A review. Quaternary Geochronology 6, 107-153.

Makou, M.C., Eglinton, T.I., Oppo, D.W., Hughen, K.A., 2010. Postglacial changes in El Niño and La Niña behavior. Geology 38(1), 43-46.

Migeon, S., Weber, O., Faugeres, J.-C., Saint-Paul, J., 1999. SCOPIX: A new X-ray imaging system for core analysis. Geo-Marine Letters 18, 251-255.

Morales, M.C., Field, D., Mayor, S., Gutierrez, D., Sifeddine, A., Ortlieb, L., Ferreira, V., Salvatteci, R., Velazco, F., 2006. Variations in foraminifera over the last 460 years from laminated sediments off the coast of Peru. Boletín de la Sociedad Geológica del Perú 101, 5-18.

Okal, E.A., Borrero, J.C., Synolakis, C.E., 2006. Evaluation of tsunami risk from regional earthquakes at Pisco, Peru. Bulletin of the Seismological Society of America 96(5), 1634-1648.

Ortlieb, L., Vargas, G., Saliège, J.-F., 2011. Marine radiocarbon reservoir effect along the northern Chile-southern Peru coast (14-24°S) throughout the Holocene. Quaternary Research 75, 91-103

Pennington, J.T., Mahoney, K.L., Kuwahara, V.S., Kolber, D.D., Calienes, R., Chavez, F.P., 2006. Primary production in the eastern tropical Pacific: A review. Progress in Oceanography 69, 285-317.

Pouclet, A., Cambray, H., Cadet, J.-P., Bourgois, J., De Wever, P., 1990. Volcanic ash from Leg 112 off Peru, in: Suess, E., von Huene, R., et al. (Eds.), Proceedings of the Ocean Drilling Program, Scientific Results, Vol. 112. pp. 465-480.

Rein, B., 2007. How do the 1982/83 and 1997/98 El Niños rank in a geological record from Peru? Quaternary International 161, 56-66.

Rein, B., Luckge, A., Sirocko, F., 2004. A major Holocene ENSO anomaly during the Medieval period. Geophysical Research Letters 31(17), 4.

Rein, B., Lückge, A., Reinhardt, L., Sirocko, F., Wolfe, A., Dullo, W.-C., 2005. El Niño variability off Peru during the last 20,000 years. Paleoceanography 20, PA4003.

Rein, B., Sirocko, F., Lückge, A., Reinhardt, L., Wolf, A., Dullo, W.-C., 2007. Abrupt Change of El Niño Activity off Peru During Stage MIS 5e-d, in: Sirocko, F., Claussen, M., Sánchez Goñi, M., Litt, T. (Eds.), The Climate of Past Interglacials. Elsevier, Amsterdam, The Netherlands, pp. 305-321.

Reinhardt, L., Kudrass, H.-R., Lückge, A., Wiedicke, M., Wunderlich, J., Wendt, G., 2002. High-resolution sediment echosounding off Peru: Late Quaternary depositional sequences and sedimentary structures of a current-dominated shelf. Marine Geophysical Researches 23(4), 335-351.

Reyss, J.L., Schmidt, S., Legeleux, F., Bonté, P., 1995. Large, low background well-type detectors for measurements of environmental radioactivity. Nuclear Instruments and Methods in Physics Research Section A: Accelerators, Spectrometers, Detectors and Associated Equipment 357(2-3), 391-397.

Salvatteci, R., Field, D.B., Baumgartner, T., Ferreira, V., Gutierrez, D., 2012. Evaluating fish scale preservation in sediment records from the oxygen minimum zone off Peru. Paleobiology 38(1), 766-792.

Sanchez, G., Calienes, R., Zuta, S., 2000. The 1997-98 El Niño and its effects on the coastal marine ecosystem off Peru. CalCOFI Report 41, 62-86.

Sanchez-Cabeza, J.A., Masqué, P., Ani-Ragolta, I. 1998. ^{210}Pb and ^{210}Po analysis in sediments and soils by microwave acid digestion. Journal of Radioanalytical and Nuclear Chemistry 227(1-2), 19-22.

Sanchez-Cabeza, J.A., Ruiz-Fernández, A.C., 2012. ^{210}Pb sediment radiochronology: An integrated formulation and classification of dating models. Geochimica et Cosmochimica Acta 82, 183-200.

Schimmelmann, A., Lange, C.B., Roark, E.B., Ingram, B.L., 2006. Resources for paleoceanographic and paleoclimatic analysis: a 6,700-year stratigraphy and regional radiocarbon reservoir-age (DR) record based on varve counting and ^{14}C-AMS dating for the Santa Barbara basin, offshore California, U.S.A. Journal of Sedimentary Research 76, 74-80.

Schnellmann, M., Anselmetti, F.S., Giardini, D., McKenzie, J.A., Ward, S.N., 2002. Prehistoric earthquake history revealed by lacustrine slump deposits. Geology 30(12), 1131-1134.

Shanmugam, G., 2010. Slides, slumps, debris flow, and turbidity currents, in: Steele, J.H., Thorpe, S.A., Turekian, K.K., (Eds.), Ocean Currents. Academic Press, Elsevier, pp. 418-437.

Sifeddine, A., Gutierrez, D., Ortlieb, L., Boucher, H., Velazco, F., Field, D., Vargas, G., Boussafir, M., Salvatteci, R., Ferreira, V., García, M., Valdes, J., Caquineau, S., Mandeng-Yogo, M., Cetin, F., Solis, J., Soler, P., Baumgartner, T., 2008. Laminated sediments from the central Peruvian

continental slope: A 500 year record of upwelling system productivity, terrestrial runoff and redox conditions. Progress in Oceanography 79, 190–197.

Skilbeck, C.G., Flink, D., 2006. Data report: Radiocarbon dating and sedimentation rates for Holocene–upper Pleistocene sediments, eastern equatorial Pacific and Peru continental margin, in: Jorgensen, B.B., D'Hondt, S.L., Miller, D.J. (Eds.), Proceedings of the Ocean Drilling Program, Scientific Results, 201, pp. 1–15.

Stuiver, M., Reimer, P.J., 1993. Extended ^{14}C database and revised CALIB radiocarbon calibration program. Radiocarbon 35, 215-230.

Suess, E., Kulm, L.D., Killingley, J.S., 1987. Coastal upwelling and a history of organic-rich mudstone deposition off Peru, in: Brooks, J., Fleet, A.J. (Eds.), Marine Petroleum Source Rocks. Geological Society, London, Special Publications, pp. 181-197.

Suess, E., von Huene, R., 1988. Ocean Drillling Program Leg 112, Peru continental margin: Part 2, Sedimentary history and diagenesis in a coastal upwelling environment. Geology 16, 939-943.

United Nations Scientific Committee on the Effects of Atomic Radiation UNSCEAR. 2000. Report to the General Assembly, with scientific annexes, Vol. I. Sources and effects of ionizing radiation. Annex C. Exposures to the public from man-made radiations.

Vargas, G., Ortlieb, L., Chapron, E., Valdes, J., Marquardt, C., 2005. Paleoseismic inferences from a high-resolution marine sedimentary record in northern Chile (23°S). Tectonophysics 399, 381-398.

Zaborska, A., Carroll, J., Papucci, C., Pempkowiak, J., 2007. Intercomparison of alpha and gamma spectrometry techniques used in ^{210}Pb geochronology. Journal of Environmental Radioactivity 93, 38-50.

CHAPTER III:

CENTENNIAL TO MILLENNIAL VARIABILITY IN OXIGEN MINIMUM ZONE INTENSITY, EXPORT PRODUCTION, AND TERRIGENOUS INPUT IN THE PERUVIAN UPWELLING ECOSYSTEM DURING THE LAST 25 KYR

III-1. Introduction

III-1.1 Scientific question to be answered

The Humboldt Current System (HCS) is one of Earth's four large and productive eastern boundary upwelling systems (EBUS) characterized by high primary productivity and an intense and shallow Oxygen Minimum Zone (OMZ; see Fig. III-1). The OMZ is a result of the lack of ventilation, long residence times and the decay of biological production (Helly and Levin, 2004; Pennington et al., 2006). The OMZ is eventually ventilated by relatively oxygen-rich waters like the Equatorial Undercurrent (EUC) and the Southern Subsurface Countercurrents (SSCCs; Montes et al., 2010; Stramma et al., 2010). The Peruvian Upwelling Ecosystem (PUE), which forms part of the larger HCS, is nourished by upwelling of cool and nutrient rich sub surface waters from the Poleward Undercurrent (PUC). Thirty percent of the PUC is fed by the EUC and the primary and secondary SSSC while the remaining part comes from an alongshore recirculation associated with flows below it, and from undercurrents south of ~9 °S (Montes et al., 2010). Nutrients subducted in the thermocline in the Subantartic Zone of the Southern Ocean as Subantartic Mode Waters (SAMW) are the dominant fuel of the EUC because SAMW feeds directly into the EUC (Martinez and Robinson, 2010). The EUC is formed in the southern high latitudes and travels all the way across the Pacific basin and then is transported poleward in the PUC (Toggweiler, 1991). The upwelling favorable winds off Peru favors productivity, and the subsequent sinking and decaying of organic matter also contribute to the subsurface oxygen deficit. Consequently, the OMZ intensity and variability off Peru is controlled by extra-tropical forcings as for example changes in the residence time of the EUC and by ventilation of the SAMW (Higginson and Altabet, 2004; Martinez and Robinson, 2010), and also by local climate variability as for example an increase in oxygen demand imposed by the decay of an increased primary productivity off Peru. In this chapter we evaluate whether extra-tropical or local climate variability dominated the subsurface ventilation and productivity off Peru during the last 25 kyr. In doing so, we also characterize the intensity of the OMZ, the export production and the terrestrial input during the Early Glacial (25.5 – 23 kyr cal BP), Last Glacial Maximum (23 – 19 kyr cal BP), Heinrich 1 Stadial (18 – 14.7 kyr cal BP), Bølling-Allerød (14.7 – 12.5 kyr BP), Early Holocene (10.5 – 8 kyr cal BP), Mid-Holocene (8 – 4 kyr cal BP), and the Late Holocene (4 – 0.05 kyr BP). The changes in OMZ intensity, the export production and the terrestrial input during the Dark Ages Cold Period, Medieval Climate Anomaly (900 – 1350 AD), the Little Ice Age (1500 – 1850 AD), and Current Warm Period (1850 to the present) are presented in detail in chapter V.
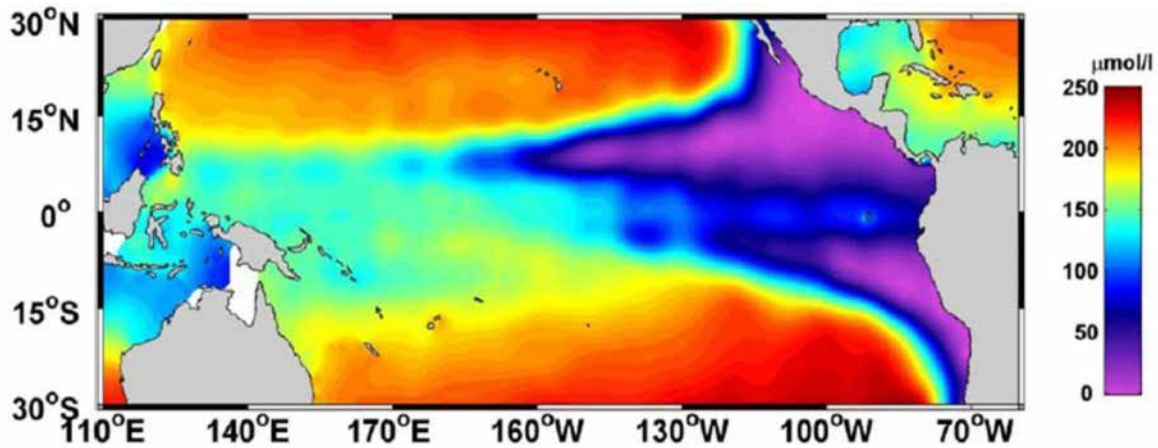
Figure III-1. Present day climatolological map of dissolved oxygen at 150 m depth (μmol L^{-1}), from the World Ocean Data Center, showing the extent of the oxygen minimum zone in the Eastern Tropical Pacific. Figure taken from Gutierrez et al. (2009). The location of the sediment records retrieved off Pisco is shown by the black dot.

The strong OMZ off Peru inhibits bioturbation and preserves high-resolution sedimentary records of past ecosystem changes in certain areas on the shelf and upper slope of the Peruvian margin (Krissek and Scheidegger, 1983; Suess and von Huene, 1988; Reinhardt et al., 2002; Gutierrez et al., 2006). Discontinuities of the sediment records are caused by repeated bioturbation events (Kim and Burnett, 1988; Levin et al 2002), erosion by bottom currents (Reinhardt et al., 2002) and slumps linked to the active and pervasive seismic activity (chapter II). The non-continuous nature of the marine sediments implies that cautious and precise core stratigraphy must be taken into account before any climatic interpretations are proposed, and that the frequently homogeneous sections observed in the sediment cores should be identified as bioturbation events or slumps. Consequently, in the cores used in the present chapter the proxies were only developed in the laminated or banded sections of the cores (avoiding the homogeneous/slumped sections) given that in many cases it is very difficult to determine the origin of the homogeneous section if a lateral correlation of sediment sequences with other cores cannot be done (chapter II). Additionally, because of the lack of foraminifers in portions of the cores, multiple ^{14}C measurements along the core on de-carbonated organic matter must be developed in order to construct a strong chronological model.

In order to determine if the OMZ off Peru was dominated by remote ventilation rather by than the oxygen demand imposed by local productivity, a multi-proxy approach was conducted. If the remote ventilation of the OMZ dominates over the local productivity then the subsurface signature of the water column should not be coupled with the inferred export production. On the contrary, if the local productivity dominates the oxygen demand, then the subsurface conditions and the export production should be closely related. Consequently in order to infer subsurface oxygenation, sediment redox conditions and export production, multiple proxies were developed on three cores (B14, G-10 and G-14), which together allowed to cover the last 25.5 kyr BP. The high sedimentation

rates of the 3 cores evaluated allow for high resolution reconstructions and detailed comparisons of continental and paleoceanographic proxies in the same record, avoiding the comparison with other records that may be biased due to age model uncertainties. While the scientific question addressed in this chapter has been in part addressed by other authors (e.g. Higginson and Altabet, 2004; Chazen et al., 2009), the chronology, the development of the proxies in laminated sections of the record and the proxies used in this chapter are different from the previous works. Additionally, terrigenous run-off proxies were also developed to determine if the terrigenous contents in the Pisco cores follows the ITCZ displacements over the continent and its consequences over the export production off Peru.

III-1.2 Changes in OMZ intensity off Peru since the Last Glacial Maximum

Water column denitrification reconstructions using sedimentary $\delta^{15}N$ in cores retrieved in the PUE, shows large changes driven by local or remote forcings (Higginson and Altabet, 2004; Agnihotri et al., 2008; Chazen et al., 2009; Gutierrez et al., 2009). An increase in $\delta^{15}N$ from 17.6 – 16.2 kyr BP was interpreted as a product of increased denitrification in response to reduced ventilation of remote southern-sourced intermediate waters, given that no similar increase in the productivity proxies that could cause enhanced respiration was found (Higginson and Altabet, 2004). Another explanation is that the increase in water column denitrification off Peru was partly produced by an increase in productivity in the whole Eastern Equatorial Pacific, which led to enhanced subsurface oxygen consumption that was ultimately transported by the EUC to Peru (Martinez and Robinson, 2010). The decoupling between productivity proxies and water column denitrification observed during the deglaciation was also observed in the Early Holocene (Chazen et al., 2009). These observations suggest remote forcings controlling the subsurface denitrification, for example changes in the source of the EUC or in the circulation of the South Pacific Gyre, which could affect the ventilation of the OMZ (Chazen et al., 2009). In contrast during the last 2 kyr subsurface denitrification and surface productivity appear to have remained coupled at centennial time-scales (Agnihotri et al., 2008; Gutierrez et al., 2009). All the studies above mentioned used different proxies to infer export production: molecular biomarkers of haptophyte species and diatoms (Higgins and Altabet, 2004); molecular biomarkers of haptophyte species and biogenic silica (Chazen et al., 2009); XRF Si/Ti ratios, Nitrogen and X-radiograph gray scale (Agnihotri et al., 2008); and Total Organic Carbon (TOC), diatom fluxes, silica fluxes and fish scales (Gutierrez et al., 2009). Additionally the age models were calibrated with different regional radiocarbon effect values (ΔR), which makes it difficult to compare the different studied records.

III-1.3 Proxies evaluated in the present study

Three kinds of paleo proxies are the primary focus of this chapter. The first group of proxies is related to terrigenous input variability from the continent. The second group of proxies is meant to estimate the OMZ intensity changes, and the seafloor redox conditions (i.e. from sub-oxic to anoxic conditions). Finally, the third group of proxies is used to estimate the export production from the water column. The proxies were developed using ICP-Mass, continuous-flow gas-ratio mass spectrometer, Rock-Eval, and XRF techniques.

III-1.3.1 Major and trace elements

In order to reconstruct the terrigenous input, sediment REDOX conditions and export production, we used a series of major and trace elements records obtained by ICP-Mass analysis. The terrigenous input was inferred by Aluminum (Al), Iron (Fe) and Titanium (Ti) contents. The terrigenous material in the shelf is principally delivered by rivers that dilute the terrigenous components of eolian origin (Scheidegger and Krissek, 1982) and thus can be used as a proxy for riverine discharge. Additionally to the Al, Fe, and Ti obtained from ICP-Mass analysis, XRF analysis were performed in cores G-10 and G-14 to reconstruct the rapid variability of these constituents. The results of these analyses are then compared with well-dated proxies of rainfall in the continent to evaluate the sensitivity of the terrestrial contents in the marine record to past changes in rainfall variability, and thus to infer the regional climate variability and tipping points.

Sediment REDOX conditions were reconstructed using a series of trace elements that exhibit different sensitivities to redox conditions such as Molybdenum (Mo), Vanadium (V), Uranium (U) and Rhenium (Re) and may permit the differentiation between anoxic (sulfate reducing conditions) or suboxic ($0.2 > [O_2] > 0$ ml.L^{-1} and no H_2S, Tyson and Pearson, 1991) conditions at the time of deposition. Additionally, Mo, V and Re are heavily enriched in OMZ sediments off Peru, have minimal detrital influence, and display a conservative behavior in the water column (Colodner et al., 1993; Boning et al., 2004; Tribovillard et al., 2006). Mo is enriched mainly under anoxic, sulfate-reducing conditions alone (Crusius, 1996; McManus et al., 2006; Tribovillard et al., 2006). V and U are reduced and can accumulate under denitrifying conditions but can also accumulate under more strongly reducing (i.e. anoxic) conditions. Re concentrations in the continental crust and in the seawater are extremely low but are heavily enriched in reducing sediments with absence of O_2 and H_2S (Crusius et al, 1996; Boning et al. 2004). Thus, sediments exhibiting concurrent enrichments in U, V, Mo and Re reflect euxinic conditions ($[O_2] = 0$; presence of H_2S) at the sediment water interface, and an enrichment of V and/or Re without Mo enrichment reflects suboxic (absence of H_2S) conditions (Tribovilliard et al., 2006).

Nickel (Ni), Copper (Cu), Cadmium (Cd), Calcium (Ca) and Silicon (Si) were used in the present work as proxies for paleoproductivity (Nameroff et al., 2004; Dean et al., 2006; Tribovillard et al., 2006) because they display a nutrient-like behavior in the column water and are present in considerable concentrations in plankton (Boning et al., 2006). Ni and Cu are used as a proxy for the original presence of organic matter; they are delivered to the sediments in association with organic matter, fixed in the sediments under reducing conditions, and are moderately enriched in sediments off Peru (Boning et al., 2006; Tribovilliard et al., 2006). Cd is delivered to marine sediments mainly in association with organic matter and then is released to interstitial waters during organic matter decay and enriched in both mildly and strongly reducing sediments (Dean et al., 2006; Tribovillard et al., 2006); additionally Cd is heavily enriched in marine sediments off Peru (Boning et al. 2006). Calcium (Ca) % was also analyzed by ICP-Mass and XRF in order reconstruct the carbonate production/preservation. Finally Si was analyzed by XRF techniques to infer siliceous productivity when normalized by Al (Si/Al).

III-1.3.2 Quantification and characterization of organic matter

The quantification and characterization of organic matter were done using Rock-Eval 6 that permits to evaluate the evolution of organic compounds during programmed pyrolysis (Lafargue et al., 1998). During the programmed pyrolysis several parameters are used in order to quantify and characterize the organic matter: S1, S2 and S3. S1 (mg HC/g rock) corresponds to the quantity of hydrocarbons (HC) released during the isothermal temperature step at 300 °C and represents the themovaporized free hydrocarbons contained in the rock (Behar et al, 2001). S2 (mg HC/g rock) corresponds to the quantity of hydrocarbons released between 300 and 650 °C and represents the hydrocarbons resulting from the cracking of sedimentary organic matter (Behar et al., 2011). Finally, S3 (mg CO_2/g rock) represents milligrams of carbon dioxide generated from a gram of sample during temperature programming up to 390 °C (Lafargue et al., 1998; Behar et al., 2001; Peters, 2005). Total Organic Carbon (TOC) is determined by summing the pyrolysable organic carbon (obtained from the S1, S2 and S3) and the residual organic carbon (Behar et al.; 2001). TOC reflects the quantity of organic matter present in the sediment and can be used to infer past export production. The hydrogen index (HI, mg HC/g TOC) is the amount of hydrocarbons released during pyrolysis and is calculated as (S2xTOC^{-1}) x100. The H-rich organic matter is the most labile and thus will be the first to be consumed by aerobic and anaerobic decomposition (Dean et al., 1994). The oxygen index (OI, mg carbon dioxide/g TOC) gives the oxygen content calculated from the amounts of CO and CO2 released during pyrolysis and is calculated as (S3xTOC^{-1}) x100 (Lafargue et al., 1998; Behar et al., 2001; Peters, 2005).

III-1.3.3 Stable isotopic composition of organic matter ($\delta^{13}C$ and $\delta^{15}N$)

The isotopic composition of modern marine phytoplankton and terrestrial plants and the organic matter derived from them often provide distinct signatures that can be used to determine the source of organic matter in sediments (Dean et al., 1994; Meyers, 1997). The $\delta^{13}C$ of particulate organic matter collected by surface pumping off Peru ranges from -18.9 to -21.2‰ (Arthur et al., 1998). In contrast, organic matter of land plants, that uses the C_3 Calvin pathway, has an average of -27 ‰ (Meyers, 1997). The mixing of terrestrial and marine organic matter is the dominant process that determines the isotopic composition of carbon in costal marine sediments; however there are other factors that can be responsible for changes in the $\delta^{13}C$ values as for example a selective diagenesis (Meyers, 1997). More detailed analyses are required to discern the origin of organic matter (i.e. petrography study); however the $\delta^{13}C$ is a rapid way to detect the organic matter origin.

$\delta^{15}N$ records from sedimentary organic matter mainly represent water-column denitrification in oxygen-deficient waters (Altabet et al., 1999; De Pol-Holz et al., 2006; Martinez and Robinson, 2010; Robinson et al., 2012). In oxygen-deficient waters bacteria reduce nitrate into N_2, leaving the remaining nitrate pool enriched in ^{15}N which is transferred by upwelling to the surface where it is used by phytoplankton and ultimately transferred to the sediments (Altabet and Francois, 1994; Agnihotri et al., 2008). Other factors can contribute to the $\delta^{15}N$ signal in the sedimentary organic matter as for example the extent of surface NO_3^- consumption by phytoplankton (Altabet and Francois, 1994; Sigman et al., 1999) or diagenetic processes (Romero et al., 2012), among other processes. However the sedimentary $\delta^{15}N$ signal off Peru is consistent with other proxies of oxygenation and productivity implying denitrification in the water column at least during great part of the Holocene (Agnihotri et al., 2006; Gutiérrez et al., 2009; Chazen et al., 2009).

III-2. Methodology

III-2.1 Cores

The cores studied in the present chapter are B-14, G-10 and G-14. Cores G-10 and G-14 were retrieved off Pisco at 312 and 400 meters depth (Fig. III-1) during the Galathea-3 expedition realized in 2007. The specific location of core B-14 is indicated in chapter II. The total length of cores G-10 and G-14 is 5.22 and 5.24 meters respectively. Both cores consist in 6 sections (S6, S5, S4, S3, S2 and S1), where S1 represent the older section in each core. Photographic images and SCOPIX images were obtained in each section in order to document the sediment structures and to define the laminated sections of the cores. Both types of images were taken at the University of Bordeaux 1. Core G-10 covers the Holocene period while G-14 contains sediments from the Last Glacial

Maximum to the Bølling-Allerød period (~13 kyr BP). In this chapter it is assumed that the sea level variations since the Last Glacial Maximum did not considerably affect the records given the steep slope off Pisco. A 125-meter lowering of sea level during the Last Glacial Maximum means that the water column above G-14 position was ~275 m; this depth coincides with the current position of the OMZ core. The results of these two cores are compared to the changes occurred during the last ~500 years recorded in core B-14. A more detailed study of the last 2 millennia is presented in the next chapter combining the results of core B-14 with the uppermost part of core G-10. In this chapter cores B-14, G-10 and G-14 are presented altogether to produce time series of the proxies of interest.

III-2.2 Development of age models

Thirty two and twenty nine samples were dated by ^{14}C measeurements from bulk de-carbonated organic matter in cores G-10 and G-14 respectively. Several dates were performed because of the complex sedimentological patterns of the cores and of the problems associated with ^{14}C content from bulk organic matter. The Accelerator Mass Spectrometry (AMS) radiocarbon measurements in core G-10 were obtained at the "*Laboratoire de mesures du Carbone-14*" (LMC14, Gif-sur Yvette, France, thanks to the IRD participation to this national facility). In core G-14 the ^{14}C dates were obtained in the Keck Carbon Cycle AMS facility (University of California, Irvine, USA). Three samples of core B04-6 retrieved also off Pisco (see chapter II) that were dated at the LMC14 were sent to the Keck Carbon Cycle AMS facility, in order to test the inter-laboratory reproducibility of the results. Two of these samples show similar conventional ages within two-sigma error: B04-6-35: 770 ±50 and 835 ±15, and B04-6-73: 1315 ±30 and 1260 ±15 conventional years (LMC14 and Keck Carbon Cycle AMS respectively); while the third sample shows rather different values: B04-6-44: 700 ±40 and 1045 ±15, respectively. The lack of reproducibility of the ^{14}C ages between different laboratories is another source of error beside the organic matter source and the problems associated with the reservoir effect, but it is here considered that it should not affect the main chronological framework.

In order to calibrate the ^{14}C ages for local reservoir effects (delta-R: ΔR), we used different values of ΔR along the cores (Tables III-1 and III-2). All the uncalibrated ^{14}C ages in core G-14 and the ages from 9800 ±40 to 6025 ±35 uncalibrated years BP in core G-10 were calibrated using a ΔR of 511 ±278 years (Tables III-1 and III-2). Ortlieb et al. (2011) reported this value of ΔR (511 ±278 years) for the period between 10400 and 6840 cal yr BP, however since there are no reported values of ΔR for the LGIG period we used this value to calibrate all the ^{14}C ages in core G-14. The ages from 4845 ±35 and 2340 ±30 in core G-10 were calibrated using a ΔR of 226 ±98, as reported by Ortlieb et al. (2011) for the period between 5180 and 1160 cal yr BP. Finally, the ages from 2645 ±30 to 1005 ±30 were calibrated using the ΔR calculated (367 ±40) in the nearby core B04-6 the ^{210}Pb$_{ex}$

profile (see chapter II and Gutierrez et al., 2009). In order to construct the age model in each core, we used the maximum probability ages obtained from the Calib 6.1 software (Tables III-1 and III-2). The one-sigma range and the two-sigma ranges, as well as the average for each range are also reported in Table III-1 and III-2 but they were not used to construct the chronological model.

An accumulated-mass age model was estimated in both cores to take into account the important changes in sediment density along the cores. This approach was used in order to avoid compaction artifacts. First the sediment density was estimated from the dry bulk density values (DBD). The DBD was calculated by subsampling 1 cm cubes along the core and dividing the dry mass by the volume. Then, we calculated the z-mass (g.cm^{-2}) of each sample by multiplying the DBD (g.cm^{-3}) by the thickness of the sample (cm). Finally, the accumulated z-mass was calculated by accumulating the individual z-mass values of each sample.

Table III-1. ^{14}C ages obtained at the LMC14 on decarbonated sediments in core G-10. The uncalibrated ^{14}C ages were calibrated using three different delta-R values taken from (Ortlieb et al., 2011) with the program CALIB 6.1 (Stuiver and Reimer, 1993). The ^{14}C cal BP for each sample used to construct the age model was taken from the maximum probability value of the plot radiocarbon age and calibrated age obtained from the CALIB 6.1 software

Sample	Depth (cm)	δ^{13}C (‰)	uncalibrated Age BP (years)	Delta-R (years)	One sigma range (calibrated years BP) start	end	average	Two sigma range (Age cal BP) (calibrated years BP) start	end	average	Max probability (calibrated years BP)
S6B - 3	2.5	-21.2	1005 ± 30	367 ± 40	239	366	303	141	412	277	280
S6B - 19	18.5	-21.1	1235 ± 30	367 ± 40	454	525	490	404	596	500	492.5
S5B - 14	32.5	-20.6	1340 ± 30	367 ± 40	525	611	568	496	644	570	547
S5B - 26	44.5	-21.4	1715 ± 30	367 ± 40	827	945	886	762	1006	884	905
S5B - 33	51.5	-21.6	1810 ± 30	367 ± 40	932	1042	987	894	1122	1008	970
S5B - 38	56.5	-21.6	2130 ± 30	367 ± 40	1265	1355	1310	1209	1423	1316	1270
S5B - 53	71.5	-21.0	2075 ± 30	367 ± 40	1223	1304	1264	1169	1343	1256	1298
S5B - 63	81.5	-21.0	2645 ± 30	367 ± 40	1821	1948	1885	1753	2026	1890	~~1880~~
S5B - 81	99.5	-21.3	2340 ± 30	226 ± 98	1569	1815	1692	1440	1937	1689	1700
S4B - 12	128.7	-20.6	3215 ± 30	226 ± 98	2665	2910	2788	2468	3031	2750	2740
S4B - 27	143.7	-21.4	2825 ± 30	226 ± 98	2126	2401	2264	2003	2595	2299	2300
S4B - 41	157.7	-21.1	3395 ± 30	226 ± 98	2836	3108	2972	2741	3236	2989	2960
S4B - 47	163.7	-21.2	3030 ± 30	226 ± 98	2423	2687	2555	2302	2758	2530	2570
S4B - 59	175.7	-21.8	3270 ± 30	226 ± 98	2717	2943	2830	2581	3129	2855	2790
S4B - 76	192.7	-21.1	3600 ± 30	226 ± 98	3102	3362	3232	2943	3468	3206	3250
S4B - 99	215.7	-21.1	4260 ± 30	226 ± 98	3913	4205	4059	3798	4375	4087	4070
S3B - 19	235.7	-21.2	4275 ± 30	226 ± 98	3930	4224	4077	3817	4382	4100	4075
S3B - 21	237.7	-21.1	4195 ± 35	226 ± 98	3828	4115	3972	3681	4267	3974	3960
S3B - 42	258.7	-21.2	4400 ± 40	226 ± 98	4110	4400	4255	3943	4530	4237	4245
S3B - 66	282.7	-20.7	4700 ± 30	226 ± 98	4534	4795	4665	4386	4895	4641	4660
S3B - 82	298.7	-21.1	4845 ± 35	226 ± 98	4688	4987	4838	4535	5137	4836	4830
S2B - 23	342.3	-21.1	6205 ± 35	511 ± 278	5776	6388	6082	5483	6711	6097	~~6100~~
S2B - 36	355.3	-21.1	6360 ± 30	511 ± 278	5935	6559	6247	5637	6888	6263	~~6260~~
S2B - 52	371.3	-21.2	7625 ± 45	511 ± 278	7342	7879	7611	7029	8164	7597	7570
S2B - 58	377.3	-20.4	7510 ± 30	511 ± 278	7232	7775	7504	6886	8028	7457	7460
S2B - 86	405.3	-21.4	8345 ± 45	511 ± 278	7971	8597	8284	7725	8993	8359	8320
S1B - 13	432.9	-21.5	8720 ± 45	511 ± 278	8397	9071	8734	8149	9433	8791	8740
S1B - 21	440.9	-22.2	8760 ± 35	511 ± 278	8437	9116	8777	8181	9452	8817	8800
S1B - 57	476.9	-21.4	9235 ± 45	511 ± 278	8996	9730	9363	8657	10133	9395	9420
S1B - 64	483.9	-21.2	9390 ± 35	511 ± 278	9248	9962	9605	9248	9962	9605	9530
S1B - 88	507.9	-22.0	9800 ± 40	511 ± 278	9712	10417	10065	9389	10757	10073	10160
S1B - 101	520.9	-21.3	9755 ± 40	511 ± 278	9657	10355	10006	9335	10676	10006	10140

Table III-2. ^{14}**C ages obtained at the Keck Carbon Cycle AMS facility on decarbonated sediments in core G-14. The δ**^{13}**C values analyzed in the same intervals or in contiguous intervals (underlined δ**^{13}**C values) are also shown. The uncalibrated** ^{14}**C ages were calibrated, using a single delta-R value taken from Ortlieb et al. (2011), with the program CALIB 6.1 (Stuiver and Reimer, 1993). The** ^{14}**C cal BP for each sample used to construct the age model was taken from the maximum probability value of the plot radiocarbon age and calibrated age obtained from the CALIB 6.1 software**

Sample	Accumulated mid-depth (cm)	δ 13-C	Accumulated mid-depth (cm) δ 13-C	Age BP	Delta R	One sigma range (Age cal BP) start	end	average	Two sigma range (Age cal BP) start	end	average	Max probability
S6A - 10	9.5	-22.2	8.5	12640 ± 30	511 ± 278	13294	13851	13573	12916	14242	13579	13550
S6A - 16	15.5	-21.9		12520 ± 30	511 ± 278	13213	13761	13487	12848	14064	13456	13420
S6A - 24	23.5	-21.3	22.5	13110 ± 30	511 ± 278	13763	14647	14205	13472	15111	14292	14025
S5A - 14	40.5	-20.8		12970 ± 30	511 ± 278	13493	14244	13869	13367	14994	14181	13900
S5A - 16	42.5	-20.9	45.5	12740 ± 30	511 ± 278	13367	13971	13669	13101	14603	13852	13700
S5A - 38	64.5	-22.1	62.5	13305 ± 35	511 ± 278	14032	14953	14493	13664	15556	14610	14400
S5A - 51	77.5	-22.8		13465 ± 35	511 ± 278	14137	15153	14645	13814	15958	14886	14680
S5A - 69	95.5	-21.5		14190 ± 40	511 ± 278	15635	16701	16168	15129	16876	16003	16500
S5A - 99	125.3	-21.9		14155 ± 35	511 ± 278	15588	16667	16128	15104	16863	15984	16260
S4A - 34	159.0	-21.5		13935 ± 35	511 ± 278	15180	16334	15757	14629	16777	15703	15825
S4A - 40	165.0	-22.2	167	14145 ± 40	511 ± 278	15573	16658	16116	15093	16862	15978	16250
S4A - 68	193.0	-22.2		14945 ± 40	511 ± 278	16855	17466	17161	16615	17889	17252	17075
S4A - 96	221.0	-21.2	220	15330 ± 40	511 ± 278	17174	17877	17526	16886	18084	17485	17580
S3A - 19	243.1	-21.2		15165 ± 40	511 ± 278	17005	17657	17331	16805	18003	17404	17250
S3A - 43	267.1	-21.2	265.1	15515 ± 40	511 ± 278	17387	18048	17718	17100	18519	17810	17720
S3A - 61	285.1	-21.1	284.1	15595 ± 45	511 ± 278	17504	18101	17803	17166	18548	17857	17920
S3A - 72	296.1	-21.2	294.1	15580 ± 45	511 ± 278	17479	18093	17786	17154	18543	17849	17910
S3A - 86	310.1	-21.8	307.1	16045 ± 45	511 ± 278	18033	18613	18323	17680	18853	18267	18200
S3A - 94	318.1	-21.6	318.1	16780 ± 50	511 ± 278	18832	19362	19097	18575	19479	19027	19180
S2A - 28	352.1	-21.3	353.1	17275 ± 45	511 ± 278	19257	19892	19575	18887	20165	19526	19450
S2A - 49	373.1	-21.3		17615 ± 50	511 ± 278	19552	20160	19856	19262	20529	19896	19640
S2A - 76	400.1	-21.6		18740 ± 60	511 ± 278	20852	21561	21207	20420	22062	21241	21340
S2A - 93	417.1	-21.4	415.1	19230 ± 60	511 ± 278	21529	22178	21854	21212	22480	21846	21960
S1A - 5	429.4	-21.9		19440 ± 70	511 ± 278	21661	22373	22017	21364	22686	22025	22150
S1A - 17	441.4	-21.6		20290 ± 80	511 ± 278	22628	23445	23037	22387	23826	23107	23040
S1A - 45	469.4	-21.6		21130 ± 90	511 ± 278	23780	24476	24128	23436	24897	24167	24110
S1A - 56	480.4	-21.7	479.4	21450 ± 90	511 ± 278	24196	24932	24564	23748	25217	24483	24460
S1A - 77	501.4	-21.5		21490 ± 90	511 ± 278	24241	24960	24601	23801	25302	24552	24500
S1A - 100	524.7	-21.5		21870 ± 90	511 ± 278	24533	25371	24952	24318	25886	25102	25000

III-2.3 Sub-sampling criteria

As shown in chapter II, the slumped, bioturbated, homogenous and massive deposits are usual in the Peruvian sediments, and the proxies obtained from these deposits thus may lead to quite erroneous climatic interpretations. In order to evaluate the origin of these deposits a correlation of sediment structures among several cores must be done. However this kind of work, realized in chapter II for the last few centuries, could not be envisaged for records as long as those of cores G-10 and G-14. Thus, the proxies studies developed in the present chapter were restricted to the laminated sections of the cores. This apporach guarantees that the analyzed sediments were deposited from the water column and not from reworking of upslope deposits. In core G-10, where the laminated sections are limited, the subsamples for ICP-Mass analyses were done at 1 cm intervals as shown with red vertical bars in Figure III-2. Sub-sampling for the quantification and characterization of organic matter and the isotopic composition of organic matter was done in the same laminated sequences where the ICP-Mass analyses were performed. However one 1-cm thick sample was used every 2 cm (broken blue line in Fig. III-2). Additionally, the subsampling for the Rock-Eval analysis and the

isotopic composition of organic matter were also performed in other laminated sequences along the core, and are shown by blue squares in Figure III-2. The total number of samples analyzed for ICP-analyses was 199, while 140 samples were analyzed for the quantification, characterization and isotopic composition of organic matter.
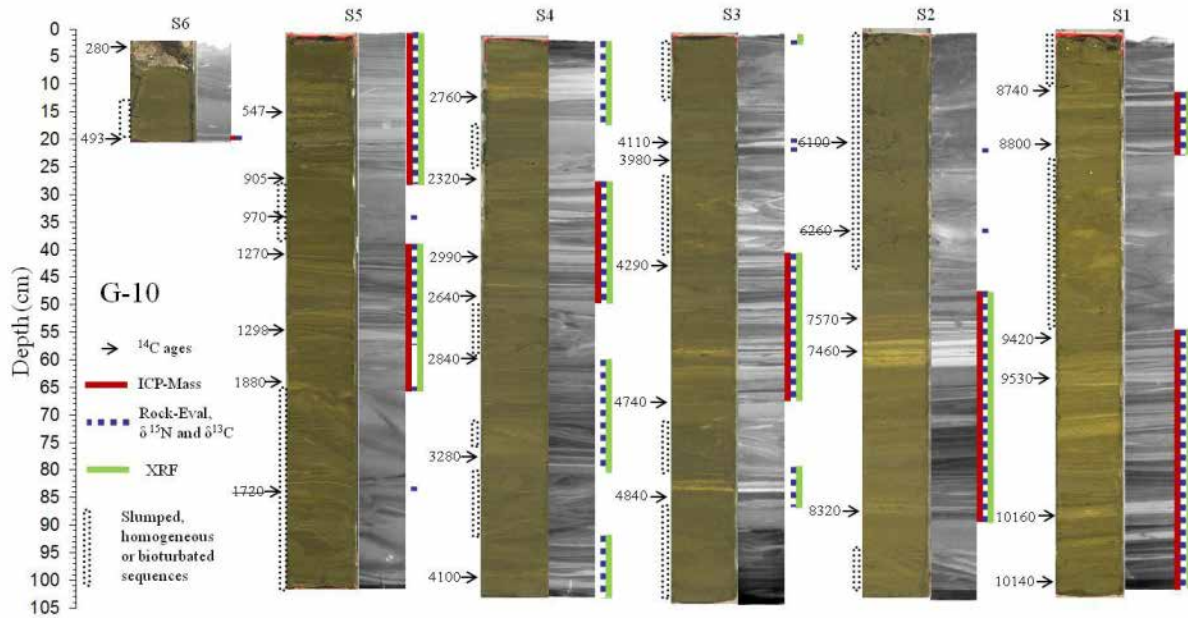
Figure III-2. SCOPIX and photographic images showing laminated sequences, massive and slumped deposits, and sampling strategy used for ^{14}C dating, ICP-Mass, Rock-Eval and the isotopic composition of the organic matter in core G-10. The ^{14}C ages are expressed in years cal BP. See Table III-1 for details. The dotted rectangle areas at the left side of the SCOPIX images indicate slumps or massive/homogeneous deposits. The arrows indicate the position of the samples taken for ^{14}C measurements. The vertical red (blue) bars indicate the samples that were analyzed for ICP-Mass analysis (Rock-Eval and the isotopic composition of the organic matter). ICP-Mass analysis in the laminated sequences were performed each cm, while the analysis for Rock-Eval and the isotopic composition of the organic matter were performed each 2 cm.

Core G-14 presents more laminated sequences and the extension of the massive/slumped sequences is lower in comparison with core G-10 (Fig. III-3), thus we conducted a different subsampling approach. Within the sequences that show finely laminated sections (e.g. base of G-14 S5 to the top of G-14 S4) we developed the proxies in one sample (1 cm thick) every 2 cm. In the sediment sequences that present more bands and more homogeneous type of material (e.g. G-14 S1), the spacing between samples was 5 cm but taking care to sample only the laminated/banded sections. In core G-14, ICP-Mass, Rock-Eval analysis and the isotopic composition of the organic matter were performed in the same intervals along the core. The total number of samples analyzed in core G-14 was 116.
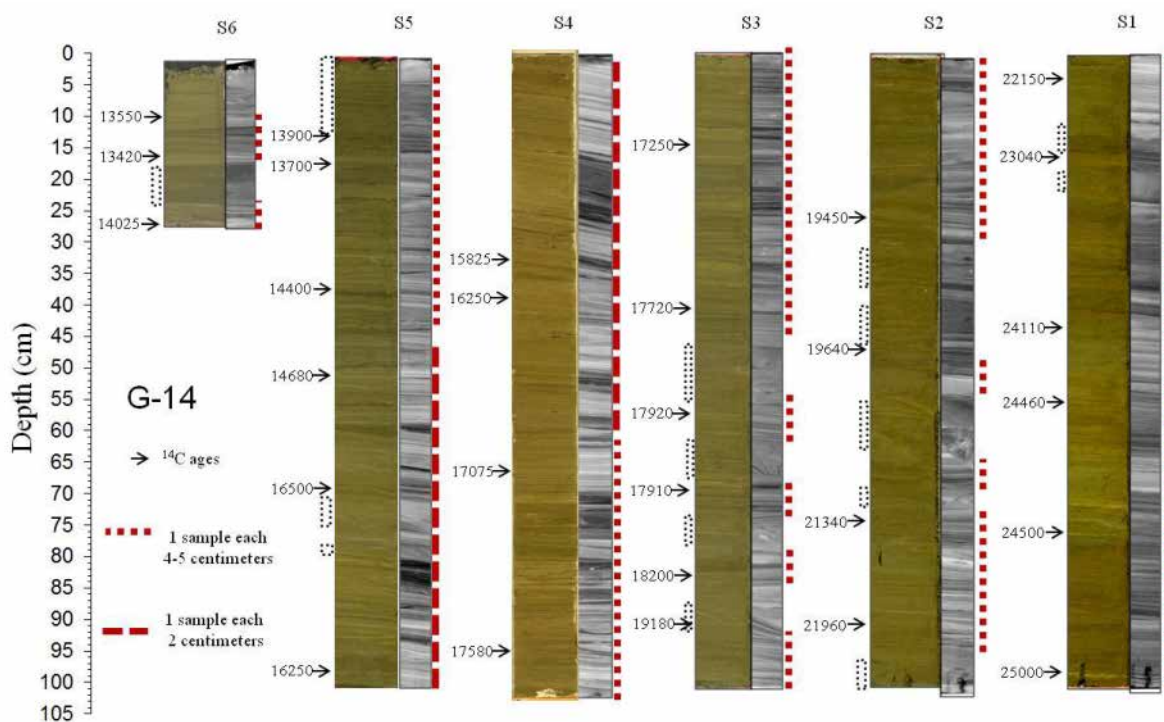
Figure III-3. SCOPIX and photographic images showing laminated sequences, homogeneous deposits, and the sampling strategy used for ¹⁴C dating, ICP-Mass, Rock-Eval and the isotopic composition of the organic matter in core G-10. The ¹⁴C ages are expressed in yrs cal BP. See Table III-2 for details. The dotted rectangle areas at the left side of the photographic images indicate massive/homogeneous deposits. The arrows indicate the position of the samples taken for ¹⁴C measurements. The vertical red bars indicate the samples that were analyzed for ICP-Mass analysis, Rock Eval and the isotopic composition of the organic matter. In the finely laminated sections the analysis were performed each 2 cm while in sequences characterized by laminations and bands the analysis were performed each 4 -5 cms. In core G-14, ICP-Mass, Rock-Eval analyses and the isotopic composition of the organic matter were performed in the same intervals along the core.

III-2.4 Inorganic fraction

III-2.4.1 Major and trace elements (ICP-Mass)

Major elements (Al, Fe, Ti, Ca and Mg) and trace elements (Manganese [Mn], Cd, Cobalt [Co], Chromium [Cr], Cu, Mo, Ni, Re, Barium [Ba], Zn [Zinc] and V) concentrations were analyzed by ICP-MS (Ultramass Varian) after hot-plate acid digestion in Polytetrafluoroethylene (PTFE) vessels. The acids employed (HF, HNO_3 and $HClO_4$) permitted to eliminate OM and remove silicates (Jarvis et al., 1992). The methodology for the sample preparation is based on Jarvis et al. (1992) and briefly summarized here. First, 25 mg of powdered sample were weighted in a high-precision micro balance and placed into the PTFE vessels. Then, 2 ml of HNO_3 (65%) and 2 ml of HF (40%) were added to the samples. The vessels were closed and immersed in an ultrasonic bath for 10 minutes to facilitate the oxidation of OM. After 2 days, the closed vessels were placed on a hot plate (150 °C) for three hours, and then the samples were removed from the hot plate to cool down. As soon as they

were cool enough, the open samples were placed again on a hot plate (150 °C) to let all the acid evaporate (duration ~5 hours). Then, 2 ml of HF (40%) and 1 ml of $HClO_4$ (70-72%) were added to the sample and the tubes were placed on a hot plate (150 °C) for 10 hours in order to let all the acid evaporate. When the evaporation was completed, 2 ml HNO_3 (65%) were added to the samples and the tubes were placed again on the hot plate to evaporate the remaining acid (2-3 hours). This last procedure was repeated twice. Finally, the samples were placed into larger plastic tubes with the aid of a funnel and HNO_3 (2%). The samples were then analyzed in an ICP-MS and the trace elements concentrations accuracy was calibrated with international standards. The measurement precision was determined by performing duplicate analyses. The average values of replicate digestions were well within the recommended ranges.

Trace elements concentrations were normalized with respect to the Al content (element/Al) to permit a correct analysis because marine sediments present variable proportions of biogenic carbonates and biogenic silica that dilute the trace elements abundances and impede a direct comparison (Boning et al., 2004; Tribovillard et al., 2006). The total metal concentrations measured contain a detrital background and an authigenic metal concentration (i.e. the part in excess of the detrital background; Böning et al., 2004; Tribovillard et al., 2006; Scholz et al., 2011). The chemical composition of andesite is an appropriate representation of the detrital background of the sediments on the Peruvian margin as proposed by Böning et al. (2004), thus we use the element/Al ratios of andesite to obtain the authigenic concentration of each trace element. These ratios were obtained from the GEOROC database (Sarbas and Nohl, 2009) taking into account the elements concentrations in andesite from whole rocks from the central Andean volcanic zone in Peru (Table III-3). The detrital metal fraction were calculated following Tribovillard et al. (2006): $X_{detrital} = (X/Al)_{andesite} * Al_{sample}$. Given that the trace elements may present, in some cases, a strong detrital fraction, we focus on the authigenic trace element content. The authigenic (or non-lithogenic) fraction is mainly enriched by post-depositional redox reactions (especially in suboxic environments) and each element exhibits different sensitivities to redox conditions along an oxic to sulfidic gradient. Consequently the authigenic fraction of element X in a sample was calculated as $X_{total} - X_{detrital}$ However not all the authigenic fraction is produced only by post-depositional reactions since some metal fraction present above the background lithogenic concentrations is also related to the flux of metals associated with settling biological material (Nameroff et al., 2004; Tribovillard et al., 2006). In order to reconstruct the environmental settings at the time of deposition, we explore if the trace elements were enriched relative to average shale (Andesite composition). The elements were presented as enrichment factors using the following formula accordingly to Tribovillard et al. (2006): $EF_{element\ x} = (X/Al)_{sample} / (X/Al)_{andesite.}$ If EF_x is greater (lower) than 1, then the element X is enriched (depleted) relative to the average shale (i.e andesite) composition.

Table III-3. Average (±sd) concentration and Metal/Al for Andesite in whole rocks from the central Andean volcanic zone in Peru taken from the GEOROC database (Sarbas and Nohl, 2009). Re/Al ratio of andesite taken from Alves et al., (2002).

Metal/Al	Average ± standard deviation		
Re/Al x10^{-9}	1.9		
Cd/Al x10^{-6}	2.6	±	2.4
Mo/Al x10^{-4}	0.3	±	0.2
Ni/Al x10^{-4}	2.6	±	2.8
Cu/Al x10^{-4}	4.4	±	3.3
Cr/Al x10^{-4}	6.7	±	9.2
Zn/Al x10^{-4}	9.2	±	3.6
V/Al x10^{-3}	1.4	±	0.6
Ba/Al x10^{-2}	0.9	±	0.4
Co/Al x10^{-4}	2.6	±	2.7

III-2.4.2 XRF

In order to capture the rapid variability of some elements, high resolution XRF measurements for Al, Ti, Fe, Si, Ca were performed on cores G-10 and G-14 at the University of Bordeaux 1. The measurements were done every 1 mm downcore at 10kV and 400uA. The counting time was 30 s for G-10 and 10s for G-14. The XRF values, expressed as "peak area", were calibrated using the Al, Ti, Fe and Ca concentrations obtained by ICP-Mass analysis (see Annexes I). In order to perform the calibration, first we obtained an average value of the XRF peak area in each 1-cm samples where ICP-Mass data was available, then the two set of data were cross-plotted and finally, a best fit was obtained.

III-2.5 Organic fraction

TOC, IH and OI parameters were measured at the Institut des Sciences de la Terre d'Orléans, Université d'Orleans, and were measured on a Rock-Eval 6 system. The sample amount varied between 10 to 20 mg of dry, powdered, sediment. The samples were placed in small capsules and then were combusted by programmed pyrolysis.

δ^{15}N and δ^{13}C of sedimentary organic matter analyses were performed at the department of Geosciences of the University of Arizona and were measured on a continuous-flow gas-ratio mass spectrometer (Finnigan Delta PlusXL) coupled to an elemental analyzer (Costech). The δ^{15}N was measured in the whole sample while the δ^{13}C was measured in de-carbonated samples. The de-carbonation was done at the University of Arizona. First the samples were put into silver capsules

and then sulfurous acid was added in order to remove the carbonates. Standardization was based on laboratory standard acetanilide, precision was better than ± 0.2 (1s).

In order to reconstruct the siliceous production we used the Si/Al ratio obtained from the XRF analyses. The Si measured by XRF analyses also incorporate Si associated with the mineral fraction, thus by dividing the Si by the Al contents the amorphous silica can be estimated. The Si/Al ratios show higher values in the intervals characterized by visual diatoms bands that support the use of the ratio to infer past siliceous production.

The trace elements and the TOC are presented as ratios and not as fluxes (sedimentation rates x dry bulk density x metal concentrations) because the fluxes are highly dependent on age model constraints (Martinez and Robinson, 2010). Moreover the mass accumulation rates (sedimentation rate x dry bulk density) should be interpreted with caution because of the influence of lateral sediment depositions, especially in a tectonic area. In the present chapter we present the trace element (and TOC) data contents (ppm or %) and also the ratio (metal/Al) to show that there are no great differences between these two methodological approaches (see Annexes I).

III-2.6 Statistic analyses

Pearson correlation coefficients (r) were calculated to establish the relationships between proxies. The probability level was corrected for multiple comparisons by dividing the probability level α (p<0.05) by the number of tests performed (Glantz, 2002). Additionally in order to test for differences of the proxies between groups, a Kruskal-Wallis test was applied (Glantz, 2002). The Kruskall-Wallis test is a non-parametric alternative to one-way (between groups) ANOVA, and tests the null hypothesis according which the different samples in the comparison were drawn from the same distribution, or from distribution with the same median. The difference between the Kruskall-Wallis and the ANOVA tests is that Kruskal-Wallis is based on ranks instead of means. Given that the data set was divided in eight different groups (Early Glacial, Last Glacial Maximum, Heinrich 1 Stadial, Bølling-Allerød, Early Holocene, Mid Holocene, Late Holocene and the Current Warm Period), and in order to avoid a significant difference obtained by chance while doing multiple analyses in the same data set, the probability level was corrected by dividing the p-value (0.05) between the number of test performed (7), giving a corrected p-value of 0.007. After the Kruskal-Wallis test was done to test if there are differences between groups, a non-parametric post-hoc analysis was performed for each proxy to detect the significant differences between groups. The post-hoc analysis choosen was the "multiple comparisons of mean ranks" (Siegel and Castellan, 1988). All the statistic analyses were perfomed in the STATISTICA 7.1 software. The results of the Kruskal-Wallis and the multiple comparisons of mean ranks are shown in Annexes I.

III-3. Results

III-3.1 Cores description

Cores G-10 and G-14 present laminated and banded sections intercalated with massive and homogeneous deposits as indicated by the dotted boxes at the left side of the photographic images (Figs. III-2 and III-3). Some of these massive deposits present clear evidence of reworked material like laminae at angle with the sedimentation subhorizontal plane. For example in G-10 the massive deposit in the lower part of S5, the one located near the base of S4 and at the top of S1, indicate that these deposits were likely caused by slumps. In G-14 massive and homogeneous deposits are also present, for example in S3 at ~63 cm depth; however they are thinner in comparison with this kind of deposits in the core G-10. There are other massive sections showing more homogeneous material like the deposit located in G-10 S5 from 26 to 37 cm depth (11 cm thickness) or the one located in G-10 S4 from 15 to 25 cm depth. Some of these homogeneous sections present signs of bioturbation; for example the homogeneous section located in G-10 S2 at ~47 cm depth presents in its base a burrow that penetrate the laminated sections underlying this homogeneous deposit. It is not possible to determine whether all the massive/homogeneous deposits were originated by bioturbation or by slumps. Sedimentological description and X-ray images of core B-14 are given in chapter II and also in Salvatteci et al. (2012).

III-3.2 Age models

The accumulated-mass age model proposed for core G-10 shows three different mass-accumulation rates (Fig. III-4). The most recent mass accumulation rate (blue diamonds in Fig. III-4) comprises the samples between the base of S6 and the base of the laminated section before the evident slump in S5 (Fig. III-2). The next mass accumulation rate (red squares in Fig. III-4) comprises the samples between the top of S4 and the first sample above the massive deposition in the base of S3 (Fig. III-2). Finally, the last mass accumulation rate (green triangles in Fig. III-4) comprises the samples below the massive deposit in S4 to the base of the core (Fig. III-2). The ages of the samples not included in the sections where the mass-accumulated rates were calculated, were estimated by linear interpolation between the uppermost and lowermost dates of the contiguous laminated sequence. Three ^{14}C ages were not included in the mass-accumulated rate calculations (black dots in Fig. III-4), the first one (1720 cal years BP, S5) was obtained in a slumped portion of the core and the other 2 (6100 and 6260 cal years BP, S2) were taken inside a massive deposit; these 3 results considered as unreliable are shown in Figure III-2 and Table III-2 with a strikethrough line. The rest of the samples for ^{14}C measurements were taken within the laminated or banded intervals of the core.
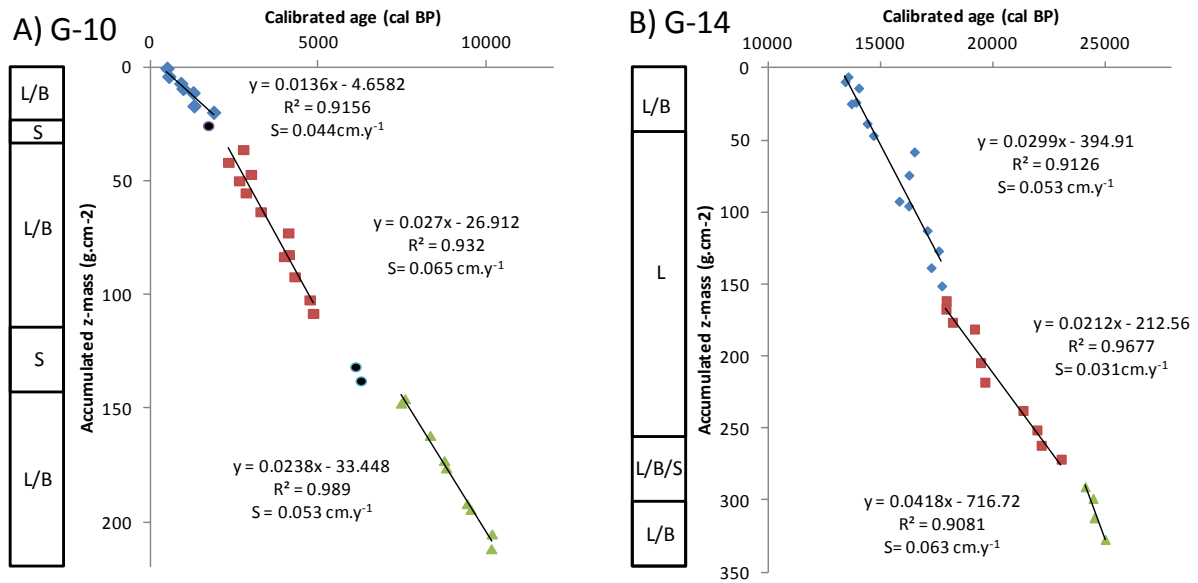
Figure III-4. Accumulated z-mass age model in cores G-10 (A) and G-14 (B) showing the different accumulation rates (S, cm.y^{-1}) and a simplified core description of laminated (L), slumped or massive deposits (S) or banded (B) sediment sequences. The 3 black dots correspond to the ages that were not used to construct the age model.

The accumulate-mass age model in core G-14 also shows three different mass-accumulation rates (Fig. III-4). The first one (blue diamonds in Fig. III-4) comprises the samples between the top of S6 to ~43 cm in S3, below this depth three massive deposits can be distinguished (Fig. III-3). The second mass-accumulation rate (red squares in Fig. III-4) was calculated with the samples between 85 cm in S3 to 17 cm in S1. Finally the last mass-accumulation rate (green triangles in Fig. III-4) comprises the samples between 44 cm depth in S1 to the base of this section. All the samples submitted to ^{14}C dating in core G-14 were taken in laminated intervals of the core.

III-3.3 Terrestrial run-off

The terrestrial run-off proxies in core B-14 show high correlations between them and large downcore changes (Table III-4 and Figure AI-1 in Annexes). Al, Ti and Fe contents show a similar variability throughout the core and are highly correlated, showing r values higher than 0.98. The average values (±sd) of Al, Ti and Fe are 2.6 ±1.4, 0.12 ±0.07 and 1.3 ±0.6% respectively. Al, Ti and Fe contents ranged from 0.3 to 5.7%, 0.01 to 0.28 % and 0.23 to 2.71% respectively. The DBD values in B-14 ranges from 0.11 to 0.41 g.cm^{-3}. The relationship of DBD with Al, Ti or Fe are high and significant (r= 0.78, 0.79 and 0.78 respectively, Table III-4).

Table III-4. Correlation matrix based on the Pearson correlation coefficient (r) between the proxies developed in core B-14. The trace elements were presented as contents (ppm) in order to perform the correlations. Boldface indicates significance after correcting for multiple comparisons (p<0.003).

	DBD	Al (%)	Ti (%)	Fe (%)	Co auth	Cr authi	Ba authi	Zn authi	V authi	Mo authi	Re authi	Re/Mo	δ15N	Ni auth	Cu auth	Cd auth	TOC	HI	OI	Ca	Bio Silica
DBD	1																				
Al (%)	**0.78**	1																			
Ti (%)	**0.79**	**0.99**	1																		
Fe (%)	**0.78**	**0.99**	**0.98**	1																	
Co auth	**-0.76**	**-0.98**	**-0.97**	**-0.95**	1																
Cr authi	**0.69**	**0.79**	**0.76**	**0.78**	**-0.72**	1															
Ba authi	0.01	-0.30	-0.28	-0.27	0.29	-0.16	1														
Zn authi	**0.40**	**0.51**	**0.52**	**0.58**	**-0.44**	0.37	-0.05	1													
V authi	-0.25	-0.17	-0.24	-0.16	0.26	0.23	-0.15	-0.23	1												
Mo authi	**-0.64**	**-0.69**	**-0.74**	**-0.71**	**0.70**	-0.38	0.03	**-0.54**	**0.60**	1											
Re authi	**0.55**	**0.65**	**0.62**	**0.65**	**-0.55**	**0.84**	-0.21	**0.45**	0.32	-0.26	1										
Re/Mo	**0.59**	**0.69**	**0.73**	**0.70**	**-0.67**	0.42	-0.14	**0.62**	**-0.50**	**-0.89**	0.38	1									
δ15N	**-0.54**	**-0.61**	**-0.67**	**-0.64**	**0.65**	-0.04	0.02	**-0.41**	**0.80**	**0.79**	0.16	**-0.68**	1								
Ni auth	0.17	**0.27**	0.21	**0.28**	-0.14	**0.69**	-0.03	0.20	**0.69**	0.10	**0.70**	0.03	**0.53**	1							
Cu auth	0.06	0.08	0.02	0.09	0.05	**0.50**	-0.04	0.09	**0.75**	0.31	**0.63**	-0.16	**0.60**	**0.78**	1						
Cd auth	**-0.42**	**-0.41**	**-0.46**	**-0.39**	0.48	-0.02	0.10	**-0.27**	**0.75**	**0.67**	0.06	**-0.53**	**0.82**	**0.59**	**0.52**	1					
TOC	0.17	**0.25**	0.18	**0.25**	-0.12	**0.66**	-0.14	0.11	**0.78**	0.23	**0.73**	-0.09	**0.62**	**0.91**	**0.88**	**0.57**	1				
HI	**-0.51**	**-0.57**	**-0.60**	**-0.61**	**0.59**	-0.25	0.19	**-0.48**	**0.40**	**0.63**	-0.24	**-0.56**	**0.72**	**0.25**	0.19	**0.68**	0.20	1			
OI	0.02	-0.07	-0.11	-0.04	0.14	0.16	0.12	-0.08	**0.41**	0.19	0.24	-0.19	**0.46**	0.38	0.37	0.44	**0.47**	0.20	1		
Ca	-0.08	-0.25	-0.26	-0.22	**0.26**	-0.10	**0.42**	-0.13	0.06	0.13	-0.10	-0.20	0.06	0.10	-0.02	**0.30**	0.04	**0.33**	**0.74**	1	
Bio Silica	**-0.66**	**-0.85**	**-0.83**	**-0.86**	**0.78**	**-0.76**	0.22	**-0.45**	-0.05	**0.50**	**-0.71**	**-0.57**	0.54	**-0.42**	-0.24	0.12	**-0.48**	**0.35**	-0.28	-0.01	1

The terrestrial run-off proxies in core G-10 show high correlations between them and large downcore changes (Table III-5 and Figure AI-2 in Annexes). Al, Ti and Fe contents show a similar variability throughout the core, but the relationship of Al with Fe is higher (0.96) than that of Al with Ti (0.86) and Ti with Fe (0.84, Table III-5). The average values (±sd) of Al, Ti and Fe are 4.7 ±1.2, 0.21 ±0.06 and 2.14 ±0.49% respectively. Al, Ti and Fe contents ranged from 0.94 to 6.69%, 0.02 to 0.35 % and 0.75 to 3.04% respectively. The DBD values in G-10 ranges from 0.16 to 0.83 g.cm^{-3}. The relationship of DBD with Al, Ti or Fe (r=0.69, 0.59 and 0.74 respectively, Table III-5) is lower in comparison to core B-14 (Table III-4) but are still high and significant.

Table III-5. Correlation matrix based on the Pearson correlation coefficient (r) between the proxies developed in core G-10. The trace elements were presented as contents (ppm) in order to perform the correlations. Boldface indicates significance after correcting for multiple comparisons (p<0.0029).

	DBD	Al	Ti	Fe	Co auth	Cr auth	Ba auth	Zn auth	V auth	Mo auth	U auth	Re auth	Re/Mo	δ15N	Ni auth	Cu auth	Cd auth	TOC	HI	OI	δ13C	Ca
DBD	1																					
Al %	**0.69**	1																				
Ti (%)	**0.59**	**0.86**	1																			
Fe (%)	**0.74**	**0.96**	**0.84**	1																		
Co auth	-0.38	**-0.90**	**-0.71**	**-0.82**	1																	
Cr auth	0.28	**0.67**	**0.61**	**0.65**	0.13	1																
Ba auth	-0.41	**-0.89**	**-0.75**	**-0.84**	**0.96**	0.13	1															
Zn auth	0.08	**0.29**	0.22	**0.36**	0.43	**0.66**	0.42	1														
V (auth.)	**-0.53**	-0.24	-0.12	-0.33	0.18	0.19	0.37	0.05	1													
Mo (auth.)	**-0.53**	**-0.52**	-0.35	**-0.58**	0.37	-0.12	0.46	-0.13	**0.66**	1												
U (auth.)	-0.07	0.04	-0.08	0.02	-0.13	0.33	-0.07	0.11	0.41	0.22	1											
Re (auth.)	0.19	**0.46**	0.37	**0.45**	-0.02	**0.79**	0.02	**0.45**	0.26	-0.03	**0.52**	1										
Re/Mo (auth	**0.49**	**0.65**	0.46	**0.67**	-0.26	**0.55**	-0.28	0.39	-0.30	**-0.74**	0.10	**0.61**	1									
δ15N	**-0.53**	**-0.63**	-0.49	**-0.64**	0.41	-0.43	0.45	-0.29	0.33	**0.70**	-0.17	-0.45	**-0.79**	1								
Ni (auth.)	-0.16	0.06	0.07	0.04	0.18	**0.45**	0.25	0.36	**0.49**	0.28	0.32	**0.48**	0.06	0.03	1							
Cu (auth.)	-0.31	-0.26	-0.18	-0.18	0.32	0.29	0.41	0.41	**0.47**	0.37	0.33	0.29	-0.15	0.07	**0.43**	1						
Cd (auth.)	-0.33	-0.34	-0.28	-0.36	0.29	0.17	0.40	0.21	**0.60**	**0.66**	**0.43**	0.23	-0.36	0.37	0.42	**0.59**	1					
TOC	-0.17	0.07	-0.02	-0.01	-0.20	**0.43**	-0.10	0.14	**0.66**	**0.60**	**0.60**	**0.67**	0.28	-0.27	**0.65**	**0.53**	0.39	1				
HI	-0.19	-0.21	-0.18	-0.22	0.09	0.02	0.11	-0.04	0.21	0.22	0.25	0.01	-0.21	0.24	0.26	0.26	**0.40**	0.01	1			
OI	-0.12	-0.19	-0.18	-0.23	0.14	-0.07	0.17	-0.02	0.26	0.19	0.19	-0.07	-0.12	0.24	0.03	-0.12	0.09	-0.21	**0.37**	1		
δ13C (‰)	**-0.44**	**-0.41**	**-0.46**	**-0.42**	0.02	-0.16	0.06	-0.12	0.32	0.35	0.29	0.06	-0.24	**0.27**	0.14	**0.31**	0.25	**0.33**	**0.27**	-0.07	1	
Ca%	-0.26	**-0.60**	**-0.53**	**-0.59**	0.28	-0.42	0.32	-0.24	0.02	**0.30**	0.12	-0.37	**-0.42**	**0.49**	-0.14	-0.02	0.14	-0.19	0.15	**0.44**	0.08	1

In core G-14 the terrestrial run-off proxies (i.e. Al, Ti and Fe) show higher average values and lower variability in comparison with core G-10 (Table III-6 and Figure AI-3 in annexes). Al, Ti and

Fe contents also show similar variability throughout the core as observed in cores B-14 and G-10. But in clear contrast to core G-10, the relationship of Al with Fe is lower (0.78) than the r values of Al with Ti (0.9) or that of Ti with Fe (0.86). The average values (±sd) of Al, Ti and Fe are 5.8 ±0.92, 0.27 ±0.04 and 2.67 ±0.33% respectively; while the Al, Ti and Fe contents ranged from 2.69 to 7.38%, 0.13 to 0.34 % and 1.56 to 3.36% respectively. The DBD values ranges from 0.34 to 1.15 g.cm^{-3}. The shared variability of DBD with Al, Ti or Fe (Table III-6) is lower in comparison with core B-14 (Table III-4) but are still high and significant (0.63, 0.68 and 0.51 respectively). In several cases, the low DBD values in G-10 and G-14 coincide with the presence of diatom layers.

Table III-6. Correlation matrix based on the Pearson correlation coefficient (r) between the proxies developed in core G-14. The trace elements were presented as contents (ppm) in order to perform the correlations. Boldface indicates significance after correcting for multiple comparisons (p<0.0029).

	DBD	Al	Ti	Fe	Co auth	Cr auth	Ba auth	Zn auth	V auth	Mo auth	U auth	Re auth	Re/Mo	$\delta^{15}N$	Ni auth	Cu auth	Cd auth	TOC	HI	OI	$\delta^{13}C$	Ca
DBD	1																					
Al	0.63	1																				
Ti	0.68	0.90	1																			
Fe	0.51	0.78	0.86	1																		
Co auth	-0.74	-0.86	-0.77	-0.55	1																	
Cr auth	-0.41	0.05	0.14	0.31	0.27	1																
Ba auth	-0.44	-0.63	-0.61	-0.55	0.52	0.03	1															
Zn auth	-0.29	0.09	0.17	0.33	0.19	0.62	0.02	1														
V auth	-0.58	-0.25	-0.21	0.04	0.61	0.79	0.14	0.49	1													
Mo auth	-0.62	-0.49	-0.42	-0.32	0.53	0.21	0.30	0.06	0.26	1												
U auth	0.01	0.23	0.21	0.12	-0.29	0.33	0.01	0.29	-0.09	0.17	1											
Re auth	-0.18	0.28	0.27	0.30	-0.15	0.70	-0.06	0.47	0.34	0.17	0.72	1										
Re/Mo	0.58	0.19	0.49	0.42	-0.44	-0.28	-0.09	-0.31	-0.32	-0.53	-0.05	-0.07	1									
$\delta^{15}N$	-0.47	-0.38	-0.45	-0.20	0.62	0.27	0.27	0.16	0.69	0.10	-0.47	-0.15	-0.17	1								
Ni auth	-0.47	-0.16	-0.16	0.01	0.46	0.79	0.20	0.48	0.82	0.23	0.09	0.51	-0.22	0.57	1							
Cu auth	-0.65	-0.42	-0.32	-0.15	0.61	0.69	0.27	0.45	0.66	0.62	0.23	0.45	-0.50	0.18	0.60	1						
Cd auth	-0.46	-0.37	-0.37	-0.26	0.57	0.44	0.40	0.27	0.62	0.26	-0.15	0.16	-0.20	0.60	0.73	0.45	1					
TOC	-0.58	-0.21	-0.23	-0.04	0.48	0.83	0.18	0.45	0.86	0.31	0.10	0.53	-0.24	0.60	0.86	0.62	0.60	1				
HI	-0.69	-0.52	-0.57	-0.38	0.73	0.47	0.38	0.22	0.78	0.34	-0.29	0.08	-0.31	0.85	0.72	0.48	0.76	0.79	1			
OI	-0.20	-0.27	-0.35	-0.27	0.35	-0.15	0.22	-0.16	0.20	-0.01	-0.42	-0.38	-0.16	0.56	0.04	-0.14	0.21	0.08	0.42	1		
$\delta^{13}C$	-0.24	-0.27	-0.28	-0.30	0.14	0.17	0.18	0.13	0.03	0.36	0.48	0.40	-0.08	-0.20	0.18	0.43	0.03	0.18	0.03	-0.36	1	
Ca	-0.24	-0.37	-0.44	-0.30	0.49	-0.08	0.20	-0.13	0.38	0.02	-0.53	-0.43	-0.16	0.69	0.18	-0.05	0.34	0.20	0.56	0.83	-0.27	1

The terrigenous runoff reconstruction (Fig. III-5) shows large multi-centennial to millennial scale variability during the last 25.5 kyr BP. The highest values were recorded during the Last Glacial Maximum and the Termination 1 period. The terrigenous input during the Last Glacial Maximum do not show large temporal variability, but during the Heinrich 1 Stadial strong centennial-scale variability can be observed with three clear minima centered at 17.2, 16.1 and 15.2 kyr BP. The more recent part of the Termination 1 period, which corresponds to the Bølling-Allerød period in the Northern Hemisphere (14.5 to 12.9 kyr BP; Steig et al., 1998), presents a trend towards lower values in the Al and Fe contents but not in the Ti contents (Figs. III-5A, B and C). The Early Holocene shows strong multidecadal scale variability imposed over millennial variability with higher values at ~10.5 kyr BP, lower values at ~9 kyr BP and finally, higher values at ~8 kyr BP which might coincide with the 8.2 kyr BP cold event (Ellison et al., 2006; Alley and Ágústsdóttir, 2005). During the Late Holocene a trend towards high terrigenous input can be observed from 5 to ~3 kyr and then a rapid decrease until 2.5 kyr BP. The last 2.5 kyr are characterized by strong multi centennial scale

variability with higher values during cold periods as the Little Ice Age and the Dark Ages Cold Period (see chapter V).
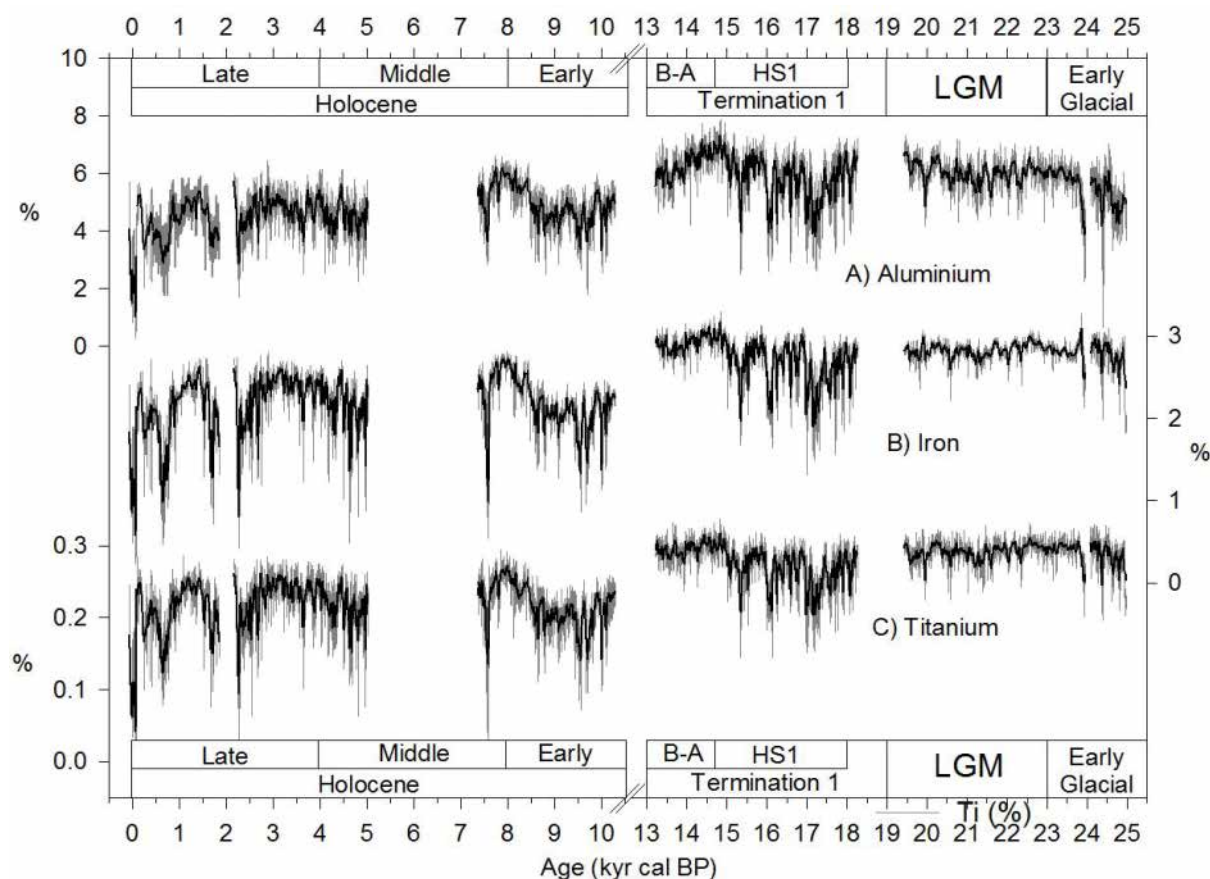
Figure III-5. Stacked record assembled using cores B-14, G-10 and G-14 showing the terrestrial runoff variability since the Last Glacial Maximum. The Al, Fe and Ti contents were obtained using the respective equations in Figure AI-4 in the annexes. A) Aluminum contents. B) Iron contents. C) Titanium contents. The thick black lines indicate a 15-point moving average. The acronyms used in this figure are Last Glacial Maximum (LGM), Heinrich 1 Stadial (H1S), and Bølling-Allerød (B-A).

III-3.4 Mode of presentation of trace elements: Authigenic values or Enrichment factors?

The average enrichment factor of each element was calculated in each core to determine which of them exhibit the highest enrichments relative to andesite (Fig. III-6). B-14 shows higher EF in comparison with G-10 and G-14, and G-14 show the lowest EFs. Re, Cd and Mo show the highest EF in all the cores which confirm their potential as paleoredox proxies. Ni shows higher EF than Cu and consequently can be used as a proxy for export production. In core G-14 Cu and V are depleted relative to andesite.
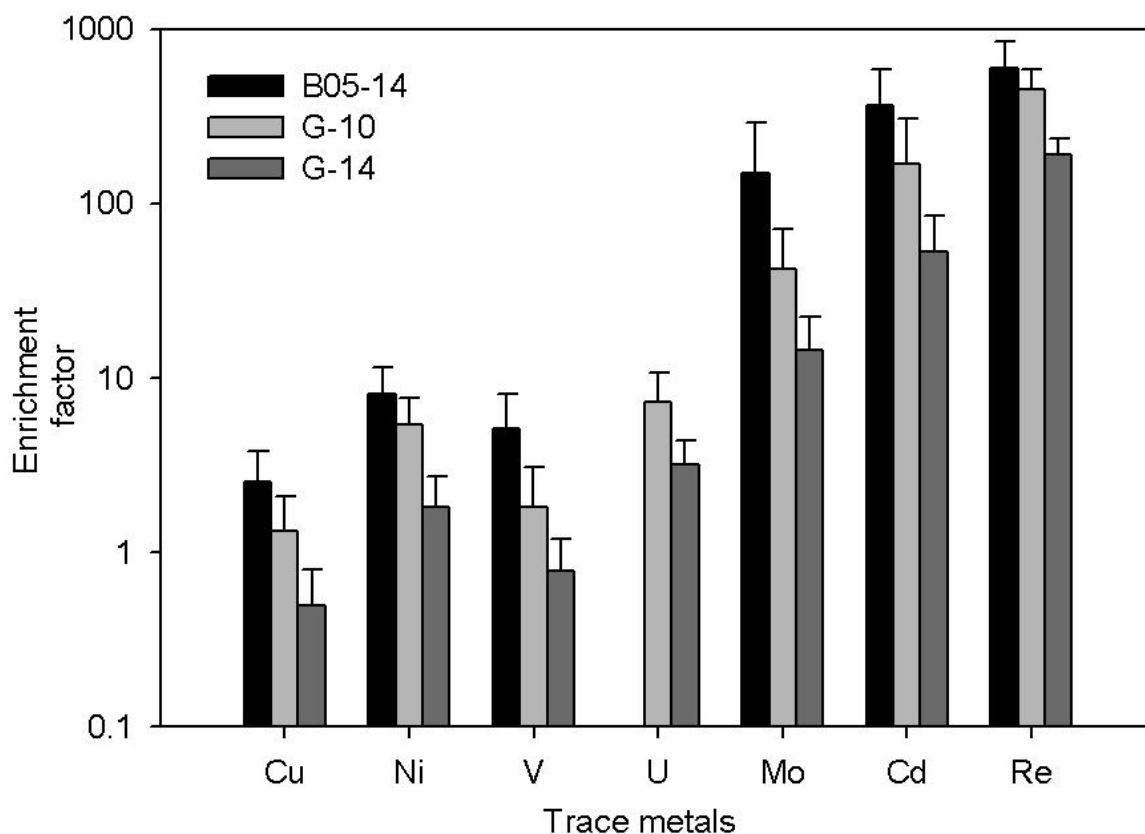
Figure III-6. Enrichment factors for Cu, Ni, V, U, Mo, Cd and Re in the 3 cores analyzed (B-14, G10 and G-14). The data used to calculate the EF were obtained only from the laminated/banded sequences.

The relationships between authigenic trace element concentrations with other parameters or with other authigenic trace elements concentrations show some differences when they are normalized to Al. In the 3 studied cores, the authigenic trace elements concentrations that were not correlated (or which presented extremely low r values) like Cd with Re (Table III-4, III-5 and III-6) show strong relationships when the data were transformed to EF (Table III-7, III-8 and III-9). Additionally, the r values of the authigenic paleoproductivity proxies with TOC (Tables III-4, III-5 and III-6) increased when the trace elements and the TOC were normalized (Tables III-7, III-8 and III-9). For example in core G-10 the correlation of authigenic Ni, Cu and Cd concentrations with TOC were 0.65, 0.53 and 0.39 respectively (Table III-5), while the correlation of Ni (EF), Cu (EF) and Cd (EF) with TOC/Al were 0.89, 0.83 and 0.86 respectively (Table III-8). These observations suggest that the presentation mode of the data could influence in the interpretation of the data set.

Table III-7. Correlation matrix based on the Pearson correlation coefficient (r) between the proxies developed in core B-14. The trace elements were presented as enrichment factors (EF) and the TOC data were normalized to Al in order to perform the correlations. Boldface indicates significance after correcting for multiple comparisons (p<0.003).

	DBD	Al (%)	Ti (%)	Fe (%)	V EF	Mo EF	Re EF	Re/Mo	$\delta^{15}N$	Ni EF	Cu EF	Cd EF	TOC/Al	HI	OI	Ca	Bio Silica
DBD	1																
Al (%)	**0.78**	1															
Ti (%)	**0.79**	**0.99**	1														
Fe (%)	**0.78**	**0.99**	**0.98**	1													
V EF	**-0.76**	**-0.87**	**-0.87**	**-0.87**	1												
Mo EF	**-0.62**	**-0.74**	**-0.72**	**-0.76**	**0.86**	1											
Re EF	**-0.61**	**-0.78**	**-0.77**	**-0.79**	**0.85**	**0.90**	1										
Re/Mo	**0.59**	**0.69**	**0.73**	**0.70**	**-0.69**	**-0.53**	**-0.52**	1									
$\delta^{15}N$	**-0.54**	**-0.61**	**-0.67**	**-0.64**	**0.78**	**0.66**	**0.69**	**-0.68**	1								
Ni EF	**-0.75**	**-0.89**	**-0.89**	**-0.89**	**0.92**	**0.79**	**0.83**	**-0.67**	**0.76**	1							
Cu EF	**-0.69**	**-0.83**	**-0.84**	**-0.84**	**0.92**	**0.80**	**0.86**	**-0.65**	**0.77**	**0.90**	1						
Cd EF	**-0.76**	**-0.87**	**-0.87**	**-0.87**	**0.89**	**0.77**	**0.73**	**-0.67**	**0.69**	**0.91**	**0.85**	1					
TOC/Al	**-0.68**	**-0.83**	**-0.83**	**-0.83**	**0.88**	**0.72**	**0.80**	**-0.63**	**0.71**	**0.89**	**0.88**	**0.85**	1				
HI	**-0.51**	**-0.57**	**-0.60**	**-0.61**	**0.41**	0.22	**0.25**	**-0.56**	**0.72**	**0.56**	**0.42**	**0.58**	**0.52**	1			
OI	0.02	-0.07	-0.11	-0.04	-0.08	**-0.29**	-0.12	-0.19	**0.46**	0.00	0.02	0.06	0.08	0.20	1		
Ca	-0.08	-0.25	-0.26	-0.22	-0.01	-0.07	0.00	-0.20	0.06	0.12	0.02	0.17	0.06	**0.33**	**0.74**	1	
Bio Silica	**-0.66**	**-0.85**	**-0.83**	**-0.86**	**0.79**	**0.76**	**0.73**	**-0.57**	0.54	**0.78**	**0.74**	**0.74**	**0.73**	**0.35**	-0.28	-0.01	1

Table III-8. Correlation matrix based on the Pearson correlation coefficient (r) between the proxies developed in core G-10. The trace elements were presented as enrichment factors (EF) and the TOC data were normalized to Al in order to perform the correlations. Boldface indicates significance after correcting for multiple comparisons (p<0.0029).

	DBD	Al	Ti	Fe	V EF	Mo EF	U EF	Re EF	Re/Mo	$\delta^{15}N$	Ni EF	Cu EF	Cd EF	TOC/Al	HI	OI	$\delta^{13}C$	Ca
DBD	1																	
Al %	**0.69**	1																
Ti (%)	**0.59**	**0.86**	1															
Fe (%)	**0.74**	**0.96**	**0.84**	1														
V EF	**-0.70**	**-0.67**	**-0.53**	**-0.71**	1													
Mo EF	**-0.67**	**-0.82**	**-0.66**	**-0.83**	**0.87**	1												
U EF	**-0.56**	**-0.72**	**-0.70**	**-0.71**	**0.67**	**0.70**	1											
Re EF	**-0.48**	**-0.57**	**-0.52**	**-0.56**	**0.64**	**0.54**	**0.73**	1										
Re/Mo	**0.49**	**0.65**	**0.46**	**0.67**	**-0.51**	**-0.73**	**-0.38**	-0.05	1									
$\delta^{15}N$	**-0.53**	**-0.63**	**-0.49**	**-0.64**	**0.56**	**0.73**	**0.37**	0.18	**-0.79**	1								
Ni EF	**-0.64**	**-0.73**	**-0.62**	**-0.72**	**0.80**	**0.77**	**0.66**	**0.68**	**-0.42**	**0.51**	1							
Cu EF	**-0.65**	**-0.85**	**-0.74**	**-0.80**	**0.77**	**0.81**	**0.74**	**0.68**	**-0.47**	**0.51**	**0.81**	1						
Cd EF	**-0.63**	**-0.80**	**-0.68**	**-0.79**	**0.85**	**0.89**	**0.74**	**0.64**	**-0.57**	**0.60**	**0.84**	**0.85**	1					
TOC/Al	**-0.74**	**-0.80**	**-0.79**	**-0.82**	**0.87**	**0.79**	**0.80**	**0.85**	-0.34	**0.41**	**0.89**	**0.83**	**0.86**	1				
HI	-0.19	-0.21	-0.18	-0.22	0.20	0.18	0.27	0.19	-0.21	0.24	0.27	0.21	**0.30**	0.15	1			
OI	-0.12	-0.19	-0.18	-0.23	**0.35**	0.29	**0.36**	0.16	-0.12	0.24	0.23	0.20	0.25	0.17	**0.37**	1		
δ13C (‰)	**-0.44**	**-0.41**	**-0.46**	**-0.42**	**0.32**	**0.38**	**0.41**	**0.38**	-0.24	0.27	**0.31**	**0.32**	**0.32**	**0.44**	0.27	-0.07	1	
Ca%	-0.26	**-0.60**	**-0.53**	**-0.59**	**0.31**	**0.49**	**0.57**	0.25	**-0.42**	**0.49**	**0.34**	**0.40**	**0.44**	**0.40**	0.15	**0.44**	0.08	1

Table III-9. Correlation matrix based on the Pearson correlation coefficient (r) between the proxies developed in core G-14. The trace elements were presented as enrichment factors (EF) and the TOC data were normalized to Al in order to perform the correlations. Boldface indicates significance after correcting for multiple comparisons (p<0.0029).

	DBD	Al	Ti	Fe	V EF	Mo EF	U EF	Re EF	Re/Mo	δ^{15}N	Ni EF	Cu EF	Cd EF	TOC/Al	HI	OI	δ^{13}C	Ca
DBD	1																	
Al	**0.63**	1																
Ti	**0.68**	**0.90**	1															
Fe	**0.51**	**0.78**	**0.86**	1														
V EF	**-0.72**	**-0.61**	**-0.57**	-0.35	1													
Mo EF	**-0.68**	**-0.76**	**-0.69**	**-0.59**	**0.55**	1												
U EF	-0.27	-0.22	-0.20	-0.22	0.12	**0.37**	1											
Re EF	**-0.59**	**-0.39**	**-0.37**	-0.26	**0.53**	**0.51**	**0.71**	1										
Re/Mo	**0.58**	0.19	**0.49**	**0.42**	**-0.40**	**-0.47**	-0.17	-0.24	1									
δ^{15}N	**-0.47**	**-0.38**	**-0.45**	-0.20	**0.71**	0.25	**-0.30**	0.09	-0.17	1								
Ni EF	**-0.67**	**-0.55**	**-0.54**	**-0.37**	**0.88**	**0.54**	0.23	**0.65**	-0.32	**0.63**	1							
Cu EF	**-0.74**	**-0.69**	**-0.61**	**-0.45**	**0.78**	**0.78**	**0.42**	**0.69**	**-0.52**	0.27	**0.74**	1						
Cd EF	**-0.60**	**-0.69**	**-0.68**	**-0.57**	**0.76**	**0.62**	0.12	**0.45**	-0.26	**0.60**	**0.83**	**0.67**	1					
TOC/Al	**-0.77**	**-0.76**	**-0.74**	**-0.57**	**0.89**	**0.68**	0.26	**0.65**	-0.32	**0.63**	**0.89**	**0.79**	**0.82**	1				
HI	**-0.69**	**-0.52**	**-0.57**	**-0.38**	**0.84**	**0.46**	-0.05	**0.42**	-0.31	**0.85**	**0.82**	**0.55**	**0.75**	**0.85**	1			
OI	-0.20	-0.27	**-0.35**	-0.27	**0.31**	0.14	-0.27	-0.16	-0.16	**0.56**	0.17	0.02	**0.31**	0.25	**0.42**	1		
δ13C	-0.24	**-0.27**	**-0.28**	**-0.30**	0.13	0.34	**0.58**	**0.55**	-0.08	-0.20	0.26	**0.42**	0.11	0.25	0.03	**-0.36**	1	
Ca	-0.24	**-0.37**	**-0.44**	**-0.30**	0.49	0.21	**-0.34**	-0.15	-0.16	**0.69**	0.34	0.13	**0.45**	0.39	**0.56**	**0.83**	-0.27	1

Uncorrelated trace elements may acquire spurious correlations when normalized through division by an immobile element during diagenesis (Van der Weijden, 2002). These problems may arise when the coefficient of variation (CV, standard deviation divided by the mean) of Al concentrations is large compared to the coefficients of variation of the other trace elements. In core B-14 the CV of Al (0.53) was relatively high in comparison with Ni (0.33), Cu (0.37), Cd (0.38), Mo (0.39), V (0.35), and Re (0.37). In contrast in cores G-10 and G-14 the CV of Al (0.25 and 0.16 for G-10 and G-14 respectively) was lower in comparison with Ni (0.29 and 0.45), Cu (0.39 and 0.51), Cd (0.29 and 0.45), Mo (0.34 and 0.38), V (0.47 and 0.47), and Re (0.25 and 0.25). Consequently, the strong shared variability of previously uncorrelated variables, especially in core B-14, may arise due to the relatively high coefficient of variation of Al. However the use of a common divisor is fundamental to avoid the effect of dilution in the sediment matrix, especially in sediments with variable carbonate and opal contents as is the case in the Pisco cores. Thus, given the complications with the Al normalization and in order to minimize normalization biases we will focus on stratigraphic variation in the elements/Al ratios rather than on the absolute values (Tribovillard et al., 2006). In the following sections the trace element EFs are presented to estimate past changes in oxygenation and export production. A comparison of the element concentration and their EFs for each element is shown in annexes I.

III-3.5. REDOX proxies with minimal detrital influences and OMZ intensity

In this sub-section the EF of several redox sensitive elements (V, Mo, U and Re), the Re/Mo, and $\delta^{15}N$ are used to reconstruct past changes in sediment redox conditions and OMZ intensity. The trace element concentrations (ppm or ppb) and their EFs in the 3 cores evaluated are shown with a depth scale in annexes I (Figs. AI-5, AI-6 and AI-7) to show the similarities and differences between the two modes of presentation of the data set. A more detailed description of the proxies developed in core B-14 and the first ~75 cm of core G-10, covering the last 2 millennia, is provided in chapter V. Results of the Kruskal-Wallis and the multiple comparisons of mean ranks test (post-hoc test) used in this section are provided in annexes I.

The EFs of the sediment redox conditions proxies (i.e. V, Mo, U and Re) show a similar pattern in the record: lower values during the Last Glacial Interglacial Period, and high values (with higher temporal variability) during the Holocene (Fig. III-7). The V, Mo, U and Re EFs during the Last Glacial Interglacial Period show low values, and no significant differences between periods in any of the proxies, except for the V EF during the Heinrich 1 Stadial that is significantly higher in comparison with the Early Glacial (Tables AI-1 to AI-6 in annexes I). The Holocene period show higher EF for all the redox sensitive proxies in comparison with the Last Glacial Interglacial Period, and in most of the cases the differences are significative (Tables AI-1 to AI-6 in annexes I). The Early Holocene and the Late Holocene show contrasting characteristics: low V, Mo, and Re EFs with low temporal variability characterize the Early Holocene, while the opposite conditions characterize the Late Holocene. Finally, the last 150 years of the record exhibits the highest EF values for V, Mo and Re. In most cases, the EFs during the last 150 years are significantly higher in comparison with EFs of these elements in the other periods (Tables AI-1 to AI-6 in annexes I).
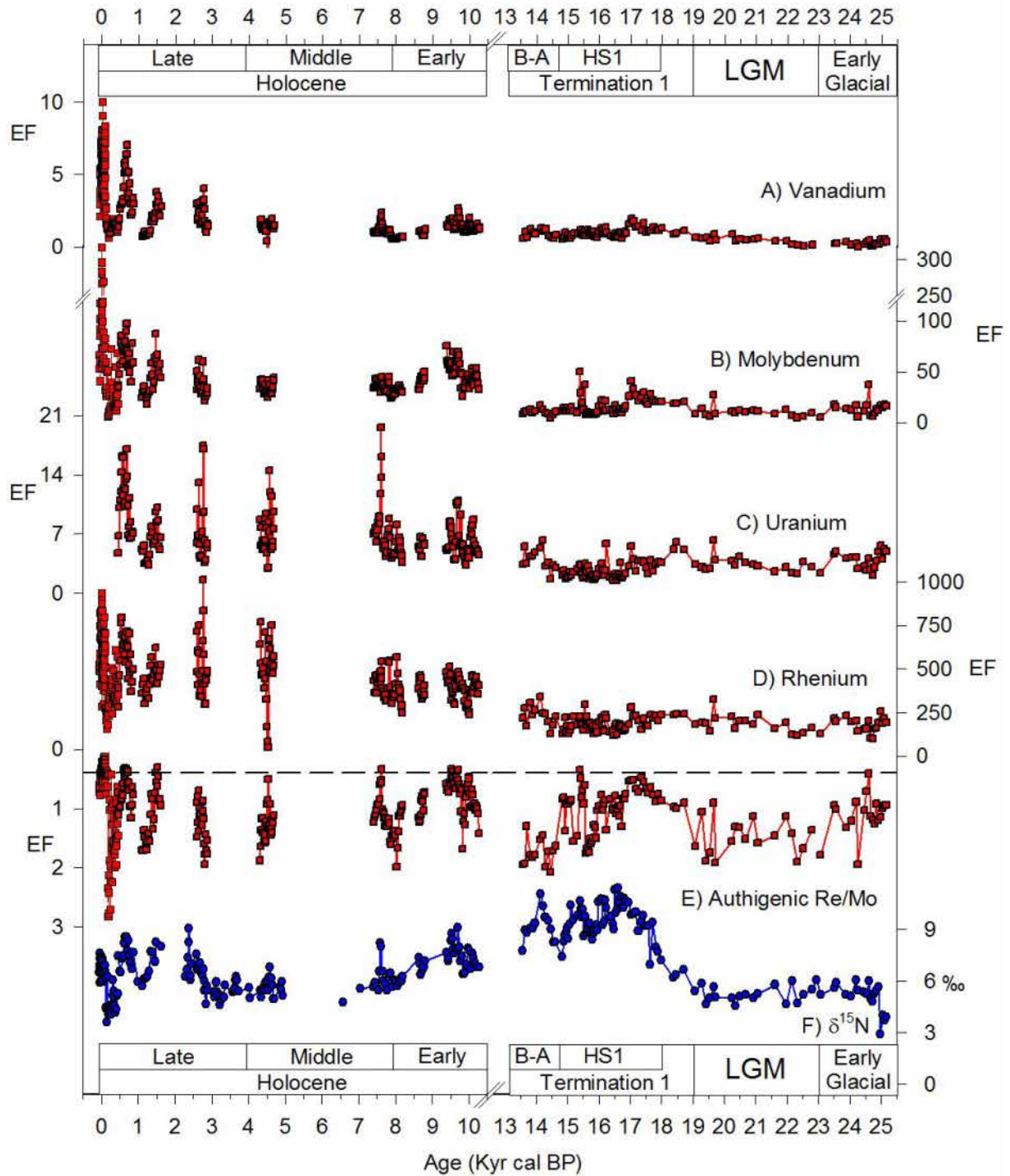
Figure III-7. Stacked record assembled using cores B-14, G-10 and G-14 showing the changes in OMZ intensity during the last 25.5 kyr BP. A) Vanadium EF. B) Molybdenum EF. C) Uranium EF. D) Re EF. E) Authigenic Re/Mo ratio, the horizontal dotted line indicates the value 0.4 x10^{-3} which corresponds to the ratio of the concentration of these metals in the sea-water, y-axis inverted. F) δ^{15}N values. The acronyms used in this figure are: Last Glacial Maximum (LGM), Heinrich 1 Stadial (H1S), and Bølling-Allerød (B-A).

The Re/Mo profile indicates that anoxic conditions in the sediments where reached in several periods during the Holocene and during the Termination 1 (Fig. III-7D). The Early Glacial and the

Last Glacial Maximum were characterized by suboxic conditions as inferred by the highest Re/Mo ratios observed (1.1 ±0.3 and 2 ±2.1 respectively, see Table AI-7 in annexes I for the averages) which is coherent with the more banded nature of the sediments during these periods (Figs. III-2, III-3 and III-4). The Last Glacial Maximum – Termination 1 transition was followed by a strong tendency towards anoxic conditions, reaching a maximum around 17 kyr BP. Afterwards, the Termination 1 period exhibits a tendency toward sub-oxic conditions from 17 to 13 kyr BP with one period with anoxic conditions centered at ~15.2 kyr BP (Fig. III-7E). The Early Holocene was characterized by lower Re/Mo ratios (0.9 ±0.3) in comparison with the former periods. During the Early Holocene anoxic conditions where associated with δ^{15}N maxima at 9.5 and 7.8 kyr BP. The few data points during the Mid Holocene indicate suboxic conditions in the sediments as evidenced by the high Re/Mo ratios, but two short periods with anoxic conditions can be observed at ~7.5 and 4.4 kyr BP (Fig. III-7E). The Late Holocene exhibits stronger centennial-scale variability in comparison with the other periods, reaching anoxic conditions during the Medieval Climate Anomaly and sub-oxic conditions during the Little Ice Age. Remarkably, the highest Re/Mo values were reached during the Little Ice Age, indicating sub-oxic conditions. Finally, the last 150 years of the record show the strongest anoxic conditions in the sediments as evidenced by the low Re/Mo ratio of 0.4 x10^{-3} (Fig. III-7E, Table AI-7 in annexes I).

The large changes in the intensity of water column denitrification during the last ~25 kyr show a similar pattern to the Re/Mo ratios (Fig. III-7E and F). The Early Glacial and the Last Glacial Maximum are characterized by low δ^{15}N values (5 ±0.8‰ and 5.2 ±0.5‰ respectively, see Table AI-8 in annexes I), indicating reduced denitrification in the water column, which is coherent with the sub-oxic conditions inferred from the Re/Mo ratios. During the Termination 1 there is a strong increase of 7 ‰ in δ^{15}N from ~19 to 17kyr BP followed by a gradual decline from ~17 to 14.5 kyr, then a increase until ~14 kyr BP and finally a decrease until 13.5 kyr BP (Fig. III-7F). The δ^{15}N values during the Heinrich 1 Stadial were significantly higher in comparison with all the other periods, except for the Bolling-Allerod episode (Table AI-8 in annexes I). The pattern of δ^{15}N during the Termination 1 is followed by anoxic conditions in the sea floor as evidenced by the Re/Mo ratio, even if the Mo EF values during this period show only a small increase from 6 to 40 (Fig. III-7B). The Early Holocene was characterized by relatively high δ^{15}N values and a tendency towards lower water column denitrification, reaching a Mid Holocene (~6.5 kyr BP) minimum of 4.8 ‰, as also observed in the Re/Mo profile (Fig. III-7E and F). The rest of the Mid Holocene is marked by very low δ^{15}N values (Fig. III-7F). The Late Holocene exhibits high temporal variability since ~2.5 kyr BP: the lowest values (~3.6‰) in all the record were reached during the Little Ice Age and the higher values (~8.5 ‰) during part of the Medieval Climate Anomaly (Fig. III-7F). The last 150 years of the record shows relatively high values (6.7 ±0.3‰) that are associated with anoxic conditions in the sediment as inferred by the Re/Mo values near to 0.4 x10^{-3} (Fig. III-7E).

III-3.6. Paleo-productivity

In this sub-section the EF of several paleo-productivity proxies (Ni, Cu and Cd), the Organic matter quantification and characterization, the carbonate production/preservation and the siliceous productivity are used to reconstruct past changes in export production and the quality and origin of the organic matter. The trace element concentrations (ppm) and their EFs in the 3 cores evaluated are shown with a depth scale in annexes I (Figs. AI-8, AI-9 and AI-10) to show the similarities and differences between the two modes of presentation of the data set. Additionally, the TOC and TOC/Al ratio, the results obtained from the Rock-Eval analysis and the $\delta^{13}C$ are also shown with a depth scale in annexes I. A more detailed description of the proxies developed in core B-14 and the first ~75 cm of core G-10, covering the last 2 millennia, is provided in chapter V. Results of the Kruskal-Wallis and the multiple comparisons of mean ranks test used in this section are provided in annexes I.

III-3.6.1 Trace metals

The EFs of the productivity proxies (i.e. Ni, Cu and Cd) show a similar pattern since the Early Glacial period: lower values during the Last Glacial-Interglacial Transition and high values (and with high temporal variability) during the Holocene (Fig. III-8A, B and C). Very low Ni, Cu and Cd EFs characterized the Early Glacial and the Last Glacial Maximum; moreover Ni and Cu EF were depleted in several samples during these periods. The first 1 kyr of the Heinrich 1 Stadial shows a small increase in the productivity proxies in comparison with the earlier periods; but from 17 to 14.5 kyr the EFs are low and comparable with the Early Glacial and the Last Glacial Maximum. There are no significant differences in the EF paleoproductivity proxies between any of the periods during the Late Pleistocene (i.e. Early Glacial, Last Glacial Maximum, Heinrich 1 Stadial and Bølling-Allerød; Tables AI-9, AI-10 and AI-11 in annexes I). The Early Holocene is marked by significant higher Ni, Cu and Cd EFs in comparison with the Last Glacial-Interglacial Transition (Tables AI-9, AI-10 and AI-11 in annexes I). During the Early Holocene the EFs of the paleoproductivity proxies do not show the strong centennial scale variability observed during the Late Holocene. From ~4.5 kyr to the present, there is a tendency towards higher EFs associated with the highest centennial-scale variability observed in all the record. The global warm periods of the Late Holocene (i.e. Medieval Climate Anomaly and the last 150 years) show high Ni, Cu and Cd EFs, while the global cold periods (Dark Ages Cold Period and Little Ice Age) show low or even depleted values as is the case for Cu EF (Fig. III-8B). Finally, the last 150 years show the highest Ni, Cu and Cd EFs, and are significantly higher in comparison with all the other periods (Tables AI-9, AI-10 and AI-11 in annexes I). Further analyses of the centennial-scale variability of the export production proxies during the last 2 millennia are developed in chapter V.
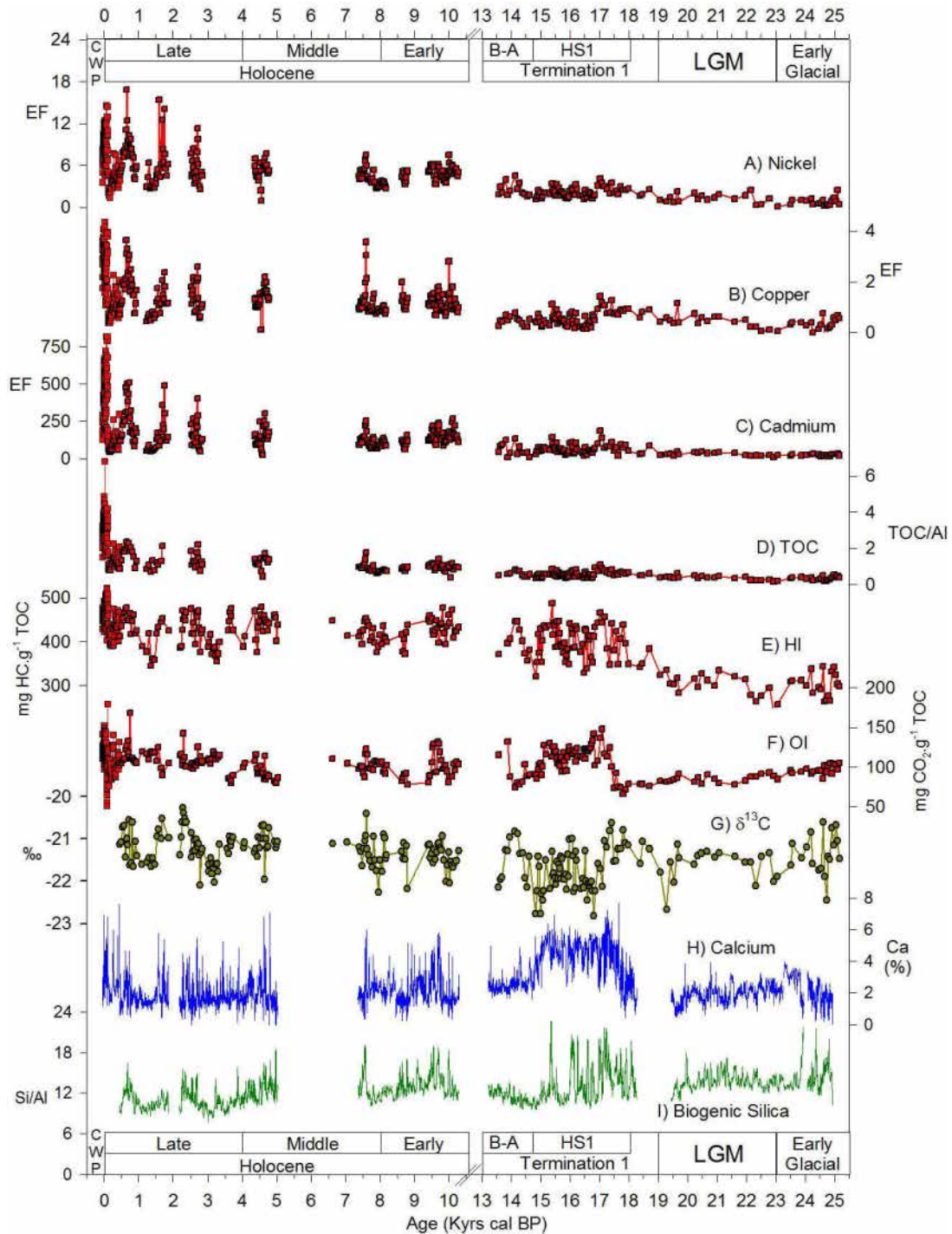
Figure III-8. Stacked record assembled using cores B-14, G-10 and G-14 showing all the proxies used to infer export production variability during the last 25.5 kyr BP. A) Nickel EF. B) Copper EF. C) Cadmium EF. D) Total Organic Carbon normalized to Al contents. E) Hydrogen index (HI). F) Oxygen Index (OI). G) δ^{13}C values. H) Calcium contents obtained using the equation shown (Figure AI-4B in annexes). I) Biogenic Silica inferred from the Si/Al ratios from the XRF analyses. The blank sections in the time series indicate discontinuities in the sediment record. The acronyms used in this figure are Last Glacial Maximum (LGM), Heinrich 1 Stadial (H1S), and Bølling-Allerød (B-A).

Ba and Zn authigenic concentrations were also evaluated as paleoproductivity proxies (profiles not shown) but their utility was proved to be very limited. Authigenic Ba shows very weak

correlations with Ni, Cu, Cd and TOC in the three studied cores (Tables III-4, III-5 and III-6). Zn contents in core B-14 do not show significant relationships with Ni, Cu and TOC, and a weak but significant negative relationship with Cd (Table III-4). In cores G-10 and G-14 the relationships of Zn with the other paleoproductivity proxies are higher in comparison with those observed in core B-14, but the relationships are lower in comparison with the r values of the other paleoproductivity proxies (i.e. Ni, Cu and Cd; Tables III-4, III-5 and III-6). Due to their limited utility as productivity proxies, Ba and Zn will no longer be discussed as such in the present work.

III-3.6.2 Organic matter quantification and characterization

The stacked TOC/Al record show a similar pattern as the trace elements EFs but the variability range during the Late Holocene is not as high as the amplitude observed with the metal EFs (Figs. III-8A, B, C and D). Very low TOC/Al values characterize the Early Glacial (0.3 ±0.1) and the Last Glacial Maximum (0.4 ±0.1), while during the first 2 kyr of the Termination 1 period, there is a small increase in the TOC/Al as observed also with the trace elements EFs (Fig. III-8A, B, C and D). There are no significant differences of the TOC/Al values between any of the Late Pleistocene periods (Tables AI-9 to AI-12). The TOC/Al values during the Early, Mid and Late Holocene and the Current Warm period are significant higher in comparison with the Heinrich 1 Stadial, Last Glacial Maximum and Early Glacial (Table AI-12 in annexes). Finally, the Current Warm Period (i.e. the last 150 years) shows the highest values in all the record (1.8 ±0.9), which is consistent with the results obtained from the paleoproductivity proxies.

The HI and OI values show a strong change toward higher values at the beginning of the Termination 1 period, even if the timing of each parameter was different, HI leads by 1kyr the OI increase (Fig. III-8). The HI shows low values during the Early Glacial and the Last Glacial Maximum, and there is no significant difference in the IH values between these periods (Table AI-12 in annexes). The HI shows high values from the Heinrich 1 Stadial towards the present, but with strong variability. The OI presents a similar pattern as the HI, with low values during the Early Glacial and the Last Glacial Maximum. The OI also shows high values from ~17 kyr BP towards the present, with the highest values observed during part of the Heinrich 1 Stadial and the Late Holocene (Fig. III-8F). The high values of the HI parameter (>400 mg HC.g^{-1}TOC) since the Termination 1 period are interpreted here as an indicator of enhanced preservation of lipid-rich organic matter, which implies a relative lack of degradation of primary organic matter (Arthur et al., 1998). In core G-14, corresponding to the Late Pleistocene, the HI and δ^{15}N values show a strong positive correlation (Table III-6) suggesting that the better preservation of organic matter was probably caused by an enhancement of water column denitrification. The organic matter preservation is significantly higher during the CWP in comparison with the other periods (Table AI-13 in annexes). The OI during the

last 150 years is significantly higher to all the periods except during the Late Holocene and the Heinrich 1 Stadial (Table AI-14 in annexes).

The average values of $\delta^{13}C$ of organic carbon do not exhibit large changes between periods, but the ranges and the temporal variability in each period are very different (Fig. III-8G and Table AI-15 in annexes). The average values ±sd of $\delta^{13}C$ were slightly more negative during the Early Glacial (-21.4 ±0.5‰), Last Glacial Maximum (-21.6 ±0.4‰), Heinrich 1 Stadial (-21.8 ±0.5‰), Bølling-Allerød (-21.5 ±0.5‰) and Early Holocene (-21.4 ±0.3‰), in comparison with the Mid Holocene (-21.2 ±0.4‰) and the Late Holocene (-21.2 ±0.4‰). However, only during the Heinrich 1 Stadial the $\delta^{13}C$ values are significantly lower in comparison with the Mid Holocene and Late Holocene (Table AI-15 in annexes). The range and amplitude were higher during the Heinrich 1 Stadial (-22.8 to -20.6, 2.2‰) in comparison with the other periods the Early Glacial (-22.4 to -20.6, 1.8‰), the Last Glacial Maximum (-22.7 to -21.1, 1.5‰), Bølling-Allerød (-22.2 to -20.8, 1.3‰), Early Holocene (-22.2 to -20.9, 1.3‰), Mid Holocene (-22.3 to -20.4, 1.9‰) and the Late Holocene (-22.1 to -20.3, 1.8‰). The average values are well within the range of $\delta^{13}C$ measured in POM off Peru, but the very low values during some periods (especially during the Heinrich 1 Stadial) suggest a contamination by terrestrial organic matter. The low values of HI during the Early Glacial and Last Glacial Maximum are interpreted as the result of a significant degradation of bulk organic matter that was originally rich in Hydrogen (as explained in the previous paragraph), and also that there is a significant fraction of admixed Hydrogen-poor terrestrial organic matter during this period (Arthur et al., 1998). The last explanation is supported by the strong relationship between $\delta^{13}C$ and IH (r = 0.76, n = 32, p<0.001) during the Early Glacial and Last Glacial Maximum, while the correlation of these parameters during the Termination 1 and all the Holocene period are lower (r = 0.34, n = 72, p<0.001 and r = 0.52, n = 135, p<0.001, respectively). Additionally, during the Early Glacial the range of $\delta^{13}C$ is wide, reaching low values as -22.4‰, which also suggests contamination with very low $\delta^{13}C$ material that likely reflects the composition of terrestrial plants.

III-3.6.3 Carbonate production/preservation

Carbonate contents derived from XRF analyses show the highest values during the Termination 1, and generally low values in the rest of the record, but with strong variability (Fig. III-8H). Ca contents are very low during the Early Glacial (1.8 ±0.6%), Last Glacial Maximum (2.1 ±0.6%), Bølling-Allerød (2.5 ±0.4%), Early Holocene (2.2 ±0.9%) and Late Holocene (1.7 ±0.8%), while the contents are high during the Heinrich 1 Stadial (4.2 ±1.2%). The high values during the Termination 1 period are also higher in comparison with the last 150 years (3.2 ±1.2%). The Ca contents in sediment cores retrieved off Peru can vary with both $CaCO_3$ production and preservation; however we cannot reliably discern the respective influences of $CaCO_3$ production and preservation.

Nevertheless, a ratio between Ca and Biogenic Silica (inferred by the Si/Al ratios) indicates higher ratios during the Termination 1 period (0.29) in comparison with the Early Glacial (0.12), the Last Glacial Maximum (0.15), the Early Holocene (0.16) and the Late Holocene (0.16). This observation supports the interpretation that during the deglaciation the upwelled water mass properties changed considerably, as a probable consequence of remote forcings.

III-3.6.4 Siliceous productivity

The highest inferred siliceous productivity (Si/Al) was recorded during the Heinrich 1 Stadial and the Early Holocene, while the lowest values were recorded during the Late Holocene (Fig. III-8I). The variation of biogenic silica abundance during the last 500 years (i.e. Little Ice Age and the Current Warm Period) was inferred through FTIR analyses, thus no direct comparison can be made with the older periods. The Early Glacial recorded the highest biogenic silica content (14.7 ±1.95), followed by the Last Glacial Maximum (14.03 ±1.36) and the period from 18 to 15 kyr BP (13.93 ±2.77). The average of the whole Termination 1 period (13.11 ±2.63) was comparable to the average during the Early Holocene (13.3 ±2.4). Finally the biogenic silica during the Late Holocene (10.5 ±2.4) was very low. During several periods of the record, the high values of Calcium contents are associated with high biogenic silica values (Fig. III-8H and I), as for example during the Heinrich 1 Stadial.

III-3.7 Proxies selected

Fe measurements obtained by XRF analysis and calibrated using the ICP-Mass results are used hereafter in order to reconstruct the multi-centennial-to millennial scale terrigenous fraction variability. Al is commonly used as a terrigenous indicator but the XRF analysis of Al within wet sediments is highly influenced by the pore water content (Tjallingli et al., 2007). Fe is a constituent of the mineral fraction present in the marine sediments off Peru, and additionally the Al and Fe contents measured by ICP-Mass analysis show high r values in the three cores studied (Table III-4, III-5 and III-6; B05-14, G-10 and G-14: r = 0.99, 0.96 and 0.90 respectively), further indicating the utility of the Fe contents to infer past changes in terrestrial runoff.

Sediment redox conditions and water column denitrification are inferred through the use of Mo EF and Re/Mo, and $\delta^{15}N$ respectively. Mo EF was preferred instead of U and V because of its higher EF (Fig. III-6) and the fact that is heavily enriched in the Peruvian sediments during anoxic episodes. Moreover the Re/Mo serves to accurately differentiate the anoxic and suboxic conditions in the sediments.

The export production is hereafter inferred through the use of the Ni EF, Ca contents and the Si/Al ratio. Ni EF is selected instead of Cu EF because Ni shows higher enrichment in the sediments than Cu (Fig. III-6). Cd is no longer discussed as an export production proxy due to post depositional processes that may affect its EF. The HI is also selected to determine the state of preservation of the OM.

III-3.8 OMZ controls by local and remote forcings

During some periods, there are strong relationships between the export production and the water column denitrification (Fig. III-9). Column water denitrification was highly tied to export production (inferred by Ni EF) during the Late Holocene, Early Holocene and Bølling-Allerød, but not during the Heinrich 1 Stadial, Last Glacial Maximum and Early Glacial. The positive correlations (r) between Ni EF and $\delta^{15}N$ were higher during the Bølling-Allerød (r = 0.69, n = 13), Early Holocene (r = 0.65, n =64), Mid Holocene (0.41, n =37), and Late Holocene (r = 0.66, n = 36), in clear contrast with the weak relationships in the Early Glacial (r = 0.32, n = 19), Last Glacial Maximum (r = 0.06, n =19), Heinrich 1 Stadial (r = 0.25, n = 62). The extremely high $\delta^{15}N$ values during the Heinrich 1 Stadial are not associated with an increase in local export production, with the exception of high values of biogenic silica during parts of this period.

The relationship between the terrestrial input proxies (that can be used as an indicator of the latitudinal displacements of the ITCZ) and the water column denitrification are higher during the Holocene in comparison with the Last Glacial-Interglacial period. The correlations during the Holocene (Early Holocene [r = -0.73, n = 64], Mid Holocene [r = -0.68, n = 37], Late Holocene [r = -0.76, n = 36]) are stronger in comparison with the Heinrich 1 Stadial (r = -0.47, n = 62), and the Bølling-Allerød (r = -0.43, n =13). Finally, the correlations between the terrestrial input proxies and the water column denitrification during the Early Glacial (r = -0.17, n = 19) and the Last Glacial Maximum (r = -0.12, n =19) display the weakest correlations.
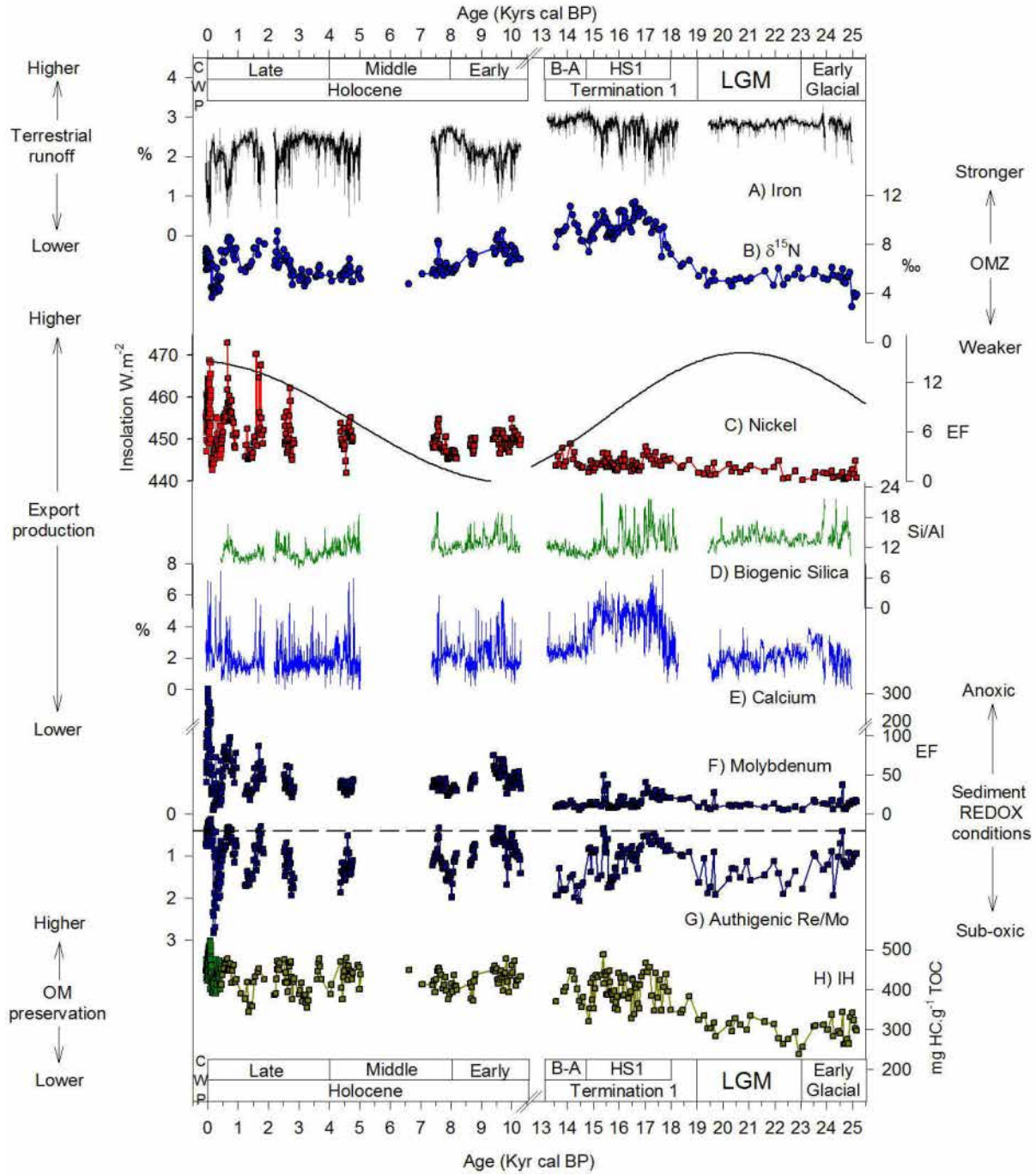
Figure III-9. Summary of the proxies used in the present chapter. A) Fe contents as a proxy for terrestrial run-off. B) δ15N values as a proxy for water column denitrification. C) Ni EF and December to February insolation at 15 °S (Berger et al., 1978). D) Biogenic Silica contents inferred by the Si/Al obtained from the XRF analysis. E) Calcium contents. F) Molybdenum EFs as a proxy for bottom water oxygenation. G)) Authigenic Re/Mo ratios as a proxy to differentiate anoxic and sub-oxic conditions in the sediments, the horizontal dotted line indicates the value 0.4 x 10^-3 which corresponds to the ratio of the concentration of these metals in the sea-water, y-axis inverted. H) Hydrogen index as a proxy for Organic matter preservation. The acronyms used in this figure are Last Glacial Maximum (LGM), Heinrich 1 Stadial (H1S), and Bølling-Allerød (B-A).

III-4. Discussion

A multi proxy approach in finely laminated sediments retrieved off Peru in the core of the actual OMZ was developed to infer subsurface oxygenation, sediment redox conditions and export production, during the last 25.5 kyr. The aim of these analyses was to evaluate whether extra-tropical or local climate variability dominated the subsurface ventilation and productivity off Peru during the last 25 kyr. The results indicate that local control (export production that consumes O_2), and remote forcings (changes in water mass properties or latitudinal displacements of the ITCZ) regulate directly or indirectly the intensity of the OMZ, and that from ~15 kyr to the date the oxygen levels in the OMZ off Pisco is more regulated by oxygen consumption of decaying organic matter in comparison with the older periods (Early Glacial, Last Glacial Maximum and Heinrich 1 Stadial). In the following discussion the use of the terrestrial input off Pisco as a recorder to ITCZ displacements are first discussed. Then the mean state of each period in terms of OMZ intensity and export production is defined using a summary of all the proxies developed (Fig. III-9). Finally the inferred conditions are compared with other relevant studies in order to substantiate a broader regional interpretation.

III-4.1 Terrestrial input proxies off Peru: proxies for ITCZ displacements?

There is an increasing interest to reconstruct rainfall variability in the Southern Hemisphere to 1) investigate whether abrupt climate events observed in the Northern Hemisphere are recorded in the Southern Hemisphere (e.g. Dansgaard Oeschger events), 2) to determine how they relate to reconstructed changes in both low- and high-latitudes, and 3) to infer the possible mechanisms that could explain the geographical patterns. South American Summer Monsoon (SASM) precipitation reconstructions for the Late Pleistocene and the Holocene are available from several locations in Peru (Bird et al., 2011a; van Breukelen et al., 2012) and Brazil (Wang et al., 2006; 2008). Trends of the same sign in southeastern Brazil and Peru during this time period were essentially synchronous across the continent (Bird et al., 2011a) implying a common forcing across the continent (Fig. III-10). The coherent millennial-scale SASM precipitation trends in these records are interpreted as a response to increasing Southern Hemisphere summer insolation, which enhanced convection over the central and western Amazon Basin while increasing subsidence to the east (Bird et al., 2011a). Decadal to multi-century variations in SASM precipitation may also reflect corresponding changes in the latitude of the ITCZ, hypothesis that is supported by a strong relationship between SASM intensity and the southward displacement of the ITCZ during the Holocene (Van Breukelen et al., 2008; Bird et al., 2011a). Laminated marine sediments are a reliable source to reconstruct at high resolution (and on longer timescales in comparison with speleothems) past changes in rainfall variability in the continent through the study of the detrital contents. However it can be debated whether the marine

sedimentary archives on the shelf integrate the discharge of terrestrial components from rivers along the Peruvian coast, as stated by Scheidegger and Krissek (1982) and Rein et al. (2005).
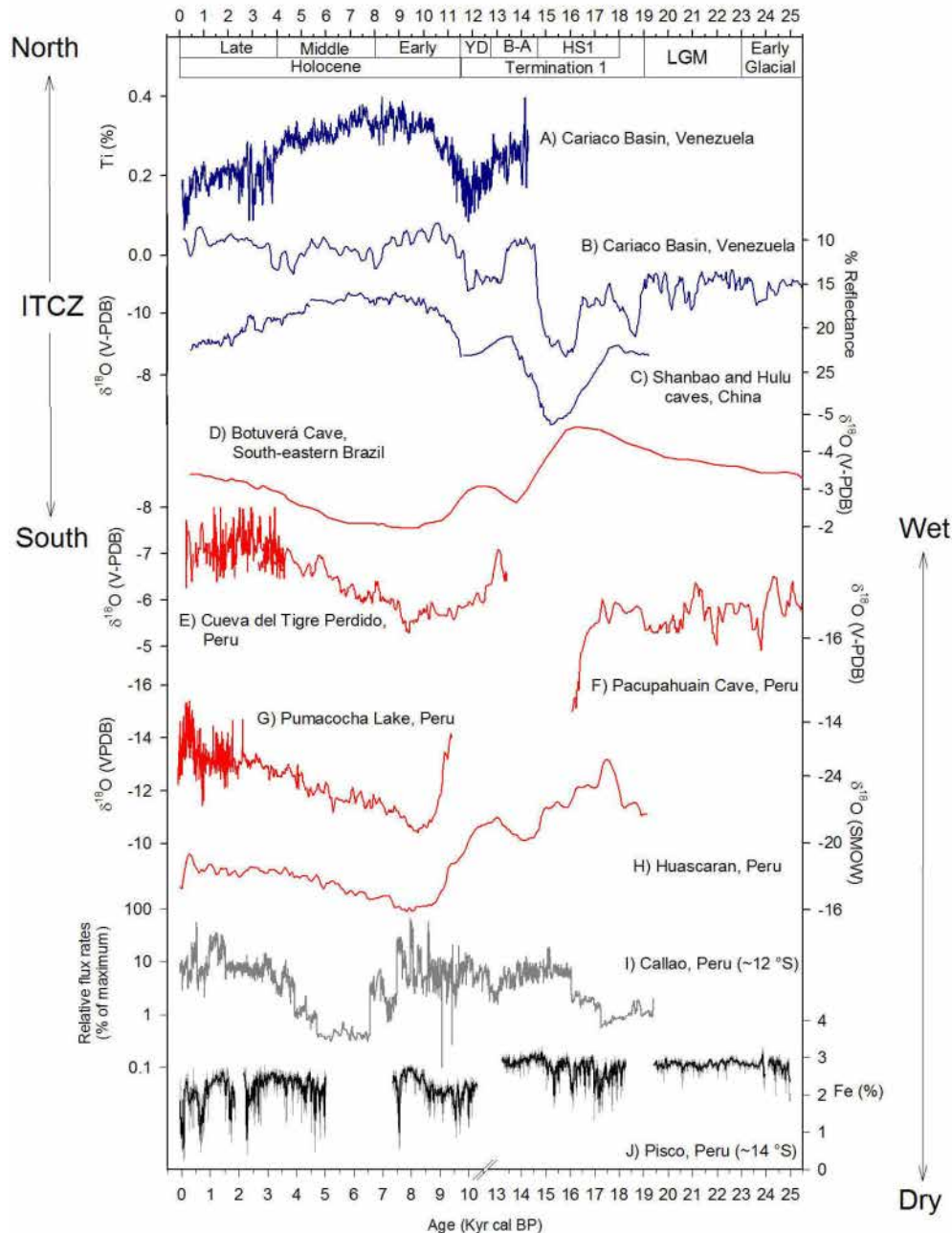
Figure III-10. Comparison between paleoclimatic records in the Northern (blue) and Southern Hemisphere (red and gray). A) Ti contents in sediment core ODP 1002 retrieved in the Cariaco Basin, Venezuela (Haug et al., 2001). B) % reflectance in sediment core ODP 1002 Cariaco Basin, Venezuela (Peterson et al., 2000). C) Speleothem $\delta^{18}O$ record collected in the Shanbao and Hulu Caves China (Wang et al., 2008). D) Speleothem $\delta^{18}O$ record collected in the Botuverá Cave South-eastern Brazil (Wang et al. 2006). E) Speleothem $\delta^{18}O$ record from "Cueva del Tigre Perdido Perú" (5°56'S, 77°18'W, elevation ~1500 m.a.s.l.; Van Breukelen et al., 2012). F) Speleothem $\delta^{18}O$ record from Pacupahuain Cave, Cajamarca, Peru (11.24°S, 75.82°W, elevation 3800 m.a.s.l.; Kanner et al., 2012). G) $\delta^{18}O$ record of authigenic calcite from Laguna Pumacocha (Bird et al. 2011a). H) $\delta^{18}O$ ice core record from Huascaran Peru (11.24°S, 75.82°W, elevation 3800 m.a.s.l.; Thompson et al., 2000). I) Relative flux rates of lithic contents off Callao, Peru (Rein et al. 2005). J) Fe contents off Pisco (present study). The acronyms used in this figure are Last Glacial Maximum (LGM), Heinrich 1 Stadial (H1S), and Bølling-Allerød (B-A).

Fe contents in our marine sediment cores are compared with well-dated speleothem records, other marine records and lake sediments that recorded past changes in precipitation to assess how well these archives off Peru are sensitive to humidity variations over the continent (Fig. III-10). The ITCZ displacements during the last 25 kyr BP are inferred from records obtained in the Northern Hemisphere (i.e. Cariaco Basin in Venezuela and Shanbao and Hulu caves in China) and Southern Hemisphere (i.e. South-eastern Brazil and Peru). The Ti contents in Cariaco Basin are considered a reliable record of past changes of the latitudinal displacement of the ITCZ from ~14.5 kyr to the Little Ice Age (Haug et al., 2001). The % reflectance data in cores retrieved in Cariaco Basin is available for longer time scales and also reflect changes in input of the fine terrigenous components because these terrestrial components are associated with the dark laminated sediments and thus with lower reflectance % (Peterson et al., 2000), even if the similarity of the Ti% contents and % reflectance do not match very well during the Holocene (Figs. III-10A and B). The striking anti-phase relationship between Northern Hemisphere (Fig. III-10A, B and C) and Southern Hemisphere records (Figs. III-10D, E, F and G) suggests that the signal needs to be transmitted in a relatively rapid manner between the two latitudes. Therefore, atmospheric interactions must be involved, likely through movement in the mean position of the ITCZ and associated change in Hadley circulation (Wang et al., 2006; 2008). During the Early Glacial and the Last Glacial Maximum the ITCZ was displaced towards the south as evidenced by the reflectance data (Fig. III-10B), and consequently the humidity in Brazil was high (Fig. III-10D), and also in Peru, which is supported by the high Fe contents off Pisco (Fig. III-10J). Strikingly during the cold Heinrich 1 (~15.5 kyr BP), the ITCZ was displaced to the south in comparison with the Last Glacial Maximum, and the record of SE Brazil (Fig. III-10D) shows an expected increase in precipitation. However the Pisco core shows lower inferred precipitation but with higher variability in comparison with the Early Glacial and the Last Glacial Maximum (Fig. III-10J), in contrast the Callao core shows the expected increase in precipitation (Fig. III-10I). During the Heinrich 1 Stadial as well, the Fe contents off Pisco show 3 centennial-minimums centered at 17.2, 16.1 and 15.2 kyr BP (Fig. III-10I), which are not clearly observed in the reflectance record (Fig. III-10B). During the Bølling-Allerød period, the ITCZ was displaced to the north (Figs. III-10A, B and C) and the inferred precipitation in Brazil was low as expected. However the Pisco core exhibits a slight decline within a period characterized by very high terrestrial input (Fig. III-10J). The lithic contents in the Callao core do not show a clear pattern in this period (Fig. III-10I), which further complicates the interpretation of the terrestrial input records off Peru.

The precipitation in Peru during the Holocene shows a gradual increase since the Early Holocene, which is associated with the southward displacement of the ITCZ (Figs. III-10A to G). During the Early Holocene the SASM precipitation was considerably reduced (Figs. III-10D, E and G) as inferred from the stalagmite records (Wang et al. 2007; van Breukelen et al. 2012) and the lake sediment record (Bird et al., 2011a). The Pisco core follows this pattern during the Early Holocene,

with a minimum in precipitation centered at 9.5 kyr BP and a maximum centered at 8 kyr BP (Fig. III-10J). However the lithic contents in the Callao core do not follow this pattern (Fig. III-10I). Following Early Holocene aridity in Peru and Southern Brazil, precipitation gradually increased throughout the Holocene (Figs. III-10D, E, G and H) as recorded by stalagmite records (Wang et al., 2008; van Breukelen et al., 2012), lake sediment record (Bird et al., 2011a) and also inferred from the Huascaran ice core (Thompson et al., 2000). The observed gradual increase throughout the Holocene, associated with a southward migration of the ITCZ (Fig. III-10A), is not observed in the marine record off Pisco, except possibly by a small increase in Fe contents from ~5 to 3.5 kyr BP (Fig. III-10J). In contrast the lithic contents off Callao show a positive tendency since ~6 kyr cal BP towards the present, interrupted by the low lithic contents observed during the MCA, which is recorded in the Pisco core as well (Figs. III-10I and J). The last 1.5 kyr of the Pisco record is consistent with precipitation records during this period (Reuter et al., 2009; Bird et al., 2011b). The satisfactory covariance of the Pisco cores and the other records during the last 2 millennia is discussed in chapter V.

The differences between the terrestrial runoff proxies off Pisco and Callao with the continental records of rainfall variability (Fig. III-10) may be explained by several processes and causes that are unrelated with the rainfall variability in the continent. Marine cores retrieved off Pisco and Callao were not located in a relatively protected basin like for example Cariaco Basin or Santa Barbara Basin. The Callao and Pisco shelf is exposed to the activity of the poleward undercurrent that may disperse the terrigenous content from the continent. Second, changes in the abundance of the components of the sedimentary matrix may dilute or concentrate the other components, for example an increase in diatom concentrations (up to 50% of the sedimentary matrix) or better preservation of carbonate material (up to 20% of the sedimentary matrix) in one interval may obscure the increase or trend in the terrigenous input (up to 40% of the sedimentary matrix). This last hypothesis may somewhat explain the contradictory terrigenous input during the Last Glacial-Interglacial transition because during this period the biogenic silica and especially the Ca contents display anomalous contents (Figs. III-9D and E). One way to correct the dilution of the constituents is to use fluxes instead of concentrations, however there are not great changes in the mass accumulation rates (Fig. III-4) that could account for the patterns observed. One wonders whether the Pisco sediments were not sensitive to the millennial increase in lithic contents since the Mid Holocene observed in the Callao core and several other precipitation records in the continent. Probably, changes in sub-surface currents off Pisco dispersed the original lithic flux. Interestingly, the terrigenous input during the last 1.5 kyr in the Pisco core fit very well with reconstructed proxies on the continent (see chapter V).

III-4.2 Early Glacial and Last Glacial Maximum

The response of the PUE to the Early Glacial and Last Glacial Maximum conditions in our record is characterized by strong terrestrial input, a weak OMZ, low export production inferred by Ni EF but high silica contents (only during the Early Glacial), and finally similar carbonate contents to the Holocene values (Fig. III-9). The terrestrial input profile does not show strong variability as during the other periods (Fig. III-9A). The reducing conditions in the sediment during these periods caused the depletion of Ni and Cu EF (Figs. III-8A and B); the Ni EF values below 1 indicate that Ni concentrations were depleted in comparison with the mineral source. Upon organic matter decay Ni may be released from organometallic complexes to pore waters and in moderately reducing conditions Ni is cycled from the sediments to the overlying waters. In contrast, under sulfate reducing conditions, Ni may be incorporated as insoluble NiS into pyrite (Tribovillard et al., 2006). However the depleted Ni and Cu values may also be due to the high concentration of Ni and Cu in the lithogenic background that caused low values of Ni and Cu EF (Boning et al., 2009). The inferred sub-oxic conditions in the sediments also contributed to stronger organic matter decay as evidenced by the lower HI values (Fig. III-9H).

SST reconstructions off Callao (~12 °S) during the Last Glacial Maximum are 3 °C below modern level (Rein et al., 2005), which is concordant with low SST in the EEP and the Western Equatorial Pacific (Lea et al., 2000; Koutavas et al., 2002; Kienast et al., 2006). During the Last Glacial Maximum, there was also a reduced Pacific east-west gradient in SST which implies weaker Walker circulation and trade winds; additionally a southward shift of the ITCZ was also evidenced by several proxies (Fig. III-10), all of which indicate a persistently "El Niño–like" pattern in the Tropical Pacific (Koutavas et al., 2002). The response of the PUE to the Early Glacial and Last Glacial Maximum conditions in the present work is consistent with an "El Niño-like" mean state, showing higher terrestrial runoff that can be associated with a southward shift of the ITCZ, and lower export production and weaker OMZ that are associated with an idealized "El Niño-like" state. Additionally, the water column denitrification remained relatively constant during these periods, as also observed by Higginson and Altabet (2004), and linked to remote forcings since there is no relationship between the productivity proxies and water column denitrification (Fig. III-9). Finally, the weak OMZ observed in the data set is consistent with an increased oxygen supply to the OMZ as a consequence of higher glacial winds speeds and lower global temperatures (Meissner et al., 2005).

III-4.3 Termination 1 (Heinrich 1 Stadial and Bølling-Allerød)

The most striking feature during the Termination 1 is the abrupt increase in water column denitrification which cannot be principally explained by an increase in oxygen demand due to an

increased export production off Pisco (Figs. III-9B and C). The abrupt increase in water column denitrification, represented by $\delta^{15}N$ records, was a phenomenon affecting a large region of the Equatorial Pacific between 15 °N and 36 °S (Martinez and Robinson, 2010). The increase in $\delta^{15}N$ in our record started at the end of the Last Glacial Maximum (~19 kyr BP) and reached a maximum peak at 16.5 kyr BP (Fig. III-9B), which is consistent with the increase observed in nearby records (Higginson and Altabet, 2004). This time period (within uncertainties) coincides with a decline in dust abundance and early deglacial rise in CO_2 as revealed by the Vostok and Byrd cores respectively (Higginson and Altabet, 2004), confirming an Antarctic influence upon the strong denitrification in the EEP (Martinez and Robinson, 2010). The causes of the strong denitrification observed in sediment cores retrieved in the Eastern Pacific margin are likely caused by two non exclusive mechanisms. The first one is related to an increase in export production and then in sub-surface oxygen demand in the EEP (Martinez and Robinson, 2010). The second mechanism is associated with changes in ventilation of the source water mass, related to a collapse of the thermocline ventilation which occurred at the mid-latitude subduction region of the Eastern South Pacific (De Pol-Holz et al., 2006). Whatever the mechanism that caused the strong denitrification and reorganization of the OMZ, it is evident that local export production did not produce the oxygen demand as evidenced by uncorrelated export production proxies and denitrification in the water column (Figs. III-9A and B, Higginson and Altabet, 2004).

The Termination 1 period also shows two periods (~ 17.2 and 15.3 Kyr BP) characterized by anoxic conditions in the water-sediment interface which were probably produced by massive deposits of diatoms (Figs. III-9D and G). These two anoxic events were associated with two peaks in silica contents, high Mo EF and Re/Mo ratios near ~0.4 x 10^{-3}. The rapid sedimentation of the diatom blooms probably originated an enhanced preservation of carbonates. The strong OMZ intensity and the anoxic conditions in the sediments likely drove the enhanced organic matter preservation as evidenced by the also abrupt change in the HI values (Fig. III-9H). Thus, it is interpreted that other organic materials (i.e. fish scales) are better preserved in this period in comparison with the earlier periods. The oceanographic conditions during the Heinrich 1 Stadial were also favorable for the production/preservation of calcium carbonate and biogenic silica, in contrast with the Bølling-Allerod period during which these two constituents returned to the glacial levels (Fig. III-9D and E).

The oceanographic conditions off Pisco during the Termination 1 are interpreted to be unrelated to La Niña or El Niño-like conditions. An idealized normal/ La Niña-like (El Niño) conditions involve higher (lower) productivity and strong (weak) OMZ, and during the Termination 1 the OMZ was strong but the export production was very low, with similar values than those observed during the glacial period. However the oceanographic conditions were favorable to the development of diatom blooms, as evidenced by the high contents of silica. (Fig. III-9D). Enhanced La Niña-like

conditions were previously associated with the period from ~16 to 12 kyr BP (Makou et al., 2010). The support for the interpretation of La Niña-like comes from the high abundance of Cholesterol, an organic biomarker that provides an integrated signal of total primary productivity and zooplankton activity in surface waters, which reached similar levels as during the last ~2 kyr (Makou et al., 2010). Our results do not support the interpretation of La Niña-like conditions during the Termination 1 period.

III-4.4 Early Holocene

The response of the PUE to the Early Glacial conditions in our record is characterized by multicentennial-scale changes in terrestrial run-off, a strong OMZ in the beginning of the Early Holocene which become weaker towards the end of the Early Holocene, higher export production inferred by Ni in comparison with the Last Glacial-Interglacial Transition and relatively higher Ca and biogenic silica contents (Fig. III-9). The terrestrial runoff presents an opposite pattern with the intensity of the OMZ and the export production. Lower terrestrial runoff (from 9.5 to 8.5 kyr) is associated with a strong OMZ and relatively high export production, while the peak in terrestrial runoff (from 8.5 to 7.5 kyr) coincides with a weaker OMZ and relatively low export production as inferred by Ni EF and Biogenic Silica contents (Fig. III-9). The stage associated with high terrestrial run-off during the Early Holocene is also associated with poor carbonate preservation (Fig. III-9E).

The inferred aridity, observed in different records in Peru and southeastern Brazil (Fig. III-10), was associated with the northernmost position of the ITCZ that favored a small increase in export production off Peru. The Early Holocene was also characterized by SST ~2 °C warmer than today and warmer than during most of the Holocene (Rein et al. 2005), which can be a result of intense warm water anomalies off Peru. The aridity in Peru was interrupted by what appears to be the cold 8.2 kyr event. The Al% record indicates that the peak in terrestrial run-off occurred at ~8 kyr (Fig. III-10J). This cold event of global extent caused an intensification of the SASM (Cheng et al., 2010) and a southern displacement of the ITCZ (Fig. III-10). These conditions were unfavorable for the export production in the PUE, and, as a consequence of the strong coupling between export production and OMZ intensity, the lower export production did not cause an intensification of the weak OMZ (Figs. III-9B and C).

III-4.5 Middle Holocene

The lack of sediment corresponding to the Mid Holocene, caused by a large hiatus in core G-10 (from 4.9 to 7.4 kyr BP) as well as in several cores retrieved off Peru, impede to characterize this period, even if the few data points suggest a weak OMZ (Fig. III-9B). However, there are two events

centered at ~7.5 and ~4.5 kyr BP characterized by a relatively strong OMZ and anoxic conditions in the sediments (Figs. III-9B and G). The Mid Holocene in our records starts with an anoxic OMZ and a slight increase in export production after the 8.2 kyr event (Figs. III-9C and D). Then from ~5 kyr to 4 kyr BP sub-oxic sediment conditions and a weak OMZ can be inferred from the high Re/Mo ratios and low $\delta^{15}N$ values respectively, although the exported production remained relatively high.

Several previous studies suggest that the Mid Holocene period was characterized by "La Niña-like" conditions in the tropical Pacific, with enhanced SST gradients and strengthened trade winds (Koutavas et al. 2002; Carré et al., 2011). Additionally, the Mid Holocene period according to model experiments was characterized by reduced El Niño activity (Clement et al., 1999). If La Niña-like conditions prevailed during the Mid Holocene we would expect constant high export production and a strong OMZ which is not the case (Figs. III-9B and C). The water column denitrification during the Mid Holocene was lower than during the last 100 years (Fig. III-9B). Sediment cores retrieved off Peru (Chazen et al., 2009) and off Chile (De Pol-Holz et al., 2006) also show a weaker column water denitrification indicating a regional signal for the low denitrification.

III-4.6 Late Holocene

The Late Holocene is characterized in our records by strong centennial to multi-centennial scale variability in terrestrial input, OMZ intensity and export production (Figs. III-9A, B and C). The export production and OMZ intensity are highly coupled during this period, thus indicating that high (low) export production off Peru play a major role in the intense (weak) OMZ. From the Mid Holocene to the present there is a strong tendency towards higher export production superimposed upon strong centennial-scale variability (Fig. III-9C). It is noteworthy that the largest changes in OMZ intensity and sediment redox conditions occurred in the last 500 years. The weak OMZ and the sub-oxic conditions in the sediments during the Little Ice Age (1500 to 1850 AD) are comparable to the conditions observed during the Last Glacial Maximum, while the Current Warm Period (last 0.15 kyr of the record) shows a strong OMZ and the more anoxic sediment conditions in comparison with all the record (Figs. III-9B, F and G). Additionally the warm periods (Medieval Climate anomaly and Current Warm Period) show inverse conditions relative to the cold periods (Dark Ages Cold Period and Little Ice Age) during the last 1.8 kyr. The globally warm (cold) periods are associated with a strong (weak) OMZ and higher (relatively lower) local productivity showing a typical El Niño – La Niña correlation between proxies during the major part of the record. The chapter V of this thesis is dedicated to the strong changes that occurred during the last 2 millennia.

The stronger centennial to multi-centennial scale variability in OMZ intensity, anoxic sediment conditions and export production since ~4.5 kyr BP was already observed in other types of

proxies obtained from cores retrieved off Callao and off Pisco (Chazen et al., 2009; Makou et al., 2010). Several studies in the Tropical Pacific also show that during the Late Holocene the variability in several El Niño related proxies increased considerably (e.g. Rodbell et al., 1999; Tudhope et al., 2001; Moy et al., 2002, Riedinger et al., 2002; Koutavas et al., 2006). The likely explanation for the increase in variability since ~4.5 kyr BP is the Mid Holocene strengthening of El Niño Southern Oscillation, which may be linked to changes in the precession of earth's orbit (Clement et al., 2000).

III-4.7 Mechanisms responsible for the increase in export production and sediment REDOX conditions during the Holocene

The upwelling enhancement since ~8 kyr BP, inferred by an increase in export production and in the anoxic conditions in the sediments, is strongly associated with the increase in December to March insolation at ~15 °S (Berger et al., 1978). The primary productivity off Pisco (and off Peru) follows a seasonal pattern: it is higher during spring/summer when surface waters are more stratified, and lower in winter because of lower surface insolation and stronger winds originating a thick mixed layer that prevent algal growth (Pennington et al., 2006; Echevin et al., 2008; Chavez and Messié, 2009; Gutierrez et al., 2011). Consequently, the increase in upwelling, export production, and anoxic sediments at millennial-scales can be explained by mechanisms related to the increased summer (December to March) insolation. Summer insolation of the Southern Hemisphere has increased gradually from a minimum centered at 9.5 kyr BP due to the variations in the Earth's orbit around the Sun (Berger et al., 1978). Higher insolation levels tend to stimulate primary production in a nutrient enriched surface water layer by the stabilization of the water column due to increased stratification. Additionally, an increase in insolation provoques an atmospheric pressure gradient between land and sea, which increases upwelling winds in spring and summer. This mechanism is explained by an inhibition of nighttime cooling and the enhancement of daytime heating leading to an intensification of the continental thermal lows adjacent to upwelling regions (Bakun, 1990; Rutllant, 1990; Rutllant et al., 2003; Bakun et al., 2010). Van Geen et al. (1992) proposed the same mechanism to explain the gradual decrease of upwelling off western North America over the past ~4 kyr BP which was associated with a decrease in insolation in the Northern Hemisphere.

An alternative, non-exclusive, explanation for the observed increase in upwelling since ~8 kyr BP is an increase in iron fertilization due to a gradual increase in rainfall over the continent throughout the Holocene. The source of the upwelled water off Peru is the nutrient-rich subsurface countercurrent in contact with the organic-rich shelf sediments that present extremely high concentrations of dissolved Fe in the near-bottom waters (Bruland et al., 2005). During the Holocene, the SASM exhibited a long term increase that tracked the summer insolation increase (Bird et al., 2011a), and a southward displacement of the ITCZ (Haug et al., 2001). The increased terrigenous

input, including iron, to the coastal ocean may have enhanced primary productivity, as proposed in another upwelling area in the HCS at ~27 °S (Dezileau et al., 2004). However this mechanism could be more important in the Southern Peru –Chile margin given that this region does not present a wide shelf to serve as a source of iron and is thus iron-limited (Bruland et al., 2005).

III-5. Conclusions

A multi proxy approach in finely laminated sediments retrieved off Peru in the core of the actual OMZ was developed to infer subsurface oxygenation, sediment redox conditions and export production, during the last 25 kyr. A detailed stratigraphic approach was conducted to construct the chronological models using multiple ^{14}C ages. Special attention was taken to develop the proxies only in the laminated or banded sections of the cores to avoid the possible slumps that would lead to erroneous interpretations of phenomenon caused by tectonic activity. The PUE during the Early Glacial and the Last Glacial Maximum was characterized by a weak OMZ and very low export production. The productivity in the PUE started to increase after the Last Glacial Maximum, then during the Holocene there is a trend towards stronger OMZ and higher export production. Finally the Late Holocene exhibited a strong centennial to multi-centennial scale changes in OMZ intensity and export production. During the Little Ice Age, the OMZ intensity was as weak as during the Last Glacial Maximum and the Early Glacial. The results of this chapter also support the view that Holocene climate variability has been increasing in recent millennia because the export production and the anoxic conditions in the sediments during the Medieval Climate Anomaly, Little Ice Age and Current Warm Period showed the largest amplitude event of the last 25 kyr. Finally, the sediments exhibited the most intense oxygen depletion during the last 100 years of the record, i.e. the Current Warm Period, and due to an enhanced export production.

The comparison of export production and water column denitrification proxies indicate that the intensity of the OMZ off Peru during the last ~25 kyr BP was controlled by local and remote forcings. The weak export production during the Early Glacial, Last Glacial Maximum and Heinrich 1 Stadial did not leave a strong imprint in the water column denitrification indicating that the OMZ signal was mainly originated by remote forcings (changes in ventilation of the source water mass and/or increase in export production and then in sub-surface oxygen demand in the eastern equatorial Pacific), as proposed in earlier works. In contrast from ~14.7 kyr to the present, the increase in export production exerts a strong control on the water column oxygenation, as evidenced by the strong coupling between export production and δ^{15}N water column denitrification.

III-6. Bibliography

Agnihotri, R., M. A. Altabet, and T. D. Herbert. 2006. Influence of marine denitrification on atmospheric N_2O variability during the Holocene. Geophysical Research Letters 33(L13704).

Agnihotri, R., M. A. Altabet, T. Herbert, and J. E. Tierney. 2008. Subdecadally resolved paleoceanography of the Peru margin during the last two millennia. Geochemistry Geophysics Geosystems 9(5):1-15.

Alley, R. B., and A. M. Ágústsdóttir. 2005. The 8k event: cause and consequences of a major Holocene abrupt climate change. Quaternary Science Reviews 24:1123-1149.

Altabet, M. A., and R. Francois. 1994. Sedimentary nitrogen isotopic ratio as a recorder for surface ocean nitrate utilization. Global Biogeochemical Cycles 8(1):103-116.

Altabet, M. A., C. Pilskaln, R. Thunell, C. Pride, D. Sigman, F. Chavez, and R. Francois. 1999. The nitrogen isotope biogeochemistry of sinking particles from the margin of the Eastern North Pacific. Deep-Sea Research I 46:655-679.

Alves, S., P. Schiano, F. Capmas, and C. J. Allègre. 2002. Osmium isotope binary mixing arrays in arc volcanism. Earth and Planetary Science Letters 198(3-4):355-369.

Arthur, M. A., W. E. Dean, and K. Laarkamp. 1998. Organic carbon accumulation and preservation in surface sediments on the Peru margin. Chemical Geology 152:273-286.

Bakun, A. 1990. Global climate change and intensification of coastal upwelling. Science 247(4939):198-201.

Bakun, A., D. Field, A. Redondo-Rodriguez, and S. J. Weeks. 2010. Greenhouse gas, upwelling-favorable winds, and the future of coastal ocean upwelling ecosystems. Global Change Biology 16:1213-1228.

Behar, F., V. Beaumont, and H. L. D. B. Penteado. 2001. Rock-Eval 6 technology: performances and developments. Oil & Gas Science and Technology - Rev. IFP 56(2):111-134.

Berger, A. L. 1978. A Simple algorithm to compute long term variations of Daily or monthly insolation Institut d'Astronomie et de Geophysique, Universite Catholique de Louvain, Louvain-la-Neuve, No. 18.

Bird, B. W., M. B. Abbott, D. T. Rodbell, and M. Vuille. 2011a. Holocene tropical South American hydroclimate revealed from a decadally resolved lake sediment $\delta^{18}O$ record. Earth and Planetary Science Letters 310:192-202

Bird, B. W., M. B. Abbott, M. Vuille, D. T. Rodbell, N. D. Stansell, and M. F. Rosenmeier. 2011b. A 2,300-year-long annually resolved record of the South American summer monsoon from the Peruvian Andes. PNAS.

Böning, P., H. J. Brumsack, E. Bottcher, B. Schnetger, C. Kriete, J. Kallmeyer, and S. L. Borchers. 2004. Geochemistry of Peruvian near-surface sediments. Geochimica et Cosmochimica Acta 68(21):4429-4451.

Bruland, K. W., E. L. Rue, G. J. Smith, and G. R. DiTullio. 2005. Iron, macronutrients and diatom blooms in the Peru upwelling regime: brown and blue waters of Peru. Marine Chemistry 93:81-103.

Carre, M., I. Bentaleb, M. Fontugne, and D. Lavallee. 2005. Strong El Nino events during the early Holocene: stable isotope evidence from Peruvian sea shells. The Holocene 15(1):42-47

Carre, M., M. Azzoug, I. Bentaleb, B. M. Chase, M. Fontugne, D. Jackson, M.-P. Ledru, A. Maldonado, J. P. Sachs, and A. J. Schauer. 2011. Mid-Holocene mean climate in the south eastern Pacific and its influence on South America. Quaternary International:1-12.

Chavez, F. P., and M. Messié. 2009. A comparison of Eastern Boundary Upwelling Ecosystems. Progress in Oceanography 83(1-4):80-96.

Chazen, C. R., M. A. Altabet, and T. D. Herbert. 2009. Abrupt mid-Holocene onset of centennial-scale climate variability on the Peru-Chile Margin. Geophysical Research Letters 36:L18704.

Cheng, H., D. Fleitmann, R. L. Edwards, M. Wang, F. W. Cruz, A. S. Auler, A. Mangini, Y. Wang, X. Kong, S. J. Burns, and A. Matter. 2010. Timing and structure of the 8.2 kyr B.P. event inferred from d^{18}O records of stalagmites from China, Oman, and Brazil. Geology 37:1007-1010.

Clement, A. C., R. Seager, and M. A. Cane. 1999. Orbital controls on the El Nino/Southern Oscillation and the tropical climate. Paleoceanography 14(4):441-456.

Colodner, D., J. Sachs, G. Ravizza, K. Turekian, J. Edmond, and E. Boyle. 1993. The geochemical cycle of rhenium: a reconnaissance. Earth and Planetary Science Letters 117(1-2):205-221

Crusius, J., S. Calvert, T. Pedersen, and D. Sage. 1996. Rhenium and molybdenum enrichments in sediments as indicators of oxic, suboxic and sulfidic conditions of deposition. Earth and Planetary Science Letters 145(1-4):65-78.

De Pol-Holz, R., O. Ulloa, L. Dezileau, J. Kaiser, F. Lamy, and D. Hebbeln. 2006. Melting of the Patagonian Ice Sheet and deglacial perturbations of the nitrogen cycle in the eastern South Pacific. Geophysical Research Letters 33:L04704.

Dean, W. E. 2006. The geochemical record of the last 17,000 years in the Guaymas Basin, Gulf of California. Chemical Geology 232:87-98.

Dean, W. E., J. V. Gardner, and R. Y. Anderson. 1994. Geochemical evidence for enhanced preservation of organic matter in the oxygen minimum zone of the continental margin of northern California during the late Pleistocene. Paleoceanography 9(1):47-61.

Dezileau, L., O. Ulloa, D. Hebbeln, F. Lamy, J. L. Reyss, and M. Fontugne. 2004. Iron control of past productivity in the coastal upwelling system off the Atacama Desert, Chile. Paleoceanography 19:PA3012.

Echevin, V., O. Aumont, J. Ledesma, and G. Flores. 2008. The seasonal cycle of surface chlorophyll in the Peruvian upwelling system: A modelling study. Progress in Oceanography 79:167-176.

Ellison, C. R. W., M. R. Chapman, and I. R. Hall. 2006. Surface and deep ocean interactions during the cold event 8200 years ago. Science 312:1929-1932.

Gutierrez, D., A. Sifeddine, D. B. Field, L. Ortlieb, G. Vargas, F. Chavez, F. Velazco, V. Ferreira, P. Tapia, R. Salvatteci, H. Boucher, M. C. Morales, J. Valdes, J. L. Reyss, A. Campusano, M. Boussafir, M. Mandeng-Yogo, M. Garcia, and T. Baumgartner. 2009. Rapid reorganization in ocean biogeochemistry off Peru towards the end of the Little Ice Age. Biogeosciences 6:835-848.

Gutierrez, D., A. Sifeddine, J. L. Reyss, G. Vargas, F. Velazco, R. Salvatteci, V. Ferreira-Bartrina, L. Ortlieb, D. Field, T. Baumgartner, M. Boussafir, H. Boucher, J. Valdes, L. Marinovic, P. Soler, and P. Tapia. 2006. Anoxic sediments off Central Peru record interannual to multidecadal changes of climate and upwelling ecosystems during the last two centuries. Advances in Geosciences 6:119-125.

Gutierrez, D., I. Bouloubassi, A. Sifeddine, S. Purca, K. Goubanova, M. Graco, D. Field, L. Méjanelle, F. Velazco, A. Lorre, R. Salvatteci, D. Quispe, G. Vargas, B. Dewitte, and L. Ortlieb. 2011. Coastal cooling and increased productivity in the main upwelling zone off Peru since the mid-twentieth century. Geophysical Research Letters 38:L07603.

Haug, G. H., K. A. Hughen, D. M. Sigman, L. C. Peterson, and U. Rohl. 2001. Southward Migration of the Intertropical Convergence Zone Through the Holocene. Science 293:1304-1308.

Helly, J., and L. Levin. 2004. Global distribution of naturally occurring marine hypoxia on continental margin. Deep-Sea Research I 51:1159-1168.

Higginson, M. J., and M. A. Altabet. 2004. Initial test of the silicic acid leakage hypothesis using sedimentary biomarkers. Geophysical Research Letters 31:L18303.

Jarvis, K. E., A. L. Gray, and R. S. Houk. 1992. Handbook of Inductively Coupled Plasma Mass Spectrometry. Blackie Academic & Professional, an imprint of Champan & Hall, Wester Cleddens Road, Bishopgriggs, Glasgow, London Glasgow New York Tokyo Merlbourne Madras.

Kanner, L. C., S. J. Burns, H. Cheng, and R. L. Edwards. 2012. High-Latitude Forcing of the South American Summer Monsoon During the Last Glacial. Science 335:570-573.

Kienast, M., S. S. Kienast, S. E. Calvert, T. I. Eglinton, G. Mollenhauer, R. François, and A. C. Mix. 2006. Eastern Pacific cooling and Atlantic overturning circulation during the last deglaciation. Nature 443:846-849.

Kim, K. H., and W. C. Burnett. 1988. Accumulation and biological mixing of Peru margin sediments. Marine Geology 80:181-194.

Koutavas, A., J. Lynch-Stieglitz, T. M. Marchitto, and J. P. Sachs. 2002. El Nino-like pattern in ice age tropical Pacific sea surface temperature. Science 297(5579):226-230.

Krissek, L. A., and K. F. Scheidegger. 1983. Environmental controls on sediment texture and composition in low oxygen zones off Peru and Oregon. Pp. 163-180. *In* E. Suess, and J. Thiede, eds. Coastal upwelling, its sediment record, Part B: Sedimentary records of ancient coastal upwelling. Plenum Press, New York.

Lafarge, E., J. Espitalié, F. Marquis, and D. Pillot. 1998. Rock-Eval 6 applications in hydrocarbon exploration, production and in soil contaminations studies. Oil & Gas Science and Technology - Rev. IFP 53(4):421-437.

Lea, D. W., D. K. Pak, and H. J. Spero. 2000. Climate Impact of Late Quaternary Equatorial Pacific Sea Surface Temperature Variations. Science 289:1719-1724.

Levin, L., D. Gutierrez, A. Rathbun, C. Neira, J. Sellanes, P. Muñoz, V. Gallardo, and M. Salamanca. 2002. Benthic processes on the Peru margin: a transect across the oxygen minimum zone during the 1997–98 El Niño. Progress in Oceanography 53:1-27.

Makou, M. C., T. I. Eglinton, D. W. Oppo, and K. A. Hughen. 2010. Postglacial changes in El Niño and La Niña behavior. Geology 38(1):43-46.

Martinez, P., and R. S. Robinson. 2010. Increase in water column denitrification during the last deglaciation: the influence of oxygen demand in the eastern equatorial Pacific. Biogeosciences 7:1-9.

McManus, J., W. M. Berelson, S. Severmann, P. R. L., D. E. Hammond, G. P. Klinkhammer, and C. Holm. 2006. Molybdenum and uranium geochemistry in continental margin sediments: Paleoproxy potential. Geochimica et Cosmochimica Acta 70:4643-4662.

Meissner, K. J., E. D. Galbraith, and C. Völker. 2005. Denitrification under glacial and interglacial conditions: A physical approach. Paleoceanography 20:PA3001.

Meyers, P. A. 1997. Organic geochemical proxies of paleoceanographic, paleolimnologic, and paleoclimatic processes. Organic Geochemistry 27(5-6):213-250.

Montes, I., F. Colas, X. Capet, and W. Schneider. 2010. On the pathways of the equatorial subsurface currents in the eastern equatorial Pacific and their contributions to the Peru-Chile Undercurrent. Journal of Geophysical Research 115:C09003.

Nameroff, T. J., S. E. Calvert, and J. W. Murray. 2004. Glacial-interglacial variability in the eastern tropical North Pacific oxygen minimum zone recorded by redox-sensitive trace metals. Paleoceanography 19:PA1010

Ortlieb, L., G. Vargas, and J.-F. Saliège. 2011. Marine radiocarbon reservoir effect along the northern Chile-southern Peru coast (14-24°S) throughout the Holocene. Quaternary Research 75:91-103.

Pennington, J. T., K. L. Mahoney, V. S. Kuwahara, D. D. Kolber, R. Calienes, and F. P. Chavez. 2006. Primary production in the eastern tropical Pacific: A review. Progress in Oceanography 69:285-317.

Peters, K. E., C. C. Walters, and J. M. Moldowan. 2005. The Biomarker Guide. Cambridge University Press.

Peterson, L. C., G. H. Haug, K. A. Hughen, and U. Röhl. 2000. Rapid Changes in the Hydrologic Cycle of the Tropical Atlantic During the Last Glacial. Science 290:1947-1951.

Rein, B., A. Lückge, L. Reinhardt, F. Sirocko, A. Wolfe, and W.-C. Dullo. 2005. El Niño variability off Peru during the last 20,000 years. Paleoceanography 20:PA4003.

Reinhardt, L., H.-R. Kudrasss, A. Lückge, M. Wiedicke, J. Wunderlich, and G. Wendt. 2002. High-resolution sediment echosounding off Peru: Late Quaternary depositional sequences and sedimentary structures of a current-dominated shelf Marine Geophysical Researches 23(4):335-351.

Reuter, J., L. Stott, D. Khider, A. Sinha, H. Cheng, and R. L. Edwards. 2009. A new perspective on the hydroclimate variability in northern South America during the Little Ice Age. Geophysical Research Letters 36:L21706.

Riedinger, M. A., M. Steinitz-Kannan, W. M. Last, and M. Brenner. 2002. A ~6100 14C yr record of El Niño activity from the Galapagos Islands. Journal of Paleolimnology 27(1):1-7

Robinson, R., M. Kienast, A. S. Albuquerque, M. A. Altabet, S. Contreras, R. De Pol-Holz, N. Dubois, R. Francois, E. D. Galbraith, T.-C. Hsu, T. S. Ivanochko, S. L. Jaccard, S.-J. Kao, T. Kiefer, S. Kienast, M. Lehmann, P. Martinez, M. McCarthy, J. H. Möbius, T. F. Pedersen, T. M. Quan, E. Ryabenko, A. Schmittner, R. Schneider, A. Schneider-Mor, M. Shigemitsu, D. Sinclair, C. J. Somes, A. S. Studer, R. Thunell, and J.-Y. T. Yang. 2012. A review of nitrogen isotopic alteration in marine sediments. Paleoceanography 27:PA4203.

Rodbell, D. T., G. O. Seltzer, D. M. Anderson, M. B. Abbott, D. B. Enfield, and J. H. Newman. 1999. An ~15,000-year record of El Niño-driven alluviation in southwestern Ecuador. Science 283(5401):516-520.

Rutllant, J. A. 1990. Natural desertification mechanisms along the arid west coast of South America. Pp. 235-253. Proc. International Workshop on Sand Transport and Desertification in Arid Lands,. Khartoum (Sudan).

Rutllant, J. A., R. Fuenzalida, and P. Aceituno. 2003. Climate dynamics along the arid northern coast of Chile: the 1997-1998 Dinamica del Clima de la Region de Antofagasta (DICLIMA) experiment. Journal of Geophysical Research 108.

Salvatteci, R., D. B. Field, T. Baumgartner, V. Ferreira, and D. Gutierrez. 2012. Evaluating fish scale preservation in sediment records from the oxygen minimum zone off Peru. Paleobiology 38(1):766-792.

Sarbas, B., and U. Nohl. 2009. The GEOROC database - a decade of "online geochemistry". Geochimica et Cosmochimica Acta 73(A1158).

Scheidegger, K. F., and L. A. Krissek. 1982. Dispersal and deposition of eolian and fluvial sediments off Peru and northern Chile. Geological Society of America Bulletin 93:150-162.

Scholz, F., C. Hensen, A. Noffke, A. Rohde, V. Liebetrau, and K. Wallmann. 2011. Early diagenesis of redox-sensitive trace metals in the Peru upwelling area – response to ENSO-related oxygen fluctuations in the water column. Geochimica et Cosmochimica Acta 75:7257-7276

Siegel, S., and N. J. Castellan. 1988. Nonparametric statistics for the behavioral sciences (2nd ed.). McGraw-Hill, New York.

Sigman, D. M., M. A. Altabet, D. C. McCorkle, R. Francois, and G. Fischer. 1999. The $\delta^{15}N$ of nitrate in the southern ocean: Consumption of nitrate in surface waters Global Biogeochemical Cycles 13(4):1149-1166.

Stramma, L., G. C. Johnson, E. Firing, and S. Schmidtko. 2010. Eastern Pacific oxygen minimum zones: Supply paths and multidecadal changes. Journal of Geophysical Research 115.

Suess, E., and R. von Huene. 1988. Ocean Drillling Program Leg 112, Peru continental margin: Part 2, Sedimentary history and diagenesis in a coastal upwelling environment. Geology 16:939-943.

Thompson, L. G., E. Mosley-Thompson, and K. A. Henderson. 2000. Ice-core palaeoclimate records in tropical South America since the Last Glacial Maximum. Journal of Quaternary Science 15(4):377-394.

Tjallingii, R., U. Röhl, M. Kölling, and T. Bickert. 2007. Influence of the water content on X-ray fluorescence core-scanning measurements in soft marine sediments. Geochemistry Geophysics Geosystems 8(2):Q02004.

Toggweiler, J. R., K. Dixon, and W. S. Broecker. 1991. The Peru Upwelling and the Ventilation of the South Pacific Thermocline. Journal of Geophysical Research 96(C11):20,467-20,497.

Tribovillard, N., T. J. Algeo, T. Lyons, and A. Riboulleau. 2006. Trace metals as paleoredox and paleoproductivity proxies: An update. Chemical Geology 232:12-32.

van Breukelen, M. R., H. B. Vonhof, J. C. Hellstrom, W. C. G. Wester, and D. Kroon. 2008. Fossil dripwater in stalagmites reveals Holocene temperature and rainfall variation in Amazonia. Earth and Planetary Science Letters 275:54-60.

van Geen, A., S. N. Luoma, C. C. Fuller, R. Anima, H. E. Clifton, and S. Trumbore. 1992. Evidence from Cd/Ca ratios in foraminifera for greater upwelling off California 4,000 years ago. Nature 358:54-56.

Van der Weijden, C. H. 2002. Pitfalls of normalization of marine geochemical data using a common divisor. Marine Geology 184:167-187.

Wang, X., A. S. Auler, R. Lawrence Edwards, H. Cheng, E. Ito, and M. Solheid. 2006. Interhemispheric anti-phasing of rainfall during the last glacial period. Quaternary Science Reviews 25:3391-3403.

Wang, X., F. W. Cruz, A. S. Auler, H. Cheng, and R. L. Edwards. 2008. Millenial-scale climate variability recorded in Brazilian speleothems. PAGES News 16(3):31-32.

CHAPTER IV:

CENTENNIAL TO MILLENNIAL-SCALE VARIABILITY IN FISH DEBRIS FLUXES FROM MARINE LAMINATED SEDIMENTS OFF PISCO, PERU DURING THE LAST 25 KYR

IV-1. Introduction

Dramatic changes in pelagic fish landings, principally of anchovies and sardines, over the last decades reveal that population dynamics are sensitive to climatic variability (Schwartzlose et al., 1999; Chavez et al., 2003; Finney et al., 2010; Alheit and Bakun, 2010). The anchovy (*Engraulis ringens*) and sardine (*Sardinops sagax sagax*) populations in the Humboldt Current System (HCS) also experienced large changes during the last 50 years. High abundances of anchovy were recorded from ~1960 to ~1970, then the decline in anchovy landings in ~1972 was followed by an increase in sardine landings from 1975 to the middle to late 1990s, finally from the late 1990s to the date anchovy abundances increased while those of sardine decreased (Chavez et al., 2003; Alheit and Bakun, 2010). The fluctuations in anchovy and sardine abundances were associated with physical oceanographic changes off Peru. The sardine period was characterized by an advance of the warmer and saltier subtropical surface waters (SSW) to the coast and by a deeper thermocline (Alheit and Bakun, 2010; Bertrand et al., 2011). In contrast, during the anchovy periods the oceanographic conditions off Peru were characterized by a dominance of Cold Coastal Waters (CCW) that favors high biomass of macro-zooplankton which is the principal prey of anchovy, and also by a shallower thermocline (Espinoza and Bertrand, 2008; Alheit and Bakun, 2010). Moreover, nowadays the spatial distribution of anchovy and sardine schools indicate a greater tolerance of anchovy to water dysoxia, compared to sardine, and available time-series indicate that anchovy were more abundant during periods with shallow oxycline conditions while sardine peaked during the period with a deeper oxycline (Bertrand et al., 2011). In longer time-scales the response of the Peruvian Upwelling Ecosystem (PUE) to the Little Ice Age period, included a weak Oxygen Minimum Zone (OMZ), low export production, and very low anchovy and sardine abundances inferred by fish scale deposited in laminated sediments off Callao and Pisco (Gutierrez et al., 2009). Consequently, records that extend beyond the available historical period are needed to define variability that occurs over multi-decadal time scales in order to help to understand the processes underlying fluctuations in fish populations (Finney et al., 2010). In this chapter we address the oceanographic and climatic conditions that favored anchovy and other species during the last 25.5 kyr. Answering this question will lead to understand the mechanisms linking physical climate changes (at global scale, basin-scale or regional/local scale) to fluctuations in anchovy abundance to identify the principal mechanism that controls biomass fluctuations at centennial to millennial timescales. But first it is mandatory to assess the degree of preservation of the fish scales in the record and determine what processes control the preservation of fish remains in the sediments.

The Tropical Pacific during the Last Glacial – Interglacial Transition and during the Holocene showed several periods characterized by large climate changes caused by different physical forcings. For example during the Mid Holocene (8 to 4 kyr BP), the cold tongue complex was cold and the

zonal Sea Surface Temperature (SST) gradient in the equatorial Pacific was enhanced, which is consistent with stronger trade winds and a more vigorous Walker Circulation (Koutavas et al., 2002). Additionally, also during the Mid Holocene, SST were ~1-4 °C cooler from the Galapagos to the southern Peruvian coast as a result of increased coastal upwelling forced by changes in longshore windfields (Carré et al., 2011). All of these evidences during the Mid Holocene suggest a "La Niña like mean state", result that is also coherent with modeling studies (Clement et al., 2000). Additionally, other north hemisphere warm periods like the Bølling-Allerød and Medieval Climate Anomaly were also characterized by La Niña-like conditions as evidenced by an enhanced SST gradient in the Tropical Pacific (Koutavas et al. 2002; Cobb et al., 2003; Conroy et al., 2010; Linsley et al., 2010; Graham et al., 2011). Moreover, the Early Holocene which is associated with a maximum in northern summer (July) insolation and a northerly mean ITCZ position shows cool SST in the equatorial cold tongue (Koutavas et al., 2002) which is also consistent with a "La Niña-like" pattern in the Tropical Pacific. In contrast, the Last Glacial Maximum (23 to 19 kyr BP) was characterized by a reduced east-west SST gradient in the Tropical Pacific with a cooler back-ground level, a southward displacement of the Inter-tropical Convergence Zone (ITCZ; Koutavas and Lynch-Stieglitz, 2003; Dubois et al., 2009), weaker Walker circulation and trade winds, all of which are consistent with an El Niño-like mean state in the Tropical Pacific (Koutavas et al., 2002). The Little Ice Age (1500 to 1850 AD) was a globally cold period characterized by a southward displacement of the ITCZ, reduced east-west SST gradient in the Tropical Pacific which also suggest an "El Niño-like" state in this region (Cobb et al., 2003; Mann et al., 2009; Conroy et al., 2010; Graham et al., 2011). Given the tightly coupled system of the Western Pacific warm pool, the East Pacific cold tongue, and the atmospheric Hadley (strongly linked with the ITCZ) and Walker circulation (Pierrehumbert, 2000); temporal changes in these systems should produce considerable changes in the HCS. Consequently the response of the anchovy biomass fluctuations to these past global changes may give important insight of the mechanisms that controls its biomass fluctuations.

Previous works using fish scales deposited in laminated sediments off Peru indicate large changes in anchovy and sardine biomass associated with global climatic changes. Anchovy and sardine scale deposition rates (SDR) off Callao (~12 °S) and off Pisco (~14 °S) show that during the Little Ice Age the anchovy and other species biomass was drastically reduced, and associated with a weak OMZ and reduced export production in comparison with the last ~100 years (Gutierrez et al., 2009). These results indicate that the anchovy population showed centennial periods with very low abundances without the appearance of other species like sardine. The responses of the HCS to the Little Ice Age were likely produced by a mean southward displacement of the ITCZ and a reduced influence of the South Pacific Sub-tropical High along the Peruvian margin (Sifeddine et al., 2008; Gutierrez et al., 2009), characteristics associated with an El Niño-like state in the Tropical Pacific. In contrast the Current Warm Period (last ~150 years) was characterized by lower SST, higher export

production, a strong OMZ, and higher anchovy biomass off Peru and Chile (Diaz-Ochoa et al., 2008; Gutierrez et al., 2009; Valdes et al., 2009; Gutierrez et al., 2011), and also by a northern position of the ITCZ (Bird et al., 2011). Anchovy and other species response to older climate changes were assessed using a core that presented several hiatus (De Vries and Pearcy, 1982), which is a common feature in sediment cores retrieved off Peru (chapter II). During the available section corresponding to the Younger Dryas period, a cold period characterized by a southward displacement of the ITCZ (Haug et al., 2001) and wetter conditions in Peru (Baker et al., 2001), sardine scales show the highest fluxes while the anchovy scale fluxes show the lowest values in the record (De Vries and Pearcy, 1982). It is not clear what is the response of the anchovy and other pelagic fish populations in the PUE to older periods with inferred El Niño or La Niña-like mean state conditions in the Tropical Pacific.

Thus, reconstructing the anchovy and other pelagic fish biomass fluctuations from fish scales preserved in laminated sediments during the Last Glacial-Interglacial Transition and during the Holocene may hold the key to understand the mechanism of changes, but the fish scale state of preservation must be first addressed in order to fulfill these interpretations. Fish scales are composed of a mixture of hydroxyapatite ($Ca_{10}(PO_4)(OH)_2$) embedded within an organic matrix that surrounds layers of fibrous collagen (Hamada and Mikuni, 1990; Varma 1990; Hutchinson and Trueman, 2006). In contrast fish bones (i.e. vertebrae, spines and other bones) present lower organic matter content (Hamada and Mikuni, 1990) and lower surface area to volume ratios in comparison to fish scale, that make the fish bones more resistant to degradation processes. Fish debris records and several preservation indices for the last 500 years (including the Little Ice Age) were developed in two cores retrieved off Pisco (~14 °S) within the OMZ but at different oxygen level exposure (Salvatteci et al., 2012). The preservation indices developed included an index of fish scale integrity; the degree of bio-erosion over fish scales and vertebrae and the ratio of fish scales to bones. The results of this work indicate that oxygenation likely plays some role in degradation, because during the Little Ice Age when the OMZ was weaker, the fish scale degradation in both cores was stronger as evidenced by the above mentioned preservation indices (Salvatteci et al., 2012). Furthermore, the core retrieved at the center of the OMZ (~300 meters depth) would be less exposed to oxygenation events than the shallower, and appears to have better scale preservation during the period of greater oxygenation (i.e. the last 100 years). The preservation indices developed by Salvatteci et al. (2012) are used in this chapter to assess the effect of degradation on the 25.5 kyr BP fish scale record.

The results of the present work serve to better understand ecosystem variability and the physical regulating processes. While the year-to-year management does not require full understanding of the cause of the fluctuations in anchovy and sardine biomass, long-term management and investment planning would certainly benefit from a model capable of predicting the long-term

dynamics of anchovy and sardine with and without fishing, or as a combined outcome of the interacting drivers of fishing and the environment (Checkley et al., 2009). Additionally, for a correct adaptative management of the pelagic fish resources it is fundamental to determine if the anchovy population is under a high or low level of abundance. Moreover given the uncertainty of the response of the anchovy and sardine population to future climatic change, the study of past biomass fluctuations of these two species to warm periods like the Early Holocene or the Medieval Climate Anomaly may give important insight, although the causes of the warming were different in each of the different periods that are studied in the present chapter.

IV-2. Study site

The cores used in the present chapter (B05-14, G-10 and G-14) were retrieved on the upper continental margin off Pisco, central-southern Peru (Fig. IV-1). The Pisco area is subjected to the most intense alongshore winds in the Peruvian coast (Goubanova et al., 2010). In the Peruvian upwelling ecosystem the seasonal cycles in production are out of phase with seasonal upwelling winds, in clear contrast to the other Eastern Boundary Upwelling Systems (Pennington et al., 2006; Chavez and Messié, 2009; Gutierrez et al., 2011). Upwelling favorable winds occur during the entire year but are stronger during austral winter and spring (Strub et al., 1998; Gutierrez et al., 2011). In contrast primary productivity is higher during austral spring and summer when surface waters are more stratified (Pennington et al., 2006; Chavez and Messié, 2009; Gutierrez et al., 2011). The seasonal changes in winds and productivity in the PUE are associated with the movement of the ITCZ from 10°N in austral winter (June-September) to 2-5°N in austral summer (December-March; Strub et al., 1998).
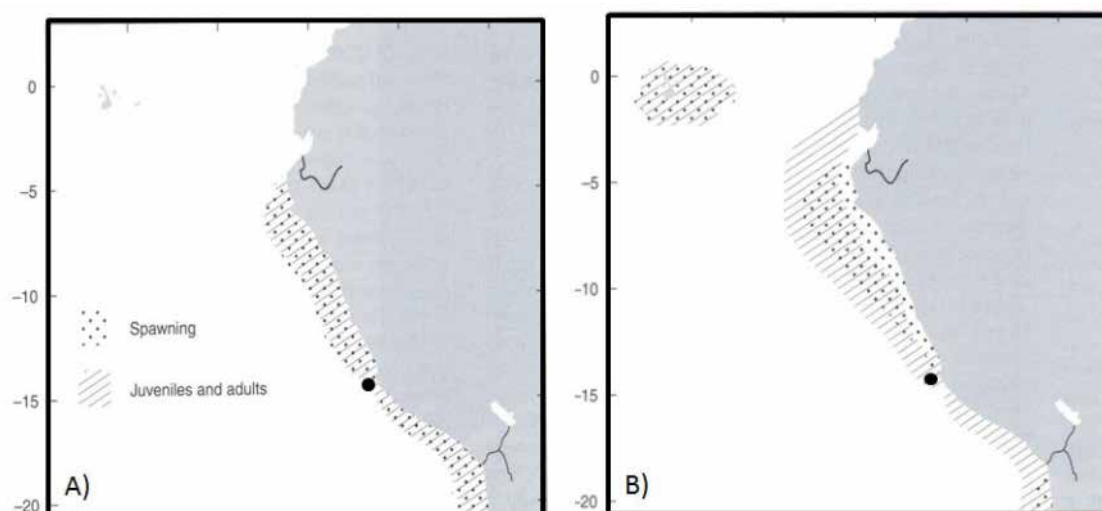
Figure IV-1. Maximal distribution range of anchovy (A) and sardine (B) and study site (black dot). Figure modified from Checkley et al. (2009).

The location of the cores studied in the present chapter permit to effectively evaluate the contraction and expansion of anchovy and sardine because the cores were retrieved near the southern limit of the northern anchovy stock and outside the distribution limits of sardine (Fig 1.). Anchovy presents two fishing stocks off Peru, the northern stock from 6 °S to 15 °S and the southern stock from 15 to 40 °S (Checkley et al., 2009). Sardine presents 4 stocks off Peru and Chile, a northern stock off north-central Peru, a stock off southern Peru and northern Chile, a Coquimbo stock (~29.5 °S) and a Talcahuano stock (~35 °S; Parrish et al., 1989). Thus, sardines are not usually present off Pisco and consequently the presence of sardine scales off Pisco should indicate a strong change in oceanographic conditions in the PUE.

IV-3. Methodology

IV-3.1 Sampling design

Subsampling for fish debris analyses in cores G-10 and G-14 was done taking into account the stratigraphy of the core (Figs. IV-2 and IV-3). Sampling the laminated sections of the core was favored because these sediments better reflect the content of the water column and are less subject to upslope remobilization. In core G-10, which consists of 6 sections (Fig. IV-2), one vertical half of each section was dedicated exclusively for fish debris analyses. The 6 sections in core G-10 were sub sampled each 1 cm. Fish debris analyses were performed continuously in the laminated sections in some segments, while in others only one out of two samples was analyzed, because of lack of time (Fig. IV-2). In core G-14, one half of each section was dedicated to fish debris analyses and several other analyses given that the reduced water content permitted to obtain sufficient dry sediment for several analyses. The 6 sections in core G-14 were sub-sampled each 1 cm as well, but approximately 75% of the material was used for fish debris analyses. In core G-14, where the thickness of the massive/slumped sequences is lower in comparison with core G-10, the spacing between samples was between 4 and 5 cm but always taking the samples in the laminated/banded sections. The total number of samples analyzed in core G-10 and G-14 was 202 and 91 respectively.
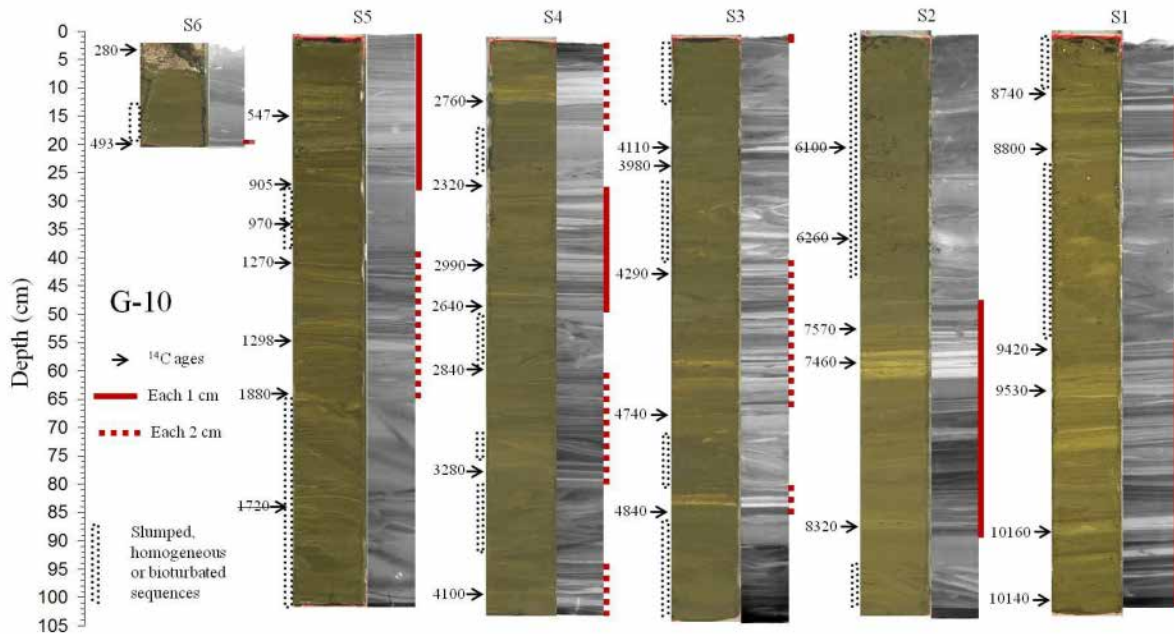
Figure IV-2. SCOPIX and photographic images showing laminated sequences, massive and slumped deposits, and sampling strategy used for fish debris analysis in core G-10. The ^{14}C ages are expressed in year cal BP. The dotted rectangle areas at the left side of the SCOPIX images indicate slumps or massive/homogeneous deposits. The arrows indicate the position of the samples taken for ^{14}C measurements. The vertical red bars indicate the samples that were analyzed for fish scale analyses. Continuous (dashed) vertical bars indicate that the sample acquisition was performed each 1 cm (2 cm). All the samples were taken in the laminated or banded sections.
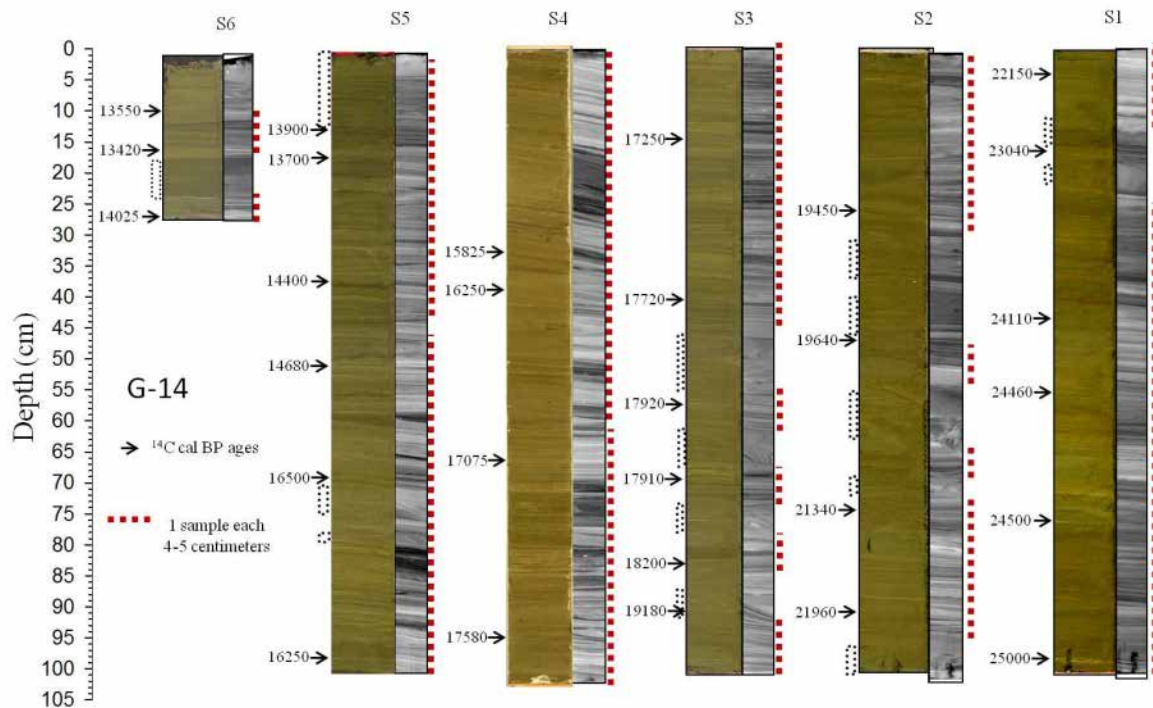
Figure IV-3. SCOPIX and photographic images showing laminated sequences, massive and slumped deposits, and sampling strategy used for fish debris analysis in core G-14. The ^{14}C ages are expressed in year cal BP. The dotted rectangle areas at the left side of the SCOPIX images indicate slumps or massive/homogeneous deposits. The arrows indicate the position of the samples taken for ^{14}C measurements. The vertical red bars indicate the samples that were analyzed for fish scale analyses. All the samples were taken in the laminated or banded sections.

The determination of the sediment sample weight is an important criterion that must be taken into account to obtain sufficient fish debris for further interpretations. In core B-14, where the fish scale preservation study was realized (Salvatteci et al., 2012) and the fish scale abundances are used in this chapter, an average of 23.6 g of wet sediment was sieved which equals to ~4.8 g of dry sediment. The quantity of fish debris in each of these samples in core B-14 resulted insufficient to perform statistical tests and consequently five contiguous intervals were grouped to solve this problem (Salvatteci et al., 2012). Consequently in core G-10 an average of 49.3 g of wet material, which yields ~17.2 dry sediment, was analyzed to perform the fish debris analyses. In core G-14 an average of 39.2 g of wet material, which yields 18.8 g of dry sediment, was analyzed. Following the sediment subsampling, the samples were heated with hydrogen peroxide and sodium pyrophosphate for 10 minutes to disaggregate the organic matter and then were gently washed through a 355μm sieve. The remains retained were then stored in an alcohol solution.

IV-3.2 Identification and quantification of fish debris

The fish debris retained in the 355 μm mesh size were quantified and identified with the help of a scale and vertebrae collection obtained from recently caught fishes (Fig. IV-4). Fish scales were identified to species level for the following species: anchovy, sardine, jack mackerel (*Trachurus murphyi*), horse mackerel (*Scomber japonicus*), hake (*Merluccius gayi peruanus*), and "agujilla" (*Scomberesox saurus scombroides*). Myctophids scales were not identified to species level and were quantified as a whole group. The rest of the fish scales were quantified as non-identified (nn). Vertebrae were identified to species for the following species: anchovy, sardine and hake; the rest of vertebrae were quantified as nn. The fish teeth, jaws, parts of the fish skull, fins, etc. were quantified as bones. Finally spines were quantified as a whole spine if more than 75% of the original spine was present, the rest of spine fragments and segments were counted as spine fragments (Fig. IV-4J). The quantification of fish debris, i.e. the distinction into complete and half scales, is described by Salvatteci et al. (2012, paper included in the annexes of this memoire).
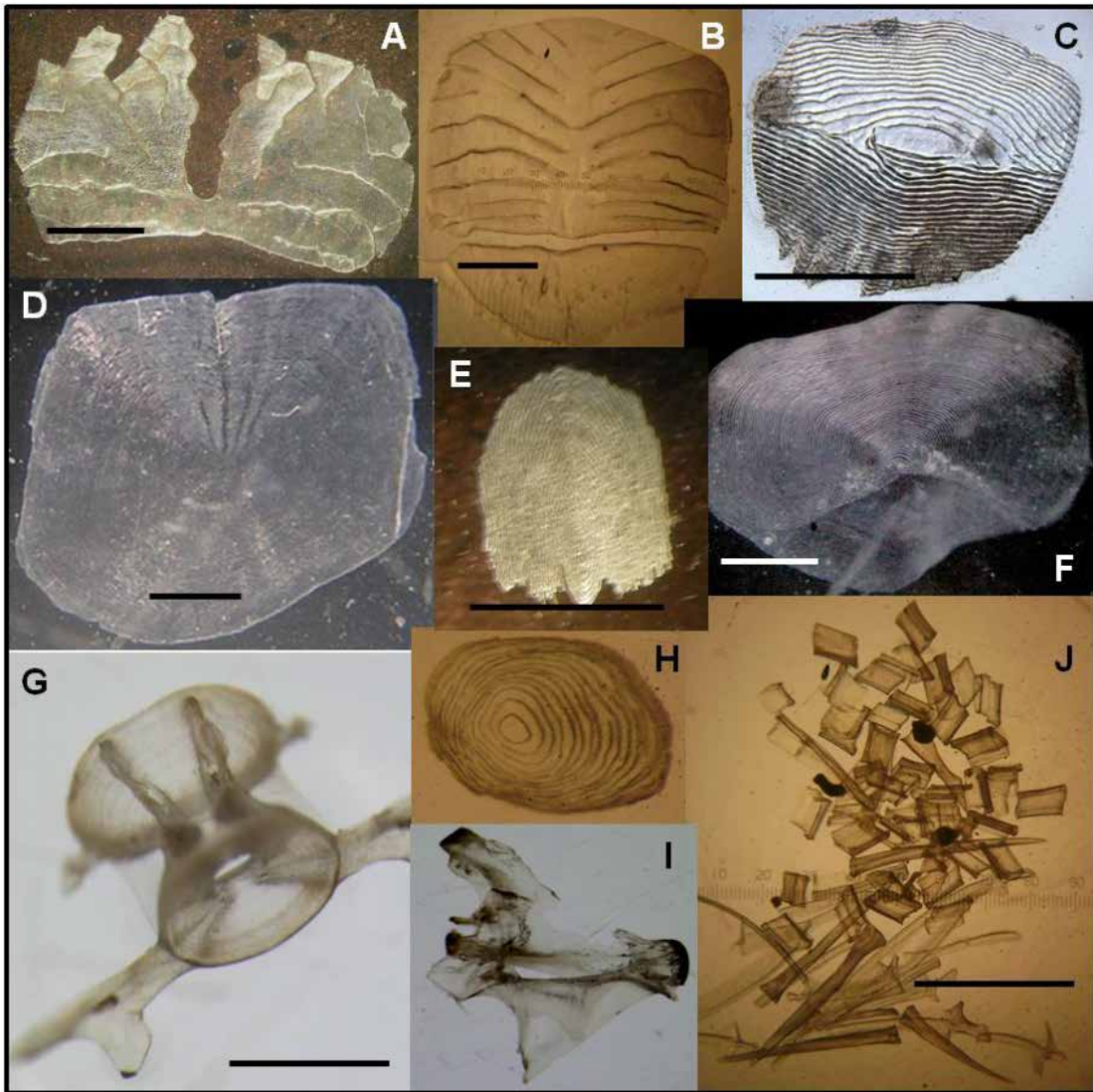
Figure IV-4. Set of fish debris from sediments and collected from live specimens. A) Anchovy (*Engraulis ringens*) scale; B) Sardine (*Sardinops sagax sagax*) scale; C) Horse mackerel (*Scomber japonicus*) scale; D) Jack Mackerel (*Scomber japonicus*) scale; E) Hake (*Merluccius gayi peruanus)* scale; F) Agujilla (*Scomberesox saurus scombroides*) scale; G) Anchovy vertebrae; H) Myctophidae scale; I) Fish bone; and J) Spines fragments (top) and spines (bottom). The horizontal line represents 1 mm. Fish debris from A, B, C, E, H. I and J were found in core B-14, while fish debris from D, F and G were collected from recently caught fish.

IV-3.3 Fish debris preservation

In order to quantify the effect of degradation, we estimated 3 preservation indices from previous studies in the same area (Salvatteci et al., 2012). The first degradation index, the "integrity index" is an estimate of scale wholeness relative to fragmentation. The second index used is the "bio-eroded free area index" over anchovy vertebrae which estimates the surface of the vertebrae that is not affected by bio-erosion. Finally, the last index used is the ratio anchovy scales to anchovy vertebrae, based on the observation that fish scales are thinner and contain more organic matter than the

vertebrae and consequently are more susceptible to degradation. Higher (lower) values of the 3 indices indicate better preservation (more degradation). A detailed explanation of the advantages and limits of these and others indices are explained by Salvatteci et al. (2012).

IV-3.4 Fish debris fluxes or scale deposition rates

The abundance of fish debris per sample (# of fish debris. g^{-1}) can be diluted by low sedimentation rates, or increased by high sedimentation rates, thus it is highly recommended to convert the abundances (fish scales or bones) to fluxes (# scales.$cm^{-2}.y^{-1}$). However the sediment rates are strongly dependent of the mass accumulation rate (W, $g.cm^{-2}.y^{-1}$), and this calculated rate W is in turn dependent on the presence of hiatus, or slumps, within the sedimentary column, features that are quite frequent in the Peruvian margin sediments. The different W values of the different periods that are studied in the present chapter are shown in Table IV-1. These values were obtained by inverting the slope value (1/slope) obtained from the age models in chapters III and V. The highest mass accumulation rate wasobserved during the CWP, Termination 1 and the Early Glacial, and the lowest during the MCA and DACP (Table IV-1). The fluxes of each fish debris component were calculated by multiplying the fish debris abundance (# of fish debris.g-1) by the corresponding W value. Given that the calculated fluxes were small, the values were multiplied by 1000. Finally, the fish debris record is presented in two ways, first the high-resolution downcore variations of fish debris in each sample are presented, and then the fish debris are grouped into the time periods of interest to permit a better visualization of the data set.

Table IV-1. Mass accumulation rate values (W, units:$g.cm^{-2}.y^{-1}$) estimated for the different time periods of interest. The Late Holocene W contains an average of the W of the Dark Ages Cold Period, Medieval Climate Anomaly , Little Ice Age and the rest of the Late Holocene period (i.e from 4 to 1.45 kyr BP).

Period	Time range (kyr BP)	W ($g.cm^{-2}.y^{-1}$)
Current Warm Period	-0.05 to 0.05	0.079
Little Ice Age	0.1 to 0.45	0.021
Medieval Climate Anomaly	0.6 to 1.05	0.015
Dark Ages Cold Period	1.05 to 1.45	0.015
Late Holocene	0.1 to 4	0.022
Middle Holocene	4 to 8	0.026
Early Holocene	8 to 10.3	0.024
Bølling-Allerød	12.7 to 14.7	0.033
Heinrich 1 Stadial	14.7 to 18	0.033
Last Glacial Maximum	19 to 23	0.022
Early Glacial	23 to 25.5	0.046

High fish debris fluxes (more than the average + 3 standard deviations) in each core were treated as outliers. Very high pulses of fish remains in the sedimentary record arise from localized events, such as single or multiple deaths (O'Connell and Tunnicliffe, 2001). The outliers were replaced by the mean + 3 sd. The occurrence of very high values is rare. For example only 1 of the 91 samples analyzed in core G-14 showed anchovy fluxes higher than the average + 3sd.

IV-3.5 Fish abundances and preservation indices compared with proxies of environmental change

The fish scale abundances and preservation indices are compared with proxies of environmental changes to understand the mechanism that control fish scale preservation and fish biomass variability off Peru. In order to identify the effects of the OMZ intensity and the sediment redox conditions in the fish scales preservation, the different preservation indices are compared with proxies of oxygenation showed in chapter III. The proxies used for this purpose include: 1) Re/Mo ratios which indicate if the sediment-water interface during the time of deposition was anoxic or sub-oxic, 2) $\delta^{15}N$ values which indicate the OMZ intensity, and 3) Hydrogen Index (HI) which indicates the organic matter preservation. In order to establish the relationship between productivity and fish biomass, the Nickel Enrichment Factor (Ni EF) were used. Finally, the calculated December to March insolation at 15 °S during the last 25 kyr BP were obtained from Paillard et al. (1996) using the formulas provided by Berger et al. (1978), to test if the changes in insolation during the Holocene are related with the anchovy and biomass fluctuation in the PUE.

IV-3.6 Statistical analyses

Pearson correlation coefficients (r) were calculated to establish the relationships between fish debris types and proxies of environmental conditions. The probability level was corrected for multiple comparisons by dividing the probability level α (p<0.05) by the number of tests performed (Glantz, 2002). Additionally in order to test for differences of the fish debris fluxes between groups, a Kruskal-Wallis test was applied (Glantz, 2002). The Kruskall-Wallis test is a non-parametric alternative to one-way (between groups) ANOVA, and tests the null hypothesis according which the different samples in the comparison were drawn from the same distribution, or from distribution with the same median. The difference between the Kruskall-Wallis and the ANOVA tests is that Kruskal-Wallis is based on ranks instead of means. Given that the data set was divided in eight different groups (Early Glacial, Last Glacial Maximum, Heinrich 1 Stadial, Bølling-Allerød, Early Holocene, Mid Holocene, Late Holocene and the Current Warm Period), and in order to avoid a significant difference obtained by chance while doing multiple analyses in the same data set, the probability level was corrected by dividing the p-value (0.05) between the number of test performed (7), giving a corrected p-value of 0.007. After the Kruskal-Wallis test was done to test if there are differences

between groups, a non-parametric post-hoc analysis was performed for each proxy to detect the significant differences between groups. The post-hoc analysis choosen was the "multiple comparisons of mean ranks" (Siegel and Castellan, 1988). All the statistic analyses were perfomed in the STATISTICA 7.1 software. The results of the Kruskal-Wallis and the multiple comparisons of mean ranks are shown in annexes II.

Finally in order to detect structure in the relationships between variables that might lead to infer processes, a Principal Component Analysis (PCA) was performed using a sub-set of the variables. The PCA analysis was performed to: 1) examine if the fluxes of anchovy and other species vertebrae are more associated with the changes in the oxygen levels or in productivity, and 2) examine if the degradation indices are more closely associated with changes in oxygenation in the water column or in the sediment. Thus, the variables selected were: δ^{15}N, the ratio Mo/Re (the Mo/Re is used instead of the Re/Mo to show the same sign as the δ^{15}N), Hydrogen Index (HI), the flux of anchovy and other species vertebrae, and the three fish debris preservation indices.

IV-4. Results

IV-4.1 Fish debris abundances

The scale fluxes of all species, anchovy, oceanic species, other species, and fish scale fragments show low values during the Early Glacial and Last Glacial Maximum, and relatively higher fluxes during the Termination 1 period (Figs. IV-5 and IV-6). There are no significant differences in any of the fish debris fluxes between the Early Glacial and the Last Glacial Maximum (Tables AII-1 to AII-7 in annexes II). The fluxes of anchovy scales, other species scales and scale fragments show an increase at ~18 kyr BP, then the anchovy scales and fragment fluxes maintain high values during all the Termination 1 period but the other species scale fluxes decrease at ~17.5 kyr BP and maintain the low values until the Current Warm Period (Figs. IV-5 and IV-6). The anchovy scales fluxes and fish scale fragments during the Bølling-Allerød and Heinrich 1 Stadial are significantly higher in comparison with the fluxes observed during the Early Glacial and Last Glacial Maximum (Tables AII-4 and AII-7 in annexes II). The fluxes of oceanic species and other species scales are very low throughout Last Glacial-Interglacial Transition, no significant differences in fluxes are observed between any of the periods (Tables AII-5 and AII-6 in annexes II).
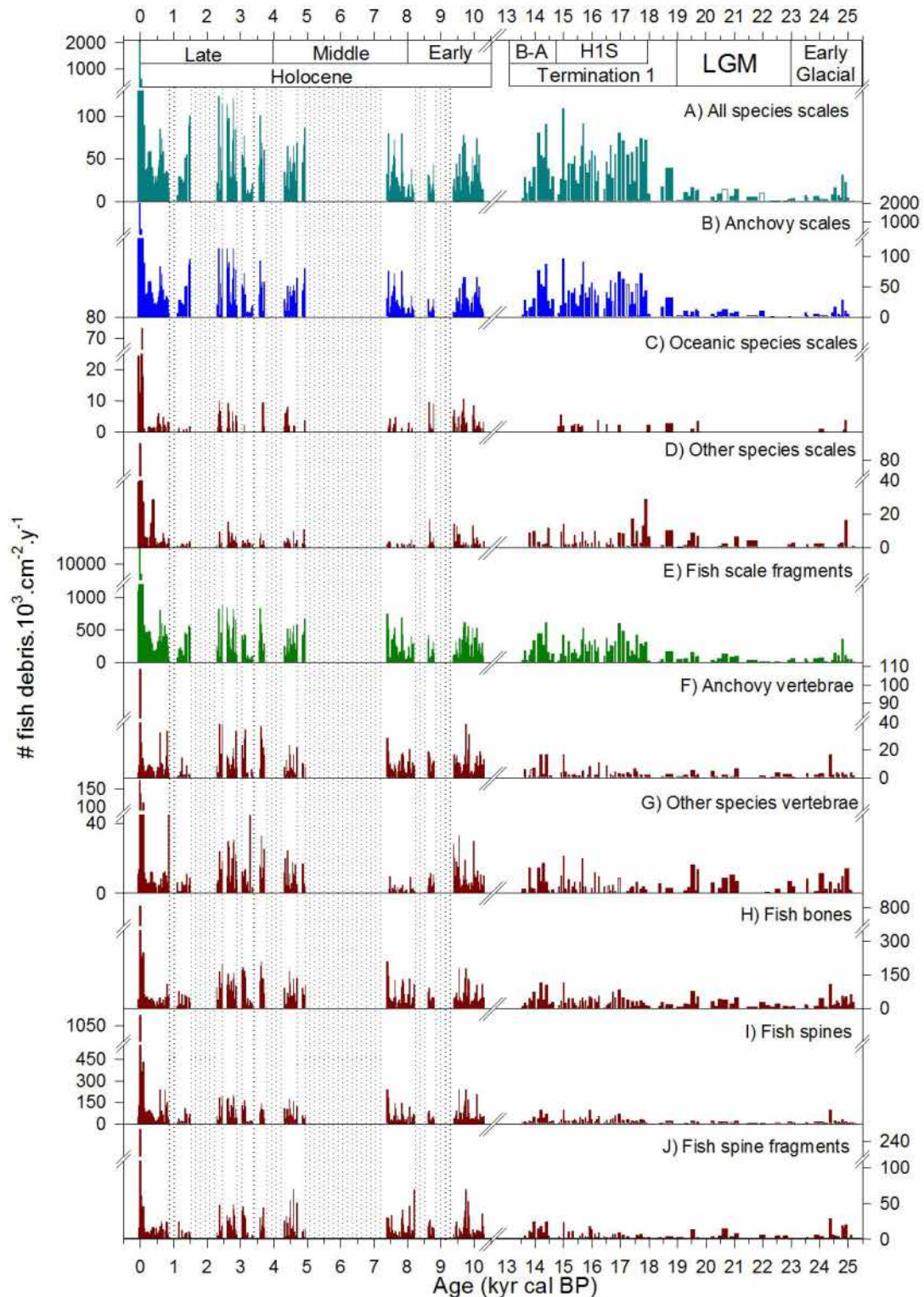
Figure IV-5. Fish remain fluxes in cores G-10 and G-14 retrieved off Pisco. From top to bottom: A) All scales, B) Anchovy (*Engraulis ringens*) scales, C) scales of oceanic species: sardine (*Sardinops sagax sagax*), mackerel (*Scomber japonicus*), jack mackerel (*Trachurus picturatus murphyi*) and agujilla (*Scomberesox saurus scombroides*), D) scales of other species, E) fish scale fragments, F) Anchovy vertebrae, G) vertebrae of other species, H) bones of all species, I) spines of all species, and J) Fish spine fragments of all species. The outliers were replaced by the average + 3 standard deviations (SD). The dotted areas indicate samples associated with homogeneous or slumped deposits. The acronyms used in this figure are: Last Glacial Maximum (LGM), Heinrich 1 Stadial (H1S), and Bølling-Allerød (B-A).
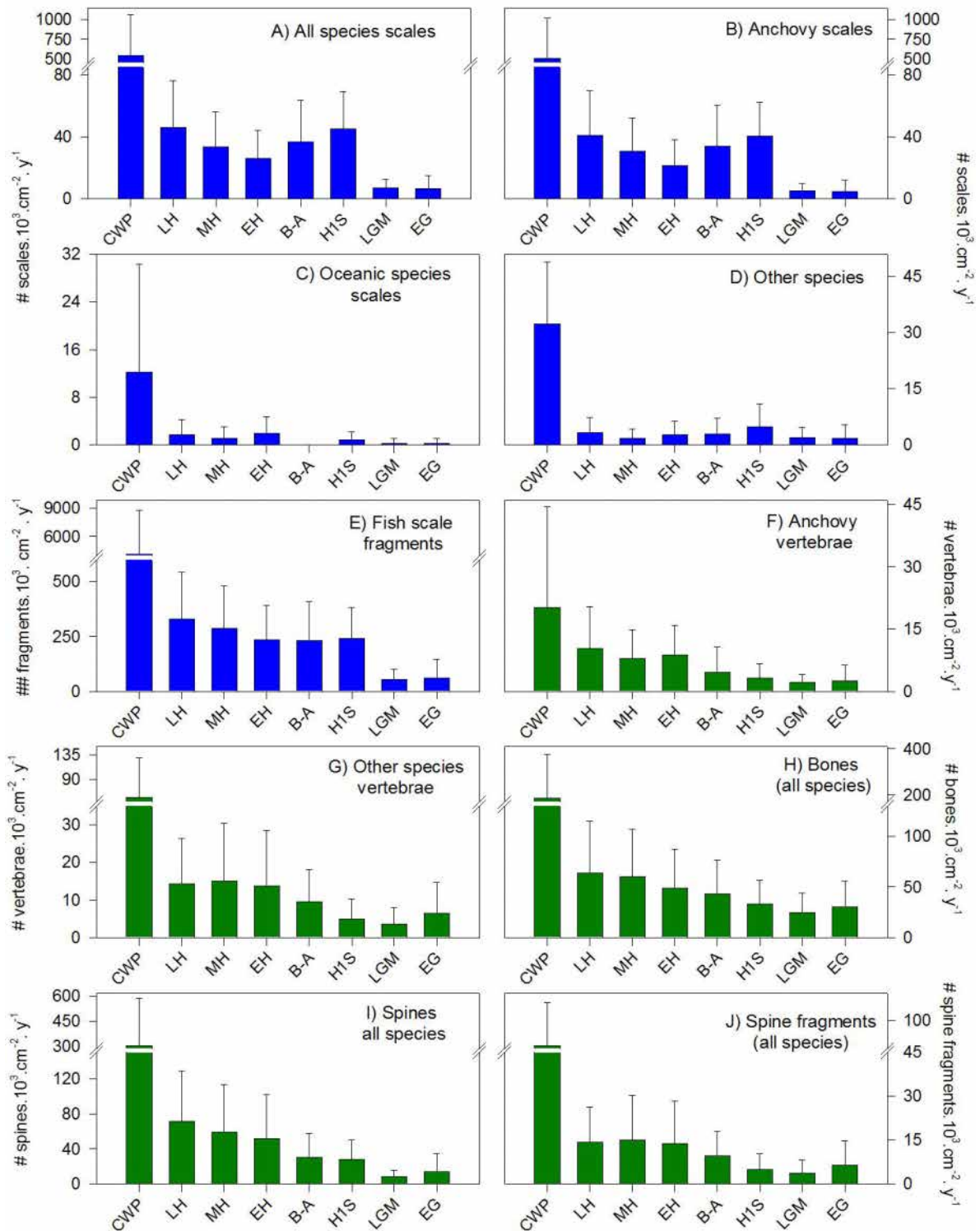
Figure IV-6. Average and standard deviation of the fish debris fluxes (fish scales in blue and the rest of debris in green) during the periods of interest: Current Warm Period (CWP), Late Holocene (LH), Mid-Holocene (MH), Early Holocene (EH), Bølling-Allerød (B-A), Heinrich 1 Stadial (H1S), Last Glacial Maximum (LGM), Early Glacial (EG). A) Anchovy scales. B) Oceanic species scales, which includes sardine, jack mackerel, horse mackerel and agujilla. C) Fish scale fragments, which mainly correspond to anchovy. D) Anchovy vertebrae. E) Vertebrae of other species and non- identified. F) Fish bones of all species. G) Spines of all species and H) Spine fragments of all species.

During the Holocene there is a positive trend towards higher anchovy scale and scale fragment fluxes from the Early Holocene to the Current Warm Period. The anchovy scales fluxes during the Late Holocene are higher in comparison with the Mid and Early Holocene, and the anchovy scales fluxes are higher during the Mid Holocene in comparison with the Early Holocene (Fig. IV-6B). However only the anchovy scale fluxes during the Late Holocene are significantly higher in comparison with the Early Holocene (Table AII-4 in annexes II). The anchovy scale fluxes during the Current Warm Period are significantly higher in comparison with all the periods except for the Heinrich 1 Stadial and the Bølling-Allerød (Table AII-4 in annexes II). The highest fluxes of any type of fish scales were recorded during the Current Warm Period (Figs. IV-5 and IV-6, and Tables AII-1 to AII-7 in annexes II).

The harder fish debris (i.e. vertebrae, bones, and spines) fluxes during the Last Glacial-Interglacial Transition show relatively low values (Figs. IV-5 and IV-6). Moreover, there are no significant differences in any of these fish debris fluxes between any of the periods corresponding to the Last Glacial-Interglacial Transition (Tables AII-8 to AII-12 in annexes II). These observations are in clear contrast with the significantly higher fluxes of anchovy scales and scale fragments during the Heinrich 1 Stadial and Bølling-Allerød periods in comparison with the Early Glacial and Last Glacial Maximum (Tables AII-4 and AII-7 in annexes II).

During the Holocene the fluxes of the harder fish debris are higher compared to the Last Glacial-Interglacial Transition (Figs. IV-5 and IV-6), although these differences were not always significant (Tables AII-8 to AII-12 in annexes II). Moreover the fluxes of the harder fish debris (i.e. vertebrae, bones, and spines) also show the highest values during the Current Warm Period and the lowest ones during the Early Glacial and the Last Glacial Maximum. The positive trend towards higher fluxes of the harder fish debris starts from the beginning of the Heinrich 1 Stadial and not from the Early Holocene as observed with the scale fluxes (Figs. IV-5 and IV-6).

Relationships between the different types of fish debris indicate the different source of deposition of the different fish debris to the sea floor (Table IV-2). The abundances of scale fragments show a higher relationship with the abundances of anchovy scales than with the abundance of all scales suggesting that the majority of scale fragments belong to anchovy scales. The slightly higher shared variability of bones, spines and spines fragments with anchovy scale abundances than with all scale abundances suggest that other species and anchovy contribute similarly to the total numbers of bones, spines and spine fragments. In general the shared variability between scales (of all species or of anchovy alone) and spines, bones and/or vertebrae is consistently lower than any combination of spines, bones and vertebrae. These relationships indicate that the similarity in the source of deposition is greater among bones, spines and vertebrae than with scales.

Table IV-2. Coefficient of determrinarion (r^2) between the different type of fish debris. Data from Figure IV-5, n = 408. Boldface indicates significance after correcting for multiple comparisons (p<0.006).

	all scales	anchovy scales	oceanic scales	other species scales	scale fragments	anchovy vertebrae	other species vertebrae	bones	spines	spines fragments
all scales	1									
anchovy scales	**0.95**	1								
oceanic scales	0.01	0.00	1							
other species scales	**0.20**	**0.07**	**0.06**	1						
scale fragments	**0.81**	**0.87**	0.00	0.05	1					
anchovy vertebrae	**0.02**	**0.03**	0.00	0.00	0.05	1				
other species vertebrae	**0.08**	**0.06**	0.05	0.04	0.04	0.03	1			
bones	**0.07**	**0.08**	0.00	0.00	0.13	0.44	0.05	1		
spines	**0.23**	**0.24**	0.00	0.02	0.31	0.31	0.07	0.55	1	
spines fragments	**0.10**	**0.11**	0.00	0.02	**0.14**	**0.36**	0.02	0.51	0.42	1

IV-4.2 Fish species composition

Fish scales composition during the last 25.5 kyr BP are largely dominated by anchovy but there are some periods were oceanic species also contributed considerably (Fig. IV-7). During the Early Glacial and Last Glacial Maximum fish scale fluxes of all species were low, but the oceanic species were particularly affected. The end of the Last Glacial Maximum is characterized by an increase in jack mackerel, hake and myctophids scale fluxes, then ~1 kyr later the anchovy scale fluxes started to increase (Fig. IV-7). The rest of the Heinrich 1 Stadial is marked by high fluxes of anchovy scales, the appearance of agujilla scales and the absence of sardine and mackerel scales. The Early Holocene is characterized by higher fluxes of all the oceanic species (sardine, jack mackerel, mackerel and agujilla) scales but also high fluxes of anchovy and myctophids scales (Fig. IV-7). The Mid Holocene shows relatively high anchovy scale fluxes and low fluxes in the rest of scales. The Late Holocene is characterized by high anchovy, sardine, jack mackerel and mackerel scale fluxes and moderate fluxes of agujilla, hake and myctophids. During the last 100 years, the anchovy scale fluxes are 1 order of magnitude higher in comparison with the rest of the record (Fig. IV-7A), and very high fluxes of the other species as well. The non identified species are more abundant in the last 100 years and from 22 to 17 kyr, but still represent a very low percentage of the fish scale assemblage.
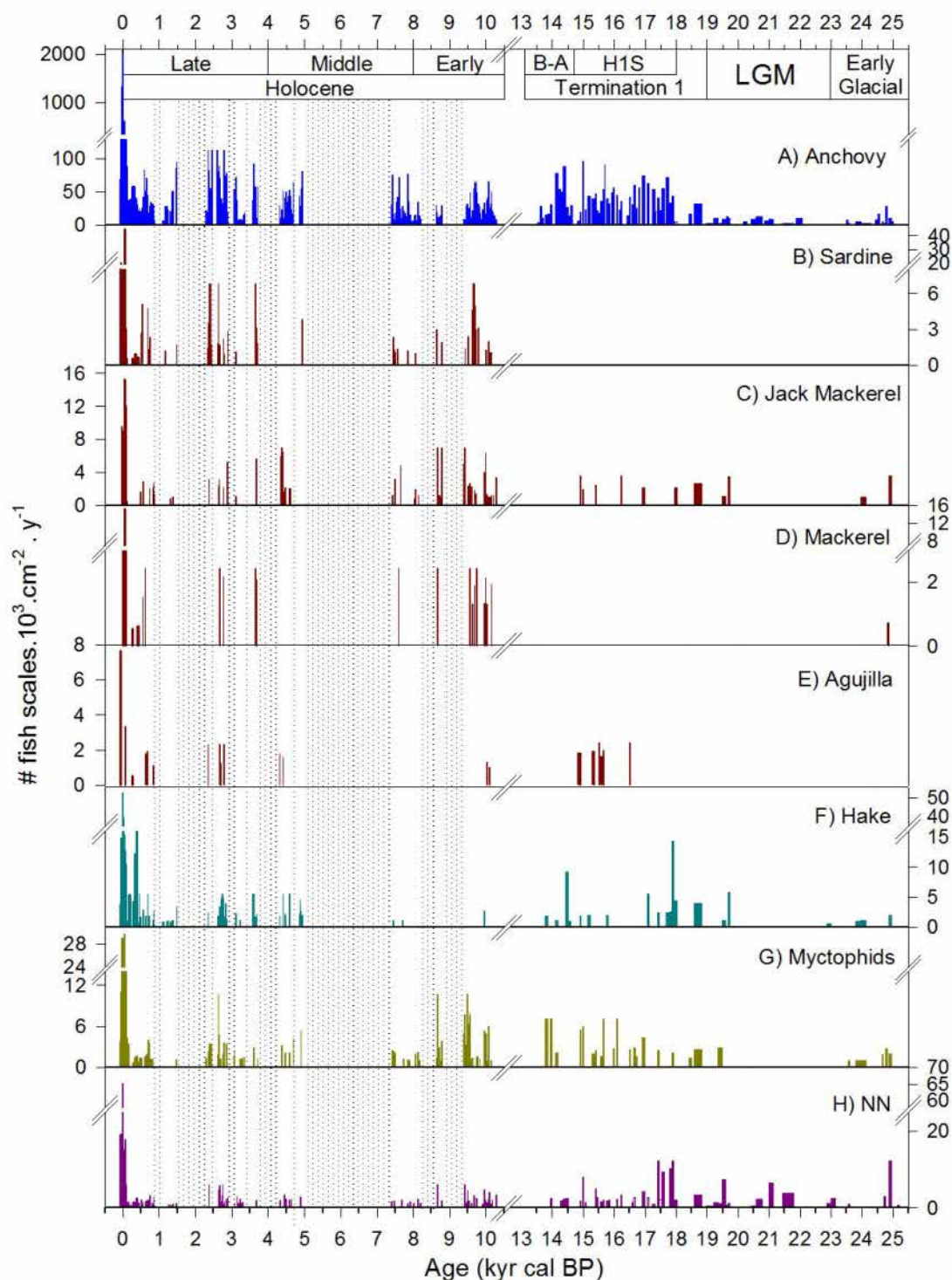
Figure IV-7. Detailed fish scale composition in cores G-10 and G-14. From top to bottom: A) anchovy (*Engraulis ringens*), B) sardine (*Sardinops sagax sagax*), C) jack mackerel (*Trachurus picturatus murphyi*, D) mackerel (*Scomber japonicus*), E) agujilla (*Scomberesox saurus scombroides*), F) hake (*Merluccius gayi peruanus*), G) myctophids and H) non identified species. The dotted areas indicate samples associated with homogeneous or slumped deposits where fish scales were not analyzed. The acronyms used in this figure are: Last Glacial Maximum (LGM), Heinrich 1 Stadial (H1S), and Bølling-Allerød (B-A).

Relationships between fish scales from different species depend on the time-scale at which the observations are done. At high termporal resolution, the relationships between fish scales from different species are very weak but display a coherent pattern according to fish species preferences in terms of oceanographic conditions (Table IV-3). Anchovy scales show no relationship with sardine or with the rest of the oceanic species, but the shared variability between anchovy and agujilla scales is significant (Table IV-3). Sardine scales show low but significant shared variability with the rest of oceanic species (i.e. jack mackerel, horse mackerel and agujilla). The highest shared variability between oceanic species was found between jack mackerel and mackerel, result that is expected due to their relatively more similar habitat, physiology and behavior in comparison with the other species. On centennial timescales during the Holocene, most of the centennial-scale maxima in sardine, jack mackerel and mackerel scale fluxes are associated with high anchovy scale fluxes (Fig. IV-7A and B). This observation is in contrast to the fact that anchovy and sardine fluctuate out of phase at decadal time-scale as observed in the fish landing records.

Table IV-3. Correlation coefficients (r^2) between the different fish scale species. Data from Figure IV-7, n =408. Boldface indicates significance after correcting for multiple comparisons (p<0.007).

	anchovy	sardine	jack mackerel	horse mackerel	agujilla	hake	myctophids	nn
anchovy	1.0							
sardine	0.00	1.0						
jack mackerel	0.00	**0.02**	1.0					
horse mackerel	0.00	**0.03**	**0.09**	1.0				
agujilla	**0.06**	**0.03**	0.01	**0.02**	1.0			
hake	**0.03**	0.01	0.00	0.00	**0.03**	1.0		
myctophids	0.01	0.00	**0.16**	0.01	0.01	0.00	1.0	
nn	**0.04**	**0.03**	0.01	0.00	0.00	0.01	0.0	1.0

IV-4.3 Anchovy scale preservation

Anchovy scales are associated with exceptionally good preservation during the Heinrich 1 Stadial, Bølling-Allerød and during the last 150 years; moderate preservation during the Holocene; and strong degradation during the Early Glacial and the Last Glacial Maximum (Figs. IV-8A to E). The three preservation indices do not show significant differences between the Early Glacial and Last Glacial Maximum, and between the Heinrich 1 Stadial and the Bølling-Allerød (Tables AII-13 to and AII-15 in annexes II), implying similar anchovy scale degradation during these periods. In contrast, the three preservation indices show higher values during the Heinrich 1 Stadial and Bølling-Allerød compared to the Early Glacial and the Last Glacial Maximum (Figs. IV-8C, D and E), however only the ratio anchovy scales to vertebrae during the Heinrich 1 Stadial is significantly higher (Tables AII-13 to and AII-15 in annexes II). During the Holocene, the three preservation indices show stronger

temporal variability compared to the Last Glacial-Interglacial Transition (Figs. IV-8A to E), and the fish debris preservation is somewhat similar during the Holocene (Tables AII-13 to and AII-15 in annexes II). During the Heinrich 1 Stadial the ratio anchovy scales to vertebrae and the bio-erosion index are significantly higher compared to all the Holocene periods, and display similar values compared to the last 150 years (Tables AII-13 to and AII-15 in annexes II). Consequently, the high anchovy scale fluxes during the Heinrich 1 Stadial are better explained by enhanced preservation rather than high anchovy abundance given that the anchovy vertebrae fluxes were very low during this period (Figs. IV-8A to E).

The HI, which is a proxy for organic matter preservation, follows the multi-centennial to millennial scale changes in fish debris preservation inferred through the 3 preservation indices (Fig. IV-8A to F). The low fish scales fluxes from 25.5 to 18 kyr BP that are associated with lower fish scale preservation, coincide with the lowest HI values registered in the core (Fig. IV-8F). Interestingly, the HI shows stronger temporal variability during the Termination 1compared to the Holocene period, while the opposite is true for the fish debris preservation indices (Fig. IV-8C, D and E). Finally, the highest HI values were recorded during the last 150 years coinciding with the best fish debris preservation. This covariation of HI and the preservation proxies at millennial timescales is not surprising because anchovy scales are largely composed of organic matter. Consequently, HI can also be used as an indicator for fish scale preservation.

The preservation of fish remains in the Last Glacial-Interglacial Transition follows the strong centennial to millennial-scale changes in OMZ intensity and sediment redox conditions (Fig. IV-8). During the Early Glacial and the Last Glacial Maximum, the weak OMZ and the sub-oxic water-sediment interface are associated with bad fish scale preservation (Figs. IV-8G and H). In contrast, the better preservation of anchovy scales during Heinrich 1 Stadial was associated with a strong OMZ (Fig. IV-8H) and anoxic conditions in the sediments (Fig. IV-8G). At the end of the Bølling-Allerød, the integrity index shows relatively low values and there is slightly more evidence of bio-erosion in the anchovy vertebrae (Fig. IV-8E) indicating higher degradation; however this pattern is not observed with the ratio anchovy scales to anchovy vertebrae (Fig. IV-8D). The relatively stronger degradation of anchovy scales during the end of the Bølling-Allerød is associated with a more oxic environment in the seafloor as inferred by the Re/Mo ratios; however the water column was strongly oxygen depleted. During the Heinrich 1 Stadial - Bølling-Allerød transition it is possible to observe the effect of the water column oxygenation and the sub-oxic conditions on the seafloor in the fish scales preservation. A minimum value in the $\delta^{15}N$ record and sub-oxic conditions in the seafloor at ~14.7 kyr BP, are associated with lower preservation of the organic matter, and a decrease in the three preservation proxies associated with very low anchovy scale fluxes (Fig. IV-8).
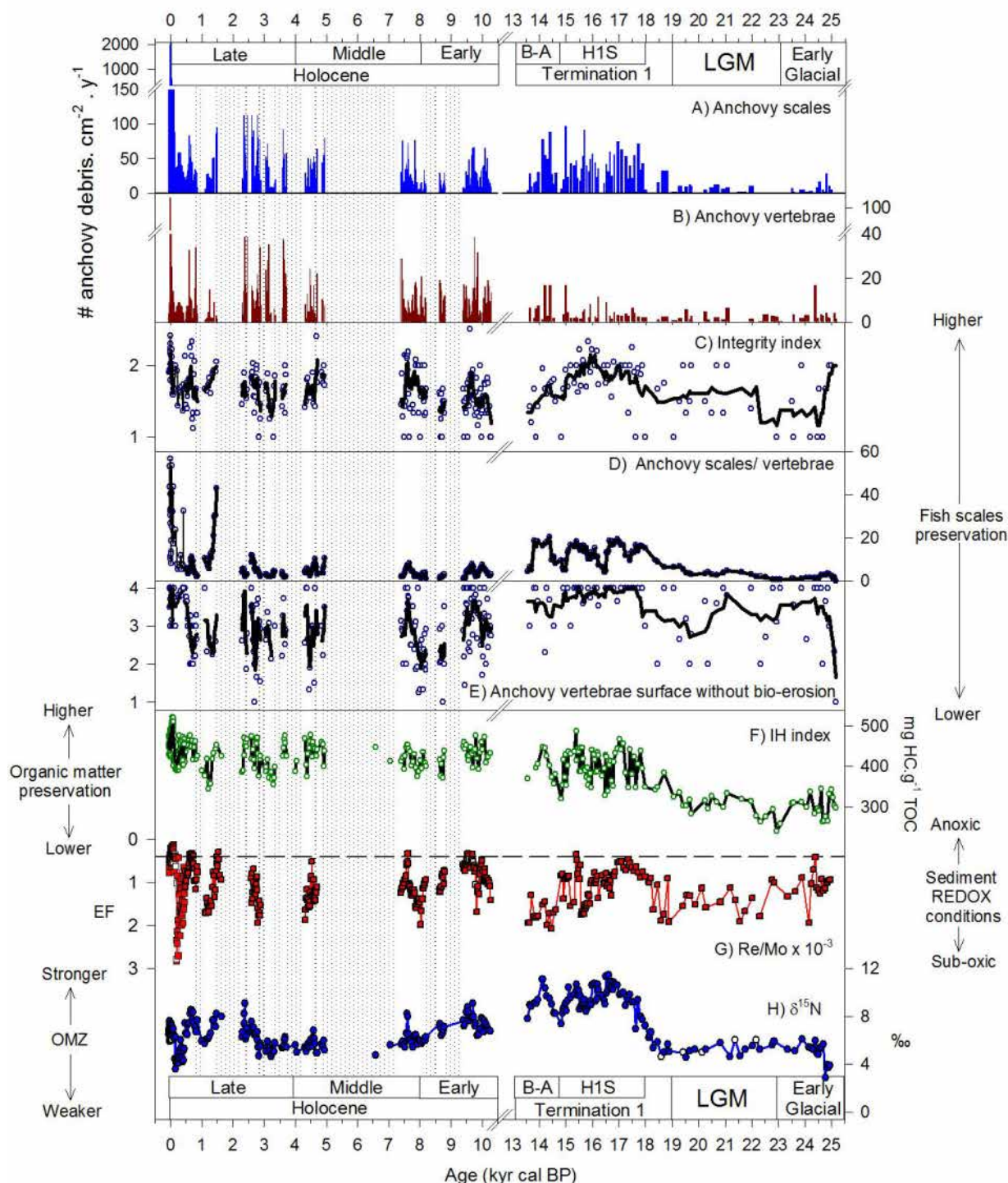
Figure IV-8. Anchovy (*Engraulis ringens*) scales and vertebrae fluxes compared with the preservation indices and oxygenation levels in the sediment and the water column. A) Anchovy scale fluxes. B) Anchovy vertebrae fluxes. C) Integrity index, the black line indicates a 7-point running mean. D) Ratio of anchovy scale to vertebrae. E) bio-erosion index. F) Hydrogen index as a proxy for organic matter preservation. G) Authigenic Re/Mo ratios as a proxy to differentiate anoxic and sub-oxic conditions, the horizontal dotted line indicates the value 0.4 x 10^{-3} which corresponds to the ratio of the concentration of these metals in the sea-water, y-axis inverted. H) δ^{15}N values as a proxy for water column denitrification, and thus OMZ intensity. The acronyms used in this figure are: Last Glacial Maximum (LGM), Heinrich 1 Stadial (H1S), and Bølling-Allerød (B-A).

During the Holocene the strong multi-centennial scale changes in OMZ intensity also affected the fish scale preservation in some parts of the record (Fig. IV-8). From the beginning of the Early Holocene to ~7 kyr BP the record shows two periods of relatively high anchovy scales fluxes (from 7.8 to 7.4 kyr BP and from 10.3 to 9.4 kyr BP) and one period with low fluxes centered at ~8.7 kyr BP. The two periods of high anchovy scale fluxes are associated in general with better fish scale preservation as evidenced by the high integrity index values, relatively high anchovy to vertebrae ratios and low bio-erosion over the anchovy vertebrae, while the opposite pattern can be observed in the low abundance period (Fig. IV-8). The better preservation of anchovy scales in the two multi-centennial periods is associated with an anoxic sediment-water interface and lower oxygen in the water column, although the older period shows a stronger OMZ (Fig. IV-8H). From 5 to ~2.5 kyr BP the positive trend towards higher anchovy scales and vertebrae fluxes are associated with variable integrity index values, low anchovy scale to vertebrae ratios and variable bio-erosion over the anchovy vertebrae (Fig. IV-8). During parts of this period the sediments were sub-oxic and the OMZ was weak as evidenced by the high Re/Mo ratios and the low $\delta^{15}N$ values respectively. The last 2 millennia of the record are characterized by strong centennial-scale variability in OMZ intensity and redox conditions, and the preservation indices follow these temporal changes. Finally, the last 150 years of the record show excellent fish scale preservation associated with a strong OMZ, anoxic sediment, and also by a shorter degradation time since deposition.

IV-4.4 Anchovy scale and vertebrae SEM observations

SEM observations of fish scales show the process of degradation of fish scales by biota that produces bio-erosion traces (Fig. IV-9). The two well defined portions of the anchovy scale: the hard upper well-mineralized portion and the several layers of fibrous collagen are readily identifiable in the anchovy scales from a recently caught specimen (Figs. IV-9A, B, C and D). The hard well mineralized portion is characterized by the growth lines over the fish scale surface and is very thin in comparison with the middle portion composed of collagen layers (Figs. IV-9B, C and D). The several organic-rich collagen layers arranged in a lamellar fashion represent the thickest part of the fish scale (Fig. IV-9B). An anchovy scale that presents evident signs of bio-erosion all over the scale (Fig. IV-9E) was observed by SEM to understand the mechanism of fish scale degradation. The SEM image of the anchovy scale surface shows no apparent signs of visible bio-erosion over the surface (Fig. IV-9F), but after a detailed observation small holes in the upper-well mineralized portion of the scale can be observed (black arrows in Figs. IV-9G, H and K), indicating that the bio-eroders dug the external layer to access the protein-rich internal layers. A vertical section of the same scale shows several burrows and channels dug by bio-eroders within the collagen layers (Figs. IV-9I, J and K). Another anchovy scale that shows parts of the upper hard layer detached from the scale (Fig. IV-9L), shows plentiful rests of needle-type organisms that consumed part of the fish scale likely originating the

detachment of parts of the upper-hard layer. Another type of degraded fish scale described by Salvatteci et al. (2012) was the rolled-up, flimsy and very thin scales (Fig. IV-9M). SEM images show evidence of bio-erosion all over this type of scale and a presumably lack of the collagen layers that probably caused the reduced thickness in this type of fish scale (Figs. IV-9N, O and P).

Anchovy vertebrae are also consumed by biota that leaves bio-erosion traces; however the vertebra retains its rigidity even if multiple bio-erosion traces are present in the vertebra (Fig. IV-10). The images of an anchovy vertebra from a recently caught anchovy (Figs. IV-10A, B, C and D) show the normal cavities in the bone structure where the dorsal spines were attached (two oval shaped structures in Fig. IV-10B). A vertical section of the same vertebra (Fig. IV-10D) shows lower quantity of cavities in the internal area. The SEM images of a half of an anchovy vertebra with bio-erosion traces all over the fish remain (Figs. IV-10E, F, G and H) show multiple burrows and channels inside the vertebrae walls. This anchovy vertebra was characterized by extensive evidence of bio-erosion in comparison with the other vertebrae found in the cores. We didn't observe holes in the external layer of the vertebrae, only in the broken section of the vertebrae (Figs. IV-10F, G and H).

Another type of degradation can be observed in vertebrae from the Early Glacial and Last Glacial Maximum periods, which were associated with the lowest fluxes of anchovy scales and a weak OMZ. SEM images of one vertebra from the Last Glacial Maximum period show the presence of mineral phases forming over its surface, suggesting another type of fish debris degradation. Additionally the surface of this vertebra presents several very thin layers, as observed in the bottom-left section of the vertebrae (Fig. IV-10K) that are easily detached with a pincer. The burrows (Figs. IV-10E, F, G and H) and the mineral phases that were formed over the scale (Figs. IV-10I, J, K and L) did not cause fragility of the vertebra even during the Early Glacial and Last Glacial Maximum periods, characterized by very low fish scale preservation and a weak OMZ (Fig. IV-8).
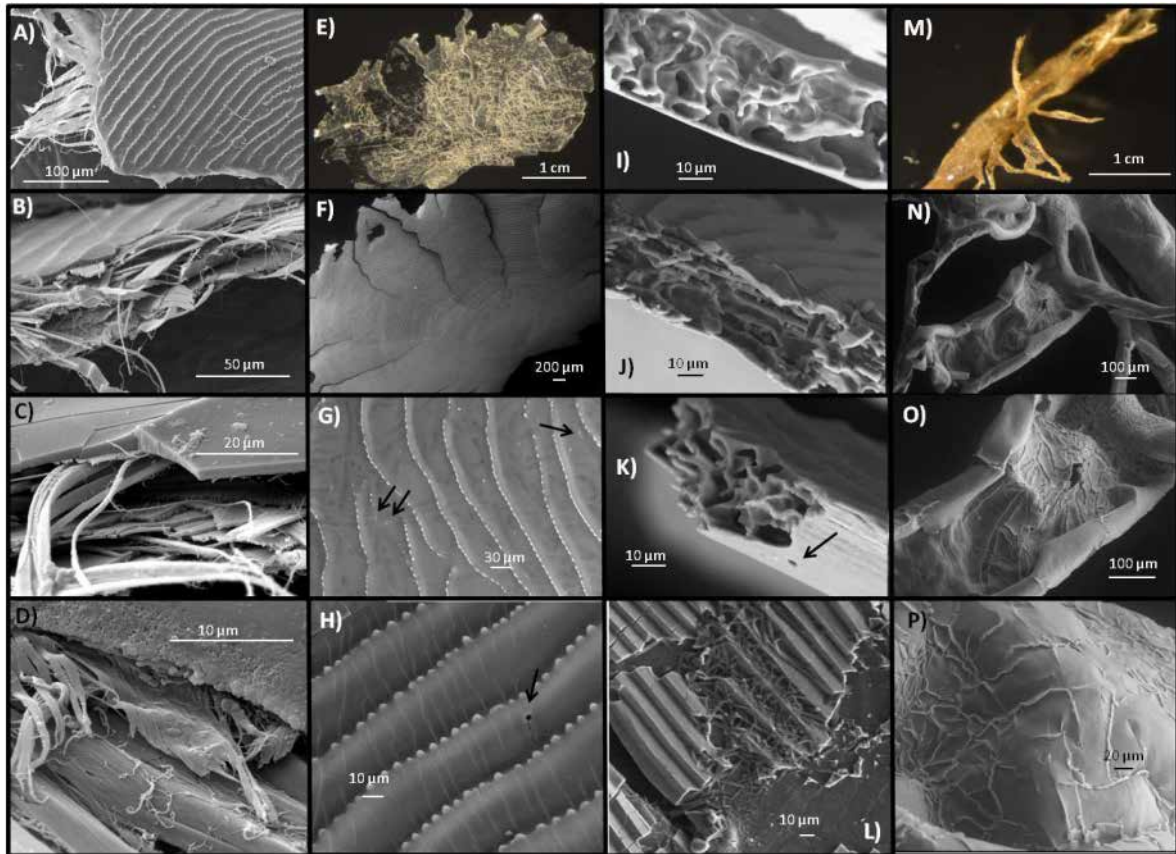
Figure IV-9. Scanning electron microscope (SEM) and conventional images of fresh and degraded anchovy scales. A) SEM image of a ripped portion of an anchovy scale taken from a recently caught fish. B) Vertical sections of the same scale shown in A. C) and D) zoom of the scale shown in A. E) Conventional image of an anchovy scale with tunnels made by bio-eroders all over the scale. F) SEM image of the surface of the same anchovy scale shown in E without any evident sign of degradation over the scale. G) and H) Zoom of the anchovy scale shown in F, showing holes over the scale surface (arrows). I), J) and K) Vertical section of the anchovy scale shown in E and F showing the multiple channels made by bio-eroders. Image show in K) also presents a hole over its surface (black arrow). L) Close-up image of another anchovy scale that present loss of the surface layer and needle-type organisms. M) Conventional photograph of a flimsy and rolled-up anchovy scale. N), O), P) SEM images of the same anchovy scale shown in M).
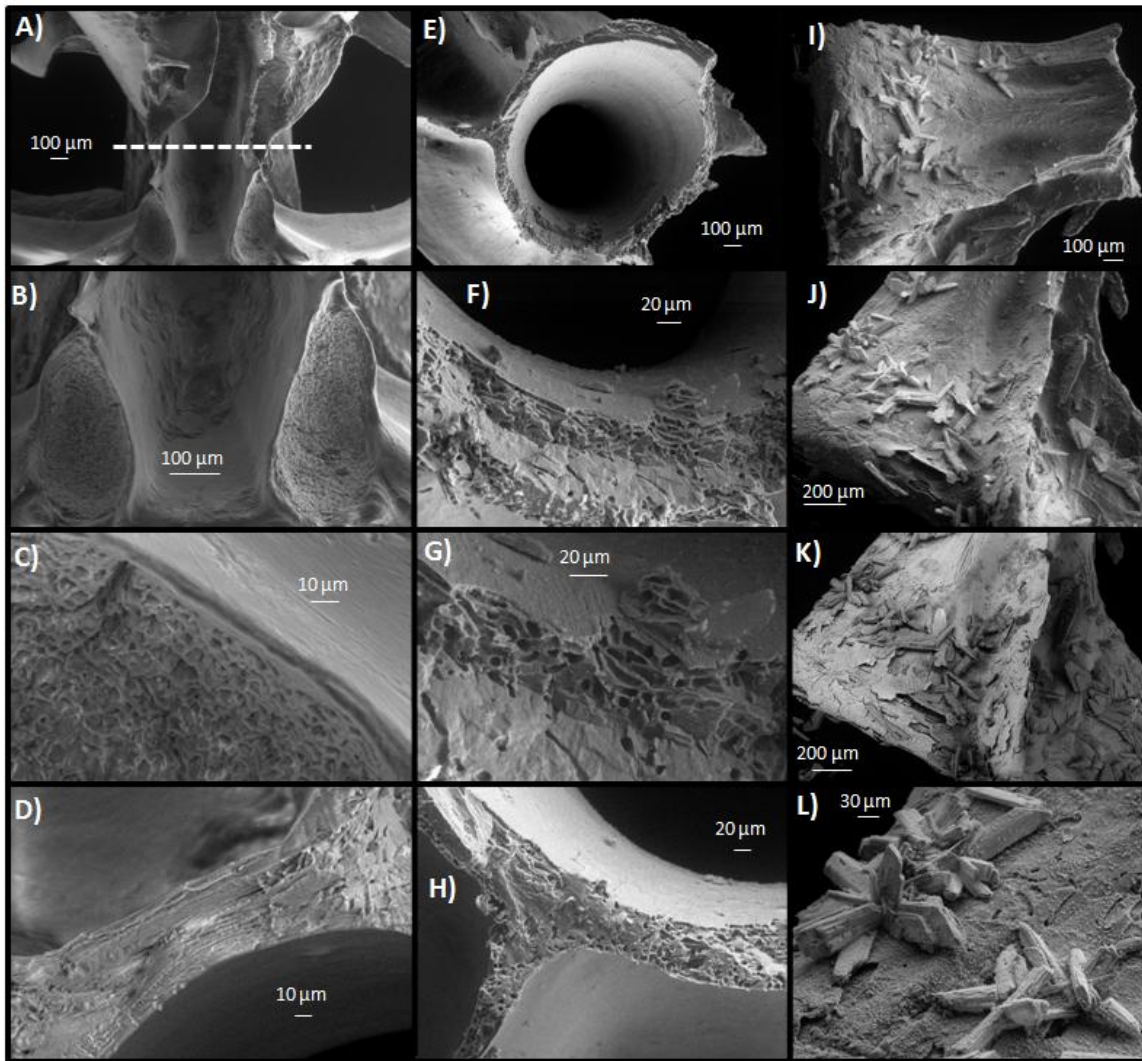
Figure IV-10. Scanning Electron Microscope (SEM) images of anchovy (*Engraulis ringens*) vertebrae from a recently caught individual (left), with strong bio-erosion evidence (middle), and with mineral crystals over the vertebrae surface (right). A) SEM image of an anchovy vertebrae, the discontinuous line indicates the position were the vertebrae was cut to observe the internal composition. B) and C) zoom of the oval structure where the dorsal spines are attached of the vertebra shown in A. D) vertical sections of the vertebrae shown in A. E) Vertebrae with strong evidence of bio-erosion. F) and G) zoom of the vertebrae shown in E) showing the galleries dag by bio-eroders. H) Vertical section of the vertebrae shown in E) showing also the presence of galleries; compare a fresh vertebra (D) with this vertebra (H). I) Vertebra found in sample G14 S1B 45 from the LGM showing the presence of minerals over the surface. J and K) zoom of the same vertebra shown in I) taken using two different techniques VPSE and CZBSD respectively. L) Zoom of the vertebrae shown in I showing the unidentified minerals.

IV-4.5 Anchovy and oceanic species biomass fluctuations during the last 25.5 kyr BP

The anchovy and other species vertebrae fluxes are compared with Ni EF, a proxy for export production, to show the similar positive trend exhibited from the Early Holocene to the present (Fig. IV-11). The anchovy and other species vertebrae are used in order to reconstruct fish biomass fluctuations instead of the fish scale fluxes, given the strong and variable preservation of fish scales

during several parts of the record (Fig. IV-8). The globally cold Early Glacial and Last Glacial Maximum show very low export production, a weak OMZ, and low fluxes of anchovy and other species vertebrae (Figs. IV-11B to F). Then, from the Early Holocene to the Current Warm Period there is a positive tend towards higher export production which is accompanied with an increase in anchovy and other species vertebrae fluxes. From the Early Holocene to the present the gradual increase in export production and anchovy abundance is apparently associated with a gradual increase in the December to March insolation at ~15 °S. Finally the highest Ni EF values and the highest anchovy and other species vertebrae are observed during the Current Warm Period. Additionally, the large variability observed in the Ni EF is also observed in the anchovy vertebrae fluxes, with higher (lower) export production associated with higher (low) anchovy fluxes, this pattern is better observed from the Late Holocene to the present. These results indicate a strong link between productivity and fish biomass abundance off Peru.

The ratio of oceanic to anchovy scales shows that during the warm Early Holocene the oceanic species were more abundant than during the other periods (Fig. IV-11G). As shown in Figure IV-8, the anchovy scales in the records are biased by differential preservation related to the changes in OMZ intensity and sediment redox conditions. By inference, the scales of the other species should also behave in the same way given the similar composition of the fish scales, although the oceanic species scales (sardine, jack mackerel and agujilla) are thicker and thus more resistant to degradation processes. Consequently the ratio of oceanic species scales to anchovy scales in each time window should indicate the original ratio of these two types of species off Pisco during periods favorable to the preservation of fish scales (i.e. from the Heinrich 1 Stadial to the present). The ratio of oceanic species to anchovy scales shows that the highest values was found during the Early Holocene, a period characterized by globally warmer temperatures and dry conditions in Peru. In contrast the Last Glacial Maximum and the Early Glacial show very low oceanic species scale abundances, only 9 fish scales were found in both periods, in clear contrast with the abundance of oceanic species during the Early Holocene (more than 100 fish scales of sardine, jack mackerel, mackerel and agujilla were found). Heinrich 1 Stadial seems to be a period favorable for anchovy but not for oceanic species as suggested by the low ratios. The strong OMZ during the Heinrich 1 Stadial may be the factor responsible for the absence of sardine. The rest of the Holocene and the Current Warm Period show moderate ratios that are not comparable in magnitude with the ratio observed during the Early Holocene (Fig. IV-11G).
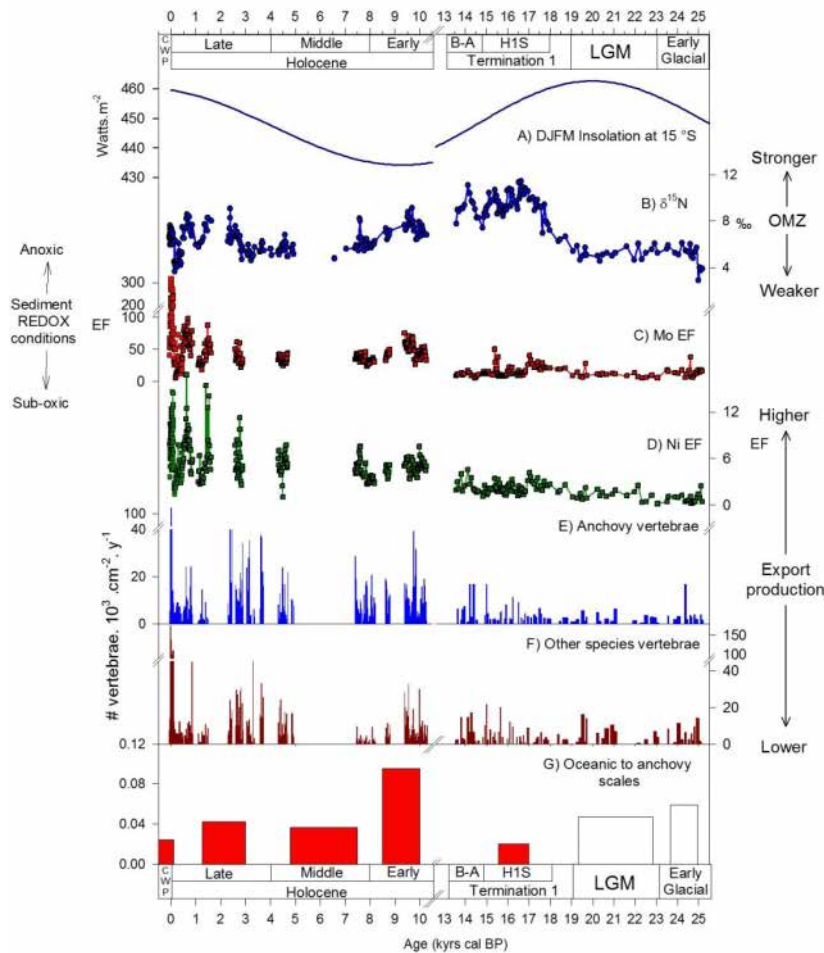
Figure IV-11. A) December-January and February insolation at 15 °S (Berger et al., 1978). B) δ¹⁵N in sedimentary organic matter as a proxy for OMZ intensity. C) Mo EF as a proxy for sediment REDOX conditions. D) Export production as inferred by the Ni EF. E) Fluxes of anchovy vertebrae as a proxy for anchovy biomass abundance. F) Fluxes of other species vertebrae as proxy for other species biomass abundance. G) Ratio of oceanic to anchovy scales, the oceanic scales are composed by sardine, jack mackerel, mackerel and agujilla. During the B-A no oceanic scales were found. The open bars during the Early Glacial and Last Glacial Maximum indicate lack of confidence in the data set due to the low number of oceanic species scales found (4 and 5 scales respectively). B-A represents the Bølling-Allerød, H1S represents Heinrich 1 Stadial and LGM represents the Last Glacial Maximum.

IV-4.6 Principal components analysis

The PCA results indicate that 53.5% of the total variance of the selected variables could be expressed by two principal components (PC, Fig. IV-12). The PC1 explained 34.5% of the data set variance and displayed the highest loadings for Mo/Re (-0.81), Ni EF (-0.76), HI (-0.57), anchovy vertebrae fluxes (-0.53), other species vertebrae fluxes (-0.66), integrity index (-0.57), the ratio anchovy scales to vertebrae (-0.6); only the $\delta^{15}N$ (-0.21) and the bio-erosion index (-0.29) show low loadings. The PC2 explained 19.1% of the data set variance and displayed the highest loadings for $\delta^{15}N$ (0.6), the anchovy vertebrae flux (-0.50), integrity index (0.44), the ratio anchovy scales to

vertebrae (0.48) and the bio-erosion index (0.60). PC1 is interpreted as a combination of sediment redox conditions and export production. PC2 is interpreted as the preservation signal given the high loadings of the three preservation indices and the degree of the water column oxygenation. Consequently, the PC1 shows that the fluxes of anchovy and other species vertebrae are more associated with the export production and oxygen contents in the sediments; while PC2 shows that the most important factor that controls fish scale preservation is the oxygen levels in the water column.
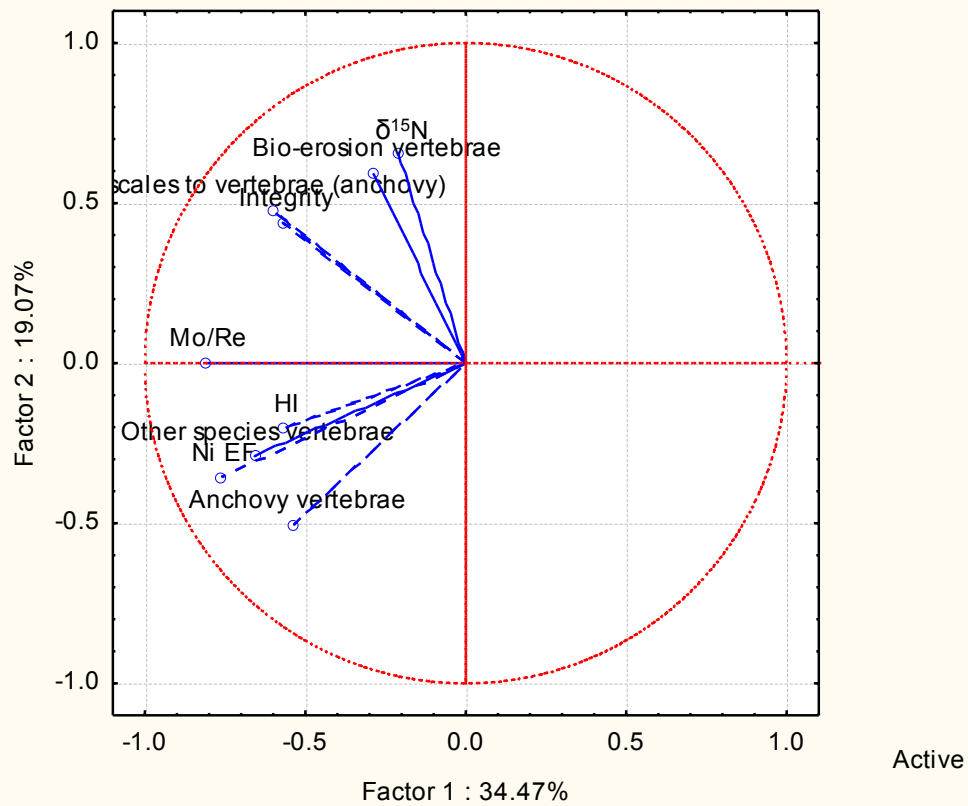
Figure IV-12. Projection of some of the variables shown in Figures IV-5, IV-8 and IV-11. The variables used in the PCA analysis were: δ^{15}N, the ratio Mo/Re, HI, the flux of anchovy (*Engraulis ringens*) and other species vertebrae, and the three preservation indices. The two principal components explain 53.5% of the data set variance.

IV-5. Discussion

IV-5.1 Fish scale preservation

The different patterns observed with the fish scale and the fish bones fluxes, and the preservation indices clearly show an important role of fish debris preservation associated with changes in OMZ intensity (Fig. IV-8). The high fluxes of anchovy scales during great part of the Heinrich 1 Stadial are not associated with high fluxes of anchovy vertebrae or with high export production. Additionally, the three preservation indices show enhanced fish scale preservation (Fig. IV-8). The combination of these results suggests that during the Heinrich 1 Stadial the anchovy biomass was low, and the high abundance of anchovy scales could be explained by enhanced

preservation. An erroneous interpretation based on the anchovy scale fluxes alone could be that during the Heinrich 1 Stadial the anchovy biomass was exceptionally favored by the environmental conditions. In the case of sardine, the absence of sardine scales during the Heinrich 1 Stadial indicates that this period was not favorable for sardine, and that the absence of sardine scales is not due to fish scale degradation. Moreover sardine scales seem to be more resistant to degradation than anchovy scales, this observation indicate that during periods with strong degradation anchovy scales should be preferentially degraded in comparison with sardine scales which is not the case during the Heinrich 1 Stadial. Thus, it is necessary to assess the degree of preservation of the fish remains prior any interpretations. This procedure is crucial in regions were the temporal intensity of the OMZ is highly variable, because the preservation of fish scales seems to be more related to the levels of oxygen in the water column than the redox conditions in the sediments, as inferred from the PCA (Fig. IV-12).

The principal mechanism of fish scale degradation is directly related to the abundance of organisms that nourish on the fibrous and organic-rich collagen layers. The mineralized external layer is avoided for these organisms; however these bio-eroders need to perforate this thick layer in order to reach the collagen fibers. Very few holes were found in the external layer while the internal collagen layers were full of channels and galleries (Fig. IV-9), these observations suggest that the external layer is more difficult to perforate. The bio-eroders were not identified and could pertain to any of the following taxa: cyanobacteria, chlorophytes, fungi and other micro-chemotrophs (Wisshak et al., 2011), and not only fungi as proposed by Salvatteci et al. (2012). The fish scales present lower evidence of bio-erosion in the periods associated with a very strong OMZ like the Heinrich 1 Stadial (Fig. IV-8), thus there should be a link between the abundance and ecology of bio-eroders and the water column oxygenation. One implication of the strong degradation of fish scales in Peruvian sediments is that isotopic analyses on fish scales (Struck et al., 2002; Hutchinson and Trueman, 2006) may be affected by the effect of bio-eroders, and that only pristine scales should be used for this kind of analyses.

IV-5.2 Use of vertebrae to infer past biomass fluctuations

The use of vertebrae, which are more resistant to degradation than fish scales, may lead to infer more reliable past fluctuations in anchovy abundances, because of the strong fish scale degradation during some periods associated with a weak OMZ. However, there are several factors that need to be considered while using vertebrae data. First, fish scales and vertebrae reach the water-sediment interface through different processes: fish scales are primarily derived from scale shedding (Shackleton, 1988; Field et al., 2009) while the majority of bones and vertebrae arrive to sediments by passing through the guts of predators (Field et al., 2009; Salvatteci et al., 2012). Thus, although the

fluxes of fish scales and vertebrae to the sediments should be somewhat dependent on population size, different modes of loss and transport of vertebrae could cause deposition patterns to differ from those of scales (Salvatteci et al., 2012). Second, the vertebrae are scarcer in comparison with fish scales and other type of fish debris (Fig. IV-6). For example in core G-10 an average of 49 g of wet material was analyzed and an average of 21 anchovy scales was found per sample, while the number of vertebrae was limited to ~6.7. Thus large quantities of sediment must be analyzed to obtain a representative sample. Third, great part of the non-identified vertebrae, which correspond to nearly ~40% of the total vertebrae abundance, could not be identified because the vertebrae belonged to juvenile specimens that cannot be easily identified. Finally, in core G-10 and G-14 only 1 vertebra of sardine and 4 of hake were found, in clear contrast with the ~4 400 anchovy vertebrae found. The higher abundance of anchovy vertebrae in the sediments is consistent with the role of anchovy in the HCS as a dominant species and a principal prey for birds, jack mackerel, mackerel, among several other species (Jahncke and Goya, 1998; Bertrand et al., 2004; Chavez et al., 2008). Consequently, it is only when large quantities of sediment can be analyzed, that vertebrae should be preferred over fish scales (O'Connell and Tunnicliffe, 2001; Salvatteci et al., 2012).

IV-5.3 Anchovy and oceanic species abundance fluctuations

The climatic and oceanographic conditions off Peru during cold Early Glacial and Last Glacial Maximum were not favorable for upwelling, primary productivity or for pelagic fishes in general. The export production and inferred fish abundance show minimum values during these periods. The sea level changes can not principally explain the observed changes that occurred off Peru. During the Last Glacial Maximum the sea level was 120 meters below present values and during the Heinrich 1 Stadial (~16 kyr BP) the sea level was only 10 meters above the Last Glacial Maximum conditions (Fleming et al., 1998) and the OMZ intensity changed abruptly likely by remote forcings (De Pol-Holz et al., 2006; Kienast et al., 2006; Martinez et al., 2010). While the physical upwelling was probably enhanced during the Last Glacial Maximum and Early Glacial due to stronger winds (Dubois et al., 2009), the increase in productivity was likely hampered by a thick mixed layer and/or a deep thermocline. All these conditions, which are consistent with El Niño-like conditions, are unfavorable for primary producers and pelagic fishes.

The Heinrich 1 Stadial was characterized by low productivity and a very strong OMZ, conditions that were to some extent favorable for anchovy but not for sardine (Figs. IV-7 and IV-11). The low productivity during this period was probably the limiting factor that impedes a higher anchovy biomass as observed during the Holocene because anchovy is strongly linked to productivity (Bertrand et al., 2004; 2011; McCall, 2009). In the case of sardine, the combination of low productivity and strong OMZ cause the absence of sardine in front of Peru because sardine benefit

from a more oxygenated-deeper habitat (Bertrand et al., 2011), which not occurred during the Heinrich 1 Stadial. The response of the pelagic community during the Heinrich 1 Stadial conditions could be an analog to future climate conditions if the OMZs continue to expand (Stramma et al., 2008).

Anchovy is restricted to the coastal waters and is more influenced by upwelling and coastal productivity than sardines (Bertrand et al., 2004; 2008; 2011; Gutierrez et al., 2007, 2008; Swartzman et al., 2008; McCall, 2009), thus it is not surprising that the upwelling enhancement observed in the trace elements record since the Early Holocene was accompanied with an increase in anchovy biomass (Fig. IV-11). The upwelling enhancement was inferred by an increase in export production associated with an increase in anoxic sediments conditions (Fig. IV-11), the anoxic conditions likely resulted from the decay of the biological production from the water column. The positive trend towards higher productivity from the Early Holocene to nowadays in the vertebrae fluxes is supported by the Ni EF values that are not dependent of the sedimentation-rates. Thus, the trend is real and not an artifact of the age model.

It is postulated that the apparent increase in productivity, anchovy biomass and reducing conditions in the surface sediments at millennial-scales are seemingly explained by mechanisms related to the increased summer (December to March) insolation. Summer insolation of the Southern Hemisphere has increased gradually from a minimum centered at 9.5 kyr BP due to the variations in the Earth's orbit around the Sun (Berger et al., 1978). A maximum in summer insolation also occurred during the Last Glacial Maximum (Fig. IV-11A), but during this time period the globally cold conditions appear to be more important than the regional conditions. An increase in insolation causes an atmospheric pressure gradient between land and sea, which enhances upwelling winds in spring and summer. This mechanism is due to an inhibition of nighttime cooling and enhancement of daytime heating leading an intensification of the continental thermal lows adjacent to upwelling regions (Bakun, 1990; Bakun et al., 2010). The primary productivity off Pisco (and off Peru in general) follows a seasonal pattern: it is higher during spring/summer when surface waters are more stratified, and lower in winter, due to lower surface insolation and stronger winds originating a thick mixed layer that prevents algal growth (Pennington et al., 2006; Echevin et al., 2008; Chavez and Messié, 2009; Gutierrez et al., 2011). Consequently, higher insolation levels tend to stratify the water column thus favoring higher primary productivity. The upwelling region off western North America shows a gradual decrease of upwelling over the past 4 kyr BP, which is also associated with a decrease in insolation in the Northern Hemisphere since the Early Holocene (van Geen et al., 1992). Van Geen et al. (1992) explained this decrease as a consequence of changes in temperature differences between air masses over land an over the ocean, which are related to changes in insolation.

Regardless the positive trend towards enhanced upwelling, higher export production and anoxic sediments, the range of variability of all these proxies is higher from the late mid-Holocene to the present (Fig. IV-11). The stronger variability of the OMZ intensity, the anoxic conditions in the sediment, the export production, and vertebrae fluxes recorded since ~4.5 kyr BP was already observed in other types of proxies obtained from cores retrieved off Callao and off Pisco (Chazen et al., 2009; Makou et al., 2010) and also in the Tropical Pacific (Moy et al., 2002). The likely explanation for the increase in variability since ~4.5 kyr BP is the mid-Holocene strengthening of El Niño Southern Oscillation, which may be linked to changes in the precession of earth's orbit (Clement et al., 2000).

The records presented show that the oceanic species are more favored during warm NH episode and extremely reduced during the globally cold periods. The ratio of oceanic species to anchovy scales can give important insights about which oceanographic and climatic conditions were favorable for the oceanic species. This ratio was higher during the Early Holocene in comparison with other periods, suggesting that warm waters intrusion were more frequent during the Early Holocene. The Early Holocene is associated with a northward displacement of the ITCZ (Haug et al., 2001), dry conditions in Peru, and very high SST off Peru between 10 – 9 kyr BP (Rein et al., 2005; Chazen et al., 2009). These conditions probably caused a strong variability in the expansion-contraction of the habitat favorable for oceanic species (Bertrand et al., 2004; 2008; 2011; Gutierrez et al., 2007, 2008; Swartzman et al., 2008). It is not clear whether the higher temperatures off Peru were a consequence of a widely observed early Holocene thermal optimum (Haug et al., 2001) or if they correspond to intense warm water anomalies off Peru (Rein et al., 2005). The latter alternative is supported by the abundant presence of oceanic species during this period. The anchovy abundance was also high during the Early Holocene, but the presence of anchovy is not surprising since the SST is not a key parameter for anchovy (Gutierrez et al., 2007; Bertrand et al., 2011). Moreover, during the Early Holocene the ^{14}C reservoir ages show higher values but also highly variable suggesting stronger upwelling (Ortlieb et al., 2011). Probably during the Early Holocene the intense warm water anomalies that can explain the appearance of sardine occurred at sub-decadal time scale that are not resolved by the sub-sampling realized since each sample during the Early Holocene represented ~20 years. The Mid Holocene, the Late Holocene and the Current Warm Period also show moderate abundance of oceanic species scales, implying that the conditions during these relatively gloabally warm periods in comparison with the glacial periods are also beneficial for oceanic species. In contrast, the global cold periods like the Early Glacial and Last Glacial Maximum are associated with very few oceanic species scales. The physical upwelling intensity was probably enhanced during the Last Glacial Maximum and Early Glacial due to stronger winds, pushing offshore the habitat favorable for sardines.

IV-6. Conclusions

Climatic forcing plays a major role in regulating fish stocks in the PUE. Anchovy biomass appears to be strongly linked with the positive trend towards enhanced upwelling, an increase in export production and redox conditions in the sediments possibly forced by a gradual increase in insolation since the Early Holocene. The warmer Holocene was favorable for anchovies and oceanic species, and the warmer Northern Hemisphere Early Holocene was more favorable for oceanic species. In contrast, the climatic-oceanographic conditions during the cold Early Glacial and Last Glacial Maximum were unfavorable for anchovy and the other species because of the lower productivity during these periods. Additionally, strong centennial scale variability in export production, OMZ intensity and fish biomass variability characterize the last 4 kyr.

Fish vertebrae are better indicators of biomass fluctuations than the fish scales. Fish scale preservation is more associated with the OMZ intensity than with the anoxic/sub-oxic conditions in the sediment-water interface during the time of deposition. The oxygen levels in the water column and the sediment-water interface have significantly changed during the last 25 kyr, originating strong degradation of fish scales during several periods. Scales are degraded more easily than vertebrae and thus vertebrae should be used to reconstruct past biomass variability, provided that analyses of sufficient volume of material is possible.

IV-7. References

Alheit, J., and A. Bakun. 2010. Population synchronies within and between ocean basins: Apparent teleconnections and implications as to physical–biological linkage mechanisms. Journal of Marine Systems 79(3-4):267-285.

Baker, P. A., C. A. Rigsby, G. O. Seltzer, S. C. Fritz, T. K. Lowenstein, N. P. Bacher, and C. Veliz. 2001. Tropical climate changes at millennial and orbital timescales on the Bolivian Altiplano. Nature 409:698-701.

Bakun, A. 1990. Global climate change and intensification of coastal upwelling. Science 247(4939):198-201.

Bakun, A., D. Field, A. Redondo-Rodriguez, and S. J. Weeks. 2010. Greenhouse gas, upwelling-favorable winds, and the future of coastal ocean upwelling ecosystems. Global Change Biology 16:1213-1228.

Berger, A. L. 1978. A Simple algorithm to compute long term variations of Daily or monthly insolation Institut d'Astronomie et de Geophysique, Universite Catholique de Louvain, Louvain-la-Neuve, No. 18.

Bertrand, A., M. Segura, M. Gutiérrez, and L. Vásquez. 2004. From small-scale habitat loopholes to decadal cycles: a habitat-based hypothesis explaining fluctuation in pelagic fish populations off Peru. Fish and Fisheries 5:296-316.

Bertrand, A., F. Gerlotto, S. Bertrand, M. Gutierrez, L. Alza, A. Chipollini, E. Diaz, P. Espinoza, J. Ledesma, R. Quesquen, S. Peraltilla, and F. Chavez. 2008. Schooling behaviour and environmental forcing in relation to anchoveta distribution: An analysis across multiple spatial scales. Progress in Oceanography 79:264-277.

Bertrand, A., A. Chaigneau, S. Peraltilla, J. Ledesma, M. Graco, F. Monetti, and F. Chavez. 2011. Oxygen: A Fundamental Property Regulating Pelagic Ecosystem Structure in the Coastal Southeastern Tropical Pacific. PLoS ONE 6(12):e29558.

Bird, B. W., M. B. Abbott, M. Vuille, D. T. Rodbell, N. D. Stansell, and M. F. Rosenmeier. 2011. A 2,300-year-long annually resolved record of the South American summer monsoon from the Peruvian Andes. PNAS.

Carre, M., M. Azzoug, I. Bentaleb, B. M. Chase, M. Fontugne, D. Jackson, M.-P. Ledru, A. Maldonado, J. P. Sachs, and A. J. Schauer. 2011. Mid-Holocene mean climate in the south eastern Pacific and its influence on South America. Quaternary International:1-12.

Chavez, F. P., and M. Messié. 2009. A comparison of Eastern Boundary Upwelling Ecosystems. Progress in Oceanography 83(1-4):80-96.

Chavez, F., J. Ryan, S. Lluch-Cota, and M. Niquen. 2003. From Anchovies to Sardines and Back: Multidecadal Change in the Pacific Ocean. Science 299:217-221.

Chavez, F., A. Bertrand, R. Guevara-Carrasco, P. Soler, and J. Csirke. 2008. The northern Humboldt Current System: Brief history, present status and a view towards the future. Progress in Oceanography 79:95-105.

Chazen, C. R., M. A. Altabet, and T. D. Herbert. 2009. Abrupt mid-Holocene onset of centennial-scale climate variability on the Peru-Chile Margin. Geophysical Research Letters 36:L18704.

Checkley, D., P. Ayon, T. Baumgartner, M. Bernal, J. Coetzee, R. Emmett, R. Guevara-Carrasco, L. Hutchings, L. Ibaibarriaga, H. Nakata, Y. Oozeki, B. Planque, J. Schweigert, Y. Stratoudakis, and C. van der Lingen. 2009. Habitats. Pp. 12-44. In D. Checkley, J. Alheit, Y. Oozeki, and C. Roy, eds. Climate Change and Small Pelagic Fish. Cambridge University Press.

Clement, A. C., R. Seager, and M. A. Cane. 2000. Suppression of El Niño during the mid-Holocene by changes in the Earth's orbit. Paleoceanography 15(6):731-737.

Cobb, K. M., C. D. Charles, H. Cheng, and R. L. Edwards. 2003. El Niño/Southern Oscillation and tropical Pacific climate during the last millennium. Nature 424:271-276.

Conroy, J. L., A. Restrepo, J. T. Overpeck, M. Steinitz-Kannan, J. E. Cole, M. B. Bush, and P. A. Colinvaux. 2009. Unprecedent recent warming of surface temperatures in the eastern tropical Pacific Ocean. Nature geoscience 2:46-50.

De Pol-Holz, R., O. Ulloa, L. Dezileau, J. Kaiser, F. Lamy, and D. Hebbeln. 2006. Melting of the Patagonian Ice Sheet and deglacial perturbations of the nitrogen cycle in the eastern South Pacific. Geophysical Research Letters 33:L04704.

De Vries, T., and W. Pearcy. 1982. Fish debris in sediments of the upwelling zone off central Peru: a late Quaternary record. Deep-Sea Research 28:87-109.

Diaz-Ochoa, J. A., C. B. Lange, S. Pantoja, G. J. De Lange, D. Gutierrez, P. Muñoz, and M. Salamanca. 2008. Fish scales in sediments from off Callao, central Peru. Deep-Sea Research Part II 56:1124–1135.

Dubois, N., M. Kienast, C. Normandeau, and T. Herbert. 2009. Eastern equatorial Pacific cold tongue during the Last Glacial Maximum as seen from alkenone paleothermometry. Paleoceanography 24:PA4207.

Echevin, V., O. Aumont, J. Ledesma, and G. Flores. 2008. The seasonal cycle of surface chlorophyll in the Peruvian upwelling system: A modelling study. Progress in Oceanography 79:167-176.

Espinoza, P., and A. Bertrand. 2008. Revisiting Peruvian anchovy (*Engraulis ringens*) trophodynamics provides a new vision of the Humboldt Current system. Progress in Oceanography 79:215-227.

Field, D. B., T. R. Baumgartner, V. Ferreira, D. Gutierrez, H. Lozano-Montes, R. Salvatteci, and A. Soutar. 2009. Variability from scales in marine sediments and other historical records. Pp. 45-63. In D. Checkley, C. Roy, J. Alheit, and Y. Oozeki, eds. Climate Change and Small Pelagic Fish. Cambridge University Press.

Finney, B. P., J. Alheit, K. C. Emeis, D. B. Field, D. Gutierrez, and U. Struck. 2010. Paleoecological studies on variability in marine fish populations: A long-term perspective on the impacts of climatic change on marine ecosystems. Journal of Marine Systems 79(3-4):316-326.

Fleming, K., P. Johnston, D. Zwartz, Y. Yokoyama, K. Lambeck, and J. Chappell. 1998. Refining the eustatic sea-level curve since the Last Glacial Maximum using far- and intermediate-field sites. Earth and Planetary Science Letters 163(1-4):327-342.

Glantz, S. A. 2002. Primer of Biostatistics. McGraw-Hill.

Goubanova, K., V. Echevin, B. Dewitte, F. Codron, K. Takahashi, P. Terray, and M. Vrac. 2010. Statistical downscaling of sea-surface wind over the Peru–Chile upwelling region: diagnosing the impact of climate change from the IPSL-CM4 model. Climate Dynamics.

Graham, N. E., C. M. Ammann, D. Fleitmann, K. M. Cobb, and J. Luterbacher. 2011. Support for global climate reorganization during the ''Medieval Climate Anomaly''. Climate Dynamics 37:1217-1245.

Gutierrez, M., G. Swartzman, A. Bertrand, and S. Bertrand. 2007. Anchovy (*Engraulis ringens*) and sardine (*Sardinops sagax*) spatial dynamics and aggregation patterns in the Humboldt Current ecosystem, Peru, from 1983–2003. Fisheries Oceanography 16(2):155-168.

Gutierrez, M., A. Ramirez, S. Bertrand, O. Moron, and A. Bertrand. 2008. Ecological niches and areas of overlap of the squat lobster 'munida' (*Pleuroncodes monodon*) and anchoveta (*Engraulis ringens*) off Peru. Progress in Oceanography 79:256-263.

Gutierrez, D., A. Sifeddine, D. B. Field, L. Ortlieb, G. Vargas, F. Chavez, F. Velazco, V. Ferreira, P. Tapia, R. Salvatteci, H. Boucher, M. C. Morales, J. Valdes, J. L. Reyss, A. Campusano, M. Boussafir, M. Mandeng-Yogo, M. Garcia, and T. Baumgartner. 2009. Rapid reorganization in ocean biogeochemistry off Peru towards the end of the Little Ice Age. Biogeosciences 6:835-848.

Gutierrez, D., I. Bouloubassi, A. Sifeddine, S. Purca, K. Goubanova, M. Graco, D. Field, L. Méjanelle, F. Velazco, A. Lorre, R. Salvatteci, D. Quispe, G. Vargas, B. Dewitte, and L. Ortlieb. 2011. Coastal cooling and increased productivity in the main upwelling zone off Peru since the mid-twentieth century. Geophysical Research Letters 38:L07603.

Hamada, M., and A. Mikuni. 1990. X-ray diffraction analysis of sardine scale ash. Nippon Suisan Gakkaishi 56(6):947-951.

Haug, G. H., K. A. Hughen, D. M. Sigman, L. C. Peterson, and U. Rohl. 2001. Southward Migration of the Intertropical Convergence Zone Through the Holocene. Science 293:1304-1308.

Hutchinson, J. J., and C. N. Trueman. 2006. Stable isotope analyses of collagen in fish scales: limitations set by scale architecture. Journal of Fish Biology 69:1874-1880.

Jahncke, J., and E. Goya. 1998. Las dietas del guanay y piquero peruano como indicadoras de la abundancia y distribución de anchoveta. Boletin del Instituto del Mar del Peru 17:15-34.

Kienast, M., S. S. Kienast, S. E. Calvert, T. I. Eglinton, G. Mollenhauer, R. François, and A. C. Mix. 2006. Eastern Pacific cooling and Atlantic overturning circulation during the last deglaciation. Nature 443:846-849.

Koutavas, A., and J. Lynch-Stieglitz. 2003. Glacial-interglacial dynamics of the eastern equatorial Pacific cold tongue-Intertropical Convergence Zone system reconstructed from oxygen isotope records. Paleoceanography 18(4):1-16.

Koutavas, A., J. Lynch-Stieglitz, T. M. Marchitto, and J. P. Sachs. 2002. El Niño-like pattern in ice age tropical Pacific sea surface temperature. Science 297(5579):226-230.

Linsley 2010

Makou, M. C., T. I. Eglinton, D. W. Oppo, and K. A. Hughen. 2010. Postglacial changes in El Niño and La Niña behavior. Geology 38(1):43-46.

Mann, M. E., Z. Zhang, S. Rutherford, R. S. Bradley, M. K. Hughes, D. Shindell, C. Ammann, G. Faluvegi, and F. Ni. 2009. Global Signatures and Dynamical Origins of the Little Ice Age and Medieval Climate Anomaly. Science 326:1256-1260.

Martinez, P., and R. S. Robinson. 2010. Increase in water column denitrification during the last deglaciation: the influence of oxygen demand in the eastern equatorial Pacific. Biogeosciences 7:1-9.

McCall, A. D. 2009. Mechanisms of low-frequency fluctuations in sardine and anchovy populations. In D. Checkley, C. Roy, J. Alheit, and Y. Oozeki, eds. Climate Change and Small Pelagic Fish. Cambridge University Press.

Moy, C. M., G. O. Seltzer, D. T. Rodbell, and D. M. Anderson. 2002. Variability of El Niño/Southern Oscillation activity at millennial timescales during the Holocene epoch. Nature 420(6912):162-165.

O'Connell, J. M., and V. Tunnicliffe. 2001. The use of sedimentary fish remains for interpretation of long-term fish population fluctuations. Marine Geology 174:177-195.

Ortlieb, L., G. Vargas, and J.-F. Saliège. 2011. Marine radiocarbon reservoir effect along the northern Chile-southern Peru coast (14-24°S) throughout the Holocene. Quaternary Research 75:91-103.

Paillard, D., L. Labeyrie, and P. Yiou. 1996. Macintosh program performs time-series analysis. Eos Trans. AGU 77:379.

Parrish, R. H., R. Serra, and W. S. Grant. 1989. The monotypic sardines, Sardina and Sardinops: their taxonomy, distribution, stock structure, and zoogeography. Canadian Journal of Fisheries and Aquatic Sciences 46(11):2019-2036.

Pennington, J. T., K. L. Mahoney, V. S. Kuwahara, D. D. Kolber, R. Calienes, and F. P. Chavez. 2006. Primary production in the eastern tropical Pacific: A review. Progress in Oceanography 69:285-317.

Pierrehumbert, R. T. 2000. Climate change and the tropical Pacific: The sleeping dragon wakes. PNAS 97(4):1355-1358.

Salvatteci, R., D. B. Field, T. Baumgartner, V. Ferreira, and D. Gutierrez. 2012. Evaluating fish scale preservation in sediment records from the oxygen minimum zone off Peru. Paleobiology 38(1):766-792.

Schwartzlose, R. A., J. Alheit, A. Bakun, T. R. Baumgartner, R. Cloete, R. J. M. Crawford, W. J. Fletcher, Y. Green-Ruiz, E. Hagen, T. Kawasaki, D. Lluch-Belda, S. E. Lluch-Cota, A. D. MacCall, Y. Matsuura, M. O. Nevarez-Martinez, R. H. Parrish, C. Roy, R. Serra, K. V. Shust, M. N. Ward, and J. Z. Zuzunaga. 1999. Worldwide large-scale fluctuations of sardine and anchovy populations. South African Journal of Marine Science 21:289-347.

Shackleton, L. Y. 1988. Scale shedding: an important factor in fossil fish studies. ICES Journal of Marine Science 44(3):259-263.

Sifeddine, A., D. Gutierrez, L. Ortlieb, H. Boucher, F. Velazco, D. Field, G. Vargas, M. Boussafir, R. Salvatteci, V. Ferreira, M. García, J. Valdes, S. Caquineau, M. Mandeng-Yogo, F. Cetin, J. Solis, P. Soler, and T. Baumgartner. 2008. Laminated sediments from the central Peruvian continental slope: A 500 year record of upwelling system productivity, terrestrial runoff and redox conditions. Progress in Oceanography 79:190–197.

Stramma, L., G. C. Johnson, J. Sprintall, and V. Mohrholz. 2008. Expanding Oxygen-Minimum Zones in the Tropical Oceans. Science 320(5876):655-658.

Strub, P. T., J. M. Mesias, V. Montecino, J. Rutllant, and S. Salinas. 1998. Coastal ocean circulation off Western South America. Coastal segment (6,E). Pp. 273-313. In A. Robinson, and K. Brink, eds. The Sea. John Wiley & Sons, Inc., New York.

Struck, U., A. V. Altenbach, K. C. Emeis, J. Alheit, C. Eichner, and R. Schneider. 2002. Changes of the upwelling rates of nitrate preserved in the δ15N-signature of sediments and fish scales from the diatomaceous mud belt of Namibia. Geobios 35:3-11.

Swartzman, G., A. Bertrand, M. Gutiérrez, S. Bertrand, and L. Vasquez. 2008. The relationship of anchovy and sardine to water masses in the Peruvian Humboldt Current System from 1983 to 2005. Progress in Oceanography 79:228-237.

Valdés, J., L. Ortlieb, D. Gutierrez, L. Marinovic, G. Vargas, and A. Sifeddine. 2008. 250 years of sardine and anchovy scale deposition record in Mejillones Bay, northern Chile. Progress in Oceanography 79:198-207.

van Geen, A., S. N. Luoma, C. C. Fuller, R. Anima, H. E. Clifton, and S. Trumbore. 1992. Evidence from Cd/Ca ratios in foraminifera for greater upwelling off California 4,000 years ago. Nature 358:54-56.

Varma, K. B. R. 1990. Morphology and dielectric properties of fish scales. Current Science 59(8).

Wisshak, M., A. Tribollet, S. Golubic, J. Jakobsen, and A. Freiwald. 2011. Temperate bioerosion: ichnodiversity and biodiversity from intertidal to bathyal depths (Azores). Geobiology 9:492-520.

CHAPTER V:

THE RESPONSE OF THE PERUVIAN UPWELLING ECOSYSTEM TO CENTENNIAL-SCALE GLOBAL CHANGE DURING THE LAST 2 MILLENNIA

V-1. Introduction

The Tropical Pacific atmosphere-ocean system may hold the key to rapid reorganizations of climate leading to changes that persist from centuries to millennia (Pierrehumbert, 2000). Given the uncertainties in the response of the Tropical Pacific to continued greenhouse forcing (Vecchi et al., 2006; Luo et al., 2012) it is important to determine the natural range of Tropical Pacific climate variability in response to the global natural forcings and the effects of these changes in the climate-ocean system in other regions (Graham et al., 2011). Throughout the last two thousand years periods of warmer cliamte (the Roman Warm Period [RWP, from ~50 to 400 AD], the Medieval Climate Anomaly [MCA, from ~900 to 1350 AD] and the Current Warm Period [CWP, from ~1900 to the date] have alternated between colder periods (the Dark Ages Cold Period [DACP, from ~500 to 900 AD] and the Little Ice Age [LIA, from ~1500 to 1850AD]) (Mann et al., 2009; Graham et al., 2011; Yan et al., 2011). The RWP, DACP, MCA and LIA were mainly identified by several proxies in the Northern Hemisphere; the intensity and global coverage of these periods are still uncertain and under discussion. In contrast the CWP is characterized by a globally warm period. In the present work we use a multi-proxy approach including organic and inorganic proxies in finely laminated sediments in the Peruvian Upwelling Ecosystem (PUE), an area which is strongly influenced by both ENSO/Walker circulation (Philander, 1990) and centennial climate variability (Agnihotri et al., 2008; Chazen et al., 2009; Gutierrez et al., 2009). The purpose is, to: 1) define the mean state of the PUE in contrasting (warm and cool) periods as the DACP, MCA, LIA and CWP, and 2) compare the results with other paleoclimatic reconstructions in the Tropical Pacific to elucidate the mechanisms that controlled the productivity and OMZ intensity off Peru during the last 2 millennia.

Paleo-oceanographic reconstructions and model simulations suggest that the MCA (LIA) was characterized by a La Niña-like (El Niño-like) mean state condition and lower El Niño (La Niña) activity (e.g. Cobb et al., 2003; Rein et al., 2004; Mann et al., 2009; Graham et al., 2011; Makou et al., 2011). One of the hypotheses is that the MCA and LIA climate changes involve opposing changes in Tropical Indo-Pacific warm pool and Central/Eastern Tropical Pacific Sea Surface Temperatures (SST), in response to changes in total solar irradiation (TSI) with the resulting circulation changes driving climate shifts around the planet (Mann et al., 2009; Graham et al., 2011). SST reconstructions indicate that the gradient between the Western and Eastern Pacific was higher during the MCA and lower during the LIA (Cobb et al., 2003; Conroy et al., 2010) suggesting a La Niña-like mean state during the MCA. Moreover, modeling experiments suggest that a northerly Inter-Tropical Convergence Zone (ITCZ) during the MCA contributes to an increased zonal SST and thus a more La Niña-like mean state (Mann et al., 2005). Given the tightly coupled system of the Western Pacific warm pool, the East Pacific cold tongue, and the atmospheric Hadley (strongly linked

with the ITCZ) and Walker circulation (Pierrehumbert, 2000), changes in the gradient between the Western and Eastern Tropical Pacific should produce considerable oceanographic changes off Peru.

Recent hydrological reconstructions point toward a different picture (Tierney et al., 2010, Yan et al., 2011b), which is inconsistent with the current mainstream theory proposing La Niña-like (El Niño-like) conditions in the Tropical Pacific during the MCA (LIA). Precipitation records in the Indo Pacific Warm Pool (IPWP, Oppo et al., 2009) and in the Galapagos Islands (Conroy et al., 2009), were used to reconstruct a Southern Oscillation Index (SOIpr) for the past two millennia (Yan et al., 2011b). The SOIpr reconstruction tends to positive values during cool periods (LIA and DACP) and negative SOI values during warm periods (RWP, MWP and CWP). Positive SOIpr and an inferred enhanced Pacific Walker Circulation (PWC) during the LIA period suggest a more La-Niña like mean state that during the MCA (Yan et al., 2011b), which contradict several of the aforementioned works. The differences in the mean-state conditions may imply that quite different mechanisms control centennial-scale shifts in the Tropical Pacific climate than those which drive and modulate interannual ENSO events, in which the sea level pressure and SST anomalies are usually coupled (Tierney et al., 2010). For example Yan et al. (2011a) showed that the north-south ITCZ migration was not the only mechanism of Tropical Pacific hydrologic variability during the last millennium, and that changes in the PWC profoundly influenced Tropical Pacific hydrology. Consequently, more paleoceanographic reconstructions in the Eastern Pacific during the last 2 millennia are needed to assess how robust the Pacific basin-wide teleconnections are and to assess the ITCZ role in modulating the oceanographic variability in this area.

The few existing paleoceanographic reconstructions off Peru suggest important changes throughout the last 2 millennia, but the results lead to different climatic interpretations. Paleoceanographic reconstructions off Callao (~12 °S) and Pisco (~14 °S) indicate that the LIA involved a dramatic reduction of export production associated with a weak Oxygen Minimum Zone (OMZ) in comparison with the last ~100 years (Diaz-Ochoa et al., 2008; Sifeddine et al., 2008; Gutierrez et al., 2009). These responses of the PUE were likely produced by a mean southward displacement of the ITCZ and a reduced influence of the South Pacific Sub-tropical High (SPSH) along the Peruvian margin (Sifeddine et al., 2008; Gutierrez et al., 2009); however the physical forcing responsible for these changes remains unclear. The MCA was inferred as a relatively constant period of extreme drought without strong flooding and with persistently weak El Niño events (Rein et al., 2004). Moreover, Agnihotri et al. (2008) showed that during the MCA the subsurface denitrification was low and that oceanographic changes were of minor intensity. In contrast to the hypothesis of a relatively homogenous period during the MCA (Rein et al., 2004; Agnihotri et al., 2008), a biomarker study showed that the first part of the MCA was characterized by lower El Niño

activity while the latter part of the MCA indicate an intensification of El Niño and La Niña events (Makou et al., 2010).

A direct comparison of different proxies from different records off Peru is difficult to make, because of chronological problems and age models reconstructions (varying reservoir ages in space and time) as well as combination of the chronology and the stratigraphy of each core (see chapter II). Consequently, the response of the PUE to centennial scale global change is not completely understood because of the lack of a widely accepted archival record. The non-continuous nature of the sedimentary marine record off central Peru produced by repeated bioturbation events, erosion by bottom currents (Reinhardt et al., 2002) and slumps linked to the active and pervasive seismic activity (Salvatteci et al., submitted). Multiple discontinuities and slumped/homogeneous sections were identified in multiple marine sediment cores off Peru, and this implies that cautious and precise core stratigraphy must be taken into account before any climatic interpretations be proposed (Salvatteci et al., submitted). For example, overlooking of a hiatus may lead to infer abrupt climate changes, and slumped sections may be erroneously interpreted as periods with low climatic variability. These problems with the sedimentary column are more relevant in works focusing in reconstructing at a high resolution level the evolution of the PUE (e.g. Rein et al., 2004; 2005; Agnihotri et al., 2008), but the centennial to millennial-scale variability may not be so much affected if a precise chronology is employed.

In view of the fact that the mean state of the PUE varied over decadal to centennial timescales (Agnihotri et al., 2008; Sifeddine et al., 2008; Chazen et al., 2009; Gutierrez et al., 2009), and is changing in response to global warming (Vargas et al., 2007; Demarcq, 2009; Gutierrez et al., 2011) it is necessary to determine what is the response of the PUE to the global climate changes and to determine which factors and processes control this variability. In the present work we use a box-core and a long gravity core retrieved off Pisco, whose sedimentary records reflect the most intense upwelling cell off the Peruvian coast (Goubanova et al., 2010), to show that productivity, water column denitrification, paleoredox proxies and fish biomass variability are associated with climatic changes in the Northern Hemisphere. These observations suggest a dynamic link between Northern Hemisphere climate and the PUE. Moreover the warm periods in the northern hemisphere, which are associated with a strong gradient in SST in the Tropical Pacific and a northward displacement of the ITCZ, favor the upwelling and productivity off Peru (i.e. normal/La Niña-like conditions). In the present work the periods with higher (lower) productivity and strong (weak) OMZ conditions are inferred to represent a persistent normal/La Niña (El Niño)-like conditions.

V-2. Proxies

Records of terrigenous input, sediment REDOX conditions and export production, were reconstructed using a series of major and trace elements. The terrigenous input was inferred from Aluminum (Al) and Titanium (Ti) contents. The terrigenous material in the shelf is principally delivered by rivers that dilute the terrigenous components of eolian origin (Scheidegger and Krissek, 1982) and thus can be used as a proxy of fluvial discharge.

In order to reconstruct sediment REDOX conditions we used a series of trace elements that exhibit different sensitivities to redox conditions such as Molybdenum (Mo), Vanadium (V) and Rhenium (Re) and may permit the differentiation between anoxic (sulfate reducing conditions) or suboxic ($0.2 > [O_2] > 0$. $ml.L^{-1}$ and no H_2S) conditions at the time of deposition. Additionally, Mo, V and Re are heavily enriched in OMZ sediments off Peru, have minimal detrital influence and display a conservative behavior in the water column (Colodner et al., 1993; Böning et al., 2004; Tribovilliard et al., 2006). Molybdenum is enriched mainly under anoxic, sulfate-reducing conditions alone, when H_2S is available (Crusius, 1996; McManus et al., 2006; Tribovillard et al., 2006). Vanadium is reduced and can accumulate under denitrifying conditions but can also accumulate under more strongly reducing (i.e. anoxic) conditions. Re concentrations in the continental crust and in the seawater are extremely low but are heavily enriched in reducing sediments with absence of O_2 and H_2S (Crusius et al., 1996; Böning et al., 2004) and also (perhaps to a lesser extent) in sulfidic sediments (Crusius et al., 1996). Re accumulates via diffusion across the sediment-water interface according to the extent of reducing conditions (Böning et al., 2004). Thus, sediments exhibiting concurrent enrichments in V, Re and Mo reflect euxinic conditions ($[O_2] = 0$; presence of H_2S) at the sediment water interface or in the water column, and an enrichment of Re (and also V in a less extent) without Mo enrichment reflect suboxic (absence of H_2S) conditions (Tribovillard et al., 2006).

Nickel (Ni), Copper (Cu) and Cadmium (Cd) are used in the present work as proxies of paleoproductivity (Nameroff et al., 2004; Dean et al., 2006; Tribovillard et al., 2006) because they display a nutrient-like behavior in the column water and are present in considerable concentrations in plankton (Böning et al., 2004). Ni and Cu were used as a proxies of the original presence of organic matter (OM); both elements are delivered to the sediments in association with OM, fixed in the sediments under reducing conditions and are moderately enriched in sediments off Peru (Tribovillard et al., 2006; Boning et al., 2004). Cd is delivered to marine sediments mainly in association with OM and then is released to interstitial waters during OM decay and enriched in both mildly and strongly reducing sediments (Dean et al., 2006; Tribovillard et al., 2006); additionally Cd is heavily enriched in marine sediments off Peru (Böning et al., 2004). Total Organic Carbon (TOC) and biogenic silica contents were also analyzed in order to infer export production.

δ^{15}N records from sedimentary OM is taken as a proxy of water-column denitrification (WCD) in oxygen-deficient waters (Altabet and Francois, 1994; Altabet et al.; 1999; De Pol-Holz et al., 2006; Martinez and Robinson, 2010). In oxygen-deficient waters bacteria reduce nitrate into N_2, leaving the remaining nitrate pool enriched in ^{15}N which is transferred by upwelling to the surface, where it is used by phytoplankton and ultimately transferred to the sediments (Altabet and Francois, 1994; Agnihotri et al., 2008). However several other factors can contribute to the δ^{15}N signal in the sedimentary organic matter, like N_2 fixation by diazotrophic bacteria, nitrification, the extent of surface NO_3^- utilization, and the anammox reaction (Robinson et al., 2012). Nevertheless the sedimentary δ^{15}N signal off Peru is consistent with other proxies of oxygenation and productivity implying denitrification in the water column at least during the last millennia (Agnihotri et al., 2008; Gutierrez et al., 2009).

In order to infer the natural biomass variability of anchovy and oceanic species prior to the development of the industrial fishery, fish scales buried in undisturbed anoxic marine sediments are used (Soutar and Isaacs, 1974; Baumgartner et al., 1992; Field et al., 2009; Finney 2010). Over time fish scales and bones as well as debris of many organisms fall to the ocean floor, get buried and accumulate. Variation in scale deposition with fish population size is attributable to natural scale shedding while the majority of bones and vertebrae arrive to sediments by passing through the guts of predators (Field et al., 2009; Salvatteci et al., 2012). If preservation conditions are favorable a record may provide a history of pelagic communities that inhabited the area; however fish scale preservation is not constant in time and depends on oxygen contents of the water column and in the sediments (Salvatteci et al., 2012). Vertebrae are more robust than scales and are better indicator of past biomass variability, but they are also less abundant and can be employed only when large quantity of sediment is sieved.

V-3. Study site

The PUE is an Eastern Boundary Upwelling Ecosystem (EBUS) characterized by a shallow surface mixed layer, a shallow thermocline and by high productivity driven by coastal upwelling of nutrient-rich cold waters that are poorly ventilated (Barber and Chavez, 1983; Pennington et al., 2006). The upper continental margin of Peru (~50 to 600 meters depth) is intersected by a strong and shallow OMZ that results from the lack of ventilation, long residence times and the decay of biological production that consumes O_2, and (Helly and Levin, 2004; Pennington et al., 2006). The strong OMZ inhibits bioturbation and preserves sediments containing millimeter-scale lamina that permit to reconstruct past ecosystem changes at high resolution levels (Gutierrez et al., 2006).

In the PUE the seasonal cycles in production are out of phase with seasonal increases in upwelling winds, in clear contrast to the other EBUS (Pennington et al., 2006; Chavez and Messié, 2009; Gutierrez et al., 2011). Upwelling favorable winds occur during the entire year but are stronger during austral winter and spring (Strub et al., 1998; Gutierrez et al., 2011). In contrast primary productivity is higher during austral spring and summer when surface waters are more stratified (Pennington et al., 2006; Chavez and Messié, 2009; Gutierrez et al., 2011). The seasonal changes in winds and productivity in the PUE are associated with the movement of the ITCZ from 10°N in austral winter (June-September) to 2-5°N in austral summer (December-March; Fig. V-1; Strub et al., 1998). The main cause of interannual variability are El Niño events that produce anomalously warm SST in the equatorial and eastern Pacific every three to eight years (Chavez et al., 2011). In contrast with seasonal warming in spring and summer, a reduction of Walker circulation during El Niño events results in an increase in sub-surface oxygenation and reduced productivity off of Peru due to a deepening of the thermocline. However the Pisco area retains a small upwelling plume even during El Niño events (Barber and Chavez, 1983).
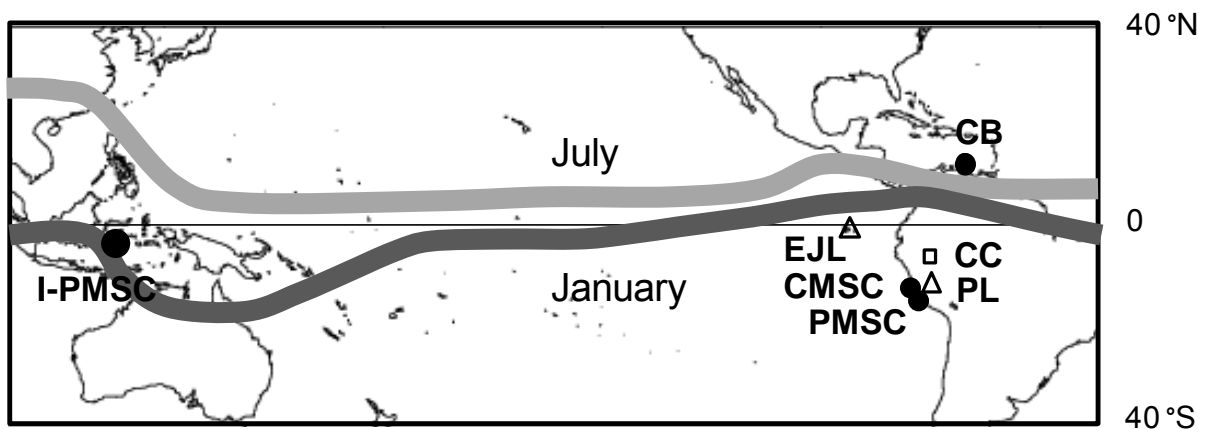
Figure V-1. Map showing modern locations of the ITCZ in July and January, modified from Newton et al. (2006), and the localities discussed in the text: I-PMSC, Indo-Pacific Marine sediment core (Oppo et al. 2009), CB, Cariaco Basin (Haug et al. 2001); EJL, El Junco lake (Conroy et al. 2009); CC, Cascayunga cave (Reuter et al. 2009); PL, Pumacocha lake (Bird et al., 2011); CMSC, Callao marine sediment core (Rein et al., 2005); and PMSC, Pisco marine sediment cores (the present study). The circles indicate the marine sediment cores, the square indicates the speleothem, and the triangles indicate the lake sediment cores.

V-4. Methodology

V-4.1 Cores used in the present study and chronology

Temporal gaps and slumps are a common feature in many cores retrieved on the Peruvian shelf as evidenced by a cross-correlation of sediment structures among several cores off Pisco (Salvatteci et al. submitted). Among all the cores used in the cross-correlation study, the box-core B0506-14 (hereafter B-14) retrieved at 301 m depth (14° 15.7S, 76°26W) presents the most

continuous, undisturbed and well-preserved laminae sequences. The presence of small-scale discontinuities and mixed sequences present in B-14 (Salvatteci et al. submitted) do not affect the centennial scale changes of the proxy records that are the focus of the present work. The 3 homogeneous deposits identified as slumps in B-14 (homogeneous deposits II, III and IV in Fig. V-2) have been removed from the record in the present work. The subsampling in core B-14 was done in stratigraphic intervals (see Salvatteci et al., 2012 for details), with a mean interval thickness of 0.46 cm.

The chronology for the most recent part of B-14 (last ~150 years) was obtained from downcore profiles of ^{241}Am and excess ^{210}Pb. The older part of B-14, which corresponds to the period below a sedimentary shift where large change in sediment density and several proxies of oxygenation and productivity occurred (Gutierrez et al., 2009), was dated using the sedimentation rates obtained from bulk organic sedimentary carbon of a nearby core B-6. A new chronological model constructed, using the ^{14}C data of Gutierrez et al. (2009) and eliminating the sedimentary sequences identified as slumps in B-6, yields a sedimentation rate of 0.07 cm.y^{-1} (Salvatteci et al. *submitted*). The sedimentation rates of core B-6 below the sedimentary shift can be used in core B-14 because both cores present similar laminae sequences and the laminae thickness are almost identical (Salvatteci et al. *submitted*). A cumulative mass-depth profile was used for the ^{210}Pb$_{ex}$ and ^{14}C profiles due to important changes in sediment density that could give erroneous age estimations.
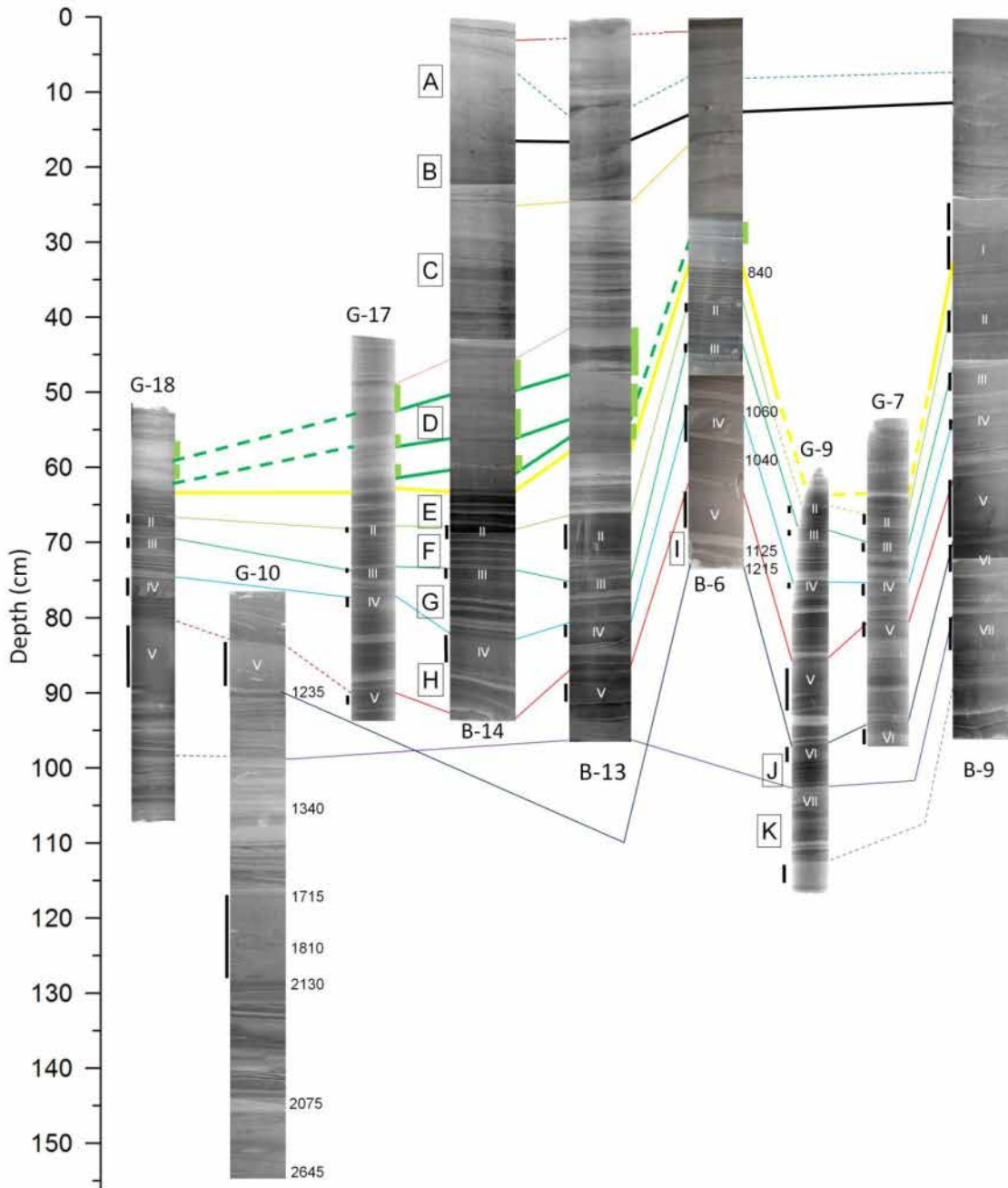
Figure V-2. Cross correlation of laminated sequences among gravity cores (G) and box-cores (B). All the cores were retrieved off Pisco, Peru. The yellow lines indicate the position of the sedimentological shift (Gutierrez et al. 2009), the upper black bold lines indicate the start of [241]Am activities and the green thick lines indicate the correlations of the diatom-rich layers. The stratigraphic markers are represented by the continuous (dashed) colored thin lines that indicate possible (less obvious) correlations and represent the base of the sediment sequences (from A to K) except for the sections A and D where the base is defined by the limit of detection of [241]Am and the sedimentary shift respectively. The capital letters from A to K indicate the position of contemporaneous sediment sequences. Black bars at the left side of the cores indicate homogeneous deposits, while green bars at the right side indicate the extent of the diatom layers. Given that the box-cores recovered surface sediments they are aligned at 0 cm; in contrast the gravity cores are aligned to the position of the shift in core B-14. In all the X-ray and SCOPIX images the colors were inverted, thus the darker (lighter) laminae represent dense (less dense) sediments. The numbers at the right side of the G-10 and B-6 X-ray images represent the uncalibrated ^{14}C ages. Figure modified from Salvatteci et al. (in revision).

Core B-14 covers approximately the last ~500 years, but in order to infer past changes in terrestrial runoff, ocean productivity, column water oxygenation and sediment redox conditions prior to the LIA, we analyzed a laminated section from a 5.2 meters long gravity core (G-10), whose upper part overlaps with core B-14 bottom. The core G-10 was retrieved during the Galathea-3 expedition in 2007 at 312 m depth (14°S 23.011, 76°W 23.906) near B-14 location. The laminated section used in the present work is located between 18 and 82 cm depth. Below this section there is a ~35 cm thick slump with laminae reworking (e.g. like bands perpendicular to the sedimentation plane). In order to date the core, 32 radiocarbon ages from bulk de-carbonated organic sedimentary carbon were obtained in core G-10, and 7 samples that were taken between 18 and 82 cm depth were used to construct an age model. The conventional radiocarbon ages were calibrated taking into account global and local reservoir (ΔR) effects using the program Calib 6.1 (Stuiver and Reimer, 1993). The ΔR to calibrate the ^{14}C ages was estimated to be 367 ±40 years and was calculated for the period between the age of the core and the last ^{210}Pb-derived age (see also Gutierrez et al., 2009 and Salvatteci et al., submitted). The age model was based on cumulative mass-depth due to important changes in sediment density. The subsampling in core G-10 was done at regular intervals of 1-cm thickness.

V-4.2 Analytical procedures

Major elements (Al, Fe, Ti, Ca and Mg) and trace elements (Manganese [Mn], Cd, Cobalt [Co], Chromium [Cr], Cu, Mo, Ni, Re, Barium [Ba], Zn [Zinc] and V) concentrations were analyzed by ICP-MS (Ultramass Varian) after hot-plate acid digestion in Polytetrafluoroethylene (PTFE) vessels. The acids employed (HF, HNO_3 and $HClO_4$) eliminated OM and removed silicates (Jarvis et al., 1992). The methodology for the sample preparation is based on Jarvis et al. (1992) and briefly summarized here. First, 25 mg of powdered sample were weighted in a high-precision micro balance and placed into the PTFE vessels. Then, 2 ml of HNO_3 (65%) and 2 ml of HF (40%) were added to the samples. The vessels were closed and immersed in an ultrasonic bath for 10 minutes to facilitate the oxidation of OM. After 2 days, the closed vessels were placed on a hot plate (150 °C) for three hours, and then the samples were removed from the hot plate to cool down. As soon as they were cool enough, the open samples were placed again on a hot plate (150 °C) to let all the acid evaporate (duration ~5 hours). Then, 2 ml of HF (40%) and 1 ml of $HClO_4$ (70-72%) were added to the sample and the tubes were placed on a hot plate (150 °C) for 10 hours in order to let all the acid evaporate. When the evaporation was completed, 2 ml HNO_3 (65%) were added to the samples and the tubes were placed again on the hot plate to evaporate the remaining acid (2-3 hours). This last procedure was repeated twice. Finally, the samples were placed into larger plastic tubes with the aid of a funnel and HNO_3 (2%). The samples were then analyzed in an ICP-MS and the accuracy of the trace elements concentrations measurement was determined through comparison with international

standards. The measurement precision was determined by performing duplicate analyses. The average values of replicate digestions were well within the recommended ranges with relative standard deviations (RSD) being <1% for Al, Mo and V, and <2.5% for Re (n = 229).

The total metal concentrations measured contain a detrital background and an authigenic metal concentration (i.e. the part in excess of the detrital background; Böning et al., 2004; Tribovillard et al., 2006; Scholz et al., 2011). Given that the trace elements may present in some cases a strong detrital fraction, we will focus on the authigenic trace element content. The chemical composition of andesite is an appropriate representation of the detrital background of the sediments on the Peruvian margin as proposed by Böning et al. (2004). Thus, we use the element contents of andesite to obtain the authigenic concentration of each trace element. These contents were obtained from the GEOROC database (Sarbas and Nohl, 2009) taking into account the elements concentrations in andesite from whole rocks from the central Andean volcanic zone in Peru (Table 1). The detrital metal fraction was calculated following Tribovillard et al. (2006): $X_{detrital} = (X/Al)_{andesite} * Al_{sample}$. Consequently the authigenic fraction of element X in a sample was calculated as $X_{total} - X_{detrital}$. The authigenic (or non-lithogenic) fraction is mainly enriched by post-depositional redox reactions (especially in suboxic environments) and each element exhibits different sensitivities to redox conditions along an oxic to sulfidic gradient. However not all the authigenic fraction is produced only by post-depositional reactions since some metal fraction present above the background lithogenic concentrations is also due to the flux of metals associated with settling biological material (Nameroff et al., 2004; Tribovillard et al., 2006). We also calculated the enrichment factor of the elements to determine if they are depleted or enriched relative to andesite. The enrichment factors were calculated using the following formula accordingly to Tribovillard et al. (2006): $EF_{element\ x} = (X/Al)_{sample} / (X/Al)_{andesite}$. If EFx is greater (lower) than 1, then the element X is enriched (depleted) relative to average shales.

Table V-1. Average (±sd) concentration and Metal/Al for Andesite in whole rocks from the central Andean volcanic zone in Peru taken from the GEOROC database (Sarbas and Nohl, 2009) and in marine sediments from the present study. Re concentration and Re/Al from andesite taken from Alves et al. (2002).

Metal	Element/Al				
	Andesite			Present study	
	average	sd		average	sd
V/Al $(x10^{-3})$	1.4	± 0.6		7.7	± 3.8
Cu/Al $(x10^{-4})$	4.4	± 3.3		15	± 5.4
Ni/Al $(x10^{-4})$	2.6	± 2.8		23	± 8.6
Mo/Al $(x10^{-5})$	2.5	± 1.9		338	± 341
Cd/Al $(x10^{-6})$	2.6	± 2.4		861	± 560
Re/Al $(x10^{-9})$	1.9			1121	± 459

The biogenic silica was quantified by Fourier transformed infrared spectrometry (FTIR) analyses (Bertaux et al., 1996). The sample preparation for FTIR analysis is described by Bertaux et al. (1996) and is briefly summarized here. Given that a particle size of less than 2 μm is required to avoid excessive scattering of infrared (IR) radiation, approximately 15 mg of dry pre-powdered sample were mechanically ground with small agate balls in an agate vial under acetone and in a cooling chamber for 90 minutes. Then, the solution containing the powdered sample and the acetone was poured onto a watch glass to let the acetone evaporate. After that, 2.5 mg of dry pre-powdered sample were weighed in a high-precision micro balance and 997.5 mg of KBr was added to the sample. Then, the powder containing the sample and KBr was mixed by hand in an agate mortar for 10 minutes and 300 mg of this powder was used to prepare a 13 mm diameter disc, by pressing the mixture in a vacuum die with up to 8 tons.cm^{-2} of compression. Finally, in order to acquire the IR spectra, the discs were placed into a Perkin-Elmer FT 16 PC spectrometer, in the 4000–250 cm^{-1} energy range with a 2 cm^{-1} resolution. In order to quantify the % of biogenic silica from the IR spectra the spectral-energy range between 1315 and 315 cm^{-1} was chosen for calculation since this region yields many absorption features that are relevant for distinguishing the biogenic silica in the mixture. The % of amorphous silica obtained from the FTIR analysis also incorporates other types of amorphous silica (e.g. volcanic ashes) but their concentrations are too low in comparison to the vast abundance of diatoms valves off Peru, thus we consider that the % of amorphous silica obtained through the FTIR analysis reflects principally the % of biogenic silica.

The quantification and characterization of organic matter were done using Rock-Eval 6 that permits evaluation of the evolution of organic compounds during programmed pyrolysis (Lafargue et al., 1998). During the programmed pyrolysis several parameters are used in order to quantify and characterize the organic matter: S1, S2 and S3. S1 (mg HC/g rock) corresponds to the quantity of hydrocarbons (HC) released during the isothermal temperature step at 300 °C and represents the themovaporized free hydrocarbons contained in the rock (Behar et al, 2001). S2 (mg HC/g rock) corresponds to the quantity of HC released between 300 and 650 °C and represents the HC resulting from the cracking of sedimentary organic matter (Behar et al., 2011). Finally, S3 (mg CO$_2$/g rock) represents milligrams of carbon dioxide generated from a gram of sample during temperature programming up to 390 °C (Lafargue et al., 1998; Behar et al., 2001; Peters, 2005). Total Organic Carbon (TOC) is determined by summing the pyrolysable organic carbon (obtained from the S1, S2 and S3) and the residual organic carbon (Behar et al.; 2001). TOC reflects the quantity of OM present in the sediment and can be used to infer past export production.

The Water column Denitrification (WCD) was inferred through δ^{15}N in sedimentary organic matter and compared to those values during the LIA and the last ~150 years obtained from a nearby core (Gutierrez et al., 2009). δ^{15}N analyses were done in the department of Geosciences of the

University of Arizona and were measured on a continuous-flow gas-ratio mass spectrometer (Finnigan Delta PlusXL) coupled to an elemental analyzer (Costech). Standardization was based on laboratory standard acetanilide, precision was better than ± 0.2 (1s). The $\delta^{15}N$ data in core B-6 reported by Gutierrez et al. (2009), and used in the present work as well, were obtained in the same facility. $\delta^{15}N$ data of core B-6 were plotted in the depth axis of core B-14 following the laminae correlations between B-6 and B-14 (see chapter II).

Fish debris were used as indicators of past fish biomass abundance variability. Anchovy vertebrae were used instead of anchovy scales because vertebrae are more resistant to degradation than the fish scales (O'Connell and Tunnicliffe, 2001; Salvatteci et al., 2012). Anchovy vertebrae abundances were transformed to fluxes by multiplying the vertebrae abundances per the mass sedimentation rate (see chapter IV for calculations). The ratio of oceanic species to anchovy scales were used as an indicator of favorable conditions for these species. Higher ratios should indicate an expansion of the habitat favorable for oceanic species. The oceanic species includes sardine (*Sardinops sagax sagax*), jack mackerel (*Trachurus murphyi),* mackerel (*Scomber japonicus*) and "agujilla" (*Scomberesox saurus scombroides)*. Fish debris abundances in core B-14 were obtained from Salvatteci et al. (2012).

V-4.3 Statistical procedures

Pearson correlation coefficients (r) were calculated to establish the relationships between proxies. The probability level was corrected for multiple comparisons by dividing the probability level α (p<0.05) by the number of tests performed (Glantz, 2002), given that 12 test were performed in the data set the corrected probability level was p<0.0042. Finally, in order to reduce the dimensionality of the data set, a Principal Component Analysis (PCA) was applied using the Statistica software to the authigenic metal values and the other proxies. The $\delta^{15}N$ data was not included in the analysis due to the low number of measurements.

V-5. Results

V-5.1 Lithology and chronology

In order to establish the connection between G-10 with B-14 and develop a continuous and reliable record we performed a laminae cross-correlation between G-10 and the 8 cores retrieved off Pisco that are well cross-correlated (Fig. V-2). The first diatom band of the laminated sequence of G-10 (below the homogeneous deposit V) was cross-correlated with the base of the sediment sequence "I" (Fig. V-2). Additional support for the fact that this diatom band is contemporaneous in both cores

came from the conventional ^{14}C ages, in core G-10 the age of this band is 1235 ±30 yr BP while in core B-6 is 1215 ±30 yr BP. Moreover there is a major slump above the sequence "I" that can be observed in G-10 and several other cores in the area, confirming the tie point of core G-10 with the other records. Consequently, the laminated sequences at the base of core B-14 were deposited just after the first diatom band in core G-10 (~89 cm depth Fig. V-2), because the laminated sequences in the base of core B-14 were deposited after the slump V.
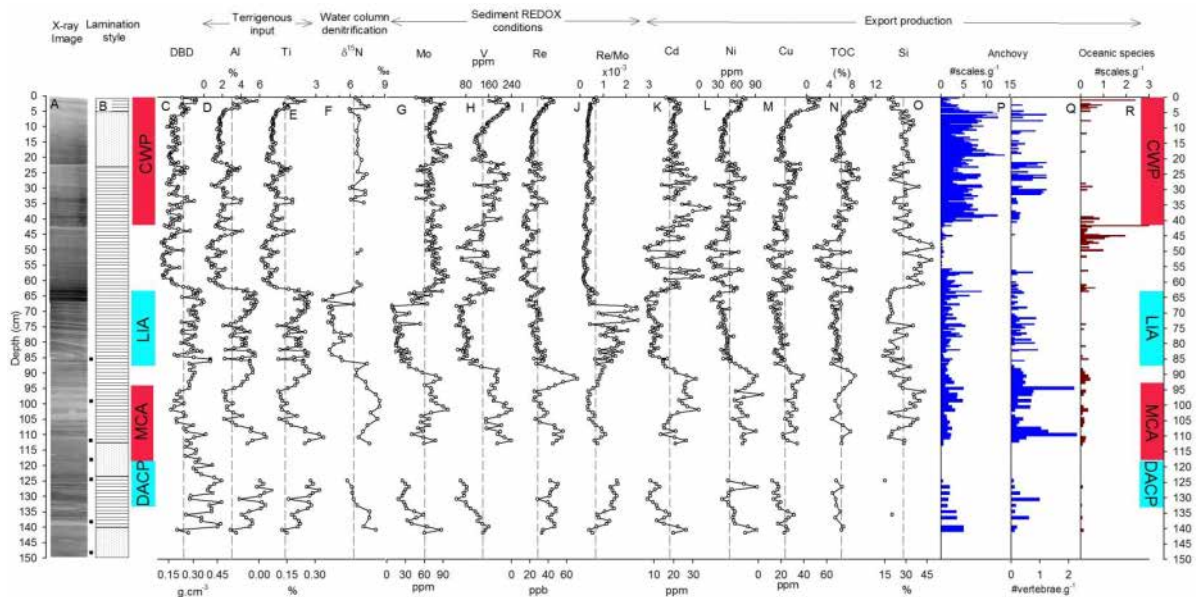
Figure V-3. X-ray images, lamination style, time periods of interest and proxies evaluated in the present study. A) Positive X-ray image of cores B-14 and G-10; the small boxes at the right side of the X-ray image indicate the position of the samples that were dated by ^{14}C in core G-10. B). Simplified lithology, the areas with horizontal lines represent finely laminated sediments and the dotted areas represent mixed sediments or more homogeneous material. C) Dry Bulk Density (DBD), data of core B-14 taken from Salvatteci et al. (2012). D) Al (%), proxy for terrigenous input. E) Ti (%) proxy for terrigenous input. F) $\delta^{15}N$ proxy of water column denitrification, $\delta^{15}N$ data of nearby core B-6 (Gutierrez et al. 2009) were plotted in the depth axis of core B-14 following the laminae correlations between B-6 and B-14 (see chapter II). G) Authigenic molybdenum (Mo, ppm), proxy for sediment REDOX conditions. H) Authigenic vanadium (V, ppm), proxy for sediment REDOX conditions. I) Authigenic rhenium (Re, ppb), proxy for sediment REDOX conditions. J) Re/Mo $(x10^{-3})$, proxy to differentiate anoxic vs. suboxic conditions. K) Authigenic cadmium (Cd, ppm), paleoproductivity proxy. L) Authigenic nickel (Ni, mg.Kg^{-1}), paleoproductivity proxy. M) Authigenic copper (Cu, mg.Kg^{-1}), paleoproductivity proxy. N) Total Organic Carbon (TOC, %), proxy for export production. O) Biogenic Silica (Si%), proxy of diatom production. P) Anchovy (*Engraulis ringens*) scale abundances. Q) Anchovy (*Engraulis ringens*) vertebrae abundances, R) Oceanic species scales, which includes sardine (*Sardinops sagax sagax*), jack mackerel (*Trachurus murphyi*), mackerel (*Scomber japonicus*) and agujilla (*Scomberesox saurus scombroides*). Fish debris data of core B-14 taken from Salvatteci et al. (2012). The vertical dashed lines indicate the average of each proxy. The colored boxes at the right and left side indicate the Current Warm Period (CWP from ~1900 to the present), Little Ice Age (LIA, from 1500 to 1850 AD), the Medieval Climate Anomaly (MCA, from 900 to 1350AD) and the Dark Ages Cold Period (DACP, from 500 to 900 AD). The DACP, MCA and LIA dates ranges from Yan et al. (2011) and Graham et al. (2011).

The assembled record shows that the sediment structures corresponding to the periods of interest (DACP, MCA, LIA and CWP) are mainly composed by undisturbed laminated sediments (Figs. V-3A and B). The assembled sediment record starts with a homogeneous sediment sequence (Figs. V-3A and B). Above this homogeneous deposit an interval containing laminated sequences, which corresponds to great part of the DACP, can be observed up to ~125 cm depth, where another homogeneous deposit is located until ~113 cm depth (Figs. V-3A and B). This last homogeneous deposit contains part of the MCA period. The remaining part of the MCA (from ~113 to ~95 cm depth) shows millimeter-scale laminae. The sediment sequences associated with the LIA period show the finest laminated sequences in the entire record. The transition between the LIA and the CWP shows thick diatom bands interspersed with laminated sequences. The CWP shows laminated sediments from ~40 cm to ~23 cm and then from ~4 to the top. The homogeneous section from ~23 to 4 cm depth (Fig. V-3B) was probably caused by bioturbation or by rapid sedimentation event since the $^{210}Pb_{ex}$ profile is relatively constant in this part of the record (Salvatteci et al. *submitted*). An angular unconformity can be observed in core B-14 at ~4 cm depth (Figs. V-2 and V-3). Finally, there is a major change in density at ~62.5 cm depth (Fig. V-3C) which coincides with a change in sediment density previously reported in a nearby core (Sifeddine et al., 2008; Gutierrez et al., 2009). Based on the sedimentological description and given that we couldn't identify the origin of the homogeneous deposits (bioturbation or slump) in core G-10 we didn't develop any proxy in these sequences to avoid uncertainty in the data set.
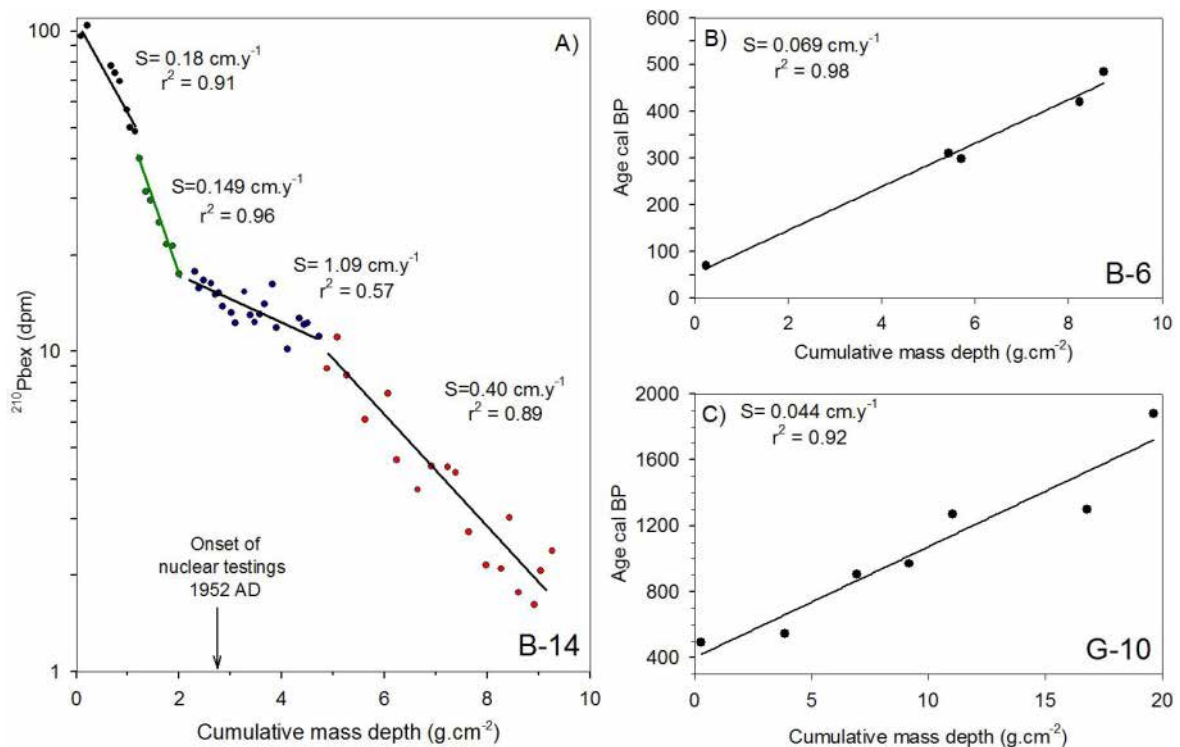
Figure V-4. Cumulative mass-depth age models showing the sedimentation rates used in the present work. A) Core B0506-14, showing 4 distinct sedimentation rates. B) Core B0405-6, ^{14}C data taken from Gutierrez et al. (2009). C) Sedimentation rates in core G-10. The local reservoir (ΔR) used to calibrate the ^{14}C ages in cores B-6 and G-10 was 367±40 years

163

The ^{210}Pb$_{ex}$ cumulative mass depth profile shows four distinct sections with different sedimentation rates (Fig. V-4A). The first section ranges from the top to 4.3 cm with a sedimentation rate of 0.184 cm.y^{-1}; the second ranges from 4.3 to 8.5 cm with a sedimentation rate of 0.149 cm.y^{-1}; the third extends from 8.5 to 23.2 cm with a high sedimentation rate of 1.09 cm.y^{-1} and the last section ranges from 23.2 to 46.6 cm and has a sedimentation rate of 0.402 cm.y^{-1}. The chronological model was adjusted using the ^{241}Am profile by assigning the date 1952AD to 15.6 cm depth. The sedimentation rate for the fourth section (0.402 cm.y^{-1}) was extrapolated up to 62.5 cm where the sedimentary shift is located. The angular unconformity at ~4 cm in core B-14 was identified as a hiatus of ~4 years that occurred approximately at ~1982 AD. Figure V-4B shows the cumulative mass depth vs. age cal BP in core B-6, showing the sedimentation rate used to determine the B-14 ages prior to the sedimentary shift (yellow lines in Fig. V-2). The sedimentation rate for the pre-shift period in core B-6 was estimated to be 0.069 cm.y^{-1} (Fig. V-4B). In core G-10 the cumulative mass depth vs. age cal BP yields a sedimentation rate of 0.044 cm.y^{-1} (Fig. V-4C). The differences in the sedimentation rates (between periods) and the different subsampling thickness (between cores) indicate that the average time spam of each sampled interval during the DACP, MCA, LIA and CWP is 21.9, 21.9, 7.5 and 1.1 years respectively.

V-5.2 Data presentation: authigenic values vs. enrichment factors

Enrichment factors (i.e. the degree of enrichment of a given element compared with the average shale composition) are often used to reconstruct the environmental setting at the time of deposition, but trace elements may acquire spurious correlations when normalized through division by an immobile element during diagenesis (Van der Weijden, 2002). Additionally the normalization procedure may increase, decrease, or even change sign of the correlations between unmodified variables (Van der Weijden, 2002). Authigenic trace element concentrations that were not correlated like Ni with Mo (Table 2, r = -0.10, n = 229, p>0.05) or Re with Cd (Table 2, r = 0.08, n = 229, p>0.05) show a strong shared variability when the data were transformed to EF (Ni and Mo: r = 0.76, n = 229, p<0.001 and Re and Cd: r = 0.73, n = 229, p<0.001). Additionally the correlation coefficients of the authigenic paleoproductivity proxies with TOC increased when the trace elements were normalized. For example the r values of authigenic Ni, Cu and Cd concentrations with TOC were 0.72, 0.80 and 0.57 respectively (Table 2), while the shared variability of Ni (EF), Cu (EF) and Cd (EF) with TOC/Al were 0.90, 0.93 and 0. 90, respectively.

Table V-2. Correlation matrix based on the Pearson correlation coefficients (r values) for authigenic metal concentrations (n = 229); biogenic Silica (n = 119); TOC (n = 202) and δ^{15}N (n = 77) in cores B-14 and G-10. Bold values indicate significant values after correcting for multiple comparisons (p < 0.004). The probability level was corrected for multiple comparisons by dividing the probability level α (p<0.05) by the number of test (12) perfomed (Glantz, 2002).

		Terrigenous input			Sediment REDOX conditions				OMZ intensity	Export production				
		DBD (g.cm^{-3})	Al %	Ti%	Mo ppm	V ppm	Re ppb	Re/Mo	δ^{15}N (‰)	Ni ppm	Cu ppm	Cd ppm	TOC (%)	Biogenic silica (%)
Terrigenous input	DBD (g.cm^{-3})	1												
	Al %	**0.67**	1											
	Ti%	**0.65**	**0.98**	1										
Sediment REDOX conditions	Mo ppm	**0.39**	**0.43**	**0.46**	1									
	V ppm	0.01	**0.08**	**0.07**	**0.10**	1								
	Re ppb	**0.39**	**0.52**	**0.50**	**0.05**	**0.34**	1							
	Re/Mo	**0.40**	**0.51**	**0.53**	**0.78**	0.03	**0.17**	1						
OMZ intensity	δ^{15}N (‰)	0.08	**0.12**	**0.14**	**0.47**	**0.36**	0.09	**0.35**	1					
Export productivity	Ni ppm	**0.18**	**0.29**	**0.26**	0.01	**0.40**	**0.58**	**0.06**	**0.24**	1				
	Cu ppm	**0.25**	**0.42**	**0.38**	0.02	**0.55**	**0.64**	**0.09**	0.06	**0.53**	1			
	Cd ppm	**0.16**	**0.13**	**0.15**	**0.49**	**0.34**	0.01	**0.29**	**0.55**	0.09	0.04	1		
	TOC (%)	0.02	**0.05**	0.03	**0.06**	**0.66**	**0.33**	0.01	**0.11**	**0.51**	**0.64**	**0.32**	1	
	Biogenic silica (%)	**0.39**	**0.57**	**0.51**	**0.23**	0.09	**0.23**	**0.33**	**0.39**	**0.15**	**0.29**	0.03	**0.23**	1

These problems may arise when the coefficient of variation (standard deviation divided by the mean) of Al concentrations is large compared to the coefficients of variation of the other trace elements. In the present work the coefficient of variation of Al (0.53) was relatively high in comparison to Ni (0.33), Cu (0.37), Cd (0.38), Mo (0.39), V (0.35) and Re (0.37). Thus, the changes observed in the modified variables may be due to the relatively high coefficient of variation of Al. Consequently, in the following sections we present the authigenic concentrations of the trace elements instead of the enrichment factors. However, the average enrichment factor of each element was calculated to determine which elements exhibit the highest enrichments relative to andesite (Fig. V-5). Re, Cd and Mo exhibited the highest enrichments factors (average ±sd): 578±236; 334 ±218 and 131 ±134; Ni and V show a moderate enrichment of 7.9 ±3.4 and 4.7 ±2.8 respectively. Finally Cu showed the lowest enrichment factor: 2.3 ±1.2. The high and moderate enrichment factors of Re, Cd, Mo, Ni, and V support their use as paleoredox or paleoproductivity proxies.
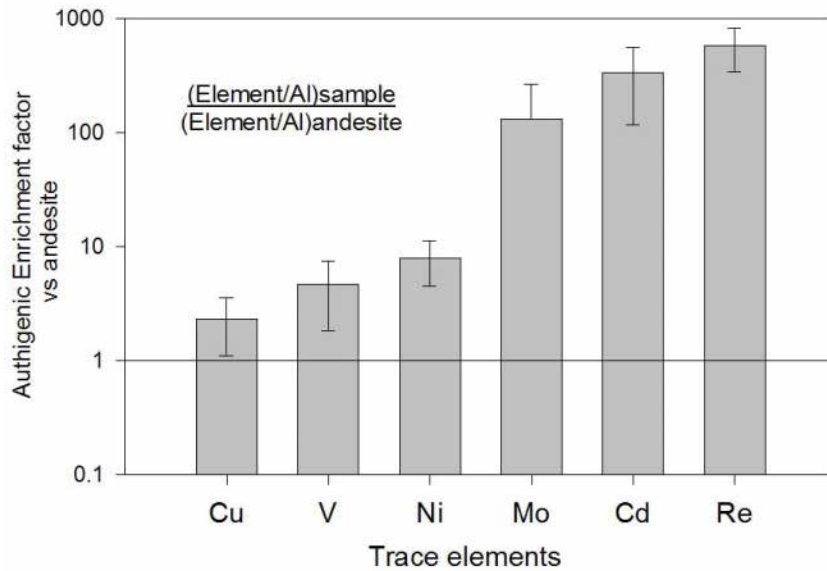
Figure V-5. Enrichment factors for several trace elements vs. average andesitic composition and standard deviation (sd). The element/Al from andesite were obtained from the GEOROC database (Sarbas and Nohl, 2009) taking into account the elements concentrations in andesite from whole rocks from the central Andean volcanic zone in Peru. Andesite Re/Al ratio was taken from Alves et al. (2002). All the data available from cores B-14 and G-10 were used to calculate the averages. The -sd of Mo is off scale.

V-5.3 Terrigenous input

Al and Ti content show similar multi-decadal to centennial-scale variability throughout the record and are highly correlated (Table 2). Al and Ti% follow the same downcore changes observed in the Dry Bulk Density (DBD) values (Figs. V-3C, D and E) and also show a strong correlation with the DBD values (Table 2). Additionally, there is a strong negative correlation of the biogenic silica contents with DBD, Al and Ti (-0.63, -0.75 and -0.72, n = 119, p < 0.001; Table 2). These results are expected because Al and Ti% represent the detrital fraction which is denser than the other components of the sedimentary matrix (i.e. OM, biogenic silica and calcium carbonate).

The terrestrial runoff proxies (Al and Ti) show lower terrestrial input during the last phase of the MCA (~1130 to 1330AD) and post-LIA, and higher values in the rest of the record (Figs. V-6A and B). During the LIA there is a period from ~1550 to 1750 AD associated with reduced terrigenous input in comparison with the start and end of this period. Additionally, several short periods of increase (decrease) in DBD, Al and Ti values can be observed during the periods characterized by low (high) terrigenous input (Figs. V-3C, D and E). The transition from the MCA to the LIA shows a gradual increase in Al and Ti contents, while the transition from the LIA to the CWP shows an abrupt decrease (Figs. V-6A and B).
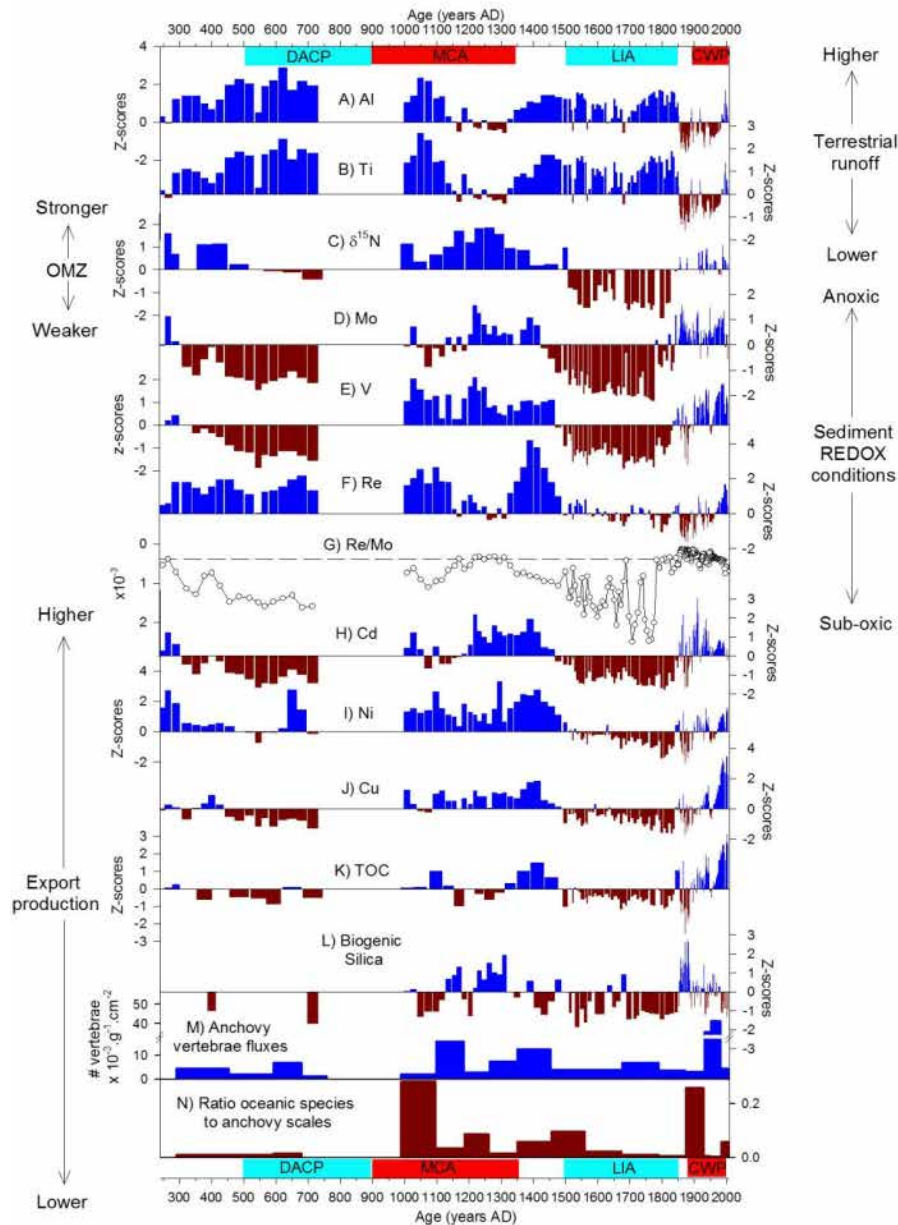
Figure V-6. Standarized values of the proxies evaluated in the present study. A) Aluminum (Al, %) proxy for terrestrial runoff. B) Titanium (Ti, %) proxy for terrestrial runoff . C) δ^{15}N, proxy of water column denitrification, data of the LIA and CWP taken from Gutierrez et al. (2009). D) Molybdenum concentrations (ppm) proxy for sediment REDOX conditions. E) Vanadium concentrations (ppm), proxy for sediment REDOX conditions. F) Rhenium concentration (ppb), proxy for sediment REDOX conditions. G) Ratio Re/Mo x 10^{-3}, proxy to differentiate anoxic versus sub-oxic conditions, the dotted line indicate the seawater value of Re/Mo = 0.4 x 10^{-3}, Crusius et al. (1996). H) Cadmium concentrations (ppm), paleoproductivity proxy. I) Nickel concentrations (ppm), paleoproductivity proxy. J) Cupper concentrations (ppm), paleoproductivity proxy. K) Total Organic Carbon (TOC, %), proxy for export production. L) % Biogenic silica, proxy of diatom export production. M) Anchovy vertebrae fluxes (# vertebrae.10[3].y[-1].cm^{-2}). N) Ratio of oceanic species to anchovy scales, oceanic species include sardine (*Sardinops sagax sagax*), jack mackerel (*Trachurus murphyi*), mackerel (*Scomber japonicus*) and agujilla (*Scomberesox saurus scombroides.* Highlighted areas indicate the Current Warm Period (CWP from ~1900 to the present), Little Ice Age (LIA, from 1500 to 1850AD) and the Medieval Climate Anomaly (MCA, from 900 to 1350AD). The LIA and MCA dates ranges from Graham et al. (2011).

V-5.4 Water column oxygenation and sediment REDOX conditions

The δ^{15}N profile shows large centennial scale changes of up to 3.1 ‰, suggesting less water column denitrification and hence a weaker OMZ during the LIA, and more intense water column denitrification and OMZ during the CWP and during the MCA (Fig. V-6C). During the section belonging to the RWP the two δ15N values are high (7.7 ‰). The δ15N values of the DACP are also relatively high (6.3 ±0.64‰, n = 5) and do not show large changes. In contrast during the MCA the average δ15N values were higher in comparison with the other periods (7.8 ±0.63‰, n =10), and shows a maxima in WCD between ~1150 and ~1300 AD. The LIA period shows the lowest values (4.7 ±0.69‰, n = 24) in comparison with the other periods. Finally, the CWP shows high values (6.7 ±0.44‰, n = 30) but not as high as during the RWP and the MCA. Finally, the CWP shows high values (6.7 ±0.44‰, n = 30) but not as high as during the MCA. Remarkably, the δ15N profile also shows a coherent pattern with Mo, V and Re/Mo (Figs. V-6C, D and G) and exhibits high and significant correlations (positive with the former two, and negative with the ratio Re/Mo; Table 2). However, during the DACP the δ^{15}N values are not low, whereas Mo and V showed low concentrations and the ratio Re/Mo was high.

Authigenic Mo and V concentrations indicate less authigenic enrichment (sub-oxic conditions) during the cold periods (DACP and LIA), and more authigenic enrichment (anoxic conditions) during the last phase of the MCA and from the end of the LIA to the present (Figs. V-6C, D and F). The Re/Mo ratio, that serves to differentiate anoxic (with available H_2S) conditions and sub-oxic conditions, is higher during the DACP and LIA, giving support to the dominance of suboxic conditions in the surface sediments. In contrast, during the last phase of the MCA (1130 to 1340 AD) and from the end of the LIA until the twentieth century, the Re/Mo values were close to or below 0.4 x 10^{-3} (dashed line in Fig. V-6G) which is similar to the seawater ratio (Crusius et al., 1996) and imply anoxic conditions. The main difference between Mo and V downcore profiles is the strong variability of the V contents from the end of the LIA to the CWP, which is better observed in the depth-scale plot (Figs. V-3G and H). V and Re show the strongest correlation among these three proxies as expected due to their behavior in the sediments. However their relationship is not so high (Table 2) probably due to the high frequency variability in the V profile after the LIA not observed in the Re profile (Figs. V-3H and I).

A closer look into the MCA reveals that this NH warm period is characterized by two different stages with contrasting characteristics in the oxygen content in the sediment-water interface and the water column. From ~1000 to ~1150 AD relatively lower values of Mo, higher values of V and Re, higher Re/Mo values, and relatively lower δ^{15}N values are all consistent with sub-oxic conditions in the sediment-water interface and a more ventilated water column. However the inferred

ventilation in this stage of the MCA is not as intense as during the LIA. In contrast, from ~1150 AD to the end of the MCA (~1350 AD) there is a concurrent increase in Mo, V, very low values of Re/Mo (ratios near to 0.4 x10^{-3}), and higher δ^{15}N, that indicate anoxic conditions in the sediment-water interface and an intense OMZ. The two different stages further indicates that the MCA is not a homogeneous period and that it is characterized by strong multi-decadal variability in oxygen content in the sediment-water interface and in the water column, which is also observed in the terrigenous input proxies.

Changes in OMZ intensity and sediment redox conditions were more gradual during the transition between a warm period and a cold period in comparison with the transition between a cold and a warm period. The MCA-LIA transition shows a gradual change from anoxic to sub-oxic conditions while the LIA-CWP transition show an abrupt change from sub-oxic to anoxic conditions. The transition MCA-LIA, which is characterized by an increase in terrestrial input (Figs. V-6A and B), was followed first by a decrease in Mo and then by a decrease in V (Figs. V-6D and E), as expected due to the behavior of these elements to a gradual change from anoxic (available H$_2$S) to suboxic conditions. The Re/Mo and δ^{15}N values also confirm this gradual pattern (Figs. V-6F and G) implying that the conditions from anoxic to suboxic were gradual in the water column and in the sediments (Fig. V-6G). In contrast the LIA-CWP transition was characterized by an abrupt change from sub-oxic to anoxic conditions as evidenced by the Re/Mo ratio that reached a value ~0.4 x10^{-3} in ~1760AD and was maintained near this value since that date until the twentieth century. Remarkably, the gradual change from anoxic to suboxic conditions occurred when the terrestrial input proxies were increasing, while the change from sub-oxic to anoxic conditions was reached when the terrigenous input was still high (Fig. V-6A and B).

V-5.5 Paleoproductivity proxies

Cd, Ni, Cu authigenic contents and TOC show similar centennial-scale variability, with high values during NH warm periods and low values during NH cold periods (Figs. V-6H, I, J and K). However during the DACP, Ni authigenic contents show relatively high values that are not reproduced by the other paleoproductivity proxies. Consistent with the proxies for oxygenation, the paleoproductivity proxies also show a gradual decrease during the MCA-LIA transition and a more abrupt change during the LIA-CWP transition. Cd, Ni and Cu show strong variability during the LIA-CWP transition (Fig. V-3K, L and M) probably resulting from the high sedimentation rates resolving high frequency variations. During the LIA-CWP transition the values of the authigenic productivity proxies in the laminated sections between the diatom bands are similar to those values recorded from ~1900 to ~1950AD (Fig. V-3K, L and M).

There are subtle differences among the productivity proxies that are better observed in the depth-scale plot (Figs. V-3K, L and M). Ni and Cu authigenic contents show higher correlation (Table 2, r = 0.73, n = 229, p<0.001) than Ni with Cd (r = 0.30, n = 229, p<0.001) or Cu with Cd (r = 0.21, n = 229, p<0.001). The similarity between the Ni and Cu profiles is likely due to the fact that both metals are exported to the sediments in association with organometallic complexes, while the differences with the Cd profile may probably arise from post-depositional processes (Tribovillard et al., 2006). The shared variability between Ni and Cu with TOC (Table 2; r = 0.72, n =229, p<0.001 and r = 0.80, n = 229, p<0.001) is higher than that of Cd and TOC (Table 2; r = 0.57, n = 229, p<0.001). Additionally, the increment in TOC% in the last ~50 years is replicated by the Ni and Cu profiles but not by the Cd profile (better observed in the depth-profile plot, Figs. V-4K, L, M and N). These results suggest that authigenic Ni and Cu are better proxies to OM flux than the authigenic Cd.

Higher biogenic silica contents are associated with visible diatoms bands in the X-ray images, which are present during the LIA-CWP transition and during some periods within the MCA and CWP (Fig. V-6L). The biogenic silica shows a strong negative relationship with Ni, Cu and TOC (Table 2; r = -0.39 n = 229, p<0.001; r = -0.54 n = 229, p<0.001 and r = - 0.48, n = 229, p<0.001). The highest values of biogenic silica during the MCA (from ~1140 to ~1310 AD) coincide in part with the anoxic episode in the sediments as recorded by the Re/Mo ratio and the strong WCD. The biogenic silica show higher relationships with proxies related to oxygenation in the water column as δ^{15}N (Table 2; r = 0.63, n = 77, p<0.001), and in the sediments as inferred by the Mo and Re/Mo (Table 2; r = 0.48, n = 119, p<0.001 and r = -0.58, n = 119, p<0.001 respectively).

The relationships between the paleoproductivity proxies with the WCD and the sediment redox conditions during the MCA-LIA and the LIA-CWP transitions indicate that changes in WCD and seafloor oxygenation occurred before the changes in export production (Fig. V-6). The highest values of the paleoproductivity proxies prior to the CWP occurred during the MCA-LIA transition (at ~1400 AD), 150 years after the strongest WCD observed in the record (Figs. V-6C, H, I, J, and K), and when the trend towards lower δ^{15}N and higher Re/Mo ratios had already started (Fig. V-6). During the LIA-CWP transition, the anoxic conditions on the seafloor also occurred before (~1760 AD) the increase in export production (~1850 AD; Fig. V-6G). The WCD in this period can not be evaluated because any δ^{15}N measurements were realized during this transition.

V-5.6 Anchovy and oceanic species changes

The warm periods (MCA and CWP) are associated with higher anchovy vertebrae fluxes and more oceanic species than the cold periods (Figs. V-6M and N). The high resolution fish debris record shown in Figures V-3P, Q and R was lumped into coarser samples of ~35 years for the past

150 years and 100 years for the LIA, MCA and DACP periods. This procedure was done to obtain sufficient fish debris to calculate the vertebrae fluxes and the ratios. Anchovy vertebrae fluxes (average ±sd) show higher values during the MCA (9.2 ±9.7) and the CWP (34.5 ±25.4) in comparison with the DACP (4.9 ±5.6) and LIA (4.9 ±2.7). Additionally the MCA and the CWP show higher oceanic to anchovy scales ratios than the colder periods (Fig. V-6N).

V-5.7 Principal Components Analysis (PCA)

The PCA results indicate that 79.9% of the total variance of the data set could be expressed by two principal components (PC; Figs. V-7 and V-8). Mo/Re ratio was used instead of Re/Mo so that all the redox proxies indicate anoxic conditions with higher values. Re authigenic concentrations were not used in the PCA to assure independence in the data set. The PC1 (Figs. V-7 and V-8) explained 41.7% of the data set variance and displayed the highest positive factor loading for Mo (0.93) and Mo/Re (0.74). Al and Ti, proxies for terrestrial input, displayed high negative factor loadings (-0.80 and -0.81 respectively). Given the highest loadings associated with proxies of sediment redox conditions, the PC1 is interpreted to represent the sedimentary redox conditions, which exhibit a strong negative correlation with the terrigenous input proxies. The PC1 and the $\delta^{15}N$ show a strong and significant shared variability ($r^2 = 0.5$, n = 77, p<0.001).
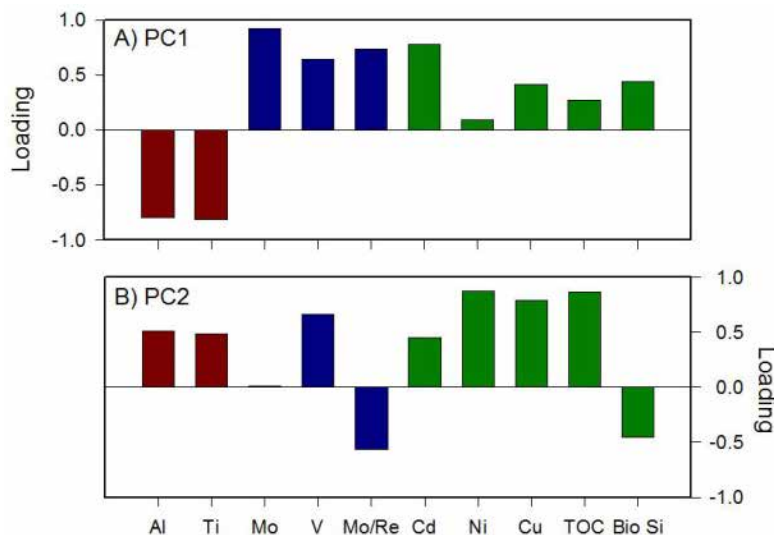
Figure V-7. Proxies loadings on PC1 and PC2. PC1 and PC2 explain 41.7% and 38.2 % of the data set variance respectively. Red bars indicate terrigenous input proxies, blue bars indicate OMZ intensity and green bars indicate productivity proxies.

PC2 explained 38.2% of the data set variance (Figs. V-7 and V-8). Ni, Cu and TOC, which are productivity proxies, showed the highest loadings (0.88, 0.79 and 0.87 respectively). Given the high correlation of Ni and Cu with TOC (Table 2), PC2 could represent the export production determined by a combination of primary productivity, transport processes to the sediments and remineralization processes. Biogenic silica shows relatively low loadings for PC1 (0.44) and PC2 (-0.46), and high loadings in the PC3, however PC3 explains only 7.2% of the data set variance and consequently the PC3 will no longer be discussed.
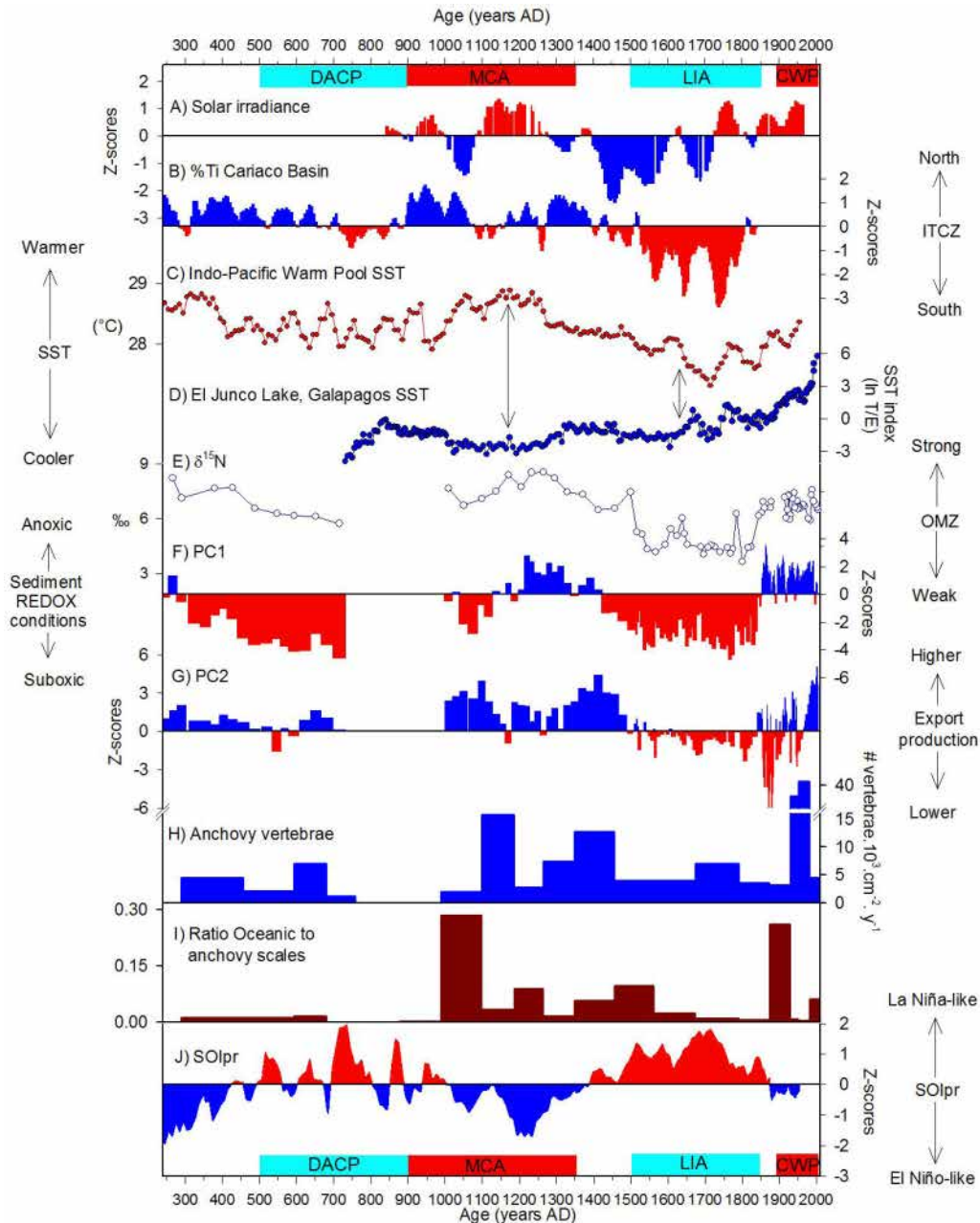
Figure V-8. Linkage between the PC1 and PC2 with solar irradiance, ITCZ displacement, SST reconstructions in the western and the SOIpr. A) Solar irradiance (Bard et al., 2001). B) 3-point average of Ti% in Cariaco Basin, (Haug et al., 2001). C) Indo Pacific Warm Pool SST reconstruction (Oppo et al., 2009). D) Eastern Equatorial Pacific SST reconstruction (ln of the number of tychoplanktonic to epiphytic diatoms in El Junco Lake, Galapagos (Conroy et al. 2009). E) Water column denitrification as inferred by δ15N values. F) First principal component (PC) that explains 41.7% of the data set variance and could represent sediment REDOX conditions. G) PC2 that explains 38.2% of the data set variance and could represent export production. H) Anchovy vertebrae fluxes (# vertebrae.10³.y⁻¹.cm⁻²). I) Ratio of oceanic species to anchovy scales, oceanic species include sardine (*Sardinops sagax sagax*), jack mackerel (*Trachurus murphyi*), mackerel (*Scomber japonicus*) and agujilla (*Scomberesox saurus scombroides.* J) Southern Oscillation Index based on precipitation records (SOIpr) in the western and eastern Tropical Pacific (Yan et al., 2011b), the SOIpr shows an inverse pattern in comparison with the results obtained from the Pisco record. Highlighted areas indicate the Current Warm Period (CWP from ~1900 to the present), Little Ice Age (LIA, from 1500 to 1850AD) and the Medieval Climate Anomaly (MCA, from 900 to 1350AD). The LIA and MCA dates ranges from Graham et al. (2011).

V-6. Discussion

Organic and inorganic proxies developed in finely laminated sediments off Peru were used to define the mean state of the PUE in contrasting periods (RWP, DACP, MCA, LIA and CWP) where the response of the tropical Pacific is controversial. The total variance of the data set can be explained by two principal components: PC1 and PC2 that could represent the sedimentary redox conditions and the export production respectively. The DACP is characterized in our records by a relatively weak OMZ, a relatively high export production and sub-oxic conditions in the sediments. The MCA is characterized by two different phases; the first one (from ~1000 to ~1150 AD) that shows a relatively weak OMZ (in comparison with the second MCA phase, but stronger in comparison with the DACP and LIA periods) and suboxic conditions in the sediments, and the second one (from ~1150 to ~1350 AD) that shows a stronger OMZ, enhanced sedimentary reducing conditions; noticeably the export production in both stages is relatively high (Fig. V-8G). Consequently, the second phase of the MCA can be catalogued as La Niña-like conditions, but the older phase can not be defined as El Niño or La Niña-like conditions. The LIA was characterized by a weaker OMZ, low productivity, and sub-oxic conditions in the sediment, thus El Niño-like condition during this period could be defined (Gutierrez et al., 2008). Finally the CWP was dominated by a stronger OMZ, high productivity, and sedimentary anoxia; these conditions are associated with normal/La Niña-like conditions. To elucidate the mechanisms that controlled the productivity and OMZ intensity off Peru during the last 2 millennia, the results of the present work are compared with other paleorecords in the following sections.

V-6.1 Changes in terrestrial run-off as records of global climatic periods

The terrestrial run-off proxies in sediment records off Pisco are coherent with changes in precipitation on the continent, registering low input during the last phase of the MCA (from ~1130 to 1350 AD) and during the CWP. The terrestrial run-off proxy (Al%) developed in the present study is compared with other hydrological proxies from several locations in order to test if the changes in the Al% are consistent with latitudinal displacements of the ITCZ (Fig. V-9). The latitudinal position of the ITCZ is associated with changes in Northern Hemisphere temperature (Fig. V-9A), migrating to the north (south) during warm (cold) periods. These latitudinal changes in the ITCZ position are reflected in the Ti concentrations (Fig. V-9B) in the varved sediments from the Cariaco Basin (~10 °N on northern Venezuela). During the MCA (LIA) the Ti% record shows high (low) values implying that the ITCZ migrated to the north (south) (Haug et al., 2001; Peterson and Haug, 2006). The multidecadal to centennial-scale latitudinal changes in the position of the ITCZ, indicating lower precipitation during the MCA in comparison to the LIA, were also registered by a speleothem oxygen isotope record ($\delta^{18}O$) of the past ~900 years (Fig. V-9C) from northeastern Peru (Reuter et al., 2009), and in an authigenic calcite record of precipitation (Fig. V-9D) from a varved lake in the Central

Peruvian Andes (~10.7 °S) (Bird et al., 2011). The main difference of our record and the Pumacocha record (Bird et al., 2011) is that during the DACP the Pisco cores suggest higher terrestrial input. The Al% in the Pisco cores agrees in general with the precipitation records in land, implying that if a good chronological framework is developed, the marine sediments of the continental margin can be used to record the South American Summer Monsoon changes which itself is highly sensitive to the ITCZ variability (Bird et al., 2011).
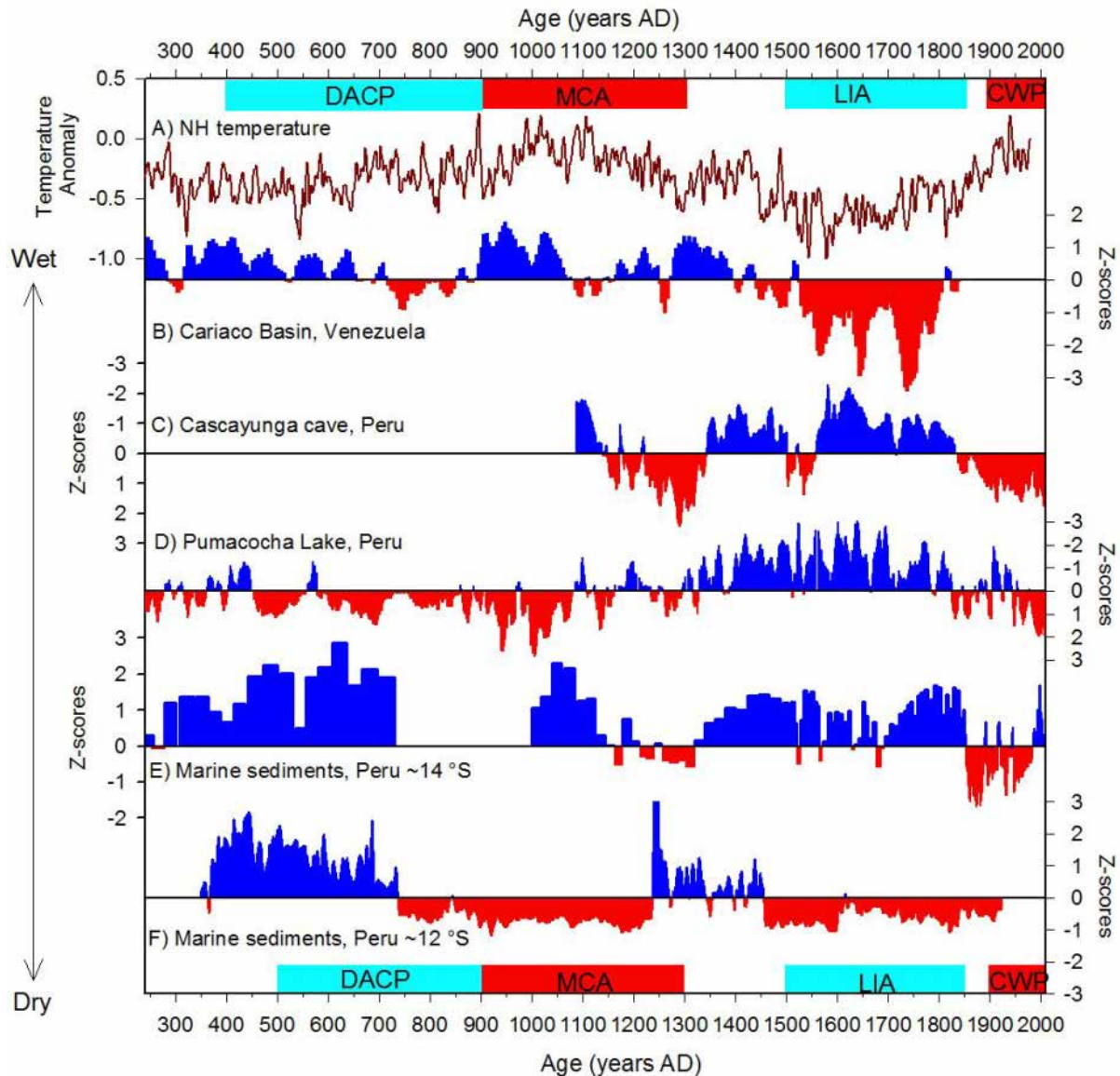
Figure V-9. Northern Hemisphere temperature reconstruction, ITCZ displacement, and hydrological proxies in Peru. A) 5-point average of the Northern Hemisphere temperature anomaly (Moberg et al., 2005), B) 3-point average of Ti% in Cariaco Basin, (Haug et al. 2001), C) 5-point average of Cascayunga cave speleothem rainfall $\delta^{18}O$ (Reuter et al., 2009), D) 5-point average Pumacocha $\delta^{18}O_{cal}$ record (Bird et al., 2011), E) Al content in the present study, F) Lithic concentration in a marine sediment core retrieved off Callao (~12 °S) (Rein et al., 2005). The series were smoothed using a running mean when indicated and then normalized to a standard Z-score.

The lithic concentrations registered in a marine sediment core at ~12 °S were used as a proxy for terrestrial input by Rein et al. (2004; 2005) and show a period between ~750 to ~1250 AD (in part coinciding with the MCA) with reduced lithic contents, that was interpreted as a dry period in Peru. The only similarity between the Callao record and our record is the high values during the DACP. While the radiochronological differences between our record and the Callao record may be related to different delta-R estimates, the nature of the MCA in the Pisco and Callao record can not be explained only by chronological misfits. Multiple lines of evidence indicate that the MCA was characterized by a range of temperatures, hydroclimate and marine changes instead of uniformly warmer temperatures (Bradley, 2000; Bradley et al., 2003; Graham et al., 2011) instead of a long period with severe drought as interpreted by Rein et al. (2004). Our record of terrestrial input (Fig. V-9E) shows a strong multi-decadal variation during the MCA that is consistent with the range of temperatures, hydroclimate and marine changes that characterized the MCA. Moreover the terrigenous input proxy in our data set displays a similar pattern than the rainfall reconstruction from continental records in Peru (Reuter et al., 2009; Bird et al., 2011), thus confirming the multidecadal climatic variability during the MCA.

V-6.2 Peruvian Upwelling Ecosystem response to global changes

The PC1 and PC2 serve to show the response of the PUE to global changes. First, PC1 shows that the cold periods (i.e. DACP and LIA) are associated with weaker reducing conditions in the seafloor, that the MCA show 2 phases, and that the CWP shows strong reducing conditions in the sediments (Fig. V-8). Second, the PC1 shows the gradual tendency towards seafloor sub-oxic conditions from ~1300 to 1760 AD, and the abrupt change from the end of the LIA to the CWP. Third, PC2 suggests that only the LIA climatic conditions caused considerable changes in the export production off Peru. Additionally, at centennial-scale the PC1, PC2 and the WCD were strongly coupled from ~1150 to the date. In contrast from ~250 to ~1150 AD the export production and WCD are decoupled with the sedimentary redox conditions.

The OMZ intensity and the sediment redox conditions have varied considerably throughout the last 2 millennia, and these changes show a strong similarity with the solar irradiance, ITCZ displacement and climate changes in the Tropical Pacific (Fig. V-8). Northern Hemisphere cold periods (DACP and LIA) are associated with weaker OMZ and sedimentary sub-oxic conditions while the globally warm periods (or the last phase of the MCA) are associated with stronger OMZ and bottom anoxia (Fig. V-8). The gradual weakening of the OMZ intensity and benthic reducing conditions from the last phase of the MCA to ~1800 AD (Fig. V-8) is also coherent with a tendency towards lower solar irradiance (Fig. V-8A) associated with a gradual southward displacement of the ITCZ (Fig. V-8B). During the MCA, the solar irradiance reconstruction (Fig. V-8A) shows two

phases as observed in our data, the first one from 1000 to ~1100 with low solar irradiance values and the second one from ~1100 to ~1250 AD; the precipitation records (Figs. V-9C and E) also show this pattern. The period of high solar irradiance coincides with the warmest SST in the Indo-Pacific Warm Pool (Oppo et al., 2009) and with very low SST reconstruction in Galapagos (Conroy et al., 2009) originating a large west-east gradient (Figs. V-8C and D). During the MCA, the strongest OMZ was found precisely during this period (Fig. V-8E). In contrast the anoxic conditions in the sediments started after this maximum gradient. The sub-oxic conditions during the LIA inferred by the Re/Mo ratio confirm the results of Gutierrez et al. (2009) and Sifeddine et al. (2008) obtained from different proxies.

The export production has also varied considerably and these changes are also associated with climate changes in the Tropical Pacific (Fig. V-8G). Higher export production, as inferred by the PC2, characterizes the DACP, the MCA, the LIA-CWP transition and the CWP while lower export production characterizes the LIA (Fig. V-8G). Additionally, high values of biogenic Silica are observed during great part of the MCA in comparison with the LIA, which also support the enhanced productivity during the MCA. The OMZ intensity change from the MCA termination towards the LIA termination is also observed in the export productivity record (Fig. V-8G). In summary, the export production was favored during both Northern Hemisphere warm periods (MCA) and global warm period (CWP) and during the cool DACP, whereas it was extremely depressed during the cold LIA.

The idea of La Niña mean-state conditions during the MCA is partially supported by the results of the present work. In our data, the MCA is characterized by two different stages; the first one (from ~1000 to ~1150 AD) that shows a weaker OMZ and suboxic sediments, while the second stage (from ~1150 to ~1350 AD) shows a stronger OMZ and anoxic sediments (Fig. V-8E and F). In contrast the export production is relatively high during all the MCA, and do not follow the pattern observed with the OMZ intensity variability. In summary, the existence of two different stages with differences in water column conditions but with high productivity partially supports the hypothesis of La Niña-like mean state conditions (Cobb et al., 2003; Graham et al., 2011).

The results of the present work definitely do not support the idea of the SOIpr (Fig. V-8J) that suggests El Niño mean-state during the MCA and La Niña mean-state during the LIA and DACP (Yan et al., 2011b). During the cold periods (DACP and LIA) we found a weak OMZ and lower export production especially during the cold LIA. These results are more coherent with an El Niño-like mean state, which contradict the SOIpr reconstruction. Additionally, during the MCA we found two different stages, where the older phase cannot be defined as nor El Niño or La Niña like conditions, while the most recent period could be defined as a La Niña-like mean state. Thus, the

response of the PUE as recorded in marine sediments off Pisco is contradictory with the expected results based on the SOIpr.

V-6.3 Anchovy and oceanic species

Anchovy and oceanic species are favored during globally warm episodes and are strongly reduced during globally cold periods. Anchovy is restricted to the coastal waters and is more influenced by upwelling and coastal productivity than sardine (Swartzman et al., 2008; McCall, 2009), thus is expected that the upwelling enhancement inferred from the export production proxies during the MCA and the CWP was accompanied with an increase in anchovy biomass. The abundance of anchovy during the MCA was high but not comparable to the abundance during the CWP. In contrast the two cold periods (DACP and LIA) show low anchovy abundances (Fig. V-8H). Oceanic species were also favored during the globally warm episodes, especially during the MCA and the LIA-CWP transition. The climatic-oceanographic conditions during the warm periods probably caused a strong variability in the expansion-contraction of the habitat favorable for oceanic species. These results suggest that climate forcing plays a major role in regulating fish stocks in the PUE.

V-6.4 Possible mechanism for the observed changes in the PUE

The observed changes in the PUE are concordant with the ocean thermostat mechanism proposed by Clement et al. (1996). In this mechanism a heating of the tropical Pacific leads to a cooling of the eastern part of the basin, which implies that the Eastern Equatorial Pacific varies negatively with changes in radiative forcing (Clement et al. 1996; Mann et al., 2005; Graham et al. 2011). In the west, where the thermocline is deep, the response to a surface heating is largely thermodynamic and the mixed layer adjusts with an increased temperature. During the MCA a strong increase is observed in the Indo-Pacific Warm Pool (Fig. V-8C; Oppo et al., 2009). In the east where the thermocline is shallow, cooling by vertical advection offsets the surface heating, producing a smaller temperature response (Fig. V-8D; Conroy et al., 2009). The increased zonal SST gradient accelerates the trade winds, which leads to further thermocline shoaling and cooling by vertical advection in the east, further accelerating the winds and originating a stronger Walker circulation (Mann et al., 2005). Additionally a northerly (southerly) ITCZ during the MCA (LIA) contributes to an increased (decreased) zonal SST and thus a more La Niña (El Niño)-like mean state (Haug et al. 2001; Koutavas et al., 2005; Mann et al., 2005; Bird et al. 2011). Under the scenario proposed by the "ocean thermostat mechanism" the MCA and the CWP should present high productivity, while the cool DACP and LIA should present low productivity, which are exactly the results obtained in the present work. Finally, the ocean warming during the recent decades favors stronger trade winds in the Western Pacific via the atmosphere and hence is likely to have contributed to the La Niña-like state

(i.e. enhanced east-west Walker circulation) through the Pacific ocean-atmosphere interactions (Luo et al., 2012).

V-7. Conclusions

Large changes in terrestrial runoff, export production, water column oxygenation and sediment REDOX conditions inferred from marine laminated cores off Peru during the last 2 millennia indicate that the centennial-scale variations have been linked to global climate variability. In general, the response of the PUE to the Northern Hemisphere cold periods (DACP and LIA) consisted in a weak OMZ, sub-oxic conditions in the sediments, low export production and low fish abundance. Moreover the effects of the globally cold LIA were stronger in comparison with those that occurred during the globally cool DACP. In contrast the response of the PUE to the warm periods consisted in a stronger OMZ, anoxic sediment conditions, higher export production and higher fish biomass. In addition the MCA shows two phases in relation to the sediment redox conditions but the export production was similar in both phases. From ~1150 AD to the present there is a strong coupling between export production and sediment redox conditions, which is not observed from ~250 to 1150 AD.

Paleo-productivity, paleo-oxygenation and paleoredox proxies developed in the present work show that the PUE was the subject of abrupt as well as gradual changes in OMZ intensity and productivity. The period between the end of the MCA and the end of the LIA, encompassing about 500 years, shows a gradual change towards lower productivity and less intense OMZ likely linked to the gradual changes in the position of the ITCZ. By contrast the transition of the PUE from the LIA to the CWP, which lasted about 50 years, was characterized by more abrupt changes as was already shown in previous works.

V-8. Bibliography

Agnihotri, R., M. A. Altabet, T. Herbert, and J. E. Tierney. 2008. Subdecadally resolved paleoceanography of the Peru margin during the last two millennia. Geochemistry Geophysics Geosystems 9(5):1-15.

Altabet, M. A., and R. Francois. 1994. Sedimentary nitrogen isotopic ratio as a recorder for surface ocean nitrate utilization. Global Biogeochemical Cycles 8(1):103-116.

Altabet, M. A., C. Pilskaln, R. Thunell, C. Pride, D. Sigman, F. Chavez, and R. Francois. 1999. The nitrogen isotope biogeochemistry of sinking particles from the margin of the Eastern North Pacific. Deep-Sea Research I 46:655-679.

Alves, S., P. Schiano, F. Capmas, and C. J. Allègre. 2002. Osmium isotope binary mixing arrays in arc volcanism. Earth and Planetary Science Letters 198(3-4):355-369.

Bakun, A. 1990. Global climate change and intensification of coastal upwelling. Science 247(4939): 198-201.

Barber, R. T., and F. Chavez. 1983. Biological consequences of El Niño. Science 222:1203-1210.

Barron, J. A., D. Bukry, and D. Field. 2010. Santa Barbara Basin diatom and silicoflagellate response to global climate anomalies during the past 2200 years. Quaternary International 215:34-44.

Baumgartner, T. R., V. Ferreira-Bartrina, J. Cowen, and A. Soutar. 1991. Reconstruction of a 20th century varve chronology from the central Gulf of California. The Gulf and Peninsular Province of the Californias.

Behar, F., V. Beaumont, and H. L. D. B. Penteado. 2001. Rock-Eval 6 technology: performances and developments. Oil & Gas Science and Technology - Rev. IFP 56(2):111-134.

Bertaux, J., F. Frohlich, and P. IIdefonse. 1998. Multicomponent analysis of FTIR spectra: Quantification of amorphous and crystallized mineral phases in synthetic and natural sediments. Journal of Sedimentary Research 68:440-447.

Bird, B. W., M. B. Abbott, M. Vuille, D. T. Rodbell, N. D. Stansell, and M. F. Rosenmeier. 2011. A 2,300-year-long annually resolved record of the South American summer monsoon from the Peruvian Andes. PNAS.

Boning, P., H. J. Brumsack, E. Bottcher, B. Schnetger, C. Kriete, J. Kallmeyer, and S. L. Borchers. 2004. Geochemistry of Peruvian near-surface sediments. Geochimica et Cosmochimica Acta 68(21):4429-4451.

Bradley, R. 2000. 1000 years of climate change. Science 288(5470): 1353-1355.

Bradley, R. S., M. K. Hughes, and H. F. Diaz. 2003. Climate in Medieval Times. Science 302:404-405.

Broccoli, A. J., K. A. Dahl, and R. J. Stouffer. 2006. Response of the ITCZ to Northern Hemisphere cooling. Geophysical Research Letters 33(L01702).

Chavez, F., A. Bertrand, R. Guevara-Carrasco, P. Soler, and J. Csirke. 2008. The northern Humboldt Current System: Brief history, present status and a view towards the future. Progress in Oceanography 79:95-105.

Chavez, F. P., and M. Messié. 2009. A comparison of Eastern Boundary Upwelling Ecosystems. Progress in Oceanography 83(1-4):80-96.

Chavez, F. P., M. Messie, and J. T. Pennington. 2011. Marine Primary Production in Relation to Climate Variability and Change. Annu. Rev. Mar. Sci. 3:227-260.

Chazen, C. R., M. A. Altabet, and T. D. Herbert. 2009. Abrupt mid-Holocene onset of centennial-scale climate variability on the Peru-Chile Margin. Geophysical Research Letters 36:L18704.

Cobb, K. M., C. D. Charles, H. Cheng, and R. L. Edwards. 2003. El Niño/Southern Oscillation and tropical Pacific climate during the last millennium. Nature 424:271-276.

Colodner, D., J. Sachs, G. Ravizza, K. Turekian, J. Edmond, and E. Boyle. 1993. The geochemical cycle of rhenium: a reconnaissance. Earth and Planetary Science Letters 117(1-2):205-221.

Conroy, J. L., A. Restrepo, J. T. Overpeck, M. Steinitz-Kannan, J. E. Cole, M. B. Bush, and P. A. Colinvaux. 2009. Unprecedent recent warming of surface temperatures in the eastern tropical Pacific Ocean. Nature geoscience 2:46-50.

Conroy, J. L., J. T. Overpeck, and J. E. Cole. 2010. El Niño/Southern Oscillation and changes in the zonal gradient of tropical Pacific sea surface temperature over the last 1.2 ka. PAGES News 18(1).

Crowley, T. 2000. Causes of Climate Change Over the Past 1000 Years. Science 289:270-289.

Crusius, J., S. Calvert, T. Pedersen, and D. Sage. 1996. Rhenium and molybdenum enrichments in sediments as indicators of oxic, suboxic and sulfidic conditions of deposition. Earth and Planetary Science Letters 145(1-4):65-78.

Dean, W. E., Y. Zheng, J. D. Ortiz, and A. van Geen. 2006. Sediment Cd and Mo accumulation in the oxygen-minimum zone off western Baja California linked to global climate over the past 52 kyr. Paleoceanography 21:PA4209.

Demarcq, H. 2009. Trends in primary production, sea surface temperature and wind in upwelling systems (1998–2007). Progress in Oceanography 83: 376-385.

De Pol-Holz, R., O. Ulloa, L. Dezileau, J. Kaiser, F. Lamy, and D. Hebbeln. 2006. Melting of the Patagonian Ice Sheet and deglacial perturbations of the nitrogen cycle in the eastern South Pacific. Geophysical Research Letters 33:L04704.

Diaz-Ochoa, J. A., C. B. Lange, S. Pantoja, G. J. De Lange, D. Gutierrez, P. Muñoz, and M. Salamanca. 2008. Fish scales in sediments from off Callao, central Peru. Deep-Sea Research Part II 56:1124–1135

Diaz-Ochoa, J. A., S. Pantoja, G. J. De Lange, C. B. Lange, G. E. Sanchez, V. R. Acuña, P. Muñoz, and G. Vargas. 2011. Oxygenation variability in Mejillones Bay, off northern Chile, during the last two centuries. Biogeosciences 8:137-146.

Disnar, J. R., B. Guillet, D. Keravis, C. Di-Giovanni, and D. Sebag. 2003. Soil organic matter (SOM) characterization by Rock-Eval pyrolysis: scope and limitations. Organic Geochemistry 34:327-343.

Field, D. B., T. R. Baumgartner, V. Ferreira, D. Gutierrez, H. Lozano-Montes, R. Salvatteci, and A. Soutar. 2009. Variability from scales in marine sediments and other historical records. Pp. 45-63. In D. Checkley, C. Roy, J. Alheit, and Y. Oozeki, eds. Climate Change and Small Pelagic Fish. Cambridge University Press.

Glantz, S. A. 2002. Primer of Biostatistics. McGraw-Hill.

Graham, N. E., M. K. Hughes, C. M. Ammann, K. M. Cobb, M. P. Hoerling, D. J. Kennett, J. P. Kennett, B. Rein, L. Stott, P. E. Wigand, and T. Xu. 2007. Tropical Pacific – mid-latitude teleconnections in medieval times. Climate Change 83:241-285

Graham, N. E., C. M. Ammann, D. Fleitmann, K. M. Cobb, and J. Luterbacher. 2011. Support for global climate reorganization during the ''Medieval Climate Anomaly''. Climate Dynamics 37:1217-1245.

Gutierrez, D., A. Sifeddine, J. L. Reyss, G. Vargas, F. Velazco, R. Salvatteci, V. Ferreira-Bartrina, L. Ortlieb, D. Field, T. Baumgartner, M. Boussafir, H. Boucher, J. Valdes, L. Marinovic, P. Soler, and P. Tapia. 2006. Anoxic sediments off Central Peru record interannual to multidecadal changes of climate and upwelling ecosystems during the last two centuries. Advances in Geosciences 6:119-125.

Gutierrez, D., E. Enriquez, S. Purca, L. Quipuzcoa, R. Marquina, G. Flores, and M. Graco. 2008. Oxygenation episodes on the continental shelf of central Peru: Remote forcing and benthic ecosystem response. Progress in Oceanography 79:177-189.

Gutierrez, D., A. Sifeddine, D. B. Field, L. Ortlieb, G. Vargas, F. Chavez, F. Velazco, V. Ferreira, P. Tapia, R. Salvatteci, H. Boucher, M. C. Morales, J. Valdes, J. L. Reyss, A. Campusano, M. Boussafir, M. Mandeng-Yogo, M. Garcia, and T. Baumgartner. 2009. Rapid reorganization in ocean biogeochemistry off Peru towards the end of the Little Ice Age. Biogeosciences 6:835-848.

Gutierrez, D., I. Bouloubassi, A. Sifeddine, S. Purca, K. Goubanova, M. Graco, D. Field, L. Méjanelle, F. Velazco, A. Lorre, R. Salvatteci, D. Quispe, G. Vargas, B. Dewitte, and L. Ortlieb. 2011. Coastal cooling and increased productivity in the main upwelling zone off Peru since the mid-twentieth century. Geophysical Research Letters 38:L07603.

Haug, G. H., K. A. Hughen, D. M. Sigman, L. C. Peterson, and U. Rohl. 2001. Southward Migration of the Intertropical Convergence Zone Through the Holocene. Science 293:1304-1308.

Helly, J., and L. Levin. 2004. Global distribution of naturally occurring marine hypoxia on continental margin. Deep-Sea Research I 51:1159-1168.

Hendy, E. J., M. K. Gagan, C. A. Alibert, M. T. McCulloch, J. M. Lough, and P. J. Isdale. 2002. Abrupt Decrease in Tropical Pacfic Sea Surface Salinity at End of Little Ice Age. Science 295.

Jahncke, J., D. M. Checkley, and G. L. Hunt. 2004. Trends in carbon flux to seabirds in the Peruvian upwelling system: effects of wind and fisheries on population regulation. Fisheries Oceanography 13(3):208-223.

Jarvis, K. E., A. L. Gray, and R. S. Houk. 1992. Handbook of Inductively Coupled Plasma Mass Spectrometry. Blackie Academic & Professional, an imprint of Champan & Hall, Wester Cleddens Road, Bishopgriggs, Glasgow, London Glasgow New York Tokyo Merlbourne Madras.

Jomelli, V., D. Grancher, D. Brunstein, and O. Solomina. 2008. Recalibration of the yellow Rhizocarpon growth curve in the Cordillera Blanca (Peru) and implications for LIA chronology. Geomorphology 93(201-212).

Khider, D., L. D. Stott, J. Emile-Geay, R. Thunell, and D. E. Hammond. 2011. Assessing El Niño Southern Oscillation variability during the past millennium. Paleoceanography 26(PA3222).

Koutavas, A., and J. Lynch-Stieglitz. 2005. Variability of the marine ITCZ over the eastern Pacific during the past 30,000 years. In E. F. Diaz, and R. S. Bradley, eds. The Hadley Circulation: Present Past and Future. Springer Academic Publishers.

Lafarge, E., J. Espitalié, F. Marquis, and D. Pillot. 1998. Rock-Eval 6 applications in hydrocarbon exploration, production and in soil contaminations studies. Oil & Gas Science and Technology - Rev. IFP 53(4):421-437.

Leduc, G., T. Herbert, T. Blanz, P. Martinez, and R. Schneider. 2010. Contrasting evolution of sea surface temperature in the Benguela upwelling system under natural and anthropogenic climate forcings. Geophysical Research Letters 37:L20705.

Licciardi, J. M., J. M. Schaefer, J. R. Taggart, and D. C. Lund. 2009. Holocene Glacier Fluctuations in the Peruvian Andes Indicate Northern Climate Linkages. Science 325:1677-1679.

Linsley, B.K., R.B. Dunbar, G.M. Wellington, and D.A. Mucciarone. 1994. A coral-based reconstruction of Intertropical Convergence Zone variability over Central America since 1707. Journal of Geophysical Research 99: 9977–9994.

Luo, J.-J., W. Sasaki, and Y. Masumoto. 2012. Indian Ocean warming modulates Pacific climate change. PNAS Early Edition.

MacDonald, G.M., Case, R.A., 2005. Variations in Pacific Decadal Oscillation over the past millennium. Geophysical Research Letters 32, L08703.

Makou, M. C., T. I. Eglinton, D. W. Oppo, and K. A. Hughen. 2010. Postglacial changes in El Niño and La Niña behavior. Geology 38(1):43-46.

Mann, M. E., and P. D. Jones. 2003. Global surface temperatures over the past two millennia. Geophysical Research Letters 30(15):1820.

Mann, M. E., Z. Zhang, S. Rutherford, R. S. Bradley, M. K. Hughes, D. Shindell, C. Ammann, G. Faluvegi, and F. Ni. 2009. Global Signatures and Dynamical Origins of the Little Ice Age and Medieval Climate Anomaly. Science 326:1256-1260.

Martinez, P., and R. S. Robinson. 2010. Increase in water column denitrification during the last deglaciation: the influence of oxygen demand in the eastern equatorial Pacific. Biogeosciences 7:1-9.

McGregor, H. V., M. Dima, H. W. Fischer, and S. Mulitza. 2007. Rapid 20th-Century Increase in Coastal Upwelling off Northwest Africa. Science 315:637-639.

McManus, J., W. M. Berelson, S. Severmann, P. R. L., D. E. Hammond, G. P. Klinkhammer, and C. Holm. 2006. Molybdenum and uranium geochemistry in continental margin sediments: Paleoproxy potential. Geochimica et Cosmochimica Acta 70:4643-4662.

Miller, C. A., B. Peucker-Ehrenbrink, B. D. Walker, and F. Marcantonio. 2011. Re-assessing the surface cycling of molybdenum and rhenium. Geochimica et Cosmochimica Acta 75:7146-7179.

Moberg, A., D. M. Sonenchkin, K. Holmgren, N. M. Datsenko, and W. Karlén. 2005. Highly variable Northern Hemisphere temperatures reconstructed from low- and high-resolution proxy data Nature 433(7026):613-617.

Nameroff, T. J., S. E. Calvert, and J. W. Murray. 2004. Glacial-interglacial variability in the eastern tropical North Pacific oxygen minimum zone recorded by redox-sensitive trace metals. Paleoceanography 19:PA1010.

Newton, A., R. Thunell, and L. Stott. 2006. Climate and hydrographic variability in the Indo-Pacific Warm Pool during the last millennium. Geophysical Research Letters 33(L19710):1-5.

Oppo, D. W., Y. Rosenthal, and B. K. Linsley. 2009. 2,000-year-long temperature and hydrology reconstructions from the Indo-Pacific warm pool. Nature 460(7259):1113-1116.

Ortlieb, L., G. Vargas, and J.-F. Saliège. 2011. Marine radiocarbon reservoir effect along the northern Chile-southern Peru coast (14-24°S) throughout the Holocene. Quaternary Research.

Pennington, J. T., K. L. Mahoney, V. S. Kuwahara, D. D. Kolber, R. Calienes, and F. P. Chavez. 2006. Primary production in the eastern tropical Pacific: A review. Progress in Oceanography 69:285-317.

Peters, K. E., C. C. Walters, and J. M. Moldowan. 2005. The Biomarker Guide. Cambridge University Press.

Pierrehumbert, R. T. 2000. Climate change and the tropical Pacific: The sleeping dragon wakes. PNAS 97(4): 1355-1358.

Rein, B., A. Luckge, and F. Sirocko. 2004. A major Holocene ENSO anomaly during the Medieval period. Geophysical Research Letters 31(17):4.

Rein, B., A. Lückge, L. Reinhardt, F. Sirocko, A. Wolfe, and W.-C. Dullo. 2005. El Niño variability off Peru during the last 20,000 years. Paleoceanography 20:PA4003.

Reuter, J., L. Stott, D. Khider, A. Sinha, H. Cheng, and R. L. Edwards. 2009. A new perspective on the hydroclimate variability in northern South America during the Little Ice Age. Geophysical Research Letters 36:L21706.

Richey, J. N., R. Z. Poore, B. P. Flower, T. M. Quinn, and D. J. Hollander. 2009. Regionally coherent Little Ice Age cooling in the Atlantic Warm Pool. Geophysical Research Letters 36:L21703.

Sarbas, B., and U. Nohl. 2009. The GEOROC database - a decade of "online geochemistry". Geochimica et Cosmochimica Acta 73(A1158).

Salvatteci, R., D. B. Field, T. Baumgartner, V. Ferreira, and D. Gutierrez. 2012. Evaluating fish scale preservation in sediment records from the oxygen minimum zone off Peru. Paleobiology 38(1):766-792.

Salvatteci, R., D. Field, A. Sifeddine, L. Ortlieb, V. Ferreira, T. Baumgartner, S. Caquineau, F. Velazco, J. L. Reyss, J. A. Sanchez-Cabeza, and D. Gutierrez. (in revision). Cross-stratigraphies from a seismically active mud lens off Peru indicate horizontal extensions of laminae, missing sequences, and a need for multiple cores for high resolution records. Marine Geology.

Scheidegger, K. F., and L. A. Krissek. 1982. Dispersal and deposition of eolian and fluvial sediments off Peru and northern Chile. Geological Society of America Bulletin 93:150-162.

Scholz, F., C. Hensen, A. Noffke, A. Rohde, V. Liebetrau, and K. Wallmann. 2011. Early diagenesis of redox-sensitive trace metals in the Peru upwelling area – response to ENSO-related oxygen fluctuations in the water column. Geochimica et Cosmochimica Acta 75:7257-7276.

Sifeddine, A., D. Gutierrez, L. Ortlieb, H. Boucher, F. Velazco, D. Field, G. Vargas, M. Boussafir, R. Salvatteci, V. Ferreira, M. García, J. Valdes, S. Caquineau, M. Mandeng-Yogo, F. Cetin, J. Solis, P. Soler, and T. Baumgartner. 2008. Laminated sediments from the central Peruvian continental slope: A 500 year record of upwelling system productivity, terrestrial runoff and redox conditions. Progress in Oceanography 79:190–197.

Strub, P. T., J. M. Mesias, V. Montecino, J. Rutllant, and S. Salinas. 1998. Coastal ocean circulation off Western South America. Coastal segment (6,E). Pp. 273-313. In A. Robinson, and K. Brink, eds. The Sea. John Wiley & Sons, Inc., New York.

Tierney, J. E., D. W. Oppo, Y. Rosenthal, J. M. Russell, and B. K. Linsley. 2010. Coordinated hydrological regimes in the Indo-Pacific region during the past two millennia. Paleoceanography 25:PA1102.

Tribovillard, N., T. J. Algeo, T. Lyons, and A. Riboulleau. 2006. Trace metals as paleoredox and paleoproductivity proxies: An update. Chemical Geology 232:12-32.

Trouet, V., J. Esper, N. E. Graham, A. Baker, J. D. Scourse, and D. C. Frank. 2009. Persistent positive North Atlantic oscillation mode dominated the medieval climate anomaly. Science 324(78).

Unkel, I., A. Kadereit, B. Mahtle, B. Eitel, B. Kromer, G. Wagner, and L. Wacker. 2007. Dating methods and geomorphic evidence of palaeoenvironmental changes at the eastern margin of the South Peruvian coastal desert (14 degrees 30 ' S) before and during the Little Ice Age. Quaternary International 175:3-28.

Van der Weijden, C. H. 2002. Pitfalls of normalization of marine geochemical data using a common divisor. Marine Geology 184:167-187.

Vargas, G., S. Pantoja, J. A. Rutlant, C. Lange, and L. Ortlieb. 2007. Enhancement of coastal upwelling and interdecadal ENSO-like variability in the Peru-Chile Current since late 19th century. Geophysical Research Letters 34.

Vecchi, G. A., B. Soden, A. T. Wittenberg, I. M. Held, A. Leetmaa, and M. J. Harrison. 2006. Weakening of tropical Pacific atmospheric circulation due to anthropogenic forcing. Nature 44:73-76.

Yan, H., L. Sun, D. W. Oppo, Y. Wang, Z. Liu, Z. Xie, X. Liu, and W. Cheng. 2011a. South China Sea hydrological changes and Pacific Walker Circulation variations over the last millennium. Nature communications 2:293.

Yan, H., L. Sun, Y. Wang, W. Huang, S. Qiu, and C. Yang. 2011b. A record of the Southern Oscillation Index for the past 2,000 years from precipitation proxies. Nature geoscience 4:611-614.

CHAPTER VI:

SUB-DECADAL TO MULTIDECADAL-SCALE CHANGES IN FISH ABUNDANCES OFF PERU DURING THE LAST 150 YEARS INFERRED BY FISH SCALES DEPOSITED IN MARINE LAMINATED SEDIMENTS

VI-1. Introduction

The highly productive upwelling environment off the coast of Peru sustains one of the world's largest fisheries, essentially based on the Peruvian anchovy (*Engraulis ringens*), but biomass variability on inter-annual to decadal timescales results in dramatic variations in catch (Schwartzlose et al., 1999; Chavez et al., 2003). A pronounced decline in anchovy landings in the Humboldt Current System (HCS) from 1972 to the late 1990s was accompagned by an increase in sardine (*Sardinops sagax* sagax). Similar patterns were observed in other upwelling ecosystems of the world (Schwartzlose et al., 1999). The interannual biomass variability of anchovy observed in the HCS could largely be explained by environmental changes associated with El Niño Southern Oscillation (ENSO) (Bertrand et al., 2004) and by fishing pressure. By contrast the decadal scale variability is largely attributed to physical and biological mechanisms, and diverse explanations have been proposed (Schwartzlose et al., 1999; Bakun and Broad, 2003; Bertrand et al., 2004; Checkley et al., 2009; Bertrand et al., 2011). In order to test hypotheses of underlying mechanisms driving decadal fish abundance variability and to determine the role of fishery in population size decline, long records of fish population variability prior to the development of industrial fishing are necessary. Moreover, an effective resource management requires the sound understanding of the natural variability of the two major pelagic species in the HCS (anchovy and sardine) at different timescales. In the present study we attempt to reconstruct at high resolution (sub-decadal time scale) the past fish population variability of anchovy, sardine, and other fishes during the last 155 years. For this purpose, we use fish scales buried in marine laminated sediments deposited under anoxic conditions off the Peruvian coast.

During the last decades the Equatorial Boundary Upwelling Ecosystems (EBUS) have been experiencing large changes in wind stress, upwelling intensity and ocean productivity likely linked to current global change as evidenced by simulation models, paleoceanographic reconstructions, observational data and analyses of satellite images (Bakun, 1990; Jahncke et al., 2004; McGregor et al., 2007; Vargas et al., 2007; Demarcq, 2009; Leduc et al.; 2010; Gutierrez et al., 2011). The Peruvian Upwelling Ecosystem (PUE), which is part of the larger Humboldt Current System (HCS), is unequalled in terms of fish productivity, producing about 10% of the global fish catch while representing less than 0.1% of the world ocean surface (Chavez et al., 2008). Like some other EBUS, the PUE experienced intensification in coastal upwelling and productivity (Jahncke et al., 2004; Demarcq, 2009; Gutierrez et al., 2011). Moreover a trophic bottom-up model indicates that since ~1925 AD an increase in primary production resulted from increasing wind stress and that this production is transferred to the Peruvian anchovy and ultimately to seabird population and anchovy fishery (Jahncke et al., 2004). Anchovy and sardine population response to future climatic change remains actually quite uncertain. If local upwelling continues to intensify, then the rates of offshore

transport and wind-driven turbulent mixing would also increase (Bakun and Weeks, 2008). One expected scenario under these conditions is that anchovy dominance may give way to the sardine dominance that seems to characterize other EBUS currently subject to relatively stronger winds and more intense turbulence generation (Bakun and Weeks, 2008). Alternatively, the increase in winds will push offshore the front between the subtropical oceanic waters and the coastal cold waters displacing the sardines offshore since this species prefer subtropical oceanic waters. These discrepant hypotheses about future EBUS response to climate change clearly illustrate the urgent need for a better understanding of the response of anchovy and sardine populations of the HCS to past climate variations and of the natural range of biomass variability of these species.

Since the beginning of industrial fishery, the landings suggested two anchovy and one sardine regimes in the HCS: anchovies dominated from ~1960 to ~1970 and from the mid 1980s up to present, whereas sardines prevailed in between the two anchovy periods (Chavez et al., 2003). This fluctuation between anchovy and sardine populations cannot be explained by interspecies competition, for at least four reasons. First, anchovies prey on large zooplankton while sardines are efficient filter feeders on phytoplankton and small zooplankton (Espinoza and Bertrand, 2008; Alheit and Bakun, 2010). Second, there is a strong relationship linking anchovy distribution to cold and highly productive cold coastal waters, while sardine populations have a slight preference for surface subtropical waters (Gutierrez et al., 2007; Swartzman et al., 2008). Third, sardines migrate more compared to anchovies (Alheit and Bakun, 2010). Fourth, anchovy and sardine cannibalize their own eggs and larvae as readily as predating upon others (Alheit, 1987). If interspecies competition cannot be the underlying mechanism inducing fluctuations in dominance between anchovy and sardine, changes in habitat and environmental conditions are the most likely cause of this pattern.

The fluctuations between anchovy and sardine populations are associated with the advance or retreat of the coastal cold and oxygen-poor upwelled waters and the warm and more oxygenated subtropical oceanic waters to the coast of Peru and Chile (Alheit and Bakun, 2010; Bertrand et al., 2011; Moron et al., in prep). The advance of the subtropical waters towards the coast seems to be adverse for anchovy, but favorable to sardine. Long-term salinity data from Peruvian waters, up to 60 nautical miles offshore show that the shifts in anchovy and sardine abundances are related to the advance and retreat of oceanic subtropical high salinity water masses (Moron et al in prep.). From 1960 up to the late 1960s, coastal waters off Peru were dominated by cold coastal water (CCW; 14–18 °C; 34.9–35.0 g/kg). Thereafter, from the late 1960s to the mid-1980s, subtropical surface water (SSW; 18–27 °C; 35.1–35.7 g/kg) was closer to the coast. Since the 1990's, the SSW retreated again offshore, being replaced by CCW. Moreover, the spatial distribution of anchovy and sardine schools indicate a greater tolerance of anchovy to water dysoxia, compared to sardine (Bertrand et al., 2011), and available time-series indicate that anchovy were more abundant during periods with shallow

oxycline conditions while sardine peaked during the period with deeper oxycline. Additionally, the cool conditions favorable to anchovies were accompanied by more nutrients in the euphotic layer and the development of large phytoplankton (chain forming centric diatoms) and zooplankton (large copepods and euphausiids), which favors anchovy that feed primarily by direct biting on large zooplankton (Espinoza and Bertrand, 2008; Bertrand et al., 2011). In contrast, the period favorable to sardines was associated with lower nutrients in the euphotic layer that favored the development of smaller phytoplankton and zooplankton that sardines can more efficiently filter feed (Espinoza et al., 2009; Ayon et al., 2011; Bertrand et al., 2011). Consequently the variability in anchovy and sardine biomass appears to be linked to large-scale atmospheric or oceanic forcing (Chavez et al., 2003).

Regarding these relationships between environmental conditions and fluctuations of anchovy and sardine biomasses, several authors have tried to link them to large-scale atmospheric or oceanic forcings as the Pacific Oscillation Index (PDO, Chavez et al., 2003). The period of higher sardine abundance occurred during the warm phase of the PDO (from 1975 to the mid-1990s), while the periods with increased anchovy population sizes have occurred during the cool phases of the PDO (from 1950 to 1975, and from the early 1990s to the present). However, Gutierrez et al. (2009) and Valdes et al. (2008) show evidence, based on anchovy and sardine biomass reconstruction using fish scale deposited in laminated sediments, that the warm phases of the PDO are not always associated with sardine since no sardine were found during a former warm phase of the PDO (from 1925 to 1950).

In order to infer the natural biomass variability of pelagic fishes prior to the development of the industrial fishery, fish scales buried in undisturbed anoxic marine sediments are used (Soutar and Isaacs, 1974; Baumgartner et al., 1992; Field et al., 2009). Over time fish scales and bones as well as debris of many organisms fall to the ocean floor, get buried and accumulate. Variation in scale deposition with fish population size is attributable to natural scale shedding while the majority of bones and vertebrae arrive to sediments by passing through the guts of predators (Field et al., 2009; Salvatteci et al., 2012). If preservation conditions are favorable a record may provide a history of pelagic communities that inhabited the area. Ideal preservation conditions are given off Central Peru, especially in front of Pisco (Gutierrez et al., 2006; IMARPE surveys), where a strong Oxygen Minimum Zone (OMZ) effectively limits bioturbation by macro-benthic fauna resulting in the preservation of high resolution laminated sediments.

Several considerations must be taken into account when using scale deposition rates (SDR), or also denominated fish scale fluxes, to reconstruct the past biomass variability of pelagic fishes. First, fish scales recovered in laminated sediments off Peru have shown evidence of degradation that could bias the fish scale record (Salvatteci et al., 2012). The degradation of fish scales was likely

induced by a weaker OMZ, as observed over a long period of time corresponding to the Little Ice Age (LIA; Sifeddine et al., 2008; Gutierrez et al., 2009; Salvatteci et al., 2012). Fish scales after the end of the LIA were better preserved, and SDR can be directly linked to changes in past variability of the fish biomass (Salvatteci et al. 2012). Second, not all fish species have the same number of scales on their body and they do not shed scales at the same rate. For example an experimental study shows that the flux of scales (# of scales.fish^{-1}.day^{-1}) of Pilchard (*Sardinops oceallata*) is higher than that of Anchovy (*Engraulis japonicus*; Shackleton, 1988). Consequently, in order to infer past biomass abundance and compare it among species, the SDR values of a given species cannot be directly compared among species. Third, sediments of the Peru slope present discontinuities caused by erosive processes and lateral re-deposition of sediments that can eliminate previously deposited laminae sequences, or add material from upslope. Assuming sedimentation continuity might therefore give rise to misleading interpretations in the fish scale downcore variability (see chapter II). A cross correlation of laminae and sedimentary structures among cores retrieved off Peru show that the two principal cores that are used in the present chapter (B05-13 and B05-14) show the most complete sedimentary sequences in comparison to multiple cores retrieved off Pisco (chapter II). Fourth, sediment records with high sedimentation rates are required to resolve sub-decadal scale variability in fish biomass fluctuations. Cores B05-13 and B05-14 show high sedimentation rates and in some parts of the record each subsample (0.4 cm) represent ~2 years. Fifth, it is possible that fish population displacements are recorded instead of real changes in biomass; however cores retrieved off Peru and northern Chile show the same multidecadal scale pattern which means that the cores are recording principally changes in biomass instead of population displacements (Gutierrez et al., 2009)

On multi-decadal time scales, fish SDR records off Peru (~12 and 14 °S) and off Mejillones (~23 °S) retrieved within the OMZ, have shown the potential to replicate similar changes in SDR, but records with higher sedimentation rates may reveal sub-decadal scale variability that could be related with changes in anchovy and sardine distribution. It is known that the pelagic fishes like anchovy changes its distribution during interannual time-scale. For example during El Niño events the anchovy distribution becomes more coastal, patchier, and asymmetrically represented towards the southern and cooler Peruvian coast, instead of being widely dispersed over the whole Peruvian coast (Ñiquen and Bouchon, 2004). However not all the El Niño events have the same effect on the distribution of anchovy, for example no strong latitudinal displacement was evidenced during El Niño 97-98 as anchovy was distributed all along the coast south of 8 °S (Bertrand et al., 2004). Following this line of reasoning, during sub-decadal or decadal periods with unfavorable conditions for anchovy, the spatial distribution of anchovy should be more southerly. Thus, well dated sediment records with high sedimentation rates collected in a latitudinal gradient may record the expansion and contraction of anchovy and sardine populations during particular time periods.

The fluctuation in anchovy and sardine populations, and its linkage with large-scale atmospheric or oceanic forcing require sediment records with high sedimentation rates that allow resolving high frequency variations. The fish scale fluxes of cores B05-13 and B05-14 lead to interpret sub-decadal scale variations in fish scale deposition rates that cannot be observed in previously reported records off Peru (Diaz-Ochoa et al., 2009; Gutierrez et al., 2009) and off Chile (Valdes et al., 2008). In the present study we use the fish scale records to fulfill two objectives. The first objective is to understand the role of climate forcing in regulating the pelagic fish biomass variability off Peru during the last ~155 years. Consequently we compare the SDR with climate indices and proxies of environmental change such as the PDO, the Southern Oscillation Index (SOI), the Cold Tongue Index (CTI), historical El Niño and La Niña events, the upwelling favorable winds (from the International Comprehensive Ocean-Atmosphere Data Set, ICOADS), export production reconstructions (chapter III and V), and finally SST reconstructions off Pisco (Gutierrez et al., 2011). The second objective is to assess the anchovy and sardine habitat contraction and expansion during the last 155 years and characterize the former multidecadal period favorable to sardines (Valdes et al., 2008; Gutierrez et al., 2009). For this purpose we use SDR obtained from 3 different sites with different distances from the coast: Callao (~12 °S), Pisco (14 °S) and Mejillones (~23 °S; Fig. VI-1). The core B04-13 retrieved off Callao is located farthest from the coast (30 nm) in comparison with the other cores and lies within the actual nucleus of the Peruvian anchovy (Checkley et al., 2009; Fig. VI-1). Pisco cores (B04-6, B05-13 and B05-14) are located at ~15 nm from the coast near the main upwelling center off Peru (San Juan, at ~15°S) and are not located near the present nucleus of sardine (Checkley et al., 2009; Fig. VI-1). The Mejillones core (F98-1A) was retrieved at ~5 nm from the coast, in a small and shallow marine sedimentary basin (15 km diameter, 125 m of maximum depth; Vargas et al., 2004), near the present nucleus of the southern fishing stock of anchovy and sardine (Checkley et al., 2009; Fig. VI-1). Consequently differences in fish scale fluxes among cores should allow to infer the changes in the range of respective habitats of anchovy and sardine throughout the last ~155 years.
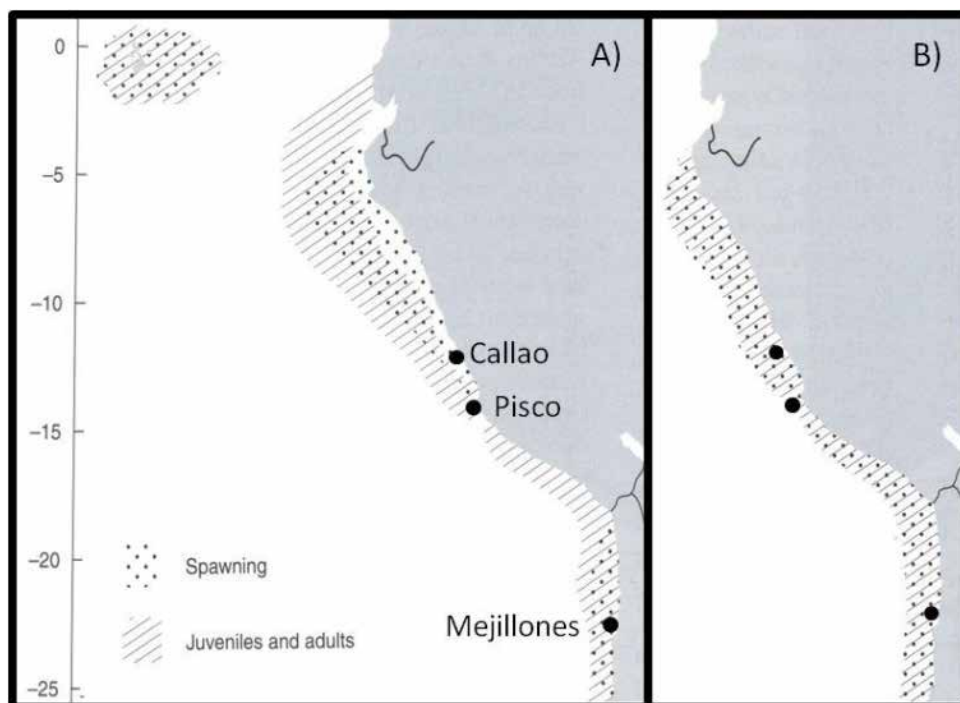
Figure VI-1. Location of the cores collected off the central-south Peruvian and off Chile coast evaluated in this study with the A) Maximal distribution range of sardine (A) and of anchovy (B). Figure modified from Checkley et al. (2009).

VI-2. Regional Setting

The PUE is characterized by a shallow surface mixed layer, a shallow thermocline and high productivity driven by coastal upwelling of nutrient-rich, poor ventilated cold waters (Barber and Chavez, 1983; Pennington et al., 2006; Chavez et al., 2008). In the PUE, the seasonal production cycles are out of phase with seasonal upwelling winds, in clear contrast to the other EBUS (Pennington et al., 2006; Chavez and Messié, 2009; Gutierrez et al., 2011). Upwelling favorable winds occur during the entire year but are stronger during austral winter and spring (Strub et al., 1998; Gutierrez et al., 2011). By contrast, primary productivity is higher during austral spring and summer when surface waters are more stratified (Pennington et al., 2006; Chavez and Messié, 2009; Gutierrez et al., 2011). The upper continental margin of Peru (~50 to 600 meters depth) is intersected by a strong and shallow OMZ that results from the decay of biological production that consumes O_2, the lack of ventilation and long residence times (Helly and Levin, 2004; Pennington et al., 2006). The main cause of interannual variability are El Niño events that produce anomalously warm SST in the equatorial and eastern Pacific every three to eight years (Chavez et al., 2011). During El Niño events, the equatorial Walker circulation is weakened, and the coast of Peru is characterized by an increase in sub-surface oxygenation and reduced productivity due to a deepening of the thermocline; however the Pisco area is under the influence of a small upwelling plume even during El Niño events (Barber and Chavez, 1983).

VI-3. Methodology

In order to fulfill the two objectives of the present work, we use the fish scale records from 5 box-cores collected off Peru: B04-13, B04-6, B05-13 and B05-14 and off Chile: F98-1A (Fig. VI-1). Fish scale records of cores B04-13 and B04-6 have already been published by Gutierrez et al. (2009) but only concerned the SDR of anchovy, sardine and other warm-water species, and focused on the multi-decennial to multi-centennial scale variability of these two types of pelagic fishes. The anchovy and oceanic species scale records of cores B05-13 and B05-14 have been published by Salvatteci et al. (2012) focusing on the fish scale preservation of anchovy scales in these two cores collected at different water depths. Fish scale records of cores B05-13 and B05-14 have not been published before within a chronological frame. Finally SDRs in core F98-1A were published by Valdes et al. (2008).

VI-3.1 Chronological models of the studied box-cores

In this chapter the chronological model for core B05-13 is developed in order to fix the time-frame of the box-core and to obtain the sediment accumulation rate required to estimate SDR. The chronological models of cores B04-6 and B04-13 were developed by Gutierrez et al. (2009) and the chronological model for core B05-14 is given in chapter IV. The ^{210}Pb activities in cores B05-13 were obtained by alpha spectrometry while in the other box-cores the activities were obtained by gamma spectrometry. As shown in chapter II, alpha and gamma spectrometry give coherent results of ^{210}Pb$_{ex}$ activities in core B05-13. Consequently, the proxy records derived from the age model obtained in core B05-13 can be compared with the proxies developed in the other box-cores. The detailed sub-sampling procedure for alpha spectrometry as well as the dry bulk density (DBD) estimations in core B05-13 is explained in chapter II. The ^{210}Pb measurements were done at intervals of 1 cm and the DBD estimations were calculated using 0.5 cm cubes along the core (DBD values taken from Salvatteci et al., 2012). Consequently the DBD values were summed or interpolated in some cases to fit the subsampling for ^{210}Pb analyses. The DBD values are shown in Table VI-1 as well as the error in the DBD values that was assumed to be 5%.

Table VI-1. Application of the CRS-^{241}Am model in core B05-13. See text for the definitions of the expressions. The average of the ^{210}Pb$_{tot}$ corresponding to the underlined samples were used to calculate the ^{226}Ra

Observations	Sample code	Depth (top) (cm)	Depth (middle) (cm)	Depth (base) (cm)	Interval thickness (cm)	Dry Bulk Density (g cm-3)	^{210}Pb$_{tot}$ (Bq kg-1)	^{210}Pb$_{ex}$ (Bq kg-1)	Mass/Area per sample (g.cm-2)	Accumulated Z-mass (g.cm-2)	Inventory ^{210}Pb$_{ex}$ per interval (Bq.cm-2)	Inv ^{210}Pb$_{ex}$ (Bq.cm-2)	Age AD CRS 241Am (base) (years)	delta-T (years)	w (g.cm-2.y-1)
	A 0-1	0.00	0.50	1	1.0	0.19 ± 0.01	1028 ± 34.3	997 ± 34.4	0.19 ± 0.01	0.2 ± 0.01	185.9 ± 11.3	3823 ± 47.2	2003.8 ± 0.87	1.7 ± 0.3	0.11 ± 0.01
	A 1-2	1.00	1.50	2	1.0	0.23 ± 0.01	1064 ± 36.8	1033 ± 36.8	0.23 ± 0.01	0.4 ± 0.01	241.5 ± 14.8	3637 ± 45.8	2001.4 ± 0.89	2.4 ± 0.2	0.10 ± 0.01
	A 2-3	2.00	2.50	3	1.0	0.25 ± 0.01	1120 ± 35.5	1089 ± 35.6	0.25 ± 0.01	0.7 ± 0.02	277.2 ± 16.6	3396 ± 43.4	1998.3 ± 0.89	3.0 ± 0.2	0.08 ± 0.01
	A 3-4	3.00	3.50	4	1.0	0.22 ± 0.01	1097 ± 36.4	1066 ± 36.4	0.22 ± 0.01	0.9 ± 0.02	239.7 ± 14.5	3118 ± 40.1	1995.5 ± 0.90	2.8 ± 0.2	0.08 ± 0.01
	A 4-5	4.00	4.50	5	1.0	0.23 ± 0.01	1032 ± 35.5	1002 ± 35.5	0.23 ± 0.01	1.1 ± 0.03	230.4 ± 14.1	2879 ± 37.4	1992.5 ± 0.91	3.0 ± 0.2	0.08 ± 0.01
	A 5-6	5.00	5.50	6	1.0	0.24 ± 0.01	973 ± 26.4	943 ± 26.4	0.24 ± 0.01	1.4 ± 0.03	222.0 ± 12.7	2648 ± 34.6	1989.3 ± 0.92	3.2 ± 0.2	0.07 ± 0.01
	A 6-7	6.00	6.50	7	1.0	0.30 ± 0.01	879 ± 29.7	849 ± 29.7	0.30 ± 0.01	1.7 ± 0.03	253.0 ± 15.4	2426 ± 32.2	1985.3 ± 0.90	4.1 ± 0.3	0.07 ± 0.01
	A 7-8	7.00	7.50	8	1.0	0.27 ± 0.01	749 ± 26.8	718 ± 26.9	0.27 ± 0.01	1.9 ± 0.03	192.1 ± 12.0	2173 ± 28.2	1981.8 ± 0.90	3.5 ± 0.2	0.08 ± 0.01
	A 8-9	8.00	8.50	9	1.0	0.24 ± 0.01	784 ± 25.3	753 ± 25.3	0.24 ± 0.01	2.2 ± 0.04	178.7 ± 10.8	1981 ± 25.6	1978.2 ± 0.89	3.6 ± 0.2	0.07 ± 0.01
	A 9-10	9.00	9.50	10	1.0	0.25 ± 0.01	692 ± 25.1	662 ± 25.2	0.25 ± 0.01	2.4 ± 0.04	165.3 ± 10.4	1802 ± 23.2	1974.5 ± 0.88	3.7 ± 0.2	0.07 ± 0.01
	A 10-11	10.00	10.50	11	1.0	0.28 ± 0.01	662 ± 12.7	631 ± 12.8	0.28 ± 0.01	2.7 ± 0.04	175.7 ± 9.5	1637 ± 20.7	1970.0 ± 0.87	4.5 ± 0.2	0.06 ± 0.00
	A 11-12	11.00	11.50	12	1.0	0.32 ± 0.02	511 ± 11.1	480 ± 11.2	0.32 ± 0.02	3.0 ± 0.04	153.4 ± 8.5	1461 ± 18.4	1965.4 ± 0.87	4.5 ± 0.3	0.07 ± 0.01
	A 12-13	12.00	12.50	13	1.0	0.24 ± 0.01	326 ± 7.3	296 ± 7.4	0.24 ± 0.01	3.3 ± 0.05	69.7 ± 3.9	1308 ± 16.4	1963.1 ± 0.89	2.3 ± 0.1	0.10 ± 0.01
	A 13-14	13.00	13.50	14	1.0	0.24 ± 0.01	289 ± 6.3	258 ± 6.5	0.24 ± 0.01	3.5 ± 0.05	62.4 ± 3.5	1238 ± 15.9	1960.9 ± 0.92	2.2 ± 0.1	0.11 ± 0.01
	A 14-15	14.00	14.50	15	1.0	0.28 ± 0.01	261 ± 6.0	230 ± 6.2	0.28 ± 0.01	3.8 ± 0.05	64.0 ± 3.6	1176 ± 15.5	1958.5 ± 0.94	2.4 ± 0.1	0.11 ± 0.01
	A 15-16	15.00	15.50	16	1.0	0.28 ± 0.01	297 ± 6.5	267 ± 6.6	0.28 ± 0.01	4.0 ± 0.05	73.8 ± 4.1	1112 ± 15.1	1955.5 ± 0.97	3.0 ± 0.2	0.09 ± 0.01
onset 241Am	A 16-17	16.00	16.50	17	1.0	0.30 ± 0.02	282 ± 6.1	251 ± 6.3	0.30 ± 0.02	4.3 ± 0.05	75.6 ± 4.2	1038 ± 14.5	1952.0 ± 1.00	3.5 ± 0.2	0.09 ± 0.01
	A 17-18	17.00	17.50	18	1.0	0.23 ± 0.01	249 ± 5.9	218 ± 6.0	0.23 ± 0.01	4.6 ± 0.05	50.6 ± 2.9	962 ± 13.9	1950.3 ± 1.03	1.7 ± 0.1	0.13 ± 0.01
	A 18-19	18.00	18.50	19	1.0	0.30 ± 0.02	270 ± 6.0	239 ± 6.2	0.30 ± 0.02	4.9 ± 0.06	72.3 ± 4.1	912 ± 13.6	1947.6 ± 1.07	2.6 ± 0.2	0.11 ± 0.01
	A 19-20	19.00	19.50	20	1.0	0.30 ± 0.02	233 ± 5.0	202 ± 5.2	0.30 ± 0.02	5.2 ± 0.06	60.7 ± 3.4	840 ± 12.9	1945.2 ± 1.11	2.4 ± 0.1	0.12 ± 0.01
	A 20-21	20.00	20.50	21	1.0	0.32 ± 0.02	271 ± 10.7	241 ± 10.8	0.32 ± 0.02	5.5 ± 0.06	77.0 ± 5.2	779 ± 12.5	1941.9 ± 1.12	3.3 ± 0.2	0.10 ± 0.01
	A 21-22	21.00	21.50	22	1.0	0.32 ± 0.02	300 ± 11.7	269 ± 11.8	0.32 ± 0.02	5.8 ± 0.06	86.2 ± 5.7	702 ± 11.3	1937.7 ± 1.10	4.2 ± 0.3	0.08 ± 0.01
	A 22-23	22.00	22.40	22.8	0.8	0.26 ± 0.01	248 ± 10.4	217 ± 10.5	0.21 ± 0.01	6.0 ± 0.06	44.9 ± 3.1	616 ± 9.8	1935.2 ± 1.13	2.4 ± 0.2	0.09 ± 0.01
	B0-1	22.80	23.30	23.8	1.0	0.23 ± 0.01	235 ± 10.4	204 ± 10.5	0.23 ± 0.01	6.3 ± 0.06	47.9 ± 3.4	571 ± 9.3	1932.4 ± 1.14	2.8 ± 0.2	0.08 ± 0.01
	B 1-2	23.80	24.30	24.8	1.0	0.23 ± 0.01	184 ± 8.0	153 ± 8.2	0.23 ± 0.01	6.5 ± 0.07	34.5 ± 2.5	523 ± 8.6	1930.2 ± 1.17	2.2 ± 0.2	0.10 ± 0.01
	B 2-3	24.80	25.30	25.8	1.0	0.25 ± 0.01	187 ± 9.3	156 ± 9.4	0.25 ± 0.01	6.7 ± 0.07	39.5 ± 3.1	488 ± 8.2	1927.5 ± 1.18	2.7 ± 0.2	0.09 ± 0.01
	B 3-4	25.80	26.30	26.8	1.0	0.20 ± 0.01	178 ± 7.5	147 ± 7.7	0.20 ± 0.01	6.9 ± 0.07	29.5 ± 2.1	449 ± 7.6	1925.3 ± 1.21	2.2 ± 0.2	0.09 ± 0.01
	B 4-5	26.80	27.30	27.8	1.0	0.23 ± 0.01	165 ± 7.0	135 ± 7.2	0.23 ± 0.01	7.2 ± 0.07	31.2 ± 2.3	419 ± 7.3	1922.9 ± 1.25	2.5 ± 0.2	0.09 ± 0.01
	B 5-6	27.80	28.30	28.8	1.0	0.23 ± 0.01	129 ± 5.8	98 ± 6.0	0.23 ± 0.01	7.4 ± 0.07	22.5 ± 1.8	388 ± 7.0	1921.0 ± 1.28	1.9 ± 0.2	0.12 ± 0.01
	B 6-7	28.80	29.30	29.8	1.0	0.28 ± 0.01	151 ± 7.5	120 ± 7.6	0.28 ± 0.01	7.7 ± 0.07	33.5 ± 2.7	366 ± 6.7	1917.9 ± 1.29	3.1 ± 0.3	0.09 ± 0.01
	B 7-8	29.80	30.30	30.8	1.0	0.24 ± 0.01	103 ± 6.1	73 ± 6.3	0.24 ± 0.01	7.9 ± 0.07	17.3 ± 1.7	332 ± 6.2	1916.1 ± 1.31	1.7 ± 0.2	0.14 ± 0.02
	B 8-9	30.80	31.30	31.8	1.0	0.21 ± 0.01	116 ± 4.4	85 ± 4.7	0.21 ± 0.01	8.1 ± 0.07	18.1 ± 1.3	315 ± 5.9	1914.2 ± 1.35	1.9 ± 0.1	0.11 ± 0.01
	B 9-10	31.80	32.30	32.8	1.0	0.32 ± 0.02	115 ± 3.8	85 ± 4.1	0.32 ± 0.02	8.4 ± 0.07	26.7 ± 1.9	297 ± 5.8	1911.2 ± 1.40	3.0 ± 0.2	0.10 ± 0.01
	B 10-11	32.80	33.30	33.8	1.0	0.19 ± 0.01	140 ± 5.4	110 ± 5.6	0.19 ± 0.01	8.6 ± 0.07	20.8 ± 1.5	270 ± 5.5	1908.6 ± 1.46	2.6 ± 0.2	0.07 ± 0.01
	B 11-12	33.80	34.30	34.8	1.0	0.24 ± 0.01	130 ± 5.1	99 ± 5.4	0.24 ± 0.01	8.9 ± 0.08	23.4 ± 1.7	249 ± 5.3	1905.5 ± 1.53	3.2 ± 0.2	0.07 ± 0.01
	B 12-13	34.80	35.30	35.8	1.0	0.22 ± 0.01	112 ± 4.5	81 ± 4.8	0.22 ± 0.01	9.1 ± 0.08	17.6 ± 1.4	226 ± 5.0	1902.9 ± 1.59	2.6 ± 0.2	0.08 ± 0.01
	B 13-14	35.80	36.30	36.8	1.0	0.21 ± 0.01	97 ± 4.2	66 ± 4.4	0.21 ± 0.01	9.3 ± 0.08	13.7 ± 1.1	208 ± 4.8	1900.7 ± 1.65	2.2 ± 0.2	0.09 ± 0.01
	B 14-15	36.80	37.30	37.8	1.0	0.22 ± 0.01	113 ± 4.4	82 ± 4.7	0.22 ± 0.01	9.5 ± 0.08	17.8 ± 1.4	194 ± 4.6	1897.6 ± 1.74	3.1 ± 0.2	0.07 ± 0.01
	B 15-16	37.80	38.30	38.8	1.0	0.23 ± 0.01	85 ± 3.0	54 ± 3.4	0.23 ± 0.01	9.7 ± 0.08	12.6 ± 1.0	176 ± 4.4	1895.2 ± 1.83	2.4 ± 0.2	0.10 ± 0.01
	B 16-17	38.80	39.30	39.8	1.0	0.24 ± 0.01	80 ± 3.5	49 ± 3.8	0.24 ± 0.01	10.0 ± 0.08	11.9 ± 1.1	164 ± 4.3	1892.8 ± 1.90	2.4 ± 0.2	0.10 ± 0.01
	B 17-18	39.80	40.30	40.8	1.0	0.17 ± 0.01	84 ± 3.7	54 ± 4.0	0.17 ± 0.01	10.2 ± 0.08	9.1 ± 0.8	152 ± 4.2	1890.8 ± 1.99	2.0 ± 0.2	0.09 ± 0.01
	B 18-19	40.80	41.30	41.8	1.0	0.14 ± 0.01	58 ± 2.7	27 ± 3.1	0.14 ± 0.01	10.3 ± 0.08	3.8 ± 0.5	143 ± 4.1	1889.9 ± 2.03	0.9 ± 0.1	0.16 ± 0.02
	B 19-20	41.80	42.30	42.8	1.0	0.11 ± 0.01	77 ± 3.6	46 ± 3.9	0.11 ± 0.01	10.4 ± 0.08	5.1 ± 0.5	139 ± 4.1	1888.8 ± 2.09	1.2 ± 0.1	0.09 ± 0.01
	B 20-21	42.80	44.80	46.8	4.0	0.27 ± 0.01			1.09 ± 0.05	11.5 ± 0.10	32.4 ± 2.4	134 ± 4.0	1879.9 ± 2.23	8.9 ± 0.8	0.12 ± 0.01
	C0-1	46.80	47.30	47.8	1.0	0.24 ± 0.01	82 ± 3.0	51 ± 3.3	0.24 ± 0.01	11.7 ± 0.10	12.1 ± 1.0	102 ± 3.3	1875.8 ± 2.41	4.1 ± 0.4	0.06 ± 0.01
	C 1-2	47.80	48.30	48.8	1.0	0.22 ± 0.01	52 ± 2.4	22 ± 2.8	0.22 ± 0.01	12.0 ± 0.10	4.9 ± 0.7	89 ± 3.1	1874.0 ± 2.49	1.8 ± 0.3	0.12 ± 0.02
	C 2-3	48.80	49.30	49.8	1.0	0.17 ± 0.01	51 ± 2.1	21 ± 2.6	0.17 ± 0.01	12.1 ± 0.10	3.6 ± 0.5	85 ± 3.0	1872.6 ± 2.57	1.4 ± 0.2	0.12 ± 0.02
	C 3-4	49.80	50.30	50.8	1.0	0.19 ± 0.01	86 ± 3.2	55 ± 3.5	0.19 ± 0.01	12.3 ± 0.10	10.5 ± 0.9	81 ± 3.0	1871.5 ± 2.81	1.2 ± 1.2	0.17 ± 0.17
	C 4-5	50.80	51.30	51.8	1.0	0.29 ± 0.01	78 ± 3.2	48 ± 3.6	0.29 ± 0.01	12.6 ± 0.10	13.7 ± 1.2	70 ± 2.9	1868.0 ± 4.50	3.5 ± 3.5	0.08 ± 0.08
	C 5-6	51.80	52.30	52.8	1.0	0.22 ± 0.01	79 ± 3.8	49 ± 4.1	0.22 ± 0.01	12.8 ± 0.10	10.8 ± 1.1	57 ± 2.6	1865.3 ± 5.25	2.7 ± 2.7	0.08 ± 0.08
	C 6-7	52.80	53.30	53.8	1.0	0.32 ± 0.02	74 ± 4.4	43 ± 4.6	0.32 ± 0.02	13.2 ± 0.10	13.8 ± 1.6	46 ± 2.4	1861.4 ± 6.52	3.9 ± 3.9	0.08 ± 0.08
	C 7-8	53.80	54.30	54.8	1.0	0.20 ± 0.01	80 ± 3.1	49 ± 3.5	0.20 ± 0.01	13.4 ± 0.10	10.0 ± 0.9	32 ± 1.7	1860.2 ± 6.64	1.2 ± 1.2	0.17 ± 0.17
	C 8-9	54.80	55.30	55.8	1.0	0.22 ± 0.01	103 ± 4.3	72 ± 4.6	0.22 ± 0.01	13.6 ± 0.10	16.1 ± 1.3	22 ± 1.5	1858.8 ± 6.77	1.3 ± 1.3	0.17 ± 0.17
Start of ^{210}Pb$_{ex}$	C 9-10	55.80	56.30	56.8	1.0	0.21 ± 0.01	59 ± 2.6	28 ± 3.0	0.21 ± 0.01	13.8 ± 0.10	6.0 ± 0.7	6 ± 0.7	1857.5 ± 6.89	1.3 ± 1.3	0.17 ± 0.17
	C 10-11	56.80	57.30	57.8	1.0	0.23 ± 0.01	35 ± 1.8	5 ± 2.3	0.23 ± 0.01	14.0 ± 0.10			1856.2 ± 7.03	1.4 ± 1.4	0.17 ± 0.17
	C 11-12	57.80	58.30	58.8	1.0	0.38 ± 0.02	30 ± 1.5		0.38 ± 0.02	14.4 ± 0.11			1851.6 ± 8.40	4.6 ± 4.6	0.08 ± 0.08
Sedimentary shift	C 12-13	58.80	59.30	59.8	1.0	0.34 ± 0.02	51 ± 2.5	20 ± 2.9	0.34 ± 0.02	14.7 ± 0.11			1847.5 ± 9.36	4.1 ± 4.1	0.08 ± 0.08
	C13-14	59.80	60.30	60.8	1.0	0.20 ± 0.01			0.20 ± 0.01	14.9 ± 0.11					
	C 14-15	60.80	61.30	61.8	1.0	0.33 ± 0.02	36 ± 1.7	6 ± 2.3	0.33 ± 0.02	15.3 ± 0.11					
	C 15-16	61.80	62.30	62.8	1.0	0.38 ± 0.02	36 ± 1.7	5 ± 2.3	0.38 ± 0.02	15.6 ± 0.11					
	C 16-17	62.80	63.30	63.8	1.0	0.41 ± 0.02	33 ± 1.6	2 ± 2.2	0.41 ± 0.02	16.1 ± 0.11					
	C 17-18	63.80	64.30	64.8	1.0	0.33 ± 0.02	33 ± 1.4	3 ± 2.1	0.33 ± 0.02	16.4 ± 0.11					
	C 18-19	64.80	65.30	65.8	1.0	0.24 ± 0.01									
	C 19-20	65.80	66.30	66.8	1.0	0.43 ± 0.02	28 ± 1.4								
	C 20-21	66.80	67.30	67.8	1.0	0.46 ± 0.02	30 ± 1.7								
	C 21-22	67.80	68.30	68.8	1.0	0.43 ± 0.02	30 ± 1.5								
	C 22-23	68.80	69.30	69.8	1.0	0.48 ± 0.02	35 ± 1.9								
	C 23-24	69.80	70.30	70.8	1.0	0.34 ± 0.02	32 ± 1.3								
	C 24-24.8	70.80	71.20	71.6	0.8	0.52 ± 0.03	28 ± 1.4								

In the following paragraph we explain the characteristics of the chronological model selected as well as the relevant parameters used in order to construct the age model. The age model in core B05-13 was constructed using the Constant Rate Supply (CRS) model (Appleby and Oldfield, 1978), also named Constant Flux (CF) model (Sanchez-Cabeza and Ruiz-Fernandez, 2012). The underlying assumption in this model is a constant ^{210}Pb$_{ex}$ flux to the sediment surface (Appleby 2001, Sanchez-Cabeza and Ruiz-Fernandez, 2012). The CRS model is robust and widely used in different environmental settings but it is recommended to validate the age model with an independent tracer when applying it to marine sediments (Sanchez-Cabeza and Ruiz-Fernandez, 2012). Therefore, we validated the age model using ^{241}Am activities (chapter II) as the onset of the ^{241}Am activities can be correlated with the start of bomb tests in the Pacific (~1952 AD). Additionally, we used the ^{241}Am

profile peaks in 1963, corresponding to its maximum concentration in the troposphere. To take into account sediment compaction, the age estimation was performed as a function of mass depth (g.cm^{-2}) instead of depth (cm) (Sanchez-Cabeza and Ruiz-Fernandez, 2012).

^{210}Pb$_{ex}$ was calculated by subtracting an inferred ^{226}Ra value from ^{210}Pb$_{tot}$ data. Given that the ^{226}Ra concentration was not measured, it was inferred by averaging the ^{210}Pb$_{tot}$ activities from the 6 deepest samples (Table VI-1), assuming that these samples did not contain ^{210}Pb$_{ex}$. This assumption is based on the expected age of these samples in adjacent cores as established by the cross-correlation of sediment structures among cores (see chapter II). The inferred ^{226}Ra value obtained by this process was 30.6 ±1.5 Bq.Kg^{-1} and was subtracted from each ^{210}Pb$_{tot}$ value to obtain ^{210}Pb$_{ex}$ amount (Table VI-1).

In order to construct an age model in function of mass depth we first multiplied the DBD value (g.cm^{-3}) by the interval thickness (cm) in order to obtain the mass/area ratio (g.cm^{-2}) for each sample. The error associated with the Mass/Area values in each sample was estimated to be 5% of the mass/area values. Then we calculated the accumulated Z-mass (g.cm^{-2}) by adding up the mass/area of all preceding samples. For example, the accumulated Z-mass of sample 4 is the sum of the mass/area of sample 1, 2, 3 and 4. The estimation of the error of the accumulated Z-mass was calculated using the following formula:

$$Accumulated\ z-mass\ error_n = \sqrt{(Mass/Area)_n + (accumulated\ Z-mass)_{n-1}}$$

In a next step we calculated the inventory of ^{210}Pb$_{ex}$ per sample by multiplying ^{210}Pb$_{ex}$ with the mass/area from each sample. In one sample (B20-21) ^{210}Pb$_{tot}$ had not been measured (Table VI-1). For this sample, we calculated the inventory of ^{210}Pb$_{ex}$ using the following formula:

$$Inv\ ^{210}Pb_{exB20-21} = Thickness_{B-} * \frac{(Pb_{ex}*DBD)_{C-} - (Pb_{ex}*DBD)_{B-}}{ln\left(\frac{(Pb_{ex}*DBD)_{C-}}{(Pb_{ex}*DBD)_{B-}}\right)}$$

The error associated with the inventory of ^{210}Pb$_{ex}$ was calculated using the following formula:

$$Error\ Inv\ ^{210}Pb_{ex_n} = Inv\ ^{210}Pb_{ex_n} * \sqrt{\left(\frac{error\ Mass/Area\ per\ sample}{Mass/Area\ per\ sample}\right)^2 + \left(\frac{Error\ ^{210}Pb_{ex}}{^{210}Pb_{ex}}\right)^2}$$

In a following step we calculated the Total $^{210}Pb_{ex}$ Inventory by adding up the $^{210}Pb_{ex}$ Inventory of the preceding samples, but starting only from the first sample with discernible $^{210}Pb_{ex}$ (i.e., sample C9-10; Table VI-1) . For example, the total $^{210}Pb_{ex}$ Inventory of sample C7-8 is the sum of $^{210}Pb_{ex}$ of samples C9-10, C8-9 and C7-8. The total $^{210}Pb_{ex}$ Inventory of core B05-13 was 3823 ±47.2 (Bq.cm^{-2}). The error associated with the total $^{210}Pb_{ex}$ Inventory was calculated using the following formula:

$$\text{Error Total } Inv\ ^{210}Pb_{ex_n} = \sqrt{\left(\text{Error } Inv\ ^{210}Pb_{ex_n}\right)^2 + \left(\text{Error Total } Inv\ ^{210}Pb_{ex_{n+1}}\right)^2}$$

The next step was the calculation of the age in years of the base of each sample. We divided the dataset into two groups based on the onset of the ^{241}Am activities. The first group includes the samples between the start of $^{210}Pb_{ex}$ (C9-10) and the first sample below the start of the ^{241}Am activities (A17-18). The second group includes the samples between the onset of the ^{241}Am activities and the top. The age of a sample n of the first group and the age of a sample n of the second group was calculated according to the following equations:

$$Age\ CRS(\quad Am)_n = \frac{1}{-\lambda} * \left(\ln e^{(\lambda* \ )} + \left(\frac{}{J}\right) * \left(-\lambda * \sum_{A\ -}^{A\ -} INV \quad Pb_{ex}\ per\ sample\right)\right)$$

$$Age\ CRS(\quad Am)_n = \frac{1}{-\lambda} * \left(\ln e^{(\lambda*T\ )} + \left(\frac{}{J}\right) * \left(\sum_{A\ -}^{C\ -} INV \quad Pb_{ex}\ per\ sample\right)\right)$$

J1 and J2 I in the formulas described above were calculated using the following equation:

$$J = \left(\lambda * \sum_{A\ -}^{A\ -} INV \quad Pb_{ex}\ per\ sample\right) / \left(e^{(-\lambda* \ )} - e^{-\lambda*(T\ )}\right)$$

$$J = \left(\lambda * \sum_{A\ -}^{C\ -} INV \quad Pb_{ex}\ per\ sample\right) / \left(e^{(-\lambda* \ )} - e^{-\lambda*(T\ )}\right)$$

T1 is 53.5 years corresponding to the time period from the base of sample A17-18 (which corresponds to the onset of ^{241}Am) to the top of the core. T1 was calculated by subtracting 1952 AD (onset of bomb tests) from 2005.5 AD (core was taken in June 2005).

The model we applied permitted to date the sediment intervals down to sample C2-3. Below this sample, thick diatom layers with low densities prevented the use of this model which is why we

used a different approach. First we calculated the mass accumulation rate W (g.cm^{-2}.y^{-1}) from sample A0-1 to sample C2-3 using the following equation:

$$W_n = \frac{Mass/Area\ per\ sample_n}{delta\ T_n}$$

where: delta T corresponds to the time (in years) that represents each sample.

The values of W for samples C3-4 to C10-11 were calculated using a different approach. First we identified the samples associated with diatom layers (samples C3-4, C7-8, C8-9, C9-10 and C10-11) and the samples characterized by laminated sequences (C4-5, C5-6 and C6-7). Samples associated with diatom layers present higher mass accumulation rates in comparison with samples characterized by laminated sequences. For the samples associated with the diatom layers, W was calculated by averaging the W values of samples B18-19, C1-2 and C2-3, which were also characterized by thick diatom layers. For the samples characterized by laminated sequences, W was calculated by averaging the W values of samples B15-16, B16-14, B17-18, B19-20 and C0-1. The error associated with W was calculated using the following formula:

$$\text{Error W}_n = W_n * \sqrt{\left(\frac{\left(Error\ Total\ Inv\ ^{210}Pb_{ex}\right)_{n+}}{\left(Total\ Inv\ ^{210}Pb_{ex}\right)_{n+}}\right)^2 + \left(\frac{\left(Error\ ^{210}Pb_{ex}\right)_n}{\left(^{210}Pb_{ex}\right)_n}\right)^2}$$

Finally, we calculated the age (AD) of the samples by subtracting 2005.5 to the ages inferred using the equations X and Y. The ages of the samples from C3-4 to C10-11 were calculated using the following formula:

$$Age\ AD\ CRS\quad Am_n = \left(Age\ AD\ CRS\quad Am_{n-}\right) * \frac{(Mass/Area)_n}{W_n}$$

In order to fit the age model to the high resolution sub-sampling applied for fish scale identification, the calculated ages were interpolated. The ^{210}Pb activities had been measured at intervals of 1 cm, but the samples used for fish scale identification and for the different proxies were sub sampled at higher resolution according to the core stratigraphy (Salvatteci et al., 2012).

VI-3.2 Fish scale abundance quantification and flux calculation

Fish scale records of anchovy and oceanic species for cores B05-13 and B05-14 were taken from Salvatteci et al. (2012) and for cores B05-13 and B04-6 from Gutierrez et al. (2009). The scale abundances of all other species have not been presented previously. The quantification of the fish

scale abundance is explained in detail in Salvatteci et al. (2012). For the present work, abundances of scales (# of scales.g-1 per interval) per sample (n) have been transformed into fluxes (or SDR) using the following formula:

$$Fish\ scale\ fluxes_n = W_n * \frac{\#scales_n}{sediment\ dry\ weight_n} *$$

VI-3.3 Proxies of environmental conditions

In order to understand the role of climate forcing in regulating fish stock variability off Peru we used several proxies to characterize the climatic and oceanographic environment. First we used the wind speed data from the International Comprehensive Ocean-Atmosphere Data Set (ICOADS, NOAA), taken from a presentation by Field et al. (2006). Although the ICOADS data is known to have some uncertainties (Bakun et al., 2010), it is the longest observational record (since ~1845) and allows detecting multidecadal trends or a centennial trend in upwelling favorable winds. Second, we used the SOI data that were obtained from the Climatic Research Unit, University of East Anglia, UK (http://www.cru.uea.ac.uk/cru/data/soi.htm). Positive anomalies of the SOI indicate strengthening of the trade winds (Bakun et al., 2010). Third, we used the Cold Tongue Index (CTI) data that were taken from http://jisao.washington.edu/enso/. Positive CTI anomalies indicate warm periods or a weakening of the CTI, for example during the strong El Niño 1982-83 and 1997-98 the CTI show positive anomalies. Fourth, we use the Pacific Decadal Oscillation (PDO) data from instrumental observations (Mantua et al., 1997, data available on http://jisao.washington.edu/pdo/). During the positive phase of the PDO, the Aleutian low pressure system deepens and shifts southwards, SSTs are anomalously warm along the coast of North America and cool in the central Pacific; during the negative phase of the PDO the conditions are generally the opposite (Lehodey et al., 2006). PDO reconstructions prior to 1900 AD show little agreement between them (see for example PDO reconstructions proposed by D'Arrigo et al., 2001; Biondi et al., 2001; MacDonald and Case, 2006), nevertheless we use the Biondi et al. (2001) PDO reconstruction to compare the oceanographic changes in the North Pacific with the observed changes off Peru. Fifth, we used the reconstructed El Niño and La Niña events that were considered extreme or very strong (Gergis and Fowler, 2006; 2009; Ortlieb et al., 2000). In order to remove the high frequency variability of the records, the ICOADS, SOI, CTI and PDO data were smoothed with a 7-point moving average and then normalized to standard units (the PDO data were not normalized).

Apart from the reconstruction of the physical properties of the system, we also used proxies to compare the SDR off Peru with other trophic levels. First, the SST reconstruction off Pisco since ~1850 AD was obtained from core B04-6 (Gutierrez et al., 2011). Second, export production was

inferred by the Total Organic Carbon (TOC) and the Biogenic Silica contents obtained in core B-14 (data from chapter IV). Third, the number of guano producing seabirds that feed almost exclusively on anchovy (Guanay *Leucocarbo bougainvillii*, Piquero *Sula variegata* and Pelicano *Pelecanus thagus*, between 6 °S and 14 °) was taken from Jahncke et al. (2004), Goya (2000); and IMARPE data. Finally, the guano harvest was taken from Cushman (2003).

VI-3.4 Composite core

A composite core combining cores B05-13 and B04-6 was assembled in order to compare the fish scale record with proxies of environmental changes since none of the cores presents an undisturbed and complete sedimentary column (see chapter II). Cores B05-13 and B05-14 show the most complete sedimentary columns, but they exhibit an apparent bioturbated section and a hiatus respectively (see chapter II), complicating the age models. Fish scale fluxes of core B05-13 (smoothed with a 3-point moving average) are used from the change in sediment density (observed in multiple cores, see chapter II) to the ^{241}Am peak. Fish scale record of B05-13 is preferred over that of B05-14 due principally to a better chronology and because the pattern of the anchovy scale record is not affected when the data is transformed to fluxes, which is the case in core B05-14 (possible problem with the age model when working at high resolution levels). The fish scale record of core B04-6 is used since ~1963 because this section does not show a hiatus or large mixing sequences as is the case with core B05-13. The peak in ^{241}Am (~1963 AD) is used to cross-correlate B04-6 and B05-13 cores, which is clearly marked in both cores (see chapter II). Additional support for this correlation is that in both cores the ^{241}Am peak coincides with the highest anchovy flux. Thus, the combined fish scale record of cores B05-13 and B04-6 is the best available to interpret changes in anchovy biomass over time.

VI-4. Results

VI-4.1 Chronological model of core B05-13

The ^{210}Pb$_{ex}$ profile of core B05-13 shows a clear decline with cumulative mass depth, with sample C9-10 representing the last interval with detectable ^{210}Pb$_{ex}$ activities (13.8 g.cm^{-2} at 56.8 cm depth, Table VI-1, Fig. VI-2). An interval with relatively constant ^{210}Pb$_{ex}$ activities can be observed between 3.3 to 5.5 g.cm^{-2} cumulative mass depth which was probably caused by a bioturbation event. Two different periods with different mass accumulation rates can be discerned: a rapid decrease with cumulative mass-depth above onset of ^{241}Am on the one hand, and a slow decrease with cumulative mass depth below the onset of ^{241}Am on the other (Fig. VI-2). The mean value of W ±sd of the samples below the onset of ^{241}Am is 0.108 ±0.031 g.cm^{-2}.y^{-1}, while that of the samples above the onset

of ^{241}Am is 0.085 ±0.016 g.cm^{-2}.y^{-1}. Yet, the W values show important changes throughout the core (Table VI-1). The age of the change in sediment density according to the CRS-^{241}Am age model is 1849.5 ±7 years AD.
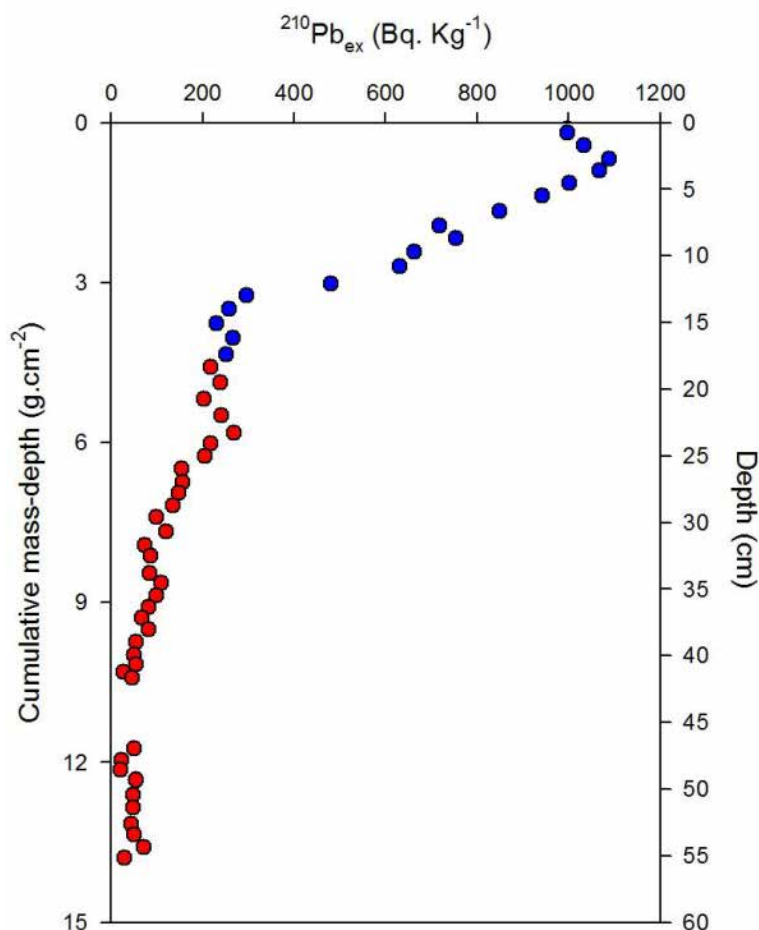
Figure VI-2. Age model of core B05-13. The blue data points correspond to the samples above the onset of ^{241}Am and the red data points correspond to the samples below the onset of ^{241}Am.

The chronology of B05-14 is explained in chapter IV however is briefly described here. The chronological model of B05-14 was obtained using ^{210}Pb$_{ex}$ and ^{241}Am activities measured by gamma spectrometry unlike the ^{210}Pb content in core B05-13 that was measured by alpha spectrometry. The ^{210}Pb$_{ex}$ cumulative mass depth profile showed 4 distinct sections with important changes in sedimentation rates: Section 1 from the top to 4.3 cm: sedimentation rate of 0.184 cm.y^{-1}; section 2 from 4.3 to 8.5 cm: 0.149 cm.y^{-1}; section 3 from 8.5 to 23.2 cm: sedimentation rate of 1.166 cm.y^{-1}, and section 4 from 23.2 to 46.6 cm: 0.442 cm.y^{-1}. Core B05-14 presents a hiatus at ~4.3 cm depth and consequently the ages of the last 40 years are less reliable than in core B05-13. In core B05-14 the estimated age of the change in sediment density was 1852.3 ± years AD. W-values in core B05-14 were calculated by multiplying DBD by the sedimentation rate of the sample (see chapter IV).

The age of the change in sediment density and several other proxies is ~1820 AD in core B04-6 and B04-13 (Gutierrez et al., 2009); however the estimated age of the same event in cores B05-13 and B05-14 are 1849.5 and 1852.3AD respectively. The discrepancy in the date of the same event among cores is likely due to the fact that core B04-6 presents a non-continuous sedimentary column that complicate the development of an age model (chapter II). Additionally cores B05-13 and B05-14 show the most complete sedimentary column in comparison with several cores retrieved off Pisco (with exception of the last ~ 40 years) and thus its chronology is interpreted to be more reliable. Additionally, sedimentation rates of cores B05-13 and B05-14 are higher than in core B04-6 and thus are more appropriate to infer the sub-decadal to multidecadal-scale variability in fish biomass variability. The high sedimentation rates after the change in sediment density in cores B05-13 and B05-14 (~ 4 mm.y^{-1}), added to the high resolution subsampling of these cores results in an average time spam of 1.1 years in both cores. In contrast, the relatively low sedimentation rate in core B04-6 (~2.1 mm.y^{-1}, Gutierrez et al., 2009) added to the relatively coarser subsampling give an average of 3.1 yr per sample.

VI-4.2 Fish scale abundances and proxies of environmental conditions

The fish scales downcore distribution in the 4 box-cores evaluated follow a similar pattern (Fig. VI-3). Anchovy scales dominate the records from the base of the cores up to a few cm above the change in sediment density, then oceanic species prevail from this point to ~20 - ~40 cm (depending of the core), and finally anchovy dominates again the record with exception of some oceanic species scales present near the top (Fig. VI-3). Anchovy scales are better preserved above the change in sediment density (dashed lines in Fig. VI-3) than below it and therefore provide a more reliable picture in this part of the record (Salvatteci et al., 2012). Highest abundance of hake scales were recorded in the Callao core (Fig. VI-3), which is more coherent with the present northerly distribution of hake (Guevara and Lleonart, 2008). The highest abundance of Myctophids scales are observed in the southern Pisco cores, which is also coherent with the latitudinal distribution of the Myctophids, for example *Myctophum nitidulum* represents 65% of the mesopelagic fishes between 14 and 18 °S (Cornejo and Kopplemann, 2006). Higher abundances of non-identified, generally small-sized, fish scales were recorded in the southern cores.
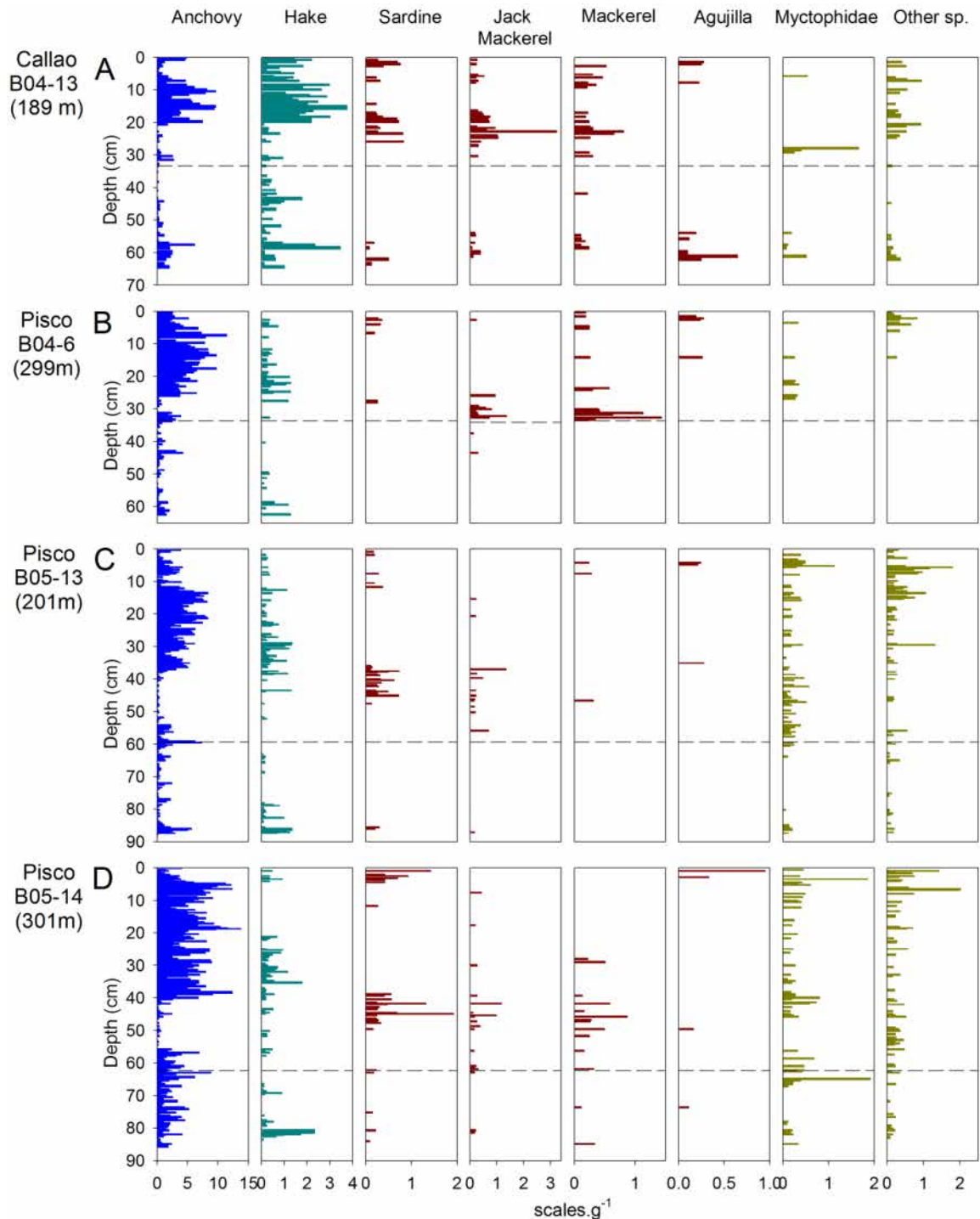
Figure VI-3. Fish scale abundances of Anchovy (*Engraulis ringens*), Hake (*Merluccius gayi peruanus*), Sardine (*Sardinops sagax sagax*), Jack mackerel (*Trachurus murphy*), mackerel (*Scomber japonicus*), "Agujilla" (*Scomberesox saurus scombroides*), Myctophidae, and Other sp. (mainly composed by unidentified fish scale) in the 4 box-cores evaluated in the present work. The dashed lines indicate the position of the sedimentary shift (Gutierrez et al. 2009). The dotted lines in each core represent the sedimentary shift reported by Gutierrez et al. (2009) and Sifeddine et al. (2008) for cores B04-6 and B04-13 and by Salvatteci et al. (2012) for cores B05-13 and B05-14 (see also chapter II).

In order to understand the historical changes within the PUE, we identified relationships among fish species by correlating the scale abundances. Despite the presence of sardine during periods characterized by low abundance of anchovy, anchovy and sardine scales do not show a negative correlation in any of the cores (Tables VI-2 to VI-5). Moroever, two cores (B05-13 and B05-14) show a negative non significant correlation while core B04-6 and the Callao core show a positive non significant correlation. The highest correlation value was observed between anchovy and hake scales in the Callao core ($r=0.71$, $p<0.007$, Table VI-2) and this correlation was also significant in core B05-13 ($r=0.21$, $p<0.07$, Table VI-5). Strong and significant relationships among some oceanic species (i.e., sardine, jack mackerel, mackerel and agujilla) were observed in several cases. In the most northerly situated Callao core, sardine, jack mackerel and mackerel are significantly correlated (Table VI-2). Further south, in core B04-6 sardine with agujilla scales and jack mackerel with mackerel scales are significantly correlated (Table VI-3). In the core closest to the coast (B05-13), only mackerel and agujilla scales show a significant relationship (Table VI-4). In core B05-14, which is located farthest from the coast in comparison with B05-13, correlations between sardine and jack mackerel, sardine and agujilla as well as jack mackerel with mackerel were significant (Table VI-5). In the Pisco cores that are located far from the coast (B04-6 and B05-14) agujilla and other sp. scales show high correlation coefficients (Table VI-3 and VI-5 respectively) in comparison with the more coastal core (B05-13).

Table VI-2. Correlation coefficients between fish scales of different species in core B04-13 retrieved off Callao. Underlined and cursive values indicate significant correlations ($p < 0.007$)

B04-13	Anchovy	Hake	Sardine	Jack Mackerel	Mackerel	Agujilla	Myctophidae	Other sp.
Anchovy	1							
Hake	0.71	1						
Sardine	0.10	0.21	1					
Jack Mackerel	-0.01	-0.01	0.30	1				
Mackerel	-0.04	0.10	0.32	0.55	1			
Agujilla	-0.03	-0.07	0.20	-0.01	-0.06	1		
Myctophidae	-0.07	-0.10	-0.09	-0.02	-0.06	0.19	1	
Other sp.	0.18	0.18	0.23	0.30	0.20	0.13	-0.05	1

Table VI-3. Correlation coefficients between fish scales of different species in core B04-6 retrieved off Pisco. Underlined and cursive values indicate significant correlations ($p < 0.007$).

B04-6	Anchovy	Hake	Sardine	Jack Mackerel	Mackerel	Agujilla	Myctophidae	Other sp.
Anchovy	1							
Hake	0.19	1						
Sardine	0.04	0.11	1					
Jack Mackerel	-0.04	-0.10	0.00	1				
Mackerel	0.01	-0.04	-0.07	0.36	1			
Agujilla	0.14	-0.05	0.45	0.00	0.05	1		
Myctophidae	0.11	0.24	-0.06	0.11	-0.03	0.14	1	
Other sp.	0.11	-0.03	0.60	-0.04	-0.01	0.69	0.12	1

Table VI-4. Correlation coefficients between fish scales of different species in core B05-13 retrieved off Pisco. Underlined values indicate significant correlations (p < 0.007).

B05-13	Anchovy	Hake	Sardine	Jack Mackerel	Mackerel	Agujilla	Myctophidae	Other sp.
Anchovy	1							
Hake	0.23	1						
Sardine	-0.14	0.05	1					
Jack Mackerel	-0.01	0.01	0.06	1				
Mackerel	-0.02	-0.06	0.06	0.04	1			
Agujilla	0.06	-0.06	-0.04	-0.02	0.27	1		
Myctophidae	0.08	0.00	0.09	0.07	0.15	0.17	1	
Other sp.	0.30	0.11	0.00	0.03	0.12	0.00	0.18	1

Table VI-5. Correlation coefficients between fish scales of different species in core B05-14 retrieved off Pisco. Underlined values indicate significant correlations (p < 0.007).

B05-14	Anchovy	Hake	Sardine	Jack Mackerel	Mackerel	Agujilla	Myctophidae	Other sp.
Anchovy	1							
Hake	0.03	1						
Sardine	-0.14	0.04	1					
Jack Mackerel	-0.10	0.01	0.30	1				
Mackerel	-0.13	-0.08	0.15	0.39	1			
Agujilla	-0.06	0.04	0.38	-0.01	0.04	1		
Myctophidae	0.06	0.10	0.10	0.14	0.08	-0.05	1	
Other sp.	0.17	-0.01	0.17	-0.03	0.01	0.35	-0.06	1

The different periods favorable to anchovy and to oceanic species were clearly associated with proxies reflecting different environmental conditions. The terrestrial input which is strongly tied to precipitation in the continent (chapter V) is inferred by the Al contents in cores B04-13, B04-6 and B05-14 and by the sediment density values in core B05-13. The sub-oxic or anoxic conditions in the water-sediment interface are inferred by the Mo contents in cores B04-13, B04-6 and B05-14. The strength of the OMZ is inferred by the $\delta^{15}N$ values of sedimentary organic matter. Finally the export production is inferred by the TOC, Nickel, Nitrogen and/or biogenic silica contents. A detailed explanation of these proxies is given in chapter III, IV and V. The low abundance of anchovy and oceanic species scales from the base of the cores up to the change in sediment density is associated with higher terrestrial input, sub-oxic conditions in the water-sediment interface, a weak OMZ and low export production. Core B04-13 shows a section (from ~65 to ~55 cm depth) where the conditions were somewhat opposite to the conditions previously described, and these conditions are not observed in the Pisco cores (Fig. VI-4). The reason for this discrepancy is interpreted to be that core B04-13 presents older sediments in comparison with the Pisco cores. The high abundance of oceanic species some cm above the change in sediment density are associated with low terrestrial input (likely diluted by the high abundance of biogenic silica), anoxic conditions in the water-sediment interface, strong OMZ, strong variability in the export production proxies and the highest biogenic silica contents. The high abundance of anchovy scales after the presence of oceanic species is associated with lower terrestrial run-off, anoxic water-sediment interface, a strong OMZ, and high export production (high values of TOC, Ni, and/or N).
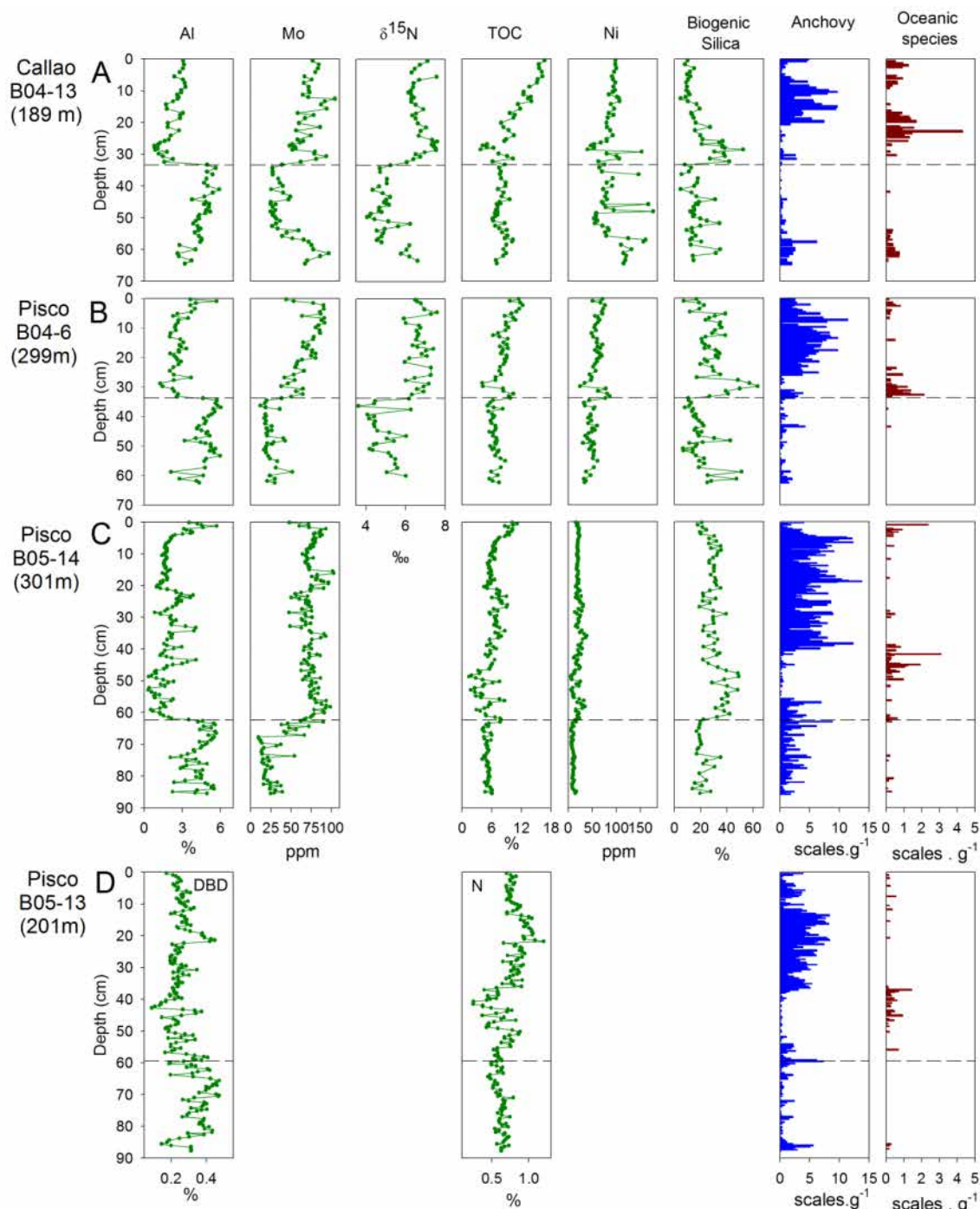
Figure VI-4. Anchovy (*Engraulis ringens*) and oceanic species scale abundances, and proxies for environmental conditions. The oceanic species include Sardine (*Sardinops sagax sagax*), Jack Mackerel (*Trachurus murphy*), Mackerel (*Scomber japonicus*) and Agujilla (*Scomberesox saurus scombroides*). The proxies for environmental conditions includes aluminum (Al) and Dry bulk Density (DBD) as a proxy for terrestrial run-off, Mo as a proxy for redox conditions in the sediments, δ¹⁵N as a proxy for OMZ intensity, total organic carbon (TOC), nitrogen (in core B05-13), nickel (Ni), and biogenic silica as a proxy for export production. A) Core B04-13 off Callao. B) Core B04-6 off Pisco. C) Core B05-14 off Pisco. D) Core B05-13.

In the next sections the emphasis is put in the fish scale record after the change in sediment density that is characterized by higher preservation of fish scales and strong decadal –scale variability. The age of the change in sediment density was estimated as ~1820 AD in cores B04-13 and B04-6,

while the age of the same event is ~1850AD in cores B05-13 and B05-14. The discrepancy in the age of what is considered the same and unique regional event is caused by the age models applied, and the continuity of the sedimentary column that in turn affects the development of an age model. Cores B05-13 and B05-14 present the most complete sedimentary column in comparison with the other Pisco cores (chapter II) and thus the age of these cores are used as a reference to present the results in the following sections. The fish scale fluxes of the other cores (B04-13 and B04-6) are used as a complement in the following sections.

VI-4.3 Fish scale fluxes

Anchovy scale fluxes in cores B04-13, B04-6, B05-13 and B05-14 show a similar pattern and a strong decadal to multidecadal-scale variability during the last ~155 years (Fig. VI-5) taking into account the chronological uncertainties in each core. In the 4 cores very low fluxes characterize the second half of the 19th century. Additionally a positive trend towards higher anchovy fluxes can be observed from the beginning of the 20th century to ~1960AD which coincides with the start of the industrial fishery; however between ~1945 to ~1960 the core B05-14 shows anomalous high fluxes related to the exceptionally elevated sedimentation rate in this part of the core. Finally moderate to low anchovy fluxes are recorded from ~1960 to 2005 AD, which coincides with the period of industrial fishery and in part with the period favorable to sardine observed in the landings records off Peru and Chile. Core B04-6 shows also a similar pattern but the chronology gave an age of ~20 years older to some important features like the start of the positive trend which is dated at ~1900 in cores B04-13, B05-13 and B05-14 while it is dated at ~1880 AD in core B04-6. However the decadal maximum in anchovy fluxes during the ~1960s coincides well with the other cores, due in part to the reliable age control in the last 50 years of the records obtained from the [241]Am activities (chapter II).

Hake scales are the second most abundant scales after anchovy scale and their highest fluxes generally coincide with the period of higher anchovy scale fluxes, especially in the Callao core (Fig. VI-5). Higher hake scale fluxes are registered between ~1900 to 2004 AD in B04-13, ~1895 to ~1965 in B05-13, and from ~1895 to ~1945AD in B05-14. Core B04-6 shows the lowest fluxes of hake scales. During the period characterized by very low anchovy fluxes (from~1865 to ~1900AD taking cores B05-13 and B05-14 as a reference), three pulses with hake scale fluxes can be observed in cores B05-13 and B05-14. These pulses of hake scales are located between the diatom bands after the change in sediment density (see chapter II). In cores B05-13 and B05-14 hake scales are absent from ~1965 to ~1980AD while present from 1980 ~2000AD, whereas the Callao core shows hake scale fluxes from the beginning of the 20th century up to 2004AD.
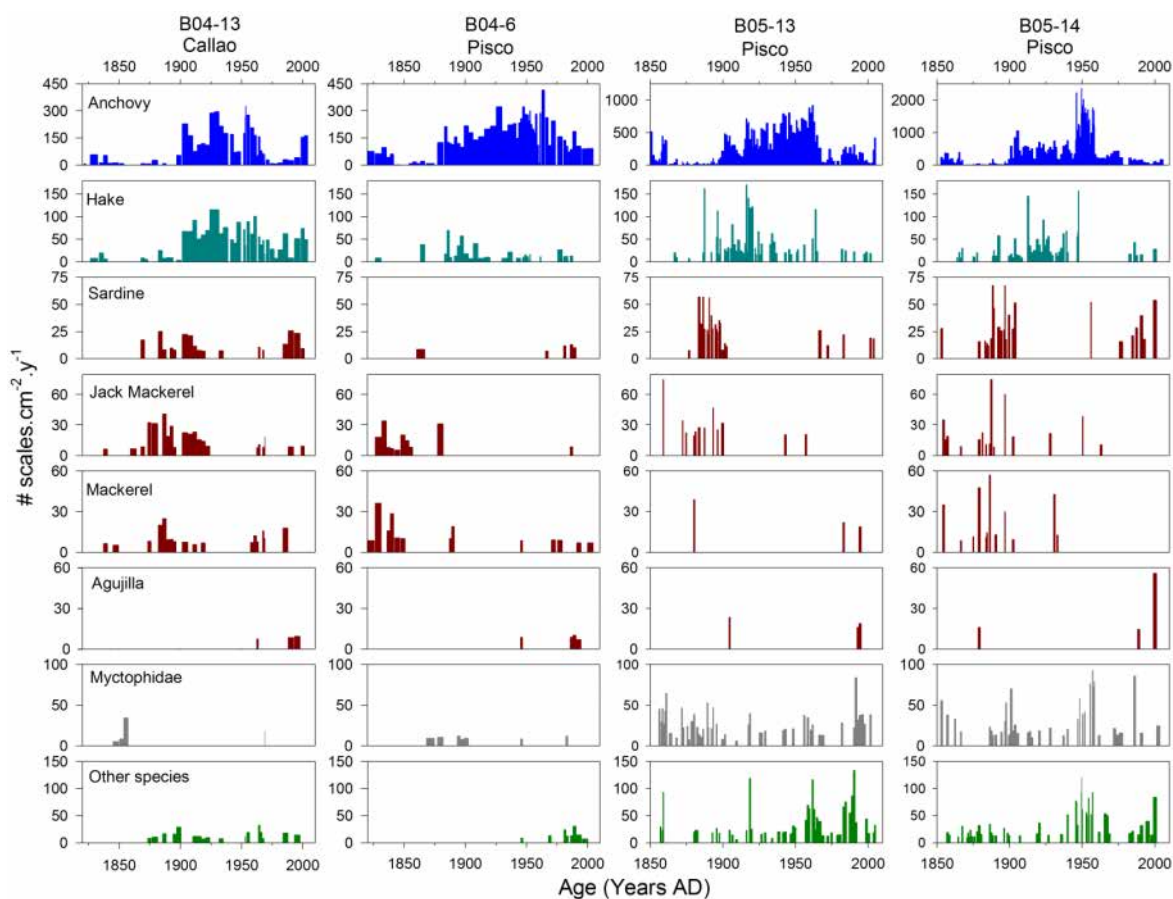
Figure VI-5. Fish scale fluxes (#scales . cm^{-2} . y^{-1}) in cores (from left to right) B04-13, B04-6, B05-13 and B05-14 after the sedimentary shift. Fish species from top to bottom: Anchovy (*Engraulis ringens*), Hake (*Merluccius gayi peruanus*), Sardine (*Sardinops sagax sagax*), Jack mackerel (*Trachurus murphy*), mackerel (*Scomber japonicus*), "Agujilla" (*Scomberesox saurus scombroides*), Myctophidae, and other sp. The range of the y-axis for each species is the same in both cores with exception of the anchovy fluxes.

Sardine, jack mackerel, mackerel and agujilla, which are usually associated with warmer and more oceanic waters, are present in two periods (the older period from ~1855 to ~1905AD and the recent period from ~1965 to ~2000AD, always taking as a reference cores B05-13 and B05-14), although not all four species are present in both periods. During the older multidecadal period (from ~1855 to ~1905AD), sardine scale fluxes are dominant between ~1880 to ~1905 in cores B05-13 and B05-14 and associated with low fluxes or no flux of anchovy scales. By contrast, both anchovy and sardine scale fluxes were present from ~1895 to ~1905AD. The Callao core (B04-13) also presents the same pattern. Sardine scales appeared again in the recent multidecadal period (from ~1965 to ~2000AD). In the four cores studied, jack mackerel and mackerel scale fluxes are more abundant in the older period in comparison with the recent period. Finally, agujilla scales are present in the four cores and during the two periods, but the scale abundance of this species is very low. There are also sparse fish scales between the two periods. The most abundant of the oceanic species was sardine, followed by jack mackerel, mackerel and agujilla

Myctophidae scale fluxes are higher in the southern cores (B05-13 and B05-14) than in the two other cores. In core B05-13, Myctophidae scale fluxes are most abundant between ~1855 to ~1900AD and between ~1990 to ~2000AD in B05-13, in part coinciding with the multidecadal periods that favor the oceanic species (Fig. VI-5). Myctophidae scales are the third most abundant after anchovy and hake scales. Other species scales fluxes (mainly composed by unidentified scales) are also higher in the southern cores (B05-13 and B05-14), and the fluxes are relatively higher from ~1955 to 1995AD, in part coinciding with the recent multidecadal period favorable to oceanic species.

VI-4.4 Multidecadal-scale changes in anchovy and sardine populations

Anchovy and sardine scale fluxes from Callao, Pisco and Mejillones (Chile) shown in Figure VI-6 indicate that the older multidecadal period favorable to oceanic species (~1855 to 1905AD) was recorded in the whole studied area in the center of the HCS. In the cores B05-13 and B05-14 the presence of oceanic species lasted from ~1855 to 1905 AD, however the presence of sardine scales occurred mainly from 1880 to ~1905 AD. The errors associated with the chronological models in each of the cores impede to make broader interpretations between the Pisco cores and the Callao and/or Mejillones core, but the patterns between anchovy and sardine in each core during the same interval can serve to understand the population changes that occurred during this multi-decadal period. For example there is negative trend towards lower sardine fluxes from ~1885 to 1905 AD in cores B05-13 and B05-14 which is associated with an increase in anchovy fluxes. In the Mejillones core the same pattern is observed, however the highest fluxes of anchovy and sardine scales is recorded ~10 years earlier than in the Pisco cores, possibly due to a problem with the age models. Off Callao the sardines lasted some decades after the decadal maximum in anchovy fluxes, which is not surprising given that the Callao core is located farthest from the coast. Additionally, the fluxes of anchovy scales during the older multidecadal period favorable to oceanic species were lower in Callao and higher in Mejillones in comparison with the anchovy fluxes in the rest of the same core (Fig. VI-6A and G); the anchovy scale fluxes in the Pisco cores (B05-13 and B05-14) also show low values but not as low as the Callao core.
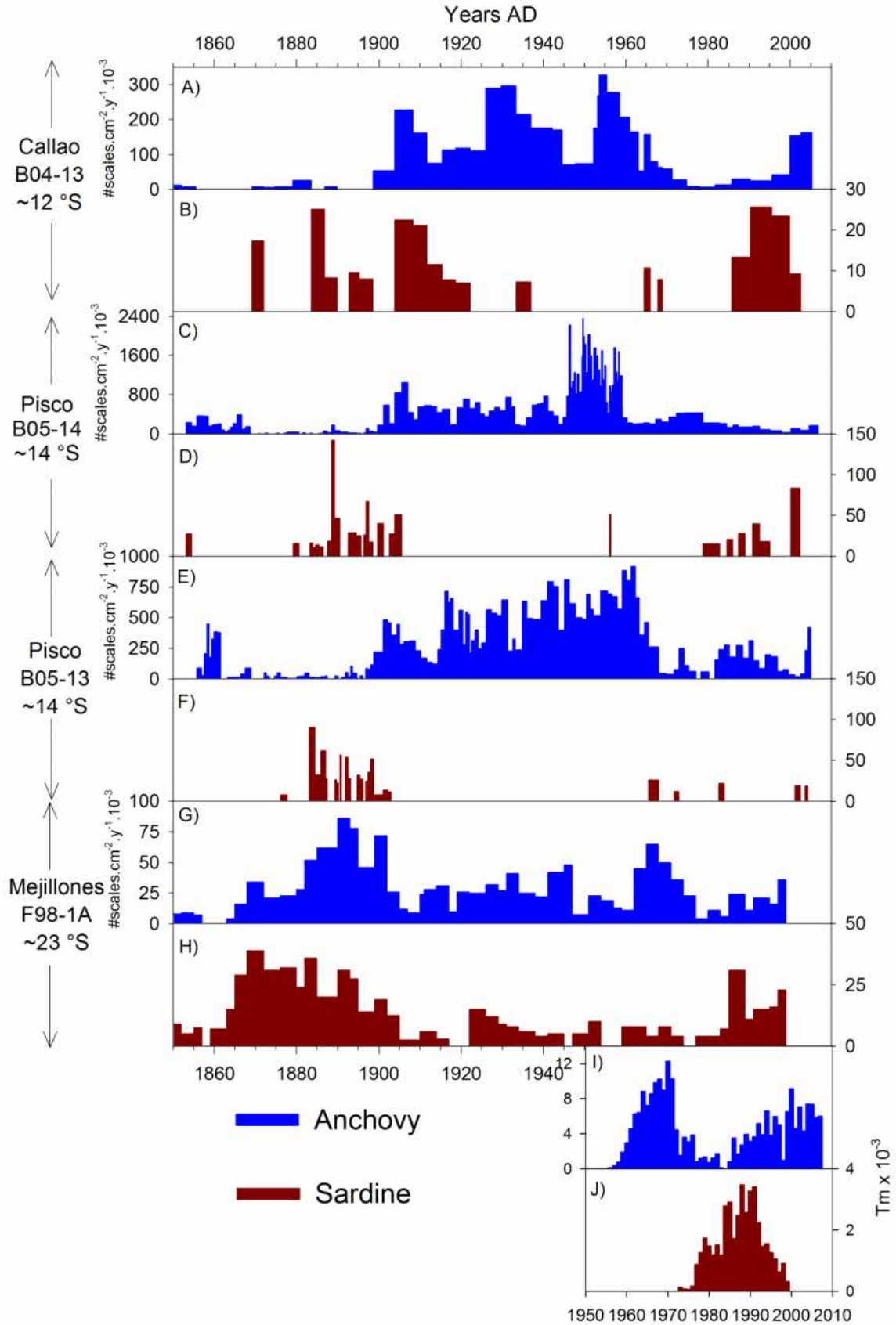
Figure VI-6. Comparison of the anchovy (blue bars) and sardine (red bars) scale fluxes in cores retrieved off Callao (B04-13), Pisco (B05-13 and B05-14) and Mejillones (F89-1A).

During the most recent multidecadal period (~1970 to 2000AD), sardine scales were recorded at all three sites (Fig. VI-6). This second period coincides with the industrial fishery (~1960 up to present) that could bias the number of fish scales deposited on the ocean floor. All the sedimentary records (especially B04-13) show high anchovy fluxes during the 1950 and 1960s, low anchovy SDR values in the '70s,'80s and beginning of the '90s, and an increase in anchovy scale fluxes during the last few years up to present. The low anchovy scale fluxes in the '70s, '80s and beginning of the '90s is associated with an increase in sardine fluxes, which is consistent with the anchovy and sardine landings off Peru (Fig. VI-6). The landings of anchovy and sardine off Peru illustrate the good coherence between the fish landings and the anchovy and sardine scale fluxes (Fig. VI-6).

There are also similarities and differences between the two multidecadal periods favorable to oceanic species. During the periods favorable to oceanic species (~1855 to 1900AD and from ~1970 to 2000AD), the initial phase was unfavorable for sardines, then the high fluxes of sardine were associated with low fluxes of anchovy, after that anchovy and sardine coexisted for a short period of time and finally sardine disappeared while anchovy flourished (Fig. VI-6). Additionally, two important differences can be observed when comparing the sardine fluxes with proxies of environmental changes as the SST and the biogenic silica contents (Fig. VI-7B, D and F). The first main difference is that the highest SSTs were recorded during the older period favorable to sardine; however during the most recent period favorable to sardine (~1970 to 2000 AD) the reconstructed SST do not show warm SST (Fig. VI-7B). Finally, some years before the appearance of sardine, the highest biogenic silica contents in all the record are observed, but the more recent multidecadal period favorable to sardines does not show this feature (Fig. VI-7D and F).
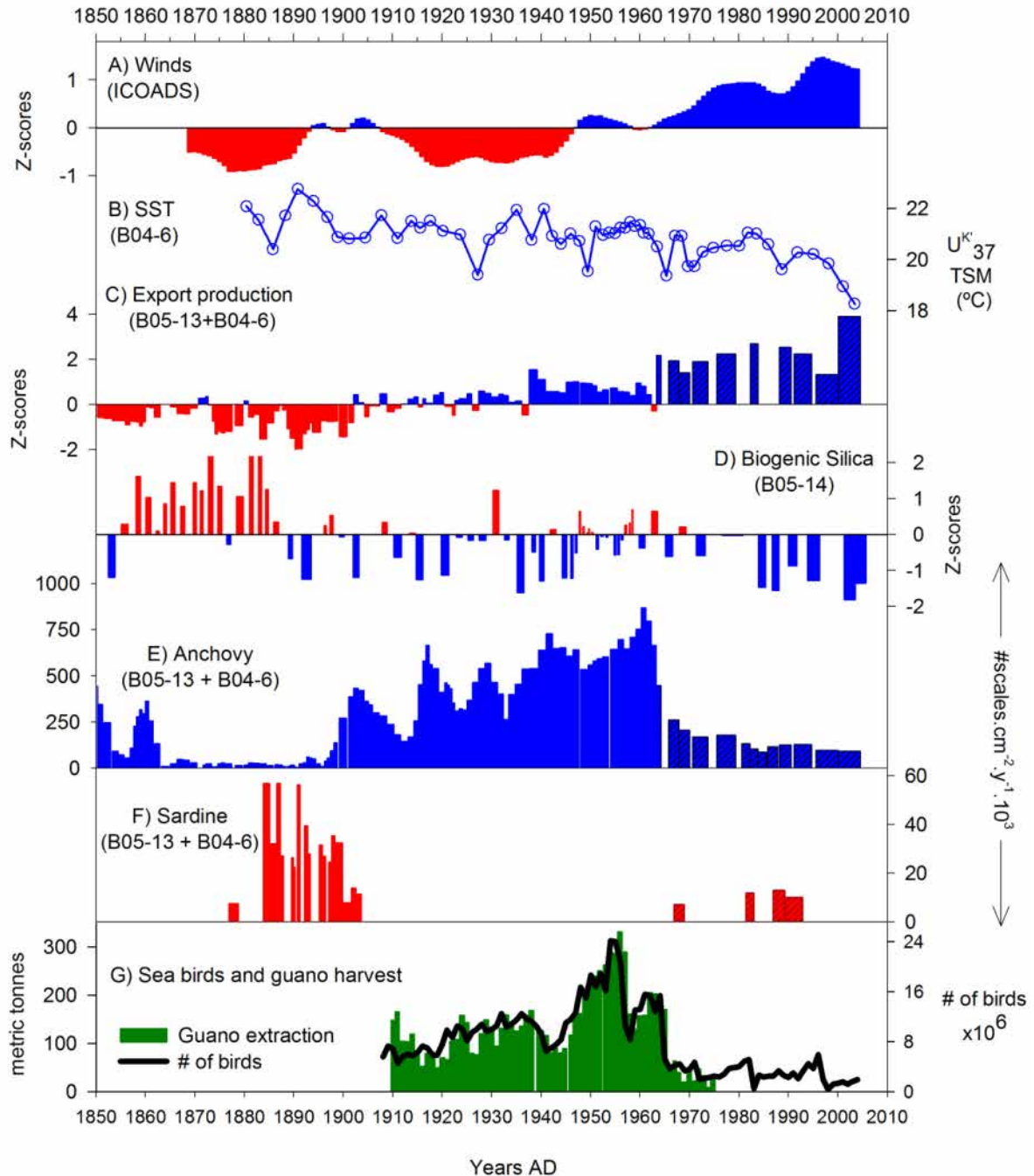
Figure VI-7. A) Regional alongshore wind stress off Pisco (Field et al., 2006), the data from ICOADS were smoothed with a 7-point moving average. **B)** Sea Surface Temperature (SST) estimations from core B04-6 (Gutierrez et al., 2011). **C)** Export production fluxes inferred by the Nitrogen content in core B05-13 and B04-6 (hatched bars). The data were smoothed with a 3-point moving average and then normalized. **D)** Biogenic silica contents in core B05-14. **E)** Anchovy scale fluxes in core B05-13 and B04-6 (hatched bars) as a proxy for anchovy biomass variability, the data were smoothed with a 3-point moving average. **F)** Sardine scale fluxes as a proxy for sardine biomass variability in core B05-13 and B04-6 (hatched bars). In core B05-13 each sample represents ~1.1 yr. **G)** Number of guano producing birds: Guanay (*Leucocarbo bougainvillii*), Piquero (*Sula variegata*) and Pelican (*Pelecanus thagus*), between 6 °S and 14 °S; alongside with guano (bird droppings) extraction off Peru (Cushman, 2003).

VI-4.5 Changes in upwelling favorable winds, SST and export production since ~1850 AD

An increase in wind intensity, accompanied with a decrease in SST, and an increase in export production since the early 20th century can be observed in the data shown in Figure VI-7. The ICOADS data suggest relatively weak winds from ~1870 to 1940, a small increase around ~1900AD and then a positive trend in the following 50 years. There is a strong and significant tendency (r = 0.75, p<0.001, using non-smoothed data) towards stronger upwelling favorable winds from the beginning of the increase in anchovy scale fluxes in core B05-13 (1895 AD) to the present (Fig. VI-7A). This upward trend in wind intensity in the direction favorable to upwelling is associated with a decrease in SST (Fig. VI-7B), as inferred by alkenone SST reconstruction in core B04-6 (Gutierrez et al., 2011). Coupled with the upwelling favorable winds increase and the SST decrease, an increase in export is evident from ~1890 to ~1960 AD (Fig. VI-7C). The intensified upwelling and increased productivity during the last ~100 years favored the anchovy production, with exception of the most recent multidecadal period favorable to oceanic species, as observed in the composite record show in Figures VI-7E and F. The increase in anchovy scale fluxes from ~1900 to ~1960 (Fig. VI-7D) is even more apparent in the Callao and Pisco cores in comparison with the Mejillones core (Fig. VI-6). This tendency continues towards the present in the export production proxy (Fig. VI-7C) but the start of the industrial fishery (~1960AD) originated a drastic diminution in the anchovy scale fluxes. In summary the oceanographic conditions off Pisco during the last 100 years conduced to an overall increase in upwelling intensity and export production.

The intensification of upwelling and the increase in anchovy abundance were also favorable to other fishes like hake and other species at the top of the food chain: the guano birds. Hake latitudinal distribution extends from 1 °N to 14 °S and under El Niño conditions (when sub-surface waters are more oxygenated) this range extends to 18 °S, but most of the stock is located between 3°S and 10 °S (Guevara-Carrasco and Lleonart, 2008). The Callao record shows abundant hake scales from the end of the older multidecadal period (~1880 to 1905AD) up to the 2004 (Fig. VI-3A). The Pisco cores also show high hake scales fluxes from the beginning of the anchovy trend (~1900 AD) to the decadal maximum in anchovy SDR (~1965 and ~1945 in core B05-13 and B05-14 respectively). Guanay cormorant (*Phalacrocorax bougainvillii*), Peruvian booby (*Sula variegata*), and Peruvian pelican (*Pelecanus thagus*) are the most abundant seabirds in the PUE and feed primarily on anchovy. The number of guano birds shows a similar increasing trend from ~1900 (when the record starts) to ~1956 (Fig. VI-7F). El Niño 1957/58 strongly decimated the bird populations but they recovered relatively fast (~1964). However, since the beginning of the industrial fishery off Peru (~1965 AD) that lowered the prey availability (Jahncke et al. 2004), the abundance of guano birds is very low (Fig. VI-7F).

The number of guano producing birds is also compared with the guano production in Peru to show that the amount of guano extracted can also be a proxy of past anchovy biomass changes (Fig. VI-7G). During the Peru's "Guano Age" (from 1840 to 1880 AD) and also before, Peru exported huge amounts of guano as a fertilizer, which consisted in the exploitation of centuries-old deposits of droppings (Cushman, 2003). In 1879 Peru exhausted its major guano deposits. However in 1909 environmental experts implemented a program that led to dramatic increases in the guano bird population and the production of excrement for human benefit. Unlike the Guano Age (which depended on the exploitation of old-deposits), this new period relied on a sustained yield of excrement from Peru's existing marine bird population. Thus, the total guano production (from ~1910 AD) as well as the number of guano birds could be used as an indicator for changes in anchovy biomass prior to the industrial fishery. Figure VI-7G shows the similarity of the number of birds and the tonnages of guano extracted; both records show a positive trend and a decrease in the late 60s as a possible consequence of the impact of the industrial fishery. Thus, the total guano production (from ~1910 AD) as well as the number of guano birds shows a very similar pattern to anchovy scale fluxes and could also be used as a broad indicator for changes in anchovy biomass prior to the industrial fishery.

VI-4.6 Anchovy and sardine scale fluxes and climate indices

In order to understand the role of climate forcing in regulating the pelagic fish biomass variability off Peru and the habitat contraction and expansion of anchovy and sardine during the last ~155 years, the fish scale records are compared in the next section with climate indices such as the PDO, the SOI, the CTI, historical El Niño and La Niña events and upwelling favorable winds (Fig. VI-8). These indices are not fully independent. The SOI index indicates stronger trade winds from ~1945 to 1980 and from ~2005 to the present, and negative anomalies during a short period in 1940s and from ~1980 to ~2005. The SOI also shows high frequency variability with mainly strong Pacific trade winds prior to ~1935, however SOI values prior to 1935 should be used with caution due to the relative quality of the Tahiti pressure values. The presence of sardine from ~1975 to 2000 is associated with the strong reduction of the trade winds as expressed by the negative anomalies of the SOI, but the short period with negative SOI values in the ~1940s was not associated with the presence of sardine.
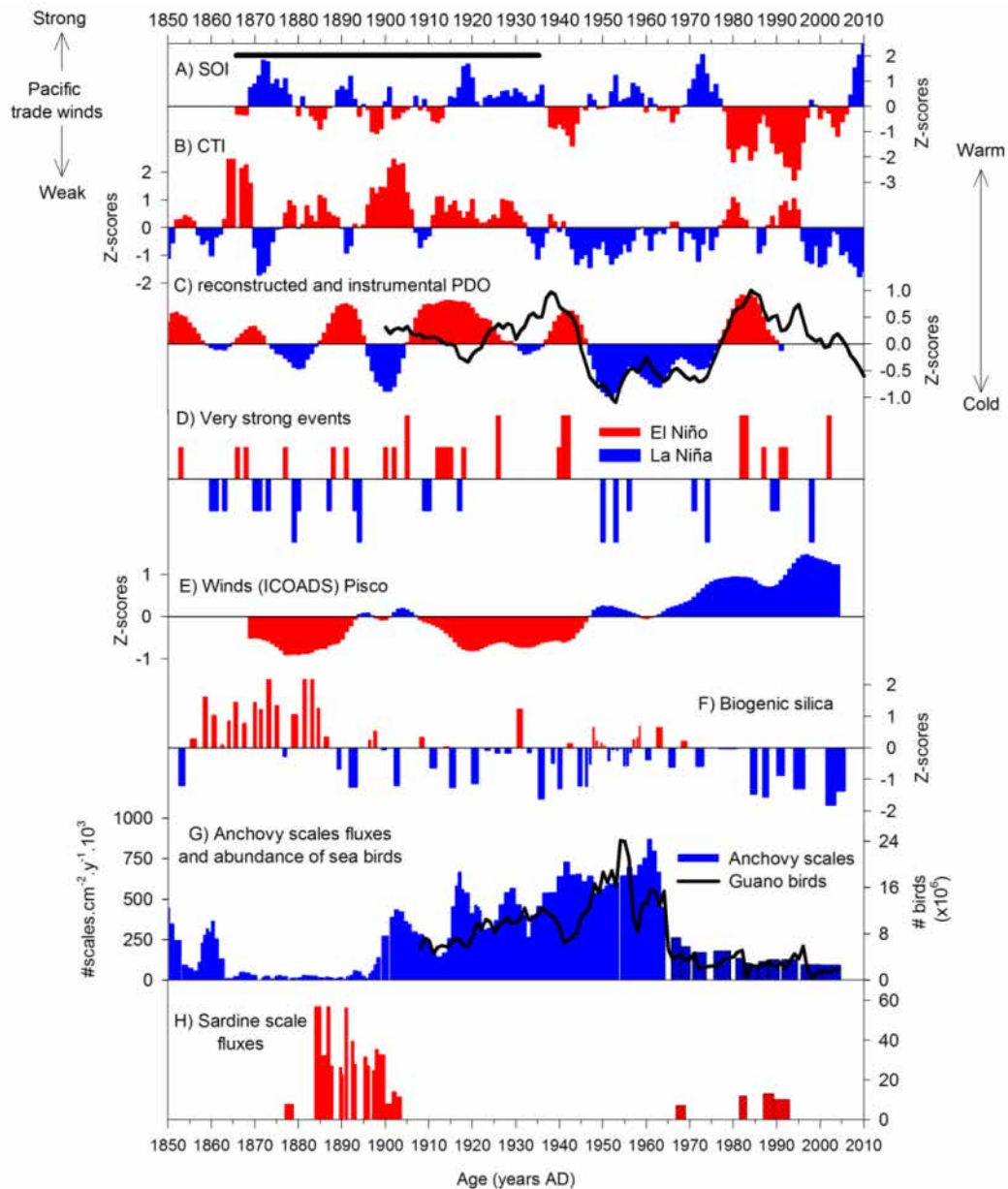
Figure VI-8. Anchovy and sardine fluxes compared with climate indices in the region. A) Southern Oscillation Index (SOI) as proxy of the strength of the Pacific trade winds, data taken from http://jisao.washington.edu/enso/. The horizontal bars indicate the SOI values associated with uncertainties. B) Cold Tongue Index (CTI), taken from http://jisao.washington.edu/enso/, The SOI and CTI data were smoothed with a 7-point moving average and then normalized. C) Instrumental (black bold line) and reconstructed Pacific Decadal Oscillation (PDO), the instrumental PDO was taken from http://jisao.washington.edu/pdo/ while the PDO reconstruction from tree rings was taken from Biondi et al. (2001). PDO data were smoothed with a 7-point moving average and then only the reconstructed PDO data were normalized. D) Extreme and very strong El Niño and La Niña events taken from Gergis and Fowler, (2000; 2006). E) Regional alongshore wind stress off Pisco (Field et al. 2006), the data from ICOADS were smoothed with a 7-point moving average and the normalized. F) Normalized biogenic silica contents in core B05-14. G) Anchovy scale fluxes in the composite record assembled with samples from core B05-13 and B04-6 (hatched bars) as a proxy for anchovy biomass variability (data were smoothed with a 3-point moving average), alongside with number of guano producing birds (black bold line). H) Sardine scale fluxes in the composite record assembled with samples from core B05-13 and B04-6 (dashed bars) as a proxy for sardine biomass variability.

211

The CTI index (Fig. VI-8B) shows a warmer cold tongue in the Equatorial Central Pacific from ~1860 to ~1935 and from ~1977 to ~1998 (suggesting El Niño-like conditions), whereas a cooler cold tongue characterizes the period from 1935 to 1975, and from ~1998 to the present (suggesting rather neutral or cold La Niña-like conditions). While the positive and negative CTI phases since ~1935 are associated with sardine and anchovy respectively, these associations are not valid for the period from 1850 to 1935, where a weak cold tongue prevailed. The period associated with the weaker cold tongue (~1860 – 1905) is associated with the low abundance of anchovy. The CTI and the SOI show higher shared variability from 1866 to the date, (r^2= 0.47, using the annual values) and this shared variability is stronger after ~1935 ($r^2 = 0.74$). Finally, the CTI shows a significant tendency since 1900 AD towards a cooler cold tongue (r = 0.48, p<0.001), which is also associated with a tendency towards stronger upwelling favorable winds (r = 0.83, p<0.001, data since 1900 AD) from the ICOADS (Fig. VI-8E).

The presence of sardine is not always associated with the warm phases of the PDO (Figs. VI-8C and 8H). During the last 50 years positive (or warm) anomalies (from 1975 to the mid-1990s) were associated with sardines while the negative (or cold) PDO period (from 1950 to 1975) was associated with anchovies (Chavez et al., 2003). By contrast, the anchovy and sardine SDR records show in the present chapter strongly indicate that before 1950, the warm phases of the PDO did not always coincide with an increase in sardine biomass. For example the warm PDO phase from 1925 to 1950 is not associated with the presence of sardine scales, and is strongly associated with an increase in anchovy fluxes (Fig. VI-8). Moreover, the older multidecadal period favorable to oceanic species (1855 to 1900AD) is characterized by higher decadal variability during a warmer period, and not by a uniform period with warmer temperatures.

There is an apparent relationship between the frequency of extreme and very strong El Niño and La Niña events with the abundance of anchovy and sardines fluxes (Fig. VI-8). The older multidecadal periods favorable to the oceanic species (1855 to 1900AD) is associated with a high frequency of extreme and very strong El Niño and La Niña events (Fig. VI-8D). In contrast, the decadal maximums in anchovy fluxes (~1940 to ~1965 AD) are associated with a period characterized by several extreme La Niña events and absence of extreme or very strong El Niño events. Finally the more recent multidecadal period favorable to oceanic species is also associated with more frequent El Niño and La Niña extreme and very strong events, but in low number in comparison with the former period.

VI-5. Discussion

Fish scale records from 5 box-cores retrieved in laminated sediments off Peru (Callao and Pisco) and off Chile (Mejillones) covering the last ~150 years were evaluated to assess the anchovy and sardine habitat contraction and expansion, and to characterize the former multidecadal period favorable to oceanic species (1855 to 1905AD). Additionally, anchovy scale fluxes of the 5 cores show a consistent, positive trend towards increased anchovy abundance from ~1900 to ~1965. After ~1965, fish scale records are biased due to the presence of the industrial fishery. However, the tendency towards higher productivity continues up to the present as evidenced by the export production proxies (Fig. VI-7C). The trend towards higher anchovy productivity is associated with an increase in upwelling favorable winds, a decrease in SST, and a higher export production (Fig. VI-7). The productivity trend propagates to species from higher trophic levels such as hake and sea birds. Additionally, two multi-decadal periods favorable to oceanic species from (~1855 to 1905 and from ~1975 to ~2000AD) were observed.

VI-5.1 Multi-decadal scale changes between anchovy and sardine

The SOI, CTI, the reconstructed PDO, and the extreme and very strong El Niño/La Niña events point out that the variable oceanographic conditions from ~1850 to ~1910 AD in the tropical Pacific, were warmer and more variable than the following mid-century, and were unfavorable to anchovies but highly favorable to oceanic species. Moreover, SST reconstructions from a suite of corals from the Tropical Pacific also indicate that the 19th century experienced stronger decadal variability than the 20th century, and that this variability is fundamentally related to ENSO activity (Ault et al., 2009). The positive anomalies of the SOI and the CTI in addition to the negative anomalies of the upwelling favorable winds point to more El Niño-like conditions, with lower productivity, sub-surface oxygenation and a weaker Walker circulation. However the OMZ during the period favorable to oceanic species do not show any weakening ($\delta^{15}N$ data in Fig. VI-4A and B), as observed in the more recent multidecadal period (Bertrand et al., 2011). The altered oceanographic conditions favored the bloom of some diatom species (Fig. VI-8F) in all the HCS (Gutierrez et al., 2009; Diaz-Ochoa et al., 2011), blooms that were not observed in this magnitude at least during the last 5 centuries off Peru (chapter V), thus confirming some anomalous conditions. During this period the SST reconstruction also shows the highest temperatures suggesting that the warm subtropical oceanic waters came closer to the coast (Fig. VI-7B). The sardines and other oceanic species followed the inshore flux of oceanic waters and then when conditions were favorable again for anchovy, the favorable sardine habitat was pushed away while anchovy habitat spread offshore around ~1905AD. This pattern is coherent with the behavior of these species during sub-annual-scale periods like the shift from the 1997-98 El Niño to the 1998-2000 La Niña events (Bertrand et al.,

2004). This multidecadal period favorable to oceanic species is related to a basin-scale reorganization of the ocean-climate system (Vargas et al., 2007) because this period represents a transition between two contrasting periods (LIA and the Current Warm Period) with different impacts on the HCS (Vargas et al., 2007; Gutierrez et al., 2009).

The fish scale records from different latitudes and distances from the coast may reflect the behavior of anchovy during periods of unfavorable conditions. The El Niño events cause the expansion or contraction of pelagic species distribution and abundance, and the latitudinal effect of each El Niño on pelagic fishes seems to be different and not directly related to its strength (Bertrand et al., 2004; Ñiquen and Bouchon, 2004; Gutierrez et al., 2012). However, in general during an El Niño event anchovy is distributed very close to the coast (Bertrand et al., 2004; Ñiquen and Bouchon, 2004). The combined fish scale records suggest that anchovies displaced to the coastal region during the warm events of the second half of the 19th century (Fig. VI-6). Support for this interpretation is that the coastal Mejillones core shows relatively high anchovy fluxes during the period favorable to oceanic species, and the Callao and Pisco cores show low abundance of anchovy scales (Fig. VI-6G). These evidences indicate that during the second half of the 19th century, anchovies concentrated in "refuge areas" such as the Mejillones bay.

The relatively warm event centered at ~1940AD, indicated by the SOI and the PDO values, suggests an El Niño-like period with an expected weakened Walker circulation, an increase in SST in the eastern Pacific, sub-surface oxygenation and reduced productivity due to a deepening of the thermocline. These characteristics should be favorable to sardines if we take as a reference the more recent multidecadal period favorable to sardine, which is not the case in the records shown in the present chapter (Fig. VI-8). One likely explanation for the fact that sardine did not flourish during that warm period is that the PUE experienced a multidecadal-scale positive trend towards higher upwelling that started at ~1900 AD. Thus, the basin-scale forcings did not have a perceptible impact on reducing the habitat favorable to anchovy.

The two observed multidecadal periods favorable to oceanic species are not fully similar. This is not surprising, as the effect of El Niño conditions on anchovy and other species differ from one event to another (Bakun and Broad, 2003; Alheit and Ñiquen, 2004; Bertrand et al. 2004). For example the recovery of anchovy was slow after El Niño events in 1972-73, 1977-78, and 1982-83, rapid after El Niño 1987 and 1997-98, and finally the El Niño of 1992-93 and 2002-03 seemed to have no perceptible impact on anchovy biomass (Alheit and Ñiquen, 2004; Bertrand et al., 2004). The older multidecadal period seems to be stronger in terms of unfavorable conditions to anchovy and longer than the more recent one. The presence of warm subtropical oceanic waters during the older period seem to be more persistent with respect to the more recent period as evidenced by higher fluxes

of more oceanic species like jack mackerel and mackerel (Fig. VI-5), the higher SST (Fig. VI-7B), and the diatoms blooms (Fig. VI-7D). Additionally the anchovy scale fluxes were lower in the older multidecadal period favorable to sardines in comparison with the most recent one (Fig. VI-8G) indicating less favorable conditions for anchovy. The duration of the older period (~45 years) is longer than the most recent period (~25 years, Fig. VI-6J) if the presence of jack mackerel and mackerel are taken into account (Fig. VI-5). The presence of jack mackerel and mackerel, which are one of the main predators of anchovy, likely increased pressure on anchovy until ~1905 when favorable conditions for anchovy permitted the increase of anchovy abundance. The presence of the industrial fishery may bias the fish scale record during the last ~50 years preventing the recording of jack mackerel and mackerel scales in the sediments or alternatively the abundance of these two species are diminished because there are not enough anchovies to provide sufficient food for the predators. This last hypothesis is supported by the diminution of the guano birds (another predator of anchovy) associated with the beginning of the industrial fishery.

VI-5.2 Bottom up trend: from physical forcings to predators

The increase in upwelling favorable winds, SST cooling and enhanced productivity in the PUE during the last decades is likely originated by local/regional process rather than basin-scale forcings. In order to understand what drives the enhancement of upwelling and productivity off Peru, and given that the variability in anchovy and sardine biomass must be linked to atmospheric or oceanic forcing (Chavez et al., 2003), the fish scale record was compared to climatic indices that affect (directly or indirectly) the upwelling off Peru (Fig. VI-8). Because each index or parameter is influenced by forcings that act on different time scales, differences between the intensification of the upwelling favorable winds, SOI, CTI and anchovy scale fluxes are expected in the trend and not in the duration of the warm or cold phases. The tendency towards stronger upwelling and productivity as evidenced by the paleoceanographic reconstructions is supported by a strong tendency towards favorable upwelling winds (Fig. VI-8A), as also noted in other works (Jahncke et al., 2004; Field et al. 2006; Narayan et al., 2010; Gutierrez et al., 2011) . The CTI (Fig. VI-8C) also shows a significant (but weaker) tendency since 1900 AD towards a cooler cold tongue (r = 0.48, p<0.001). The tendency in the CTI data is not surprising because the horizontal advection of cool water upwelled along the coast of Peru as well as the equatorial upwelling are the main sources of temperature changes on this cold tongue (Wyrtki, 1981). By contrast, the SOI index (Fig. VI-8B), which can be considered as a proxy for the strength of the Pacific trade winds, does not show a tendency like the one deduced off Peru from several independent proxies since ~1900 (Fig. VI-7). Finally, the PDO index (Fig. VI-8D) does not indicate a cooler period from ~1900 to 1960 that would be expected to favor anchovy conditions. These evidences indicate that a regional/local mechanism may be causing the trend towards stronger upwelling and productivity off Peru.

The dissimilarity between the basin-scale oscillations (like the SOI and the PDO) and the trends observed in our data set rules out an alteration of upwelling intensity off Peru other than due to regional/local processes. One proposed mechanism involve a greenhouse-associated intensification of thermal low-pressure cells over the coastal land masses of upwelling regions that cause an intensification of wind-driven ocean upwelling in coastal upwelling regions (Bakun, 1990). If this mechanism is valid the Pisco area should be more influenced than other areas off Peru like Callao, because of the local semi-permanent low-pressure areas found to the south of Bahia Paracas at 14 °S off the Ica Desert (Strub et al., 1998). Moreover the proposed mechanism should be more intense in summer due to higher insolation, but the positive trend in upwelling winds occurs in spring and not in summer (Gutiérrez et al., 2011), indicating that some component of the proposed mechanism is not fully understood. The Bakun mechanism has been used to explain the upwelling enhancement in the HCS and other EBUS (Bakun 1990; McGregor et al. 2007; Vargas et al., 2007; Leduc et al., 2010; Gutierrez et al., 2011). However other physical factors like an intensification of the Southeastern Pacific Anticyclone (Falvey and Garreaud, 2009), changes in stratification atmospheric aerosols and solar variability could not be excluded in order to explain the increase in upwelling in the EBUS (Narayan et al., 2010). Both the intensification of the Southeastern Pacific Anticyclone and the enhancement of local alongshore winds in response to increasing land-sea pressure gradient, are triggered by anthropogenic global warming (Bakun, 1990; Falvey and Garreaud, 2009).

The cooling and enhanced productivity in the PUE during the last decades were favorable to anchovy, hake and also to the guano birds (Fig. VI-7). The southern limit of the spatial distribution of hake is located at ~6 °S, even though the pelagic juvenile individuals of hake can be found off Callao (Guevara and Lleonart, 2008). Additionally, during El Niño events, when the subsurface waters off Peru are oxygenated, adult hakes can be caught off Callao and the juveniles may reach farther south. The Callao record (Fig. VI-5A) show abundant hake scales from the end of the older multidecadal period favorable to sardine (~1880 to 1905AD) up to the 2004 (when the box-core was retrieved). The Pisco cores also show relative abundance of hake scales from the beginning of the anchovy trend (~1900 AD) to the decadal maximum in anchovy SDR (~1965 and ~1945 in core B05-13 and B05-14 respectively), which further confirms the increase in hake abundance (Fig. VI-5). Given the existence of a tight link between anchovy and guano birds, it is not surprising that the increase in anchovy abundance was also favorable to the guano birds. The proportion of anchovy found in the diet of cormorants and boobies is strongly correlated with anchovy biomass (Jahncke and Goya, 1998), confirming the close relationship between anchovy abundance and guano birds. Finally, the annual variability in the number of birds could be explained by the effects of the El Niño events while the decadal variability in the anchovy fluxes and the number of birds (from ~1910 to ~1960) could be explained by fluctuations in productivity during a centennial-scale increase trend in productivity since the beginning of the 20th century.

VI-5.3 Fish scale fluxes and uncertainties with the chronological model

The anchovy fluxes obtained from core B05-13 from ~1850 to 1963 and from core B04-6 from ~1963 to 2005 were used in order to relate the anchovy and sardine biomass variability to proxies of environmental change; however an integrated fish scale record off Pisco (using the 3 available fish records: B04-6, B05-13 and B05-14) would be a better approach to perform this task. The three records show considerable high frequency variability (Fig. VI-5) and the decadal maxima and decadal minima (after a 3-point moving average) match well among cores (Salvatteci et al., 2012). Moreover, the sedimentary structures of the three records are well correlated (chapter II) and independently support the correlation of decadal maxima and minima in anchovy fluxes. However, the application of the chronological model induces a shift of sections that are contemporaneous among cores (based on the cross-correlations of sediment structures and decadal maximum and minimums of anchovy). For example the highest decadal maximum is dated at ~1960 in core B05-13 but ~1950 in core B05-14. On the other hand the chronological models in cores B05-13 and B05-14 that were developed independently, using different ^{210}Pb measurements techniques, and different age models, indicate that the change from sardine to anchovy occurred at ~1900 AD and that the change in sediment density occurred at ~1850 AD in both cores, which indicate that in general the chronology was correctly developed in both cores. By contrast, core B04-6 represents a bigger challenge to cross-correlate the sediment structures with cores B05-13 and B05-14, and to develop a precise chronological model, due to the low sedimentation rates that dilutes the high frequency variability of the records and the hiatus observed in parts of the core (chapter II). Beside the application of the chronological model the correct identification of high sedimentation events in each core entails other difficulties. Thus, more work is needed to develop the chronological models using the cross-correlation of sedimentary structures to better constrain the chronology and assemble one record from the 3 Pisco box-cores in order to resolve sub-decadal variability in anchovy biomass variability. However we consider that the anchovy and sardine scale fluxes obtained from the composite record (B04-6 + B05-13) is the current best estimate of the anchovy and sardine biomass fluctuations.

VI-6. Conclusions

Fish scale records from 5 cores retrieved in laminated sediments off Peru and Chile show a positive trend towards increased anchovy abundance since the beginning of the 20th century. The tendency towards higher anchovy productivity is supported by an increase in winds favorable to upwelling, a tendency towards lower SST and higher exported productivity. The productivity trend does not stop at the base of the trophic levels (i.e. anchovy) but propagates to species located at higher trophic levels such as hake and sea birds. These results indicate that the whole PUE is submitted to large changes if oceanographic conditions change, as for example during older periods like the LIA or

during the multidecadal periods favorable to oceanic species, putting at stake a whole ecosystem and the social and economical activities associated with.

Population fluctuations of anchovy and sardine occur at different time scales that involve different underlying mechanisms. Regional/local processes induce a centennial tendency towards stronger upwelling and productivity favorable for anchovies, which can be explained by Bakun's mechanism (i.e. intensification of thermal low-pressure cells over the coastal land masses of upwelling regions that cause an intensification of wind-driven ocean upwelling). By contrast, perturbations in the ocean-climate system in the Pacific basin lead to two multidecadal periods (with stronger El Niño and La Niña events in the former one) favorable for sardines and a contraction of the habitat for anchovies. These results suggest that in order to model the HCS behavior, the different time scales and local/regional vs. basin-scale processes must be taken into account.

The presence of oceanic species off Peru and Chile indicates a stronger and longer multidecadal period (from ~1855 to ~1905) in comparison with the last multidecadal period favorable to sardines (~1975 to ~1995AD). During this former period favorable to oceanic species, anchovy biomass was extremely reduced and the anchovies were displaced to the south and close to the coast as can be observed in the Mejillones record. This latitudinal displacement of anchovy during adverse conditions further suggests that several cores along a latitudinal gradient must be studied to better assess the contraction and expansion of pelagic fishes from fish scale preserved in laminated sediments.

VI-7. Bibliography

Alheit, J., and M. Niquen. 2004. Regime shifts in the Humboldt Current ecosystem. Progress in Oceanography 60:201-222.

Alheit, J., and A. Bakun. 2010. Population synchronies within and between ocean basins: Apparent teleconnections and implications as to physical–biological linkage mechanisms. Journal of Marine Systems 79(3-4):267-285.

Alheit, J.,1987. Egg cannibalism versus egg predation: their significance in anchovies. In: Payne, A.I.L., Gulland, J.A., Brink, K.H. (Eds.), The Benguela and Comparable Ecosystems. S. Afr. J. Mar. Sci. 5, pp. 467–470.

Appleby, P. G. 2001. Chronostratigraphic techniques in recent sediments. In W. M. L. J. P. S. (eds.), ed. Tracking Environmental Change Using Lake Sediments. Volume 1: Basin Analysis, Coring, and Chronological Techniques. Kluwer Academic Publishers, Dordrecht, The Netherlands.

Appleby, P. G. and F. Oldfield. 1978. the calculation of 210Pb dates assuming a constant rate of supply of unsupported 210Pb to the sediment. Catena 5:1-8.

Ault, T. R., J. E. Cole, M. N. Evans, H. Barnett, N. J. Abram, A. W. Tudhope, and B. K. Linsley. 2009. Intensified decadal variability in tropical climate during the late 19th century. Geophysical Research Letters 36:L08602.

Ayón, P., G. Swartzman, P. Espinoza, and A. Bertrand. 2011. Long-term changes in zooplankton size distribution in the Peruvian Humboldt Current System: conditions favouring sardine or anchovy. Marine Ecology Progress Series 422:211-222.

Bakun, A. 1990. Global climate change and intensification of coastal upwelling. Science 247(4939):198-201.

Bakun, A., and K. Broad. 2003. Environmental 'loopholes' and fish population dynamics: comparative pattern recognition with focus on El Niño effects in the Pacific. Fisheries Oceanography 12(4/5):458-473.

Bakun, A., and S. J. Weeks. 2008. The marine ecosystem off Peru: What are the secrets of its fishery productivity and what might its future hold? Progress in Oceanography 79:290-299.

Bakun, A., D. Field, A. Redondo-Rodriguez, and S. J. Weeks. 2010. Greenhouse gas, upwelling-favorable winds, and the future of coastal ocean upwelling ecosystems. Global Change Biology 16:1213-1228.

Barber, R. T. and F. Chavez. 1983. Biological consequences of El Niño. Science 222:1203-1210.

Baumgartner, T., A. Soutar, and V. Ferreira-Bartrina. 1992. Reconstruction of the history of pacific sardine and northern anchovy populations over the past two millennia from sediments of the Santa Barbara basin, California. CalCOFI Rep. 33:24-40.

Bertrand, A., A. Chaigneau, S. Peraltilla, J. Ledesma, M. Graco, F. Monetti, and F. Chavez. 2011. Oxygen: A Fundamental Property Regulating Pelagic Ecosystem Structure in the Coastal Southeastern Tropical Pacific. PLoS ONE 6(12):e29558.

Bertrand, A., M. Segura, M. Gutiérrez, and L. Vásquez. 2004. From small-scale habitat loopholes to decadal cycles: a habitat-based hypothesis explaining fluctuation in pelagic fish populations off Peru. Fish and Fisheries 5:296-316.

Biondi, F., A. Gershunov, and D. R. Cayan. 2001. North Pacific Decadal Climate variability since AD 1661. Journal of Climate 14(1):5-10.Chavez, F. P., and M. Messié. 2009. A comparison of Eastern Boundary Upwelling Ecosystems. Progress in Oceanography 83(1-4):80-96.

Chavez, F., J. Ryan, S. Lluch-Cota, and M. Niquen. 2003. From Anchovies to Sardines and Back: Multidecadal Change in the Pacific Ocean. Science 299:217-221.

Chavez, F., A. Bertrand, R. Guevara-Carrasco, P. Soler, and J. Csirke. 2008. The northern Humboldt Current System: Brief history, present status and a view towards the future. Progress in Oceanography 79:95-105.

Chavez, F. P., and M. Messié. 2009. A comparison of Eastern Boundary Upwelling Ecosystems. Progress in Oceanography 83(1-4):80-96.

Chavez, F. P., M. Messie, and J. T. Pennington. 2011. Marine Primary Production in Relation to Climate Variability and Change. Annu. Rev. Mar. Sci. 3:227-260.

Checkley, D., P. Ayon, T. Baumgartner, M. Bernal, J. Coetzee, R. Emmett, R. Guevara-Carrasco, L. Hutchings, L. Ibaibarriaga, H. Nakata, Y. Oozeki, B. Planque, J. Schweigert, Y. Stratoudakis, and C. van der Lingen. 2009. Habitats. Pp. 12-44. In D. Checkley, J. Alheit, Y. Oozeki, and C. Roy, eds. Climate Change and Small Pelagic Fish. Cambridge University Press.

Cornejo, R., and R. Koppelmann. 2006. Distribution patterns of mesopelagic fishes with special reference to Vinciguerria lucetia Garman 1899 (Phosichthyidae: Pisces) in the Humboldt Current Region off Peru. Marine Biology 149:1519-1537.

Cushman, G. T. 2003. The Lords of Guano: Science and the Management of Peru's Marine Environment, 1800-1973. University of Texas at Austin, Texas.

D'Arrigo, R., R. Villalba, and G. Wiles. 2001. Tree-ring estimates of Pacific decadal climate variability. climate Dynamics 18(3/4):219-224.

Demarcq, H. 2009. Trends in primary production, sea surface temperature and wind in upwelling systems (1998–2007). Progress in Oceanography 83:376-385.

Diaz-Ochoa, J. A., C. B. Lange, S. Pantoja, G. J. De Lange, D. Gutierrez, P. Muñoz, and M. Salamanca. 2008. Fish scales in sediments from off Callao, central Peru. Deep-Sea Research Part II 56:1124–1135.

Diaz-Ochoa, J. A., S. Pantoja, G. J. De Lange, C. B. Lange, G. E. Sanchez, V. R. Acuña, P. Muñoz, and G. Vargas. 2011. Oxygenation variability in Mejillones Bay, off northern Chile, during the last two centuries. Biogeosciences 8:137-146.

Espinoza, P., and A. Bertrand. 2008. Revisiting Peruvian anchovy (*Engraulis ringens*) trophodynamics provides a new vision of the Humboldt Current system. Progress in Oceanography 79:215-227.

Espinoza, P., A. Bertrand, C. D. van der Lingen, S. Garrido, and B. Rojas de Mendiola. 2009. Diet of sardine (Sardinops sagax) in the northern Humboldt Current system and comparison with the diets of clupeoids in this and other eastern boundary upwelling systems. Progress in Oceanography 83:242-250.

Falvey, M., and R. D. Garreaud. 2008. Regional cooling in a warming world: Recent temperature trends in the southeast Pacific and along the west coast of subtropical South America (1979–2006). Journal of Geophysical Research 114:D04102.

Field et al. 2006. Análisis de datos de ICOADS que faltan para probar hipótesis de surgencia e interpretar registros. Humboldt Current Conference November 2006

Field, D. B., T. R. Baumgartner, V. Ferreira, D. Gutierrez, H. Lozano-Montes, R. Salvatteci, and A. Soutar. 2009. Variability from scales in marine sediments and other historical records. Pp. 45-63. In D. Checkley, C. Roy, J. Alheit, and Y. Oozeki, eds. Climate Change and Small Pelagic Fish. Cambridge University Press.

Gergis, J. L., and A. M. Fowler. 2006. How unusual was late 20th century El Nino-Southern Oscillation (ENSO)? Assessing evidence from tree-ring, coral, ice-core and documentary palaeoarchives, A.D. 1525–2002. Advances in Geosciences 6:173-179.

Gergis, J. L., and A. M. Fowler. 2009. A history of ENSO events since A.D. 1525: Implications for future climate change. Climatic Change 92:343-387.

Goya, E. 2000. Abundancia de aves guaneras y su relación con la pesquería de anchoveta peruana de 1953 a 1999. Boletín del Instituto del Mar del Perú 19:125-131.

Guevara-Carrasco, R., and J. Lleonart. 2008. Dynamics and fishery of the Peruvian hake: Between nature and man. Journal of Marine Systems 71:249-259.

Gutierrez, D., A. Sifeddine, J. L. Reyss, G. Vargas, F. Velazco, R. Salvatteci, V. Ferreira-Bartrina, L. Ortlieb, D. Field, T. Baumgartner, M. Boussafir, H. Boucher, J. Valdes, L. Marinovic, P. Soler, and P. Tapia. 2006. Anoxic sediments off Central Peru record interannual to multidecadal changes of climate and upwelling ecosystems during the last two centuries. Advances in Geosciences 6:119-125.

Gutierrez, M., G. Swartzman, A. Bertrand, and S. Bertrand. 2007. Anchovy (*Engraulis ringens*) and sardine (*Sardinops sagax*) spatial dynamics and aggregation patterns in the Humboldt Current ecosystem, Peru, from 1983–2003. Fisheries Oceanography 16(2):155-168.

Gutierrez, D., A. Sifeddine, D. B. Field, L. Ortlieb, G. Vargas, F. Chavez, F. Velazco, V. Ferreira, P. Tapia, R. Salvatteci, H. Boucher, M. C. Morales, J. Valdes, J. L. Reyss, A. Campusano, M. Boussafir, M. Mandeng-Yogo, M. Garcia, and T. Baumgartner. 2009. Rapid reorganization in ocean biogeochemistry off Peru towards the end of the LIA. Biogeosciences 6:835-848.

Gutierrez, D., I. Bouloubassi, A. Sifeddine, S. Purca, K. Goubanova, M. Graco, D. Field, L. Méjanelle, F. Velazco, A. Lorre, R. Salvatteci, D. Quispe, G. Vargas, B. Dewitte, and L. Ortlieb. 2011. Coastal cooling and increased productivity in the main upwelling zone off Peru since the mid-twentieth century. Geophysical Research Letters 38:L07603.

Helly, J., and L. Levin. 2004. Global distribution of naturally occurring marine hypoxia on continental margin. Deep-Sea Research I 51:1159-1168.

Jahncke, J., and E. Goya. 1998. Las dietas del guanay y piquero peruano como indicadoras de la abundancia y distribucion de anchoveta. Boletin del Instituto del Mar del Peru 17:15-34.

Jahncke, J., D. M. Checkley, and G. L. Hunt. 2004. Trends in carbon flux to seabirds in the Peruvian upwelling system: effects of wind and fisheries on population regulation. Fisheries Oceanography 13(3):208-223.

Leduc, G., T. Herbert, T. Blanz, P. Martinez, and R. Schneider. 2010. Contrasting evolution of sea surface temperature in the Benguela upwelling system under natural and anthropogenic climate forcings. Geophysical Research Letters 37:L20705.

Lehodey, P., J. Alheit, M. Barange, T. Baumgartner, G. Beaugrand, K. Drinkwater, J.-M. Fromentin, S. R. Hare, G. Ottersen, R. I. Perry, C. Roy, C. D. van der Lingen, and F. Werner. 2006. Climate Variability, Fish and Fisheries. 19:5009-5030.

MacDonald, G. M., and R. A. Case. 2005. Variations in Pacific Decadal Oscillation over the past millennium. Geophysical Research Letters 32:L08703.

McGregor, H. V., M. Dima, H. W. Fischer, and S. Mulitza. 2007. Rapid 20th-Century Increase in Coastal Upwelling off Northwest Africa. Science 315:637-639.

Mantua, N. J., S. R. Hare, Y. Zhang, J. M. Wallace, and R. C. Francis. 1997. A Pacific interdecadal climate oscillation with impacts on salmon production. Bulletin of the American Meteorological Society 78(6):1069-1079.

McGregor, H. V., M. Dima, H. W. Fischer, and S. Mulitza. 2007. Rapid 20th-Century Increase in Coastal Upwelling off Northwest Africa. Science 315:637-639.

Moron, O., W. Garcia and M. Sarmiento.(in prep.). Promedios y variabilidad interanual de la salinidad frente a la costa peruana. Boletin del Instituto del Mar del Peru.

Narayan, N., A. Paul, S. Mulitza, and M. Schulz. 2010. Trends in coastal upwelling intensity during the late 20th century. Ocean Science 6:815-823.

Niquen, M., and M. Bouchon. 2004. Impact of El Niño events on pelagic fisheries in Peruvian waters. Deep-Sea Research II 51:563-574.

Ortlieb, L. (2000). The documentary historical record of El Niño events in Peru: An update of the Quinn record (sixteenth through nineteenth centuries). In: El Niño and the Southern Oscillation: Variability, Global and Regional Impacts, H. Diaz & V. Markgraf (Eds.), Cambridge University Press. p. 207-295.

Pennington, J. T., K. L. Mahoney, V. S. Kuwahara, D. D. Kolber, R. Calienes, and F. P. Chavez. 2006. Primary production in the eastern tropical Pacific: A review. Progress in Oceanography 69:285-317.

Salvatteci, R., D. B. Field, T. Baumgartner, V. Ferreira, and D. Gutierrez. 2012. Evaluating fish scale preservation in sediment records from the oxygen minimum zone off Peru. Paleobiology 38(1):766-792.

Sanchez-Cabeza, J. A., and A. C. Ruiz-Fernández. 2012. 210Pb sediment radiochronology: An integrated formulation and classification of dating models. Geochimica et Cosmochimica Acta 82:183-200.

Schwartzlose, R. A., J. Alheit, A. Bakun, T. R. Baumgartner, R. Cloete, R. J. M. Crawford, W. J. Fletcher, Y. Green-Ruiz, E. Hagen, T. Kawasaki, D. Lluch-Belda, S. E. Lluch-Cota, A. D. MacCall, Y. Matsuura, M. O. Nevarez-Martinez, R. H. Parrish, C. Roy, R. Serra, K. V. Shust, M. N. Ward, and J. Z. Zuzunaga. 1999. Worldwide large-scale fluctuations of sardine and anchovy populations. South African Journal of Marine Science 21:289-347.

Shackleton, L. Y. 1988. Scale shedding: an important factor in fossil fish studies. ICES Journal of Marine Science 44(3):259-263.

Sifeddine, A., D. Gutierrez, L. Ortlieb, H. Boucher, F. Velazco, D. Field, G. Vargas, M. Boussafir, R. Salvatteci, V. Ferreira, M. García, J. Valdes, S. Caquineau, M. Mandeng-Yogo, F. Cetin, J. Solis, P. Soler, and T. Baumgartner. 2008. Laminated sediments from the central Peruvian continental slope: A 500 year record of upwelling system productivity, terrestrial runoff and redox conditions. Progress in Oceanography 79:190–197.

Soutar, A., and J. Isaacs. 1974. Abundance of pelagic fish during the 19th and 20th century as recorded in anaerobic sediment off the Californias. Fisheries Bulletin 72:257-273.

Swartzman, G., A. Bertrand, M. Gutiérrez, S. Bertrand, and L. Vasquez. 2008. The relationship of anchovy and sardine to water masses in the Peruvian Humboldt Current System from 1983 to 2005. Progress in Oceanography 79:228-237.

Valdés, J., L. Ortlieb, D. Gutierrez, L. Marinovic, G. Vargas, and A. Sifeddine. 2008. 250 years of sardine and anchovy scale deposition record in Mejillones Bay, northern Chile. Progress in Oceanography 79:198-207.

Vargas, G., L. Ortlieb, J. J. Pichon, J. Bertaux, and M. Pujos. 2004. Sedimentary facies and high resolution primary production inferences from laminated diatomacous sediments off northern Chile (23°S). Marine Geology 211:79-99.

Vargas, G., S. Pantoja, J. A. Rutlant, C. Lange, and L. Ortlieb. 2007. Enhancement of coastal upwelling and interdecadal ENSO-like variability in the Peru-Chile Current since late 19th century. Geophysical Research Letters 34.

Wyrtki, K. 1981. An estimate of equatorial upwelling in the Pacific. Journal of Physical Oceanography 11:1205-1214.

CHAPTER VII:
GENERAL DISCUSSION

VII-1. General Discussion

A multi-proxy approach using paleontological techniques, organic and inorganic proxies was carried out on several laminated cores retrieved off Pisco in the core of the Oxygen Minimum Zone (OMZ) to elucidate the following questions: 1) **Which were the driving mechanisms originating the changes in OMZ intensity and export production off Peru during the last 25 kyr?**, and 2) **Which were the factors influencing anchovy and sardine fluctuations during the last 25 kyr?**. The results of the thesis finally assert to better understand the ecosystem variability and the physical regulating processes in the Peruvian Upwelling Ecosystem (PUE). In the following paragraphs the questions proposed are answered with the results obtained in this thesis.

VII-1.1. Which were the driving mechanisms originating the changes in OMZ intensity and export production off Peru during the last 25 kyr?

The comparison of export production and water column denitrification proxies indicate that the intensity of the OMZ off Peru during the last ~25 kyr was controlled by local and remote forcings. The weak export production during the Early Glacial, Last Glacial Maximum and Heinrich 1 Stadial did not leave a strong imprint in the water column denitrification, indicating that the OMZ signal was mainly originated by remote forcings (changes in ventilation of the source water mass and/or increase in export production and then in sub-surface oxygen demand in the Eastern Equatorial Pacific), as proposed in earlier works (Higginson and Altabet, 2004; De Pol-Holz et al., 2006; Chazen et al., 2009; Martinez and Robinson, 2010). In contrast, from ~15 kyr BP to the present, the increase in export production exerted a strong control on the water column oxygenation, as evidenced by the strong coupling between export production and $\delta^{15}N$ water column denitrification at centennial timescales.

The upwelling enhancement since ~8 kyr BP, inferred by an increase in export production and in the anoxic conditions in the sediments is strongly associated with the increase in December to March insolation at ~15 °S (Berger et al., 1978). The primary productivity off Pisco (and off central Peru) follows a seasonal pattern: it is higher during spring/summer when surface waters are more stratified, and lower in winter due to lower surface insolation and stronger winds originating a thick mixed layer that prevent algal growth (Pennington et al., 2006; Chavez and Messié, 2009; Gutierrez et al., 2011). Consequently, the increase in upwelling, export production, and anoxic sediments at millennial timescales could all be explained by mechanisms related to the increased summer (December to March) insolation. Summer insolation in the Southern Hemisphere has increased gradually from a minimum centered at 9.5 kyr BP due to the variations in the Earth's orbit around the Sun (Berger et al., 1978). A maximum in summer insolation in the Southern Hemisphere also

occurred during the Last Glacial Maximum, but during this period the globally cold conditions appear to be more important than the regional conditions. Higher insolation levels tend to stimulate primary production in a nutrient enriched surface water layer by the stabilization of the water column. Additionally, an increase in insolation produces an atmospheric pressure gradient between land and sea, which drives an increase of upwelling winds in spring and summer, increase. This mechanism is due to an inhibition of nighttime cooling and enhancement of daytime heating, leading an intensification of the continental thermal lows adjacent to upwelling regions (Bakun, 1990; Bakun et al., 2010). Upwelling regions in the Northern Hemisphere should present an opposed pattern because insolation in the Northern Hemisphere is decreasing since the Early Holocene. The upwelling region off western North America shows a gradual decrease of upwelling over the past 4 kyr BP, which is explained as a consequence of changes in temperature differences between air masses over land an over the ocean, themselves related to changes in insolation (Van Geen et al., 1992).

The southward displacement of the ITCZ throughout the Holocene (Haug et al., 2001), which is intimely coupled with the Walker circulation and the South Pacific Subtropical High (Pierrehumbert 2000), may also be an important factor that directly or indirectly controlled the productivity off Peru. The low productivity off the coast of Peru during the Little Ice Age has been linked to a southward migration of the ITCZ, likely associated with a weaker Walker circulation and consequently a deeper thermocline off Peru (Sifeddine et al., 2008; Gutierrez et al., 2009). During the Little Ice Age the Ti contents in the Cariaco Basin show the lowest values in the 14 kyr record, possible implying that the ITCZ was located at its southernmost location (Haug et al., 2001). Interestingly, the export production, the OMZ intensity and redox conditions off Pisco also show the lowest or very low values during the Little Ice Age, with values as similar as recorded during the glacial times (chapter III). These observations indicate the role of climate-driven phenomena in producing large changes in marine ecossytems. The northward displacement of the ITCZ during the last decades as a consequence of global warming (Sachs et al., 2009), is producing considerable changes in the southern Caribbean Sea (Chavez et al., 2012; Taylor et al., 2012) highlighting the importance of the ITCZ in producing large changes in marine ecossytems. However the Caribbean Sea is more linked to the ITCZ than the PUE, and consequently more affected by its changes.

An alternative non-exclusive explanation for the observed increase in upwelling since ~8 kyr BP is an increase in iron fertilization which might be related to a gradual increase in rainfall over the continent throughout the Holocene. The source of the upwelled water off Peru is the nutrient-rich subsurface countercurrent in contact with the organic-rich shelf sediments that presents extremely high concentrations of dissolved Fe in the near-bottom waters (Bruland et al., 2005). During the Holocene, the South American Summer Monsoon (SASM) exhibited a long term increase that tracked the summer insolation increase (Bird et al. 2011), and a southward displacement of the ITCZ (Haug et

al., 2011). The increased terrigenous input, including iron, to the coastal ocean may have enhanced primary productivity, as proposed in another upwelling area in the HCS at ~27 °S (Dezileau et al., 2004). However, this mechanism might be more important in the Southern Peru –Chile margin that is iron-limitied, given that this Southern region does not present a wide shelf to serve as a source of iron (Bruland et al., 2005).

The amplitude of the temporal changes in the water column denitrification, the export production, and the anoxic conditions in the sediments is higher from the late mid-Holocene to the present in comparison with the older periods. The stronger variability of the OMZ intensity, the anoxic conditions in the sediment and the export production, recorded since ~4.5 kyr BP was already observed in other types of proxies obtained from cores retrieved off Callao and off Pisco (Chazen et al., 2009; Makou et al., 2010) and also in the Tropical Pacific (Tudhope et al., 2001; Moy et al., 2002). The likely explanation for the increase in variability since ~4.5 kyr BP is the mid-Holocene strengthening of El Niño Southern Oscillation, which may be linked to changes in the precession of earth's orbit (Clement et al., 2000).

VII-1.2. Which were the factors influencing anchovy and sardine fluctuations during the last 25 kyr?.

Regardless of the mechanism that caused the enhancement of upwelling off Pisco since the Early Holocene, the increase in export production was accompanied by an increase in anchovy biomass which is not surprising given that anchovies are more influenced by upwelling and coastal productivity than sardines (Bertrand et al., 2004; Gutierrez et al., 2007; Swartzman et al., 2008; McCall, 2009). Therefore, the periods associated with weaker productivity like the Early Glacial and Last Glacial Maximum show low abundance of anchovy as expected, while the periods associated with an enhanced upwelling like the Late Holocene show higher anchovy abundance, though highly variable. The response of the PUE to globally cold periods of either relatively short duration (like the Little Ice Age 1500 – 1850 AD) or long duration (e.g. Last Glacial Maximum 23– 19 kyr BP) are all characterized by a decrease in productivity and in anchovy abundance. The strong link between anchovy and the productivity can be observed in the records obtained for the last 100 years where the tendency towards higher anchovy productivity is related to an increase in alongshore winds favorable to upwelling, a tendency towards lower SST and higher productivity (Gutierrez et al., 2011). Therefore, productivity is the main factor that controls the fluctuations in anchovy biomass at several timescales.

The high resolution reconstruction of anchovy and sardine biomass fluctuations during the last 150 years show that the multidecadal fluctuations are not always related to the PDO. During the last ~60 years the period of higher sardine abundance occurred during the warm phase of the PDO

(from 1975 to the mid-1990s), while the periods with increased anchovy population sizes have occurred during the cool phase of the PDO (from 1950 to 1975, and from the early 1990s to the present; Chavez et al., 2003). However, the high resolution record obtained in chapter VI show that the former warm phase of the PDO (from 1925 to 1950) is not associated with an increase in sardine, result that confirms previous records (Valdes et al., 2008; Gutierrez et al., 2009). Moreover the natural fluctuation of anchovy biomass size (from ~1900 to ~1960) is in the order of ~15 – 20 years and is not related at all with the PDO fluctuations in this time period.

The oceanic species, especially sardines, were more favored during warm Northern Hemisphere episode and inversely, significantly reduced during the globally cold periods. The Early Holocene, specifically from 10.5 to 9.5 kyr BP, shows one of the highest fluxes of sardine and other oceanic species. This period was characterized by a maximum in Northern summer insolation (Berger et al., 1978) and a northward displacement of the ITCZ (Haug et al., 2001) that is consistent with dry conditions in Peruvian Andes (Bird et al., 2011). Off Southern Peru, ^{14}C reservoir ages were higher (and highly variable) during this period, suggesting generally stronger, but highly variable upwelling intensity (Ortlieb et al., 2011). In addition, proxy records indicate warmer and variable SSTs off central and southern Peru (Callao and San Juan), suggesting strong changes in upwelling and stratification (Rein et al., 2005; Chazen et al., 2009). These conditions probably induced a strong variability in the expansion-contraction of the habitat favorable for oceanic species. This observation is concordant with the general observation that sardines are usually associated to highly variable climatic-oceanographic conditions (Bakun and Weeks, 2008). For example, the period from 1855 to 1905 AD favorable to sardines, was characterized by perturbations in the ocean-climate system in the Pacific basin (with stronger El Niño and La Niña events). The globally warm periods, like the Early Holocene, Medieval Climate anomaly and the Current Warm Period, seem to induce more variable conditions in the PUE than the globally cold periods, which are more favorable to oceanic species. By contrast, during the globally cold Early Glacial, Last Glacial Maximum, Dark Ages cold Period and Little Ice Age the sardine and other oceanic species abundance were strongly reduced. Finally, the reconstruction of fish biomass fluctuations at high resolution levels during the last 150 years show that sardine is not always associated with the warm PDO phases (see Figure VI-8).

Changes in OMZ intensity is also an important factor influencing the fluctuations of anchovy and sardine at several timescales, and the OMZ intensity during the Heinrich 1 Stadial and during the last 50 years (Bertrand et al., 2011) are good examples. The Heinrich 1 Stadial was characterized by low productivity and a very strong OMZ, conditions that were to some extent favorable for anchovy but not for sardine (see Figs. IV-7 and IV-11). The low productivity during this period was probably the limiting factor that impeded a higher anchovy biomass because anchovy is strongly linked to productivity (Bertrand et al., 2004; 2011; McCall, 2009). In the case of sardine, the combination of

low productivity and strong OMZ caused the absence of sardine in front of Peru because sardine benefit from a more oxygenated-deeper habitat (Bertrand et al., 2011), which not occurred during the Heinrich 1 Stadial. The response of the pelagic community during the Heinrich 1 Stadial conditions could be an analog to future climate conditions if the OMZs continue to expand (Stramma et al., 2008). Consequently, it seems that productivity and oxygen in the water column are the limiting factor for sardine. A high resolution reconstruction of the OMZ intensity for the last 150 years is in progress and may elucidate if the presence of sardine from ~1880 to ~1905 AD is associated or not with a weaker OMZ, which may confirm or not the 3D model proposed by Bertrand et al. (2011).

VII-2. Comparison of the fish scale records off Peru with other records of fish abundance

One of the best examples of past population variability of pelagic fishes inferred by fish scale deposition rates of the last 1600 years is the one developed in the Santa Barbara Basin off Southern California (Baumgartner et al., 1992; Fig VII-1C). Off California the periods of high sardine biomass are from ~500 to 800AD, 1050 to 1350 AD and 1700 to 1950 (Fig. VII-1C). The presence of sardine in the Pisco record is scarcer than off California, but sardine is abundant from 1050 to 1400AD and from 1850 to 2000AD (Fig. VII-1B). These observations indicate that only during the Medieval Climate Anomaly sardines were favored off California and Peru. One important difference between the records off Peru and California is that during the last 100 years the anchovy scale record off Peru are higher in comparison with the whole record and that there is an increase in anchovy fluxes during the last 100 years that are not observed off California (Fig. VII-1B).
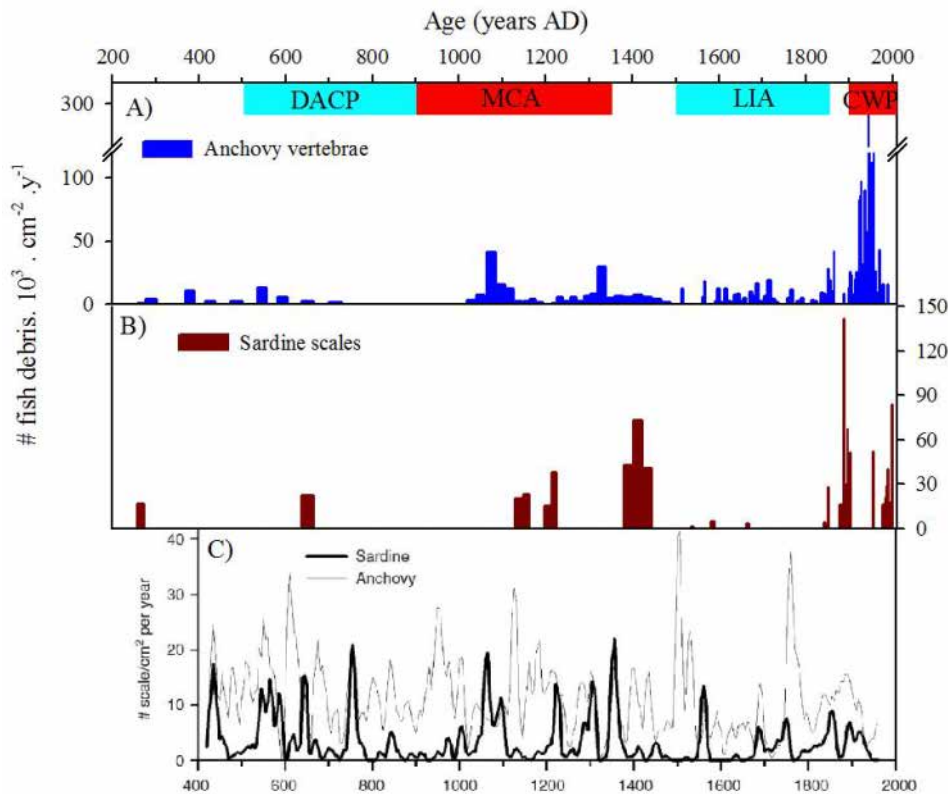
Figure VII-1. Fish debris deposition rates off Pisco and off California. A) Anchovy vertebrae fluxes (# vertebrae.10^3.y^{-1}.cm^{-2}) in cores B-14 and G-10 (see chapter V). B) Sardine (*Sardinops sagax sagax*) scale fluxes (# scales.10^3.y^{-1}.cm^{-2}) in cores B-14 and G-10 (see chapter V). C) Pacific sardine (*Sardinops sagax*) and northern anchovy (*Engraulis mordax*) scale fluxes resolved into 5-year samples. Highlighted areas indicate the Current Warm Period (CWP from ~1900 to the present), Little Ice Age (LIA, from 1500 to 1850AD), the Medieval Climate Anomaly (MCA, from 900 to 1350AD) and the Dark Ages Cold Period (500 – 900 AD). The LIA and MCA dates ranges from Graham et al. (2011).

Comparison of anchovy and sardine landings obtained from the coastal waters off North-Western, North-Eastern and South-Eastern Pacific and the South-Eastern Atlantic lead to detect decade-scale regimes of these two pelagic species (Schwartzlose et al., 1999). Particularly in the 1980s and 1990s, sardine in the North-Western (i.e. off Japan) and South-Eastern Pacific (i.e. off Peru and Chile) were fluctuating in phase (Fig. VII-2) which supports a synchronicity between sardine populations in the Pacific. During the 1980s the Californian sardine did not show high abundance, as observed off Japan and off Peru and Chile, which was explained as a consequence of heavy fishing pressure (Kawasaki, 1983; Schwartzlose et al., 1999). During the 1930s and early 1940s sardine population off Japan and California also show a period of relatively high abundance, further supporting the idea of a synchronicity of sardine in the Pacific. In contrast, there is no evidence of synchronicity between the different anchovy populations, except in the simultaneous collapse of the populations in Japan and the Humboldt Current in the late 1960s/early 1970s (Kawasaki, 1983; Schwartzlose et al., 1999; Lehodey et al., 2006). The limited number of observed cycles and the lack of consistency in some landings time series did not permit to establish a firm conclusion of whether

anchovy or sardine fluctuate in synchrony on a global scale (Lehodey et al., 2006). The most convincing observation for a basin-scale synchrony was based on sardine landings in Japan and in the HCS (Lehodey et al., 2006). However, the fish scale records for the last 150 years off Peru (and also off Chile) do not support the idea of a basin-scale synchrony of sardine in the Pacific (Fig. VII-2), because no sardine scales were found during the 1930s and early 1940s. Thus, the combined results off Peru, off Japan and off California indicate no support for the apparent synchrony of sardines in the Pacific. The different historical records (fish landings and fish scale deposition rates) suggest that the ecosystem paradigms that were constructed based on 20th century observations are only a small part of the range of ecosystem response to cliamte change and intrinsic variability (Field et al., 2009)
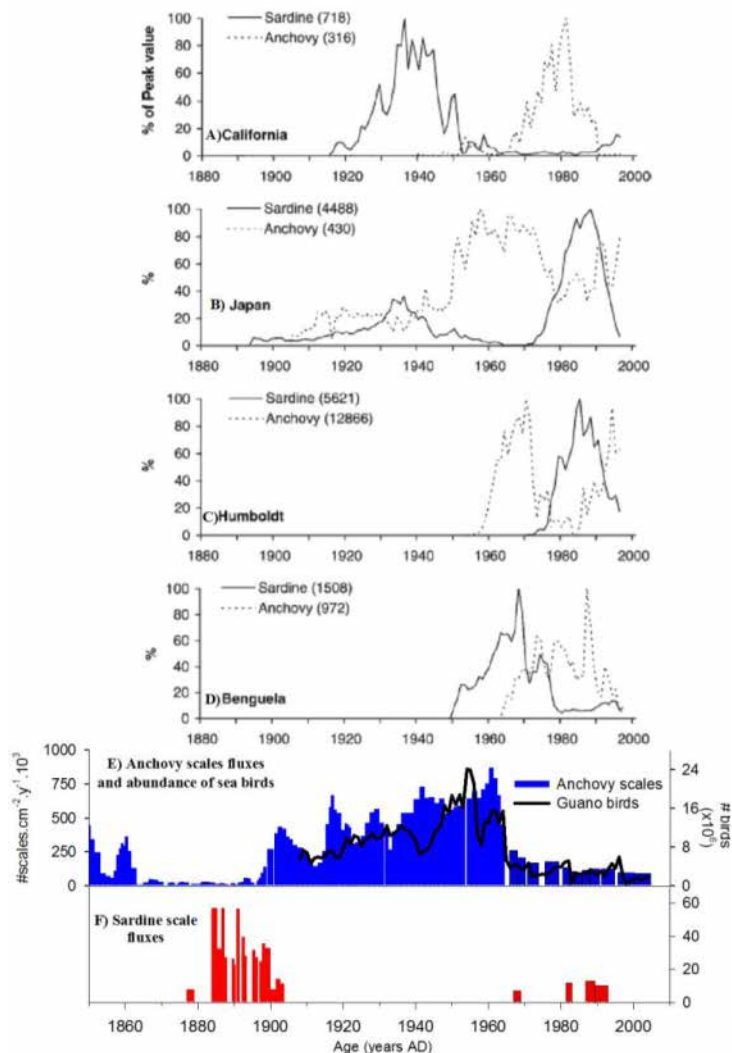
Figure VII-2. Observed catch of anchovy and sardine relative to the maximum peak value of their series (value in thousand of tons between brackets) during the last century in the Pacific: A) California, B) Japan-Kuroshio, and C) Peru-Humboldt systems, and Atlantic: D) Benguela system. Figure taken from Lehodey et al. (2006) that was redrawn from Schwartzlose et al. (1999). E) Anchovy scale fluxes in the composite record assembled with samples from core B05-13 and B04-6 (hatched bars) as a proxy for anchovy biomass variability (data were smoothed with a 3-point moving average), alongside with number of guano producing birds (black bold line). F) Sardine scale fluxes in the composite record assembled with samples from core B05-13 and B04-6 (dashed bars) as a proxy for sardine biomass variability.

Anthropogenic activities lead to global warming, inducing an enhancement of local alongshore winds in response to 1) increasing land-sea pressure gradient (Bakun, 1990), and/or 2) an intensification of the Southeastern Pacific Anticyclone (Falvey and Garreaud, 2009). This in turn favors the enhancement of primary productivity off Peru. Our results show that during the last ~100 yr a strong tendency towards higher anchovy productivity is supported by an increase in upwelling intensity and higher export production. Nevertheless the last 4.5 kyr shows that large and rapid

changes in export production and OMZ intensity accompanied with major changes in anchovy and sardine biomass can occur. In the near future it is uncertain if oceanographic conditions will change as it happened in the past (as for example in the Medieval Climate Anomaly-Little Ice Age transition). This would have important consequences to the whole ecosystem and the associated social and economical activities, given that the productivity trend does not stop in the first chains of the trophic levels (i.e. anchovy) but instead propagates to species located in higher trophic levels as hake and sea birds.

VII-3. Perspectives

Different types of analyses can be perfomed to develop the interpretations proposed in the present work. For example, measurement of $\delta^{15}N$ in pristine anchovy or sardine scales during the last 25 kyr and its comparison with the $\delta^{15}N$ of the bulk organic matter could serve to gain insight about the trophic chain dynamics in the PUE (Struck et al., 2002). Additionally, Strontium (Sr) and Neodymium (Nd) radiogenic isotope ratios in fish debris can be performed to study the provenance and transport pathways of water masses (Gleason et al., 2009). The Nd contents in fish teeth and bones is acquired through rapid postmortem uptake at the sediment/water interface via adsorption and substitution mechanisms while still on the seafloor (Reynard et al., 1999; Gleason et al., 2009). Consequently, the apatite present in the fish remains should faithfully record the average Nd isotopes composition of waters flowing across the seafloor over very short duration time spans (hundreds to thousands of years; Gleason et al., 2009). This method, applied to several latitudinal cores in the HCS, should be powerful enough to test whether the sources of the Peruvian Under-Current were the same or not during the last Glacial-Interglacial transition and during the Holocene. Finally, another potential study could be to study the effects of the OMZ intensity and export production changes on the fish biomass fluctuations in the three others Eastern Boundary Upwelling Ecosystems (i.e. California, Benguela and Canarias) at decadal to millennial timescales.

VII-4. Bibliography

Bakun, A. 1990. Global climate change and intensification of coastal upwelling. Science 247(4939):198-201.

Bakun, A., D. Field, A. Redondo-Rodriguez, and S. J. Weeks. 2010. Greenhouse gas, upwelling-favorable winds, and the future of coastal ocean upwelling ecosystems. Global Change Biology 16:1213-1228.

Bakun, A., and S. J. Weeks. 2008. The marine ecosystem off Peru: What are the secrets of its fishery productivity and what might its future hold? Progress in Oceanography 79:290-299.

Berger, A. L. 1978. A Simple algorithm to compute long term variations of Daily or monthly insolation Institut d'Astronomie et de Geophysique, Universite Catholique de Louvain, Louvain-la-Neuve, No. 18.

Bertrand, A., M. Segura, M. Gutiérrez, and L. Vásquez. 2004. From small-scale habitat loopholes to decadal cycles: a habitat-based hypothesis explaining fluctuation in pelagic fish populations off Peru. Fish and Fisheries 5:296-316.

Bertrand, A., A. Chaigneau, S. Peraltilla, J. Ledesma, M. Graco, F. Monetti, and F. Chavez. 2011. Oxygen: A Fundamental Property Regulating Pelagic Ecosystem Structure in the Coastal Southeastern Tropical Pacific. PLoS ONE 6(12):e29558.

Bird, B. W., M. B. Abbott, D. T. Rodbell, and M. Vuille. 2011. Holocene tropical South American hydroclimate revealed from a decadally resolved lake sediment δ18O record. Earth and Planetary Science Letters 310:192-202.

Bruland, K. W., E. L. Rue, G. J. Smith, and G. R. DiTullio. 2005. Iron, macronutrients and diatom blooms in the Peru upwelling regime: brown and blue waters of Peru. Marine Chemistry 93:81-103. Chavez, F. P., and M. Messié. 2009. A comparison of Eastern Boundary Upwelling Ecosystems. Progress in Oceanography 83(1-4):80-96.

Chavez, F., J. Ryan, S. Lluch-Cota, and M. Niquen. 2003. From Anchovies to Sardines and Back: Multidecadal Change in the Pacific Ocean. Science 299:217-221.

Chavez, F. 2012. Climate change and marine ecosystems. PNAS 109(47):19045-19046.

Chazen, C. R., M. A. Altabet, and T. D. Herbert. 2009. Abrupt mid-Holocene onset of centennial-scale climate variability on the Peru-Chile Margin. Geophysical Research Letters 36:L18704.

Clement, A. C., R. Seager, and M. A. Cane. 2000. Suppression of El Niño during the mid-Holocene by changes in the Earth's orbit. Paleoceanography 15(6):731-737.

De Pol-Holz, R., O. Ulloa, L. Dezileau, J. Kaiser, F. Lamy, and D. Hebbeln. 2006. Melting of the Patagonian Ice Sheet and deglacial perturbations of the nitrogen cycle in the eastern South Pacific. Geophysical Research Letters 33:L04704.

Dezileau, L., O. Ulloa, D. Hebbeln, F. Lamy, J. L. Reyss, and M. Fontugne. 2004. Iron control of past productivity in the coastal upwelling system off the Atacama Desert, Chile. Paleoceanography 19:PA3012. Falvey, M., and R. D. Garreaud. 2008. Regional cooling in a warming world: Recent temperature trends in the southeast Pacific and along the west coast of subtropical South America (1979–2006). Journal of Geophysical Research 114:D04102.

Field, D. B., T. R. Baumgartner, V. Ferreira, D. Gutierrez, H. Lozano-Montes, R. Salvatteci, and A. Soutar. 2009. Variability from scales in marine sediments and other historical records. Pp. 45-63. In D. Checkley, C. Roy, J. Alheit, and Y. Oozeki, eds. Climate Change and Small Pelagic Fish. Cambridge University Press.

Gleason, J. D., D. J. Thomas, T. C. Moore Jr, J. D. Blum, R. M. Owen, and B. A. Haley. 2009. Early to middle Eocene history of the Arctic Ocean from Nd-Sr isotopes in fossil fish debris, Lomonosov Ridge. Paleoceanography 24:PA2215.

Gutierrez, M., G. Swartzman, A. Bertrand, and S. Bertrand. 2007. Anchovy (*Engraulis ringens*) and sardine (*Sardinops sagax*) spatial dynamics and aggregation patterns in the Humboldt Current ecosystem, Peru, from 1983–2003. Fisheries Oceanography 16(2):155-168.

Gutierrez, D., A. Sifeddine, D. B. Field, L. Ortlieb, G. Vargas, F. Chavez, F. Velazco, V. Ferreira, P. Tapia, R. Salvatteci, H. Boucher, M. C. Morales, J. Valdes, J. L. Reyss, A. Campusano, M. Boussafir, M. Mandeng-Yogo, M. Garcia, and T. Baumgartner. 2009. Rapid reorganization in ocean biogeochemistry off Peru towards the end of the Little Ice Age. Biogeosciences 6:835-848.

Gutierrez, D., I. Bouloubassi, A. Sifeddine, S. Purca, K. Goubanova, M. Graco, D. Field, L. Méjanelle, F. Velazco, A. Lorre, R. Salvatteci, D. Quispe, G. Vargas, B. Dewitte, and L. Ortlieb. 2011. Coastal cooling and increased productivity in the main upwelling zone off Peru since the mid-twentieth century. Geophysical Research Letters 38:L07603.

Haug, G. H., K. A. Hughen, D. M. Sigman, L. C. Peterson, and U. Rohl. 2001. Southward Migration of the Intertropical Convergence Zone through the Holocene. Science 293:1304-1308. Makou, M.C., Eglinton, T.I., Oppo, D.W., Hughen, K.A., 2010. Postglacial changes in El Niño and La Niña behavior. Geology 38(1), 43-46.

Higginson, M. J., and M. A. Altabet. 2004. Initial test of the silicic acid leakage hypothesis using sedimentary biomarkers. Geophysical Research Letters 31:L18303.

Kawasaki, T. 1983. Why do some pelagic fishes have wide fluctuations in their numbers? Biological basis of fluctuation from the viewpoint of evolutionary ecology. FAO Fish. Rep. 291:1065-1080.

Lehodey, P., J. Alheit, M. Barange, T. Baumgartner, G. Beaugrand, K. Drinkwater, J.-M. Fromentin, S. R. Hare, G. Ottersen, R. I. Perry, C. Roy, C. D. van der Lingen, and F. Werner. 2006. Climate Variability, Fish and Fisheries. Journal of Climate 19:5009-5030.

Martinez, P., and R. S. Robinson. 2010. Increase in water column denitrification during the last deglaciation: the influence of oxygen demand in the eastern equatorial Pacific. Biogeosciences 7:1-9.

McCall, A. D. 2009. Mechanisms of low-frequency fluctuations in sardine and anchovy populations. In D. Checkley, C. Roy, J. Alheit, and Y. Oozeki, eds. Climate Change and Small Pelagic Fish. Cambridge University Press.

Moy, C. M., G. O. Seltzer, D. T. Rodbell, and D. M. Anderson. 2002. Variability of El Niño/Southern Oscillation activity at millennial timescales during the Holocene epoch. Nature 420(6912):162-165.

Pennington, J. T., K. L. Mahoney, V. S. Kuwahara, D. D. Kolber, R. Calienes, and F. P. Chavez. 2006. Primary production in the eastern tropical Pacific: A review. Progress in Oceanography 69:285-317.

Reynard, B., C. Lécuyer, and P. Grandjean. 1999. Crystal-chemical controls on rare-earth element concentrations in fossil biogenic apatites and implications for paleoenvironmental reconstructions. Chemical Geology 155:233-241.

Rein, B., Lückge, A., Reinhardt, L., Sirocko, F., Wolfe, A., Dullo, W.-C., 2005. El Niño variability off Peru during the last 20,000 years. Paleoceanography 20, PA4003.

Schwartzlose, R. A., J. Alheit, A. Bakun, T. R. Baumgartner, R. Cloete, R. J. M. Crawford, W. J. Fletcher, Y. Green-Ruiz, E. Hagen, T. Kawasaki, D. Lluch-Belda, S. E. Lluch-Cota, A. D. MacCall, Y. Matsuura, M. O. Nevarez-Martinez, R. H. Parrish, C. Roy, R. Serra, K. V. Shust, M. N. Ward, and J. Z. Zuzunaga. 1999. Worldwide large-scale fluctuations of sardine and anchovy populations. South African Journal of Marine Science 21:289-347.

Struck, U., A. V. Altenbach, K. C. Emeis, J. Alheit, C. Eichner, and R. Schneider. 2002. Changes of the upwelling rates of nitrate preserved in the δ15N-signature of sediments and fish scales from the diatomaceous mud belt of Namibia. Geobios 35:3-11.

Swartzman, G., A. Bertrand, M. Gutiérrez, S. Bertrand, and L. Vasquez. 2008. The relationship of anchovy and sardine to water masses in the Peruvian Humboldt Current System from 1983 to 2005. Progress in Oceanography 79:228-237

Taylor, G. T., F. Muller-Karger, R. Thunell, M. I. Scranton, Y. Astor, R. Varela, L. Troccoli Ghinaglia, L. Lorenzoni, K. A. Fanning, S. Hameed, and O. Doherty. 2012. Ecosystem responses in the southern Caribbean Sea to global climate change. PNAS 109(47):19315-19320.

Tudhope, A. W., C. P. Chilcott, M. T. McCulloch, E. R. Cook, J. Chappel, R. M. Ellam, D. W. Lea, J. M. Lough, and G. B. Shimmield. 2001. Variability in the El Niño-Southern Oscillation through a Glacial-Interglacial cycle. Science 291:1511-1517.

Valdés, J., L. Ortlieb, D. Gutierrez, L. Marinovic, G. Vargas, and A. Sifeddine. 2008. 250 years of sardine and anchovy scale deposition record in Mejillones Bay, northern Chile. Progress in Oceanography 79:198-207.

van Geen, A., S. N. Luoma, C. C. Fuller, R. Anima, H. E. Clifton, and S. Trumbore. 1992. Evidence from Cd/Ca ratios in foraminifera for greater upwelling off California 4,000 years ago. Nature 358:54-56.

ANNEXES

Annexes I: Supplementary Tables and Figures for chapter III: Centennial to millennial variability in OMZ intensity, export production, and terrigenous input in the Humboldt Current System during the last 25 kyr.

AI-1 Terrestrial run-off proxies in cores G-14, G-10 and B-14

In this sub-section the terrestrial run-off proxies in cores B-14, G-10 and G-14 are shown with a depth scale (Figs. 1, 2 and 3) to show the similarities and differences among the different proxies. In core B-14 the Dry Bulk Density (DBD) and the 3 terrestrial run-off proxies (Al, Fe and Ti) show a coherent pattern (Fig. 1). Core B-14 shows an important change in sediment density at ~62.5 cm depth (Fig. 1) that was correlated with multiple nearby cores in chapter II. This so-called "sedimentary shift" was dated towards the end of the Little Ice Age (Gutierrez et al., 2009). The three terrigenous runoff proxies and the DBD values display strong variability throughout the core; however from ~22 to 5 cm from the top, the contents do not display changes. This coincides with the sediment sequence with more homogeneous material/ rapid sedimentation event, represented by the hatched area in Figure 1. Finally, a clear increase in the terrigenous input proxies can be observed in the upper 5 cm (Fig. 1). In cores G-10 and G-14 the DBD and the 3 terrestrial run-off proxies also show a coherent pattern (Figs. 2 and 3) with large changes along the cores.
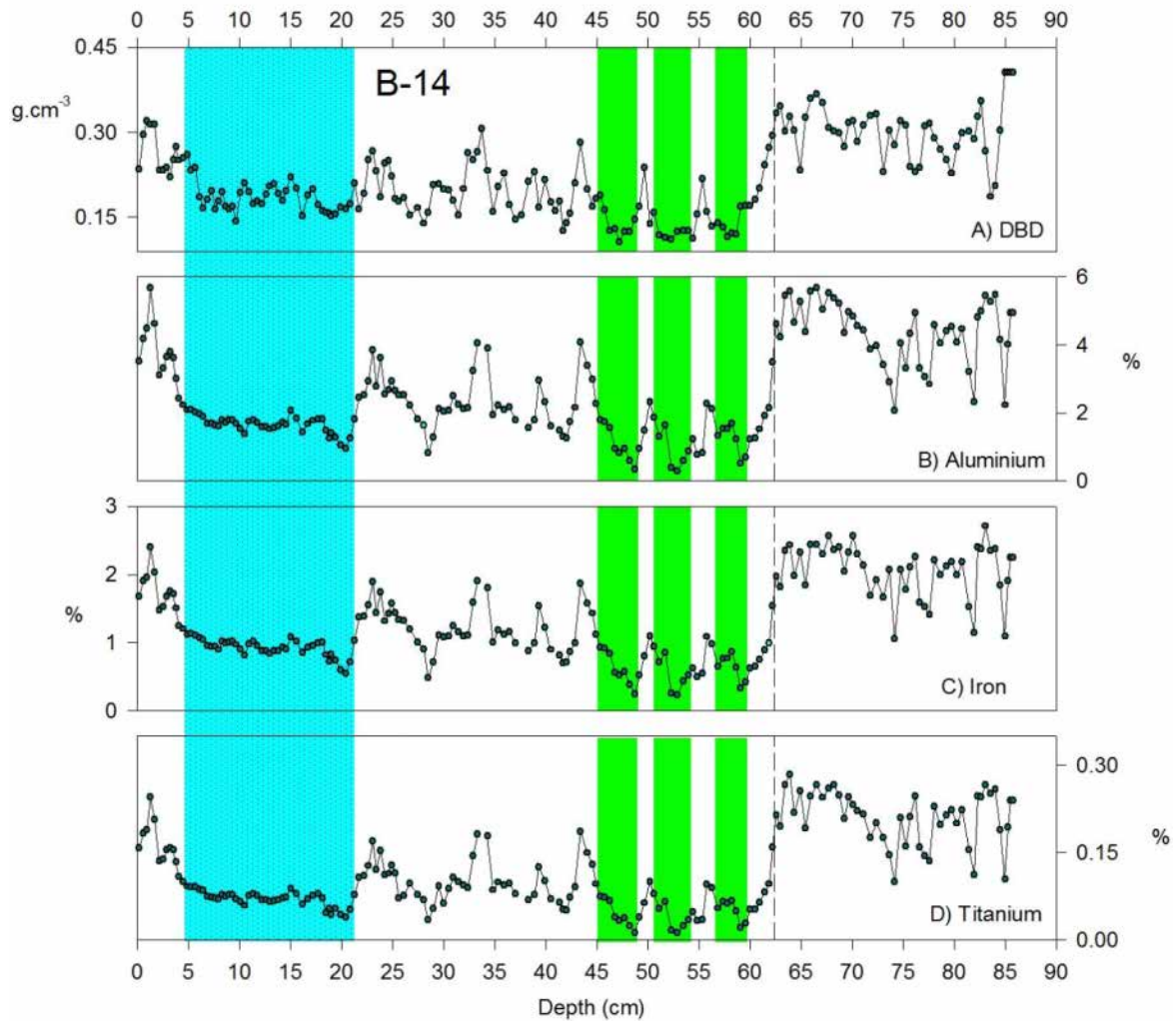
Figure AI-1. Sediment density and proxies of terrestrial runoff recorded in core B-14. A) Dry bulk Density (g.cm^{-3}). B) Aluminum contents (%). C) Titanium contents (%). D) Iron contents (%). The Dashed area corresponds to a sediment sequence with more homogeneous material. The highlighted areas correspond to the position of the diatom bands (see chapter II). The dashed lines represent the sedimentary shift reported by Gutierrez et al. (2009).
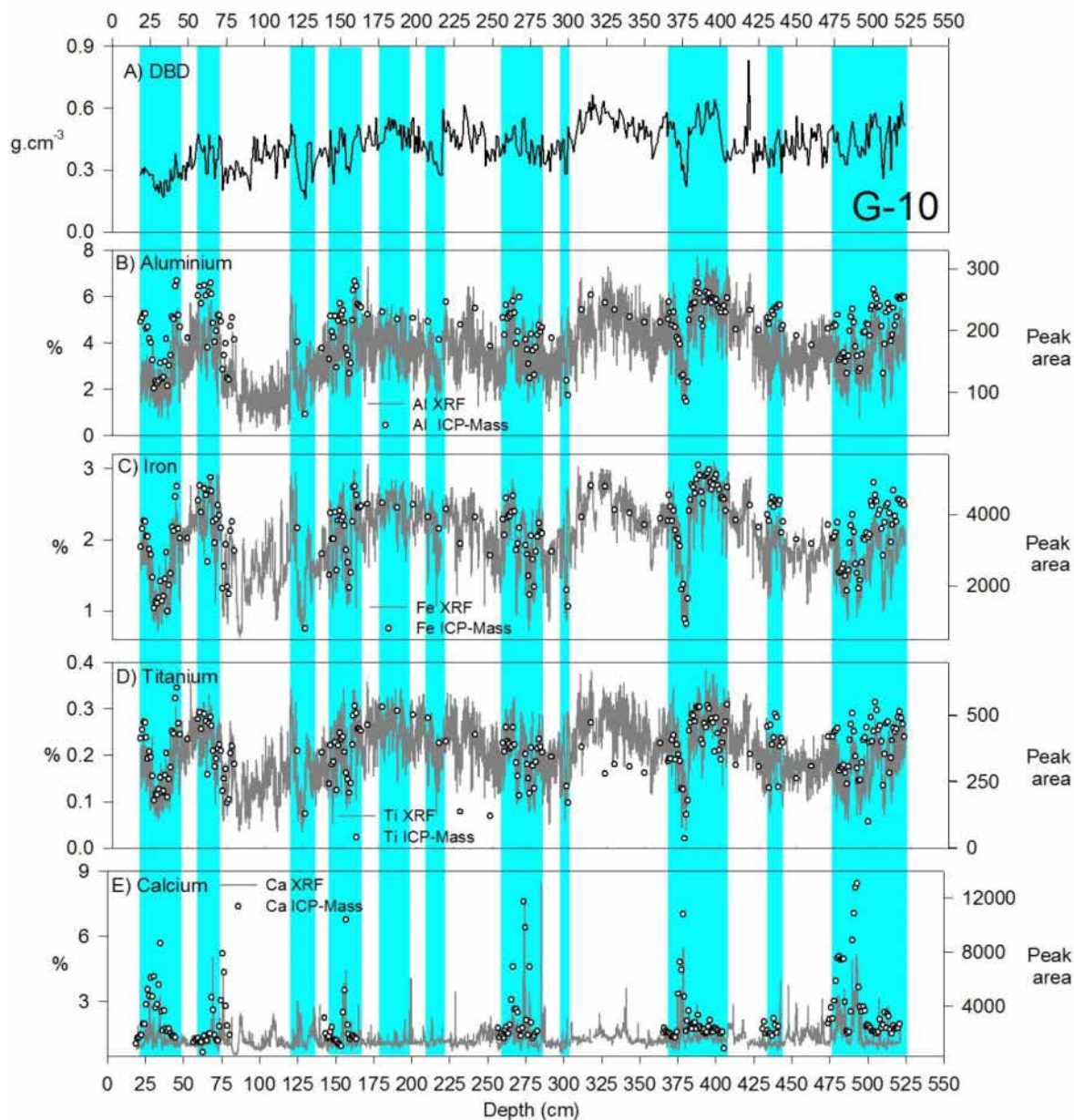
Figure AI-2. Sediment density, proxies of terrestrial runoff and Calcium contents recorded in core G-10. A) Dry bulk Density (g.cm^{-3}). B) Aluminum contents (%). C) Titanium contents (%). D) Iron contents (%). E) Ca contents. The blank circles (continuous lines) indicate the values obtained by ICP-Mass (XRF). The shaded areas correspond to the intervals with laminated sediments. Note that the ICP-Mass analyses were only obtained within the laminated sequences.
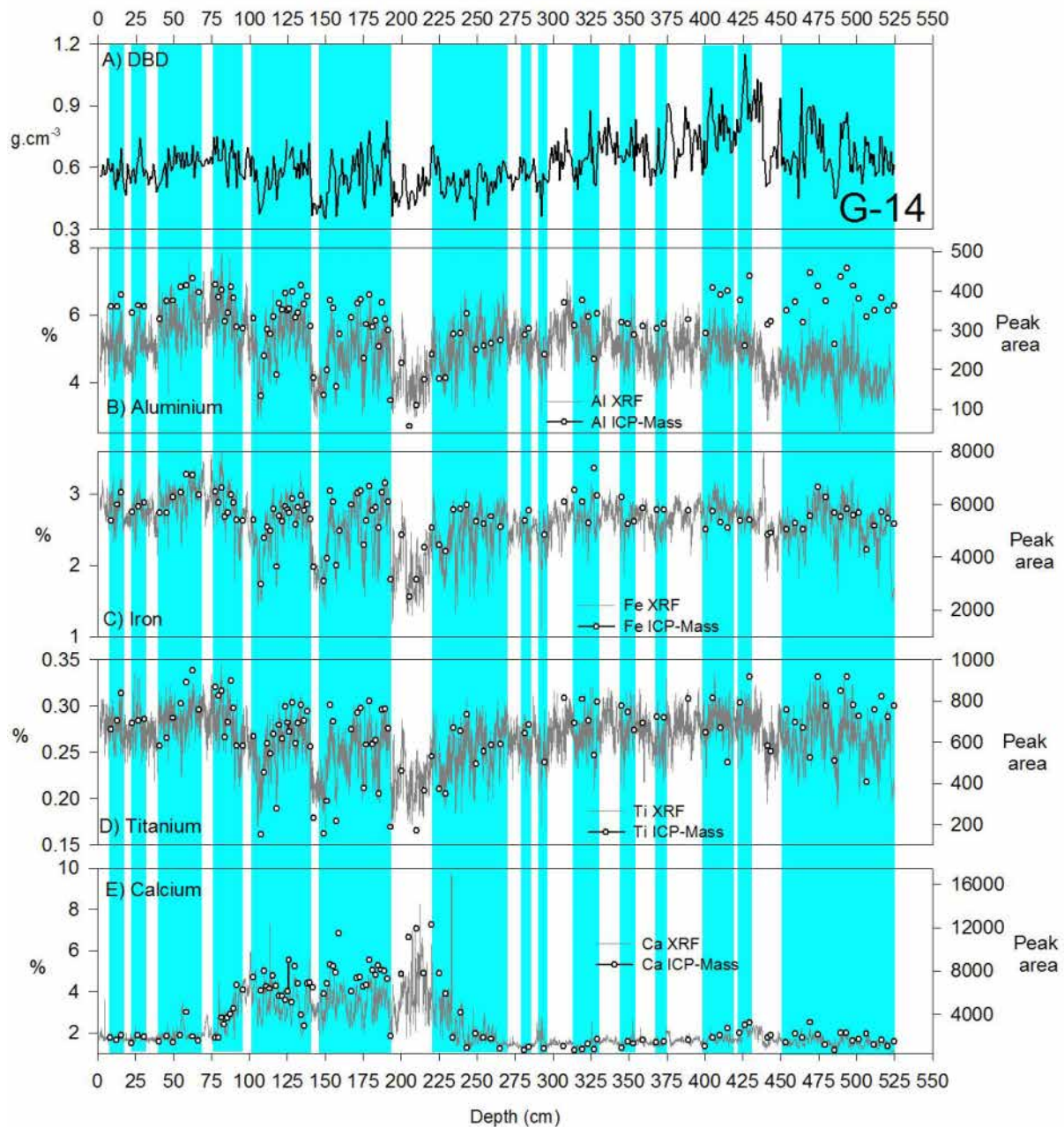
Figure AI-3. Sediment density, proxies of terrestrial runoff and Calcium contents recorded in core G-14. A) Dry bulk Density (g.cm^{-3}). B) Aluminum contents (%). C) Titanium contents (%). D) Iron contents (%). E) Ca contents. The blank circles (continuous lines) indicate the values obtained by ICP-Mass (XRF). The shaded areas correspond to the intervals with laminated sediments. Note that the ICP-Mass analyses were obtained within the laminated sequences.

AI-2 XRF calibration

There is a good agreement between the contents of Al, Fe and Ti obtained by XRF and ICP-Mass techniques in cores G-10 and G-14 (Figs. 2 and 3), but there are several data points that do not fit very well (e.g. Al contents at the base of core G-14, Fig. 3B). A best fit between XRF and ICP-Mass measurements for Al, Fe, and Ti, using all the samples of G-10 and G-14, was obtained using a

logarithmic relationship instead of a linear relationship (Figs. 4A, B and C). The log-relationship is possibly due to the limitations of the XRF to detect very low and very high element concentrations. The higher fit was obtained for Fe ($r^2 = 0.79$, n = 300, p<0.01) in comparison with Al ($r^2 = 0.58$, n = 300, p<0.01) and Ti ($r^2 = 0.57$, n = 300, p<0.01).
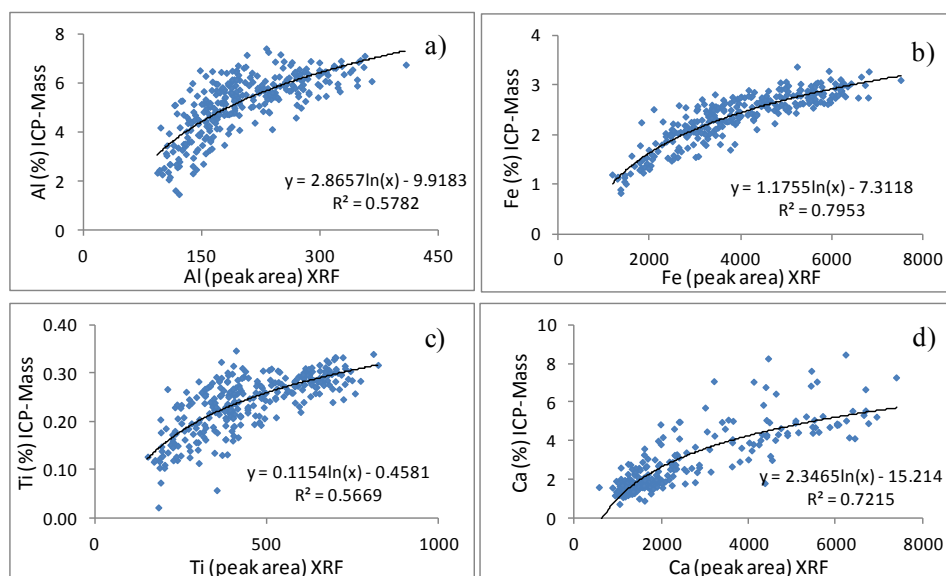
Figure AI-4. Calibration plots of major elements Al (A), Fe (B), Ti (C) and Ca (D) measured by scanning XRF and ICP-Mass analyses for cores G-10 and G-14.

AI-3 Sediment redox proxies

In this sub-section the trace element concentrations (ppm or ppb) and their EFs in the 3 cores evaluated are shown with a depth scale (Figs. 5, 6 and 7) to show the similarities and differences between the two modes of presentation of the data set. There are some differences between the redox trace metal authigenic contents and the metal EFs in core B-14 which are not observed in cores G-10 and G-14 (Figs. 5, 6 and 7). One remarkable difference is that in core B-14 the three diatom bands (highlighted areas in Fig. 5) show elevated EF values of V, Mo and Re and the lowest Re/Mo ratios. In contrast, the trace elements contents show low values of V and Re and no great change in Mo concentrations. The Mo EF for example was 3 times greater in the diatom bands in comparison with the average value during the post-sedimentary shift period. The high EF in the diatom bands likely indicates that the rapid diatom deposition produced anoxic events in the ocean floor. Additionally there is an increase in V, Mo and Re contents during last ~10 cm of the record which is not observed in their respective EFs (Fig. 5), and might be related to the high Al contents in this part of the record (Fig. 1B). In spite of the differences between the trace element concentrations and EF, both of them indicate anoxic conditions after the "sedimentary shift" (Fig. 5). Redox sensitive elements in core G-10 (Figs. 6A, B, C and D) and G-14 (Figs. 7A, B, C and D) show a stronger similarity between the two modes of presentation of the data set in comparison with core B-14. This resemblance is better

observed in core G-14 that is a more continuous record. In core G-10 this correspondence is better observed in the maximums and minimums from ~80 cm to the top of the core.
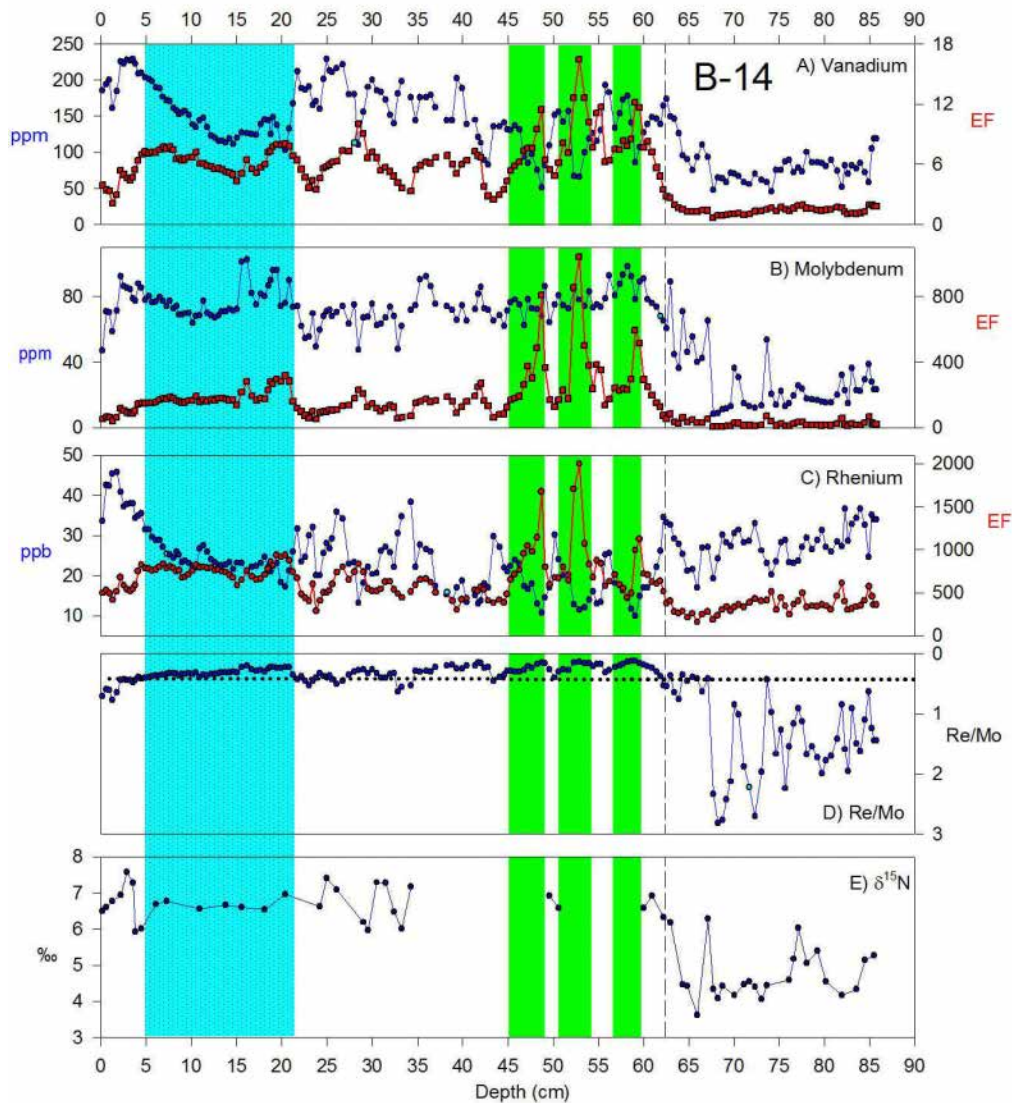
Figure AI-5. Proxies used to evaluate the OMZ intensity in core B-14, comparing the trace element contents (blue) and their EFs (red). A) Vanadium contents and EF. B) Molybdenum contents and EF. C) Re contents and EF. D) Authigenic Re/Mo, the horizontal dotted line indicates the value 0.4 x 10^{-3} which corresponds to the ratio of the concentration of these metals in the sea-water, y-axis inverted. E) δ^{15}N values from core B-6, plotted in the B-14 depth axis following the cross-stratigraphy shown in chapter II. The dashed area corresponds to a sediment sequence with more homogeneous material. The highlighted areas correspond to the position of the diatom bands (see chapter II). The dashed lines represent the sedimentary shift reported by Gutierrez et al. (2009).
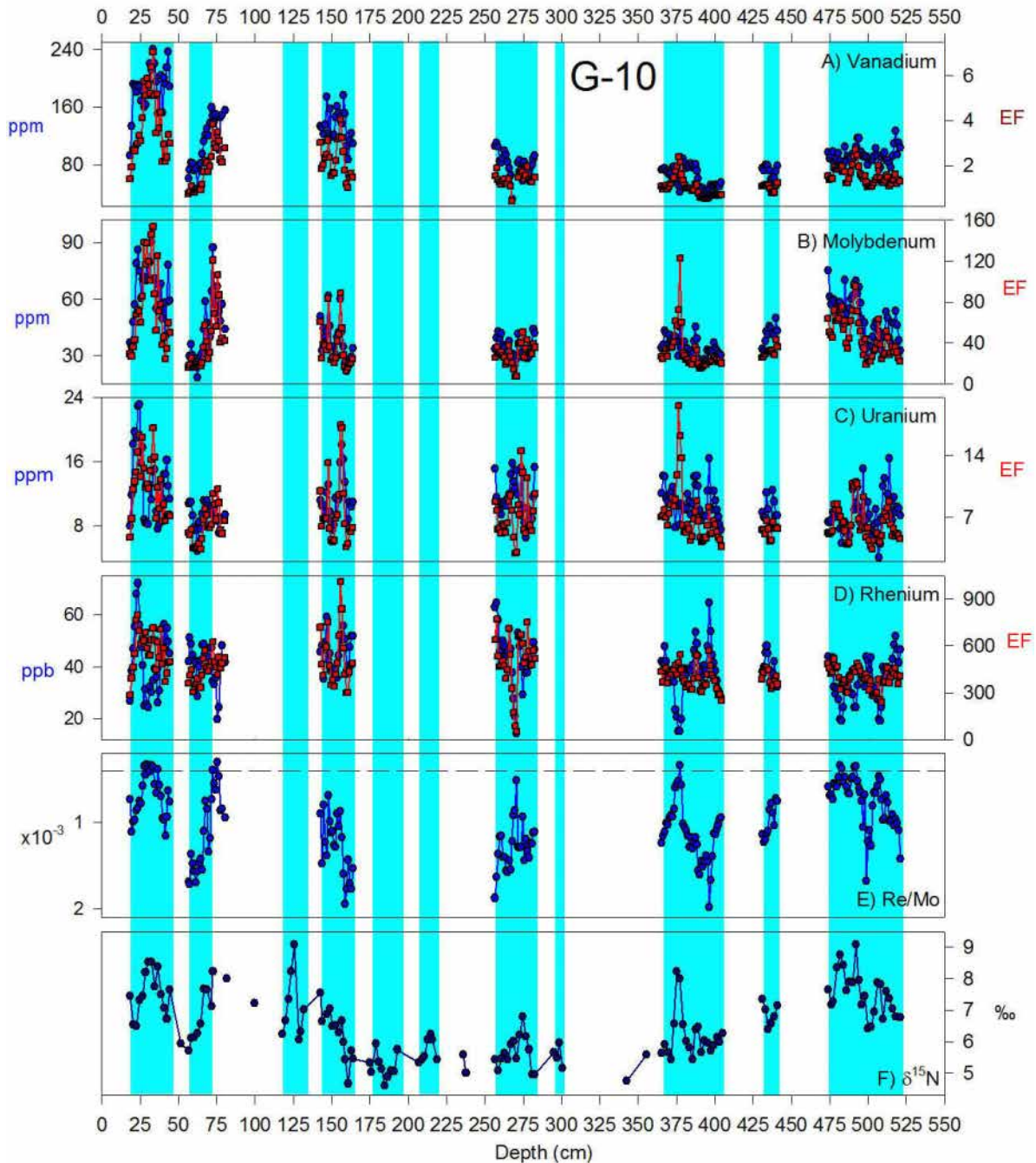
Figure AI-6. Proxies used to evaluate the OMZ intensity in core G-10, comparing the trace element contents (blue) and their EFs (red). A) Vanadium contents and EF. B) Molybdenum contents and EF. C) Uranium contents and EF. D) Re contents and EF. E) Authigenic Re/Mo, the horizontal dotted line indicates the value 0.4 x 10⁻³ which corresponds to the ratio of the concentration of these metals in the sea-water, y-axis inverted. F) δ¹⁵N values. The shaded areas correspond to the intervals with laminated sediments
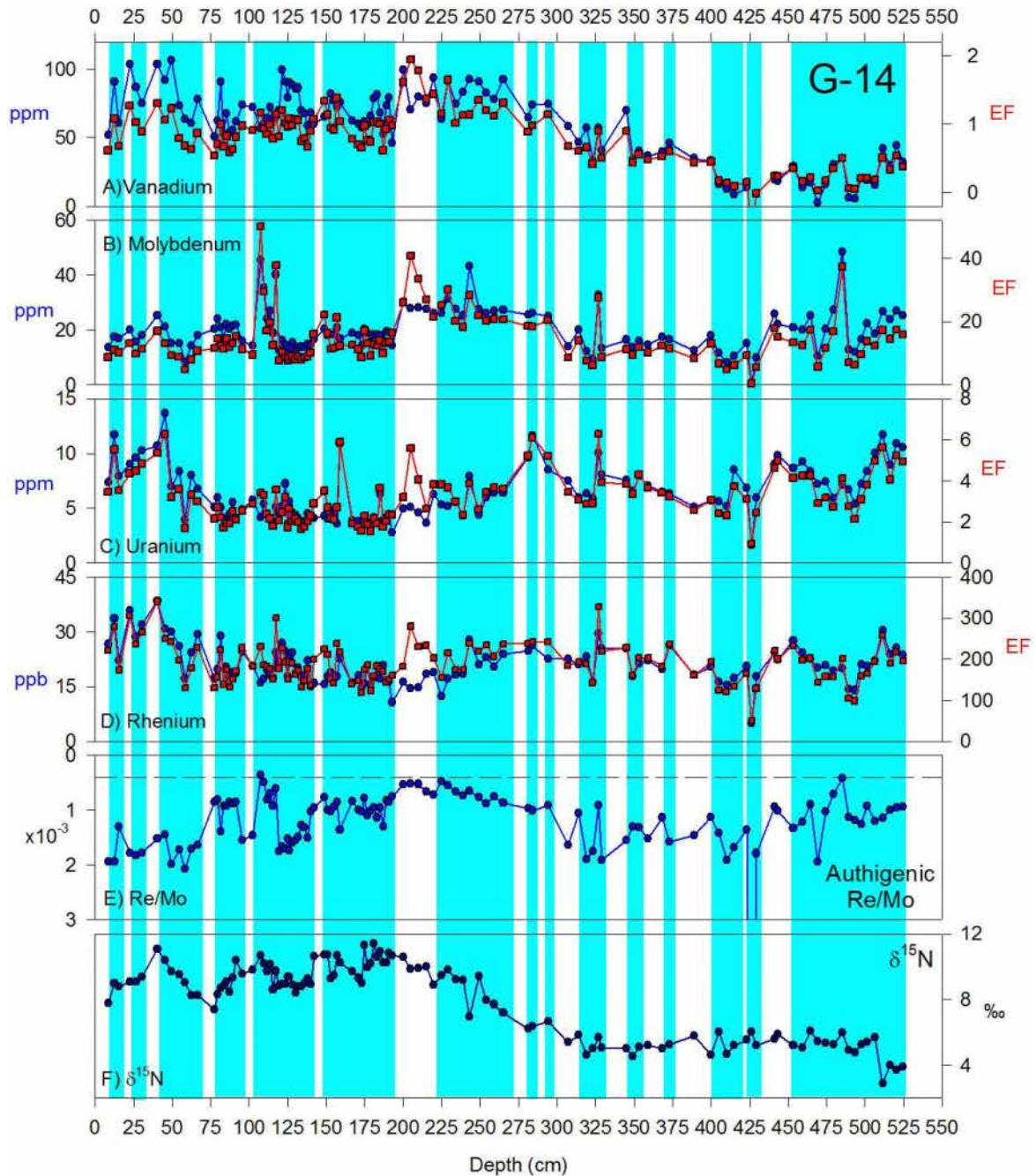
Figure AI-7. Proxies used to evaluate the OMZ intensity in core G-14, comparing the trace element contents (blue) and their EFs (red). A) Vanadium contents and EF. B) Molybdenum contents and EF. C) Uranium contents and EF. D) Re contents and EF. E) Authigenic Re/Mo, the horizontal dotted line indicates the value 0.4 x 10^{-3} which corresponds to the ratio of the concentration of these metals in the sea-water, y-axis inverted. F) δ^{15}N values. The shaded areas correspond to the intervals with laminated sediments.

AI-4 Paleo-productivity proxies

AI-4.1 Trace elements

In this sub-section the trace elements concentrations (ppm) and their Enrichment Factor (EF) in the three studied cores are shown with a depth scale (Figs. 8, 9 and 10) to show the similarities and differences between the two modes of presentation of the data set.   There are some differences between the productivity trace metal contents and the EF in the 3 cores but they are more subtle in comparison with the redox trace elements and their EFs (Figs. 5, 6 and 7). One remarkable difference in core B-14 is that the three diatom bands (highlighted areas in Fig. 8) show relatively high EF values of Ni, Cu and Cd while the concentrations of these elements are very low (Figs. 8A, B and C). Additionally in core B-14 the Ni and Cu contents show a tendency towards higher values in the first 5 cm of the record, while the EFs show a decline (Figs. 8A and B). These two differences between the productivity trace metal contents and the EFs in B-14 were also observed with the paleoredox proxies. Regardless of these small differences, the productivity proxies in core B-14 show higher values from the "sedimentary shift" to the top of the core and lower values downcore from the "sedimentary shift" to the base of the core. In core G-10 and G-14, both modes of data presentation are very similar (Figs. 9 and 10).

AI-4.2 Organic matter quantification and characterization

There are some differences between the TOC contents and the TOC/Al in the 3 cores, especially in core B-14 (Figs. 8D, 9D and 10D). As also shown by the paleo-redox proxies and the export production proxies, the TOC and TOC/Al contents in the three diatom bands (highlighted areas in Fig. 8) show relatively high TOC/Al values, while the TOC % are very low (Figs. 8D). Additionally, in core B-14 the TOC% shows a tendency towards higher values in the first 5 cm of the record, which is not observed in the TOC/Al profile (Figs. 8D). Regardless of these small differences, the TOC % and TOC/Al values in core B-14 show higher values from the "sedimentary shift" to the top of the core and lower values downcore from the "sedimentary shift" to the base of the core. In core G-10 and especially in core G-14 the TOC % and TOC/Al values are very similar.
.
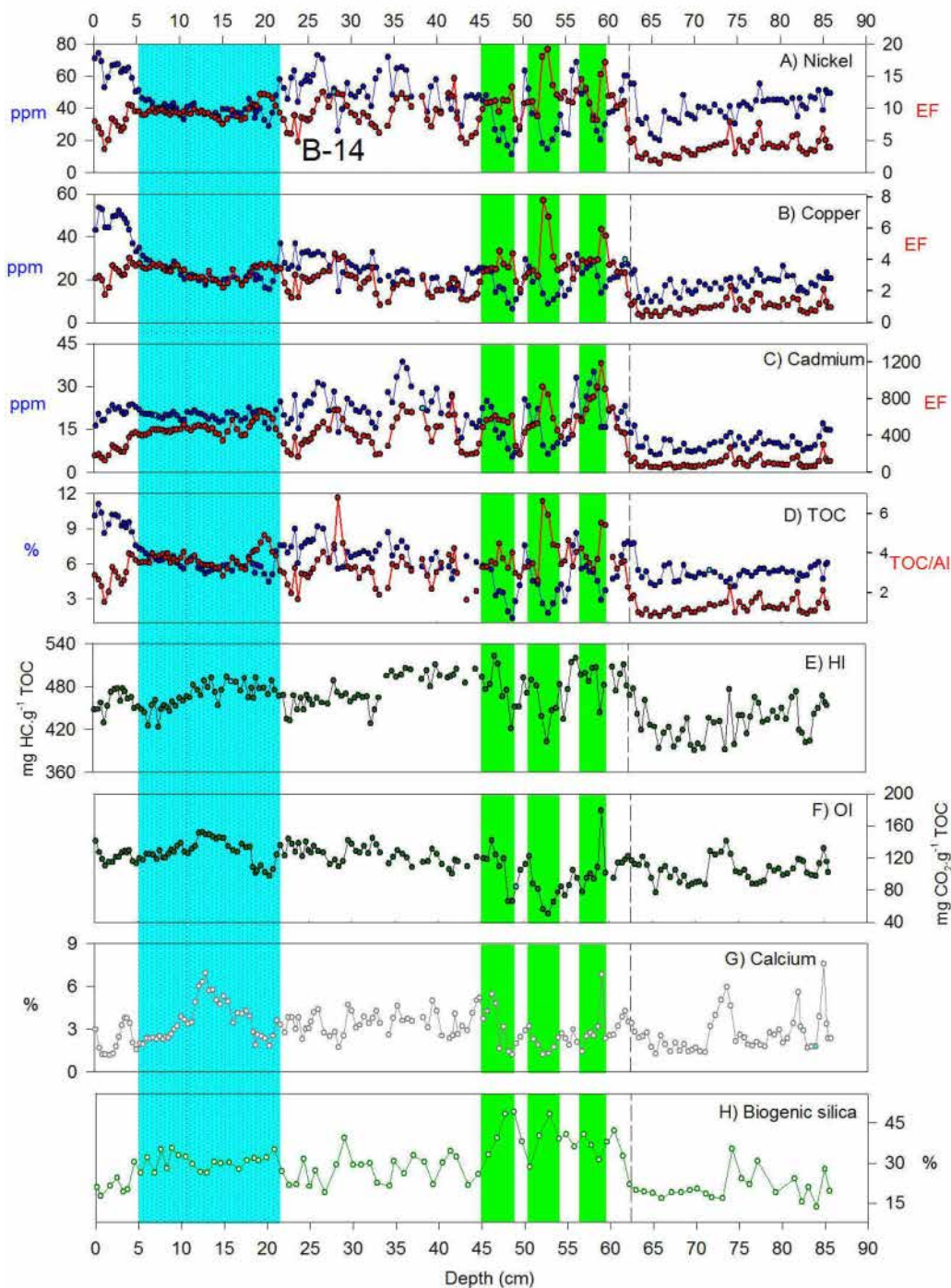
Figure AI-8. Proxies used to evaluate the export production in core B-14, comparing the trace element contents (blue) and their EFs (red), and the Rock-Eval parameters. A) Ni content and EF. B) Copper contents and EF. C) Cadmium content and EF. D) Total Organic Carbon (TOC) percentages (blue) and TOC/Al (red). E) Hydrogen index (HI). F) Oxygen index (OI). G) Calcium contents. H) Biogenic Silica contents. The dashed area corresponds to a sediment sequence with more homogeneous material. The highlighted areas correspond to the position of the diatom bands (see chapter II). The dashed lines represent the sedimentary shift reported by Gutierrez et al. (2009).
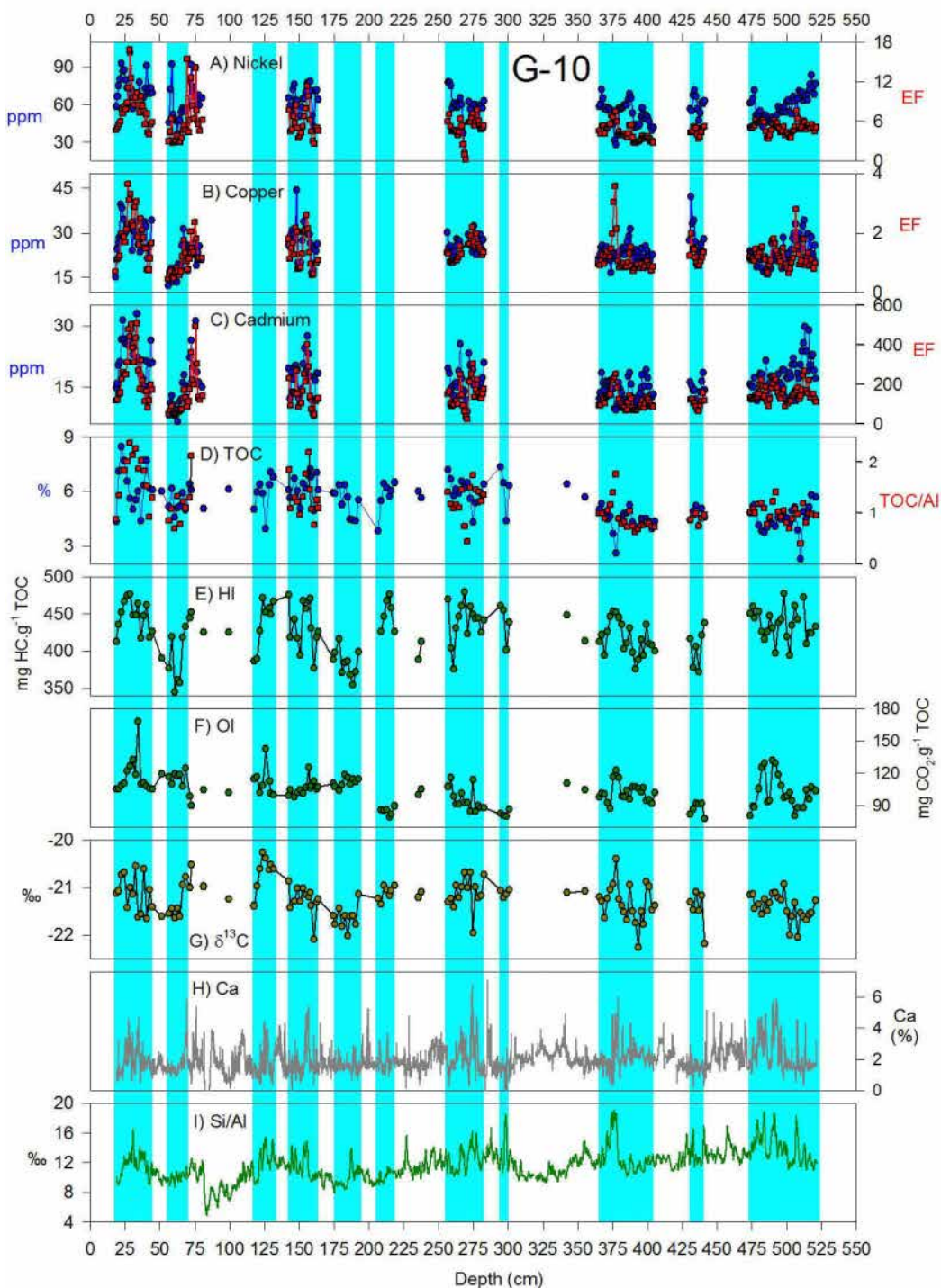
Figure AI-9. Proxies used to evaluate the export production in core G-10, comparing the trace element contents (blue) and their EFs (red), the Rock-Eval parameters and the δ¹³C values. A) Ni content and EF. B) Copper contents and EF. C) Cadmium content and EF. D) Total Organic Carbon (TOC) percentages (blue) and TOC/Al (red). E) Hydrogen index (HI). F) Oxygen index (OI). G) δ¹³C values. H) Calcium contents obtained using the equation shown in Fig. 8D. I) Biogenic Silica inferred from the Si/Al ratios obtained from the XRF analyses. The shaded areas correspond to the intervals with laminated sediments
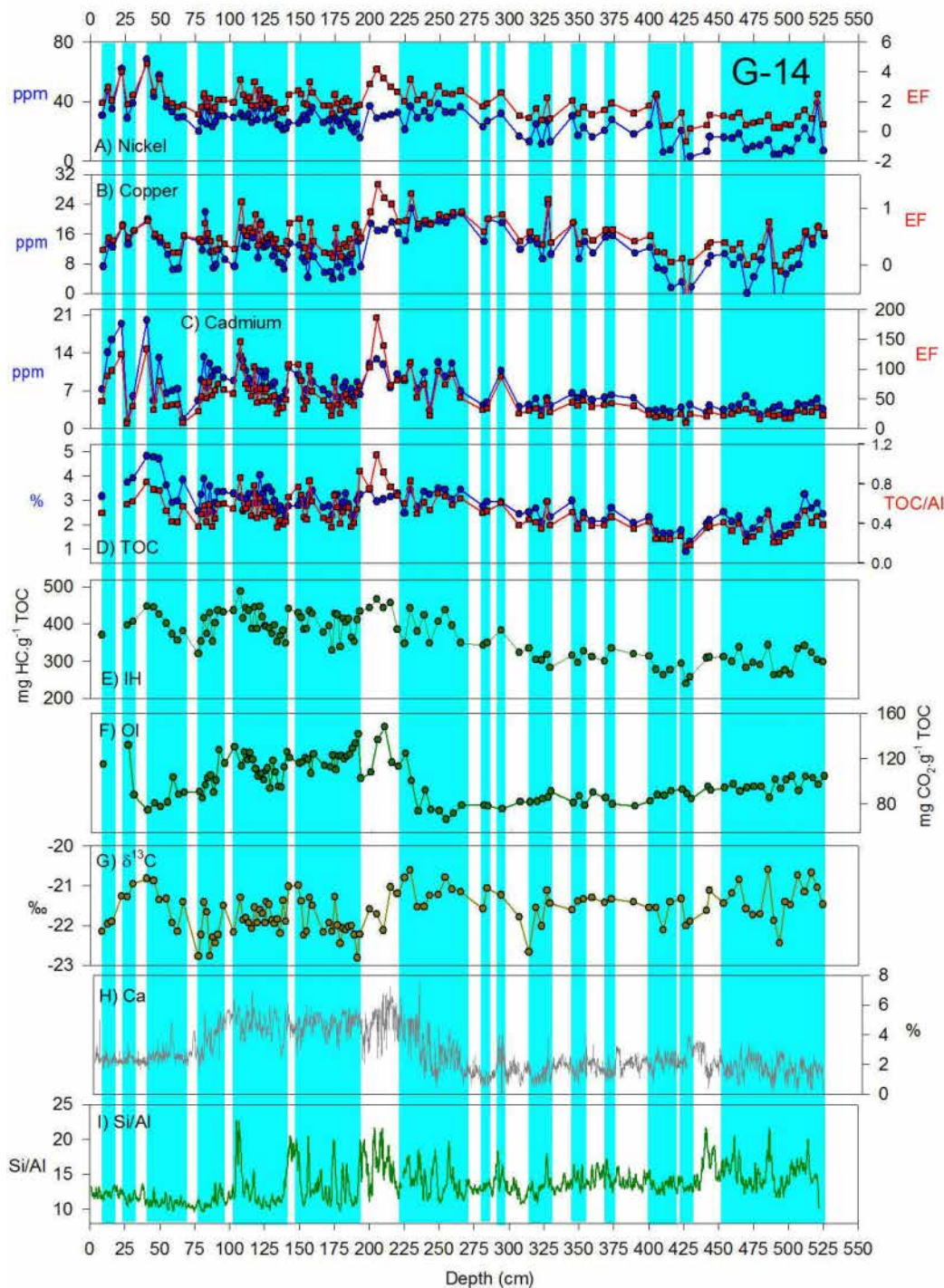
Figure AI-10. Proxies used to evaluate the export production in core G-14, comparing the trace element contents (blue) and their EFs (red), the Rock-Eval parameters and the δ¹³C values. A) Ni content and EF. B) Copper contents and EF. C) Cadmium content and EF. D) Total Organic Carbon (TOC) percentages (blue) and TOC/Al (red). E) Hydrogen index (HI). F) Oxygen index (OI). G) δ¹³C values. H) Calcium contents obtained using the equation shown in Fig. 8D. I) Biogenic Silica inferred from the Si/Al ratios obtained from the XRF analyses. The shaded areas correspond to the intervals with laminated sediments.

AI-4.3 Carbonate production/preservation

There is a good agreement between the contents of Ca in cores G-10 and G-14 obtained by XRF and ICP-Mass techniques (Figs. 2E and 3E), even if there are several data points that do not fit well (especially in core G-10, Fig. 3E). A best fit between XRF and ICP-Mass measurements for Ca using all the samples of G-10 and G-14, was obtained using a logarithmic relationship instead of a linear relationship (r^2 = 0.72, Figs. 4D).

AI-5. Statistical analyses

In this sub-section the results of the Kruskal-Wallis non-parametric ANOVA are presented (Tables 1 and 2) as well as the post-hoc tests (Tables 3-15).

Table AI- 1. Results of the Kruskal-Wallis non-parametric ANOVA (H statistic and *p*- values) used to test for differences in sediment redox conditions and OMZ intensity between the periods of interest.

Period	V EF H= 218 p = 0.000 Valid N	Sum of Ranks	Mo EF H= 215 p = 0.000 Valid N	Sum of Ranks	U EF H = 189 p = 0.000 Valid N	Sum of Ranks	Re EF H= 245 p = 0.000 Valid N	Sum of Ranks	Re/Mo H= 131 p = 0.000 Valid N	Sum of Ranks	δ^{15}N H= 196 p = 0.000 Valid N	Sum of Ranks
Last 150 years	27	8966	27	8958	-	-	27	8359	27	581	16	2245
Late Holocene	83	20837	83	18257	73	16271	83	20126	83	14749	77	8509
Mid Holocene	57	8987	57	10496	57	12241	57	12692	57	12425	37	3034
Early Holocene	69	12191	69	15087	69	12717	69	13028	69	9643	36	5676
Bolling Allerod	13	1419	13	559	13	1392	13	1209	13	4168	13	3012
Heinrich 1 Stadial	62	7646	62	5572	62	2870	62	3500	62	10399	62	14887
Last Glacial Maximum	19	681	19	746	19	1421	19	1079	19	5338	19	864
Early Glacial	19	348	19	1400	19	1916	19	1082	19	3772	19	833

Table AI-2. Results of the Kruskal-Wallis non-parametric ANOVA (H statistic and *p* values) used to test for differences in export production, organic matter quality and δ^{13}C values between the periods of interest.

Period	Ni EF H= 242 p = 0.000 Valid N	Sum of Ranks	Cu EF H= 209 p = 0.000 Valid N	Sum of Ranks	Cd EF H= 220 p = 0.000 Valid N	Sum of Ranks	TOC/Al H= 180 p = 0.000 Valid N	Sum of Ranks	HI H= 151 p = 0.000 Valid N	Sum of Ranks	OI H= 87 p = 0.000 Valid N	Sum of Ranks	δ^{13}C H= 53 p = 0.000 Valid N	Sum of Ranks
Last 150 years	27	8705	27	8890	27	8869	27	5690	27	6898	27	5767	-	-
Late Holocene	83	19674	83	18352	83	18201	46	8412	76	12575	76	12767	67	10616
Mid Holocene	57	11458	57	11735	57	11180	29	4964	37	6247	37	4077	37	6130
Early Holocene	69	14019	69	13875	69	14682	36	5478	36	5909	36	4219	36	4553
Bolling Allerod	13	1255	13	849	13	1110	13	1081	10	1149	10	829	13	1554
Heinrich 1 Stadial	62	4849	62	5363	62	5990	62	4952	62	7505	62	10835	62	4918
Last Glacial Maximum	19	719	19	1198	19	636	19	583	19	389	19	730	19	1842
Early Glacial	19	396	19	813	19	407	19	466	19	369	19	1817	19	2518

Table AI-3. Results of the multiple comparisons of mean ranks test (*p*-values) of the Vanadium Enrichment Factor differences between the periods of interest. Values between parentheses indicate the average, standard deviation and the valid number of samples used for the analysis. Boldface indicates significance after correcting for multiple comparisons (p<0.007).

Vanadium Enrichment Factor (V EF)	Last 150 years	Late Holocene	Mid Holocene	Early Holocene	Bølling-Allerød	Heinrich 1 Stadial	Last Glacial Maximum	Early Glacial
Last 150 years (6.4 ±1.8; n= 28)								
Late Holocene (2.6 ±1.4; n= 82)	0.008							
Mid Holocene (1.2 ±0.5; n= 57)	**0.000**	**0.000**						
Early Holocene (1.3 ±0.5; n= 69)	**0.000**	**0.000**	1.000					
Bølling Allerød (0.9 ±0.2; n= 13)	**0.000**	**0.000**	1.000	0.752				
Heinrich 1 Stadial (1 ±0.3; n= 62)	**0.000**	**0.000**	1.000	0.070	1.000			
Last Glacial Maximum (0.4 ±0.3; n= 19)	**0.000**	**0.000**	**0.000**	**0.000**	1.000	0.026		
Early Glacial (0.3 ±0.2; n= 19)	**0.000**	**0.000**	**0.000**	**0.000**	0.346	**0.002**	1.000	

Table AI-4. Results of the multiple comparisons of mean ranks test (*p*-values) of the Molybdenum Enrichment Factor differences between the periods of interest. Values between parentheses indicate the average, standard deviation and the valid number of samples used for the analysis. Boldface indicates significance after correcting for multiple comparisons (p<0.007).

Molybdenum Enrichment Factor (Mo EF)	Last 150 years	Late Holocene	Mid Holocene	Early Holocene	Bølling-Allerød	Heinrich 1 Stadial	Last Glacial Maximum	Early Glacial
Last 150 years (192 ±107; n= 28)								
Late Holocene (49.7 ±35.4; n= 82)	**0.000**							
Mid Holocene (32 ±17.5; n= 57)	**0.000**	1.000						
Early Holocene (40.3 ± 18.5; n= 69)	**0.000**	1.000	1.000					
Bølling Allerød (10.4 ±3; n= 13)	**0.000**	**0.000**	**0.000**	**0.000**				
Heinrich 1 Stadial (16.5 ±8.8; n= 62)	**0.000**	**0.000**	**0.000**	**0.000**	1.000			
Last Glacial Maximum (9.9 ±5.4; n= 19)	**0.000**	**0.000**	**0.000**	**0.000**	1.000	1.000		
Early Glacial (14.1 ±7; n= 19)	**0.000**	**0.000**	**0.001**	**0.000**	1.000	1.000	1.000	

Table AI-5. Results of the multiple comparisons of mean ranks test (*p*-values) of the Uranium Enrichment Factor differences between the periods of interest. Values between parentheses indicate the average, standard deviation and the valid number of samples used for the analysis. Boldface indicates significance after correcting for multiple comparisons (p<0.007). Uranium contents were not analyzed in core B05-14

Uranium Enrichment Factor (U EF)	Last 150 years	Late Holocene	Mid Holocene	Early Holocene	Bølling-Allerød	Heinrich 1 Stadial	Last Glacial Maximum	Early Glacial
Last 150 years	-							
Late Holocene (8.1±3.7; n= 73)	-							
Mid Holocene (7.4 ±3.1; n= 57)	-	1.000						
Early Holocene (6 ±1.8; n= 69)	-	0.228	1.000					
Bølling Allerød (4 ±1.2; n= 13)	-	**0.000**	**0.002**	0.097				
Heinrich 1 Stadial (2.6 ±0.9; n= 62)	-	**0.000**	**0.000**	**0.000**	0.571			
Last Glacial Maximum (3.3 ±1; n= 19)	-	**0.000**	**0.000**	**0.000**	1.000	1.000		
Early Glacial (3.9 ±1; n= 19)	-	**0.000**	**0.000**	0.007	1.000	0.443	1.000	

Table AI-6. Results of the multiple comparisons of mean ranks test (*p*-values) of the Rhenium Enrichment Factor differences between the periods of interest. Values between parentheses indicate the average, standard deviation and the valid number of samples used for the analysis. Boldface indicates significance after correcting for multiple comparisons (p<0.007).

Rhenium Enrichment Factor (Re EF)	Last 150 years	Late Holocene	Mid Holocene	Early Holocene	Bølling-Allerød	Heinrich 1 Stadial	Last Glacial Maximum	Early Glacial
Last 150 years (679 ±183; n= 28)								
Late Holocene (495 ±146; n= 82)	0.075							
Mid Holocene (453 ±141; n= 57)	**0.006**	1.000						
Early Holocene (391 ± 68; n= 69)	**0.000**	0.031	1.000					
Bølling Allerød (235 ±57; n= 13)	**0.000**	**0.000**	**0.001**	0.047				
Heinrich 1 Stadial (184 ±39; n= 62)	**0.000**	**0.000**	**0.000**	**0.000**	1.000			
Last Glacial Maximum (180 ±57; n= 19)	**0.000**	**0.000**	**0.000**	**0.000**	1.000	1.000		
Early Glacial (180 ±42; n= 19)	**0.000**	**0.000**	**0.000**	**0.000**	1.000	1.000	1.000	

Table AI-7. Results of the multiple comparisons of mean ranks test (*p*-values) of the Re/Mo differences between the periods of interest. Values between parentheses indicate the average, standard deviation and the valid number of samples used for the analysis. Boldface indicates significance after correcting for multiple comparisons (p<0.007).Uranium contents were not analyzed in core B05-14

Re/Mo	Last 150 years	Late Holocene	Mid Holocene	Early Holocene	Bølling-Allerød	Heinrich 1 Stadial	Last Glacial Maximum	Early Glacial
Last 150 years (0.3 ± 0.1; n= 28)								
Late Holocene (1 ±0.5; n= 82)	**0.000**							
Mid Holocene (1.2 ±0.3; n= 57)	**0.000**	0.568						
Early Holocene (0.9 ± 0.3; n= 69)	**0.000**	0.587	**0.000**					
Bølling Allerød (1.7 ±0.2; n= 13)	**0.000**	**0.000**	0.026	**0.000**				
Heinrich 1 Stadial (1 ±0.4; n= 62)	**0.000**	1.000	0.186	1.000	**0.000**			
Last Glacial Maximum (2 ±2.1; n= 19)	**0.000**	**0.002**	0.517	**0.000**	1.000	**0.001**		
Early Glacial (1.1 ±0.3; n= 19)	**0.000**	1.000	1.000	0.687	0.022	1.000	0.331	

Table AI-8. Results of the multiple comparisons of mean ranks test (*p*-values) of the $\delta^{15}N$ differences between the periods of interest. Values between parentheses indicate the average, standard deviation and the valid number of samples used for the analysis. Boldface indicates significance after correcting for multiple comparisons (p<0.007).

$\delta^{15}N$	Last 150 years	Late Holocene	Mid Holocene	Early Holocene	Bølling-Allerød	Heinrich 1 Stadial	Last Glacial Maximum	Early Glacial
Last 150 years (6.7 ± 0.3‰; n= 17)								
Late Holocene (6.3 ±1.2‰; n= 76)	1.000							
Mid Holocene (5.8 ±0.7‰; n= 37)	0.440	1.000						
Early Holocene (7.2 ± 0.8‰; n= 36)	1.000	0.106	**0.002**					
Bølling Allerød (9.2 ±0.9‰; n= 13)	0.068	**0.000**	**0.000**	0.128				
Heinrich 1 Stadial (9.5 ±1‰; n= 62)	**0.000**	**0.000**	**0.000**	**0.000**	1.000			
Last Glacial Maximum (5.2 ±0.5‰; n= 19)	0.015	0.046	1.000	**0.000**	**0.000**	**0.000**		
Early Glacial (5 ±0.8‰; n= 19)	0.012	0.035	1.000	**0.000**	**0.000**	**0.000**	1.000	

Table AI-9. Results of the multiple comparisons of mean ranks test (*p*-values) of the Ni EF differences between the periods of interest. Values between parentheses indicate the average, standard deviation and the valid number of samples used for the analysis. Boldface indicates significance after correcting for multiple comparisons (p<0.007).

Nickel Enrichment Factor (Ni EF)	Last 150 years	Late Holocene	Mid Holocene	Early Holocene	Bølling-Allerød	Heinrich 1 Stadial	Last Glacial Maximum	Early Glacial
Last 150 years (9.7 ± 1.8; n= 28)								
Late Holocene (6.3 ±3; n= 82)	**0.004**							
Mid Holocene (4.7 ±1.7; n= 57)	**0.000**	1.000						
Early Holocene (4.7 ± 1; n= 69)	**0.000**	1.000	1.000					
Bølling-Allerød (2.6 ±0.9; n= 13)	**0.000**	**0.000**	0.021	0.013				
Heinrich 1 Stadial (2.2 ±0.7; n= 62)	**0.000**	**0.000**	**0.000**	**0.000**	1.000			
Last Glacial Maximum (1.2 ±0.7; n= 19)	**0.000**	**0.000**	**0.000**	**0.000**	1.000	1.000		
Early Glacial (0.8 ±0.6; n= 19)	**0.000**	**0.000**	**0.000**	**0.000**	1.000	0.844	1.000	

Table AI-10. Results of the multiple comparisons of mean ranks test (*p*-values) of the Cu EF differences between the periods of interest. Values between parentheses indicate the average, standard deviation and the valid number of samples used for the analysis. Boldface indicates significance after correcting for multiple comparisons (p<0.007).

Copper Enrichment Factor (Cu EF)	Last 150 years	Late Holocene	Mid Holocene	Early Holocene	Bølling-Allerød	Heinrich 1 Stadial	Last Glacial Maximum	Early Glacial
Last 150 years (3.1 ± 0.7; n= 28)								
Late Holocene (1.4 ±0.7; n= 82)	**0.000**							
Mid Holocene (1.2 ±1.7; n= 57)	**0.000**	1.000						
Early Holocene (1.2 ± 0.4; n= 69)	**0.000**	1.000	1.000					
Bølling-Allerød (0.5 ±0.2; n= 13)	**0.000**	**0.000**	**0.000**	**0.000**				
Heinrich 1 Stadial (0.6 ±0.3; n= 62)	**0.000**	**0.000**	**0.000**	**0.000**	1.000			
Last Glacial Maximum (0.4 ±0.4; n= 19)	**0.000**	**0.000**	**0.000**	**0.000**	1.000	1.000		
Early Glacial (0.3 ±0.2; n= 19)	**0.000**	**0.000**	**0.000**	**0.000**	1.000	1.000	1.000	

Table AI-11. Results of the multiple comparisons of mean ranks test (*p*-values) of the Cd EF differences between the periods of interest. Values between parentheses indicate the average, standard deviation and the valid number of samples used for the analysis. Boldface indicates significance after correcting for multiple comparisons (p<0.007).

Cadmium Enrichment Factor (Cd EF)	Last 150 years	Late Holocene	Mid Holocene	Early Holocene	Bølling-Allerød	Heinrich 1 Stadial	Last Glacial Maximum	Early Glacial
Last 150 years (463 ± 150; n= 28)								
Late Holocene (180 ±118; n= 82)	**0.000**							
Mid Holocene (135 ±60; n= 57)	**0.000**	1.000						
Early Holocene (141 ± 43; n= 69)	**0.000**	1.000	1.000					
Bølling-Allerød (59 ±41; n= 13)	**0.000**	**0.000**	0.010	**0.001**				
Heinrich 1 Stadial (67 ±31; n= 62)	**0.000**	**0.000**	**0.000**	**0.000**	1.000			
Last Glacial Maximum (31 ±11; n= 19)	**0.000**	**0.000**	**0.000**	**0.000**	1.000	0.476		
Early Glacial (25 ±5; n= 19)	**0.000**	**0.000**	**0.000**	**0.000**	1.000	0.125	1.000	

Table AI-12. Results of the multiple comparisons of mean ranks test (*p*-values) of the TOC/Al differences between the periods of interest. Values between parentheses indicate the average, standard deviation and the valid number of samples used for the analysis. Boldface indicates significance after correcting for multiple comparisons (p<0.007).

TOC/Al	Last 150 years	Late Holocene	Mid Holocene	Early Holocene	Bølling-Allerød	Heinrich 1 Stadial	Last Glacial Maximum	Early Glacial
Last 150 years (1.8 ± 0.9; n= 28)								
Late Holocene (1.3 ±0.5; n= 45)	1.000							
Mid Holocene (1.1 ±0.3; n= 29)	1.000	1.000						
Early Holocene (0.9 ± 0.2; n= 36)	0.043	1.000	1.000					
Bølling-Allerød (0.6 ±0.1; n= 13)	**0.000**	**0.000**	0.008	0.093				
Heinrich 1 Stadial (0.6 ±0.2; n= 62)	**0.000**	**0.000**	**0.000**	**0.000**	1.000			
Last Glacial Maximum (0.4 ±0.1; n= 19)	**0.000**	**0.000**	**0.000**	**0.000**	1.000	0.274		
Early Glacial (0.3 ±0.1; n= 19)	**0.000**	**0.000**	**0.000**	**0.000**	0.696	0.102	1.000	

Table AI-13. Results of the multiple comparisons of mean ranks test (*p*-values) of the Hydrogen Index (HI) differences between the periods of interest. Values between parentheses indicate the average, standard deviation and the valid number of samples used for the analysis. Boldface indicates significance after correcting for multiple comparisons (p<0.007).

Hydrogen index (mg HC.g^{-1}TOC)	Last 150 years	Late Holocene	Mid Holocene	Early Holocene	Bølling-Allerød	Heinrich 1 Stadial	Last Glacial Maximum	Early Glacial
Last 150 years (473 ± 18; n= 28)								
Late Holocene (425 ±34; n= 75)	**0.000**							
Mid Holocene (429 ±27; n= 37)	**0.001**	1.000						
Early Holocene (439 ± 81; n= 36)	**0.000**	1.000	1.000					
Bølling-Allerød (400 ±31; n= 10)	**0.000**	1.000	1.000	1.000				
Heinrich 1 Stadial (403 ±37; n= 62)	**0.000**	0.048	0.152	0.361	1.000			
Last Glacial Maximum (302 ±25; n= 19)	**0.000**	**0.000**	**0.000**	**0.000**	0.097	**0.000**		
Early Glacial (300 ±28; n= 19)	**0.000**	**0.000**	**0.000**	**0.000**	0.088	**0.000**	1.000	

Table AI-14. Results of the multiple comparisons of mean ranks test (*p*-values) of the Oxygen index (OI) differences between the periods of interest. Values between parentheses indicate the average, standard deviation and the valid number of samples used for the analysis. Boldface indicates significance after correcting for multiple comparisons (p<0.007).

Oxygen index (mg CO$_2$.g^{-1}TOC)	Last 150 years	Late Holocene	Mid Holocene	Early Holocene	Bølling-Allerød	Heinrich 1 Stadial	Last Glacial Maximum	Early Glacial
Last 150 years (118 ± 17; n= 28)								
Late Holocene (109 ±14; n= 75)	0.388							
Mid Holocene (98 ±11; n= 37)	**0.000**	0.014						
Early Holocene (102 ± 24; n= 36)	**0.000**	0.067	1.000					
Bølling-Allerød (93 ±18; n= 10)	**0.001**	0.062	1.000	1.000				
Heinrich 1 Stadial (110 ±18; n= 62)	1.000	1.000	**0.005**	0.025	0.031			
Last Glacial Maximum (85 ±5; n= 19)	**0.000**	**0.000**	0.059	0.022	1.000	**0.000**		
Early Glacial (96 ±6; n= 19)	**0.000**	0.018	1.000	1.000	1.000	0.007	0.924	

Table AI-15. Results of the multiple comparisons of mean ranks test (*p*-values) of the δ^{13}C differences between the periods of interest. Values between parentheses indicate the average, standard deviation and the valid number of samples used for the analysis. Boldface indicates significance after correcting for multiple comparisons (p<0.007). δ^{13}C values were not measured in core B05-14.

δ^{13}C	Last 150 years	Late Holocene	Mid Holocene	Early Holocene	Bølling-Allerød	Heinrich 1 Stadial	Last Glacial Maximum	Early Glacial
Last 150 years	-							
Late Holocene (-21.2 ±0.4‰; n= 67)	-							
Mid Holocene (-21.2 ±0.4‰; n= 37)	-	1.000						
Early Holocene (-21.4 ± 0.3‰; n= 36)	-	0.724	0.464					
Bølling-Allerød (-21.5 ±0.5‰; n= 13)	-	1.000	1.000	1.000				
Heinrich 1 Stadial (-21.8 ±0.5; n= 62)	-	**0.000**	**0.000**	0.044	1.000			
Last Glacial Maximum (-21.6 ±0.4; n= 19)	-	0.026	0.018	1.000	1.000	1.000		
Early Glacial (-21.4 ±0.5; n= 19)	-	1.000	1.000	1.000	1.000	0.117	1.000	

Annexes II: Supplementary Tables and Figures for chapter IV: Centennial to millennial-scale variability in fish debris fluxes from marine laminated sediments off Pisco, Peru during the last 25 kyr

AII-1 Statistical analyses

Table AII- 1. Results of the Kruskal-Wallis non-parametric ANOVA (H statistic and *p-* values) used to test for differences in fish debris fluxes between the periods of interest.

Period	All fish scales H= 147 p =0.000		Anchovy scales H= 134 p =0.000		Oceanic species H= 45 p =0.000		Other species H= 87 p =0.000		Fish scale fragments H= 108 p =0.000	
	Valid N	Sum of Ranks	Valid N	Sum of Ranks	Valid N	Sum of Ranks	Valid N	Sum of Ranks	Valid N	Sum of Ranks
Last 150 years	28	8478	28	7974	28	6343	28	8488	28	7719
Late Holocene	92	17425	92	17527	92	16052	92	15886	92	17381
Mid Holocene	48	7518	48	7892	48	7257	48	5845	48	8206
Early Holocene	71	9304	71	9062	71	13004	71	10559	71	10795
Bølling-Allerød	13	2160	13	2234	13	1255	13	1757	13	1906
Heinrich 1 Stadial	37	7278	37	7412	37	5389	37	6660	37	5925
Last Glacial Maximum	19	773	19	829	19	2117	19	2359	19	806
Early Glacial	19	692	19	698	19	2213	19	2076	19	890

Period	Anchovy vertebrae H= 63 p =0.000		Other spp. vertebrae H= 87 p =0.000		Bones H= 45 p =0.000		Spines H= 113 p =0.000		Spine fagments H= 53 p =0.000	
	Valid N	Sum of Ranks	Valid N	Sum of Ranks	Valid N	Sum of Ranks	Valid N	Sum of Ranks	Valid N	Sum of Ranks
Last 150 years	28	5824	28	8234	28	6603	28	7548	28	6094
Late Holocene	92	17320	92	17534	92	16568	92	17960	92	17076
Mid Holocene	48	8490	48	5642	48	8680	48	8440	48	8710
Early Holocene	71	13381	71	11306	71	11471	71	11848	71	12403
Bølling-Allerød	13	1532	13	1828	13	1880	13	1574	13	1937
Heinrich 1 Stadial	37	3893	37	4492	37	4569	37	4384	37	3756
Last Glacial Maximum	19	1556	19	2259	19	1763	19	805	19	1558
Early Glacial	19	1633	19	2335	19	2096	19	1070	19	2096

Table AII- 2. Results of the Kruskal-Wallis non-parametric ANOVA (H statistic and *p-* values) used to test for differences in the preservation indices between the periods of interest.

Period	Anchovy scales integrity index H= 70 p =0.000		Ratio anchovy scales to vertebrae H= 109 p =0.000		Bio-erosion on anchovy vertebrae H= 70 p =0.000	
	Valid N	Sum of Ranks	Valid N	Sum of Ranks	Valid N	Sum of Ranks
Last 150 years	27	6632	21	5421	22	4716
Late Holocene	91	13927	86	12671	86	10409
Mid Holocene	48	8040	42	5263	42	4816
Early Holocene	71	7465	66	6537	66	7524
Bølling-Allerød	12	1457	10	1800	9	1650
Heinrich 1 Stadial	37	7678	29	6190	29	6508
Last Glacial Maximum	13	1502	15	1310	15	2167
Early Glacial	10	1196	13	713	13	2115

Table AII-3. Results of the multiple comparisons of mean ranks test (*p*-values) of the fish scale fluxes differences between the periods of interest. Values between parentheses indicate the average, standard deviation and the valid number of samples used for the analysis. Boldface indicates significance after correcting for multiple comparisons (p<0.007).

Fish scale fluxes (all species)	Last 150 years	Late Holocene	Mid Holocene	Early Holocene	Bølling-Allerød	Heinrich 1 Stadial	Last Glacial Maximum	Early Glacial
Last 150 years (545 ±520; n=28)								
Late Holocene (46 ±30; n=82)	**0.000**							
Mid Holocene (33 ±22; n=57)	**0.000**	1.000						
Early Holocene (26 ±18; n= 69)	**0.000**	**0.003**	1.000					
Bølling-Allerød (37 ±27; n=13)	**0.000**	1.000	1.000	1.000				
Heinrich 1 Stadial (45 ±24; n=62)	**0.000**	1.000	1.000	0.017	1.000			
Last Glacial Maximum (7 ±6; n=19)	**0.000**	**0.000**	**0.000**	**0.006**	**0.006**	**0.000**		
Early Glacial (6 ±8; n=19)	**0.000**	**0.000**	**0.000**	**0.003**	**0.004**	**0.000**	1.000	

Table AII-4. Results of the multiple comparisons of mean ranks test (*p*-values) of the anchovy scale fluxes differences between the periods of interest. Values between parentheses indicate the average, standard deviation and the valid number of samples used for the analysis. Boldface indicates significance after correcting for multiple comparisons (p<0.007).

Anchovy scale fluxes	Last 150 years	Late Holocene	Mid Holocene	Early Holocene	Bølling-Allerød	Heinrich 1 Stadial	Last Glacial Maximum	Early Glacial
Last 150 years (503 ±518; n=28)								
Late Holocene (41 ±29; n=92)	**0.000**							
Mid Holocene (31±21; n=48)	**0.000**	1.000						
Early Holocene (21 ±17; n= 71)	**0.000**	**0.001**	1.000					
Bølling-Allerød (34 ±26; n=13)	0.010	1.000	1.000	1.000				
Heinrich 1 Stadial (40 ±22; n=37)	0.010	1.000	1.000	**0.004**	1.000			
Last Glacial Maximum (5 ±4; n=19)	**0.000**	**0.000**	**0.000**	0.016	**0.005**	**0.000**		
Early Glacial (5 ±7; n=19)	**0.000**	**0.000**	**0.000**	**0.006**	**0.002**	**0.000**	1.000	

Table AII-5. Results of the multiple comparisons of mean ranks test (*p*-values) of the oceanic species scale fluxes differences between the periods of interest. Values between parentheses indicate the average, standard deviation and the valid number of samples used for the analysis. Boldface indicates significance after correcting for multiple comparisons (p<0.007).

Oceanic species scale fluxes	Last 150 years	Late Holocene	Mid Holocene	Early Holocene	Bølling-Allerød	Heinrich 1 Stadial	Last Glacial Maximum	Early Glacial
Last 150 years (12.2 ±18.1; n=28)								
Late Holocene (1.7 ±2.6; n=92)	0.301							
Mid Holocene (1.1 ±2; n=48)	0.023	1.000						
Early Holocene (2 ±2.7; n= 71)	1.000	1.000	1.000					
Bølling-Allerød (0)	**0.001**	0.150	1.000	0.067				
Heinrich 1 Stadial (0.8 ±1.3; n=37)	0.018	1.000	1.000	1.000	1.000			
Last Glacial Maximum (0.2 ±0.8; n=19)	**0.001**	0.227	1.000	0.092	1.000	1.000		
Early Glacial (0.3 ±0.9; n=19)	**0.003**	0.416	1.000	0.176	1.000	1.000	1.000	

Table AII-6. Results of the multiple comparisons of mean ranks test (*p*-values) of the other species scale fluxes differences between the periods of interest. Values between parentheses indicate the average, standard deviation and the valid number of samples used for the analysis. Boldface indicates significance after correcting for multiple comparisons (p<0.007).

Other species scale fluxes	Last 150 years	Late Holocene	Mid Holocene	Early Holocene	Bølling-Allerød	Heinrich 1 Stadial	Last Glacial Maximum	Early Glacial
Last 150 years (32.3 ±16.5; n=28)								
Late Holocene (3.4 ±4; n=92)	**0.000**							
Mid Holocene (1.8 ±2.5; n=48)	**0.000**	0.070						
Early Holocene (2.8 ±3.5; n= 71)	**0.000**	1.000	1.000					
Bølling-Allerød (3 ±4.2; n=13)	**0.000**	1.000	1.000	1.000				
Heinrich 1 Stadial (4.9 ±6; n=37)	**0.000**	1.000	0.136	1.000	1.000			
Last Glacial Maximum (2 ±2.7; n=19)	**0.000**	1.000	1.000	1.000	1.000	1.000		
Early Glacial (1.7 ±3.7; n=19)	**0.000**	0.218	1.000	1.000	1.000	0.225	1.000	

Table AII-7. Results of the multiple comparisons of mean ranks test (*p*-values) of the fish scale fragment fluxes differences between the periods of interest. Values between parentheses indicate the average, standard deviation and the valid number of samples used for the analysis. Boldface indicates significance after correcting for multiple comparisons (p<0.007).

Fish scale fragment fluxes	Last 150 years	Late Holocene	Mid Holocene	Early Holocene	Bølling-Allerød	Heinrich 1 Stadial	Last Glacial Maximum	Early Glacial
Last 150 years (4155 ±4623; n=28)								
Late Holocene (330 ±240; n=92)	**0.001**							
Mid Holocene (286 ±196; n=48)	**0.000**	1.000						
Early Holocene (234 ±159; n= 71)	**0.000**	0.379	1.000					
Bølling-Allerød (230 ±180; n=13)	**0.001**	1.000	1.000	1.000				
Heinrich 1 Stadial (243 ±141; n=37)	**0.000**	1.000	1.000	1.000	1.000			
Last Glacial Maximum (53±46; n=19)	**0.000**	**0.000**	**0.000**	**0.000**	0.062	**0.000**		
Early Glacial (63 ±84; n=19)	**0.000**	**0.000**	**0.000**	**0.000**	0.094	**0.001**	1.000	

Table AII-8. Results of the multiple comparisons of mean ranks test (*p*-values) of the anchovy vertebrae fluxes differences between the periods of interest. Values between parentheses indicate the average, standard deviation and the valid number of samples used for the analysis. Boldface indicates significance after correcting for multiple comparisons (p<0.007).

Anchovy vertebrae fluxes	Last 150 years	Late Holocene	Mid Holocene	Early Holocene	Bølling-Allerød	Heinrich 1 Stadial	Last Glacial Maximum	Early Glacial
Last 150 years (20.2 ±24.3; n=28)								
Late Holocene (10.3 ±10.1; n=92)	1.000							
Mid Holocene (8 ±6.8; n=48)	1.000	1.000						
Early Holocene (8.8±7.2; n= 71)	1.000	1.000	1.000					
Bølling-Allerød (4.7± 5.9; n=13)	0.126	0.335	1.000	0.372				
Heinrich 1 Stadial (3.3 ±3.5; n=37)	**0.000**	**0.000**	0.015	**0.000**	1.000			
Last Glacial Maximum (2.1 ±2; n=19)	**0.000**	**0.000**	**0.006**	**0.000**	1.000	1.000		
Early Glacial (2.5 ±3.7; n=19)	**0.000**	**0.000**	0.011	**0.001**	1.000	1.000	1.000	

Table AII-9. Results of the multiple comparisons of mean ranks test (*p*-values) of the other species vertebrae fluxes differences between the periods of interest. Values between parentheses indicate the average, standard deviation and the valid number of samples used for the analysis. Boldface indicates significance after correcting for multiple comparisons (p<0.007).

Other spp. vertebrae fluxes	Last 150 years	Late Holocene	Mid Holocene	Early Holocene	Bølling-Allerød	Heinrich 1 Stadial	Last Glacial Maximum	Early Glacial
Last 150 years (59± 71; n=28)								
Late Holocene (14 ± 12; n=92)	**0.000**							
Mid Holocene (15 ±15; n=48)	**0.000**	**0.000**						
Early Holocene (14 ±15; n= 71)	**0.000**	1.000	0.510					
Bølling-Allerød (10 ±9; n=13)	**0.000**	1.000	1.000	1.000				
Heinrich 1 Stadial (5 ±5; n=37)	**0.000**	**0.005**	1.000	1.000	1.000			
Last Glacial Maximum (4 ±4; n=19)	**0.000**	0.073	1.000	1.000	1.000	1.000		
Early Glacial (6 ±8; n=19)	**0.000**	0.125	1.000	1.000	1.000	1.000	1.000	

Table AII-10. Results of the multiple comparisons of mean ranks test (*p*-values) of the fish bones fluxes differences between the periods of interest. Values between parentheses indicate the average, standard deviation and the valid number of samples used for the analysis. Boldface indicates significance after correcting for multiple comparisons (p<0.007).

Bones fluxes	Last 150 years	Late Holocene	Mid Holocene	Early Holocene	Bølling-Allerød	Heinrich 1 Stadial	Last Glacial Maximum	Early Glacial
Last 150 years (185 ±193; n=28)								
Late Holocene (64 ±52; n=92)	0.176							
Mid Holocene (60 ±47; n=48)	0.404	1.000						
Early Holocene (49 ±38; n= 71)	0.012	1.000	1.000					
Bølling-Allerød (43 ±33; n=13)	0.113	1.000	1.000	1.000				
Heinrich 1 Stadial (33 ±23; n=37)	**0.000**	0.059	0.156	1.000	1.000			
Last Glacial Maximum (25±19; n=19)	**0.000**	**0.007**	0.017	0.136	1.000	1.000		
Early Glacial (31 ±26; n=19)	**0.000**	0.095	0.166	1.000	1.000	1.000	1.000	

Table AII-11. Results of the multiple comparisons of mean ranks test (*p*-values) of the spine fluxes differences between the periods of interest. Values between parentheses indicate the average, standard deviation and the valid number of samples used for the analysis. Boldface indicates significance after correcting for multiple comparisons (p<0.007).

Spine fluxes	Last 150 years	Late Holocene	Mid Holocene	Early Holocene	Bølling-Allerød	Heinrich 1 Stadial	Last Glacial Maximum	Early Glacial
Last 150 years (303 ±283; n=28)								
Late Holocene (72 ±57; n=92)	0.008							
Mid Holocene (60 ±54; n=48)	**0.001**	1.000						
Early Holocene (52 ±50; n= 71)	**0.000**	1.000	1.000					
Bølling-Allerød (31± 27; n=13)	**0.000**	0.227	1.000	1.000				
Heinrich 1 Stadial (28 ±22; n=37)	**0.000**	**0.001**	0.156	0.325	1.000			
Last Glacial Maximum (8 ±7; n=19)	**0.000**	**0.000**	**0.000**	**0.000**	0.582	0.121		
Early Glacial (14 ±21; n=19)	**0.000**	**0.000**	**0.000**	**0.000**	1.000	0.553	1.000	

Table AII-12. Results of the multiple comparisons of mean ranks test (*p*-values) of the spine fragment fluxes differences between the periods of interest. Values between parentheses indicate the average, standard deviation and the valid number of samples used for the analysis. Boldface indicates significance after correcting for multiple comparisons (p<0.007).

Spine fragment fluxes	Last 150 years	Late Holocene	Mid Holocene	Early Holocene	Bølling-Allerød	Heinrich 1 Stadial	Last Glacial Maximum	Early Glacial
Last 150 years (59 ±71; n=28)								
Late Holocene (14 ±12; n=92)	1.000							
Mid Holocene (15 ±15; n=48)	1.000	1.000						
Early Holocene (14 ±15; n= 71)	1.000	1.000	1.000					
Bølling-Allerød (10 ±0.9; n=13)	0.856	1.000	1.000	1.000				
Heinrich 1 Stadial (5 ±5; n=37)	**0.000**	**0.000**	**0.003**	**0.004**	1.000			
Last Glacial Maximum (4 ±4; n=19)	**0.000**	**0.000**	**0.003**	**0.004**	1.000	1.000		
Early Glacial (6 ±8; n=19)	**0.004**	0.044	0.153	0.234	1.000	1.000	1.000	

Table AII-13. Results of the multiple comparisons of mean ranks test (*p*-values) of the anchovy scales integrity index differences between the periods of interest. Values between parentheses indicate the average, standard deviation and the valid number of samples used for the analysis. Boldface indicates significance after correcting for multiple comparisons (p<0.007).

Anchovy scales integrity index	Last 150 years	Late Holocene	Mid Holocene	Early Holocene	Bølling-Allerød	Heinrich 1 Stadial	Last Glacial Maximum	Early Glacial
Last 150 years (2 ±0.2; n=27)								
Late Holocene (1.7 ±0.3; n=91)	**0.000**							
Mid Holocene (1.7 ±0.4; n=48)	0.008	1.000						
Early Holocene (1.5 ±0.3; n= 71)	**0.000**	0.020	**0.005**					
Bølling-Allerød (1.6±0.3; n=12)	**0.002**	1.000	1.000	1.000				
Heinrich 1 Stadial (1.8 ±0.3; n=37)	1.000	0.050	1.000	**0.000**	0.104			
Last Glacial Maximum (1.5±0.4; n=13)	**0.000**	1.000	1.000	1.000	1.000	0.039		
Early Glacial (1.5 ±0.4; n=10)	**0.004**	1.000	1.000	1.000	1.000	0.162	1.000	

256

Table AII-14. Results of the multiple comparisons of mean ranks test (*p*-values) of the ratio anchovy scales to vertebrae differences between the periods of interest. Values between parentheses indicate the average, standard deviation and the valid number of samples used for the analysis. Boldface indicates significance after correcting for multiple comparisons (p<0.007).

Ratio anchovy scales to vertebrae	Last 150 years	Late Holocene	Mid Holocene	Early Holocene	Bølling-Allerød	Heinrich 1 Stadial	Last Glacial Maximum	Early Glacial
Last 150 years (29.8 ±15.1; n=21)								
Late Holocene (7.2 ±8.6; n=86)	**0.000**							
Mid Holocene (4.5 ±3.3; n=42)	**0.000**	1.000						
Early Holocene (3.6 ±3.6; n= 66)	**0.000**	0.008	1.000					
Bølling-Allerød (14.1 ±21.7; n=10)	0.352	1.000	1.000	0.097				
Heinrich 1 Stadial (13.5 ±7.4; n=29)	1.000	**0.004**	**0.000**	**0.000**	1.000			
Last Glacial Maximum (2.9 ±2.7; n=15)	**0.000**	0.240	1.000	1.000	0.151	**0.000**		
Early Glacial (1.7 ±2.3; n=13)	**0.000**	**0.004**	0.182	1.000	0.007	**0.000**	1.000	

Table AII-15. Results of the multiple comparisons of mean ranks test (*p*-values) of the anchovy vertebrae surface without bio-erosion differences between the periods of interest. Values between parentheses indicate the average, standard deviation and the valid number of samples used for the analysis. Boldface indicates significance after correcting for multiple comparisons (p<0.007).

Anchovy vertebra without bio-erosion	Last 150 years	Late Holocene	Mid Holocene	Early Holocene	Bølling-Allerød	Heinrich 1 Stadial	Last Glacial Maximum	Early Glacial
Last 150 years (3.8 ±0.4; n=22)								
Late Holocene (3 ±0.7; n=86)	**0.000**							
Mid Holocene (2.9 ±0.8; n=42)	**0.000**	1.000						
Early Holocene (2.9 ±0.8; n= 66)	**0.000**	1.000	1.000					
Bølling-Allerød (3.5±0.6; n=9)	1.000	0.822	0.615	0.470				
Heinrich 1 Stadial (3.9 ±0.3; n=29)	1.000	**0.000**	**0.000**	**0.000**	1.000			
Last Glacial Maximum (3.2 ±0.8; n=15)	0.293	1.000	1.000	1.000	1.000	0.057		
Early Glacial (3.2 ±1; n=13)	1.000	1.000	1.000	1.000	1.000	0.652	1.000	

Annexes III: Article published in Paleobiology (Winter 2012, Vol. 38, No. 1, pp. 52-78):

"Evaluating fish scale preservation in sediment records from the oxygen mimimum zone off Peru"

Authors: Renato Salvatteci[1]*, David B. Field[2], Timothy Baumgartner[1], Vicente Ferreira[1], and Dimitri Gutierrez[3].

Affiliations:

[1]Centro de Investigación Científica y de Educación Superior de Ensenada, Apartado Postal 2732, Ensenada, Baja California C.P., 22860, México. e-mail: renato.salvatteci@ird.fr.

[2]Hawaii Pacific University, College of Natural Sciences, 45-045 Kamehameha Highway,Kaneohe, Hawaii, 96744-5297

[3]Instituto del Mar del Perú, Esquina Gamarra y General Valle s/n, Callao, 22000 Peru

*Present address: LOCEAN, UMR 7159 (IRD, CNRS, UPMC, MNHN), Institut Pierre Simon Laplace, Laboratoire d'Océanographie et du Climat: Expérimentations et Analyses Numériques. Center IRD France Nord, 32 avenue Henri Varagnat, 93143 Bondy cedex, France

Evaluating fish scale preservation in sediment records from the oxygen minimum zone off Peru

Renato Salvatteci, David B. Field, Timothy Baumgartner, Vicente Ferreira, and Dimitri Gutierrez

Abstract.—Fish scales accumulating in marine laminated sediments can provide a record of population variability of small pelagic fishes. Although some studies have noted signs of scale degradation that could affect estimates of population variability, there are presently no well-developed means to evaluate degradation. We developed several indices as indicators of fish scale preservation in two box-cores that we collected off Pisco (14°S), one at 301 m near the center of the oxygen minimum zone (OMZ), and the other at 201 m near the upper limit of the OMZ. These indices include (1) an index of fish scale integrity (estimate of scale wholeness relative to fragmentation), (2) the fungi-free area of fish scales and vertebrae, (3) the ratio of fish scales to vertebrae (as well as fish scales to vertebrae and bones), and (4) the ratio of whole scales to fragments. We address whether lower numbers of anchovy scales occurring in association with reduced total organic carbon fluxes and higher bottom-water oxygen concentrations are due entirely to lower abundances of anchovy or whether differential preservation of the fish scales in the sediments plays an important role in reduced scale abundances. Comparison of temporal sequences between the two cores provides the means to assess whether there are differences in the preservation of fish scales. The combined indices indicate that the lower numbers of fish scales in the earliest period have been affected by degradation, and to a greater degree in the box-core from 201 meters, which can be subject to higher oxygen concentrations. On the other hand, decadal-scale variations in fish scale abundance within the period of better preservation are unlikely to be caused by degradation. We discuss the utility and drawbacks of different indices of preservation for reconstructing past changes in fish population sizes with fluxes of fish debris and also briefly discuss the utility of these indices to other paleobiological systems.

Renato Salvatteci,* Timothy Baumgartner, and Vicente Ferreira. Centro de Investigación Científica y de Educación Superior de Ensenada, Apartado Postal 2732, Ensenada, Baja California C.P., 22860, México. E-mail: renato.salvatteci@ird.fr. *Present address: LOCEAN, UMR 7159 (IRD, CNRS, UPMC, MNHN), Institut Pierre Simon Laplace, Laboratoire d'Océanographie et du Climat: Expérimentations et Analyses Numériques. Center IRD France Nord, 32 avenue Henri Varagnat, 93143 Bondy cedex, France
David B. Field. Hawaii Pacific University, College of Natural Sciences, 45-045 Kamehameha Highway, Kaneohe, Hawaii, 96744-5297
Dimitri Gutierrez. Instituto del Mar del Perú, Esquina Gamarra y General Valle s/n, Callao, 22000 Perú

Introduction

Quantifying variations in fish scale deposition to marine sediments has been used to infer past variability in fish populations prior to the development of industrial fisheries and catch records (Soutar and Isaacs 1974; Baumgartner et al. 1992; Field et al. 2009; Finney et al. 2002, 2010; Wright et al. 2005). Such work has been limited in scope because high sedimentation rates and anoxic or disoxic bottom waters that inhibit bioturbation are required to preserve high-resolution laminated sediments and fish scales (Field et al. 2009). Although degradation of scales occurs in oxygenated sediments, it is not yet clear if all laminated sediments preserve scales

equally throughout their sequences (O'Connell and Tunnicliffe 2001), which is an important assumption for reconstructing variability in fish populations. In the Humboldt Current region high-resolution paleoecological archives are found within laminated and banded sequences present off central Peru within the oxygen minimum zone (OMZ), especially offshore of Pisco (DeVries and Pearcy 1982; Gutierrez et al. 2006; Gutierrez et al. 2009). Previously reported studies indicate high variability of fish scale abundances, yet some of these also suggest associated changes in degradation (DeVries and Pearcy 1982; Valdes et al. 2008; Gutierrez et al. 2009). We develop various indices to quantify fish scale preservation and determine the influence of

scale degradation in the fish scale deposition records.

The highly productive upwelling environment off the coast of Peru sustains one of the world's largest fisheries, for the Peruvian anchoveta (*Engraulis ringens*), but biomass variability on interannual to decadal time scales results in dramatic fluctuations in catch (Chavez et al. 2008). The interannual biomass variability of anchovy observed in the Humboldt Current system (HCS) could largely be explained by environmental changes associated with El Niño Southern Oscillation (ENSO) and by fishing pressure. The decadal-scale variability is largely attributed to physical and biological mechanisms, although varying explanations have been proposed (Schwartzlose et al. 1999; Bakun and Broad 2003; Checkley et al. 2009a). Testing these hypotheses of mechanisms driving decadal variability in fish abundances and determining the role of fisheries in affecting population sizes require long records of fish population variability prior to the development of industrial fishing, which is best achieved through the development of fish scale records from marine sediments.

Fish scales fluxes off Pisco and Callao show dramatically lower rates prior to ca. 1820, which coincide with lower inferred primary productivity and a weaker OMZ (Diaz-Ochoa et al. 2008; Sifeddine et al. 2008; Gutierrez et al. 2009). Figure 1 shows the down-core variability of fish scales, organic carbon (as an indicator of primary productivity), molybdenum (Mo) concentrations (a proxy for sedimentary redox and thus the intensity of the OMZ), and $\delta^{15}N$ values (a proxy for water column oxygenation) in two box-cores collected off Callao (B0405-13) and Pisco (B0405-6). Both cores were taken within the OMZ (dissolved oxygen <0.5 ml.L^{-1}), a feature that intersects the upper Peruvian continental margin from approximately 50 m to 600 m depth (Helly and Levin 2004). The Pisco and Callao cores are separated by approximately 300 kilometers (Fig. 2) and were collected at different depths within the OMZ (299 m and 184 m respectively), thus the spatial and vertical differences between them prevents direct comparisons. The diminished abundance of anchovy scales in both cores prior to 1820, which is more notable off Callao, could reflect a decrease in the local biomass of the anchovy during this less productive period. The less dramatic reduction off Pisco could be due to the presence of a strong upwelling cell and anchovy refuge during periods of lower productivity (Barber and Chavez 1983; Mendo 1991). Alternatively, the diminished scale abundances could be a direct consequence of greater scale degradation associated with increased oxygenation, particularly within the Callao core at 184 m. Or the diminished abundances could reflect a combination of both lower productivity and greater degradation (Sifeddine et al. 2008; Gutierrez et al. 2009). Our study compares records from two different cores taken at different depths but from the same region to determine the role of degradation.

Variation in scale deposition with fish population size is attributable to natural scale shedding, as inferred from two major lines of evidence as discussed in detail by Field et al. (2009). First, down-core variability in scale flux from cores taken hundreds of meters apart are quite similar (Baumgartner et al. 1992). Second, scale morphology is species specific and also varies with the location on a fish (Lozano-Montes 1997; Salvatteci 2008; Shackleton and Johnson 1988). Observations of scales shed from fish in controlled aquarium environments have shown that the "typical scales" (those scales derived from the lateral line) are highly disproportionately shed from living fish (Shackleton 1988; Lozano-Montes 1997). The majority of scales in marine sediments are typical scales as well, reiterating that scale shedding is the major source of deposition (Field et al. 2009). In contrast, the majority of bones and vertebrae arrive to sediments by passing through the guts of predators. Thus, although the fluxes of these remains to the sediments should be somewhat dependent on population size, different modes of loss and transport could cause deposition patterns to differ from those of scales. Consequently, if the bones and vertebrae that arrive to sediments covary temporarily with scales, all sources of fish debris are varying primarily with population size rather than random predation events.
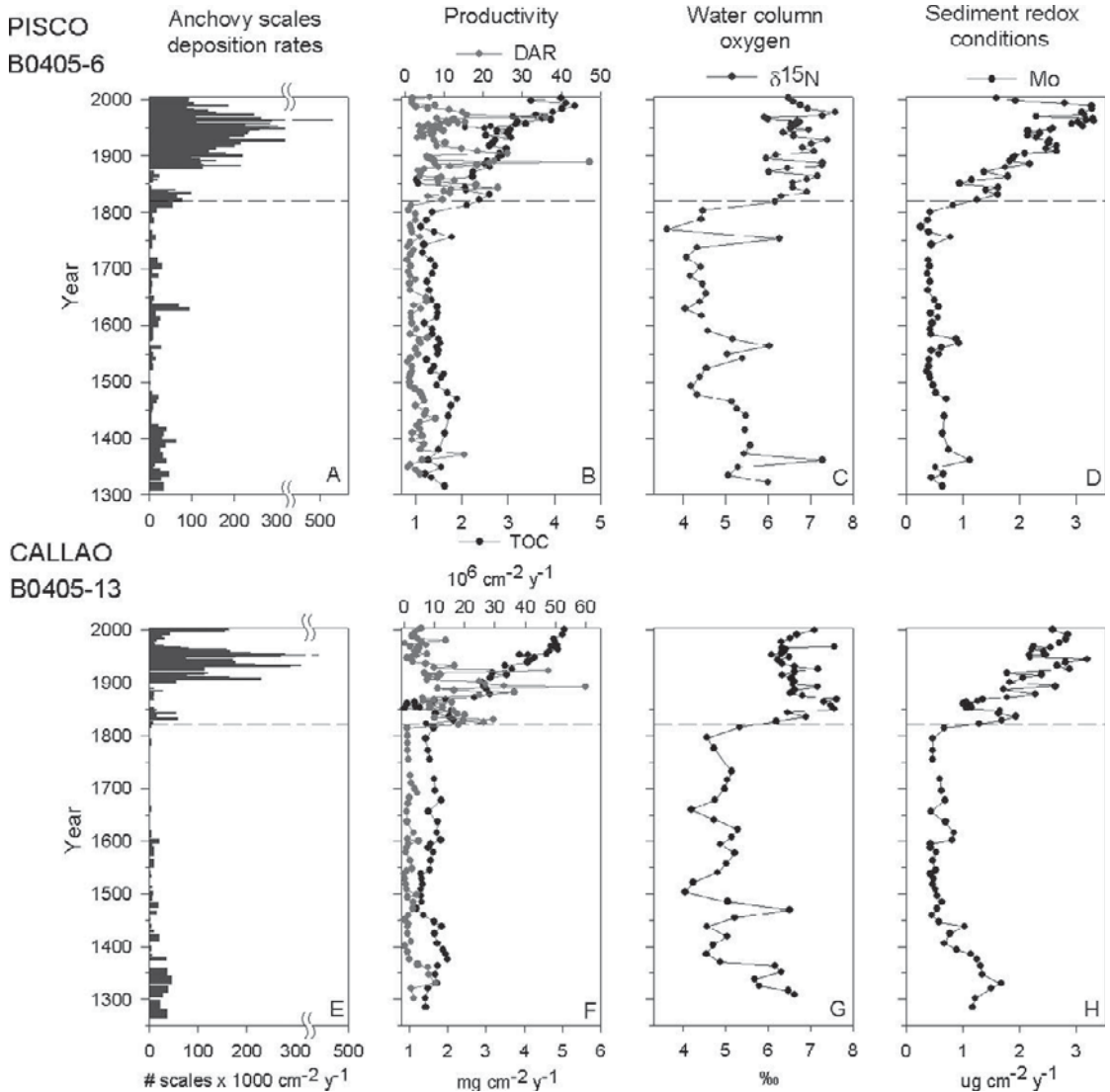
FIGURE 1. Fish scale deposition rates and proxies of environmental conditions developed in cores B0405-6 (299 m depth) and B0405-13 (189 m depth) retrieved off Pisco and Callao, respectively. Records are anchovy scale fluxes as indicators of anchovy biomass (A, E); fluxes of total organic carbon (TOC) and diatom accumulation rates (DAR) as proxies of primary productivity (B, F); δ^{15}N values of organic matter as an indicator of water column oxygenation, where higher values indicate lower oxygenation (C, G); and molybdenum (Mo) fluxes as an indicator of redox conditions where higher values indicate more anoxic conditions (redrawn from Gutierrez et al. 2009) (D, H). The dashed lines indicate a shift from a period characterized by lower productivity and weaker OMZ (from the base of the core to ca. 1820) to a period characterized by higher productivity and intense OMZ (following Sifeddine et al. 2008 and Gutierrez et al. 2009).

Fish scales are composed of a mixture of hydroxyapatite ($Ca_{10}(PO_4)_6(OH)_2$) embedded within an organic matrix that surrounds layers of fibrous collagen (Hamada and Mikuni 1990; Varma 1990; Hutchinson and Trueman 2006). Consequently, each of these constituents of fish scales could be affected by degradation processes. Seawater is undersat- urated with respect to oceanic apatite (Atlas and Pytkowicz 1977), which could result in dissolution of apatite within scales and bones. In addition, there is evidence of a loss of organic matter in fish scales retrieved from marine sediments relative to scales from living fish (Field et al. 2009), which might be explained by bacterial processes. Vertebrae,
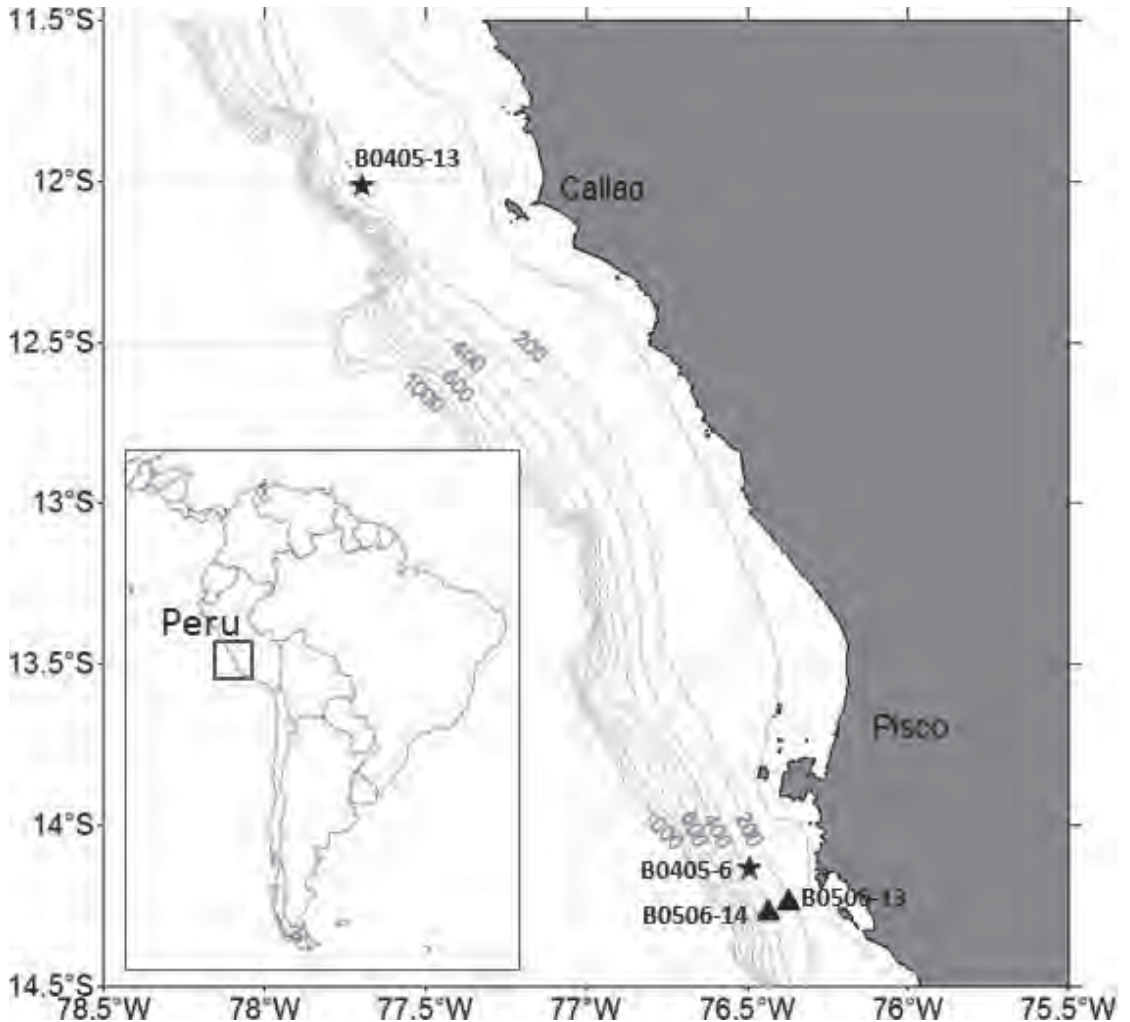
FIGURE 2. Location of box-cores collected off the central-south Peruvian coast discussed in this study. The stars indicate the position of cores B0405-13 (189 m) and B0405-6 (299 m) where the sedimentary and biogeochemical shift was described (Sifeddine et al. 2008; Gutierrez et al. 2009). The triangles indicate the position of cores B0506-13 (201 m) and B0506-14 (301 m) analyzed in this study. Bathymetric contour lines are in 100-m intervals.

bones, and spines are also composed of apatite (Hamada and Mikuni 1990). However, vertebrae and bones have lower surface area to volume ratios and less organic matter than scales; thus, scales may be degraded more easily than vertebrae and bones. Consequently, the ratio of scales to vertebrae and bones may be a good indication of degradation. DeVries and Pearcy (1982) found that the ratio of scales to vertebrae in a laminated section of a core collected from 186 m depth, near the upper limits of the OMZ, was higher than the ratios found in cores collected at water depths deeper than 400 m, near the

lower boundary of the OMZ (Helly and Levin 2004). Their results suggest an effect of bottom-water oxygenation on scale preservation. However, because ratios of scales to vertebrae may also be affected by species composition and predation, other indices of degradation are needed.

The intensity of the OMZ off Peru has been observed to vary on seasonal to interannual time scales, whereas variability on decadal- to centennial-scale time scales has been inferred by $\delta^{15}N$ of organic matter and other proxies in sediment records (Agnihotri et al. 2008; Sifeddine et al. 2008; Gutierrez et al. 2009)

(Fig. 1). During extreme El Niño events (e.g., El Niño 1997–1998) the upper boundary of the OMZ may deepen to 250 m (Sánchez et al. 2000). Sediments from a shallower core would be more exposed to oxygenated events that could result in degradation of fish scales.

Here, we develop an index of down-core variability of the scales-to-vertebrae (and other bones) ratios and other indices of degradation from two box-cores retrieved from laminated sediments. We collected one core within the core of the OMZ and the other near the upper boundary of the OMZ, to quantify the effect of degradation in the fish scale deposition rates. Our results will provide a better basis for interpreting fish scale deposition records in the HCS and other regions where preservation of scales may be influenced by degradation.

Regional Settings

The HCS is characterized by high productivity driven by coastal upwelling of nutrient-rich waters from the subsurface undercurrent. The upper Peruvian continental margin (~50 to ~600 m depth) is intersected by an intense OMZ (dissolved oxygen <0.5 ml.L^{-1}) that results from high regional primary productivity and large-scale circulation patterns (Helly and Levin 2004). The presence of the OMZ inhibits bioturbation and facilitates the preservation of high-resolution records of past ecosystem changes in disoxic sediments in suitable topographic conditions (Krissek and Scheidegger 1983). Previous studies (Suess et al. 1990; Reinhardt et al. 2002) and exploratory coring on the upper slope off Callao and Pisco at depths varying between 50 and 500 m (IMARPE unpublished data) indicate that the regions of good laminations and highest accumulation rates frequently occur between 200 and 300 m. Accumulation rates may vary regionally with differences in surface productivity, proximity to riverine input, and subsurface currents.

Materials and Methods

Sampling Sites and Box-Core Subsampling

Based on previous surveys, two box-cores six miles apart (Fig. 2) were retrieved off Pisco in June 2005 using a Soutar box-corer. Core B0506-13 was taken at 201 m depth (14°13.428S,76°22.203W) and core B0506-14 was taken at 301 m (14°15.733S,76° 26.01W). The two box-cores remained refrigerated as water drained until subsampling. The cores were cut lengthwise into four sections (~25 cm each) and six vertical slabs (two slabs of 1 cm, two slabs of 2.4 cm, one slab of 1.9 cm, and one slab of 3.5 cm). One thin slab (~1.0 cm) was used for X-radiography; the X-ray image was used to construct a high-resolution, subsampling template following the stratigraphy. Each sampling interval consisted of a couplet of dark and light laminae in the X-ray image or a banded sequence. Any couplet or band thicker than 0.6 cm was subsampled into equidistant thinner samples (no less than 0.3 cm). The thickest slab (slab VI; 3.5 cm) was subsampled for fish remains following the template. The subsamples were heated with hydrogen peroxide and sodium pyrophosphate to disaggregate the organic matter and then were gently washed through a 355-μm sieve. The remains retained were stored in an alcohol solution. One slab of 2.4 cm (slab III) was used to calculate the dry bulk density (DBD) of the cores.

Stratigraphic Correlation and Preliminary Chronology

The X-ray images were scanned and then printed in positive for stratigraphic correlation, which was done by visual inspection of the laminae and bands as well as DBD estimates. A preliminary chronology for B0506-13 and B0506-14 was developed on the basis of ^{241}Am concentrations for the upper layers and stratigraphic correlations between these cores and a nearby core B0405-6 (Fig. 2). Core B0405-6 has a developed chronology as described by Gutierrez et al. (2009) and briefly summarized here. The down-core profiles of the bomb-derived ^{241}Am in core B0405-6 show a peak at ~8 cm, which was dated as 1964. In cores B0506-13 and B0506-14 the down-core profiles of ^{241}Am show a peak in activity at ~12 cm and at ~7.6 cm depth respectively. Thus, the peaks in activity in cores B0506-13 and B0506-14 also were dated as 1964, which corresponds to the
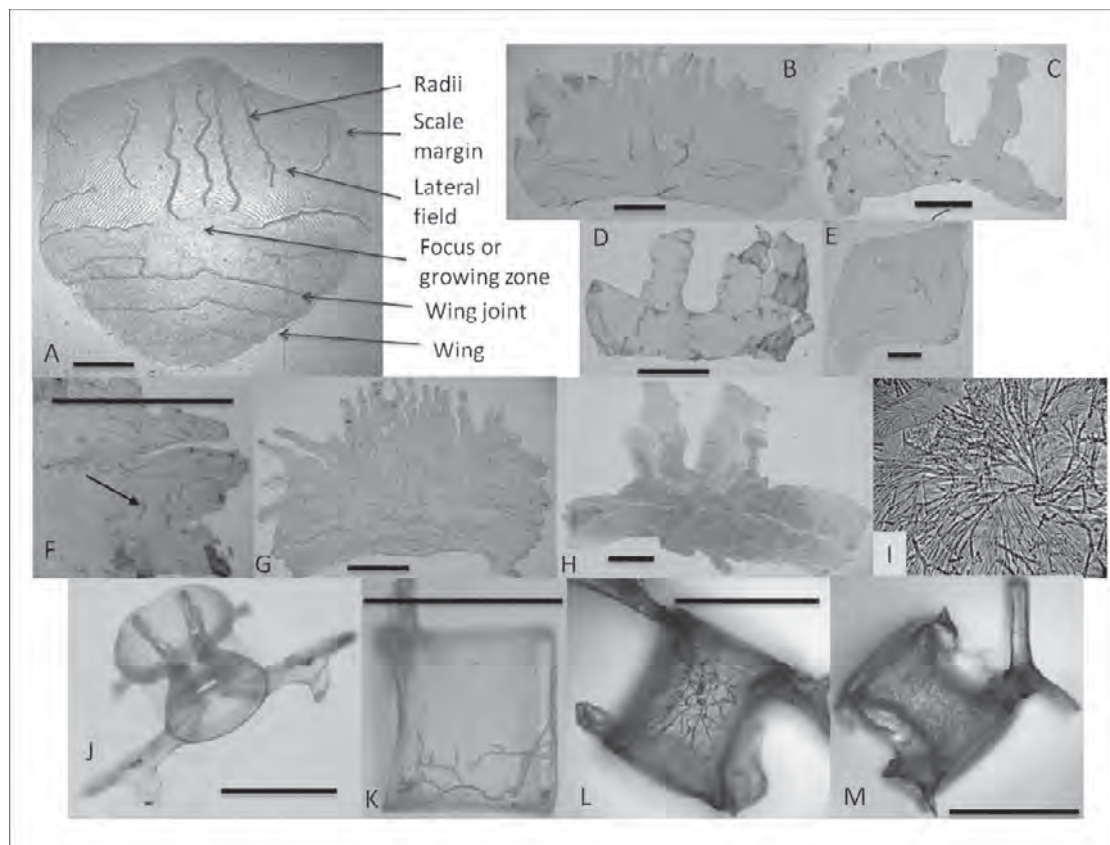
FIGURE 3. Photographs illustrating a typical, or type-X, scale showing the scale parts (A), an anchovy vertebra (J), and the different defined states of scales and vertebrae used for developing degradation indices (B–M). A, Anchovy type-X scale taken from a recently living anchovy showing the scale parts (based on nomenclature of Shackleton and Johnson 1988). B, Complete scale with both lateral fields and part of the scale margins. C, Incomplete scale with only the left lateral field and part of the left margin. D, Focus-only scale without lateral fields and scale margins. E, Half scale with half of the central part of the scale and only one lateral field with its margin. F, Scale with fungal coverage over less than one-third of the scale surface (the arrow indicates the presence of fungus). G, Scale with fungal coverage over less than two-thirds of the scale surface. H, Scale with fungal coverage over more than two-thirds of the scale surface. I, $60\times$ zoom of a scale showing a fungus colony. J, Anchovy vertebra taken from a recently living anchovy. K, Unidentified vertebra with fungal coverage over less than one-third of its surface. L, Anchovy vertebra with fungal coverage over less than two-thirds of its surface. M, Anchovy vertebra with fungal coverage over more than two-thirds of its surface. Images A–E and J are all without fungus. Scale bar, 1 mm in all images.

first years of the fully developed stage of the industrial fisheries (Schwartzlose et al. 1999; Chavez et al. 2008). A shift in sedimentary characteristics in core B0405-6 was dated at ca. 1820 using the down-core distribution of natural excess ^{210}Pb, ^{241}Am, and radiocarbon ages resulting in an approximate sedimentation rate of 2.2 mm yr^{-1} after ca. 1870 and of 1 mm yr^{-1} before ca. 1870 (Gutierrez et al. 2009).

Abundances of Fish Scales and Bones

The fish debris retained in the 355-μm mesh size was quantified with stereo-microscopy with the aid of a scale and vertebrae collection obtained from recently caught fishes. Scales were identified to species level and vertebrae were identified as either anchovy or other species. Nearly all scale fragments belonged to anchovy but were not quantified by species. Other bones and spines could not be distinguished by species.

Fish scales were quantified with the following criteria according to the scale parts (Fig. 3A):

- Fish scales were considered complete when both lateral fields were present (Fig. 3B).
- Fish scales with one complete lateral field, the focus, and a nearly complete opposing

lateral field were counted as 1 scale but considered ''incomplete'' scale (Fig. 3C).

- Fish scales that contain the focus but only a portion of the lateral fields without the presence of the scale margins were counted as 1 scale and considered ''focus-only'' (Fig. 3D).
- Fish scales that have part of the focus but only half of the scale were counted as 0.5 scale and denoted as ''half scale'' (Fig. 3E).
- The remainder of fish scale remains consisted of fragments of different sizes that were counted as ''fragments.''

Fish scales were divided into three groups. The first group consists of only anchovy scales. Anchovy is a pelagic fish that preferentially inhabits cold and productive water masses (Swartzman et al. 2008), feeds on phytoplankton and zooplankton (Espinoza and Bertrand 2008) and is the major prey of the principal top predators in the Humboldt Current system, including marine mammals, seabirds, cephalopods, and fishes like jack mackerel (*Trachurus picturatus murphyi*) and mackerel (*Scomber japonicus*). The second group includes the scales from oceanic species, those that generally live farther offshore in warmer, less productive waters, which are sardine (*Sardinops sagax*), jack mackerel, and mackerel (Checkley et al. 2009b). The last group has no clear oceanographic affinity and includes the scales of hake (*Merluccius gayi gayi*), agujilla (*Scomberesox saurus scombroides*), myctophids, and other unidentified scales.

The deposition of a part of a single fish can occur on rare occasions and result in a multitude of different debris from the same fish within a sampling interval (O'Connell and Tunnicliffe 2001; Field et al. 2009). The abundance of fish debris within a sampling interval associated with this feature is clearly higher than the background levels and may not represent the fish density in a given time period. Thus, in order to avoid a potential bias of high abundances caused by the deposition of a part of a single fish, abundance of anchovy scales, vertebrae, spines, and other bones from the sampling intervals that fell more than three standard deviations from the mean were treated as outliers

(O'Connell and Tunnicliffe 2001) and replaced by the average +3 standard deviations (SD). Because of the small sample size of ''oceanic species scales'' and ''other species scales,'' we could not reliably detect outliers; thus, the outlier treatment was not applied in these cases. The outlier replacement occurred in a maximum of six samples out of 187 (3.2% of the data) in the case of ''other species vertebrae'' in core B0506-14 (see Fig. 5).

Fish Scale Preservation

In order to quantify the effect of degradation, we estimated the following indices:

Integrity index.—Each anchovy scale that had a focus and was counted as one scale was rated from 1 to 3 according to the scale's integrity. Complete scales were rated as 3, incomplete scales were rated as 2, and focus-only scales were rated as 1. A scale integrity index was calculated for each sample by calculating the average of all scales in the sampling interval with a higher (lower) index indicating more whole (broken) scales and consequently better preservation.

Fungi-free area index on anchovy scales and vertebrae.—Scales and vertebrae from the Peruvian margin have been observed to have fungi throughout the scale as shown in Figure 3F-I and 3K–M. Scales with a high degree of fungal coverage were observed to be more brittle and some would fragment during handling (Ohwada et al. 1983 and personal observations). Each fish scale and vertebra was rated according to the percentage of its surface covered by fungi (Fig. 3F–I, K–M). Fish remains lacking fungi altogether were rated as 4. Scales and vertebrae with fungi covering up to one-third of their surface were rated as 3 (Fig. 3F,K), those with fungi covering one-third to two-thirds of the surface were rated as 2 (Fig. 3G,L), and those remains with fungi covering between two-thirds and the entire surface were rated as 1 (Fig. 3H,M). The fungi-free area index was calculated as the weighted average of all scales and vertebrae within a sample. Higher values indicate less fungal coverage over the fish remains. We did not calculate a similar index for fish scales and vertebrae of other

species because the dearth of fish debris would have yielded unreliable estimates.

Ratios of scales to fragments.—We examined ratios of whole scales (of all species) to scale fragments in order to determine whether fragmentation is a good index of degradation.

Ratios of scales to vertebrae and bones.—Because scales are thinner and more susceptible to dissolution or degradation than other forms of debris, ratios of scales to other debris were also calculated. These include anchovy scales to anchovy vertebrae, scales to vertebrae from all species, and scales to vertebrae and other bones from all species. Higher (lower) values could indicate better (worse) preservation of anchovy scales. The spines were not included in the calculation of the ratios because they are as thin as the fish scales and the ratio of area to volume is more similar to fish scales than to the other bones and vertebrae. Thus the ratio of scales to spines may not be as good an indicator of preservation as the ratio of scales to other bones and vertebrae.

Compound preservation index of anchovy remains.—To best describe the preservation of anchovy scales we calculated a compound index by using the average of three normalized indices: the integrity index of anchovy scales, the fungi-free area index over anchovy vertebrae, and the ratio of anchovy scales to anchovy vertebrae. We normalized each variable by subtracting its average and dividing by its standard deviation. We did not include in our calculations the ratio of anchovy scales to anchovy vertebrae during the fishery period. Higher (lower) values indicate better (less) preservation of anchovy scales.

Types of fish scales.—Anchovy scales in the sediment samples were identified by type relative to their position on the body, using the nomenclature proposed by Shackleton and Johnson (1988) for *Engraulis capensis* and by Salvatteci (2008) for *Engraulis ringens*. The typical scales (X-type), found along the lateral line, are thicker and more robust and have fewer cracks or radii than the other scale types. Consequently, they may be more resistant to degradation and thus the percentages of different scale types may also be affected by changes in degradation. Therefore, the comparison of the ratios of X-type scales to all scales and of the ratios of all the other scale types to all scales under contrasting conditions would yield information about scale preservation.

Carbon and nitrogen composition.—In order to elucidate the processes of degradation, we analyzed % carbon (C) and nitrogen (N) of the total weights of groups of anchovy scales for two different types of degraded fish scales and compared these with measurements from typical scales. Degraded scales either were considered flimsy (and often rolled up on their own, giving the appearance of a lack of apatite) or had substantial fungal coverage. Groups of scales (usually 4–15) were loaded into tin capsules and analyzed on an elemental analyzer at the University of California, Santa Cruz.

Effect of Fishery in Fish Scales and Bones Abundances

To determine if the fishery affected the relative flux of fish spines, bones, and vertebrae to the sediments, we compared the ratios of scales to vertebrae; scales to bones; and vertebrae and scales to bones, spines, and vertebrae between the fishery period and the pre-fishery period.

Statistical Analysis

To establish the relationships between fish debris types within each core, a simple linear regression was carried out to calculate the shared variability (r^2 values). The probability level was corrected for multiple comparisons by dividing the probability level α ($p < 0.05$) by the number of tests performed (Glantz 2002).

We grouped the different indices and ratios examined in this work and used a nonparametric Mann-Whitney U-test to test differences in (a) fish scale preservation/degradation within cores, (b) fish scale preservation/degradation between cores, (c) preservation/degradation within the period of higher abundance of anchovy scales using the compound preservation index of anchovy scales, and (d) fish scale to bone ratios during the period of industrial fishing. The probability level was corrected for multiple comparisons on the same data set, using a Bonferroni correction, by dividing the probability level α

($p < 0.05$) by the number of tests performed (Glantz 2002).

To test differences in the proportions of types of anchovy scales between the period of high abundances of anchovy scales and the period of low abundances of anchovy scales, we used a Z-test for two proportions. Finally, we tested the differences in %C and %N of the different types between degraded fish scales and the normal anchovy scales using a Mann-Whitney U-test. STATISTICA 7.1 (Stat-Soft, Inc. 2005) computer software was used for all the statistical analysis.

Results

Sediment Characteristics and Preliminary Chronology

Cores B0506-13 and B0506-14 show a visual change in the sediment structure as well as DBD at ~59 and ~63 cm respectively, which can be correlated with a nearby core in Pisco (B0405-6) (Fig. 4). Above this level the sediments are less dense and have fewer distinct laminae. Below this shift the sediments are denser and more finely laminated (Fig. 4). The change in color within a slab, from darker (lighter) at the base (top) of some slabs in cores B0506-13 and B0506-14 shown in Figure 4, is due to the X-ray focus and does not represent a real change in density (e.g., the third slab of core B0506-14 approximately between 42 and 69 cm in Fig. 4). The X-ray images show evidence of at least three homogeneous layers that appear to result from instantaneous lateral depositions: (1) ~70 cm depth in both cores, (2) ~78 cm in core B0506-13 and ~76 cm in core B0506-14, and (3) ~84 cm in core B0506-13 and ~86 cm in core B0506-14. The samples associated with these apparently instantaneous lateral deposits are shown in Figures 4 and 5 and were excluded from the analyses shown in Figures 6 and 7. We excluded these samples because all three cores showed evidence of instantaneous deposition (Fig. 4). Other discordances (e.g., ~49 cm core B0506-13) and a large bioturbated section in core B0506-13 between ~14 and 23 cm depth are present and may result in minor discontinuities in the records.

From the sedimentation rates calculated from core B0405-6 (Gutierrez et al. 2009) and the presence of the sedimentary shift, we estimate that the average sedimentation rates in cores B0506-13 and B0506-14 after the shift are 3.2 mm yr^{-1} and ~3.4 mm yr^{-1} respectively whereas those before the shift are on the order of ~1 mm yr^{-1}. Applying these sedimentation rates and eliminating the instantaneous deposits, we inferred that the age of the bottom of the cores would be ca. 1481 and ca. 1585 for cores B0506-13 and B0506-14, respectively. These are preliminary chronological estimates. A chronology based on radiocarbon analyses is in progress but is not necessary for the objectives of this study.

Characterization of Different Temporal Periods

On the basis of multi-proxy studies, Gutierrez et al. (2009) determined that dramatically different environmental conditions were present for two different centennial-scale periods during the last seven hundred years. A period of low productivity and higher oxygenation up to ca. 1820, as inferred from the proxies shown in Figure 1, was followed by a period of higher productivity and lower oxygenation (in cores B0405-6 and B0405-13 retrieved off Pisco and Callao, respectively). In the cores used in our study these different centennial-scale environmental periods are inferred from DBD values (Fig. 4). Our cores also exhibit the important down-core variations in fish debris observed in the records off Callao and Pisco (Fig. 1). Major temporal variations in fish debris within the period of high productivity that are coherent between our cores merit characterization into different periods (as shown in Fig. 5) and are briefly described here, with the average ± SD of anchovy scale abundances for each period shown in parentheses.

Greater Oxygenation and Lower Abundance of Anchovy Scales.—Anchovy scale abundances are low (B0506-13: 1.06 ± 1.51, $n = 73$; B0506-14: 2.2 ± 1.71, $n = 47$), from the bottom of each core to the ca. 1820 shift (Fig. 5), with visual evidence of greater degradation. The upper limit of this period is located at ~35 cm in core B0405-6 and at ~59 cm and ~63 cm depth in our cores (B0506-13 and B0506-14).
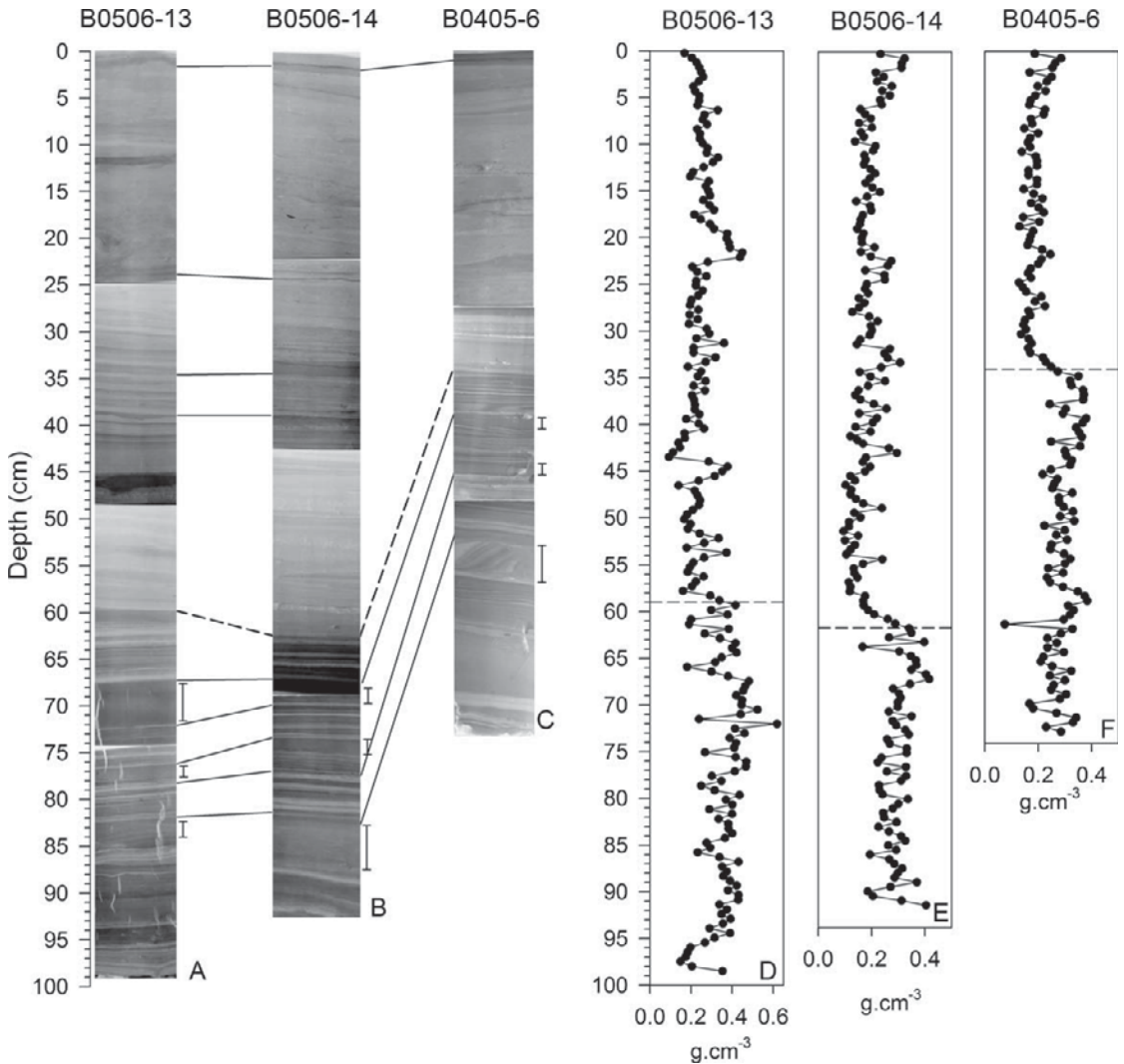
FIGURE 4. Stratigraphic correlation among the three cores retrieved off Pisco: B0506-13 (A), B0506-14 (B), and B0405-6 (C), and Dry Bulk Density (DBD) of cores B0506-13 (D), B0506-14 (E), and B0405-6 (F). Brackets indicate homogenous intervals that can be identified in each core (based on X-radiographs), which are interpreted as instantaneous depositions. The dashed lines indicate the stratigraphic correlation, based on both DBD values and X-radiographs, of the shift from a less productive period to a more productive period (Gutierrez et al. 2009) (Fig. 1). Data for this figure are reported in the online supplemental material.

Presence of Oceanic Species.—The second period is characterized by the notable lack of anchovy scales (B0506-13: 0.50 ± 0.68, $n = 48$; B0506-14: 1.19 ± 1.48, $n = 47$) and the presence of scales from species generally inhabiting more oceanic waters—sardine, mackerel, and jack mackerel (Fig. 5). Although this period lies within the period of higher productivity and lower oxygenation, there is a multidecadal period of low TOC and Mo indicating environmental conditions more similar to pre-1820.

Lower Oxygenation and High Abundance of Anchovy Scales.—The third period is characterized by high abundances of anchovy scales (B0506-13: 4.90 ± 1.86, $n = 58$; B0506-14: 6.36 ± 2.45, $n = 73$) and extends from the "oceanic species period" to the period of industrial fishing, from ~40 cm to ~12.4 cm in core B0506-13 and from ~40 cm to ~7.6 cm in core B0506-14 (Fig. 5). This period is characterized by higher productivity and lower oxygen concentrations, both in the water column and within the sediments (Fig. 1)
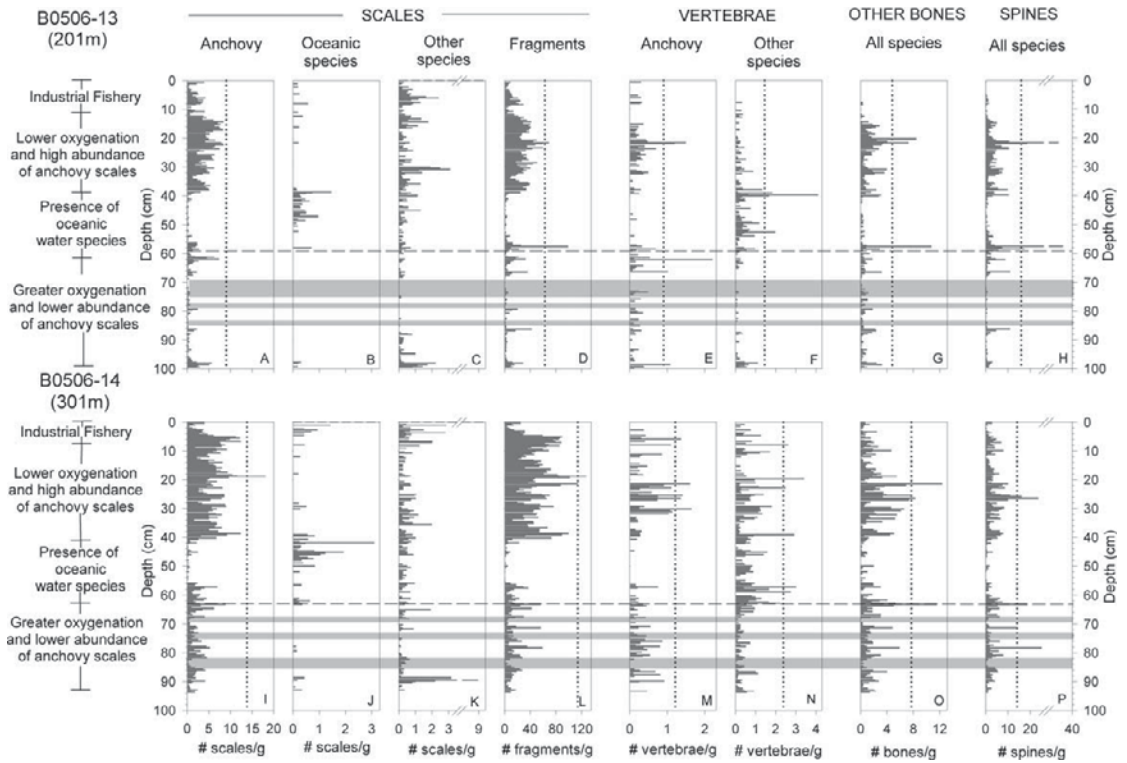
FIGURE 5. Abundance of fish remains in cores B0506-13 (top) and B0506-14 (bottom). A, I, Anchovy (*Engraulis ringens*) scales. B, J, Scales of oceanic species: sardine (*Sardinops sagax sagax*), mackerel (*Scomber japonicus*), and jack mackerel (*Trachurus picturatus murphyi*). C, K, Scales of other species. D, L, Fish scale fragments. E, M, Anchovy vertebrae. F, N, Vertebrae of other species. G, O, Bones. H, P, Spines. The vertical dashed lines indicate the position of the average + 3 standard deviations (SD); all values above this level were replaced by the average + 3 SD for the statistical analyses. The horizontal bars indicate samples associated with inferred instantaneous deposits shown in Figure 4. The horizontal dashed line indicates the shift from a less productive period to a higher productive period (Gutierrez et al. 2009) (Fig. 1). Data for this figure are reported in the online supplemental material.

Industrial Fishery.—The fourth and last period spans the time of the industrial fishery on small pelagic fishes (anchovy and sardines), from ~12.4 cm in core B0506-13 and ~7.6 cm in core B0506-14 to the top of the cores (Fig. 5). There are no major differences in environmental conditions between this period and the preceding period. A higher presence of sardine scales occurs during a period of low anchovy scale abundances from the mid 1970s to 1990s, a period when fish landings indicate a drop in anchovy and increase in sardine populations. A high ratio of scales to all bones suggests an effect of the industrial fisheries on the deposition of fish bones (Gutierrez et al. 2009), which is not driven by an increase in anchovy scale abundances (B0506-13: 1.86 ± 1.35, $n = 28$; B0506-14: 5.45 ± 3.81, $n = 20$).

The major down-core changes in other forms of fish debris, in addition to scales, are similar between cores across these four different periods, although the deeper core (B0506-14) has higher abundances (#/g) of scales of both anchovy and oceanic species, scale fragments, vertebrae, and other bones (Fig. 5). Unlike anchovy scales, anchovy vertebrae show no marked decrease in abundance in either core during the period of "low anchovy scale abundance." However, the abundances of vertebrae from other species are lower during this period of lower productivity. Low abundances of anchovy vertebrae, other bones, and spines are observed in both cores from ~40 to 55 cm, coinciding with the decrease of anchovy scales. The abundance of vertebrae from "other species" in the shallower core (B0506-13) shows a peak from

~40 to 55 cm, during the ''oceanic species period.'' In the deeper core (B0506-14) the peak in abundance of vertebrae from ''other species'' is not clear, but the abundances of vertebrae from ''other species'' is much higher throughout the record and there were observations of many small, thin vertebrae, which were less frequently observed in the shallower core (B0506-13). In both cores the abundances of vertebrae, other bones, and spines show a marked reduction during the ''industrial fishery'' period.

Relationships between Fish Debris Types within Cores

There is considerable shared variability of different components of fish debris within each of the two cores, which is due both to the down-core differences between the four different periods and to the higher-resolution variations. The shared variability (r^2 values) between different down-core variations in fish debris is shown in Tables 1 and 2. In general, there are stronger relationships (range in parentheses) between anchovy scale abundances, scale fragments, bones, and spines in each of the cores (B0506-13: 0.25–0.77; B0506-14: 0.17–0.84), which is likely due to the higher abundances of these debris types in each core. In contrast, relationships of vertebrae with other types of debris are lower (B0506-13: 0–0.36; B0506-14: 0–0.27), because the abundances of vertebrae were much lower and do not resolve the high-resolution down-core variations.

The abundances of scale fragments show higher shared down-core variability with the abundances of anchovy scales than with the abundances of all scales (Tables 1, 2). The stronger relationship likely reflects that the majority of the scale fragments are from anchovy because anchovy scales are most abundant and fragment more readily than those of other species (and they visually appear to be anchovy in most cases). However, the relationships between spines and other bones with anchovy scales are similar in variability to the relationships between spines and bones with scales of all species, suggesting that other species and anchovy may

contribute similarly to the total numbers of spines and other bones.

Taking into consideration that relationships between debris types with lower abundances (e.g., vertebrae) result in lower r^2 values, the shared variability between scales (of all species or anchovy) and spines, bones, and/or vertebrae is consistently lower than for any combination of spines, bones, and vertebrae in each of the cores (Tables 1 and 2). For example, the shared variability (r^2) between all scales and all vertebrae is 0.04 and that between anchovy scales and anchovy vertebrae is 0.16 in core B0506-13. In contrast, the r^2 values between spines and either all vertebrae (0.26) or anchovy vertebrae (0.36) are much higher, as are the r^2 values for other bones with either all vertebrae (0.20) or with anchovy vertebrae (0.29). These relationships indicate that the similarity in the source of deposition is greater among bones, spines, and vertebrae than with scales. The same results were obtained when the fishery period was excluded (data not shown), implying that these relationships are not driven by the fishery period.

Relationships between fish species are of great interest in order to understand the historical changes within the pelagic ecosystem as well as which species may be contributing to unidentifiable fish debris (bones, spines, and some vertebrae). However, the down-core variations in scale abundances of anchovy, oceanic species, and ''other species'' show no significant relationships with one another in either core (Tables 1 and 2), except for a weak relationship between anchovy scales and other species scales in core B0506-13. Consequently, the shared variability between anchovy scales and anchovy vertebrae is higher (B0506-13 = 0.16; B0506-14 = 0.10) than between scales and vertebrae from all species combined (B0506-13 = 0.04; B0506-14 = 0.05). However, there is a weak but significant relationship between the vertebrae from other species with scales of oceanic species in the shallower core B0506-13 (Table 1), but not in the deeper core B0506-14 (Table 2).

Preservation of Fish Remains

The different indices of preservation developed in this study are compiled in two

TABLE 1. Coefficients of determination (r^2 values) indicating shared variability between different fish remains (#/per gram) in core B0506-13 ($n = 207$). Data from Figure 5, excluding samples associated with instantaneous deposits and replacing outliers by the average + 3 standard deviations. Underlined values indicate significant values after correcting for multiple comparisons ($p < 0.005$). The asterisks replace values derived from two categories that share the same data (e.g., all species scales and anchovy scales). Data for this figure are reported in the online supplemental material.

	All species scales	Anchovy scales	Oceanic species scales	Other species scales	Scales fragments	All bones (vertebrae + spines + other bones)	All vertebrae	Anchovy vertebrae	Other species vertebrae	Spines	Other bones
All species scales	-										
Anchovy scales	*	-									
Oceanic species scales	*	0.01	-								
Other species scales	*	0.13	0.01	-							
Scales fragments	0.74	0.77	0.01	0.11	-						
All bones (vertebrae + spines + other bones)	0.27	0.27	0.00	0.05	0.47	-					
All vertebrae	0.04	0.03	0.02	0.02	0.04	*	-				
Anchovy vertebrae	0.13	0.16	0.01	0.00	0.18	*	*	-			
Other species vertebrae	0.00	0.00	0.05	0.02	0.00	*	*	0.00	-		
Spines all species	0.25	0.25	0.00	0.04	0.46	*	0.26	0.36	0.05	-	
Other bones all species	0.30	0.30	0.00	0.06	0.41	*	0.20	0.29	0.04	0.58	-

TABLE 2. Coefficients of determination (r^2 values) indicating shared variability between different fish remains (#/per gram) in core B0506-14 ($n = 187$). Details as in Table 1. Data for this figure are reported in the online supplemental material.

	All species scales	Anchovy scales	Oceanic species scales	Other species scales	Scales fragments	All bones (vertebrae + spines + other bones)	All vertebrae	Anchovy vertebrae	Other species vertebrae	Spines	Other bones
All species scales	-										
Anchovy scales	*	-									
Oceanic species scales	*	0.03	-								
Other species scales	*	0.00	0.01	-							
Scales fragments	0.76	0.84	0.02	0.00	-						
All bones (vertebrae + spines + other bones)	0.21	0.22	0.01	0.01	0.28	-					
All vertebrae	0.05	0.05	0.01	0.00	0.04	*	-				
Anchovy vertebrae	0.09	0.10	0.01	0.00	0.12	*	*	-			
Other species vertebrae	0.02	0.01	0.03	0.00	0.00	*	*	0.08	-		
Spines all species	0.21	0.22	0.01	0.00	0.28	*	0.15	0.27	0.04	-	
Other bones all species	0.16	0.17	0.02	0.01	0.24	*	0.15	0.27	0.04	0.62	
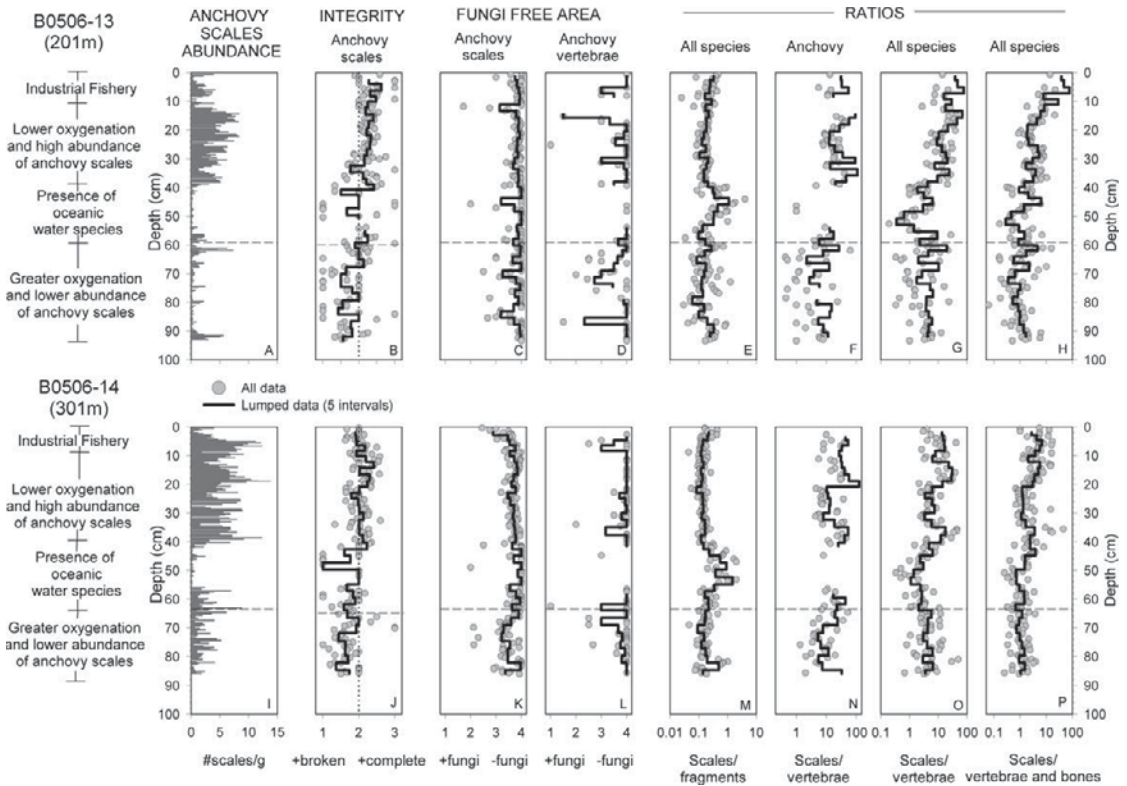
FIGURE 6. Anchovy scale abundances, ratios, and indices developed in this study from cores B0506-13 (top) and B0506-14 (bottom). A, I, Anchovy scales. B, J, Integrity index of anchovy scales. C, K, Fungi-free area index on anchovy scales. D, L, Fungi-free area index on anchovy vertebrae. E, M, Ratio of scales to fragments. F, N, Ratio of scales to vertebrae from anchovy. G, O, Ratio of scales to vertebrae from all species. H, P, Ratio of scales to all bones from all species. The thick black line represents a five-interval lumped average. Ratios are shown in logarithmic scale for better visualization of the data set. Ratios with zero in the denominator are not shown. The horizontal dashed line indicates the shift from a less productive period to a more productive period (Gutierrez et al. 2009) (Fig. 1). Data for this figure are reported in the online supplemental material.

different ways and compared with the abundances of anchovy scales in Figures 6 and 7. Figure 6 shows the high-resolution downcore temporal variations whereas Figure 7 emphasizes the major differences between periods.

First, the indices were tabulated in a way that would allow statistical comparisons between cores and within cores (Fig. 6). Because the low counts of scales and vertebrae in many sampling intervals can affect the estimates of the degradation indices (particularly the ratios), data from five continuous sampling intervals were lumped together into one "lumped interval." The averages of lumped intervals would be identical to having a coarser sampling resolution with greater counts of debris per sample. The black lines in Figure 6 indicate averages of all the

data from the "lumped intervals." In many cases the lumped values have higher averages than the averages of each sampling interval, because ratios with zero in the denominator, which are not shown as symbols, elevate the ratios when the data of five sampling intervals are lumped together. The averages of the indices estimated from the data within each lumped interval were used to test if there are significant differences in preservation of anchovy fish scales between the period characterized by higher oxygenation (low abundance of anchovy scales) and the period characterized by lower oxygenation (high abundance of anchovy scales). The average values for the integrity index, the fungi-free area on anchovy scales and anchovy vertebrae, and the different ratios examined in this work were ranked and used to test
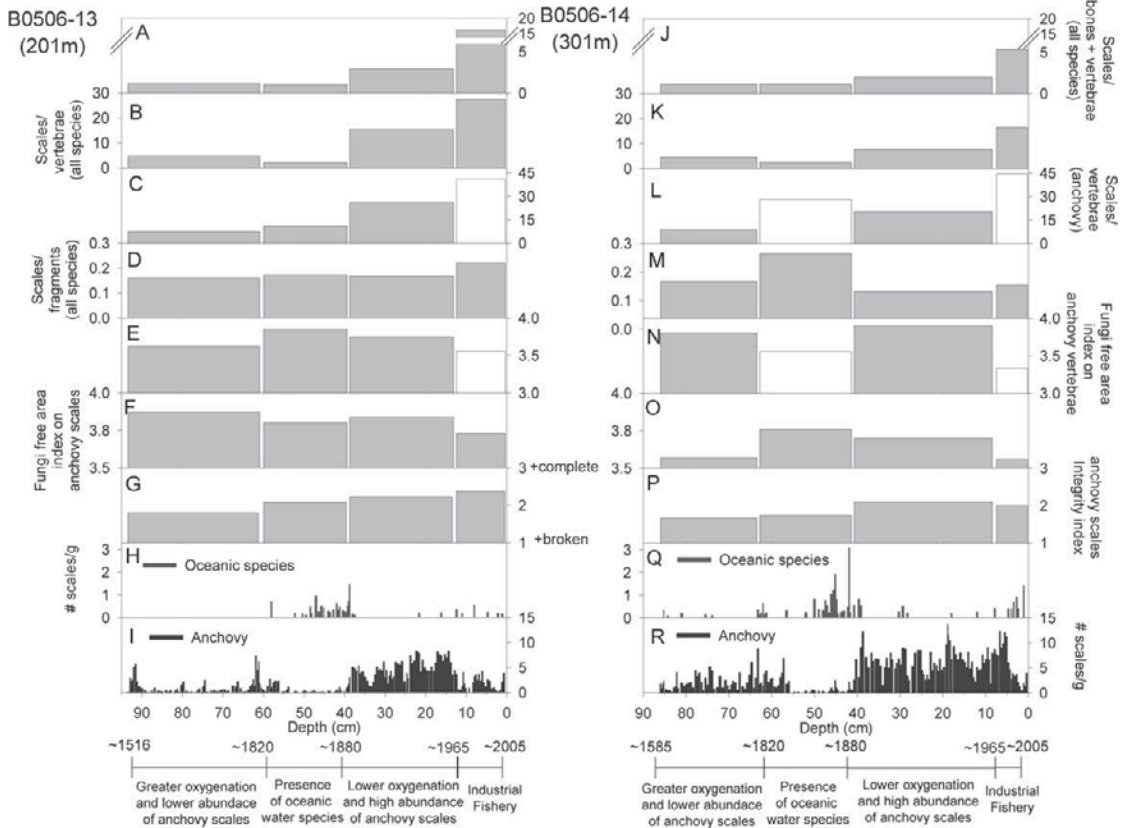
FIGURE 7. Degradation indices and ratios evaluated in this study in four periods based on the down-core variability of fish remains abundance of cores B0506-13 (left, B0506-14 (right) as well as geochemical proxies shown in Figure 1. A, J, Ratio of scales to bones and vertebrae from all species. B, K, Ratio of scales to vertebrae from all species. C, L, Ratio of anchovy scales to anchovy vertebrae. D, M, Ratios of scales to scale fragments from all species. E, N, Fungi-free area index on anchovy vertebrae. F, O, Fungi-free area index on anchovy scales. G, P, Integrity index. H, Q, Oceanic species scale abundance. I, R, Anchovy scale abundance. Estimates based on fewer than ten observations (e.g., scales or vertebrae) are not filled. Data for this figure are reported in the online supplemental material.

for differences within and between cores with a nonparametric Mann-Whitney *U*-test (Tables 3, 4).

Because the number of observations of the preservation indices and ratios within the lumped intervals is still often low and variable, we calculated a second compilation of the preservation indices to illustrate the mean differences between periods and between cores. Figure 7 shows estimates for each of the preservation indices and ratios based on all the data within all sampling intervals within each period, for each of the four different periods.

Differential Preservation of Fish Remains within each Core.—Our primary interest is to determine if there are differences in preservation between the period of greater oxygenation (low anchovy scale abundance) and the period of lower

oxygenation (high anchovy scale abundance). Thus we focus our comparisons of degradation on these two periods. The ''industrial fishery'' period is considered separately because of the possible effect of the fisheries on the ratios (Gutierrez et al. 2009). The period ''presence of oceanic species'' is also considered separately because the low anchovy scale abundances in this period result in unreliable estimates of the preservation indices. Down-core changes in the preservation indices of fish scales in cores B0506-13 and B0506-14 show similar patterns within each core (Fig. 6), nearly all of which indicate greater degradation during the more oxygenated period.

The results of the comparison of the degradation indices from the lumped intervals between the periods of higher and lower

TABLE 3. Results of the Mann-Whitney U-test of the degradation indices and fish debris ratios (within the cores B0506-13 and B0506-14) comparing the period characterized by higher abundance of anchovy scales with the period characterized by lower abundance of anchovy scales. Boldface indicates significance after correcting for multiple comparisons ($p < 0.0125$) and italics indicates those values that are significant at $p < 0.05$.

| | B0506-13 (201 m) | | | | | | B0506-14 (301 m) | | | | | |
| | Lower oxygenation and high abundance of anchovy scales | | Greater oxygenation and lower abundance of anchovy scales | | | | Lower oxygenation and high abundance of anchovy scales | | Greater oxygenation and lower abundance of anchovy scales | | | |
Index/ratio	Mean	n	Mean	n	U	p-value	Mean	n	Mean	n	U	p-value
Anchovy scales integrity	2.22	12	1.77	14	9	**<0.001**	2.09	15	1.68	9	4	**<0.001**
Fungi-free area on anchovy scales	3.84	12	3.77	14	81	0.877	3.69	15	3.54	9	37	0.069
Fungi-free area on anchovy vertebrae	3.56	12	3.57	13	72.5	0.765	3.91	15	3.78	9	40.5	0.107
Ratio scales to fragments	0.17	12	0.17	14	70	0.471	0.13	15	0.19	9	33	*0.040*
Ratio scales to vertebrae (anchovy)	44.54	12	9.12	13	11	**<0.001**	33.57	15	13.26	9	24	**0.009**
Ratio scales to vertebrae (all species)	21.06	12	5.75	14	18	**0.001**	11.86	15	4.52	9	25	**0.011**
Ratio scales to bones and vertebrae	3.30	12	1.31	14	18	**0.001**	2.62	15	1.10	9	13	**0.001**

TABLE 4. Results of the Man-Whitney U-test of the degradation indices and fish debris ratios between cores B0506-13 and B0506-14 in the periods characterized by lower abundance of anchovy scales and high abundance of anchovy scales. Details as in Table 3.

| Index/ratio | Lower oxygenation and high abundance of anchovy scales | | | | | | Greater oxygenation and lower abundance of anchovy scales | | | | | |
| | B0506-13 (201 m) | | B0506-14 (301 m) | | | | B0506-13 (201 m) | | B0506-14 (301 m) | | | |
	Mean	n	Mean	n	U	p-value	Mean	n	Mean	n	U	p-value
Anchovy scales integrity	2.22	12	2.09	15	47	0.036	1.76	10	1.68	9	37.5	0.540
Fungi-free area on anchovy scales	3.84	12	3.69	15	18	**<0.001**	3.79	10	3.54	9	21	0.050
Fungi-free area on anchovy vertebrae	3.56	12	3.91	15	56.5	0.102	3.56	9	3.78	9	28.5	0.289
Ratio scales to fragments	0.17	12	0.13	15	30	**0.003**	0.14	10	0.19	9	31	0.253
Ratio scales to vertebrae (anchovy)	44.54	12	33.57	15	71	0.354	9.00	9	13.26	9	27	0.233
Ratio scales to vertebrae (all species)	21.06	12	11.86	15	54	0.079	6.09	10	4.52	9	44	0.935
Ratio scales to bones and vertebrae	3.30	12	2.62	15	62	0.172	1.33	10	1.10	9	33	0.327

oxygenation within each core are shown in Table 3. In both cores the anchovy scale integrity index, the ratio of anchovy scales to anchovy vertebrae, the ratio of all scales to all vertebrae, and the ratio of all scales to bones and vertebrae were statistically higher, after correcting for multiple testing, in the period of lower oxygenation (Table 3). In the deeper core the ratio of anchovy scales to fragments is significantly higher at the $p < 0.05$ level, but not after correcting for multiple testing.

Although the period characterized by ''presence of oceanic species'' has insufficient quantities of fish debris for statistical comparisons, the dramatic change in species composition during this period serves to illustrate the effect that species composition may have on the preservation indices. Because anchovy scales fragment more readily than scales of other species, species composition could change the ratio of scales to scale fragments without affecting degradation. Figure 6 shows that there is an increase in this ratio in both cores, although Figure 7 shows that the increase is more noteworthy in the deeper core (B0506-14) than in the shallower core (B0506-13). The ratio of all scales to all vertebrae is also lower during this period in both of the cores, perhaps due to the change in species composition as well.

Preservation of Fish Remains between Cores.—In addition to assessing preservational differences between time periods, a major objective is to determine if the deeper core (B0506-14; 301 m) has better preservation than the shallower core (B0506-13; 201 m).

We compare the degradation indices and ratios from the lumped intervals to detect changes in preservation between cores. There are few significant differences between the cores during the period of ''high abundance of anchovy scales'' (and lower oxygenation), but some suggestion of greater degradation in the shallower core. However, the fungi-free area index on anchovy scales is statistically lower in the deeper core whereas the fungi-free area index on anchovy vertebrae is actually slightly higher in this same core (Table 4). This contrast between the fungal coverage on scales and on vertebrae is consistent with the different temporal changes

observed in the fungi-free area indices on scales and on vertebrae. Scales covered with considerable fungus were observed to break frequently and become fragments, whereas vertebrae were not observed to fragment.

A greater difference in preservation between cores was expected during the period of higher oxygenation (prior to ca. 1820). However, a direct comparison of these two periods could be affected by differential time-averaging because B0506-13 has older sediment than B0506-14. During the less productive period several laminated sequences above ~83 cm are well correlated between the cores (Fig. 4) and thus should represent the same time period. Consequently, we compared degradation indices and ratios from the lumped intervals from the first 20 cm below the shift to constrain the comparison to similar temporal sequences. No statistical differences were detected in the degradation indices or ratios between cores for this time period (Table 4) but the ratio of scales to scale fragments, the fungi-free area index on anchovy vertebrae, and the ratio of anchovy scales to anchovy vertebrae all indicate better preservation in the deeper core (Fig. 7). During this period as well, the fungi-free area index on anchovy scales is actually lower in the deeper core, whereas the fungi-free area index on anchovy vertebrae is lower in the shallower core (Fig. 7).

Compound Preservation Index of Anchovy Remains.—We developed a compound index to describe the preservation of anchovy scales because of the variability and potential biases in each individual index. The down-core variability of anchovy scale abundances and the compound preservation index are shown in Figure 8. Higher (lower) values indicate better (less) preservation of anchovy scales. Because the compound preservation index is based on anchovy scales, the period characterized by oceanic species (between 40 and 56 cm in both cores) should not be considered reliable, given the low numbers of anchovy scales and vertebrae during this period. The compound preservation index clearly shows better preservation of anchovy scales after ca. 1880 than during the period before 1820. Some minor decadal-scale fluctuations are also apparent in the index.

The decadal-scale variations in scale abundance within each core during the period of greater anchovy scale abundance may be consistent between cores and are of great interest in understanding population dynamics of anchovy and other pelagic species (Fig. 8). To determine whether these fluctuations could be affected by degradation, we compared the average of the degradation index of the anchovy scales between the decadal minimums and maximum within each core. Consecutive sampling intervals of relatively high (low) sustained abundance relative to neighboring sequences were selected for grouped comparisons (clear and dark horizontal bars in Fig. 8). The average of the compound index values during the decadal maximums is 0.38 ± 0.17 ($n = 5$) and 0.53 ± 0.4 ($n = 4$) in cores B0506-13 and B0506-14, respectively, whereas the average during the decadal minimums is 0.28 ± 0.25 ($n = 5$) and 0.14 ± 0.43 ($n = 5$) in cores B0506-13 and B0506-14, respectively. However, no differences were found in the average compound preservation index between decadal-scale maximums and minimums within each core (Mann-Whitney U-test; B0506-13: U = 9, $p = 0.465$; B0506-14: U = 4, $p = 0.142$). Thus the variations in scale abundance are likely to primarily reflect variability in anchovy scale deposition (Fig. 8).

Type of Fish Scales.—X-type scales are clearly the most abundant anchovy scale type in both cores during the periods of high abundance and lower abundance of anchovy scales (Fig. 9). The comparison of the proportions of X-type to all scales versus the sum of all the other scale types to all scales between the two periods show a significant increase of X-type scales during the more oxygenated period in both cores. The difference is slightly higher in the shallower core (B0506-13: $z = 4.715$, $p < 0.05$) than in the deeper core (B0506-14: $z = 2.695$, $p < 0.05$). These results further indicate that scale preservation in the shallower core, in particular, was lower during the period of greater oxygenation.

Organic Matter Content in Anchovy Scales.—Dissolution of the hard and well-mineralized outer layer of fish scales might accelerate degradation processes and affect fish scale
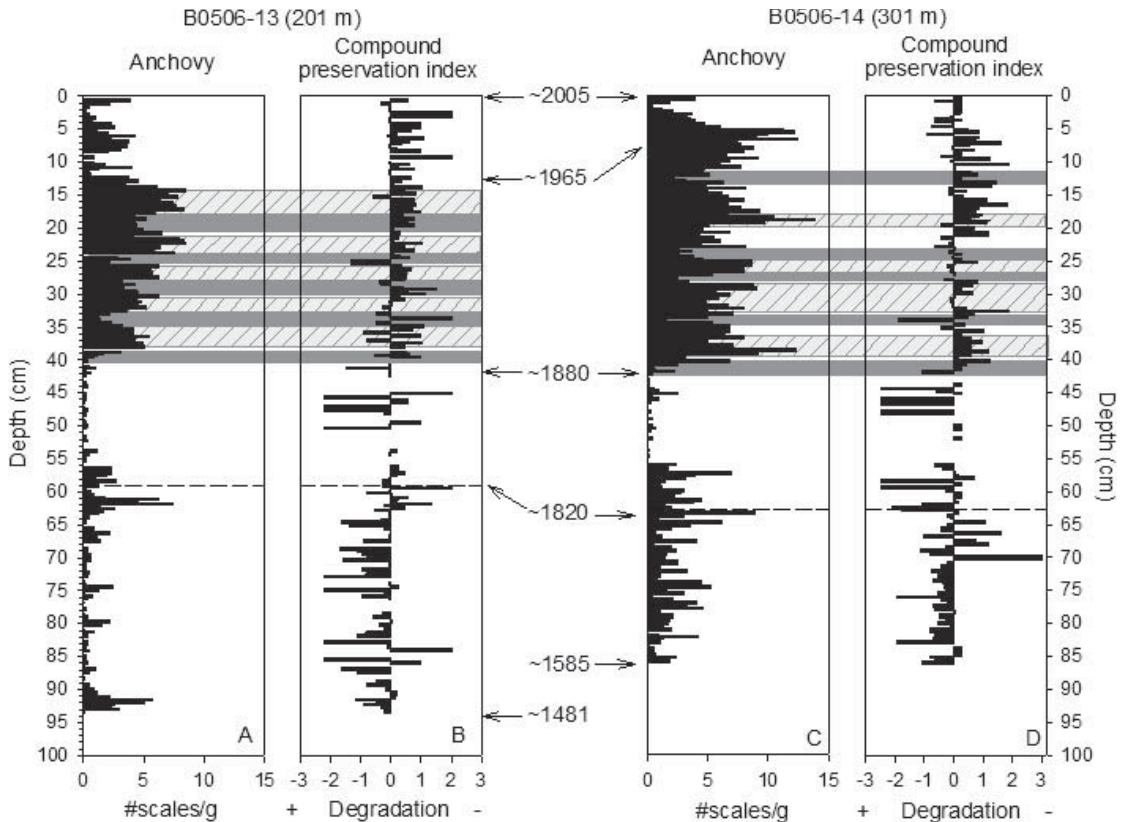
FIGURE 8. Anchovy scale abundances and compound preservation index of anchovy scales in cores B0506-13 (A, B) and B0506-14 (C, D). The compound index was calculated from the average of three normalized indices: the integrity index of anchovy scales, the fungi-free area index on anchovy vertebrae, and the ratio of anchovy scales to anchovy vertebrae. Dark (clear with diagonal lines) horizontal bars indicate samples associated with decadal-scale minimums (maximums). The dashed lines indicate a shift from a period characterized by lower productivity and weaker OMZ (from the base of the core to ca. 1820) to a period characterized by higher productivity and intense OMZ (following Sifeddine et al. 2008 and Gutierrez et al. 2009). Data for this figure are reported in the online supplemental material.

firmness (Hutchinson and Trueman 2006). Anchovy scales within the oxygenated period (prior to 1820) that were observed to be quite flimsy, folded, and/or rolled up have higher percentages of carbon and nitrogen than other scales, which is consistent with a loss of apatite (Fig. 10). The percentages of carbon and nitrogen in the flimsy and rolled-up scales ($n = 5$) are significantly higher (Mann-Whitney U-test, $U = 0$, $p < 0.0001$) than in the normal scales ($n = 56$). However, there are no significant differences in either the percentage of carbon (Mann-Whitney U-test, $U = 359$, $p = 0.637$) or the percentages of nitrogen (Mann-Whitney U-test, $U = 388$, $p = 0.96$) between the well normal scales (n = 56) and the scales with fungus ($n = 14$).

Effect of Fishery in Fish Scales and Bones Abundances

During the period of the industrial fishery development, abundances of vertebrae, bones, and spines decreased in both cores relative to the abundances of scales (Figs. 6, 7). The ratios of scales to fish vertebrae and scales to vertebrae and bones show a marked increase during the ''industrial fishery,'' which is attributed to an absence of bones and vertebrae rather than an increase in scale flux (Figs. 6, 7). To determine if the fishery affected the relative flux of fish spines, bones, and vertebrae to the sediments, we used a Mann-Whitney U-test to compare the ratios (scales to vertebrae; scales to bones and vertebrae; and scales to bones, vertebrae, and spines) between the fishery
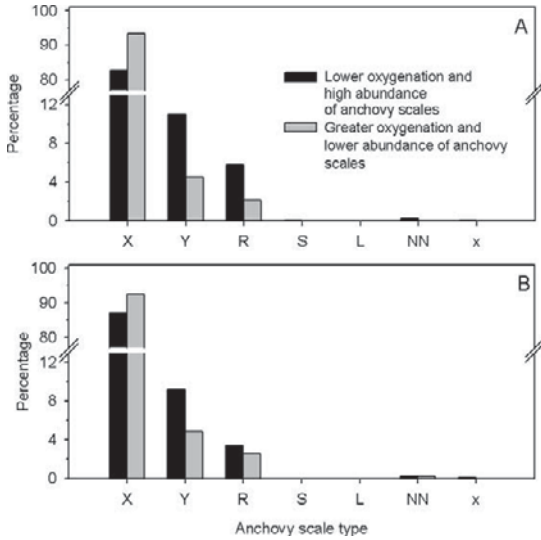
FIGURE 9. Percentage of the different types of anchovy scales in cores B0506-13 (A, B0506-14 (B): X, Y, R, S, L, x, and NN (not identified) following Shackleton and Johnson (1988). X-type scales are considered thicker and more resistant to degradation. Data for this figure are reported in the online supplemental material.

period and the "period of high abundance of anchovy scales" from the lumped intervals (Fig. 6). The ratios of scales to vertebrae for all species combined are much higher during the fishery although the results are not significant (Table 5). However, the ratios of all scales to bones and vertebrae and all scales to bones,

vertebrae, and spines are significantly higher during the period of the fishery in the shallower core (Table 5) and are significantly different at the $p < 0.05$ level in the deeper core, although this result is not significant after correcting for multiple testing (Table 5).

Discussion

Processes of Degradation

The multiple indices of degradation developed here give primarily consistent results between one another with respect to comparisons of different temporal periods within cores and between the cores. The compound degradation index clearly reveals patterns of detectable degradation in both cores during the period of higher oxygenation, as inferred from independent proxies (Fig. 1).

The evidence indicates that a substantial portion of scales in the region are degraded through the development of fungus, which might be nourished on the organic matter within the scale. Unlike scales with light to moderate fungal coverage, heavily covered scales break into fragments that can dissolve or pass through sieves. The vertebrae are more robust and much less likely to fragment with fungal coverage. The fragmentation and subsequent absence of scales with heavy
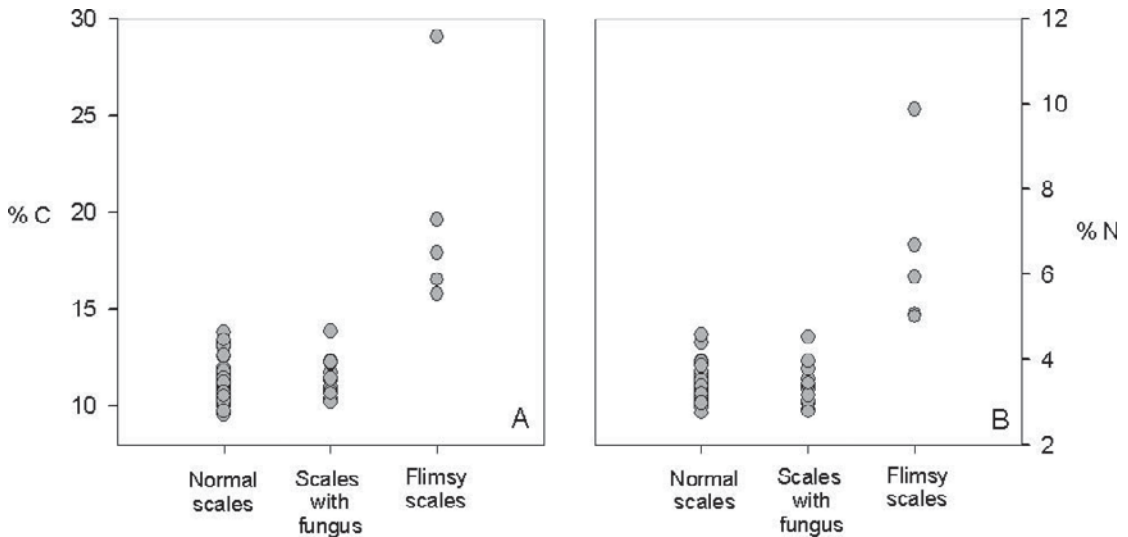
FIGURE 10. Percent carbon (A, nitrogen (B) in normal anchovy scales ($n = 56$), in scales with fungus ($n = 14$, and in scales that were flimsy and/or rolled up ($n = 5$). Fish scales taken from cores B0405-6, B0506-13, and B0506-14. Data for this figure are reported in the online supplemental material.

fungal coverage explains the differences in the fungi-free area index between scales and vertebrae both between and within cores (Fig. 7). Although we did not observe a loss of carbon and nitrogen in fungus-covered scales, perhaps a localized (and hence non-detectable) loss of organic matter destroyed the collagen binding or somehow altered the scale chemically, causing fungus-covered scales to become brittle.

Although many observations support scale fragmentation due to fungal coverage as a mode of degradation, there is also evidence for degradation through dissolution of apatite (Fig. 10). In addition to having higher concentrations of carbon and nitrogen (Fig. 10), total scale weights were considerably lower in these scales; this indicates a loss of apatite, because the hard and well mineralized upper layer contributes a considerable portion of the total scale weight (Hutchinson and Trueman 2006). Some of these scales were also discolored—yellow, orange, or more transparent. Vertebrae and bones also showed visual signs of dissolution during the period of greater oxygenation. Some vertebrae were also discolored (usually yellow, orange, or darker) or had missing structures (apparently from dissolution), and portions of these vertebrae occasionally crumbled off when being manipulated with a forceps. Likewise, some bones and spines were discolored, and some spines and smaller bones were quite flimsy, indicating a loss of structure. It is unclear what conditions would favor one mechanism of degradation over another.

Oxygenation likely plays some role in degradation, because when oxygenation is lower, as inferred from independent proxies (Fig. 4), preservation in both cores is better. Furthermore, the deeper core (B0506-14) would be less exposed to oxygenation than the shallower, and appears to have better scale preservation during the period of greater oxygenation.

Sedimentation rates could also affect degradation of either type. Lower sedimentation rates could result in prolonged exposure to bottom waters with oxygen and/or undersaturated in apatite, which might increase dissolution and/or fungal growth. Lower

TABLE 5. Results of the Mann-Whitney U-test comparing ratios from the fisheries period with those from the high abundance of anchovy scales period. Details as in Table 3.

| | B0506-13 (201 m) | | | | | | B0506-14 (301 m) | | | | | |
| | Fishery | | Pre-Fishery | | | | Fishery | | Pre-Fishery | | | |
Ratios	Mean	n	Mean	n	U	p-value	Mean	n	Mean	n	U statistic	p-value
Ratio scales to vertebrae (anchovy)	33.63	4	44.54	12	23	0.903	43.01	3	33.57	15	12	0.214
Ratio scales to vertebrae (all species)	37.52	6	21.06	12	17	0.075	15.34	4	11.86	15	17	0.194
Ratio scales to bones and vertebrae	34.64	6	3.30	12	0	**<0.001**	4.85	4	2.62	15	9	0.036
Ratio scales to bones, vertebrae, and spines	8.30	6	0.99	12	0	**<0.001**	2.03	4	1.15	15	9	0.036

fluxes of TOC could also result in less oxygen consumption, and hence higher levels of free dissolved oxygen in bottom water and/or a deeper oxidized layer, as inferred from Mo (Fig. 1), which could also affect preservation.

Patterns of Temporal and Spatial Preservation

Statistical tests (Table 3) and the compound degradation index (Fig. 8) clearly point to degradation of anchovy scales during the period of greater oxygenation. The centennial-scale differences in preservation are apparent from all of the indices and ratios examined except for the ratio of scales to scale fragments (Fig. 7), which may be affected by species composition. During this period, the fungi-free area on vertebrae is lower in both cores (Fig. 7). Although the fungi-free area index on scales is lower during the period of greater oxygenation in the deeper core, the opposite pattern is observed in scales from the shallower core (Fig. 8). As mentioned above, these opposing patterns of fungi-free area index on scales and vertebrae indicate that some of the scales with highest fungal coverage have already degraded through fragmentation. Temporal differences in degradation are further supported by the differences between the less robust scales and the more robust type-X scales during the period of higher oxygenation (Fig. 9).

Although changes in oxygen likely play an important role in preservation of fish remains (Simon et al. 1994), changes in sedimentation rate could also account for some of the differences in scale abundances between cores and between periods because scale abundances reported here are #/g rather than flux (#/cm²/yr). The rate of sedimentation prior to the sedimentological shift are estimated to have been half of the rates that occurred after the shift (Gutierrez et al. 2009), which would signify that the lower abundance of anchovy scales in this period (Fig. 5) resulted in much lower estimates of scale fluxes to the sediments. Likewise, fluxes of anchovy vertebrae during this period (before ca. 1820) would be much lower than in the high abundance period (from ca. 1880 to ca. 1965). However, the difference in fluxes of anchovy vertebrae between periods is not as dramatic as in the fluxes of anchovy scales.

Thus, the lower abundance of anchovy scales before ca. 1820 is likely a result of the combination of lower local biomass supported by inferred lower productivity (Gutierrez et al. 2009) and more degradation of fish scales.

Remarkably, during the period characterized by greater oxygenation (prior to ca. 1820) both cores show fine laminations (Fig. 4). This suggests that the weakening of the OMZ was not strong enough to destroy the laminated sequences. In discussing the apparent discrepancy between laminations and oxygen proxies, Gutierrez et al. (2009) attributed such circumstances to (1) a deepening of the redox layer within the sediments with little change in oxygen concentrations at the sediment interphase, (2) a small change in oxygen that affected degradation but did not permit macrofaunal colonization, and/or (3) greater seasonal (or interannual) differences in particle density to the sediments. The evidence for higher oxygenation depletion after the shift of ca. 1820 comes from multiple proxies and cores (Díaz-Ochoa et al. 2008; Sifeddine et al. 2008; Gutierrez et al. 2009) and thus can be considered reliable.

There is some evidence that degradation is greater in the shallower core than in the deeper core, but the evidence is based on different indices than the temporal changes. The fungi-free area index on vertebrae is lower throughout the shallower core than in the deeper core (Fig. 7), as would be expected if the fungi-free area index on vertebrae is an indicator of degradation. In contrast, the index of fungi-free area on anchovy scales is lower throughout the deeper core (Fig. 7), indicating that some scales with greater fungal coverage have fragmented in the shallower core. Finally, the changes in scale type across different periods were greatest in the shallower core, further indicating greater degradation in the shallower core. The relatively lower abundance of anchovy scales throughout the shallower core could in part be explained by this greater degradation, although conclusive evidence requires better estimates of sedimentation rates.

Use of Degradation Indices

Each degradation index can be affected by factors other than degradation, which emphasizes

the importance of developing multiple indices. For example, although the anchovy scale integrity index does reflect the effect of degradation through fragmentation; the index is sensitive to the number of anchovy scales counted. During the period dominated by scales of oceanic species, the integrity index of anchovy scales would not be reliable because of the small sample size of anchovy scales. Furthermore, a scale integrity index should be species specific because different species fragment differently.

The fungi-free area index on fish scales can be biased because scales with high fungal development fragment and disintegrate. The presence of fungal coverage over fish remains is unlikely to be an artifact of core storage. Fungal coverage of fish scales and bones examined immediately after a short gravity core was retrieved off Callao was similar to that observed in the cores of this study. The fungi-free area index on vertebrae is a more useful index for evaluating the preservation of fish remains, but larger sample sizes are required to obtain a sufficient number of vertebrae.

The ratio of scales to scale fragments is relatively constant across time periods when other indices vary, and thus reveals little about the preservation of fish scales. In contrast, a measure of how complete a scale is (the integrity index) is a good indicator of degradation. This is not surprising, because the size and number of scale fragments resulting from scale fragmentation may be quite variable and could be affected during sieving as well (O'Connell and Tunnicliffe 2001). Fragmentation also varies by species; for example, sardine scales are thicker than the anchovy scales (Shackleton and Johnson 1988 and personal observations) and could resist degradation better in situ and during the sieving process.

The ratios of fish scales to vertebrae and fish scales to vertebrae and bones are meaningful but quite variable in individual sampling intervals and even in the lumped intervals. Also, the ratios may be affected by factors other than degradation. The different values of the coefficient of determination of fish debris (bones, spines, and vertebrae have stronger relations between each other than with scales) further confirms the different modes of flux of fish debris; that scales reach the sediment via shedding whereas bones and vertebrae likely reach the sediments only after death (usually after ingestion by a predator). We have on rare occasion observed within a sediment sample a sequence of vertebrae and bones that was clearly derived from a portion of a fish carcass (Field et al. 2009). However, the down-core counts of spines, bones, and vertebrae are generally consistent with one another and with scales, indicating that all sources of fish debris vary primarily with population size rather than random predation events. Furthermore, replacing the outlier values of the abundances of vertebrae, bones, and spines (O'Connell and Tunnicliffe 2001) by the mean + 3 SD reduces the possible bias that the deposition of a piece of fish carcass could have on the ratios. Although the Humboldt Current is largely dominated by anchovy, this index works best when scales and vertebrae are identified to species and would be much less effective in periods, or other regions, having more equal distributions of different species. As discussed below, ratios of debris would not indicate preservation state during periods of industrial fishing. The results presented here confirm the usefulness of the ratio of scales to vertebrae as a good indicator of preservation, as proposed by DeVries and Pearcy (1982), and indicate that the ratio of scales to vertebrae and bones may be more appropriate depending on the amount of fish debris quantified.

Schenau and De Lange (2000) quantified the amount of phosphorus from fish remains (P_{fish}) to determine presence of fish debris in surface samples from the Arabian Sea. Higher concentrations of P_{fish} were found in sediments located at depths associated with higher accumulation rates and lower concentrations of bottom-water oxygen (presumably flux of fish debris was equal across sampling sites). Thus P_{fish} could be used to indicate spatial patterns of relatively higher preservation of total fish debris.

Díaz-Ochoa et al. (2008) discussed preservation of fish scales off Callao in a short gravity core based on several proxies of productivity and oxygen and proposed the use of P_{fish} to total phosphorus (P_{total}), as an indicator of preservation. The ratio P_{fish}/P_{total} shows higher values occurring after the shift reported by Gutierrez

et al. (2009). However, there is great uncertainty as to whether this ratio reflects dissolution of fish debris, changes in the total amount of fish debris arriving to the sediments, or changes in the amount of organic matter arriving to the sediments. Furthermore, there is no information on the relative contribution of fish scales, bones, and vertebrae to P_{fish} nor is there information on the species composition composing P_{fish}. Our results illustrate that information on species composition of scales, bones, and vertebrae, as well as on their fragmentation, is essential for understanding degradation of fish debris, and hence for differentiating past variations in population size of pelagic fishes from changes in preservation of fish debris.

Our evaluation of the utility and drawbacks of several indices to detect and quantify fish scales degradation could also be relevant to other paleobiological systems. For example, the fact that both vertebrae and scales had fungal coverage but scales degraded more easily implies that different surface area to volume ratios might be important factors affecting other marine fossils, particularly if fungus plays a role in degradation. Additionally, because of species-specific differences in the fragments or the loss of fragments during sieving, we found that the integrity index proved more useful than the ratio of scales to fragments. Therefore, the degree of completeness of other marine fossils may better reflect the degree of degradation than a ratio of whole fossils to their fragments. Finally, our study clearly showed that determining degradation in marine fossils requires the use of several indices, because each of them has particular advantages and limitations that may affect the evaluation.

Effect of Fisheries in Fish Scales and Bones Fluxes

Our results, combined with those of Gutierrez et al. (2009), provide strong evidence that the flux of bones and vertebrae off Pisco and Callao has diminished since the development of the industrial fishery in the 1960s. Although our results do not clearly indicate an effect on vertebrae alone, the significant effect on the ratio of scales to bones and vertebrae and the ratio of scales to bones,

spines, and vertebrae suggests that the fishery did reduce the flux of bones, spines, and by inference, vertebrae as well. The fishery, which at its peak is capable of extracting over 10 million tons of anchovy annually, would definitely remove a significant quantity of bones and vertebrae from the system. At the same time, any possible effect on scale shedding would likely be to increase rates of scale shedding (by scale loss during fishing operations resulting from trauma to the fish). We should therefore expect higher rates of deposition of scales relative to bones during industrial fishing operations, which would increase the ratio of scale to bone deposition.

The likely effect of the fishery is that spines, bones, and vertebrae now end up as fish meal and no longer arrive to the sediments after passing through the guts of predators because the fishery has removed so many anchovy from the ecosystem. Although fishing may or may not alter scale flux (caused by live shedding rather than mortality), the removal of anchovy by fishing clearly reduces their availability to top predators (Jahncke et al. 2004) and this effect is observed in the sedimentary record.

Conclusions

This study has clearly shown differences in fish scale preservation, both between different cores and between different temporal periods, corresponding to a sedimentological shift at ca. 1820 within each core (higher productivity and lower water column oxygenation versus lower productivity and higher water column oxygenation). The shallower core, which was more exposed to oxygenation events, shows more degradation than the deeper core. The results of this work indicate that diminished abundances of fish scales during the less productive period, which is characterized by more oxygen in the bottom waters at both core sites, reflect a combination of lower local biomass of anchovy and increased degradation of fish scales. A deeper oxidized layer and lower sedimentation rates during the increased oxygenation period may be the environmental factors that result in greater degradation.

During the period of lower oxygenation, higher productivity, and higher abundances of anchovy scales, there was no clear evidence that degradation affected the decadal variability observed in anchovy scale abundances. Thus variations in abundance should be related primarily to past fish population variability.

Determining degradation in fish scales requires the use of several indices, each of which may have particular uncertainties or other factors that affect the index. The scale integrity index (completeness of scales) of anchovy scales is an appropriate index, although the ratio of scales to scale fragments can be affected by the type of fragments remaining and of course by species composition of scales. The ratio of anchovy scales to anchovy vertebrae is a good index for assessing the degradation of fish scales, although it has been affected by industrial fishing during recent times. The ratio of all scales to all vertebrae is also useful but can be affected by species composition (in addition to fishing) and large sample sizes are required to obtain reliable data at high-resolution sampling. The ratio of scales to vertebrae and bones may be a more useful index, particularly with lower sample sizes. If larger sample sizes can be analyzed, the fungi-free area index on vertebrae (but not scales) is a good index for evaluating degradation of fish remains. Moreover, the compound preservation index—the average of the normalized indices of the anchovy scale integrity index, the ratio anchovy scales to anchovy vertebrae, and the fungi-free area index on anchovy vertebrae—is a good means of detecting differences in fish scale preservation.

Acknowledgments

Literature Cited

Agnihotri, R., M. A. Altabet, T. Herbert, and J. E. Tierney. 2008. Subdecadally resolved paleoceanography of the Peru margin during the last two millennia. Geochemistry, Geophysics, Geosystems 9:1–15.

Atlas, E., and R. M. Pytkowicz. 1977. Solubility behavior of apatites in seawater. Limnology and Oceanography 22:290–300.

Bakun, A., and K. Broad. 2003. Environmental ''loopholes'' and fish population dynamics: comparative pattern recognition with focus on El Niño effects in the Pacific. Fisheries Oceanography 12:458–473.

Barber, R. T., and F. Chavez. 1983. Biological consequences of El Niño. Science 222:1203–1210.

Baumgartner, T., A. Soutar, and V. Ferreira-Bartrina. 1992. Reconstruction of the history of pacific sardine and northern anchovy populations over the past two millennia from sediments of the Santa Barbara basin, California. CalCOFI Report 33:24–40.

Chavez, F., A. Bertrand, R. Guevara-Carrasco, P. Soler, and J. Csirke. 2008. The northern Humboldt Current System: brief history, present status and a view towards the future. Progress in Oceanography 79:95–105.

Checkley, D., J. Alheit, Y. Oozeki, and C. Roy. 2009a. Climate change and small pelagic fish. Cambridge University Press, Cambridge.

Checkley, D., P. Ayon, T. Baumgartner, M. Bernal, J. Coetzee, R. Emmett, R. Guevara-Carrasco, L. Hutchings, L. Ibaibarriaga, H. Nakata, Y. Oozeki, B. Planque, J. Schweigert, Y. Stratoudakis, and C. van der Lingen. 2009b. Habitats. Pp. 12–44 in Checkley et al. 2009a.

DeVries, T., and W. Pearcy. 1982. Fish debris in sediments of the upwelling zone off central Peru: a late Quaternary record. Deep-Sea Research 28:87–109.

Díaz-Ochoa, J. A., C. B. Lange, S. Pantoja, G. J. De Lange, D. Gutierrez, P. Muñoz, and M. Salamanca. 2008. Fish scales in sediments from off Callao, central Peru. Deep-Sea Research Part II 56:1124–1135.

Espinoza, P., and A. Bertrand. 2008. Revisiting Peruvian anchovy (*Engraulis ringens*) trophodynamics provides a new vision of the Humboldt Current system. Progress in Oceanography 79:215–227.

Field, D. B., T. R. Baumgartner, V. Ferreira, D. Gutierrez, H. Lozano-Montes, R. Salvatteci, and A. Soutar. 2009. Variability from scales in marine sediments and other historical records. Pp. 45–63 *in* Checkley et al. 2009a.

Finney, B. P., I. Gregory-Eaves, M. S. V. Douglas, and J. P. Smol. 2002. Fisheries productivity in the northeastern Pacific Ocean over the past 2200 years. Nature 416:729–733.

Finney, B. P., J. Alheit, K. C. Emeis, D. B. Field, D. Gutierrez, and U. Struck. 2010. Paleoecological studies on variability in marine fish populations: a long-term perspective on the impacts of climatic change on marine ecosystems. Journal of Marine Systems 79:316–326.

Glantz, S. A. 2002. Primer of biostatistics. McGraw-Hill, New York.

Gutierrez, D., A. Sifeddine, J. L. Reyss, G. Vargas, F. Velazco, R. Salvatteci, V. Ferreira-Bartrina, L. Ortlieb, D. Field, T. Baumgartner, M. Boussafir, H. Boucher, J. Valdes, L. Marinovic, P. Soler, and P. Tapia. 2006. Anoxic sediments off Central Peru record interannual to multidecadal changes of climate and upwelling ecosystems during the last two centuries. Advances in Geosciences 6:119–125.

Gutierrez, D., A. Sifeddine, D. B. Field, L. Ortlieb, G. Vargas, F. Chavez, F. Velazco, V. Ferreira, P. Tapia, R. Salvatteci, H. Boucher, M. C. Morales, J. Valdes, J. L. Reyss, A. Campusano, M. Boussafir, M. Mandeng-Yogo, M. Garcia, and T. Baumgartner. 2009. Rapid reorganization in ocean biogeochemistry off Peru towards the end of the Little Ice Age. Biogeosciences 6:835–848.

Hamada, M., and A. Mikuni. 1990. X-ray diffraction analysis of sardine scale ash. Nippon Suisan Gakkaishi 56:947–951.

Helly, J., and L. Levin. 2004. Global distribution of naturally occurring marine hypoxia on continental margin. Deep-Sea Research Part I 51:1159–1168.

Hutchinson, J. J., and C. N. Trueman. 2006. Stable isotope analyses of collagen in fish scales: limitations set by scale architecture. Journal of Fish Biology 69:1874–1880.

Jahncke, J., D. M. Checkley, and G. L. Hunt. 2004. Trends in carbon flux to seabirds in the Peruvian upwelling system: effects of wind and fisheries on population regulation. Fisheries Oceanography 13:208–223.

Krissek, L. A., and K. F. Scheidegger. 1983. Environmental controls on sediment texture and composition in low oxygen zones off Peru and Oregon. Pp. 163–180 *in* E. Suess and J. Thiede, eds. Coastal upwelling; its sediment record, Part B. Sedimentary records of ancient coastal upwelling. Plenum, New York.

Lozano-Montes, H. 1997. Reconstruction of marine fish populations using fossil fish scales deposited in Santa Barbara Basin (U.S.A.). M.S. thesis. Centro de Investigación Científica y de Educación Superior de Ensenada, Ensenada, Mexico.

Mendo, J. 1991. Stock identification of Peruvian anchoveta (*Engraulis ringens*): morphometric, tagging/recapture, electrophoretic and ecological studies. Ph.D. thesis. University of Bremen, Germany.

O'Connell, J. M., and V. Tunnicliffe. 2001. The use of sedimentary fish remains for interpretation of long-term fish population fluctuations. Marine Geology 174:177–195.

Ohwada, K., N. Tanaka, and M. Sugiyama. 1983. Penetration of microorganisms into deposited fish scales in the sediment of a coastal finfish culture grounds. Bulletin of the Japanese Society of Scientific Fisheries 49:657.

Reinhardt, L., K. H.-R., A. Lückge, M. Wiedicke, J. Wunderlich, and G. Wendt. 2002. High-resolution sediment echosounding off Peru: late Quaternary depositional sequences and sedimentary structures of a current-dominated shelf. Marine Geophysical Researches 23:335–351.

Salvatteci, R. 2008. Preservation and abundance of fish debris in the oxygen minimum zone off Pisco, Peru in the last 400 years. M.S. thesis. Centro de Investigación y de Educación Superior de Ensenada, Ensenada, Mexico.

Sánchez, G., R. Calienes, and S. Zuta. 2000. The 1997–1998 El Niño and its effects on the coastal marine ecosystem off Peru. CalCOFI Report 41:62–86.

Schenau, S. J., and G. J. De Lange. 2000. A novel chemical method to quantify fish debris in marine sediments. Limnology and Oceanography 45:963–971.

Schwartzlose, R. A., J. Alheit, A. Bakun, T. R. Baumgartner, R. Cloete, R. J. M. Crawford, W. J. Fletcher, Y. Green-Ruiz, E. Hagen, T. Kawasaki, D. Lluch-Belda, S. E. Lluch-Cota, A. D. MacCall, Y. Matsuura, M. O. Nevarez-Martinez, R. H. Parrish, C. Roy, R. Serra, K. V. Shust, M. N. Ward, and J. Z. Zuzunia. 1999. Worldwide large-scale fluctuations of sardine and anchovy populations. South African Journal of Marine Science 21:289–347.

Shackleton, L. Y. 1988. Scale shedding: an important factor in fossil fish studies. ICES Journal of Marine Science 44:259–263.

Shackleton, L. Y., and R. F. Johnson. 1988. Identification of and distinction between the scales of South African pilchard *Sardinops ocellatus* and Cape anchovy *Engraulis capensis*. South African Journal of Marine Science 6:207–216.

Sifeddine, A., D. Gutierrez, L. Ortlieb, H. Boucher, F. Velazco, D. Field, G. Vargas, M. Boussafir, R. Salvatteci, V. Ferreira, M. García, J. Valdes, S. Caquineau, M. Mandeng-Yogo, F. Cetin, J. Solis, P. Soler, and T. Baumgartner. 2008. Laminated sediments from the central Peruvian continental slope: a 500 year record of upwelling system productivity, terrestrial runoff and redox conditions. Progress in Oceanography 79:190–197.

Simon, A., M. Poulicek, B. Velimirov, and F. T. Mackenzie. 1994. Comparison of anaerobic and aerobic biodegradation of mineralized skeletal structures in marine and estuarine conditions. Biogeochemistry 25:167–195.

Soutar, A., and J. Isaacs. 1974. Abundance of pelagic fish during the 19th and 20th century as recorded in anaerobic sediment off the Californias. Fisheries Bulletin 72:257–273.

StatSoft, Inc. 2005. STATISTICA (data analysis software system), Version 7.1. www.statsoft.com.

Suess, E., R. Von Huene, K. Emeis, J. Bourgois, et al. 1990. Proceedings of the Ocean Drilling Program. Scientific Results 112:738.

Swartzman, G., A. Bertrand, M. Gutiérrez, S. Bertrand, and L. Vasquez. 2008. The relationship of anchovy and sardine to water masses in the Peruvian Humboldt Current System from 1983 to 2005. Progress in Oceanography 79:228–237.

Valdes, J., L. Ortlieb, D. Gutierrez, L. Marinovic, G. Vargas, and A. Sifeddine. 2008. 250 years of sardine and anchovy scale deposition record in Mejillones Bay, northern Chile. Progress in Oceanography 79:198–207.

Varma, K. B. R. 1990. Morphology and dielectric properties of fish scales. Current Science 59:420–422.

Wright, C. A., A. Dallimore, R. E. Thomson, R. T. Patterson, and D. M. Ware. 2005. Late Holocene paleofish populations in Effingham Inlet, British Columbia, Canada. Paleogeography, Paleoclimatology, Palaeoecology 224:367–384.